

Coupling of Computational Fluid Dynamics and Population Balance Modelling for Liquid-Liquid Extraction

vom Fachbereich Maschinenbau und Verfahrenstechnik der
Technischen Universität Kaiserslautern zur Verleihung des
akademischen Grades

Doktor-Ingenieur (Dr.-Ing.)

genehmigte Dissertation

von

Herrn

Dipl.-Ing. Christian Drumm

aus Frohnhofen

Tag der mündlichen Prüfung : 21. Mai 2010

Dekan: Prof. Dr.-Ing. S. Ripperger

Prüfungskommission:

Prüfungsvorsitzender: Prof. Dr.-Ing. M. Böhle

1. Berichterstatter: Prof. Dipl.-Ing. Dr. techn. H.-J. Bart

2. Berichterstatter: Prof. Dr.-Ing. M. Kraume

PREFACE

The research work of this thesis was carried out at the Technical University Kaiserslautern, in the Department of Separation Science and Technology, during the years 2005-2009. Parts of the thesis were done in close cooperation with the Fraunhofer ITWM in Kaiserslautern, the Technomathematics Group of the University Kaiserslautern and the Al Balqa Applied University in Amman, Jordan.

I would like to thank Prof. Hans-Jörg Bart for the opportunity of studying this interesting and challenging research work and for supervising this thesis. I am also truly grateful to Professor Matthias Kraume and Professor Martin Böhle for being members of my PhD commission.

I would also like to thank my colleagues and co-authors Prof. Menwer Attarakih, Mark Hlawitschka, Dr. Jörg Kuhnert, Vikash Sharma and Dr. Sudarshan Tiwari for their cooperation, ideas and contribution on this project. Furthermore, I wish to thank my colleagues and the staff of the department of Separation Science and Technology for pleasant working atmosphere.

Finally, the warmest thanks to my wife and parents for their patience, trust and support. Special thanks to my little baby for her smile of happiness and love.

This work was financially supported by the Deutsche Forschungsgemeinschaft (DFG).

Kaiserslautern, May 2010

Christian Drumm

ABSTRACT

The aim of this thesis was to link Computational Fluid Dynamics (CFD) and Population Balance Modelling (PBM) to gain a combined model for the prediction of counter-current liquid-liquid extraction columns. Parts of the doctoral thesis project were done in close cooperation with the Fraunhofer ITWM. Their in-house CFD code Finite Pointset Method (FPM) was further developed for two-phase simulations and used for the CFD-PBM coupling. The coupling and all simulations were also carried out in the commercial CFD code Fluent in parallel. For the solution methods of the PBM there was a close cooperation with Prof. Attarakih from the Al-Balqa Applied University in Amman, Jordan, who developed a new adaptive method, the Sectional Quadrature Method of Moments (SQMOM).

At the beginning of the project, there was a lack of two-phase liquid-liquid CFD simulations and their experimental validation in literature. Therefore, stand-alone CFD simulations without PBM were carried out both in FPM and Fluent to test the predictivity of CFD for stirred liquid-liquid extraction columns. The simulations were validated by Particle Image Velocimetry (PIV) measurements. The two-phase PIV measurements were possible when using an iso-optical system, where the refractive indices of both liquid phases are identical. These investigations were done in segments of two Rotating Disc Contactors with 150mm and 450mm diameter to validate CFD at lab and at industrial scale. CFD results of the aqueous phase velocities, hold-up, droplet raising velocities and turbulent energy dissipation were compared to experimental data. The results show that CFD can predict most phenomena and there was an overall good agreement.

In the next steps, different solution methods for the PBM, e.g. the SQMOM and the Quadrature Method of Moments (QMOM) were implemented, varied and tested in Fluent and FPM in a two-fluid model. In addition, different closures for coalescence and breakage were implemented to predict drop size distributions and Sauter mean diameters in the RDC DN150 column. These results show that a prediction of the droplet size distribution is possible, even when no adjustable parameters are used. A combined multi-fluid CFD-PBM model was developed by means of the SQMOM to overcome drawbacks of the two-fluid approach. Benefits of the multi-fluid approach could be shown, but the high computational load was also visible. Therefore, finally, the One Primary One Secondary Particle Method (OPOSPM), which is a very easy and efficient special case of the SQMOM, was introduced in CFD to simulate a full pilot plant column of the RDC DN150. The OPOSPM offers the possibility of a one equation model for the solution of the PBM in CFD. The predicted results for the mean droplet diameter and the dispersed phase hold up agree well with literature data. The results also show that the new CFD-PBM model is very efficient from computational point of view (two times less than the QMOM and five times less than the method of classes).

The overall results give rise to the expectation that the coupled CFD-PBM model will lead to a better, faster and more cost-efficient layout of counter-current extraction columns in future.

ZUSAMMENFASSUNG

Ziel der Arbeit war die Verknüpfung von Computational Fluid Dynamics (CFD) und des Populationsbilanzmodells (PBM), um mit diesem kombinierten Werkzeug die Simulation von gerührten Gegenstromextraktionskolonnen weiterzuentwickeln und zu verbessern. Die Simulation von Gegenstromextraktionskolonnen basiert zurzeit auf einfachen Methoden wie dem Dispersionsmodell, bei dem ein Parameter, der Dispersionskoeffizient, die gesamten Strömungsnichtidealitäten subsummiert. Mit der Tropfenpopulationsbilanzmodellierung (TPBM) werden Koaleszenz und Zerfall der Tropfen berücksichtigt, wodurch eine höhere Güte der Beschreibung erreicht wird. Die Nichtidealitäten der Strömung werden in reinen Tropfenpopulationsbilanzmodellen jedoch weiterhin durch einfache Modelle wie dem Dispersionsmodell beschrieben und es werden homogene Bedingungen in einem Extraktionskompartiment vorausgesetzt. Im Gegensatz dazu können mit Hilfe von CFD turbulente Strömungen lokal aufgelöst werden, wodurch eine Verknüpfung von CFD und PBM die genannten Vereinfachungen beseitigen und zu einer verbesserten Auslegung und Vorhersage von Extraktionskolonnen führen kann. In einem gekoppelten Modell liefert CFD die turbulenten Strömungsinformationen und PBM detaillierte Informationen zum Tropfenschwarm, wobei beide Methoden durch diese Kopplung voneinander profitieren.

Teile der Arbeit entstanden in Kooperationen mit dem Fraunhofer ITWM in Kaiserslautern und dem Lehrstuhl für Technomathematik an der TU Kaiserslautern. Im Rahmen der Kooperation mit dem ITWM wurde die Finite Pointset Methode (FPM) als CFD Code für die Kopplung verwendet. Parallel dazu wurde die Kopplung auch eigenständig mit dem kommerziellen CFD Code Fluent durchgeführt.

Zunächst wurde die Leistungsfähigkeit der CFD-Methoden für die Simulation von Gegenstromextraktionskolonnen untersucht und eine Grundlage für die spätere Verknüpfung zwischen CFD und PBM geschaffen. Speziell zweiphasige Simulationen gerührter Gegenstromextraktionskolonnen waren in der Literatur kaum vorhanden. Die wenigen Veröffentlichungen zu diesem Thema zeigen keinen Vergleich mit experimentellen Ergebnissen oder haben Konvergenzprobleme. Die Ein- und Zweiphasenströmung in einer RDC (rotating disc contactor) Extraktionskolonne (150 mm) wurde daher sowohl mit FPM als auch mit dem kommerziellen CFD Code Fluent simuliert. Zur Validierung der CFD Simulationen wurden experimentelle Particle Image Velocimetry (PIV) Messungen durchgeführt, wobei im zweiphasigen Betrieb ein isooptisches Stoffsystem (Glycerin/Wasser-Heptan) verwendet wurde. Es zeigte sich, dass die durchgeführten CFD Simulationen die Strömung der wässrigen Phase und den Hold-up in einer Extraktionskolonne, bei richtiger Wahl des Turbulenzmodelles und der Randbedingungen, gut wiedergeben. Die gitterfreie Methode FPM lieferte hierbei ähnlich gute Ergebnisse wie der kommerzielle Code und muss den Vergleich nicht scheuen. Auf dieser Basis wurde die weitere Verknüpfung zwischen CFD und PBM aufgebaut.

Um die Vorhersagbarkeit von CFD auch für den industriellen Maßstab zu testen, wurden die CFD Simulationen und PIV Messungen auch an einem Segment einer RDC Kolonne, im industriellen Maßstab, mit 450 mm Durchmesser durchgeführt. Die Ergebnisse zeigen, dass CFD auch in dieser Größenordnung brauchbare Vorhersagen liefert, wobei die

Vorhersagegenauigkeit im Vergleich zur kleinen Geometrie im zweiphasigen Betrieb etwas abnimmt. Zusätzlich wurde in der großen Kolonne auch die turbulente Energiedissipation aus den PIV Messungen berechnet und mit der Simulation verglichen. Diese ist eine wichtige Größe bei der Modellierung von Koaleszenz- und Zerfallsvorgängen in den gekoppelten CFD-PBM Modellen. Gerade das Experiment gestaltet sich hier schwierig, da man eine Auflösung hinunter bis zu den kleinsten turbulenten Skalen kaum realisieren kann und die Ergebnisse mit Hilfe von Turbulenzspektren skalieren muss. Es ergab sich hier im einphasigen Fall eine gute Übereinstimmung mit den CFD Simulationen. Bei der zweiphasigen Betriebsweise steigt die mit CFD vorhergesagte Energiedissipation am Rührer um etwa das doppelte an. Dieser Anstieg im Bereich des Rührers scheint zu stark zu sein, da hier der Hauptenergieeintrag vom Rührer kommt und nicht von der dispersen Tropfenphase. Diese Simulationen konnten nicht mit Hilfe von Messungen validiert werden, da im zweiphasigen Betrieb keine ausreichende Auflösung in den PIV Messungen erreicht werden konnte.

Im Rahmen der Verknüpfung von CFD und des TPBM wurden verschiedene Lösungsmethoden in CFD implementiert und getestet. Bei der Verknüpfung zwischen CFD und PBM gibt es grundsätzlich mehrere Möglichkeiten, ein Zwei-Fluid oder Multi-Fluid Modell für die Kopplung und man kann aus einer Reihe verschiedener Lösungsmethoden wie z.B. der Klassenmethode (CM) (Kumar & Ramkrishna, 1996a) und der Quadrature Method of Moments (QMOM) (Marchisio et al., 2003a) wählen. Auf dem Gebiet der Lösungsmethoden erfolgte eine enge Kooperation mit Prof. Attarakih von der Al Balqa Applied University in Amman, Jordanien. Im Rahmen dieser Kooperation wurde von Prof. Attarakih eine neue Lösungsmethode der PBM entwickelt, die Sectional Quadrature Method of Moment (SQMOM) (Attarakih et al., 2009a). Diese Methode stellt eine adaptive Methode dar, die die Vorteile der Klassen- und Momentenmethode vereint und sich der Nachteile entledigt, wobei die klassischen Lösungsmethoden (CM, QMOM) als Spezialfälle der SQMOM betrachtet werden können.

Die SQMOM wurde in ein Zwei-Fluid Modell in FPM programmiert und 2D und 3D Testsimulationen für eine Sektion mit 5 Kompartments eines RDC Extraktors mit konstanten Zerfalls- und Koaleszenzkernen durchgeführt. In der 2D Geometrie wurden hierbei die Parameter angepasst, um die Tropfengröße am Ausgang beschreiben zu können. Mit den gleichen Parametern wurde im Anschluss die Tropfengröße in der 3D Geometrie erfolgreich vorhergesagt. Des Weiteren wurde in FPM die Anzahl der primären Partikel in der SQMOM variiert, um die Einflüsse darzustellen.

In Fluent wurden verschiedene Modelle für Zerfall und Koaleszenz (Luo & Svendsen, 1996; Coualaloglou & Tavlarides, 1977; Martínez-Bazán et al., 1999; Prince and Blanch, 1990) als user defined functions eingebunden und getestet, unter Variation der CM und der QMOM. Hierbei zeigte sich, dass für eine Vorhersage der Tropfengrößenverteilung in einer 5 Kompartments Sektion der RDC Kolonne im Normalfall anpassbare Parameter in den Modellen nötig sind. Mit Hilfe eines modifizierten Modells und eines gemischten Modells war aber auch eine Vorhersage ohne anpassbare Parameter möglich. Die Abweichung bei der Vorhersage des Sauter Durchmessers war hierbei <30% für die Stoffsysteme Toluol/Wasser und Butylacetat/Wasser bei unterschiedlichen Rührerumdrehungen. Die Literaturmodelle für Zerfall und Koaleszenz wurden diskutiert und mögliche Verbesserungsvorschläge gemacht.

Vor- und Nachteile der Klassen- und Momentenmethoden und die Einflüsse der Klassen- und Momentenanzahl konnten gezeigt werden. Darüber hinaus war es möglich aus den Momenten eine idealisierte Verteilung zu rekonstruieren.

Auch wenn die in CFD vorhergesagten Tropfenanstiegsgeschwindigkeiten eine gute Übereinstimmung mit experimentellen Daten lieferten, zeigte der Vergleich die Schwächen des Zwei-Fluid Modells: tropfengrößenabhängige Aufstiegsgeschwindigkeiten können nicht beschrieben werden, da sich die ganze Verteilung im gleichen Geschwindigkeitsfeld, basierend auf dem Sauter Durchmesser (d_{32}) bewegt. Daher wurde mit Hilfe der SQMOM in Fluent ein Multi-Fluid CFD Modell realisiert und getestet. Die Ergebnisse konnten die Vorzüge eines Multi-Fluid Modells zeigen. Des Weiteren wurde aber auch deutlich, dass diese Modelle einen sehr hohen Rechenaufwand mit sich bringen und für die Kolonnenauslegung momentan noch nicht geeignet sind.

Da der allgemeine Rechenaufwand in den gekoppelten Simulationen sehr hoch ist, wurde zum Abschluss der entgegengesetzte Weg gegangen und anstatt immer genauerer und aufwändigerer Modelle (wie z.B. SQMOM) ein vereinfachtes Eingleichungsmodell zur Lösung der Populationsbilanzen realisiert. Die One Primary One Secondary Particle Method (OPOSPM) (Attarakih et al., 2009b), die einen einfachen Spezialfall der SQMOM darstellt, wurde in einem Eingleichungs-Populationsbilanzmodell in CFD verwendet. Mit dieser einfachen Methode war es möglich eine ganze Pilotkolonne des RDC mit 50 Kompartments zu simulieren. Es wurde das in der 5 Kompartments Sektion modifizierte Modell von Luo und Svendsen (1996) ohne weitere anpassbare Parameter verwendet. Hierbei konnte der Durchmesser am oberen Ende der Kolonne für unterschiedliche Rührerumdrehungen mit einem Fehler von $<20\%$ vorhergesagt werden. Die Rechenzeit war dabei im Vergleich zur effizienten QMOM um mehr als die Hälfte reduziert.

Das Ziel der gekoppelten CFD-PBM Modelle ist eine geometrieunabhängige Simulation von Extraktionskolonnen, die z.Z. nicht gegeben ist und für die technische Maßstabsvergrößerung von großer wirtschaftlicher Bedeutung ist. Gekoppelte CFD-PBM Simulationen werden in der Literatur erst seit dem Jahre 2000 untersucht. Bis das Ziel einer vollständigen Simulation von Apparaten mit hoher Vorhersagegenauigkeit mit einem solchen Modell möglich ist, müssen noch eine Reihe weiterer Forschungen und Untersuchungen durchgeführt werden. Die Ergebnisse dieser Arbeit und der bisher in der Literatur veröffentlichten Arbeiten zeigen jedoch, dass der Ansatz vielversprechend ist und in Zukunft eine schnellere, einfachere und kostengünstigere Auslegung von Apparaten möglich sein wird. Die vorliegende Arbeit hat ihr Ziel erreicht, beide Methoden zu koppeln, wobei verschiedene Möglichkeiten vorgestellt wurden. Auch im Bereich der Vorhersagbarkeit der Fluidynamik und der Vorhersage der Tropfengröße konnten gute Ergebnisse und Fortschritte erzielt werden. Die Arbeit hat einen entscheidenden Beitrag geleistet und einen Grundstein gelegt für die zukünftige Modellierung und Auslegung von Extraktionskolonnen, oder auch anderen mehrphasig betriebenen Apparaten.

LIST OF PUBLICATIONS

This thesis is based on the following publications, which are reprinted in the appendix and which are referred to in the text by their roman numerals. The order is chronological. The complete list of publications can be found in the references section.

- [I] Drumm, C., Bart, H.-J. (2006). Hydrodynamics in a RDC Extractor: Single and Two-Phase PIV Measurements and CFD Simulations, *Chemical Engineering Technology*, 29, 1297.
- [II] Drumm, C., Bart, H.-J. (2007). Coupling of CFD with DPBM: Drop Size Distributions and Flow Fields in a RDC Extractor, *Proc. International Conference on Multiphase Flow ICMF 2007*, M. Sommerfeld (Ed.), Leipzig.
- [III] Drumm, C., Attarakih, M.M., Tiwari, S., Kuhnert, J., Bart, H.-J. (2008). Implementation of the Sectional Quadrature Method of Moments in a CFD code, *Proc. 6th International Conference on Computational Fluid Dynamics in the Oil & Gas, Metallurgical and Process Industries CFD 2008*, Johansen, S.T., Olsen, J.E., Ashrafiyan, A. (Eds.), Trondheim, Norway.
- [IV] Attarakih, M. M., Zeidan, D., Drumm, C., Tiwari, S., Kuhnert, J., Allaboun, H., Bart, H.-J. (2008). Dynamic Modelling of Liquid Extraction Columns using the Direct Primary and Secondary Particle Method (DPSPM), *Proc. 6th International Conference on Computational Fluid Dynamics in the Oil & Gas, Metallurgical and Process Industries CFD 2008*, Johansen, S.T., Olsen, J.E., Ashrafiyan, A. (Eds.), Trondheim, Norway.
- [V] Tiwari, S., Drumm, C., Sharma, V.K., Kuhnert, J., Attarakih, M.M., Klar, A. and Bart, H.-J. (2008). A Meshfree CFD-Population Balance Equation Coupled Model, *Proc. 6th International Conference on Computational Fluid Dynamics in the Oil & Gas, Metallurgical and Process Industries CFD 2008*, Johansen, S.T., Olsen, J.E., Ashrafiyan, A. (Eds.), Trondheim, Norway.
- [VI] Drumm, C., Tiwari, S., Attarakih, M.M., Kuhnert, J., Bart, H.-J. (2008). CFD-PBM coupled model using the Finite Pointset Method and the SQMOM, *Proc. International Solvent Extraction Conference ISEC 2008*, Moyer, B. (Ed.), Canadian Institute of Mining, Metallurgy and Petroleum, Montreal, Vol. 2, 1177-1182.
- [VII] Drumm, C., Tiwari, S., Kuhnert, J., Bart, H.-J. (2008). Finite Pointset Method for Simulation of the Liquid-Liquid Flow Field in an Extractor, *Computers & Chemical Engineering*, 32, 2946.
- [VIII] Tiwari, S., Drumm, C., Kuhnert, J., Bart, H.-J. (2008). Coupling of the CFD and the Droplet Population Balance Equation with Finite Pointset Method, *Lecture Notes in Computational Science and Engineering: Meshfree Methods for Partial Differential Equations IV*, M. Griebel; M.A. Schweitzer (Eds.), Vol. 65, Springer., 315-344.

- [IX] Drumm, C., Attarakih, M.M., Bart, H.-J. (2009). Coupling of CFD with DPBM for a RDC Extractor, *Chemical Engineering Science*, 64, 721.
- [X] Attarakih, M.M., Drumm, C., Bart, H.-J. (2009). Solution of the Population Balance equation using the Sectional Quadrature Method of Moments, *Chemical Engineering Science*, 64, 742.
- [XI] Drumm, C., Hlawitschka M., Bart, H.-J. (2010). CFD Simulations and Particle Image Velocimetry Measurements in an Industrial Scale Rotating Disc Contactor, *AIChE Journal*, doi:10.1002/aic.12249, *in press*.
- [XII] Drumm, C., Attarakih, M.M., Hlawitschka M., Bart, H.-J. (2010). One-Group Reduced Population Balance Model for CFD Simulation of a Pilot-Plant Extraction Column, *Industrial and Engineering Chemistry Research*, 49, 3442.
- [XIII] Attarakih, M.M., Jaradat. M., Drumm, C., Bart, H.-J., Tiwari, S., Sharma, V.K., Kuhnert, J., Klar, A. (2009). Solution of the Population Balance Equation using the One Primary and One Secondary Particle Method (OPOSPM). *Proc. ESCAPE 19*, Jezowski J., Thullie, J. (Eds.), Cracow, Poland.

TABLE OF CONTENTS

1	Introduction	3
1.1	Scope of this work	4
2	CFD Simulations: motivation and theory.....	6
2.1	Introduction.....	6
2.2	Two-phase flow modelling	7
2.2.1	Euler-Euler & Euler-Lagrange	7
2.2.2	Governing equations.....	7
2.2.3	Two-fluid & multi-fluid models	8
2.3	Finite Pointset Method (FPM)	9
3	Particle Image Velocimetry & experimental setup	10
3.1	Introduction / PIV in liquid-liquid extraction	10
3.2	Investigated Rotating Disc Contactors.....	10
3.3	PIV setup and analysis	11
3.4	Single- and two-phase PIV	11
3.5	Turbulent energy dissipation from PIV analysis	12
4	Results of the CFD simulations and the PIV measurements.....	14
4.1	Introduction.....	14
4.1.1	PIV results (RDC DN150).....	14
4.1.2	Fluent results (RDC DN150).....	14
4.1.3	FPM results.....	16
4.1.4	RDC DN450 - flow fields.....	16
4.1.5	Turbulent energy dissipation	17
5	Droplet Population Balance Modelling.....	19
5.1	Introduction / DPBM in liquid-liquid extraction	19
5.2	Population balance equation	19
5.3	Closure models for coalescence & breakage	20
5.4	Solution methods of the PBM.....	21
5.4.1	Classes Method.....	22
5.4.2	Quadrature Method of Moments	22
5.4.3	Sectional Quadrature Method of Moments	23
5.4.4	The One Primary and One Secondary Particle Methods (OPSPM).....	24
6	Coupled CFD-PBM model: theory and implementation.....	25

6.1	Introduction / state-of-the-art	25
6.2	Implementation of the PBM in CFD.....	27
6.2.1	Fluent population balance add-on.....	27
6.2.2	Implementation of the SQMOM in Fluent	27
6.2.3	Implementation of the OPOSPM in Fluent	28
7	Coupled CFD-PBM: results	29
7.1	Fluent population balance add-on.....	29
7.2	PBM in FPM.....	31
7.3	SQMOM in a multi-fluid model	31
7.4	OPOSPM in Fluent	32
8	Summary & outlook	35
9	Symbols.....	37
10	References	38
	Own publications.....	47
	Lectures	48
	Supervised diploma thesis	50
	Appendix	51
	Figures	
	Publications	

1 Introduction

Liquid-Liquid extraction, also called solvent extraction, is a separation process, which is based on the different distribution of the separable components between two liquid phases. The process is used primarily when distillation is impractical or too costly to use. Liquid-liquid extraction involves contacting the feed stream (raffinate stream) with an immiscible liquid solvent in which one or more of the feed stream components is soluble. The component or components that are absorbed by this solvent are called the solute (Erwin, 2004). It may be more practical than distillation when the relative volatility for two components falls between 1.0 and 1.2 (Robbins & Cusack, 1997) or if they are thermal instable. This unit operation is widely applicable in chemical, biochemical industries, pharmacy and hydrometallurgy.

The modelling of extraction columns still demands improvement. The layout of an extractor is mainly based on manufacturer's knowledge and simplified stage-wise models, e.g. the HTU-NTU concept. Flow models such as the dispersion or backmixing model, describe the non-ideal flow, where one parameter accounts for all deviations from the ideal plug flow behaviour (Thornton, 1992). These models are too simple to describe the real hydrodynamics, where one of the liquid phases is normally dispersed as droplets in the second continuous phase (Bart & Stevens, 2004). Therefore, the influences of droplet movement, droplet interaction (breakage and coalescence), energy input (stirrer, pulsation) and mass transfer cannot be described satisfactorily. Due to the complex nature of the dispersed phase behaviour there is a discrepancy between theoretical and actual performance. That is why the design of extraction columns requires pilot plant experiments. Besides the selection of the solvent and the thermodynamic data, pilot plant experiments are a time and money consuming factor during the layout process. Apparatus scale-up from lab scale to industrial scale carries risk and needs experience. Further information about the basic principles of liquid-liquid extraction and column layout could be found in literature (e.g. Bart, 2001; Deibele & Dohrn, 2006; Goedecke, 2006; Godfrey & Slater, 1994; Mohanty, 2000; Rydberg et al., 1992; Sattler, 1988; Thornton, 1992).

In contrary, there is an ongoing claim by the industry for more straightforward, faster and money saving simulation methods. A process and apparatus layout with low expenditure of work, time and money is required. The development of new layout processes and methods that meet these requirements is one of the most important tasks of modern engineering science (Modes, 2000). New design methods that meet these requirements also with potential to improve column modelling are Population Balance Modelling (PBM) and Computational Fluid Dynamics (CFD). The use of CFD software in many materials processing industries has grown tremendously in recent years. CFD has been widely utilized for conducting virtual experiments, prototype testing, and parametric studies. Analysis using CFD complements and reduces physical testing, and it can result in a significant time and cost savings (Mukhopadhyay et al., 2004). CFD can predict fluid dynamics and turbulence and gives a fully resolved local resolution of the flow in an apparatus. PBM with its origin in crystallization (Hulburt & Katz, 1964) can specify droplet movement, coalescence, breakage and drop size distribution of the dispersed phase and considers the particulate behaviour in an extraction column. The population balance framework has found its way in numerous

scientific and engineering disciplines such as mining, water and wastewater treatment, nanoparticle generation, fermentation, crystallization (Nopens et al., 2009) and of course dispersed phase size distribution in multiphase flows. In a 2005 DECHEMA Colloquium "From Single Droplet to Extraction Column – Requirements and New Development" the scale-up from a mini plant to a pilot plant column could be successfully obtained from single droplet experiments when PBM was applied. There was also a further demand from industry in regard to process intensification with the idea to link PBM and CFD for high precision engineering and a direct modelling of industrial scale column design (Bart et al., 2006; Bart et al., 2008; Bart et al., 2009; Pfennig et al., 2006; Schmidt, 2006).

Both methods are subject to restrictions when they are applied independently. PBM needs information of the fluid dynamics such as drop velocity and turbulence (energy input), which are normally incorporated by simplified correlations in stand-alone PBM codes (e.g. LLECMOD, Attarakih et al., 2006a). In two-phase CFD simulations, generally a two-fluid model is applied, whereas a constant Sauter mean diameter represents the different sizes of the particles in the dispersed phase. If the particle size distribution is very wide or multimodal this approach is more likely to fail. Aggregation or breakage of particles and a change in the particle size distribution are not considered.

1.1 Scope of this work

The aim of this thesis was to link CFD and PBM to gain a combined model for the prediction of counter-current liquid-liquid extraction columns. The coupling of CFD and PBM can eliminate above mentioned shortcomings of stand-alone models. CFD can predict the hydrodynamics and turbulence and give a fully resolved local resolution of the two-phase flow in all three external coordinates, while the PBM can account for the droplet coalescence and breakup and predict the size distribution of the dispersed phase. Both methods can benefit from each other due to the coupling. In their preface of the 3rd Population Balance Conference in Quebec 2007 the scientific committee stated that Computational fluid dynamics/discrete element methods (CFD-DEM) has become an integral part of analyzing fluid systems that include population balances. In that respect, further development of more efficient solution methods continues to receive great attention (Nopens et al., 2009).

Parts of the doctoral thesis project were done in close cooperation with the Fraunhofer ITWM (Institut für Techno- und Wirtschaftsmathematik). Their in-house CFD code Finite Pointset Method (FPM) was further developed for two-phase simulations and used for the CFD-PBM coupling. The coupling and all simulations were also carried out in the commercial CFD code Fluent in parallel. For the solution methods of the PBM there was a close cooperation with Prof. Attarakih from the Al-Balqa Applied University in Amman, Jordan.

At the beginning of the project, there was a lack of two-phase liquid-liquid CFD simulations and their experimental validation in literature. Therefore, stand-alone CFD simulations without PBM were carried out both in FPM and Fluent to test the predictivity of CFD for stirred liquid-liquid extraction columns. These simulations were validated by means of Particle Image Velocimetry measurements in the papers [I], [VII] and [XI]. In the next step, PBM were incorporated in CFD using classical solution methods of the PBM such as the

classes method (CM) (Kumar & Ramkrishna, 1996a) and the Quadrature Method of Moments (QMOM)(Marchisio et al., 2003a) and different models for coalescence and breakage were varied and tested. The coupled CFD-PBM models were applied to predict drop size distributions in small column sections ([II], [V], [VI], [IX]). New solution methods, the Sectional Quadrature Method of Moments (SQMOM) and its special cases as the One Primary One Secondary Particle Method (OPOSPM) were developed by Prof. Menwer Attarakih at the Al-Balqa Applied University as part of the cooperation [IV], [X], [XIII]. These methods were incorporated in CFD [III], [V], [VI], [VIII], [XII] to realize a multi-fluid model [III] and a one equation model of the PBM in CFD [XII]. The latter was applied to simulate a whole pilot plant column without simplifications [XII]. The basis of the present investigations was a Rotating Disc Contactor type extraction column, which is very easy to implement in CFD because of its rotational symmetry.

The structure of the work is as follows: In each main chapter a short introduction and a literature survey on the topic are given. For the details of theory and results it will be pointed to the relevant publications in the appendix. The computational model (single- and two-phase flow) and the Finite Pointset Method (FPM) are introduced in chapter 2. Principles of Particle Image Velocimetry (PIV), the experimental setup and the data analysis are given in chapter 3. Results of the single- and two-phase flow stand-alone CFD simulations and their validation with PIV are presented in chapter 4. In the next chapter, the evolution of the PBM from the past using stand-alone PBM codes to the present is summarized as well as different solution methods of the PBM, which are suitable for the coupling with CFD. New solution methods as the SQMOM and the OPOSPM, are also described. Chapter 6 finally deals with the implementation of PBM in CFD and chapter 7 shows results of these simulations. Conclusions are given in chapter 8.

2 CFD Simulations: motivation and theory

2.1 Introduction

Although CFD simulations have been used with great success in chemical engineering applications in recent years, there was a lack of two-phase CFD simulations for stirred liquid-liquid extraction columns in literature at the beginning of this project in the year 2005. Only a few working groups focused on the CFD simulations of the hydrodynamics in counter-current stirred liquid-liquid extraction columns in the past. The majority of these groups considered only single-phase flow in the column (Modes & Bart, 2001; Fei et al., 2000; Haderer, 2004). Fei et al. (2000) and Haderer et al. (2005) conducted Laser Doppler Anemometry measurements for validation at discrete points but could not provide velocity fields over the whole compartment. Modes & Bart (2001) and recently Gurker et al. (2008) simulated the single-phase flow in an RDC and compared the residence time distribution to experiments. Kolb (2004) and Kolb et al. (2002) used the commercial code Fluent in order to evaluate residence time distribution, energy input and impeller discharge rates for a Kühni column geometry. Different single-phase turbulence models were tested and adjusted by You & Bart (2003). Several attempts were made to use CFD for a better understanding of the two-phase flow in countercurrent extraction columns. Weiss & Bart (1993) used the CFD code FIRE to simulate a segment of an RDC column. Rieger et al. (1996) employed the Euler-Euler model to predict the two-phase flow patterns at low hold-up in a DN 150 RDC. The predicted velocities could be confirmed by LDA-measurements at several points. Two-phase flow fields were also simulated and investigated by You & Xiao (2005) and Vikhansky & Kraft (2004). Researchers also reported convergence problems in two-phase simulations (Rieger et al., 1996; Haderer, 2004). Ghaniyari-Benis et al. (2009) recently simulated an RDC using the Euler-Euler approach. Newer work also dealt with liquid-liquid problems in pulsed extraction columns (Bujalski et al., 2006; Retieb et al., 2007). Bujalski et al. (2006) investigated a single water phase and compared the results to experimental PIV measurements. Retieb et al. (2007) compared the simulated hold-up within two-phase countercurrent pulsed columns. A literature survey is also given in [I],[VII] and [XI].

Recapitulatory, either only single-phase flow was investigated and/or a validation and comparison to experimental data of the complete flow field were not given. Consequently, there was need to establish two-phase liquid-liquid simulations and to validate and compare the simulations to experimental data. A coupled CFD-PBM model would be useless if the predictions of the fluid dynamics are not reliable. Therefore, the single and two-phase flow field of a RDC (rotating disc contactor) extraction column was simulated by means of Computational Fluid Dynamics (CFD). The simulations were validated by Particle Image Velocimetry (PIV) measurements ([I], [VII], [XI]). Both the commercial CFD code Fluent and the Fraunhofer Finite Pointset Method were applied.

The theory of the computational model and the governing equations both in FPM and Fluent are shortly described in this chapter and references to the papers in the appendix are given. Results are shown in chapter 4. This chapter is structured as follows: The

computational model (two-phase flow and governing equations) is described first. The Finite Pointset Method (FPM) is introduced in chapter 2.3.

2.2 Two-phase flow modelling

2.2.1 Euler-Euler & Euler-Lagrange

For the modelling of two-phase flows one may choose to treat both the dispersed and continuous phase as interpenetrating pseudo-continua as in the Euler-Euler approach or the dispersed phase as discrete entities as in the Euler-Lagrange approach. The Eulerian model is appropriate to cases where the volume fraction of the dispersed phase is high and varies widely, which is actually the situation in an extractor (Kankaanpää, 2007). Over the last years the Euler-Euler approach emerged as the standard approach to model multiphase problems at higher hold-up. For the two-phase flow Haderer (2005) argues that the Euler-Euler model is the only applicable multiphase model for the simulation of counter-current extraction columns. While Eulerian two-phase CFD simulations of liquid-liquid systems are hardly found (Ghaniyari-Benis et al., 2009; Retieb et al., 2007; Rieger et al. 1996), CFD simulations of gas-liquid dynamics in bubble columns (Pfleger & Becker, 2001; Sanyal et al., 1999; Santos et al., 2007; Zhang et al., 2006) and stirred tanks (Gosman et al., 1992; Lane et al., 2005; Scargiali et al., 2007) are widely applied.

The Euler-Lagrange approach, also known as the discrete phase model, is best used for flow regimes where the difference between the volume fractions of the two phases is large. The discrete phase model injects a large number of particles into the primary phase and then uses a force-balance equation in the Lagrangian reference frame to calculate the effect that the primary phase has upon the trajectory of each particle. Typically, the secondary phase should not make up more than 10% of the total volumetric flowrate (Newton et al., 2007). Two-phase simulations at higher hold-up have problems with convergence together with an increased computational load. Therefore, the Euler-Lagrange approach was mainly applied to determine dispersion coefficients from a small amount of droplets, but fails to predict column behaviour at higher hold-up (Kolb, 2004, Haderer et al, 2005). Nevertheless, the model was applied by other authors to simulate stirred extraction columns at this lower hold-up (Vikhansky & Kraft, 2004, You & Xiao, 2005). Both groups did not show an experimental verification of the two-phase flow field. Again, more references on Euler-Lagrange simulations can be found for gas-liquid systems in bubble columns (Buwa et al, 2006; Laín et al., 2002).

The meshfree code FPM is based on the Lagrangian approach. The highlights of this method are summarized in chapter 2.3. In Fluent, the Euler-Euler approach is most suitable for the present liquid-liquid flow and was therefore applied.

2.2.2 Governing equations

The conservation equations of continuity and momentum are solved for each phase. The continuity equation for the liquid phase I is:

$$\frac{\partial(\alpha_l \rho_l)}{\partial t} + \nabla \cdot (\alpha_l \rho_l \vec{u}_l) = 0, \quad (1)$$

where α is the volume fraction, which represents the space occupied by each phase, ρ is the phase density, u is the phase velocity. The conservation of momentum for phase l is:

$$\frac{\partial(\alpha_l \rho_l \bar{u}_l)}{\partial t} + \nabla \cdot (\alpha_l \rho_l \bar{u}_l \bar{u}_l) - \nabla \cdot \tau_l = -\alpha_l \nabla p + \alpha_l \rho_l g + F_k, \quad (2)$$

where τ is the stress-strain tensor, p is the pressure shared by all phases, g is the gravitational acceleration and F represents the interfacial forces. In addition the constraint for the volume fractions must also be satisfied:

$$\alpha_1 + \alpha_2 = 1. \quad (3)$$

The inter-phase interaction term F_k consists of different momentum exchange mechanisms. Only the drag force was taken into account, while the virtual mass force and the lift force can be neglected for liquid-liquid interactions as shown by Wang & Mao (2005) in a stirred tank. For the evaluation of the drag coefficient, the model of Schiller & Naumann (1935) is applied (see [IX], Eq.4-9). In addition one may chose between different turbulence models, wall functions and boundary conditions. In this work, the standard k - ϵ , realizable k - ϵ , RNG k - ϵ and the Reynolds Stress Model were varied and tested (Launder & Spalding, 1972; Shih et al., 1995; Launder et al., 1975). For the multiphase turbulence, the Fluent mixture turbulence model and the per-phase model were applied (Fluent Inc., 2005). The mixture turbulence model is applicable when phases separate and when the density ratio between phases is close to one (Fluent Inc., 2005), which is the case for a liquid-liquid problem.

The complete set of governing CFD equations and above details are given in publications [I], [II], [VII], [IX]. Details of the governing equations and models could also be found in the Fluent manual (Fluent Inc., 2005).

2.2.3 Two-fluid & multi-fluid models

In an Euler-Euler multiphase flow, usually a two-fluid model is applied with a constant size for the bubbles, droplets or particles in the dispersed phase, whereas the Sauter mean diameter (d_{32}) could represent the different sizes of the particles in the dispersed phase, while the influence of the size-specific terminal velocity resulting from the drop size distribution, could be neglected (Wang and Mao, 2005). If the particle size distribution is very wide or multimodal this approach is more likely to fail. In reality, a wide particle size distribution can exist in the apparatus often together with growth, aggregation or breakage of the particles and different velocities of the particles depending on their size. Therefore, such an approach cannot describe the particulate behaviour of the dispersed phase. Bhole et al. (2009) and Drumm et al. (2009) ([IX], Fig.5) have shown the variation of the terminal rising velocities with bubble and droplet diameters. The results show that there is no a priori justification for the assumption of equal rise velocities (Bhole et al., 2009). As a possible solution, multi-fluid models (Tomiyama & Shimada, 2001; Hosokawa et al., 2007) divide the dispersed phase into different size classes with one fluid for each class but are highly CPU-time consuming. They can predict size dependent velocities since each size class moves in its own velocity field. These multi-fluid models are still in development and highly CPU-time consuming. A multi-fluid model was applied in [III].

2.3 Finite Pointset Method (FPM)

The Finite Pointset Method (FPM) is a numerical meshfree and Lagrangian method for solving fluid dynamic equations developed at the [Fraunhofer ITWM](#). The basis of the computations is a point cloud which is referred to as particles or numerical grid points. Particles move with the fluid velocity and they carry all relevant physical information. The point cloud represents the flow field, where they have to cover completely the whole flow domain, i.e. the point cloud should fulfill certain adaptivity criteria (particles are not allowed to form "holes" which means particles have to find sufficiently many neighbors; also, particles are not allowed to cluster; etc.). The point cloud is a geometrical basis, which allows for a numerical formulation, making FPM a general finite difference idea applied to continuum mechanics. If the point cloud would reduce to a regular cubic point grid, then FPM would reduce to a classical finite difference method. FPM is a strong formulation technique which models differential equations by direct approximation of the occurring differential operators. The method uses a moving least squares idea which was especially developed for FPM. The primary (continuous) phase is modeled by the Navier-Stokes equations. The motion of the secondary (dispersed) phase is calculated by solving the equation of motion in which the inertia, drag and buoyancy forces are taken into account. The coupling strategy within FPM framework is as follows: the separate point clouds are established for each phase. Primary and secondary phase equations are solved in their respective point clouds. These point clouds are decoupled from each other; however the necessary information like velocities, volume fractions, etc. will be exchanged between these clouds. This method is found to be appropriate for multiphase problems, e.g. a two-phase immiscible flow (Tiwari & Kuhnert, 2007). In general, one can say that FPM is able to handle the problems associated with the Lagrangian approach.

Details of the numerical approach and the treatment of the point cloud: initialization, neighbour searching, filling holes, removing points as well as a literature survey of meshfree methods are summarized in papers [VI]-[VIII] and could also be found elsewhere (Tiwari & Kuhnert, 2002; Tiwari et al., 2006). The FPM was applied in papers [V], [VI], [VII] and [VIII].

3 Particle Image Velocimetry & experimental setup

3.1 Introduction / PIV in liquid-liquid extraction

The Particle Image Velocimetry (PIV) is a non-intrusive laser technique which provides instantaneous velocity fields over global domains. PIV records the position over time of small tracer particles introduced into the flow to extract the local fluid velocity (Prasad, 2000). Principles of PIV and its development can be found in literature (e.g. Adrian, 2005; Raffel et al., 1998).

PIV as a full field method can deliver information over the whole flow domain in contrast to other methods such as Laser-Doppler anemometry (LDA). For the validation of CFD simulations in stirred extraction columns so far only LDA measurements at distinct points were carried out (Fei, 2000; Haderer, 2004; Rieger 1996). These measurements did not allow a comparison of the velocity field over the whole domain, so that only a few data points at different points (e.g. at the rotor level) could be compared. Bujalski et al. (2006) measured the single-phase flow in a pulsed extraction column with PIV. The authors used Laser Doppler Velocimetry as a crosscheck of PIV measurements and could confirm the PIV data. LDA is slow compared to PIV for velocity measurement. That is why PIV is the preferred method for investigating the velocity field (Bujalski et al., 2006).

PIV measurements are widely applied nowadays in various problems studying ring packings (Fei et al., 2003), tee mixers (Pan & Meng, 2001), aerodynamics in wind tunnels (Kompenhans et al., 1998) and stirred tanks (Deen & Hjertager, 1999).

The references which deal with CFD simulations in liquid-liquid extraction (see chapter 2.1) lack in a comparison with experimental data. Therefore, single- and two-phase flow PIV measurements were performed in this work to validate the CFD simulations over the whole extraction compartment in the RDC. The PIV setup and data analysis are introduced in this chapter. Specifics of the single- and two-phase PIV measurements are given. First the experimental setup and the investigated column type, the Rotating Disc Contactor (RDC), are described.

3.2 Investigated Rotating Disc Contactors

The RDC is the most commonly used extractor for aromatics extraction in the petrochemical industry. Two types of RDC (see Fig. A.1) extractors were investigated. A pilot plant RDC with 150 mm inner diameter and an industrial scale RDC with 450 mm inner diameter. The pilot plant column with an inner diameter of 150 mm is often applied for scale-up purposes.

A 1m section of a 150 mm diameter column with 5 RDC compartments as internals was used as the experimental basis. For this column type literature data for drop size distributions, Sauter mean diameters and hold-up were available for a 5 compartment section (Simon, 2004) and a pilot plant column with 50 compartments (Modes, 2000).

In addition, the hydrodynamics were investigated for an industrial scale RDC with 450 mm inner diameter. For a future process layout it should be ensured that CFD can predict fluid

dynamics at bigger scales. The RDC DN450 section with 3 compartments was planned and designed as part of the project. The layout rule by Kusters (1983) was applied for the scale-up of the RDC geometry of a DN450 column. Three RDC compartments were installed in the test rig with an overall height of around 1m.

Both column sections can be operated in one and two-phase conditions, the aqueous phase entering at the top and leaving at the bottom. For both types of RDC different rotational speeds and volume flow rates of the phases were investigated. The small column sections were chosen to allow PIV measurements in the compartments and the comparison with CFD simulations. Details of the experimental setup and the compartment dimensions can be found in the governing publications [I], [VII] and [XI].

3.3 PIV setup and analysis

Some key data are shortly summarized in this chapter. An ILA (Intelligent Laser Applications GmbH) 2D PIV system was used. It includes a pair of Nd :YAG Lasers, the CCD camera (PCO SensiCam, 1280x1024 px²) and the ILA synchronizer. The flow is seeded with small tracer particles that follow the flow. A cross section of the flow is illuminated with the use of a laser light sheet. The CCD camera is used to record images of the particles in the illuminated plane. Two subsequent images of the flow, separated by a short time delay, Δt , are divided into small interrogation areas. In the time interval between light pulses, the particles move a short distance. Their displacements are then calculated and can be converted into a velocity vector field by a cross correlation in knowing the pulse separation and the image scale. ILA's VidPIV software version 4.6XP was applied for the data analysis (see Fig. A2). A linear mapping was used to assign the pixels of a picture to physical units. The pulse distance was varied between 250 and 1500 μs . The interrogation areas for the cross correlation were 64 x 64 pixel with a 50% overlapping, followed by an 32 x 32 pixel adaptive cross correlation. The erroneous vectors were removed and replaced by a global velocity filter and local 3x3 median filters. The outliers were finally interpolated to fill the holes in the vector field. Images were captured at a rate of 4Hz for 50s. 200 pairs of pictures were taken for the determination of ensemble-averaged velocity fields.

A detailed description of the PIV setup is given in [I] & [XI]. Photographs of the PIV setup and the column sections could be found in the appendix (Fig. A3, A4)

3.4 Single- and two-phase PIV

For the single-phase water experiments polyamide tracer particles with a diameter of 50 μm and a density of 1060 kg/m³ were applied. The density difference between the particles and the water phase and the resulting errors can be neglected.

In multiphase flow, the presence of the dispersed phase introduces problems to the PIV method, which are not present in single-phase flows. Several PIV techniques have been developed and applied to analyse two-phase bubbly flows. Well-known methods are shadowgraphy, the digital masking technique and PIV/LIF technique (Laser induced fluorescence) (Bröder & Sommerfeld, 2002; Deen et al., 2002; Lindken & Merzkirch, 2002). However, these techniques are not working for a dense liquid-liquid flow as in an extraction column. The dispersed phase masks the measurement plane and a clear view on the

illuminated plane is not possible ([I], Fig.1). For the two-phase PIV a refractive index matching technique is the method of choice. The measurement of the aqueous phase velocities is possible by the use of an iso-optical system, where the refractive index of both liquid phases is identical.

In this work the refractive index matching method introduced by Augier et al. (2003) was adopted. The liquid-liquid system is composed of n-heptane as the dispersed phase and a water/glycerine (44/56 wt%) mixture as the continuous phase. The fluorescent dye Rhodamine 6G only soluble in the aqueous phase allows the discrimination of the phases and makes an estimation of the phase fractions possible. The second system with matching refractive indices is composed of butylacetate and a calcium chloride/water mixture (30/70 wt%, Fig. A5). For both systems, hollow glass spheres with a diameter of 10 μm and a density of 1100 kg/m^3 only soluble in the aqueous phase seeded the two-phase flow. Other refractive index matching methods were introduced by Budwig (1994) and Svensson and Rasmuson (2004). For the bigger geometry the second iso-optical system (butylacetate-chloride/water mixture) was applied due to safety reasons. Approximately 100l of organic phase in a storage tank and inside the column were necessary to carry out the measurements, which was dangerous with regard to explosion protection. The organic phase butylacetate has a lower vapour pressure than n-heptane in the first system and was therefore more suitable. As a drawback, it was not possible to use the fluorescent dye since it was soluble in both phases.

3.5 Turbulent energy dissipation from PIV analysis

PIV offers the possibility to estimate turbulent kinetic energy k and its dissipation rate ε . The dissipation rate is an important parameter in modelling coalescence and breakage (see 5.3). The determination of dissipation rate through direct PIV measurement of fluctuating velocity gradients is widely investigated and further information could be found in relevant literature (Alekseenko et al., 2007; Gabriele et al., 2009; Saarenrinne et al., 2001; Saarenrinne and Piirto, 2000; Baldi et al., 2004; Baldi and Yianneskis, 2003; 2004). The approach is shortly described here. A detailed description is found in [XI].

The turbulent kinetic energy and its dissipation rate can be derived from the fluctuating velocities and their spatial derivatives. First, the ensemble-averaged velocity field \bar{u} is subtracted from the instantaneous velocity fields u to obtain the local fluctuating velocity fields u' in VidPIV.

$$u' = u - \bar{u} \quad (4)$$

The local energy dissipation ε is defined as follows:

$$\varepsilon = \nu \left[2 \left(\overline{\left(\frac{\partial u'_i}{\partial x_i} \right)^2} + \overline{\left(\frac{\partial u'_j}{\partial x_j} \right)^2} + \overline{\left(\frac{\partial u'_k}{\partial x_k} \right)^2} \right) + \overline{\left(\frac{\partial u'_i}{\partial x_j} \right)^2} + \overline{\left(\frac{\partial u'_j}{\partial x_i} \right)^2} + \overline{\left(\frac{\partial u'_i}{\partial x_k} \right)^2} + \overline{\left(\frac{\partial u'_k}{\partial x_i} \right)^2} + \overline{\left(\frac{\partial u'_j}{\partial x_k} \right)^2} + \overline{\left(\frac{\partial u'_k}{\partial x_j} \right)^2} + 2 \left(\overline{\left(\frac{\partial u'_i}{\partial x_j} \frac{\partial u'_j}{\partial x_i} \right)} + \overline{\left(\frac{\partial u'_i}{\partial x_k} \frac{\partial u'_k}{\partial x_i} \right)} + \overline{\left(\frac{\partial u'_j}{\partial x_k} \frac{\partial u'_k}{\partial x_j} \right)} \right) \right] \quad (5)$$

Only 5 of the 12 terms can be determined from 2D PIV measurements. The remaining seven terms can be obtained by employing the local isotropy hypothesis. Therefore the equation for ε becomes, in cylindrical coordinates:

$$\varepsilon = \nu \left[2 \left(\overline{\left(\frac{\partial u'_r}{\partial r} \right)^2} + \overline{\left(\frac{\partial u'_z}{\partial z} \right)^2} + \overline{\left(\frac{\partial u'_r}{\partial z} \right)^2} \right) + 3 \overline{\left(\frac{\partial u'_z}{\partial r} \right)^2} + 2 \overline{\frac{\partial u'_r}{\partial z} \frac{\partial u'_z}{\partial r}} \right] \quad (6)$$

The fluctuating velocity fields were exported to Tecplot. In Tecplot, the velocity gradients were derived and the energy dissipation was determined. To fully resolve the spatial behaviour of the turbulence quantities of a turbulent three-dimensional flow field, it is necessary to measure down to the Kolmogorov length scale (Saarenrinne et al., 2001).

$$\eta = \left(\frac{\nu^3}{\varepsilon} \right)^{1/4} . \quad (7)$$

Therefore, for the determination of the turbulent energy dissipation, an additional adaptive cross correlation with a 16 x 16 pixels interrogation area was carried out in VidPIV to improve the spatial resolution. The resulting vector field has a resolution of 8 x 8 pixels because of the 50% overlap. The measurement of the turbulent energy dissipation and influence of the spatial resolution are shown in [XI].

4 Results of the CFD simulations and the PIV measurements

4.1 Introduction

The predictivity of the CFD codes for the liquid-liquid flow in a stirred extractor were tested prior achieving a link between CFD and PBM. In literature, there was also a lack of CFD simulations of two-phase counter-current extraction columns (see 2.1). The single and two-phase flow fields of a RDC extraction column (DN150) were simulated in CFD. The simulations for the DN150 RDC were carried out both in FPM and Fluent. In Fluent, the single-phase setup was used to test different turbulence models and a 2D and 3D grid approach. For the two-phase simulations a 2D computational grid and the Euler-Euler model were used. In FPM, a 3D geometry without a mesh can be applied together with the Euler-Lagrange approach. The CFD results were validated by PIV measurements (see chapter 3). For the single phase experiments and simulations, a water phase is considered while iso-optical systems were applied for the two-phase case ([I], [VII]). In addition, single- and two-phase simulations were also carried out for the DN450 column in Fluent and validated by PIV measurements [XI].

The Fluent results could be found in publication [I], [IX] and [XI]. Results with the FPM are given in [VII]. Paper [XI] deals with the industrial scale RDC DN450 column.

4.1.1 PIV results (RDC DN150)

The results of the PIV measurements were published in [I] and [VII]. The main results are summarized here.

The velocity field of the continuous water phase could be measured by means of PIV. For the single-phase flow, two big vortices can be estimated in the compartment; one between the stators and the other between the rotating discs (see [I], Fig.3). A small third vortex is visible above the stirrer because the flow field turns around at this position towards the stirrer tip ([I], Fig.3; [VII], Fig.6). In the two-phase scenario, still two big vortices can be estimated in the compartment. Because of the rising droplets the vortices shift or turn around and are directed to the top of the column, so that the vortex between the stirrer moves to the position above the stirrer and vice versa. The small third vortex is now visible under the stirrer because of the opposite rotating direction ([I], Fig.7, [VII], Fig.11). A PIV picture of the iso-optical system is shown in ([I], Fig.1). The path of droplets is visible because of the Rhodamine in the aqueous phase. The droplets move mainly through the middle of the compartments, do not penetrate the outer regions of the compartment and accumulate under stirrer and walls. Unfortunately, the overall image quality was not good enough to calculate a hold-up inside the compartment. Nevertheless, a qualitative comparison is possible.

4.1.2 Fluent results (RDC DN150)

In Fluent, a single-phase setup was used to test different turbulence models and a 2D and 3D grid approach. A 2D axis-symmetric grid ([I], Fig.2) and a 3D one ([VII], Fig.2) of the RDC were modeled in Gambit. Because of the rotational symmetry of a Rotating Disc Contactor the 2D grid can be adopted without losing information. Different setups, a grid with

only one compartment and periodic boundary conditions and grids including 5 compartments with velocity inlet and pressure outlet boundary conditions were tested. A 90° section of the extraction compartments was mapped in the 3D grid. In addition the influence of the cell edge length was tested varying the length down to 0.05 mm [I]. Different turbulence models were varied and tested, the standard -, RNG -, realizable k-ε model and the Reynolds stress model (RSM). For modelling the two-phase system, an Eulerian-Eulerian two-fluid approach is used. The conservation equations of continuity and momentum are solved for each phase (see 2.2.3) [I]. Details of the numerical schemes including boundary conditions, time steps, and solver settings are given in [I], [II] and [IX].

Results of the single- and two-phase simulations were published in [I], [II] and [IX] and are shortly summarized here. Single and two-phase simulations are in good agreement with the PIV measurements. Because of the reduction in numerical effort, a 2D axisymmetric approach is recommended and yields reliable results. In principle, 2D and 3D grids gave the same results and the same accounts for the different grid spacings. In Fig. A6 results for a 3D simulation are depicted. All turbulence models can describe the overall flow structures. The RSM describes the velocities with more accuracy than the k-ε models ([I], Fig.4, 5) Murthy and Joshi (2008) also found out that the RSM performs better than the standard k-ε model in a stirred tank. While the RSM is the best turbulence model in the single phase simulation, there are shortcomings in the prediction of the two-phase flow (see Fig. A7). For the two-phase flow, the realizable k-ε describes the flow field best ([I], Fig.7-9). Haderer (2004) also recommended the realizable-k-ε and the Reynolds stress model (RSM) for single-phase flow. The simulation of the counter-current two-phase flow was possible by means of the chosen velocity boundary conditions, either velocity-inlet/velocity-inlet (see [I], Fig.6) or velocity-inlet/ pressure-outlet (see [II], Fig.2). All the phenomena that occurred in the single and two-phase flow and were visible in PIV measurements as vortices and path of the droplets could be predicted with CFD [I]. In addition, the drag model of Schiller and Naumann (1935) can describe the droplet rising velocities ([IX], Fig.5).

Some test simulations were also carried out with additional lift and virtual mass forces, which were not published. The lift force introduced convergence problems in general but did not affect the velocities. The results could confirm the results of Mao and Wang (2005) that these forces can be neglected for liquid-liquid interactions. Test simulations using an enhanced wall treatment and the per-phase mixture model were also tested (see Fig.A6-A10). The influence of the per-phase model on the velocities was small and did not result in an improvement. The enhanced wall-treatment with a fine near wall grid ($y^+ = 1$, Fluent Inc., 2005) totally failed for the prediction of the two-phase flow (Fig. A10). That's why the mixture model together with standard wall functions was chosen for the CFD-PBM coupling (see also 4.5). Typical residuals of a two-phase simulation are shown in Fig.A11.

The overall results show that CFD is suitable for the prediction of the fluid dynamics in stirred extraction column and give rise to the expectation that a future link between CFD and PBM will lead to a better prediction and simulation of counter-current stirred extraction columns [I].

4.1.3 FPM results

The validation of the FPM was done in paper [VII]. The simulations were carried out by Dr. Tiwari from Fraunhofer ITWM and compared to the same PIV measurements in the RDC DN150. The comparison shows that FPM can predict the one- and two-phase flow field in the RDC, whereas the predicted velocities and the path of the droplets are in good agreement with the experimental ones ([VII], Fig.3-15). FPM also bears comparison with the results of the standard k- ϵ model in the commercial CFD code Fluent. All phenomena that occur in single and two-phase flows in an extraction column which were visible in PIV measurements could be predicted with FPM [VII]. As a drawback, turbulence in FPM is calculated directly from the Navier-Stokes equations and no averaging or turbulence modelling is applied as in a Direct Numerical Simulations (DNS) without having a turbulence model. On the other hand, the space between the points of the point cloud is not dense enough to reach the integral length scale. A suitable turbulence model will be incorporated in FPM in future, which can predict turbulence and energy dissipation and helps in modelling breakage and coalescence. In summary, FPM was successfully applied to model the flow fields in the RDC extractor [VII].

4.1.4 RDC DN450 - flow fields

The RDC DN450 was investigated to test the predictivity of CFD at industrial scale. For a future process layout it should be ensured that CFD can predict fluid dynamics at bigger scales. The resulting measurement area in the 450 mm test rig is around 10 times larger as in the 150 mm column. The dimensions of the RDC DN450 and details of the numerical scheme can be found in [XI].

The single- and two-phase simulations have been performed with three turbulence models, namely the standard k- ϵ , realizable k- ϵ and the RSM, in the framework of Fluent. PIV measurements have been conducted for the single- and two-phase flow. The CFD simulations are in overall good agreement with the simulations. The same big vortex can be estimated in the compartment between the stators as in the small column ([XI], Fig.5-6). PIV and CFD velocities are compared along a line at the stirrer level from the stirrer to the column wall ([XI], Fig. 7, 10, 13, 26, 28). All turbulence models can predict the fluid dynamics and the shape of the vortex at low stirrer speeds. At 300 rpm the standard k- ϵ fails to predict the shape of the vortex and the maximum velocities. Therefore, these results confirm the results in the RDC 150 column, where the realizable k- ϵ and the RSM were best [XI]. CFD and PIV results for different stirrer speeds are depicted in ([XI], Fig.5-13, Fig.25-30).

For the two-phase flow, one big vortex can be estimated in the compartment between the stators as in the single-phase flow ([XI], Fig.25, 27, 30). The vortex shift or turn around as it was observed in the RDC DN150. In contrast to the RDC DN150, all turbulence models can describe the vortex and the dead zones and predict almost identical results at 100 rpm and 300 rpm. However, the vortex in PIV is smaller and compressed and therewith the dead zone is also shifted. In contrast to the single-phase flow, the deviations are now higher because of the different location of the dead zones and the different shape of the vortices. Nevertheless, the maximum velocities and the qualitative velocity distribution in the compartment are predicted well.

The flow field in the upscaled RDC DN 450 seems to be comparable to the one in the smaller RDC DN150. At least this accounts for the part of the compartment between the stators (see [XI], Fig. 2). It was not possible to measure the area between the shaft and the stirrer tip (left side of the compartment in [XI], Fig. 2) since the illumination of the tracer particles and the overall picture quality in the dense system were not good enough to guarantee reliable measurements [XI]. Nevertheless, this part was studied in CFD. It is visible in ([XI], Fig.30) that the velocities at the left side of the compartment, near to the shaft are very small. A swirl of dispersed phase at the shaft is predicted in CFD at 300 rpm. The same swirl of dispersed phase is also visible in the PIV pictures ([XI], Fig.29). A more detailed comparison of the droplet phase was not possible since no fluorescent dye was applied. It seems that the layout rule of Kosters (1983) produces similar flow conditions between the stators. However, the shaft was held constant for the scale-up without applying the scale-up rule to avoid a 160 mm shaft. A bigger shaft would probably avoid the small velocities and the accumulation near the shaft.

As expected, the overall prediction of the velocity fields in the RDC DN450 is reasonable but worse than in the smaller RDC DN150 pilot plant column. The results show that CFD can predict fluid dynamics at bigger scales but still needs some minor improvements.

4.1.5 Turbulent energy dissipation

The turbulent energy dissipation was calculated within the framework of PIV analysis from Eq.(6) and compared to CFD (RDC DN450) results using different turbulence models to investigate the predictivity of CFD for the turbulence characteristics [XI]. A correct prediction of the turbulent energy dissipation in CFD is crucial for a correct modelling of the breakage and coalescence phenomena and a coupling with Population Balance Models.

The spatial resolution of the PIV measurements affects the magnitude of the measured dissipation rate. To fully resolve the spatial behaviour of the turbulence quantities of a turbulent flow field, it is necessary to measure down to the Kolmogorov length scale (Eq.7) (Saarenrinne and Piirto, 2000, [XI]). Because of the huge compartment area in the industrial scale RDC a small measurement zone (see [XI], Fig.2, zone 2) at the stirrer was chosen, to increase the spatial resolution. This zone is also of main interest, since the main energy input is at the stirrer and the stirrer tip. In practice, the droplets break in this region at the stirrer wall or in the stirrer outflow. The influence of the spatial resolution (interrogation areas $64 \times 64 \text{px}^2$, $32 \times 32 \text{px}^2$, $16 \times 16 \text{px}^2$) on the maximum measured energy dissipation for 100 rpm is shown in ([XI], Fig.14). From this figure, it becomes clear, that the smaller measurement zone 2 around the stirrer was necessary to reach a lower spatial resolution together with 16×16 pixels interrogation areas. The influence of the spatial resolution in PIV on the underestimation coefficient ([XI], Eq. 11) of the turbulent energy dissipation was shown by Alekseenko et al. (2007) (see [XI], Fig.19). Alekseenko et al. also proposed a fit function ([XI], Eq. 12) to scale the measured energy dissipation as a function of the Kolmogorov length scale and the spatial resolution. In the present analysis, the spatial resolution was around 5 to 20 times the Kolmogorov length scale. Due to these considerations, the measured energy dissipation was scaled to reach the real values. Different approaches were followed to scale the measured values which are described in paper [XI] in detail.

The different turbulence models predict almost identical results for the energy dissipation in the CFD simulations (see [XI], Table 3-4 & Fig.15). The maximum values in CFD are higher than the maximum PIV values (see [XI], Fig.16-17, Fig.20-23, Table 3-4). Because of a small angular deviation and resulting small oscillations of the stirrer in the experiments, it is not possible to measure exactly close to the stirrer wall. That's why the higher values in CFD can neither be negated nor confirmed. At least these values are in the same order of magnitude and they are also dependent on the grid near the wall and the wall functions. In this work, the standard wall functions were applied without giving closer attention to this aspect, since it is not possible to compare the near wall values to experimental PIV data. Nevertheless, a good agreement is reached for the average value, when the energy dissipation is scaled based on the Kolmogorov length scale analysis [XI, Table 3-4].

On the other hand, the turbulent kinetic energy k is less dependent on the spatial resolution and the measured results agree well with the CFD results ([XI], Fig.24). For the turbulent kinetic energy it was even possible to fully resolve it for the full measurement zone without choosing the smaller zone. For the maximum values of the kinetic energy around 20η are reached for zone 1 and around 10η are reached for the smaller zone 2. The negligible influence of the resolution in this region (resolution below 20η) can confirm the work of Saarenrinne et al. (2000).

In conclusions, different methods based on a Kolmogorov length scale analysis were applied to scale the local measured energy dissipation. The scaled energy dissipation derived from PIV measurements agree quite well with the CFD results at low stirrer speeds but remains challenging at higher stirrer speeds. Especially the areas near the stirrer cannot be investigated by means of PIV because of the experimental non-idealities.

A comparison was only possible for the single-phase flow. At two-phase flow conditions it is not possible to achieve such a high resolution in the PIV measurements. That's why a comparison was not done for the two-phase flow in paper [XI]. Nevertheless, one could assume that the energy dissipation is mainly influenced by the stirrer and not the rising droplets. Therefore, two-phase CFD results of the turbulent energy dissipation for the same operating conditions as in [XI] are shown in the appendix (Fig. A12). Here it is visible that the predicted two-phase turbulent energy dissipation in the mixture is increased in comparison to the single-phase energy dissipation. Predicted single- and two-phase maximum and average energy dissipation for the RDC DN 450 are compared in Table A1. Due to the lack of two-phase experimental investigations one can hardly estimate the accuracy of these two-phase predictions. Nevertheless, it is questionable if the increase near the stirrer can be explained by the second phase. On the other hand, it is well-known in literature that the currently available multiphase turbulence models demand improvement (Andersson et al., 2004). In general, experimental investigations or direct measurements of the dissipation rate for two-phase flows were not found in the literature [IX]. There is a need for future investigations on the measurement and modeling of two-phase turbulence. Due to the lack of a more exact comparison and validation, the mixture multiphase turbulence model together with the standard wall functions was applied for the CFD-PBM coupling. These models gave the best results for the hydrodynamics and best convergence was reached during the simulations.

5 Droplet Population Balance Modelling

5.1 Introduction / DPBM in liquid-liquid extraction

Droplet Population Balance Modelling (DPBM) with its origin in crystallization (Hulburt & Katz, 1964) can specify droplet movement, coalescence and breakage of the dispersed phase and consider the particulate behaviour in an extraction column (Gourdon et al. 1994). Valentas & Amundson (1966) were the first who applied a PBM for liquid-liquid dispersions to describe the stationary drop size distribution for a continuous stirred tank. The first one who developed a differential model using the DPBM for hydrodynamics and mass transfer in an agitated liquid-liquid extraction column was Casamatta (1981). The resulting differential model takes into account the droplet transport, breakage and coalescence as well as the necessary boundary conditions. The basic differential equation of the model includes the axial dispersion to consider the non-idealities of the flow such as random drop motion due to flow instability because of agitation and internals (Gourdon et al. 1994).

Current PBM codes by Attarakih et al. (2006a) (LLECMOD) or Kronberger et al. (1995) also use the dispersion model for the hydrodynamics. The codes are based on average compartment conditions (pseudo-homogeneous) and contain only one external coordinate. It could be shown by Steinmetz et al. (2005) and Schmidt et al. (2006) that the population balance modelling based on these codes (Attarakih et al., 2006a) is able to predict the hold-up profile and the Sauter mean diameter of the droplets in a liquid-liquid extraction column. Although this approach has a huge advantage over the currently used design methods from the introduction, there are still experiments in small lab-scale devices necessary. These are needed to establish correlations for the droplet rising velocities, the dispersion coefficient in the dispersion model and to fit adjustable parameters in the coalescence and breakage kernels.

This chapter outlines the modelling framework that has been used to describe the droplet breakup and coalescence in the coupled CFD-PBM approach. First, the population balance equation is shortly summarized. A review of different source terms for coalescence and breakage is given. Well-known solution methods are reviewed as well as the new solution methods which were used for the CFD-PBM coupling.

5.2 Population balance equation

The population balance equation (PBE) is a simple continuity statement. It can be derived as a balance for particles in some fixed subregion of internal-coordinate and physical space. The general multi-dimensional population balance equation for a number density function $n(x,r,t)$ with external (x) and internal (r) coordinates can be written as (Ramkrishna, 2000):

$$\frac{\partial}{\partial t} n + \nabla_x \cdot \dot{X} n + \nabla_r \cdot \dot{R} n = h, \quad (8)$$

where h is the net rate of generation of particles due to birth and death processes and \dot{X} and \dot{R} are the velocities for external and internal coordinates. The derivation of the equation and a literature review of the state-of-the-art in population balances could be found elsewhere (Ramkrishna, 2000; Nopens, 2005; Marchisio & Fox, 2007).

In the present case, the continuity equation for the number density function $n(x,V,t)$, which denotes the spatial position x of a particle as an external coordinate and the droplet volume V as an internal coordinate, is given by:

$$\frac{\partial}{\partial t} [n(V,t)] + \nabla \cdot [\bar{u}n(V,t)] = S(V,t), \quad (9)$$

where $S(V,t)$ are the source terms due to breakage and coalescence of the droplets. These can be further written as:

$$S(V,t) = B^C(V,t) - D^C(V,t) + B^B(V,t) - D^B(V,t). \quad (10)$$

B^B , D^B , B^C and D^C are the birth and death rates of droplets of volume V due to coalescence and breakup. The breakage and coalescence terms were first given by Valentas et al. (1966) and Valentas & Amundson (1966). A description of the source terms could be found in [IX] ([IX], Eq.12-15). How to model the different functions in the source terms is described in the next section.

5.3 Closure models for coalescence & breakage

Breakage

The breakage rate expression includes the breakage frequency g , which represents the fraction of droplets splitting per unit time and the probability density function (PDF) β , which describes the distribution of the daughter droplets from the splitting mother particle [IX]:

$$g(V')\beta(V|V'). \quad (11)$$

Several authors proposed models for the breakage rate of drops or bubbles (Alopaeus et al., 2002, Coualaloglou & Tavlarides, 1977; Hagesaether et al., 2002; Lehr et al., 2002; Luo & Svendsen, 1996; Martínez-Bazán et al., 1999a; Prince & Blanch, 1990; Andersson & Andersson, 2006a). The breakage term considers the interaction of a single droplet with the turbulent continuous phase where the droplet undergoes breakage if the turbulent kinetic energy transmitted to the droplet exceeds its surface energy (Coualaloglou & Tavlarides, 1977). In most models the authors assume drop or bubble deformation and breakup under the influence of local pressure fluctuations in a locally isotropic flow field or on the arrival of turbulent eddies to the surface of the droplets. The resulting diameter is heavily dependent on the turbulent energy dissipation. To determine the daughter droplet distribution, it is necessary to specify the number of daughter drops. Valentas et al. (1966) used a normal density function for the daughter droplet distribution, which assumes binary breakage. Instead of the binary breakup assumptions in the other models, a beta distribution by Bahmanyar et al. (1991) can describe more than two daughter droplets. Other PDF are by Martínez-Bazán et al. (1999b) or Diemer and Olson (2002). Binary breakup is suitable for bubbles but normally not for droplets, where more than two daughter droplets are formed (Schmidt, 2006). Modes (2000) measured the number of daughter droplets around 2.2 for the present RDC extractor (Kühni column up to 8 daughter droplets). A review of daughter size distributions and breakage models in the literature is given by Wang et al. (2003) and Lasheras et al. (2002). The experimental investigation and modelling of breakage phenomena as well as daughter drop/bubble distribution in gas-liquid and liquid-liquid systems is still a research topic

(Andersson & Andersson, 2006b; Eastwood et al., 2004; Maaß et al., 2007; Maaß et al., 2009; Vankova et al., 2007).

Coalescence

Droplet coalescence is expected to occur due to the interaction between two droplets and the turbulent continuous phase. The coalescence between these two droplets is considered to occur if the intervening liquid film has sufficient contact time to be drained out (Chatzi & Lee, 1987). The coalescence source terms consist of the aggregation kernel which accounts for the probability of successful collisions between pairs of droplets (V and V'). It is normally defined as the product of two quantities, the collision frequency h and the coalescence efficiency λ .

$$a(V, V') = h(V, V') \cdot \lambda(V, V'). \quad (12)$$

Most models are based on this film drainage assumption (Coulaloglou & Tavlarides, 1977; Chesters, 1991; Luo (1993), Prince & Blanch (1990), Tsouris & Tavlarides, 1994). Other approaches replaced the film drainage by a mechanism based on the effect of collision impact (Sovová, 1981) but could not achieve acceptance. The influence of pH-value, salts, detergents and mass transfer direction is usually neglected in spite of the fact that the droplet-droplet coalescence is responding very sensitive to changes in local chemical composition (Simon & Bart, 2002). Therefore, coalescence phenomena are difficult to tackle and there are only a few models in literature which have a predictive character. Coalescence in liquid-liquid systems and above influences are up to now not fully understood and an important research topic (Eiswirth & Bart, 2008; Henschke et al., 2002; Simon, 2004; Tobin & Ramkrishna, 1999).

The well-known models by Coulaloglou & Tavlarides (1977), Luo & Svendsen (1996), Martínez-Bazán et al. (1999) and Prince & Blanch (1990) were applied in this work. The governing equations could be found in the original literature or in the papers [II] and [IX].

5.4 Solution methods of the PBM

There exist many numerical methods in the literature as attempts to solve certain type of the PBEs. These methods can be roughly divided into five categories: the method of moments, the method of characteristics, the method of weighted residuals/orthogonal collocation, Monte Carlo simulation, and finite difference methods/discretized population balances. An exhaustive review of the available numerical methods is presented by Attarakih et al. (2004, 2006b) or Ramkrishna (1985, 2000).

Classical solution methods of the PBM which were used for the CFD-PBM coupling in literature and also in this work are the Classes Method (CM) (Kumar & Ramkrishna, 1996a) and the Quadrature Method of Moments (QMOM) (McGraw, 1997; Marchisio et al., 2003a,b,c). Most approaches in literature are based on these two methods. Monte Carlo simulation can be found in coupled Euler-Lagrange simulations (Vikhansky & Kraft, 2004) but is seldom. Newer solution methods are the Direct Quadrature of Moments (DQMOM) introduced by Marchisio & Fox (2005) or the Sectional Quadrature Method of Moments (SQMOM) [X]. Other promising solution methods which are not discussed in this work are the Parallel Parent and Daughter Classes (Bove et al., 2005) and the High-Order Moment-

Conserving Method of Classes (Alopaeus et al., 2006), which is able to conserve more than two moments of the distribution.

In this work, the fixed pivot technique by Kumar & Ramkrishna (1996a) ([II],[IX]), the QMOM ([V],[VII], [VIII], [IX]) and the SQMOM ([III], [V], [XII]) were applied. A review of the different solution methods is given in [IX], [X] and [XII].

5.4.1 Classes Method

Widely applied schemes for the method of classes, which include both aggregation and breakage, are by Hounslow et al. (1988), Litster et al. (1995) and Kumar & Ramkrishna (1996a). A reasonably up to date comparison of various classes methods can be found in Vanni (2000). Hounslow et al. (1988) proposed a discretisation technique that conserves droplet number and volume during coalescence and growth using a grid with a geometric factor equals 2 ($V_i/V_{i-1}=2$). Lister et al. (1995) improved the work of Hounslow et al. (1988) by introducing an adjustable geometric factor instead of 2 for droplet coalescence and growth. The fixed pivot technique by Kumar & Ramkrishna (1996a) allows a non regular grid that distribute newly formed particles that do not coincide with an existing class into neighbor classes. This method was extended in the moving pivot technique (Kumar & Ramkrishna, 1996b), which allows a varying pivot location within each interval (class). In the CM the particle population is discretized into a finite number of intervals that are used to track the population density directly.

The PBE could then be written in terms of the volume fraction of particle size i :

$$\frac{\partial}{\partial t}[\alpha_i] + \nabla \cdot [u_d \alpha_i] = V_i S_i, \quad (13)$$

where α_i is the volume fraction of particle size i and is defined as:

$$\alpha_i = N_i V_i = V_i \int_{V_i}^{V_{i+1}} n(V, t) dV. \quad (14)$$

(N_i & V_i =number and volume of particles).The CM is particularly useful when the particle sizes do not vary widely. On the other hand, one limitation is its inability to predict accurately integral quantities (low-order moments as an especial case) associated with populations of sharp shapes (Ramkrishna, 2000, Attarakih, et al., 2006b). For example, the fixed pivot method by Kumar & Ramkrishna (1996a) can conserve mass and number of the distribution. The CM was applied in publication [II] and [IX].

5.4.2 Quadrature Method of Moments

The QMOM as first introduced by McGraw (1997) to solve the PBE with pure growth is found very efficient from accuracy and computational cost point of view. The method was extended to aggregation-breakage processes by Marchisio (2003a, 2003c). Unlike the sectional methods, the QMOM has a drawback of destroying the shape of the distribution and the information about the distribution is only stored in its moments. The r th moment is defined by integrating the population number density function with respect to certain

population property (e.g. particle sizes) weighted with this property raised to its r th power. The k th moment is then defined as:

$$m_k(x, t) = \int_0^{\infty} n(L, x, t) L^k dL, \quad (15)$$

where L is the droplet size. When r equals zero the zero moment represents the total number of particles per unit volume; on the other hand, when r equals three the third moment represents the volume fraction (volume concentration) of the particles. The QMOM tracks the population moments (e.g. the zero and third moments) rather than its size and hence it does not depend on the minimum and maximum particle sizes. The QMOM is based on the Product-Difference algorithm to find weights and abscissas from the moments, which requires the solution of an eigenvalue problem in terms of the population low order moments.

The DQMOM (Marchisio & Fox, 2005) is based on the idea of tracking directly the variables (weights and abscissas) appearing in the quadrature approximation, rather than tracking the moments of the distribution. DQMOM was proposed to eliminate two main disadvantages of the QMOM: (i) if applied to multi-variate distributions QMOM loses simplicity and efficiency, and (ii) by tracking only the moments of the distributions, it does not represent realistically polydisperse systems with strong coupling between the internal coordinates and phase velocities (Marchisio & Fox, 2005). Therefore, the transport equations for weights and abscissas of the moments are directly solved. A drawback of the QMOM and DQMOM methods is that a full reconstruction of the distribution is not possible. The algebraic linear system has the same numerical difficulties as the eigenvalue problem associated with the Product-Difference algorithm used in the QMOM. Grosch et al. (2007) analysed and tested the QMOM using different case studies concerned with crystallization. They highlighted the problem of ill-conditioning associated with either the Standard or Direct QMOM when the number of abscissas increases.

The QMOM is applied as solution method in [III], [VI], [VIII] and [IX].

5.4.3 Sectional Quadrature Method of Moments

The Sectional Quadrature Method of Moments, invented by Prof. Attarakih, (Attarakih et al, 2009a, [X]) combines the advantages of classes method and the method of moments and tries to minimize their drawbacks. The SQMOM is based on the concept of primary and secondary particles, where the primary particles are responsible for the distribution reconstruction (classes), while the secondary ones (method of moments) are responsible for breakage and coalescence events and carry detailed information about the distribution. The main idea behind the SQMOM is to divide the population density function into sections followed by the application of the classical QMOM to each section. The method can track accurately any set of low-order moments with the ability to reconstruct the shape of the distribution. The SQMOM has three major advantages over the different QMOM: First, the inversion of the moment problem using the product difference algorithm or the direct QMOM is no longer needed since two equal weights and abscissas are analytically derived. Second, the problem of ill-conditioning is reduced due to the limited number of abscissas to two.

Third, the convergence of the solution could now be tested by increasing the number of sections, which is not available at all in the standard QMOM (Attarakih et al., 2009a).

The method is derived in paper [X]. It was implemented in Fluent in a three-fluid model using two primary particles in the SQMOM [III], while up to five primary particles were applied in a two-fluid model in FPM [V]. These results are shown in chapter 7.

5.4.4 The One Primary and One Secondary Particle Methods (OPSPM)

In the simplest case of the SQMOM, for one primary and one secondary particle, the method becomes The One Primary and Secondary Particle Method (OPOSPM) ([XII], [XIII]). In terms of the SQMOM, the primary and secondary particles coincide with each other in this case. So, the population density is represented by a single particle whose position (size) is set according to the variation of the population density and is given by:

$$d_{30} = \sqrt[3]{\frac{\pi\alpha_i}{6N_i}} \quad (16)$$

where N and α are the total number and volume concentrations of the population of real particles. The transport equations for the integral quantities N and α are solved in the method. By assigning two distinct integral properties to the secondary particle, it is equivalent to a one-point Gauss-like quadrature according to the QMOM framework (McGraw, 1997). So, the population balance equation is represented by a couple of transport equations conserving both the total number and volume concentrations of the whole population. The OPOSPM is equivalent to taking one secondary and one primary particle using the SQMOM. The method is derived in detail in [IV] but with a different name as the Direct One Primary and One Secondary Particle Method (DOPOSPM). A shorter derivation is given in [XIII] now as OPSPM. A comprehensive test of the method is presented in [IV] and [XIII], where the model is found to produce exact solutions for many popular breakage and coalescence kernels. In addition, the source terms ([XII], Eq.10) are very simple and allow fast and easy implementation of coalescence and breakage models

$$S = (n_d(d_{30}) - 1)g(d_{30})N_d - \frac{1}{2}a(d_{30}, d_{30})N_d^2. \quad (17)$$

Here n_d is the mean number of daughter particles due to breakage, g and a are the breakage and coalescence kernels (frequencies).

The method was implemented in Fluent in a one equation CFD-PBM model [XII]. A full pilot plant extraction column of a Rotating Disc Contactor (RDC) type consisting of 50 compartments was simulated with the new model (see chapter 7).

For the sake of completeness, another variation of the SQMOM is the Direct Primary and Secondary Particle Method (DPSPM) with up to N primary particles and one secondary particle (Attarakih et al., 2008), which was not used in this project.

6 Coupled CFD-PBM model: theory and implementation

6.1 Introduction / state-of-the-art

Both CFD and PBM are subject to restrictions when they are applied independently. PBM needs information of the fluid dynamics such as drop velocity and turbulence (energy input), which are normally incorporated by simplified correlations in stand-alone PBM codes (e.g. LLECMOD, Attarakih et al., 2006a). In two-phase CFD simulations, generally a two-fluid model is applied, whereas a constant Sauter mean diameter represents the different sizes of the particles in the dispersed phase. If the particle size distribution is wide or multimodal this approach is more likely to fail. A change in the particle size distribution due to aggregation or breakage is also not considered. In reality, a wide drop size distribution can exist in the apparatus and even in a single extraction compartment (Schmidt et al., 2006). Smallest droplets can be found near the stirrers due to breakage, while coalescence under stators or less turbulent regions lead to bigger droplets. These differences in the local distribution influence the hydrodynamics and account for changes in velocities and volume fraction of the dispersed phase. A constant diameter can not reflect these influences and the resultant complex behaviour is simplified in CFD simulations without PBM. Therefore, both CFD and PBM can benefit from each other in a coupled model.

The coupling between CFD and PBM just started at the beginning of this millennium. A literature survey is also given in [III], [IX] and [XII]. Lo (2000) was the first who implemented a MUSIG (Multiple-Size-Group) model for the solution of the population balance equations in the commercial CFD code CFX. Herewith a complete coupling is achieved, the bubble size distribution is divided into a number M of discrete size classes, while it is assumed that particles of all sizes share a common velocity field, where the Sauter mean diameter influences the drag term (Fig.1). Several authors applied such an approach for the solution of multiphase flows (Andersson et al., 2004; Chen et al., 2005; Cheung et al., 2007; Ekambara et al., 2007; Kerdouss et al., 2008; Laakkonen et al., 2007; Olmos et al., 2001; Podila et al., 2007; Sanyal et al., 2005). Sanyal et al. (2005) implemented a classes-method (CM) and a method of moments (MOM) in the CFD code Fluent in conjunction with the Eulerian multiphase model. The QMOM was first implemented in CFD by Marchisio (2003b) and applied by many researchers in a two-fluid model (Sanyal et al., 2005; Wan et al., 2006; Petitti et al., 2007) [XII]. One simplification in the coupled CFD-PBM model is the two-fluid model (see chapter 2) where the influence of the different drop sizes is blurred, since all droplets in the secondary phase move at the same velocity based on an idem Sauter mean diameter. Krepper et al., (2007, 2008), Sha et al. (2006) and Bhole et al. (2008) developed a multi-fluid multi-size group model based on the CM in which each fluid is represented by one class. Depending on the number of fluids and the number of classes in the PBM the accuracy is increased at the expense of increased CPU time. The computing time is always high because of the CM, which normally needs more than 20 classes even for a narrow distribution, and one has to find an effective trade-off between accuracy, furnished information and computing time [IX]. Other coupled multi-fluid models are based on the DQMOM (Fan & Fox, 2008; Fan et al., 2004). The DQMOM was carried out for 2,3 or 4

nodes by Fan & Fox. However, the DQMOM is limited to this small number of fluids since inversion of ill-conditioned linear system is encountered as the number of quadrature nodes increases. Multi-fluid CFD-PBM models have a high computational complexity and their application is therefore limited.

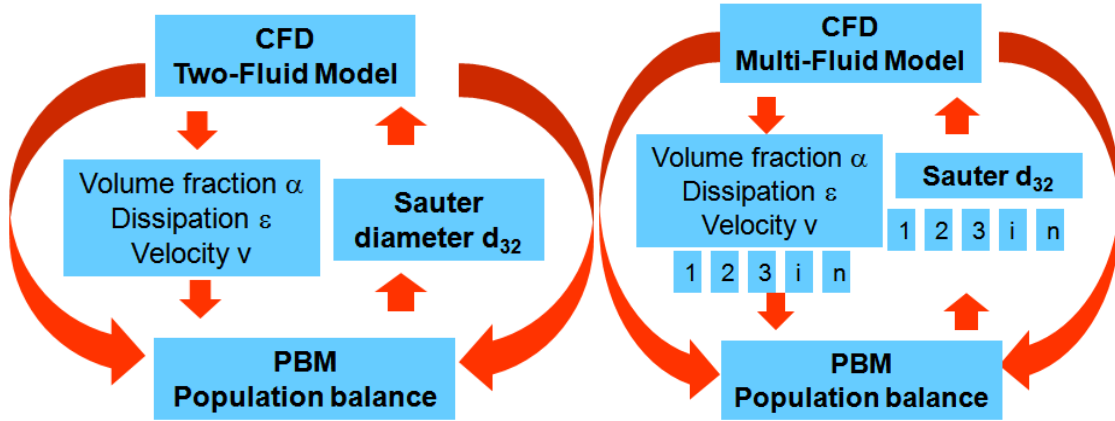


Fig. 1: Two-fluid and multi-fluid CFD-PBM model

Combined CFD-PBM models are investigated mainly in the gas-liquid field (e.g. Andersson et al., 2004; Chen et al., 2005; Jakobsen et al. 2005, Lehr et al., 2002; Wang et al., 2006). Laakonen et al. (2007) and Wang & Wang (2007) implemented gas-liquid mass transfer for a bubble column and a stirred tank in a coupled CFD-PBM code. For the liquid-liquid problem in the field of extraction, only few research groups investigated a combined CFD-PBM model. First, researchers adopted a simplified approach by employing a one-way coupling. This means that only the result of the flow simulation is used for the calculation of the drop size distributions, while the influence of the droplets on the flow field is neglected (Schlauch, 2006). A multi block approach, where the investigated geometry is subdivided into sub-regions, is another alternative in that respect (Alopaeus et al., 1999). Vikhansky et al. (2006) implemented the PBM in an Euler/Lagrange CFD code using Monte Carlo simulation for the solution of the PBM. Monte Carlo simulations are typically computationally expensive and most suitable for stochastic population balance equations, especially for complex systems (Ramkrishna, 1985).

In summary, one can choose between different approaches for the coupling: a two-fluid or multi-fluid model in CFD (see chapter 2) and a whole set of models for the solution of the PBM (CM, QMOM, DQMOM, SQMOM chapter 5). Therefore, the existing coupling approaches vary according to accuracy, efficiency and recovered information about the distribution. Nowadays, coupled CFD-PBM models are widely investigated especially in bubbly flows. On the other hand, there was a lack of investigations in the liquid-liquid or extraction field at the beginning of this project.

In the following chapter the implementation of the applied solution methods (QMOM, SQMOM, OPOSPM, models for coalescence and breakage) in CFD is described, while the results are shown in chapter 7.

6.2 Implementation of the PBM in CFD

For the solution of the PBM in CFD, the additional transport equations for the bins in the CM (Eq.13) or the moments (Eq.15) in the QMOM or SQMOM have to be introduced. These transport equations can be defined by means of user-defined scalars in Fluent (see [III] and [XII]). In a two-fluid model, the Sauter mean diameter of the droplets is calculated in every time step and returned to the drag force for the coupling with the fluid dynamics (e.g.[III],Eq.10). The velocity \dot{X} in Eq. (8) is derived from the Navier-Stokes equations, thus a complete two-way coupling between CFD and PBM is assured. The governing values in the source terms for coalescence and breakage (see [IX]), e.g. the turbulent energy dissipation and the volume fraction α can be returned for each cell from the Fluent solver. Using this approach, all information come from the simulation and the need for experimental data and geometrically dependent correlations is eliminated [IX]. The implementation of the SQMOM [VIII] and the QMOM [VI] in the FPM is similar to the one in Fluent, but in Lagrangian form (see [VI] and [VIII] for details).

6.2.1 Fluent population balance add-on

In Fluent 6.3 the CM and the QMOM are already built-in and can be activated in a two-fluid model (Fluent Inc., 2006). The CM was applied in paper [II] and both the CM and the QMOM were applied in publication [IX]. The volume coordinate in the CM was discretised using a geometric factor (Litster et al., 1995) and up to 30 classes, while 4,6 and 8 moments were applied in the QMOM [IX]. The boundary conditions of the bins/moments at the velocity inlet were taken from experimental data (Simon, 2004) and were specified. The different models for coalescence and breakage (see [II] and [IX]) were written as user-defined functions (UDF) and coupled to the PBM scalars. In this connection, one has to specify the breakage rate expression (Eq.11) and the aggregation kernel (Eq.12) (Fluent Inc., 2006). In detail, the models of Coulaloglou and Tavlarides (1977), Luo and Svendsen (1996; Luo, 1993), Martínez-Bazán et al. (1999) and Prince and Blanch (1990) were applied together with different probability density functions (Valentas et al., 1966; Bahmanyar and Slater, 1991) (see [IX], Eq.37-48). The model of Luo & Svendsen includes a double integral for the breakage frequency (e.g. [II], Eq.33) which was solved by means of the incomplete gamma function (Hagesaether, 2002; Press et al., 2007) and a numerical integration (rectangle rule) (Hagesaether, 2002).

6.2.2 Implementation of the SQMOM in Fluent

The SQMOM and QMOM [III] were implemented in Fluent by defining own user-defined scalars for the moments of the distribution. In the SQMOM, two primary particles and therewith two fluids for the dispersed phase were applied resulting in a three-fluid model (see [III] for details). For coupling with the fluid dynamics the Sauter mean diameter of the droplets is calculated in each section and returned to the drag force of the respective phase. So each section moves with its own velocity field based on the Sauter mean diameter of this section ([III],Eq.18). The weights and abscissas of the moments in the QMOM and SQMOM were calculated at the beginning of each time step and stored in user-defined memory. The need for the Product-Difference algorithm was eliminated by using the two-equal-weight

quadratures (see [X], Eq.11,12). Two secondary particles result in 4 moments for each section, which is sufficient to carry detailed information about the distribution. These moments were defined as user-defined scalars. The source terms for coalescence and breakage ([III], Eq.14-17) were written as UDF and coupled to the transport equations. The SQMOM considers the movement of mass between the sections. Therefore, in each single equation additional source terms were introduced which describe the mass movement between the classes. Details of the implementation and the governing equations can be found in [III] and [X].

6.2.3 Implementation of the OPOSPM in Fluent

In comparison, the implementation of the OPOSPM (chapter 5.4.4, [XIII]) in paper [XII] was straightforward. The transport equations for the integral quantities N and α are solved in the method. Since the volume fraction of the dispersed phase is already solved in the continuity equation in CFD, only one additional transport equation for the total number of the particles N_d was introduced as UDF.

$$\frac{\partial}{\partial t}(\rho_d N_d) + \nabla \cdot (\rho_d u_d(d_{30}) N_d) = \rho_d S \quad (18)$$

The population density is represented by a single particle, whose position is the d_{30} diameter (Eq.16). For the purpose of the two-way coupling with the fluid dynamics the coupling is now based on the available d_{30} . The source terms, which were written as UDF, are very simple (Eq.17) in comparison to the other solution methods, which consist of integrals, sums or vector and matrices multiplications [XII]. Here two single terms account for breakage and coalescence of the droplets. Since only the total number of the droplets is of interest, functions for the daughter droplet distribution are implicitly implied and reflected by N . The same could be said about the aggregation kernel where only collision of equal sized droplets is considered ($a(d_{30}, d_{30})$). The reduced model is described in detail in paper [XII].

7 Coupled CFD-PBM: results

Results of the coupled CFD-PBM simulations are presented in this chapter. Applied solution methods of the PBM and the models for coalescence and breakage were introduced in chapter 5. In Chapter 6 the implementation of the different solution methods and models for coalescence and breakage were summarized.

7.1 Fluent population balance add-on

The Fluent population balance add-on was applied to simulate the drop size distributions and flow fields in a 5 compartment segment of a liquid-liquid RDC extractor (see [IX], Fig.2) [II], [IX]. Simulated drop size distributions for the systems toluene-water and butylacetate-water are compared to the experimental measurements of Simon (2004). Theoretical models for coalescence and breakup, the models of Luo & Svendsen (1996) and Coualoglou & Tavlarides (1977), as well as a mixed model, where the breakup kernel comes from Martínez-Bazán et al. (1999) and the coalescence kernel from Prince and Blanch (1990) were implemented in the CFD code as user-defined functions. For the solution of the PBM the CM (Kumar & Ramkrishna, 1996a) and the QMOM (Marchisio, 2003a) were used. Here the focus was on the prediction of the drop size distribution, varying QMOM, CM and closures for coalescence and breakage, in a proved, tested and cost-efficient framework, namely the two-fluid model.

Different scenarios were carried out for the CM and the QMOM varying the number of classes ($N_c=8, 15, 29$) and the number of moments ($N_m= 4, 6, 8$) to investigate their influence. In addition, the drop size distribution was reconstructed from the moments based on the statistically most probable distribution for turbulent flames (Pope, 1979; Bałdyga et al., 2001) ([IX], Eq.34-35). The following conclusions can be drawn: 15 classes in the CM are sufficient for the description of the problem and seem to be a good trade-off ([IX], Fig.7), the number of tracked moments (4, 6 or 8) does not significantly influence the reconstruction of the distributions for the present problem ([IX], Fig.8). The maximum deviation was only around 0.01% between 4 and 8 moments. These results show that 4 moments as in the SQMOM are sufficient to describe the sectional or overall d_{32} . It is even possible to reconstruct an idealized distribution from the moments (see also John et al., 2007).

The model of Coualoglou & Tavlarides described the droplet size distribution accurately because of the 4 adjustable parameters. Both CM (15 classes) and QMOM (6 moments) using the same parameter set give reliable results ([II], Fig.8, [IX], Fig.9). In terms of the QMOM the number of scalars to be tracked is reduced from 15 to 6. This comes together with a lower CPU time and no lower and upper limit on the classes (Marchisio et al., 2003a). For the model of Luo & Svendsen, the simulation results are shown in [IX] (Fig.10-11). Since the original model overestimates the coalescence, the only parameter in the model c_1 in the coalescence efficiency ([IX], Eq.44), which is normally of order unity, was adjusted. Good predictions were achieved when the parameter c_1 was set to 7.0 for toluene-water and 4.5 for butylacetate-water. Chen et al. (2005) tested the model of Luo & Svendsen in a CFD-PBM model for a bubble column and made similar observations that the model predicted

coalescence rates are about a factor of 10 higher than the predicted breakup rate. They proposed a constant decrease of the coalescence kernel by a factor 10 (increase breakage tenfold respectively). When the whole coalescence kernel is reduced by a factor 10 almost the same results were achieved ([IX], Fig.10). So the constant factor for the whole coalescence kernel seems to be independent from the applied system and allows for a major predictability, since the constant factor 0.1 is more an engineering estimate than an adjustment. Finally a mixed model was chosen, where the breakup kernel of Martínez-Bazán is very simple and gives results in the same order of magnitude as the model of Luo & Svendsen, while the CPU time is much lower. On the other hand, because of slightly different assumptions the collision frequency in the model of Prince & Blanch is four times less than in the model of Luo & Svendsen. The results for 150 rpm are slightly deviant, while the prediction for the higher stirrer speed (300 rpm) is very good ([IX], Fig.12-13). The original model of Luo & Svendsen calculates a Sauter mean diameter, which is more than 100%, oversized. When the parameter c_1 is adjusted or the whole aggregation kernel is tweaked by a factor 0.1 the deviation is less than 30% for both systems in respect to the experiments. For the mixed model the deviation for the Sauter mean diameter is less than 30% for both systems without using any adjustable parameters. The results show that a prediction of the droplet size distribution is possible, even when no adjustable parameters are used. However, the selected mixed model was tailor-made and a lot of future work is needed to allow for a prediction of the drop size distribution in extractions columns without any adjustable parameters. More details can be found in papers [II] and especially [IX].

Mainly, there seems to be a need for more investigations on multiphase turbulence models and experimental work on breakage and coalescence. The results in chapter 4.1.5 for the RDC DN450 have shown that the predicted two-phase energy dissipation is probably too high near the stirrer. In Fig.A13 and Fig.A14 single- and two-phase predicted turbulent energy dissipations for the same operating conditions as in paper [IX] (RDC DN150) are shown. Results of the single-phase turbulent energy dissipation estimated from single-phase PIV measurements [I] using an underestimation coefficient as in [XI] are presented in Fig.A15 for comparison. The same trend as in the RDC DN450 is obvious. While the single-phase prediction is quite good, the two-phase prediction seems to overestimate the dissipation near the stirrer. Nevertheless, a decrease of the energy dissipation in the two-phase simulations would result in even less breakage and more coalescence, which is already dominant in the present literature models (Luo & Svendsen, Prince & Blanch). A comparison of some currently available literature models for coalescence and breakage is shown in Fig.A16-A18. Breakage frequencies of different literature models are given in Fig.A16 as a function of the droplet diameter. These results show the huge deviations (factor 1000) of the different models although they have almost the same assumption of turbulent eddy/particle collisions (see Prince & Blanch, 1990; Luo & Svendsen, 1996; Andersson & Andersson, 2006a). Especially the model of Luo & Svendsen depends on the lower and upper limits of integration ([IX], Eq.41), where it is assumed that only a turbulent eddy, which is smaller than the droplet, causes breakage and the upper limit is therefore 1. Although the model of Andersson & Andersson results in even less breakage (Fig. A16) their experimental results (Andersson & Andersson, 2006b) have shown that also eddies bigger than the size of the fluid particle can cause breakup. An increase of the upper limit ($\xi=2$) in the model of Luo & Svendsen

increases the breakage frequency and could further improve the model (see Fig.A16). On the other hand, predictions for the particle collision frequency (h) in the coalescence terms are quite equal (Fig.A17), while a slightly different behaviour can be observed for the coalescence efficiency in Fig.A18 (Lehr et al., 2002; Venneker et al., 2002; Tsouris & Tavlarides, 1994). Nevertheless, the collision frequency seems to be too high in all models for the present case of an RDC extractor. These results show the need for future investigations and improvements on multiphase turbulence models and models for coalescence and breakage, which are a strong function of the local turbulence in an apparatus (see 5.3). A discussion of the different models and possible model improvements are also given in [II] and [IX].

7.2 PBM in FPM

The SQMOM was implemented in FPM and results are presented in [VI] and [VIII]. A complete two-way coupling is achieved and the coupled model accounts for breakage and coalescence using constant kernels. The flexibility of the method through its reduction to the standard QMOM, when the primary particle equals one, makes it very attractive from computational point of view. Three test cases were considered: only breakage, only aggregation and breakage and aggregation both. In ([VIII], Fig.3) the Sauter mean diameter for all three cases is plotted. The SQMOM in FPM is found extremely accurate and the number of primary particles was varied between one ([VI], [VIII]) and five [V] while two secondary particles were solved for tracking the sectional moments.

For the simulation of the RDC DN150, in order to find some estimation on the aggregation and breakage kernels, some parameter studies in 2D geometry where the rotor is fixed were performed. The 2D computational domain is depicted in ([VIII], Fig. 2), where 5 compartments (as in the 3D domain, [VIII], Fig. 1) are considered. The constant kernels were fitted to experimental data of the five compartment section in the 2D geometry ([V], [VIII]) and give suitable results. In the next step, the same breakage and coalescence kernels were applied in the 3D domain. As in the 2D domain, the Sauter mean diameter is equal to the experimental data and the parameters, which were achieved in the CPU-time saving 2D simulation, are also suitable for the simulation of the real column ([VI], [VIII], Fig.4-5). The approach of the 2D domain for parameter studies was chosen because parameter studies are not feasible in a complex 3D domain. This approach was possible since only constant kernels were applied. Real models should and will be applied in FPM in future. Flow fields and dispersed phase hold-up were also studied in the FPM framework ([VI], Fig.2-4; [VIII], Fig.4-5).

7.3 SQMOM in a multi-fluid model

Although the results in [II] and [IX] are promising, a comparison of the size-specific rise velocities ([IX], Fig.5) points at the main drawback of the two-fluid model. The influence of the different drop sizes is blurred because it is assumed that all droplets with different sizes move in the same velocity field based on the Sauter mean diameter d_{32} . It is obvious that the assumption of the two-fluid model results in errors for droplets at the left-most and right-most position of the distribution [IX]. Therefore, there is a future need for investigations in multi-fluid CFD-PBM frameworks, which already started (Krepper et al., 2008; Bhole et al., 2008)

(see 2.2.3). Nevertheless, the benefit of the two-fluid model is the moderate computational effort, which is anyway very high in coupled CFD-PBM models. Multi-fluid models will further increase the computational effort. One has to make a compromise between limited computing power and accuracy, whereas the two-fluid model seems reasonable [IX]. Combined CFD-PBM multi-fluid models are still in development, highly CPU-time consuming, limited and not recommended as long as the correct modelling of coalescence and breakage is not guaranteed. The problems of the currently available multi-fluid CFD-PBM models (Krepper et al., 2008; Bhole et al., 2008; Fan & Fox, 2008), are summarized in chapter 6.1 or in [XII].

As a promising alternative a multi-fluid based on the SQMOM was developed in [III]. The SQMOM offers the possibility to use a multi-fluid model depending on the number of primary particles in the SQMOM. The SQMOM has also several advantages over the different QMOM methods (5.4.3, [X]). Two primary particles and therewith two fluids for the dispersed phase were introduced in Fluent resulting in a three-fluid model (see 6.2.2). Four moments were tracked in each section, while this number can be reduced to two moments, whereas m_2 is estimated by interpolation and m_3 is equal the continuity equation of the dispersed phase as in the OPOSPM [III]. Constant kernels in the model account for breakage and coalescence. Detailed results and a comparison between the SQMOM with two primary particles and a two-fluid model using the QMOM are presented in [III]. The simulation results for three test cases and a bimodal inlet distribution show the accuracy and benefit of the three-fluid model with the SQMOM in comparison to the two-fluid model with the QMOM ([III], Fig.3-13). The local movement of the droplets between the two fluids in the SQMOM is working smoothly while the overall Sauter mean diameter is calculated correctly. The SQMOM represents a perfect basis to couple CFD and PBM in a multi-fluid model. An unlimited amount of additional fluids or primary particles could also be easily added, while only the computational power sets the limit [III]. However, the SQMOM is most efficient for a small number of fluids. For each primary particle (fluids) the total number of tracked sectional moments increases by 4 (2 respectively) and at a higher number of sections one could just as well apply the CM (Krepper et al., 2008).

7.4 OPOSPM in Fluent

The main drawback of the multi-fluid models is the computational load. Although the shown three-fluid model with the SQMOM is very efficient, such an approach does not allow the simulation of full columns with the currently available computing power. Therefore, finally, the One Primary One Secondary Particle Method (OPOSPM) (see 5.4.4), which is a very easy and efficient special case of the SQMOM, was introduced in CFD via user-defined functions and user-defined scalars [XII]. The OPOSPM offers the possibility of a one equation model for the solution of the PBM in CFD based on the d_{30} diameter instead of the classical Sauter mean droplet diameter.

As a test case, the predictions of the one equation model are compared to the results of the well-known QMOM using constant source terms for breakage and coalescence. A monomodal drop size distribution at the dispersed phase inlet was assumed. Therefore, both diameters d_{30} and d_{32} are equal at the bottom of the section ($d_{30}=d_{32}=2.66$). A Uniform daughter droplet distribution was assumed for the QMOM, while the OPOSPM does not need

assumptions for the daughter droplet distribution [XII]. The differences in the results and therefore in the coupling were shown ([XII], Fig.3-4). The results show that the diameter d_{30} is approximately equal in both methods as expected. This is because the OPOSPM can conserve the zero and third moments of the distribution like the QMOM. Furthermore, the Sauter mean diameter (d_{32}) is different in the QMOM as expected and therefore we have a different coupling to the fluid dynamics with the present new model [XII]. Although the coupling with d_{30} is different from the common coupling in CFD-PBM models using d_{32} , it is not necessarily worse, but one should keep in mind the differences.

As a case study, a full pilot plant extraction column of a Rotating Disc Contactor (RDC) type consisting of fifty compartments ([XII], Table 1, Fig. 2) was simulated with the new model. The model of Luo and Svendsen (1990), which was modified in the previous work ([IX], 7.1), by introducing a scaling factor, was used to account for breakage and coalescence of droplets.

$$a(d_{30}, d_{30}) = 0.1 \cdot a_{Luo\&Svendsen}(d_{30}, d_{30}) \quad (19)$$

The number of daughter droplets in Eq. (17) was taken as 2.5 according to a daughter droplet distribution given by Schmidt et al. (2006). The predicted results for the mean droplet diameter and the dispersed phase volume fraction (hold up) agree well with published literature data of Modes (2000) ([XII], Fig.5-9). The overall deviation between the experimental and predicted mean droplet diameters is below 20% at the different stirrer speeds ([XII], Table 2).

The contours of the mean droplet diameter (d_{30}) inside the compartments are shown in ([XII], Fig.7). It is clear that the droplets break up near the tip of the stirrer (due to the shearing force) resulting in small mean droplet diameters which are around 2 mm. Moreover, breakage and coalescence are strong functions of the turbulent energy dissipation, which reaches the highest values at the tip of the stirrer. On the contrary, the largest mean droplet diameters are found under the stators where the droplets accumulate in the stagnant regions under the stirrers [XII]. A comparison of the predicted local droplet mean mass diameter with the experimental data is not possible since measurements of the local droplet size distributions are not available in the published literature. Nevertheless, the local drop sizes in the compartment agree well with experimental observations, is reasonable and encouraging.

These results also point at the main drawbacks of the experimental literature data (Kolb, 2004; Modes, 2000; Simon, 2004; Steinmetz et al., 2005). In the governing experiments hold-up and drop size distributions were measured as an average over the whole compartment. On the other hand, the CFD simulations give local resolutions of these properties and cannot be compared. Furthermore, the experimental PIV and the CFD results show that there was a huge spread in the local distribution of the hold-up and the drop sizes. Future experimental investigations should provide local drop size, volume fraction and droplet velocities in one compartment for a better comparison and a further improvement of the models [XII].

The results further show that the new CFD-PBM model is very efficient from computational point of view (two times less than the QMOM and five times less than the method of classes) ([XII], Table 3). This is because the OPOSPM requires the solution of only one equation (the total number concentration) when coupled to the CFD solver (Eq.18).

It is therefore suitable for fast and efficient simulations of small scale devices and even large scale industrial processes. Thus the OPOSPM coupled to CFD solvers provides a feasible tool for checking scale up of extraction columns. As a possible future approach, one could estimate parameters in the models for coalescence and breakage in lab-scale or small column parts, and then use them for large scale devices as already done by Schmidt et al. (2006) [XII].

8 Summary & outlook

The aim of this thesis was to link Computational Fluid Dynamics (CFD) and Population Balance Modelling (PBM) to gain a combined model for the prediction of the behaviour of counter-current liquid-liquid extraction columns. Parts of the doctoral thesis project were done in close cooperation with the Fraunhofer ITWM (Institut für Techno- und Wirtschaftsmathematik). Their in-house CFD code Finite Pointset Method (FPM) was further developed for two-phase simulations and used for the CFD-PBM coupling. The coupling and all simulations were also carried out in the commercial CFD code Fluent in parallel. For the solution methods of the PBM there was a close cooperation with Prof. Attarakih from the Al-Balqa Applied University in Amman, Jordan.

At the beginning of the project in 2005, there was a lack of two-phase liquid-liquid CFD simulations and their experimental validation in literature. Therefore, prior achieving the link between CFD and PBM, stand-alone CFD simulations without PBM were carried out both in FPM and Fluent to test the predictivity of CFD for stirred liquid-liquid extraction columns. These investigations were done in a segment of a Rotating Disc Contactor (RDC) with 150mm diameter. Single- and two-phase simulations were validated by means of Particle Image Velocimetry measurements (PIV). The two-phase PIV measurements were possible when using iso-optical systems, where the refractive indices of both liquid phases are identical. During the simulations different turbulence models and boundary conditions were varied and tested. In addition, same investigations were carried out in an RDC with 450mm diameter to test the CFD predictivity at industrial scale, which is important for a future column layout. CFD results of the aqueous phase velocities, hold-up, droplet raising velocities and turbulent energy dissipation were compared to experimental data. The results show that CFD can predict most phenomena in the one- and two-phase flow field and there was an overall good agreement.

In the next step, the link of CFD and PBM was achieved in a two-fluid model. The Sectional Quadrature Method of Moments (SQMOM, Attarakih et al. 2008) was implemented in FPM. As a start, only one primary particle was used in SQMOM resulting in the well known Quadrature Method of Moments (QMOM). First simulations of the coupled algorithms were conducted for the RDC (DN150) extractor in which droplet coalescence and breakage (with constant kernels) are used. The constant kernels were fitted to experimental data in a 2D geometry of the column section and predict also suitable results for the 3D geometry. In addition, the number of primary particles was varied up to five primary particles for a 2D test case.

CFD-PBM simulations were also carried out in the framework of Fluent. The CM and QMOM are already implemented in version 6.3. Different models for coalescence and breakage were implemented as user-defined functions (Luo & Svendsen 1996, Coualoglou & Tavlarides 1977, Martínez-Bazán et al. 1999, Prince and Blanch 1990) to predict drop size distributions and Sauter mean diameters in the RDC DN150 column. These results showed that a prediction of the droplet size distribution is possible, even when no adjustable parameters are used. A modified model of Luo & Svendsen was proposed with a scaled

aggregation kernel. Pros and Cons of the different solution methods and a reconstruction of the distribution from the moments were shown. Good agreement was also obtained compared to the experimental drop hold-up, path of the droplets and velocity fields, showing that the coupled model can predict the hydrodynamics in a stirred extraction column.

In addition, a combined multi-fluid CFD-PBM model was developed by means of the SQMOM to overcome the shown drawbacks of the two-fluid approach. Benefits of the three-fluid approach using two primary particles in the SQMOM could be shown and compared to results of a two-fluid QMOM model. Nevertheless, the high computational load of such a multi-fluid model was also visible and discussed. Therefore, finally, the One Primary One Secondary Particle Method (OPOSPM), which is a very easy and efficient special case of the SQMOM, was introduced in CFD to simulate a pilot plant column of the RDC DN150. The OPOSPM offers the possibility of a one equation model for the solution of the PBM in CFD based on the d_{30} diameter instead of the classical Sauter mean droplet diameter. The previously modified model of Luo and Svendsen was applied as model for coalescence and breakage without changing parameters. The predicted results for the mean droplet diameter and the dispersed phase hold-up agree well with literature data. The results also show that the new CFD-PBM model is very efficient from computational point of view (two times less than the QMOM and five times less than the method of classes).

In summary, the CFD-PBM framework, the link between both tools and the solution methods for PBM were all well established, tested and validated. The predictivity of the coupled model varying different available closures for coalescence and breakage was also demonstrated for small column sections and even for a full pilot plant. Therefore, a platform is available for further investigations. This work should and will be continued to realize and establish a direct modelling and prediction of extraction columns in future. To accomplish this, future work should also include mass transfer, which was not considered in this work. The results already show that the coupled CFD-PBM algorithm is a suitable design tool, which has a huge potential for the layout of industrial columns. Besides, this software could be also applied to other industrial multiphase problems. On the other hand the results also pointed at some weaknesses of the combined approach, which are the models for coalescence and breakage, the multiphase turbulence models and the experimental data. The closures for coalescence and breakage still demand improvement, both phenomena are still not fully understood and are still important research topics. The same accounts for the multiphase turbulence models, especially the experimental validation. In addition, future experimental investigations should provide local drop sizes, volume fractions and droplet velocities in one compartment instead of measuring properties at fixed points for a better comparison and a further improvement of the CFD models.

The current results give rise to the expectation that the coupled CFD-PBM model will lead to a better prediction and simulation of the behaviour of counter-current extraction columns in future. The present work could achieve its aim and made an important step in this direction.

9 Symbols

a	coalescence kernel
B	birth rates
d	droplet diameter
d_{32}	Sauter mean diameter
d_{30}	mean mass diameter
D	death rates
F	interaction force
g	gravity
g	breakage frequency
h	collision frequency
h	source term
L	droplet size
L	abscissa
m_k	kth moment
n	number density function
n_d	number of daughter droplets
N_i	local average number density
N	number of droplets
p	pressure
r	internal coordinate
\dot{R}	velocity internal coordinate
Re	Reynolds number
S	source term
t	time
u	velocity
u'	instantaneous velocity
u'	fluctuating velocity
\bar{u}	average velocity
V	volume
x	external coordinate
\dot{X}	velocity external coordinate

Greek letters

α	volume fraction
β	probability density function
ε	turbulent energy dissipation
λ	coalescence efficiency
μ	dynamic viscosity
ν	kinematic viscosity
η	Kolmogorov length scale
ρ	density

Subscripts / Superscripts

l	liquid phase 1
d	dispersed phase
C	coalescence
B	breakage

Abbreviations

CFD	computational fluid dynamics
CM	classes method
DN	diameter nominal
DPBM	droplet population balance model
DPSPM	Direct Primary and Secondary Particle Method
DQMOM	Direct Quadrature Method of Moments
MOM	method of moments
MUSIG	Multiple-Size-Group
OPOSPM	One Primary One Secondary Particle Method
PBE	population balance equation
PBM	population balance model
PDF	probability density function
PIV	Particle Image Velocimetry
QMOM	Quadrature Method of Moments
RDC	Rotating Disc Contactor
rpm	revolutions per minute
SQMOM	Sectional Quadrature Method of Moments
UDF	user-defined functions

10 References

- Adrian, R.J. (2005). Twenty years of Particle Image Velocimetry. *Experiments in Fluids* 39, 159-169.
- Alekseenko, S.V., Bilsky, AV., Dulin, V.M., Markovich, D.M. (2007). Experimental study of an impinging jet with different swirl rates, *International Journal of Heat and Fluid Flow* 28, 1340-1359.
- Alopaeus, V., Koskinen, J., Keskinen, K.I. (1999). Simulation of the population balances for liquid-liquid systems in a nonideal stirred tank. Part 1 description and qualitative validation of the model. *Chemical Engineering Science* 54, 5887-5899.
- Alopaeus, V., Koskinen, J., Keskinen, K.I. (2002). Simulation of the population balances for liquid-liquid systems in a nonideal stirred tank. Part 2 Parameter fitting and the use of the multiblock model for dense dispersions. *Chemical Engineering Science* 57, 1815-1825.
- Alopaeus, V., Laakkonen, M., Aittamaa, J. (2006). Solution of population balances with breakage and agglomeration by high-order moment-conserving method of classes. *Chemical Engineering Science* 61, 6732-6752.
- Andersson, R., Andersson, B., Chopard, F., Noren, T. (2004). Development of a multi-scale simulation method for design of novel multiphase reactors. *Chemical Engineering Science* 59, 4911-4917.
- Andersson, R., Andersson, B. (2006a). Modeling the breakup of fluid particles in turbulent flows. *A.I.Ch.E. Journal* 52, 6, 2031-2038.
- Andersson, R., Andersson, B. (2006b). On the breakup of fluid particles in turbulent flows. *A.I.Ch.E. Journal* 52, 6, 2020-2030.
- Attarakih, M.M., Bart, H.-J., Faqir, N.M (2004). Numerical solution of the spatially distributed population balance equation describing the hydrodynamics of interacting liquid-liquid dispersions. *Chem. Eng. Sci.* 59, 2567-2592.
- Attarakih, M.M., Bart, H.-J., Lagar, L. G., Faqir N.M. (2006a). LLECMOD: A Windows-based program for hydrodynamics simulation of liquid-liquid extraction columns. *Chemical Engineering Processing* 45, 113.
- Attarakih, M.M., Bart, H.-J., Faqir, N.M (2006b). Numerical solution of the bivariate population balance equation for the interacting hydrodynamics and mass transfer in liquid-liquid extraction columns., *Chem. Eng. Sci.* 61, 113-123.
- Augier, F., Masbernat, O., Guiraud, P. (2003). Slip Velocity and Drag Law in a Liquid-Liquid Homogeneous Dispersed Flow. *A.I.Ch.E. Journal* 49, 2300-2316.
- Bahmanyar, H., Slater, M.J. (1991). Studies of drop-break-up in liquid-liquid systems in a rotating disc contactor part I: conditions of no mass transfer. *Chemical Engineering Technology* 14, 79-89.
- Baldi, S., Ducci, A., Yianneskis, M. (2004). Determination of Dissipation Rate in Stirred Vessels through Direct Measurement of Fluctuating Velocity Gradients, *Chemical Engineering Technology* 27, 275-281.
- Baldi, S., Yianneskis, M. (2003). On the Direct Measurement of Turbulence Energy Dissipation in Stirred Vessel with PIV, *Industrial & Engineering Chemistry Research* 42, 7006-7016.

- Baldi, S., Yianneskis, M. (2004). On the quantification of energy dissipation in the impeller stream of a stirred vessel from fluctuating velocity gradient measurements”, *Chemical Engineering Science* 59, 2659-2671.
- Bałyga, J., Orciuch, W. (2001). Barium Sulphate precipitation in a pipe – an experimental study and CFD modelling. *Chemical Engineering Science* 56, 2435-2444.
- Bart, H.-J. (2001). *Reactive Extraction*. Springer, Berlin.
- Bart, H.-J., Stevens, G. (2004). Reactive solvent extraction. In: *Ion Exchange and Solvent Extraction 17*, M. Kertes, A.K. Sengupta (Eds.), Marcel Dekker, New York, 37.
- Bart, H.-J., Garthe, D., Grömping, T., Pfennig, A., Schmidt, S., Stichlmair, J. (2006). Vom Einzeltropfen zur Extraktionskolonne. *Chemie Ingenieur Technik* 78, 5.
- Bart, H.-J., Drumm, C., Attarakih, M.M. (2008). Process Intensification with reactive extraction columns, *Chemical Engineering Processing* 47, 745.
- Bart, H.-J., Drumm, C., Steinmetz, T. (2009). Skalierung von Extraktionskolonnen. *CIT Plus* 1/2, 37-39.
- Bhole, M.R., Joshi, J.B., Ramkrishna, D. (2008). CFD simulation of bubble columns incorporating population balance modeling. *Chemical Engineering Science* 63, 2267-2282.
- Bove, S., Solberg, T., Hjertager, B.H. (2005). A novel algorithm for solving population balance equations: the parallel parent and daughter classes. Derivation, analysis and testing. *Chemical Engineering Science* 60, 1449-1464.
- Bröder, D., Sommerfeld, M. (2002). An advanced LIF-PLV system for analyzing the hydrodynamics in a laboratory bubble column at higher void fractions. *Experiments in Fluids* 33, 826-837.
- Budwig, R. (1994). Refractive index matching methods for liquid flow investigations. *Experiments in Fluids* 17, 350-355.
- Bujalski, J.M., Yang, W., Nikolov, J., Solnordal, C.B., Schwarz, M.P. (2006). Measurement and CFD simulation of single-phase flow in solvent extraction pulsed column. *Chemical Engineering Science* 61, 2930-2938.
- Buwa, V.V., Dhanannjay, S.D., Ranade, V.V. (2006). Eulerian-Lagrangian simulations of unsteady gas-liquid flows in bubble columns. *International Journal of Multiphase Flow* 32, 864-885.
- Casamatta, G. (1981): Comportement de la population des gouttes dans une colonne d'extraction: Transport, rupture, coalescence, transfer de matiere, Phd Thesis, Institut National Polytechnique De Toulouse.
- Chatzi, E., Lee, J.L. (1987). Analysis of interaction for liquid-liquid dispersion in agitated vessels. *Industrial & Engineering Chemistry Research* 26,2263-2267.
- Chen, P., Sanyal, J., Dudukovic, M. P. (2005). Numerical simulation of bubble column flows: effect of different breakup and coalescence closures. *Chemical Engineering Science* 60, 1085-1101.
- Cheung, S.C.P., Yeoh, G.H., Tu, J.Y. (2007). On the numerical study of isothermal vertical bubbly flow using two population balance approaches. *Chem. Eng. Sci.* 62, 4659-4674.
- Coulaloglou, C.A., Tavlarides, L.L. (1977). Description of interaction processes in agitated liquid-liquid dispersions. *Chemical Engineering Science* 32, 1289-1297.
- Chesters, A.K. (1991). The modelling of coalescence processes in fluid-liquid dispersions. A review of current understanding. *Trans IChemE* 69(A), 259-281.

- Deen, G.D., Hjertager, B.H. (1999). Multiphase Particle Image Velocimetry Measurements in an Aerated Stirred Tank. presented at Annual Meeting AIChE, Dallas.
- Deen, N.G., Westerweel, J., Delnoij, E. (2002). Two-phase PIV in Bubbly Flows: Status and Trends. *Chemical Engineering Technology* 25, 97-101.
- Deibele, L., Dohrn, R. (Eds.) 2006. *Miniplant-Technik in der Prozessindustrie*. Wiley-VCH, Weinheim.
- Diemer, R.B., Olson, J.H. (2002). A moment methodology for coagulation and breakage problems: Part 3 – generalized daughter distribution functions. *Chemical Engineering Science* 57, 4187-4198.
- Eastwood, C.D., Armi, L., Lasheras, J.C. (2004). The breakup of immiscible fluids in turbulent flows. *Journal of Fluid Mechanics* 502, 309-333.
- Ekambara, K., Dhotre, M.T. (2007). Simulation of oscillatory baffled column: CFD and population balance. *Chem. Eng. Sci.* 62, 7205-7213.
- Eiswirth, R.T., Bart, H.-J. (2008). Experimental Investigation of Droplet-Droplet Coalescence in Liquid-Liquid Systems. Proc. International Solvent Extraction Conference ISEC 2008, Moyer, B. (Ed.), Canadian Institute of Mining, Metallurgy and Petroleum, Montreal, Vol. 2, 1177-1182.
- Erwin, D.L. (2004). Liquid-Liquid Extraction. In: *Industrial Chemical Process Design*. McGraw-Hill, New York.
- Fan, R., Fox, R.O. (2008). Segregation in polydisperse fluidized beds: Validation of a multi-fluid model. *Chemical Engineering Science* 63, 272.
- Fan, R., Marchisio, D.L., Fox, R.O. (2004). Application of the Direct Quadrature Method of Moments to Polydisperse Gas-Solid Fluidized Beds. *Powder Technology* 139, 7.
- Fei, W.Y., Wang, Y.D., Wan, Y.K. (2000). Physical modeling and numerical simulation of velocity fields in rotating disc contactor via CFD simulation and LDV measurements. *Chemical Engineering Journal* 78, 131-139.
- Fei, W.Y., Wang, Y.D., Song, X.Y., Yin, Y.D., Sun, L.Y. (2003). Intensification of random packing via CFD simulation, PIV measurement and traditional experiments. *Journal of Chemical Technology and Biotechnology* 78, 142-145.
- Fluent Inc. (2005). *Fluent 6.2 User's Guide*. Lebanon, USA.
- Fluent Inc. (2006). *Fluent 6.3 Population Balance Module Manual*. Lebanon, USA.
- Gabriele, A., Nienow, A.W., Simmons, M.J.H. (2009). Use of angle resolved PIV to estimate local specific energy dissipation rates for up-and down-pumping pitched blade agitators in a stirred tank. *Chemical Engineering Science* 64, 126-143.
- Ghaniyari-Benis, S., Hedayat, N., Ziyari, A., Kazemzadeh, M., Shafiee, M. (2009). Three-Dimensional Simulation of Hydrodynamics in a Rotating Disc Contactor using Computational Fluid Dynamics. *Chemical Engineering Technology* 32, 93-102.
- Godfrey, J.C, Slater, M.J. (Eds.) (1994). *Liquid – Liquid Extraction Equipment*. John Wiley & Sons, West Sussex.
- Goeddecke, R. (Ed.) 2006. *Fluidverfahrenstechnik*. Wiley-VCH, Weinheim.
- Gosman, A.D., Lekakou, C., Politis, S., Issa, R.I., Looney, M.K. (1992). Multidimensional Modelling of Turbulent Two-Phase Flows in Stirred Vessels. *A.I.Ch.E. Journal* 38, 1946-1956.

- Gourdon, C., Casamatta, G.A., Muratet, G. (1994). Population balance based modelling. In: Liquid – Liquid Extraction Equipment., J.C. Godfrey and M.J. Slater (Eds.), John Wiley & Sons, West Sussex, 141-226.
- Grosch, R., Briesen, H., Marquardt, W. (2007). Generalization and Numerical Investigation of QMOM. *A.I.Ch.E. Journal* 53, 207-227.
- Gurker, T., Haderer, T., Marr, R. (2008). CFD-Supported Design in Liquid-Liquid Extraction. *Proc. International Solvent Extraction Conference ISEC 2008*, Moyer, B. (Ed.), Canadian Institute of Mining, Metallurgy and Petroleum, Montreal, Vol. 2, 1177-1182.
- Haderer, T. (2004). CFD-Simulation der Hydrodynamik einer gerührten Extraktionskolonne und Vergleich mit experimentell ermittelten hydrodynamischen Kenngrößen. PhD thesis, TU Graz.
- Haderer, T., Marr, R., Martens, S., Siebenhofer, M. (2005). Bestimmung auslegungsrelevanter hydrodynamischer Kenngrößen einer RDC-Extraktionskolonne mit CFD, *Chemie Ingenieur Technik* 77, 1055-1055.
- Hagesaether, L., Jakobsen, H.A., Svendsen, H.F. (2002). A model for turbulent binary breakup of dispersed fluid particles. *Chemical Engineering Science* 57, 3251-3267.
- Hagesaether, L. (2002). Coalescence & Break-up of Drops and Bubbles. PhD thesis, Norwegian University of Science and Technology, Trondheim, Norway.
- Henschke, M., Schlieper, L.H., Pfennig, A. (2002). Determination of Coalescence Parameter from Batch-Settling Experiments. *Chemical Engineering Journal* 85, 369.
- Hosokawa, S., Sou, A., Tomiyama, A. (2007). Multi-fluid simulation of turbulent bubbly pipe flows, *Proceedings of the ICMF-2007*, M. Sommerfeld (Ed.), 6th International Conference on Multiphase Flow, Leipzig.
- Hounslow, M.J., Ryall, R.L., Marshall, V.R. (1988). A discretized population balance for nucleation, growth and aggregation. *A.I.Ch.E. Journal* 34, 1821-1832.
- Hulburt, H.M., Katz, S. (1964). Some problems in particle technology. *Chemical Engineering Science* 19, 555-574.
- Jakobsen, H.A., Lindborg, H., Dorao, C.A. (2005). Modeling of bubble column reactors: Progress and limitations. *Industrial Engineering & Chemistry Research* 44, 5107-5151.
- John, V., Angelov, I., Öncül, A.A., Thévenin, D. (2007). Techniques for the reconstruction of a distribution from a finite number of its moments. *Chemical Engineering Science* 62, 2890-2904.
- Kankaanpää, T. (2007). CFD Procedure for Studying Dispersion Flows and Design Optimization of the Solvent Extraction Settler. PhD thesis, Helsinki University of Technology, Finland.
- Kerdouss, F., Bannari, A., Proulx, P., Bannari, R., Skrga, M., Labreque, Y. (2008). Two-phase mass transfer coefficient prediction in stirred vessel with a CFD model. *Computers and Chemical Engineering* 32, 1943-1955.
- Kolb, P. (2004). Hydrodynamik und Stoffaustausch in einem gerührten Miniplantextraktor der Bauart Kühni. PhD thesis, TU Kaiserslautern.
- Kolb, P., Bart, H.-J., Fischer, L. (2002). Entwicklung einer Miniplant-Extraktionskolonne, *Chemie Ingenieur Technik* 74, 243-247.
- Kompenhans, J., Raffel, M., Dieterle, L., Dewhirst, T. Vollmers, H., Ehrenfried, K., Willert, C., Pengel, K., Kähler, C., Schröder, A., Ronneberger, O. (1998). Particle Image

- Velocimetry in Aerodynamics: Technology and Applications in Wind Tunnels. Proc. Of VSJ-SPIE98, Yokohama.
- Kosters, W.C.G. (1983). Rotating Disc Contactor. In: Handbook of Solvent Extraction, T.C. Lo, M.H.I. Baird, C. Hanson (Eds.), John Wiley & Sons, New York.
- Krepper, E., Frank, T., Lucas, D., Prasser, H.-M., Zwart, P.J., (2007). Inhomogeneous MUSIG model – a population balance approach for polydispersed bubbly flows. In Proc. of the 6th International Conference on Multiphase Flow ICMF-2007, Sommerfeld, M. Ed., Leipzig, Germany.
- Krepper, E., Lucas, D., Frank, T., Prasser, H.-M., Zwart, P.J., (2008). The Inhomogeneous MUSIG model for the simulation of polydispersed flows. Nuclear Engineering and Design 238, 1690.
- Kronberger, T.A., Ortner, A., Zulehner, W., Bart, H.-J., (1995). Numerical simulation of extraction columns using a drop population model. Computers and Chemical Engineering 19, 639-644.
- Kumar, S., Ramkrishna, D. (1996a). On the solution of population balance equations by discretization – I. A fixed pivot technique. Chemical Engineering Science 51, 1311-1332.
- Kumar, S., Ramkrishna, D. (1996b). On the solution of population balance equations by discretization – II. A moving pivot technique. Chemical Engineering Science 51, 1333-1342.
- Laakkonen, M., Moilanen, P., Alopaeus, V., Aittamaa, J. (2007). Modelling Local Gas-Liquid Mass Transfer in Agitated Vessels. Chemical Engineering Research and Design 85, 665-675.
- Laín, S., Bröder, D., Sommerfeld, M., Göz, M.F. (2002). Modelling hydrodynamics and turbulence in a bubble column using the Euler-Lagrange procedure. International Journal of Multiphase Flow 28, 1381-1407.
- Lane, G.L., Schwarz, M.P., Evans, G.M. (2005). Numerical Modelling of gas-liquid flow in stirred tanks. Chemical Engineering Science 60, 2203-2214.
- Lasheras, J.C., Eastwood, C., Martínez-Bazán, C., Montañés, J.L. (2002). A review of statistical models for the break-up of an immiscible fluid immersed into a fully developed turbulent flow. International Journal of Multiphase Flow 28, 247-278.
- Launder B.E., Spalding, D.B. (1972). Lectures in Mathematical Models of Turbulence. Academic Press, London, England.
- Launder B.E., Reece, G.J., Rodi, W. (1975). Progress in the Development of a Reynolds-Stress Turbulence Closure. Journal of Fluid Mechanics 68, 537-566.
- Lehr, F., Millies, M., Mewes, D. (2002). Bubble-size distributions and flow fields in bubble columns. A.I.Ch.E. Journal 48, 2426-2442.
- Lindken, R., Merzkirch, W. (2002). A novel PIV technique for measurements in multiphase flows and its application to two-phase bubbly flows. Experiments in Fluids 33, 814-825.
- Litster, J.D., Smit, D.J., Hounslow, M.J. (1995). Adjustable discretization population balance for growth and aggregation. A.I.Ch.E. Journal 41, 591-603.
- Lo, S. (2000). Application of population balance to CFD modelling of gas-liquid reactors. Proc. “Trends in numerical and physical modeling for industrial multiphase flows”, Corsica, France.
- Luo, H. (1993). Coalescence, Breakup and Liquid Circulation in Bubble Column Reactors. PhD thesis, University of Trondheim, Norway.

- Luo, H., Svendsen, H.F. (1996). Theoretical model for drop and bubble breakup in turbulent dispersions. *A.I.Ch.E. Journal* 42, 1225-1233.
- Maaß, S., Gäbler, A., Zaccone, A., Paschedag, A.R., Kraume, M. (2007). Experimental Investigations and Modelling of Breakage Phenomena in Stirred Liquid/Liquid Systems. *Chemical Engineering Research and Design* 85, 703-709.
- Maaß, S., Wollny, S., Sperling, R., Kraume, M. (2009). Numerical and experimental analysis of particle strain and breakage in turbulent dispersions. *Chemical Engineering Research and Design* 87, 565-572.
- Marchisio, D.L., Pikturna, J.T., Fox, R.O., Vigil, R.D., Barresi, A.A., (2003a). Quadrature method of moments for population-balance equations. *A.I.Ch.E. Journal* 49, 1266-1276.
- Marchisio, D.L., Vigil, R.D., Fox, R.O., (2003b). Implementation of the quadrature method of moments in CFD codes for aggregation-breakage problems. *Chemical Engineering Science* 58, 3337-3351.
- Marchisio, D.L. Vigil, R.D., Fox, R.O. (2003c). Quadrature method of moments for aggregation-breakage processes. *Journal of Colloid and Interface Science* 258, 322-334.
- Marchisio, D.L., Fox, R.O. (2005). Solution of population balance equation using the direct quadrature method of moments. *Journal of Aerosol Science* 36, 43-73.
- Marchisio, D.L., Fox, R.O. (Eds.) (2007). *Multiphase reacting flows: modelling and simulation*, CISM International Centre for Mechanical Sciences , Number 492, Springer, Wien New York.
- Martínez-Bazán, C., Montañés, J.L., Lasheras, J.C., (1999a). On the breakup of an air bubble injected into a fully developed turbulent flow. Part 1. breakup frequency. *Journal of Fluid Mechanics* 401, 157-182.
- Martínez-Bazán, C., Montañés, J.L., Lasheras, J.C., (1999b). On the breakup of an air bubble injected into a fully developed turbulent flow. Part 2. Size PDF of the resulting daughter bubbles. *Journal of Fluid Mechanics* 401, 183-207.
- McGraw, R. (1997). Description of Aerosol Dynamics by the Quadrature Method of Moments. *Aerosol Science and Technology* 27, 255-265.
- Modes, G.. (2000). *Grundlegende Studie zur Populationsdynamik einer Extraktionskolonne auf Basis von Einzeltropfenuntersuchungen*. Dr.-Ing. Thesis TU Kaiserslautern, Shaker Verlag, Aachen.
- Modes, G., Bart, H.-J. (2001). CFD simulation of nonideal dispersed phase flow in stirred extraction columns. *Chemical Engineering Technology* 24, 1242-1245.
- Mohanty, S. (2000). Modeling of liquid-liquid extraction column: A review. *Reviews in Chemical Engineering* 16, 199.
- Mukhopadhyay, A., Devulapalli, B., Dutta, A., Grald, E.W. (2004). Computational Fluid Dynamics: A virtual prototyping tool for materials engineering. *Journal of the Minerals, Metals and Materials Society* 56, 44.
- Murthy, B.N., Joshi, J.B. (2008). Assessment of standard k- ϵ , RSM and LES turbulence models in a baffled stirred vessel agitated by various impeller designs. *Chemical Engineering Science* 63, 5468-5495.
- Newton, T., Connolly, D., Mokhatab, S. (2007). Tools to model multiphase separation. *Chemical Engineering Progress* 103, 26-32.
- Nopens, I. (2005). *Modelling the activated sludge flocculation process: a population balance approach*. Ph.D. thesis, Universiteit Gent.

- Nopens, I., Briesen, H., Ducoste, J. (2009). Celebrating a milestone in Population Balance Modelling. *Chemical Engineering Science* 64, 627.
- Olmos, E., Gentric, C., Vial, C., Wild, G., Midoux, N. (2001). Numerical simulation of multiphase flow in bubble column reactors. Influence of bubble coalescence and break-up. *Chem. Eng. Sci.* 56, 6359-6365.
- Pan, G., Meng, H. (2001). Experimental Study of Turbulent Mixing in a Tee Mixer Using PIV and PLIF. *A.I.Ch.E. Journal* 47, 2653-2665.
- Petitti, M., Caramellino, M., Marchisio, D.L., Vanni, M. (2007). Two-scale simulations of mass transfer in an agitated gas-liquid tank. In *Proc. of the 6th International Conference on Multiphase Flow ICMF-2007*, Sommerfeld, M. Ed., Leipzig, Germany.
- Pfennig, A., Pilhofer, T., Schröter, J. (2006). Flüssig-Flüssig Extraktion. In: *Fluidverfahrenstechnik Band 2*, Goedecke, R. (Hrsg.), Wiley-VCH, Weinheim.
- Pfleger, D., Becker, S. (2001). Modelling and simulation of the dynamic flow behaviour in a bubble column. *Chemical Engineering Science* 56, 1737-1747.
- Podila, K., Al Taweel, A.M., Koksal, M., Troshko, A., Gupta, Y.P. (2007). CFD simulation of gas-liquid contacting in tubular reactors. *Chem. Eng. Sci.* 62, 7151-7162.
- Pope, S.B. (1979). Probability distributions of scalars in turbulent shear flow. In *Turbulent shear flows 2: Selected Papers from the Second International Symposium. on Turbulent Shear Flows*, Springer, Berlin, 7–16.
- Prasad, A.K. (2000). Particle Image Velocimetry. *Current Science*, 79, 51-60.
- Press, W.H., Teukolsky, S.A., Vetterling, W.T., Flannery B.P. (2007). *Numerical Recipes: The Art of Scientific Computing*. Third Edition, Cambridge University Press.
- Prince, M. J., Blanch, H.W. (1990). Bubble coalescence and break-up in air-sparged bubble columns. *A.I.Ch.E Journal* 36, 1485-1499.
- Raffel, M., Willert, C., Kompenhans, J. (1998). *Particle image velocimetry, a practical guide*. Springer, Berlin Heidelberg New York.
- Ramkrishna, D. (1985). The Status of Population Balances. *Reviews in Chemical Engineering* 3, 49.
- Ramkrishna, D. (2000). *Population balances : theory and applications to particulate systems in engineering*. Academic Press, San Diego.
- Retieb, S., Guiraud, P., Angelov, G., Gourdon, C. (2007). Hold-up within two-phase countercurrent pulsed extraction columns via Eulerian simulations. *Chemical Engineering Science* 62, 4558-4572.
- Rieger R., Weiss, C., Wigley, G., Bart, H.-J., Marr, R. (1996). Investigating the process of liquid-liquid extraction by means of computational fluid dynamics. *Computers and Chemical Engineering* 20, 1467-1475.
- Robbins, L.A., Cusack, R.W. (1997). Liquid-Liquid Extraction Operations & Equipment. In: *Perry's Chemical Engineers' Handbook*, Perry, R.H., Green, D.W., Maloney, J.O. (Eds.), 7th Edition, McGraw-Hill, New York.
- Rydberg, J., Musikas, C., Choppin, G.R. (1992). *Principles and Practices in Solvent Extraction*. Marcel Dekker, New York.
- Saarenrinne, P., Piiro, M. (2000). Turbulent kinetic energy dissipation rate estimation from PIV velocity vector fields, *Experiments in Fluids* 29, 300-307.
- Saarenrinne, P., Piiro, M., Eloranta, H. (2001). Experiences of turbulence measurement with PIV", *Measurement Science and Technology* 12, 1904-1910.

- Santos, C.M., Dionisio, R., Cerqueira, H.S., Sousa-Aguiar, E.F., Mori, M., d'Avila, M.A. (2007). Three-Dimensional Gas-Liquid CFD Simulations in Cylindrical Bubble Columns. *International Journal of Chemical Reactor Engineering* 5, 1.
- Sanyal, J., Vasquez, S., Shantau, R., Dudukovic, M.P. (1999). Numerical Simulation of gas-liquid dynamics in cylindrical bubble column reactors. *Chemical Engineering Science* 54, 5071-5084.
- Sanyal, J., Marchisio, D.L., Fox, R.O., Dhanasekharan, K., (2005). On the comparison between population balance models for CFD simulation of bubble columns. *Industrial & Engineering Chemistry Research* 44, 5063-5072.
- Sattler, K. (1988). *Thermische Trennverfahren*. Wiley VCH, Weinheim.
- Scargiali, F., D'Orazio, A., Grisafi, F., Brucato, A. (2007). Modelling and Simulation of Gas-Liquid Hydrodynamics in Mechanically Stirred Tanks. *Chemical Engineering Research and Design* 85, 637-646.
- Schlauch, S., (2006). Numerical simulation of stirred liquid-liquid systems. *Proceedings in Applied Mathematics and Mechanics* 6, 541-542.
- Schiller, L., Naumann, Z., (1935). Über die grundlegenden Berechnungen bei der Schwerkraftaufbereitung. *Zeitschrift des Vereines Deutscher Ingenieure* 77, 318.
- Schmidt, S.A., (2006). Populationsdynamische Simulation gerührter Extraktionskolonnen auf der Basis von Einzeltropfen- und Tropfenschwarmuntersuchungen. Dr.-Ing. Thesis, Shaker Verlag, Aachen.
- Schmidt, S.A., Simon, M., Attarakih, M.M., Lagar, L.G., Bart, H.-J., (2006). Droplet population balance modelling - hydrodynamics and mass transfer. *Chemical Engineering Science* 61, 246-256.
- Sha, Z., Laari, A., Turunen, I. (2006). Multi-Phase-Multi-Size-Group Model for the Inclusion of Population Balances into the CFD simulation of Gas-Liquid Bubbly Flows. *Chem. Eng. Tech.* 29, 550-559.
- Shih, T.-H., Liou, W.W., Shabbir, A., Yang Z., Zhu, J. (1995). A New k-Eddy-Viscosity Model for High Reynolds Number Turbulent Flows - Model Development and Validation. *Computers and Fluids* 24, 227-238.
- Simon, M., Bart H.-J. (2002). Experimental Studies of Coalescence in Liquid-Liquid Systems. *Chemical Engineering Technology* 25, 481-484.
- Simon, M., (2004). Koaleszenz von Tropfen und Tropfenschwärmen. Dr.-Ing. Thesis TU Kaiserslautern, Kaiserslautern.
- Sovova, H. (1981). Breakage and Coalescence of Drops in a Batch Stirred Vessel – II Comparison of Model and Experiment. *Chem. Eng. Sci.* 36, 1567-1573.
- Steinmetz, T., Schmidt, S., Attarakih, M.M., Bart, H.-J., (2005). Droplet population balancing for column simulation, Proc. of the International Solvent Extraction Conference (ISEC 2005), China Academic Journal (compact disc version) Electronic Publishing House, Beijing, 997-1003.
- Svensson, F.J.E., Rasmuson, A. (2004). LDA-Measurements in a Stirred Tank with a Liquid-Liquid System at High Volume Percentage Dispersed Phase. *Chemical Engineering Technology* 27, 335-339.
- Thornton, J.D. (1992). *Science and Practice of Liquid-Liquid Extraction*. University Press, Oxford.

- Tiwari, S., Kuhnert, J. (2002). A meshfree method for incompressible fluid flows with incorporated surface tension, *Revue Européenne des Éléments Finis (Meshfree and particle based approaches in computational mechanics)*, Breitkopf, P., Huerta, A. (Eds.), 11, 965-987.
- Tiwari, S., Kuhnert, J. (2007). Modeling of two-phase flows with surface tension by Finite Pointset Method (FPM), *Journal of Computational and Applied Mathematics* 203, 376-386.
- Tiwari, S., Antonov, S., Hietel, D., Kuhnert, J., Olawsky, F., Wegener, R. (2006). A meshfree Method for Simulations of Interactions between Fluids and Flexible Structures, *Lecture Notes in Computational Science and Engineering: Meshfree Methods for Partial Differential Equations III*, M. Griebel, M.A. Schweitzer (Eds.), Vol. 57, 249-264, Springer.
- Tobin, T., Ramkrishna, D. (1999). Modeling the Effect of Drop Charge in Turbulent Liquid-Liquid Dispersions. *Canadian Journal of Chemical Engineering* 77, 1090-1104.
- Tomiyama, A., Shimada, N., (2001). A numerical method for bubbly flow simulation based on a multi-fluid model. *Journal of Pressure Vessel Technology* 123, 510-516.
- Tsouris, C., Tavlarides, L.L. (1994). Breakage and Coalescence Models for Drops in Turbulent Dispersions. *A.I.Ch.E. Journal* 40, 395-406.
- Valentas, K.J., Amundson, N.R. (1966). Breakage and coalescence in dispersed phase systems. *Industrial & Engineering Chemistry Fundamentals* 5, 533-542.
- Valentas, K.J., Bilous, O., Amundson, N.R. (1966). Analysis of breakage in dispersed phase systems. *Industrial & Engineering Chemistry Fundamentals* 5, 271-279.
- Vankova, N., Tcholakova, S., Denkov, N.D., Vulchev, V.D., Danner, T. (2007). Emulsification in turbulent flow 2. Breakage rate constants. *Journal of Colloid and Interface Science* 313, 612-629.
- Vanni, M. (2000). Approximate population balance equations for aggregation-breakage processes. *Journal of Colloid & Interface Science* 221, 143-160.
- Venneker, B.C.H., Derksen, J.J., Van den Akker, H.E.A. (2002). Population Balance Modeling of Aerated stirred vessels based on CFD. *AIChE Journal* 48, 673-685.
- Vikhansky, A., Kraft, (2004). Modelling of a RDC using a combined CFD-population balance approach. *Chemical Engineering Science* 59, 2597-2606.
- Wan, B., Ring, T.A., Dhanasekharan, K., Sanyal, J. (2006). Verification of SMOM and QMOM Population Balance Modeling in CFD code Using Analytical Solutions for Batch Particulate Processes. *China Particuology* 4, 243-249.
- Wang, T., Wang, J., Jin, Y. (2003). A novel theoretical breakup kernel function for bubbles/droplets in a turbulent flow. *Chemical Engineering Science* 58, 4629-4637.
- Wang, F., Mao, Z.-S., (2005). Numerical and experimental investigation of liquid-liquid two-phase flow in stirred tanks. *Industrial & Engineering Chemistry Research* 44, 5776-5787.
- Wang, T., Wang, J., Jin, Y., (2006). A CFD-PBM coupled model for gas-liquid flows. *A.I.Ch.E. Journal* 52, 125-140.
- Wang, T., Wang, J. (2007). Numerical Simulations of Gas-Liquid Mass Transfer in Bubble Columns with a CFD-PBM coupled model. *Chemical Engineering Science* 62, 7107-7118.
- Weiss, C., Bart, H.-J., (1993). Calculation of Flow Patterns in an RDC based on Computational Fluid-Dynamic Methods. In *Solvent Extraction in the Process Industry*, vol. 2, D.H. Logsdail and M.J. Slater, (Eds.), Elsevier Applied Science, London, 1191-1197.

- You, X., Bart, H.-J., (2003). Comparison of the Reynolds-averaged Turbulence Models on Single Phase Flow Simulation in Agitated Extraction Columns. *Chinese Journal of Chemical Engineering* 11, 362-366.
- You, X., Xiao, X., (2005). Simulation of the three-dimensional two-phase flow in stirred extraction columns by Lagrangian-Eulerian method. *Chemical and biochemical engineering quarterly* 19, 1-11.
- Zhang, D., Deen, N.G., Kuipers, J.A.M. (2006). Numerical simulation of the dynamic flow behaviour in a bubble column: A study of closures for turbulence and interface forces. *Chemical Engineering Science* 61, 7593-7608.

Own publications

- Attarakih, M. M., Zeidan, D., Drumm, C., Tiwari, S., Kuhnert, J., Allaboun, H., Bart, H.-J. (2008). Dynamic Modelling of Liquid Extraction Columns using the Direct Primary and Secondary Particle Method (DPSPM), Proc. 6th International Conference on Computational Fluid Dynamics in the Oil & Gas, Metallurgical and Process Industries CFD 2008, Johansen, S.T., Olsen, J.E., Ashrafiyan, A. (Eds.), Trondheim, Norway.
- Attarakih, M. M., Drumm, C., Bart, H.-J. (2009a). Solution of the Population Balance equation using the Sectional Quadrature Method of Moments, *Chemical Engineering Science* 64, 742.
- Attarakih, M. M., Jaradat, M., Drumm, C., Bart, H.-J., Tiwari, S., Sharma, V.K., Kuhnert, J., Klar, A. (2009b). Solution of the Population Balance Equation using the One Primary and One Secondary Particle Method (OPOSPM). Proc. ESCAPE 19, Jezowski J., Thullie, J. (Eds.), Cracow, Poland.
- Attarakih, M. M., Jaradat, M., Drumm, C., Bart, H.-J., Tiwari, S., Sharma, V.K., Kuhnert, J., Klar, A. (2009c). A multivariate Population Balance Model for Liquid Extraction Columns. Proc. ESCAPE 19, Jezowski J., Thullie, J. (Eds.), Cracow, Poland.
- Bart, H.-J., Drumm, C., Steinmetz, T. (2009). Skalierung von Extraktionskolonnen. *CIT Plus* 1/2, 37-39.
- Bart, H.-J., Drumm, C., Attarakih, M.M. (2008). Process Intensification with reactive extraction columns, *Chemical Engineering Processing* 47, 745.
- Drumm, C., Bart, H.-J. (2006a). Hydrodynamics in a RDC Extractor: Single and Two-Phase PIV Measurements and CFD Simulations, *Chemical Engineering Technology* 29, 1297.
- Drumm, C., Bart, H.-J. (2006b). Bestimmung der Hydrodynamik in einer gerührten Extraktionskolonne vom Typ RDC mit Hilfe der Particle Image Velocimetry, Proc. 14. Gala Fachtagung Lasermethoden in der Strömungsmesstechnik, Braunschweig.
- Drumm, C., Bart, H.-J. (2007a). Computational Fluid Dynamics-Simulation der Ein- und Zweiphasenströmung in einer Rotating Disc Contactor-Extraktionskolonne. *Chemie Ingenieur Technik* 79, 68.
- Drumm, C., Bart, H.-J. (2007b). Coupling of CFD with DPBM: Drop Size Distributions and Flow Fields in a RDC Extractor, Proc. International Conference on Multiphase Flow ICMF 2007, M. Sommerfeld (Ed.), Leipzig.
- Drumm, C., Attarakih, M.M., Tiwari, S., Kuhnert, J., Bart, H.-J. (2008a). Implementation of the Sectional Quadrature Method of Moments in a CFD code, Proc. 6th International

- Conference on Computational Fluid Dynamics in the Oil & Gas, Metallurgical and Process Industries CFD 2008, Johansen, S.T., Olsen, J.E., Ashrafian, A. (Eds.), Trondheim, Norway.
- Drumm, C., Tiwari, S., Attarakih, M. M., Kuhnert, J., Bart, H.-J. (2008b). CFD-PBM coupled model using the Finite Pointset Method and the SQMOM, Proc. International Solvent Extraction Conference ISEC 2008, Moyer, B. (Ed.), Canadian Institute of Mining, Metallurgy and Petroleum, Montreal, Vol. 2, 1177-1182.
- Drumm, C., Tiwari, S., Kuhnert, J., Bart, H.-J. (2008c). Finite Pointset Method for Simulation of the Liquid-Liquid Flow Field in an Extractor, Computers & Chemical Engineering 32, 2946.
- Drumm, C., Attarakih, M.M., Bart, H.-J. (2009). Coupling of CFD with DPBM for a RDC Extractor, Chemical Engineering Science 64, 721.
- Drumm, C., Hlawitschka M., Bart, H.-J. (2010a). CFD Simulations and Particle Image Velocimetry Measurements in an Industrial Scale Rotating Disc Contactor, AIChE Journal, doi:10.1002/aic.12249.
- Drumm, C., Hlawitschka M., Attarakih, M.M., Bart, H.-J. (2010b). One-Group Reduced Population Balance Model for CFD Simulation of a Pilo-Plant Extraction Column, Industrial Engineering Chemistry Research 49, 3442.
- Tiwari S., Drumm, C., Kuhnert, J., Bart, H.-J. (2008a). Coupling of the CFD and the Droplet Population Balance Equation with Finite Pointset Method, Lecture Notes in Computational Science and Engineering: Meshfree Methods for Partial Differential Equations IV, M. Griebel, M.A. Schweitzer (Eds.), Vol. 65, Springer.
- Tiwari, S., Drumm, C., Sharma, V.K., Kuhnert, J., Attarakih, M.M., Klar, A. and Bart, H.-J. (2008b). A Meshfree CFD-Population Balance Equation Coupled Model, Proc. 6th International Conference on Computational Fluid Dynamics in the Oil & Gas, Metallurgical and Process Industries CFD 2008, Johansen, S.T., Olsen, J.E., Ashrafian, A. (Eds.), Trondheim, Norway.

Lectures

(presenting author is underlined)

- C. Drumm, M.M. Attarakih, V.K. Sharma, S. Tiwari, J. Kuhnert, H.-J. Bart (2009). „Eingleichungsmodell zur Lösung der Populationsbilanzen in CFD“. ProcessNet Fachausschüsse Extraktion, CFD & Mischvorgänge, March 30 - April 1, Fulda.
- H.-J. Bart, T. Steinmetz, C. Drumm (2008). "Kolonnenskalierung mit Miniplants, Populationsbilanzen und CFD". ProcessNet Jahrestagung, October 7-9, Karlsruhe.
- C. Drumm, S. Tiwari, M.M. Attarakih, J. Kuhnert, H.-J. Bart (2008). "CFD-PBM coupled model using the Finite Pointset Method and the SQMOM". International Solvent Extraction Conference ISEC 2008, September 15-19, Tucson, USA.
- C. Drumm, S. Tiwari, M.M. Attarakih, J. Kuhnert, H.-J. Bart (2008). "Implementation of the Sectional Quadrature Method of Moments in a CFD code". 6th International Conference on Computational Fluid Dynamics in the Oil & Gas, Metallurgical and Process Industries CFD 2008, June 10-12, Trondheim.

- M.M. Attarakih, D. Zeidan, C. Drumm, S. Tiwari, J. Kuhnert, H.-J. Bart (2008). "Dynamic Modelling of Liquid Extraction Columns using the Direct Primary and Secondary Particle Method (DPSPM)". 6th International Conference on Computational Fluid Dynamics in the Oil & Gas, Metallurgical and Process Industries CFD 2008, June 10-12, Trondheim.
- S. Tiwari, C. Drumm, V.K. Sharma, J. Kuhnert, M. Attarakih, A. Klar and H.-J. Bart (2008). "A Meshfree CFD-Population Balance Equation Coupled Model". 6th International Conference on Computational Fluid Dynamics in the Oil & Gas, Metallurgical and Process Industries CFD 2008, June 10-12, Trondheim.
- C. Drumm, H.-J. Bart (2008). "Verknüpfung von CFD und Populationsbilanzen – Lösungsmethoden und Modelle". Annual meeting ProcessNet Fachausschüsse Extraktion & Phytoextraktion, April 16-18, Clausthal-Zellerfeld.
- C. Drumm, M.M. Attarakih, H.-J. Bart, S. Tiwari, J. Kuhnert (2008). "Computational Fluid Dynamics und Populationsbilanzen: Aktuelle Entwicklungen und Anwendungsbeispiele aus der flüssig-flüssig Extraktion". Annual meeting ProcessNet Fachausschüsse Adsorption und Fluidverfahrenstechnik, March 13-14, Bingen.
- C. Drumm, S. Tiwari, J. Kuhnert, H.-J. Bart (2007). "Verknüpfung von Populationsbilanzmodellen PBM und der Finite Pointset Methode FPM bei der Extraktion". ProcessNet Jahrestagung, October 16-18, Aachen.
- C. Drumm, H.-J. Bart (2007). "Coupling of CFD with DPBM for a RDC Extractor". International Conference on Population Balance Modelling, September 19-21, Quebec.
- S. Tiwari, J. Kuhnert, C. Drumm, H.-J. Bart (2007). "Coupling of the CFD and the Droplet Population Balance Equation with Finite Pointset Method". International Workshop Meshfree Methods for Partial Differential Equations, September 17-20, Bonn
- C. Drumm, H.-J. Bart (2007). "Coupling of CFD with DPBM: Drop Size Distributions and Flow Fields in a RDC Extractor". International Conference on Multiphase Flow, July 9-13, Leipzig.
- C. Drumm, H.-J. Bart (2007). "Verknüpfung von Computational Fluid Dynamics mit den Tropfenpopulationsbilanzen", Annual meeting ProcessNet Fachausschuss "Extraktion", March 22-23, Asselheim.
- C. Drumm, H.-J. Bart (2007). "CFD Simulationen der turbulenten Strömung in einer gerührten Extraktionskolonne", Annual meeting ProcessNet Fachausschuss CFD, March 5-6, Würzburg.
- C. Drumm, H.-J. Bart (2006). "Bestimmung der Hydrodynamik in einer gerührten Extraktionskolonne vom Typ RDC mit Hilfe der Particle Image Velocimetry". Gala Lasermethoden in der Strömungsmesstechnik, September 5-7, Braunschweig.
- C. Drumm, H.-J. Bart (2006). "Two-Phase Simulation of a RDC Extractor". Multi-Phase Flow: Simulation, Experiment and Application, July 26-29, Dresden.
- C. Drumm, H.-J. Bart (2006). "CFD Simulation der Ein- und Zweiphasenströmung in einer RDC Extraktionskolonne", Annual meeting DECHEMA/GVC Fachausschuss "Extraktion", May 22-24, Würzburg.

Supervised diploma thesis

- Nowatschin, M. (2006). Untersuchung der Zweiphasenströmung in einer RDC Extraktionskolonne mit Hilfe der Particle Image Velocimetry, Diplomarbeit, TU Kaiserslautern.
- Hlawitschka, M. (2007). CFD Simulation der Zweiphasenströmung in einer RDC Extraktionskolonne, Studienarbeit, TU Kaiserslautern.
- Gruselle, C. (2008). CFD-Simulation der Einphasenströmung in einer RDC-Extraktionskolonne mit 450 mm Durchmesser, Studienarbeit, TU Kaiserslautern.
- Robineau, J.-L. (2008). Particle Image Velocimetry Messungen der Einphasenströmung in einer RDC-Extraktionskolonne mit 450 mm Durchmesser, Studienarbeit, TU Kaiserslautern.
- Elfendahl, C. (2009). CFD-Simulation einer RDC-Extraktionskolonne im Technikumsmaßstab, Studienarbeit, TU Kaiserslautern

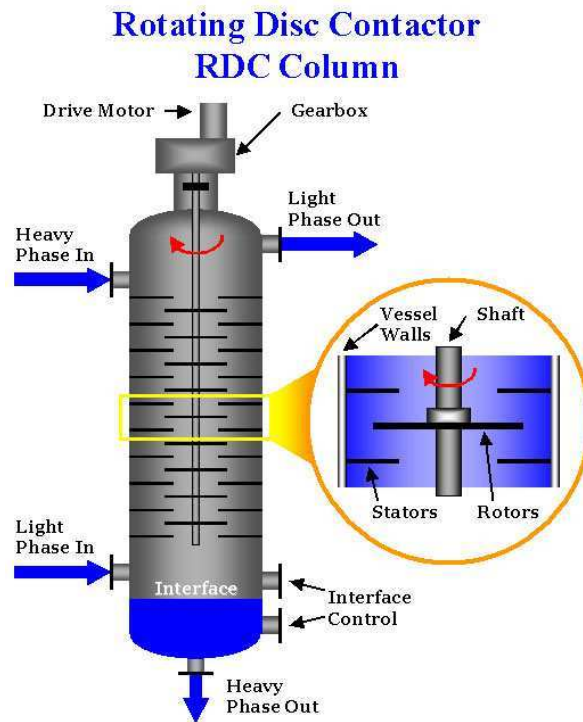


Fig. A1: RDC; Source: <http://www.liquid-extraction.com/rdc-column.htm>

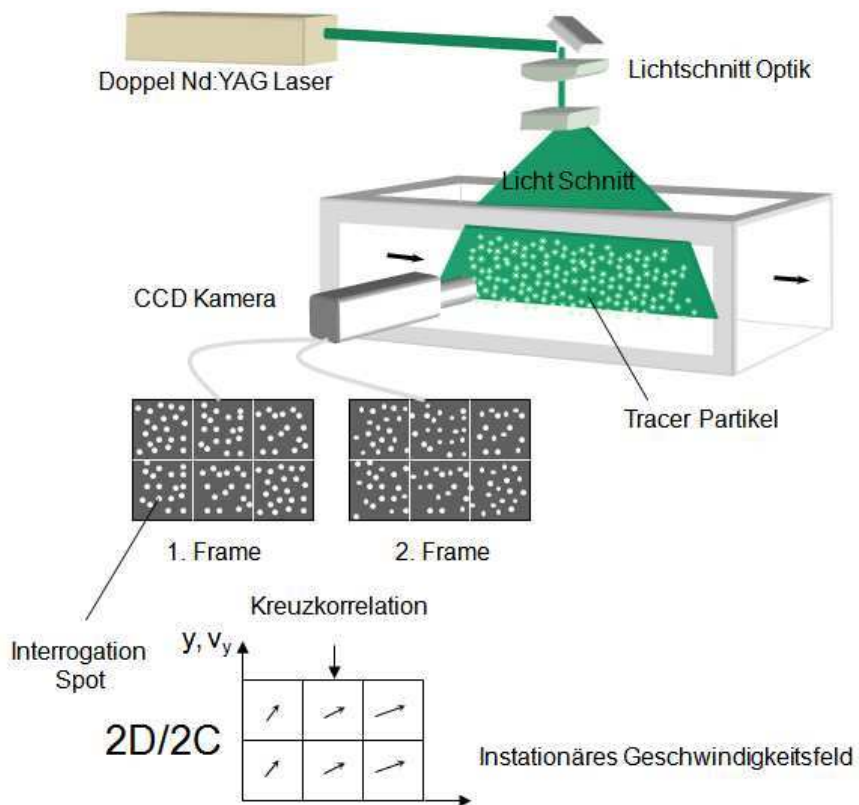


Fig. A2: PIV principles, Source: ILA PIV education, ILA GmbH, Juelich



Fig. A3: PIV Setup, DN150 column section



Fig. A4: PIV Setup, DN450 column section

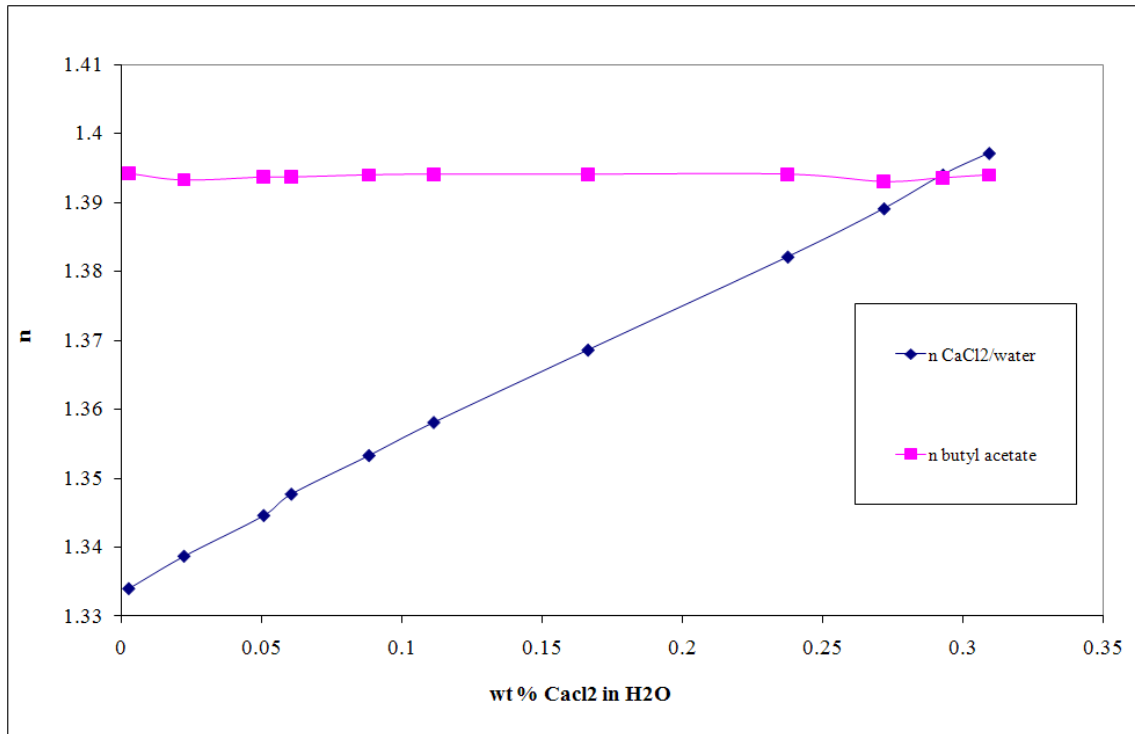
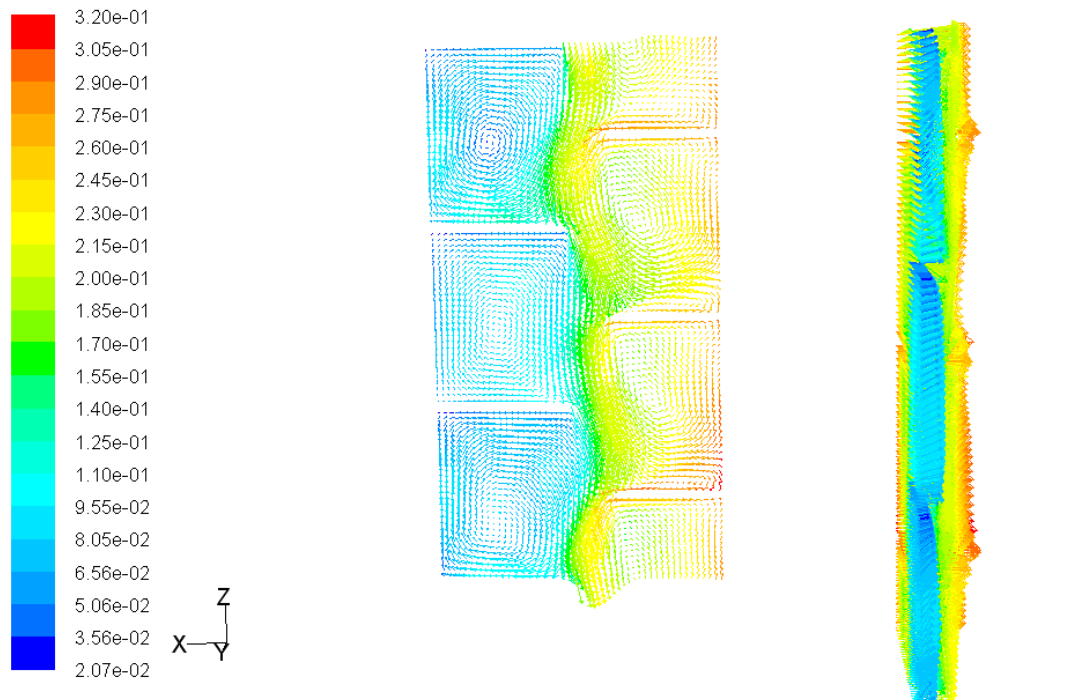


Fig. A5: Refractive indices CaCl₂/water, butyl acetate



Velocity Vectors Colored By Velocity Magnitude (m/s)

Jun 16
FLUENT 6.2 (3d, segregated)

Fig. A6: 3D geometry, single-phase flow, realizable k-ε: contours and vectors of aqueous phase velocity, $V_{aq} = 200$ l/h, $n_{stirrer} = 150$ rpm

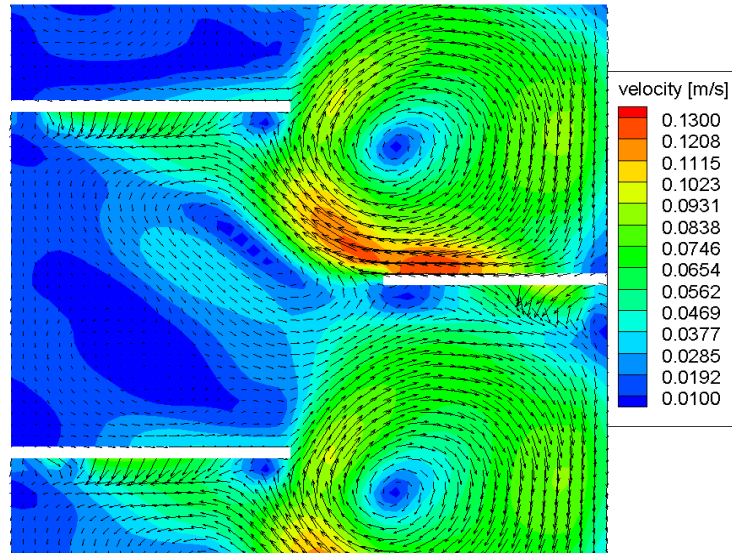


Fig. A7: Two-phase flow, RSM, contours and vectors of aqueous phase velocity, $V_{aq} = 200$ l/h, $V_{org} = 100$ l/h, $n_{stirrer} = 150$ rpm

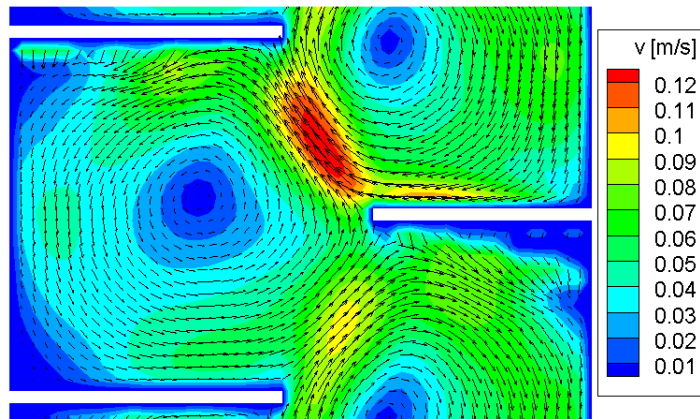


Fig. A8: Two-phase flow, realizable k-ε, mixture turbulence model, standard wall functions: contours and vectors of aqueous phase velocity, $V_{aq} = 200$ l/h, $V_{org} = 100$ l/h, $n_{stirrer} = 150$ rpm

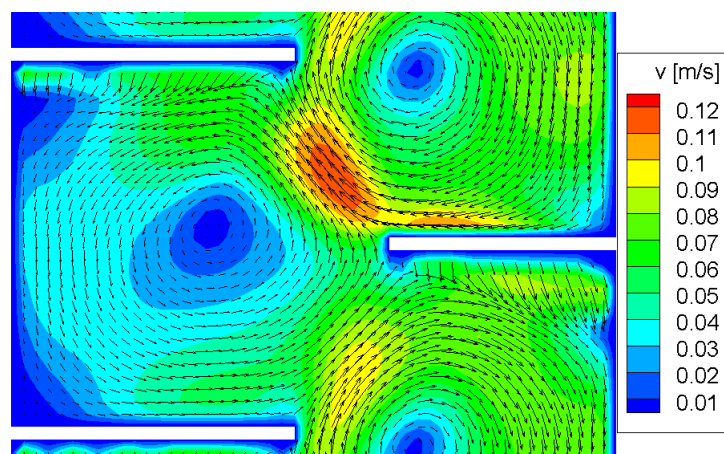


Fig. A9: Two-phase flow, realizable k-ε, per-phase turbulence model, standard wall functions: contours and vectors of aqueous phase velocity, $V_{aq} = 200$ l/h, $V_{org} = 100$ l/h, $n_{stirrer} = 150$ rpm

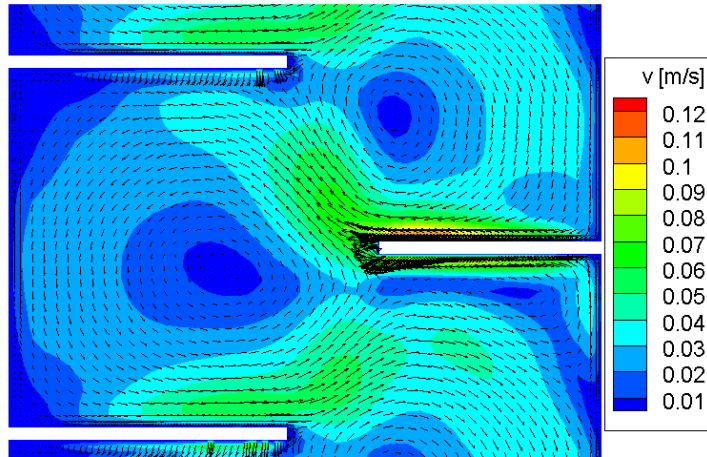


Fig. A10: Two-phase flow, realizable k- ϵ , mixture turbulence model, enhanced wall-treatment: contours and vectors of aqueous phase velocity, $V_{aq} = 200$ l/h, $V_{org} = 100$ l/h, $n_{stirrer} = 150$ rpm

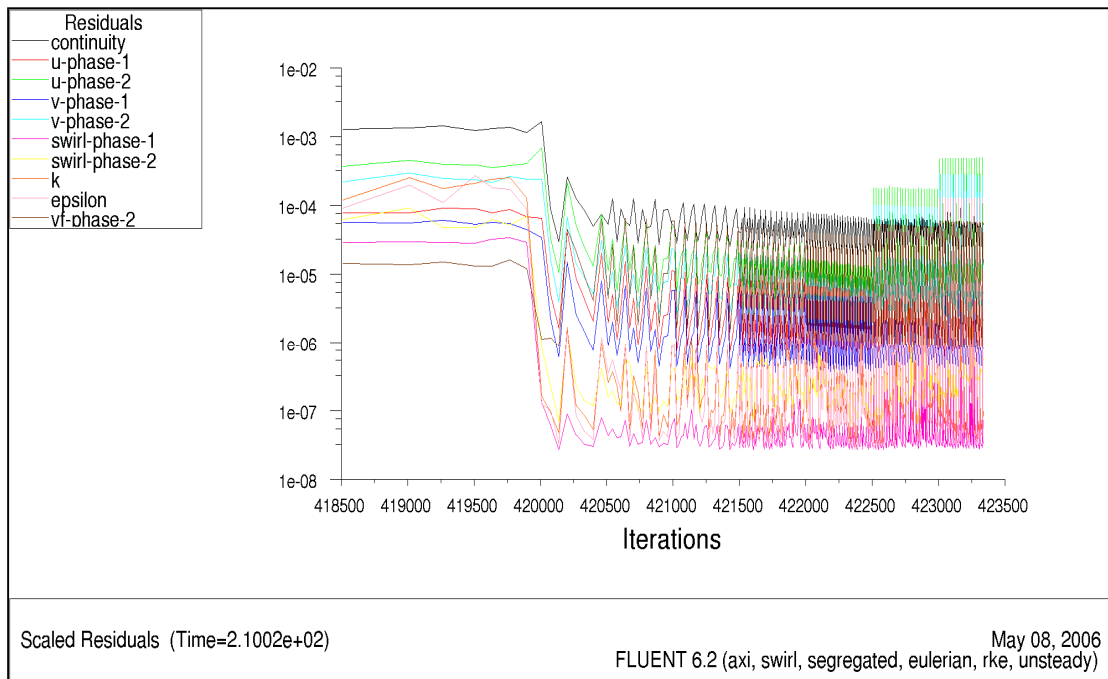


Fig. A11: Residuals, realizable k- ϵ , two-phase flow, $V_{aq} = 200$ l/h, $V_{org} = 100$ l/h, $n_{stirrer} = 150$ rpm

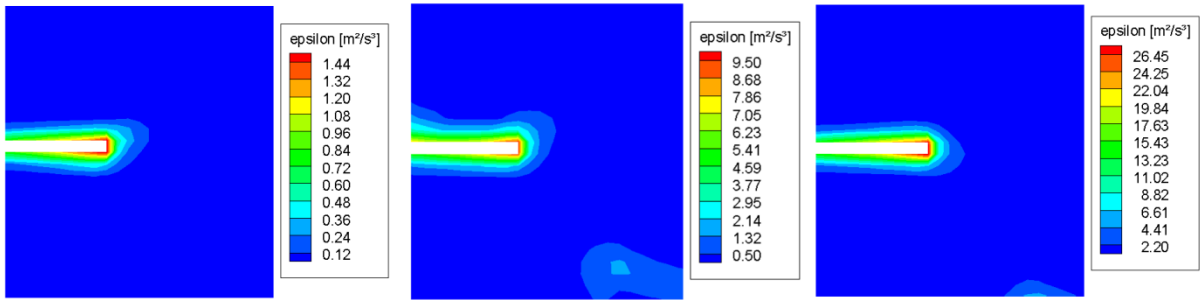


Fig. A12: CFD, two-phase turbulent energy dissipation at 100-300rpm (left to right), mixture realizable k-epsilon model

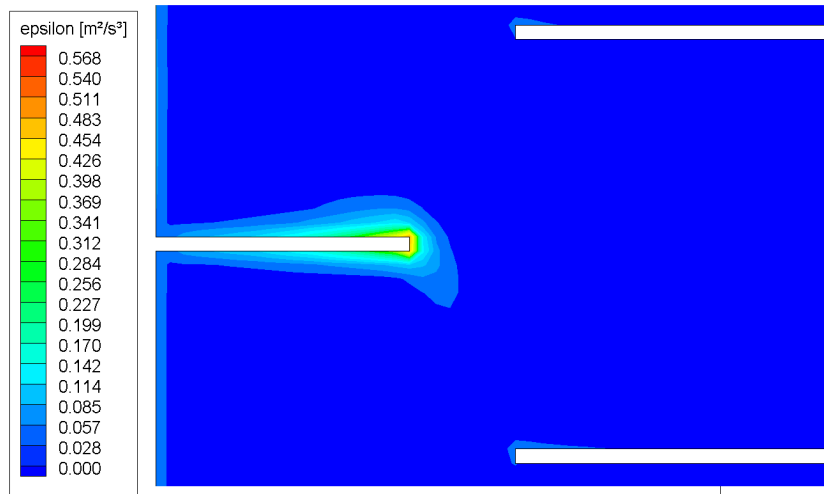


Fig. A13: CFD, single-phase turbulent energy dissipation standard wall treatment 150 rpm, operating conditions as in [I],

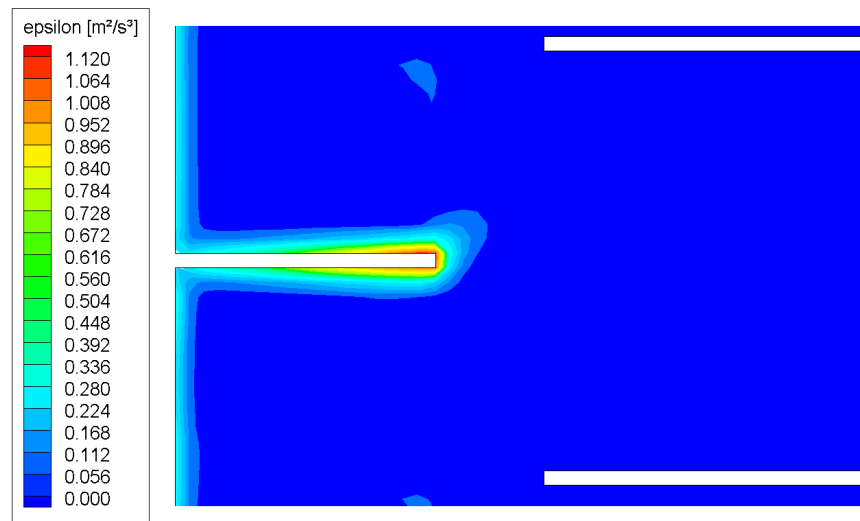


Fig. A14: CFD, two-phase turbulent energy dissipation standard wall treatment, toluene-water, 150 rpm, operating conditions as in [IX],

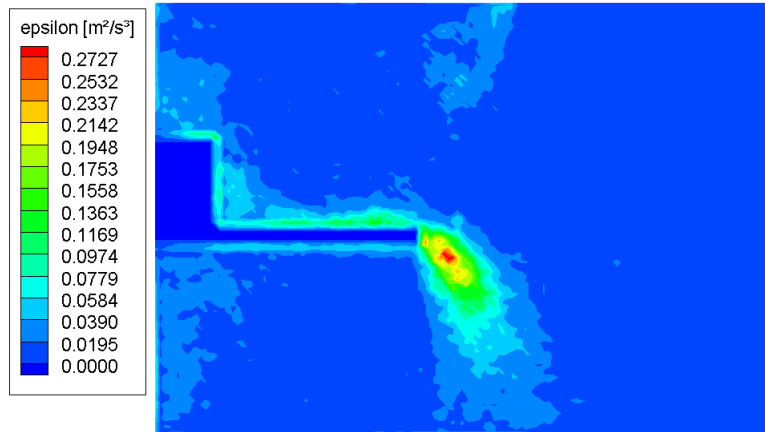


Fig. A15: PIV, single-phase turbulent energy dissipation standard wall treatment 150 rpm, operating conditions as in [I], scaled with Pao Spectrum ([XI], Eq.10)

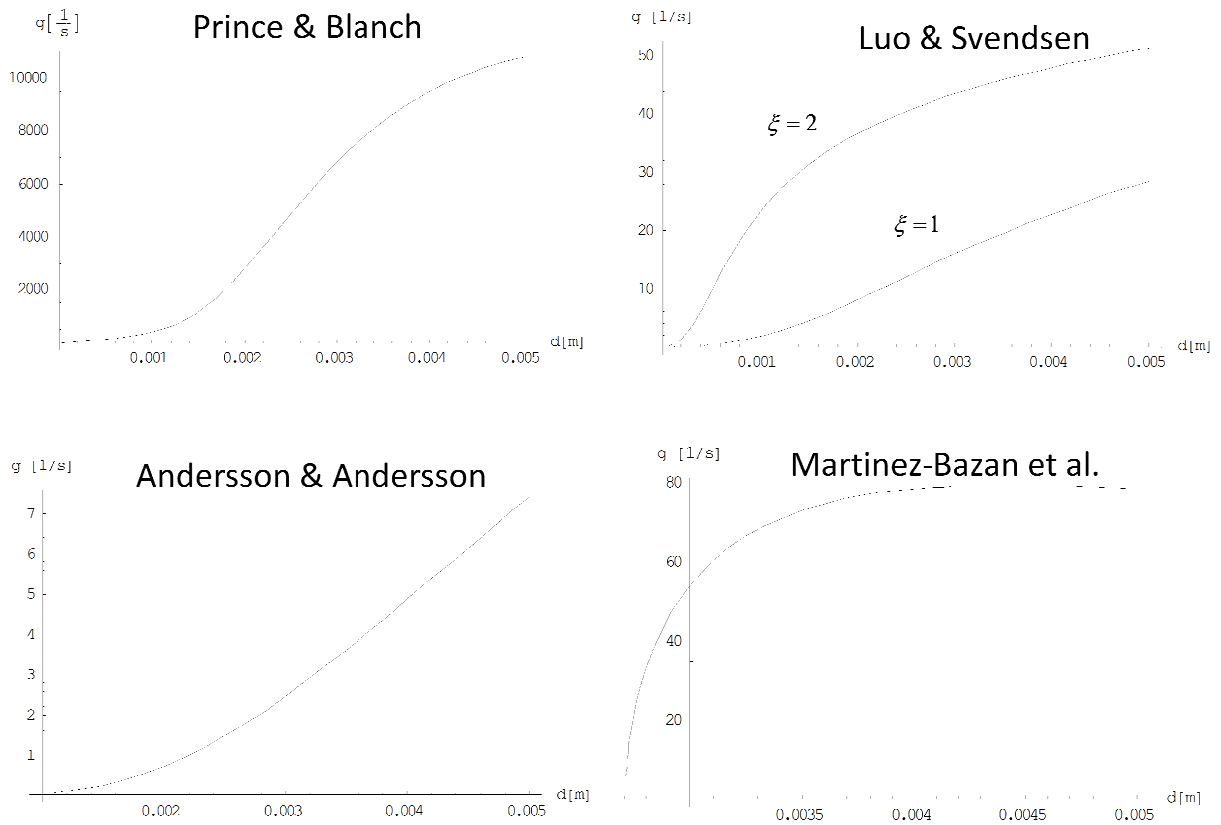


Fig. A16: Comparison of various breakage frequency g models, $\sigma=0.36$ Nm, $\rho=1000$ kg/m³, $\varepsilon=1$ m²/s³, $\alpha=0.1$,

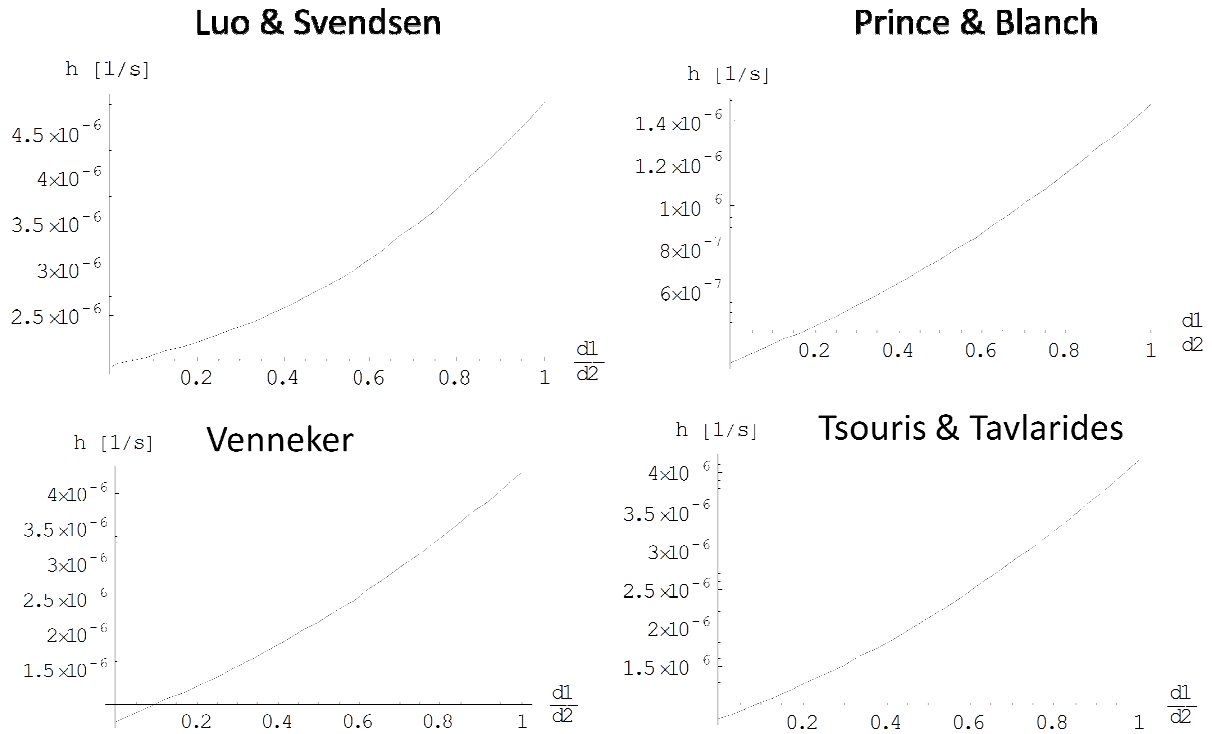


Fig. A17: Comparison of various collision frequency h models, $\sigma=0.36$ Nm,
 $\rho=1000$ kg/m³, $\varepsilon = 0.05$ m²/s³, $\alpha=0.05$

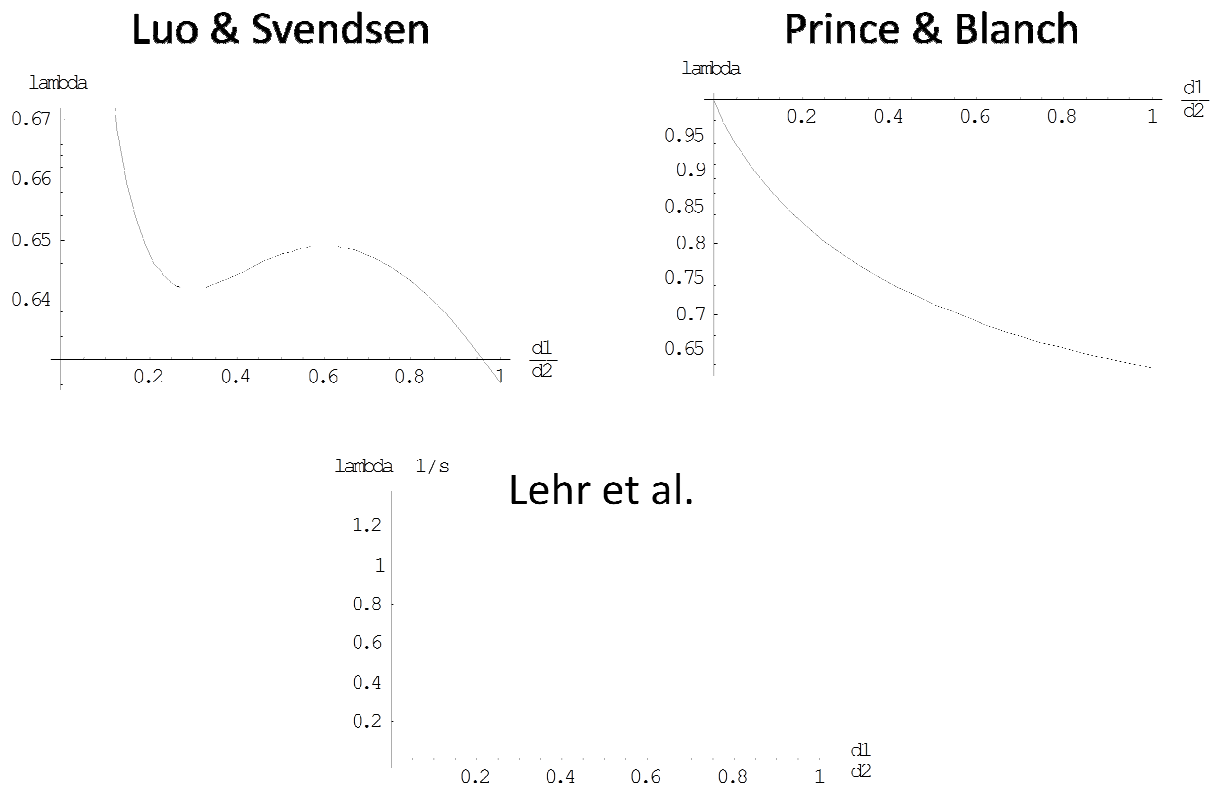


Fig. A18: Comparison of various coalescence probability λ models, $\sigma=0.36$ Nm,
 $\rho=1000$ kg/m³, $\varepsilon = 0.05$ m²/s³, $\alpha=0.05$

Table A1. CFD maximum and average values for ϵ , (RDC DN450),
single- and two-phase simulations, 3 compartment section

Stirrer speed (rpm)	Turbulence model	energy dissipation ϵ (m^2/s^3)	
		Maximum value at stirrer	Average value in compartment
100	2ph mixture realizable k- ϵ	1.32	0.0115
200	2ph mixture realizable k- ϵ	8.9	0.0654
300	2ph mixture realizable k- ϵ	25.8	0.2157
100	1ph realizable k-epsilon	0.63	0.00236
200	1ph realizable k-epsilon	3.65	0.0153
300	1ph realizable k-epsilon	9.87	0.046

Publication I

Reprinted from Chemical Engineering & Technology, 29, 1297-1302, **2006**,

Christian Drumm, Hans-Jörg Bart,

Hydrodynamics in a RDC Extractor: Single and Two-Phase PIV Measurements and CFD Simulations.

Reprinted with permission from Wiley-VCH.

<http://dx.doi.org/10.1002/ceat.200600212>

Hydrodynamics in a RDC Extractor: Single and two-phase PIV Measurements and CFD Simulations *

By Christian Drumm and Hans-Jörg Bart**

[*] Based on the presentation at the DECHEMA/GVC Extraction Annual Meeting, Würzburg (Germany), May 22-24, 2006

[**] C. Drumm, H.-J. Bart (author to whom correspondence should be addressed, bart@mv.uni-kl.de), Institut für Thermische Verfahrenstechnik, Universität Kaiserslautern, Postfach 3049, 67653 Kaiserslautern, Germany

ABSTRACT

The single and two-phase flow field of a RDC (rotating disc contactor) extraction column is simulated with the help of computational fluid dynamics (CFD). The simulations were validated by particle image velocimetry (PIV) measurements. The single-phase setup was used to test different turbulence models and a 2D and 3D grid approach. For the two-phase simulations a 2D computational grid and the Euler-Euler model was used. The two-phase PIV measurements are possible when using an iso-optical system, where the refractive indices of both liquid phases are identical.

1 Introduction

Liquid-liquid extraction is a separation process, which is based on the different distribution of the components to be separated between two liquid phases. Liquid-liquid extraction processes are widely applied in chemical and biochemical industries. Classical extraction equipment used are mixer-settler cascades and different types of counter-current extraction columns like the RDC type, which is analysed here.

The simulation of these counter-current liquid-liquid extraction columns still demands improvement. The layout of an extractor is mainly based on manufacturer's knowledge and simplified models, e.g. the HTU-NTU concept methods, where flow models such as the back-flow or dispersion model are used to account for the flow non-idealities. In most cases, these models are too simple to describe the real hydrodynamics. Current research focus on a more fundamental description using the droplet population balance (DPBM), which can describe droplet coalescence and breakage of the dispersed phase [1]. As state of the art in DPBM codes the hydrodynamic non-idealities are still described with simplified flow models like the dispersion model and are based on average compartment conditions [2]. The combination of CFD and DPBM can eliminate these shortcomings by giving a local resolution of the two-phase flow. For a successful link of CFD and DPBM the performance of CFD simulations for extraction columns needs to be tested.

In recent years only a few working groups focussed on the simulation of the hydrodynamics in counter-current stirred liquid-liquid extraction columns. Modes [3] investigated the velocity profile of a single water phase with the help of the CFD code FIDAP. Kolb [4] simulated the single-phase flow in a Kühni column and compared it with PIV experiments. Velocity fields in a single-phase flow RDC were measured using a Laser Doppler Velocimeter (LDV) and simulated with CFD by Fei et al [5]. Rieger et al. [6] investigated the one- and two-phase flow in a RDC extraction column employing an Euler-Euler and a Euler-Lagrange model, but had

problems with convergence. Haderer et al. [7] investigated different turbulence models for the one-phase flow and applied the Euler-Euler model for two-phase flow simulations. The Laser-Doppler anemometry (LDA) velocity measurements for validation by Haderer [7] and Rieger [6] did not allow a comparison of the whole velocity profile, so that only a few data points at rotor level could be compared. Haderer recommended the realizable-k- ϵ and the Reynolds stress model (RSM) for single-phase flow but annotated that it is without a proper validation. For the two-phase flow Haderer argues that the Euler-Euler model is the only applicable multiphase model for the simulation of counter-current extraction columns. He focussed on hold-up and drop size estimation but did not show flow fields for both phases. Vikhansky [8] proposed a combined CFD-population balance approach using an Euler-Lagrange model for the two-phase flow. For comparison of the numerical procedure only the droplet size distribution is compared with experimental results, while the two-phase flow field was not compared with experimental results. Also You [9] simulated the three dimensional two-phase flow for a Kühni column by means of an Euler-Lagrange method without any experimental verification.

In this paper the one- and two phase flow in a RDC extractor is simulated and validated by PIV Measurements. The simulations are carried out with the commercial CFD code Fluent 6.2. For the single-phase experiments and simulations a water phase is considered while an iso-optical water / glycerine-heptane system is applied for the two-phase case.

2 Experimental PIV technique

A 1m section of a 150 mm diameter column with 3 RDC compartments as internals was used as the experimental basis. The column can be operated in one and two-phase conditions, the aqueous phase entering at the top and leaving at the bottom. In the single-phase scenario water was used. The counter-current two-phase operating method was done with a glycerine-water mixture as the continuous phase and n-heptane as the dispersed phase. The organic phase is fed into the column through a distributor at the bottom which generates droplets in the millimetre range ($d_{32} = 2.5\text{mm}$). Variable rotation of the disc stirrers was warranted by an agitator. The optical measurement area (48 x 30 mm) in one extraction compartment is the height of one compartment and the symmetry region from the shaft to the wall of the column. The RDC column was operated at different throughputs for the aqueous (100-200 l/h) and the organic phase (50-100 l/h). The stirrer revolution was varied between 150 and 250 rpm.

An ILA (Intelligent Laser Applications GmbH) PIV system was used. It includes a pair of Nd:YAG Lasers, the CCD camera (PCO SensiCam) and the ILA synchronizer. For the single-phase water experiments polyamide tracer particles with a diameter of 50 μm and a density of 1060 kg/m^3 were applied. For the two-phase PIV a refractive index matching technique introduced by Augier [8] was adopted. The measurement of the aqueous phase velocities is possible by the use of an iso-optical system, where the refractive index of both liquid phases are identical. The liquid-liquid system is composed of n-heptane as the dispersed phase and a water/glycerine (44/56 wt%) mixture as the continuous phase. This system is optically homogenous at a temperature of 25°C. The organic droplets do not mask the measurement area and allows a clear view. The fluorescent dye Rhodamine 6G only soluble in the aqueous phase allows the discrimination of the phases and makes an estimation of the phase fractions possible. Hollow glass spheres with a diameter of 10 μm and a density of 1100 kg/m^3 only soluble in the aqueous phase seeded the two-phase flow. The measurement area used 970 x 600 pixels of the CCD array, thus one pixel is 0,05 mm in real length scale. The interrogation areas for the cross correlation were 64 x 64 pixel with a 50% overlapping, followed by an 32 x 32 pixel adaptive cross correlation. Local median filters

were used to eliminate outliers, which were interpolated. 200 pairs of pictures were taken for the determination of ensemble-averaged velocity fields. Fig. 1 shows the experimental 2D PIV-setup and the dimensions of the internals as well as the difference between such an iso-optical and a common non-iso-optical system.

3 Computational Model

3.1 Single-phase flow

Because of the axis-symmetry a 2D grid that contained one compartment of the RDC extractor was modelled in the pre-processor Gambit. The dimensions were the same as in the pilot column. The grid was implemented in the commercial CFD code Fluent 6.2. Periodic boundary conditions were applied at the in- and outflow boundaries of the aqueous phase. Fig. 2 shows the rectangular mesh with a cell edge length of 0.5 mm and the boundary conditions.

The conservation of mass and momentum were determined with the help of the Reynolds averaged approach leading to the Reynolds-averaged Navier-Stokes equations:

$$\frac{\partial \rho}{\partial t} + \frac{\partial (\rho u_i)}{\partial x_i} = 0 \quad (1)$$

$$\frac{\partial}{\partial t} (\rho u_i) + \frac{\partial}{\partial x_j} (\rho u_i u_j) = -\frac{\partial p}{\partial x_i} + \rho g_i + \frac{\partial}{\partial x_j} (\tau_{ij} - \overline{\rho u_i u_j}) \quad (2)$$

The Reynolds stresses in eq. 2 which represent the effects of turbulence must be modelled in order to close the equations. Different turbulence models were applied to test their performance. The standard -, RNG - and the realizable k- ϵ model which relate the Reynolds stresses to the mean velocity gradients by the use of the Boussinesq hypothesis were compared with the Reynolds stress model (RSM) which solves transport equations for each of the terms in the Reynolds stress tensor. The problem was solved stationary using Fluent.

In addition to the 2D axis symmetric grid a 90° section of the extraction compartments was modelled in a 3D grid and also another 2D grid including 6 compartments with velocity inlet and pressure outlet boundary conditions was tested. This was done for a comparison of the different grids and to see if application of the 2D axis symmetric grid with one compartment and axial and rotational periodic conditions gives meaningful results [6]. In addition the influence of the cell edge length was tested varying the length down to 0.05 mm.

3.2 Two-phase flow

An Euler-Euler model where both phases are treated mathematically as interpenetrating continua was applied for the two-phase simulations of the extraction column. The volume fraction α which represent the space occupied by each phase and the inter-phase interaction term $F_{k,i}$ representing the momentum exchange between the continuous and dispersed phase are introduced in the continuity and Navier-Stokes equations

$$\frac{\partial(\alpha_k \rho_k)}{\partial t} + \frac{\partial}{\partial x_i} (\alpha_k \rho_k u_{k,i}) = 0 \quad (3)$$

$$\frac{\partial(\alpha_k \rho_k u_{k,i})}{\partial t} + \frac{\partial(\alpha_k \rho_k u_{k,j} u_{k,i})}{\partial x_j} = -\alpha_k \frac{\partial p}{\partial x_i} + \alpha_k \rho_k g_i + \frac{\partial(\alpha_k \tau_{k,ij})}{\partial x_j} + F_{k,i} \quad (4)$$

The subscripts k signifies one phase ($k=1, 2$) and i, j represent the cartesian coordinate directions ($i, j=1, 2, 3$). In addition to (3) and (4) the summation equation for the volume fractions must be satisfied:

$$\alpha_1 + \alpha_2 = 1$$

The inter-phase interaction term consists of different momentum exchange mechanisms. Only the drag force was taken into account, while the added mass force and the lift force can be neglected for a liquid-liquid interaction as shown by Wang and Mao in a stirred tank [11]. The drag force can be described as:

$$F_{c,i} = -F_{d,i} = \frac{3\rho_c \alpha_c \alpha_d C_D |\bar{u}_d - \bar{u}_c| (u_{d,i} - u_{c,i})}{4d_d}$$

where the drag coefficient C_D was described by the model of Schiller-Naumann in simulation [12]. As in the single-phase simulations the RSM and the realizable k - ϵ model were applied. A 2D axis symmetric grid of a whole column with 6 compartments was modelled in Gambit. Because of the phase separation at the top and the bottom in an extraction column the velocities at the in- and outlet of the phases can be easily calculated when mass transfer is neglected. That is why 4 velocity inlet boundary conditions were chosen in Fluent. The common approach with pressure outlet conditions at the top and velocity-inlet at the bottom is also possible, but assumptions for the volume fraction at the in- and outlets are necessary. The droplet phase was treated as a mono disperse phase with a droplet diameter of 2.5 mm which corresponds with the mean droplet diameter in the experimental setup. The simulation were carried out unsteady reducing the time step from 0.1 to 0.001 s. The simulations were first carried out using the first order implicit solver. After convergence was reached it was switched to the second order implicit solver to gain the final solution.

4 Results and discussion

4.1 Single-phase results

The velocity field of the continuous water phase both for CFD simulation and PIV measurements is depicted in Fig. 3 for a 200 l/h throughput and a stirrer revolution of 150 rpm. Fig. 3 shows the contour and vectors of the velocities. The RSM was used as turbulence model and the computations were performed on the mesh shown in Fig. 2. It can be seen that the CFD simulations are in good agreement with the measurements. Two big vortices can be estimated in the compartment, one between the stators and one between the rotating discs. A small third vortex is visible above the stirrer because the flow field turns round at this position towards the stirrer tip. All this phenomena are both obvious in the simulations and experiments. When the three k - ϵ models were used to describe the turbulence it was obvious that they describe the vortex especially between the stirrers worse (Fig 4.). Furthermore, using the k - ϵ models the maximal velocities are computed too low. In Fig. 5 measured and calculated mean velocities at the rotor level are given and are in qualitative good agreement

for all turbulence models. Here it is also obvious that the RSM describes the velocities better than the $k-\epsilon$ models with a maximum deviation of 15% near the stirrer while the $k-\epsilon$ models predict the velocities at the wall and near the stirrer too low. The RNG and realizable $k-\epsilon$ models express the velocities still better than the standard $k-\epsilon$ model. A comparison of the results performed on the mesh shown in Fig.2 with the results of the 3D section mesh and the 2D grid including 6 compartments and velocity inlet and pressure outlet boundary conditions yield that the simulated flow profile is almost independent from the chosen mesh. Therefore the periodic boundary conditions adopted here are applicable and are recommended because of the much lower computation time. Similar observations was made by Rieger [5] et al. and Haderer [6]. Furthermore a node spacing of 0.5 mm was satisfactory for the predicted velocity profiles. A finer mesh do not change the magnitude of the velocities but on the other hand the computational time was increased dramatically.

4.2 Two-phase results

Results for the two-phase operating method of the column are shown for an aqueous throughput of 200 l/h and an organic throughput of 100 l/h, while the stirrer revolution was set to 150 rpm. In Fig. 6 both the computed volume fraction of the aqueous phase and the boundary conditions for the two-phase simulation are shown. The velocity contours and vectors of the continuous aqueous phase for CFD simulation and PIV are shown in Fig. 7. For the results of both figures the realizable $k-\epsilon$ model was applied in the simulation. Compared to the single-phase operating method the vortices shift so that the vortex between the stators moves at the position above the stirrer. At the positions between the stators and the stirrers the vortices reverse, because the throughput of the ascending droplets is high enough to modify the flow pattern. CFD simulations predict this behaviour and as can be seen in Fig. 7 there is also a good agreement between CFD and PIV. Even the small vortex which was above the stirrer in the single-phase case and is now below the stirrer is reflected in the simulation when the second order implicit solver is used. In Fig. 6 one can see the path of the dispersed phase, with a volume fraction of 6%, through the compartment. The droplets do not penetrate the outer regions of the compartment and accumulate under stirrer and walls. This was also visible in the PIV measurements for these operating conditions (Fig. 1).

In Fig. 8 and Fig. 9 the measured and calculated velocities of the aqueous phase at the rotor level and above the rotor level at half compartment height are compared. The two levels are depicted in Fig. 2 as black lines. As in the single flow case the realizable $k-\epsilon$ model predicts the velocities too low and there is also a small shift obvious. Nevertheless there is still a good agreement between simulation and experimental results. Though a good convergence was reached when using the RSM for the single-phase flow, the RSM was not able to reproduce the expected flow field and could not show the vortex between the stators. Instead there was a second dead zone near the lower stator of the compartment. Therefore the RSM is inadvisable for the two-phase simulation, while we recommend the realizable $k-\epsilon$ model.

5 Summary and Conclusion

Single and two-phase simulations of a RDC extractor are discussed and are in good agreement with the PIV measurements. Because of the reduction of numerical effort a 2D axis symmetric approach is recommended and gives reliable results. While the RSM is the best turbulence model in the single-phase simulation, there are shortcomings in the prediction of the two-phase flow. The simulation of the counter-current two-phase flow was possible by means of the chosen velocity boundary conditions, while an Euler-Euler model where the realizable $k-\epsilon$ model describing the turbulence was used. All phenomena that occur in single and two-phase flows in an extraction column which were visible in PIV measurements could be

predicted with CFD. The results give rise to the expectation that a future link of CFD and DPBM will lead to a better prediction and simulation of counter-current stirred extraction columns.

References

- [1] T. Steinmetz, S. Schmidt, M. Attarakih, H.-J. Bart, *Proc. of ISEC*, **2005**, Peking, China
- [2] M. Attarakih, H.-J. Bart, L. Lagar, N. Faqir, *Chem. Engng. Proc.*, **2006**, 45, 113
- [3] G. Modes, H.-J. Bart, *Chem. Ing. Techn.*, **2001**, 73, 332.
- [4] P. Kolb, *PhD thesis*, TU Kaiserslautern, **2004**
- [5] W. Fei, Y. Wang, Y. Wan, *Chem. Eng. J.*, **2000**, 78, 131
- [6] R. Rieger, C. Weiss, G. Weigley, H.-J. Bart, R. Marr, *Computers Chem. Engng.*, **1996**, 12, 1467
- [7] T. Haderer, *PhD thesis*, TU Graz, **2004**
- [8] A. Vikhansky, M. Kraft, *Chem. Eng. Sc.*, **2004**, 59, 2597
- [9] X. You, X. Xiao, *Chem. Biochem. Eng.*, **2005**, 19, 1
- [10] F. Augier, O. Masbernat, P. Guiraud, *AIChE J.*, **2003**, 49, 230
- [11] F. Wang, Z.-S. Mao, *Ind. Eng. Chem. Res.*, **2005**, 44, 5776
- [12] L. Schiller, Z. Naumann., *Z. Ver. Deutsch. Ing.*, **1935**, 77, 318

Symbols used

C_D	[-]	drag coefficient
d	[m]	droplet diameter
F	[N]	interaction force
p	[Nm ⁻²]	pressure
u	[ms ⁻¹]	velocity
t	[s]	time
x	[m]	coordinate

Greek symbols

α	[-]	volume fraction
δ	[-]	Kronecker delta
μ	[m ² s ⁻¹]	kinematic viscosity
ρ	[kgm ⁻³]	density
τ	[Nm ⁻²]	shear stress

Subscripts

c,d	continuous and disperse phase
i,j	directions
k	k th phase

List of Figures

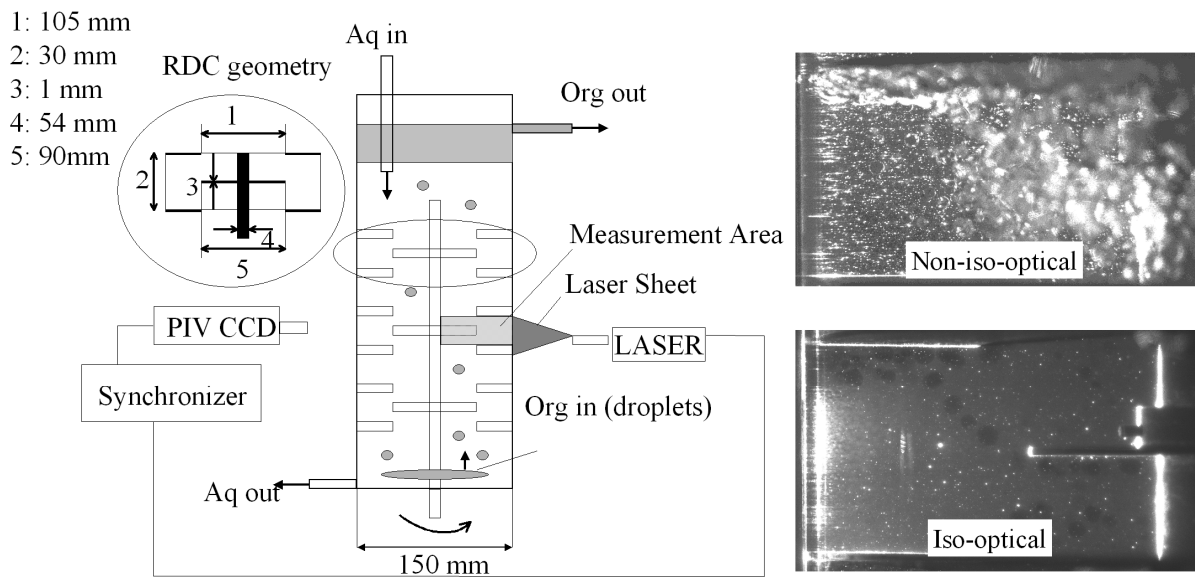


Figure 1. Experimental setup

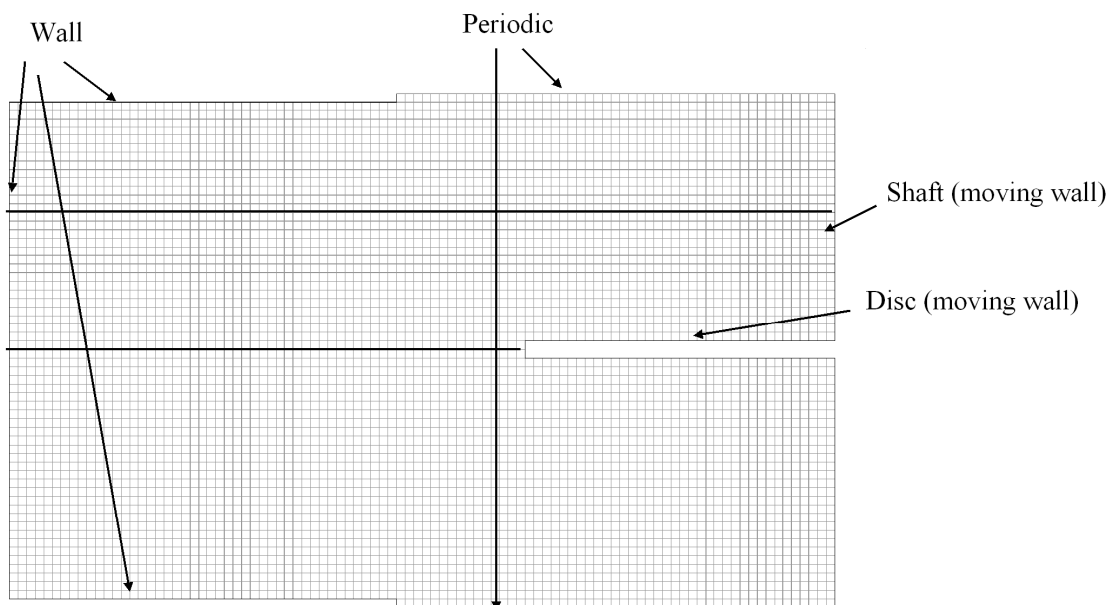


Figure 2. Computational grid (single-phase simulations)

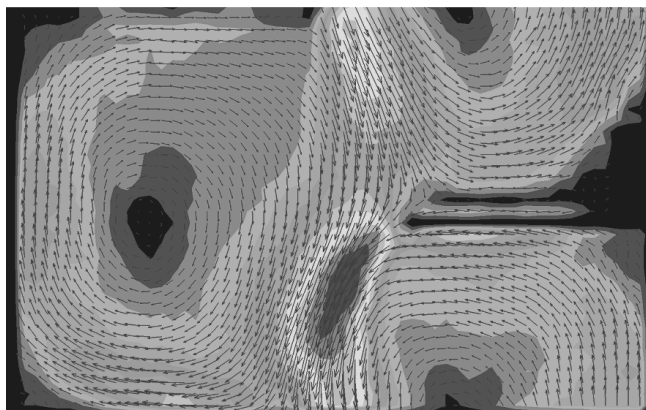
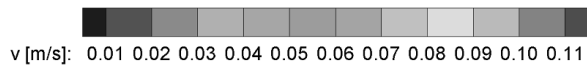
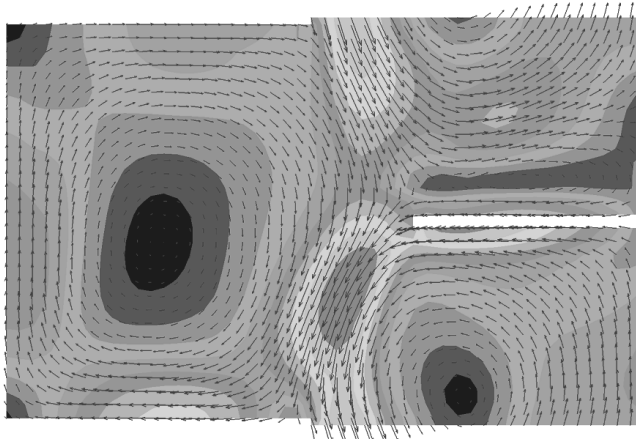
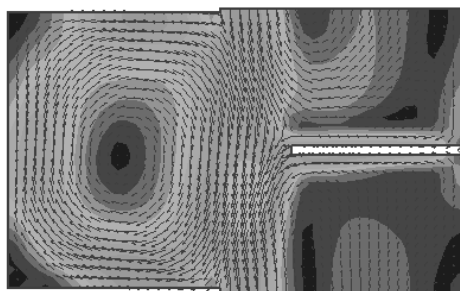
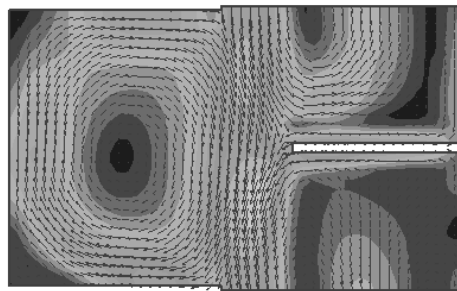


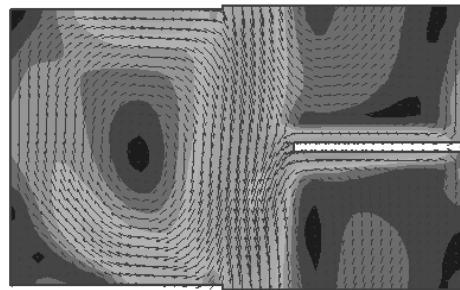
Figure 3. Comparison single-phase contours and vectors of velocity, CFD (top) and PIV (bottom), RSM, $V_{aq} = 200$ l/h



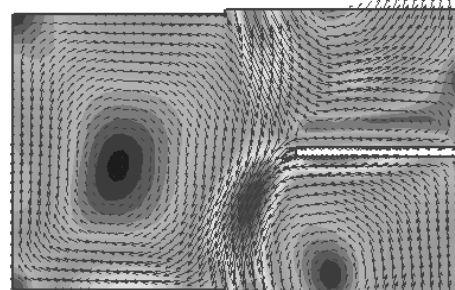
realizable k-epsilon



RNG k-epsilon



standard k-epsilon



Reynolds Stress Model

Figure 4. Comparison of different turbulence models: single-phase contours and vectors of velocity, $V_{aq} = 200$ l/h

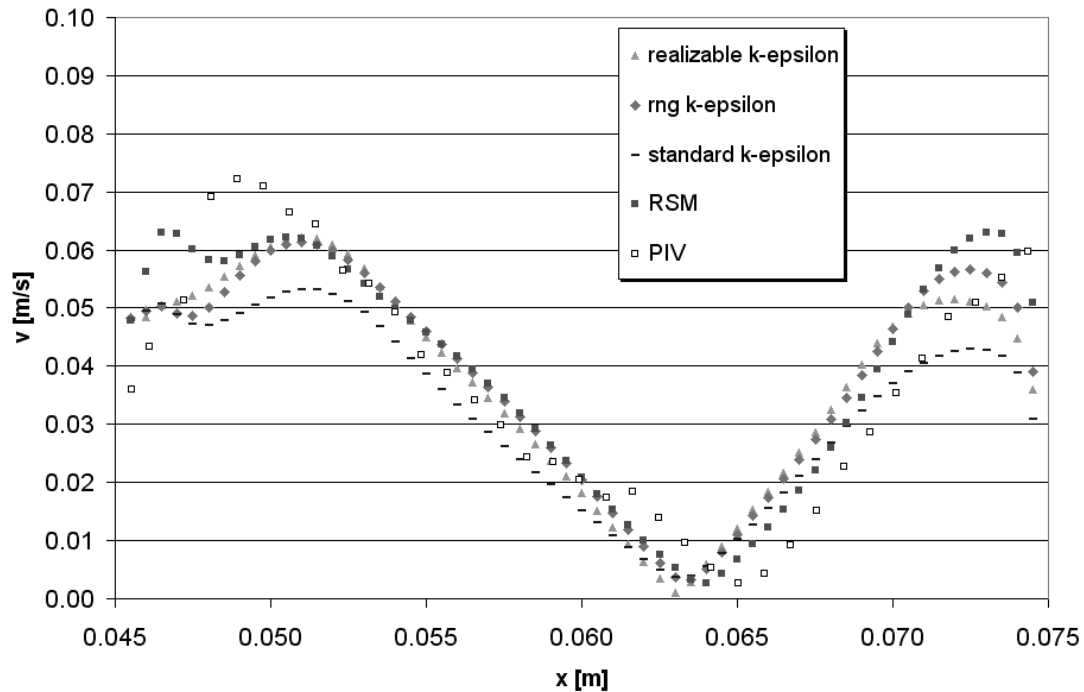


Figure 5. Single-phase measured and calculated velocities at rotor level, $V_{aq} = 200$ l/h, $n_{stirrer} = 150$ rpm

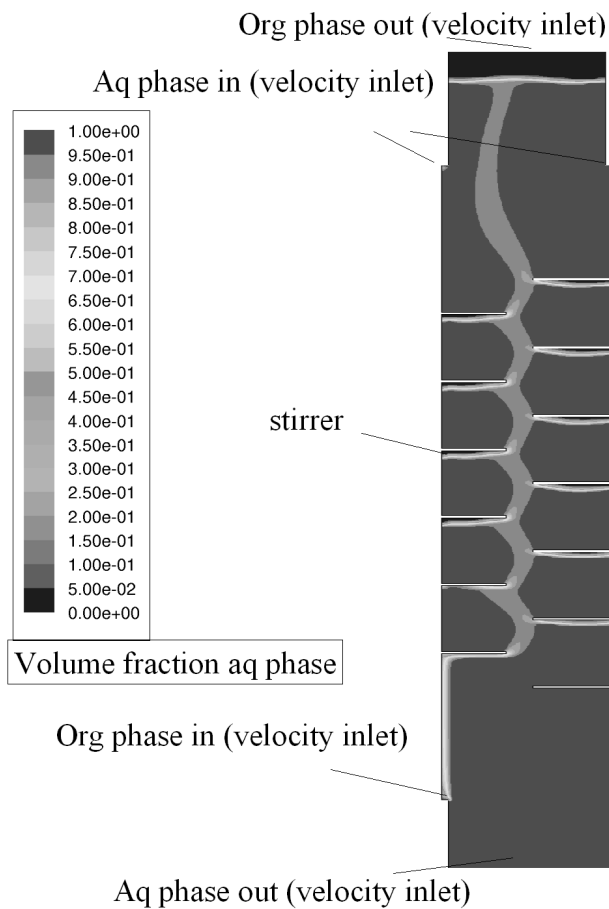


Figure 6. Two-phase CFD simulation: boundary conditions and volume fraction aqueous phase, $V_{aq} = 200$ l/h, $V_{org} = 100$ l/h, $n_{stirrer} = 150$ rpm

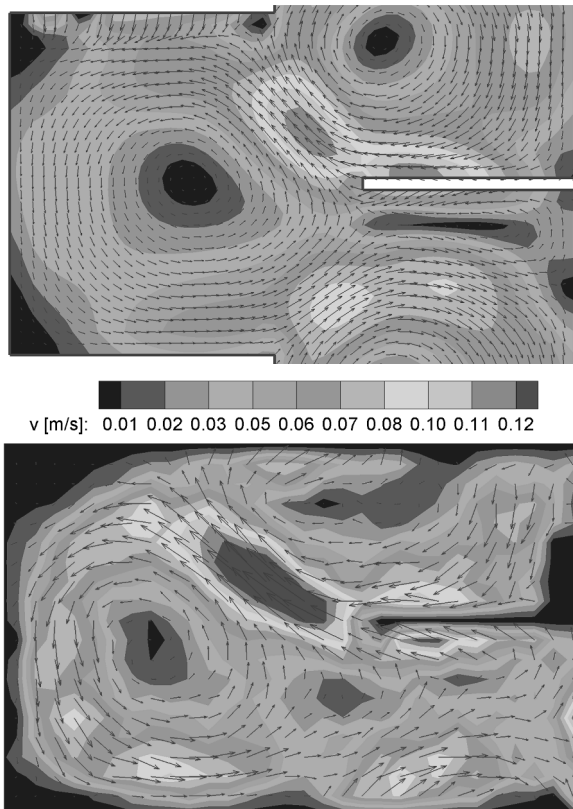


Figure 7. Comparison two-phase flow: contours and vectors of aqueous phase velocity, CFD (top) and PIV (bottom), RSM, $V_{aq} = 200$ l/h, $V_{org}=100$ l/h, $n_{stirrer}=150$ rpm

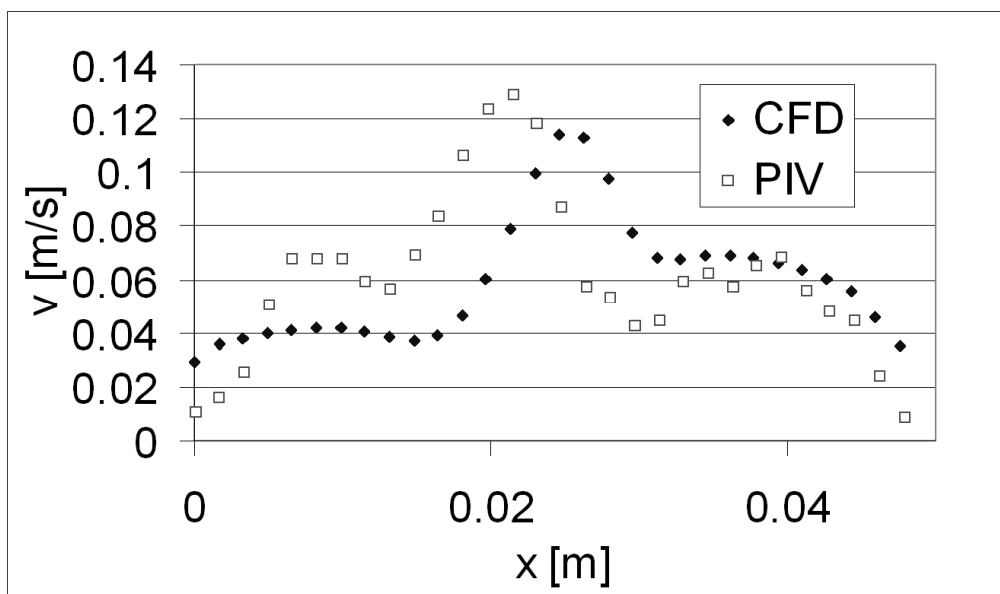


Figure 8. Two-phase flow: measured and calculated mean velocities at half compartment height above stirrer, $V_{aq} = 200$ l/h, $V_{org}=100$ l/h, $n_{stirrer}=150$ rpm

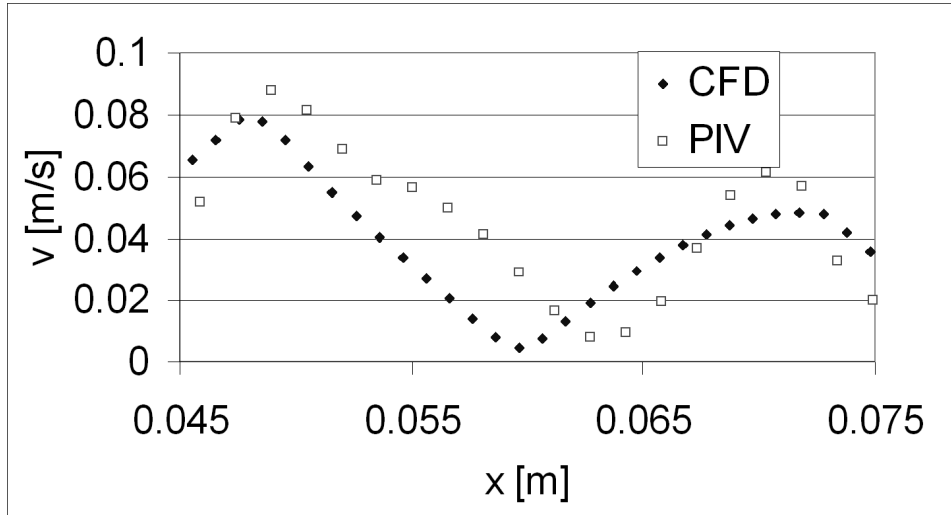


Figure 9. Two-phase flow: measured and calculated mean velocities at rotor level, $V_{aq} = 200$ l/h, $V_{org} = 100$ l/h, $n_{stirrer} = 150$ rpm

Publication II

Reprinted from Proceedings International Conference on Multiphase Flow ICMF 2007,
M. Sommerfeld (Ed.), Leipzig, **2007**,

Christian Drumm, Hans-Jörg Bart,

**Coupling of CFD with DPBM: Drop Size Distributions and Flow Fields in a RDC
Extractor.**

Coupling of CFD with DPBM: Drop Size Distributions and Flow Fields in a RDC Extractor

Drumm Christian, Bart Hans-Jörg

TU Kaiserslautern, Lehrstuhl für Thermische Verfahrenstechnik
Postfach 3049, Kaiserslautern, 67663, Germany
bart@mv.uni-kl.de

Keywords: CFD, PBM, population balances, extraction, liquid-liquid, coalescence, breakup

Abstract

For the layout of counter-current liquid-liquid extraction columns, there is an ongoing claim for more straightforward, faster and money-saving simulation methods. One possibility in this direction with great potential is the coupling of computational fluid dynamics (CFD) with population balance models (PBM). Therefore, in the present work, a combination of computational fluid dynamics and droplet population balance modeling (DPBM) is applied to simulate the drop size distributions and flow fields in a liquid-liquid RDC extractor. The simulations are carried out in the commercial CFD code Fluent. The liquid-liquid flow is modeled using a Reynolds averaged turbulence model in conjunction with the Eulerian two-fluid equations. Two theoretical models for coalescence and breakup, the models of Luo & Svendsen (1996) and Coulaloglou & Tavlarides (1977) are implemented in the CFD code as user defined functions. Simulated droplet distributions for the system toluene-water are compared to experimental measurements by Simon (2004). The first results show that the link of PBM and CFD presents a powerful simulation tool, which could significantly improve the layout of industrial columns.

Introduction

Liquid-liquid extraction is a separation process, which is based on the different distribution of the components to be separated between two liquid phases. Liquid-liquid extraction processes are widely applied in chemical and biochemical industries. Classical extraction equipments used are mixer-settler cascades and different types of counter-current extraction columns like the RDC type, which is analysed here. The simulation of these counter-current liquid-liquid extraction columns still demands improvement. Today, the layout of an extractor is mainly based on manufacturer's knowledge and simplified models, e.g. the HTU-NTU concept methods, where flow models, such as the back-flow or dispersion model, are used to account for non-ideal flow. In most cases these models are too simple to describe the real hydrodynamic behaviour. That is why the design of extraction columns often requires pilot plant experiments and is time and money consuming. On the other hand, there is an ongoing claim by the industry for more straightforward, faster and money saving simulation methods.

Research recently focused on a more fundamental design method when using the droplet population balance models (DPBM) (Gourdon et al. 1994) with its origin in crystallization (Hulburt & Katz 1964). DPBM can specify droplet movement, coalescence and breakage of the

dispersed phase and consider the particulate behaviour in an extraction column. Current DPBM codes by Attarakih et al. (2006) or Kronberger et al. (1995) also use above simplified models, e.g. the dispersion model for the hydrodynamics. They are based on average compartment conditions (pseudo-homogeneous) and contain only one external coordinate. It could be shown by Steinmetz et al. (2005) and Schmidt et al. (2006) that the population balance modelling based on these codes (Attarakih et al. 2006) is able to predict the hold-up profile and the Sauter mean diameter of the droplets in a liquid-liquid extraction column. Although this approach has a huge advantage over the currently used design methods, there are still experiments in small lab-scale devices necessary. These are needed to establish correlations for the droplet rising velocities, the dispersion parameter in the dispersion model and to fit adjustable parameters in the coalescence and breakage kernels.

Current research in the last years tried to improve the predictability of the PBM when coupling it with CFD (Vikhansky et al. 2006). The link can, on the one hand, eliminate the simplifications and shortcomings of the dispersion model by giving a local resolution of the two-phase flow and on the other hand save at least some of the small lab-scale experiments. The pseudo-homogeneous conditions can be removed and, therewith, also the simple dispersion model, since CFD can account for hydrodynamics and turbulence of the fluid. The models for

coalescence and breakage of the droplets usually need the local turbulence, more precisely the turbulent energy dissipation, which can be supplied by the turbulence model, also locally resolved.

First publications adopted this approach with simplifications when only using a one-way coupling. This means that only the result of the flow simulation is used for the calculation of the drop size distributions, while the influence of the drops on the flow field is neglected. A multi block approach, where the investigated geometry is subdivided into sub-regions, is another alternative in that respect. Alopaeus et al. (1999) divided the investigated stirred tank into 11 sub-regions, while the turbulent energy dissipation entering the population balances came from CFD simulations by integrating over the volumes of the sub-regions. They stated that by assuming a stirred extraction column to be homogeneous, a serious error might be introduced, since turbulent energy dissipation is several orders of magnitude greater near the impeller than far from it. Schlauch (2006) simulated a liquid-liquid stirred tank by means of the CFD code Featflow and the commercial PBM code Parsival (Wulkow et al. 1999) also using an one-way coupling. The tank is subdivided into 4 regions, and only the velocity fields of the CFD simulations enter the PBM code.

These simplifications in the coupling procedure can be reduced by implementing the population balance equations in a CFD code. Lo (2000) realised a more complete description by implementing the population balance equations in the commercial CFD code CFX via the MUSIG (Multiple-Size-Group) model of Lo. Herewith a complete coupling is achieved, the bubble size distribution is divided into a number M of discrete size classes, while it is assumed that bubbles of all sizes share a common velocity field, where the Sauter mean diameter influences the drag term. Sanyal et al. (2005) implemented a classes-method (CM) and a method of moments (MOM) in the CFD code Fluent in conjunction with the Eulerian multiphase model. Since the main focus of the work was the investigation of alternate approaches for solving the population balance equations and not the detailed modelling of the hydrodynamics in a column the results were not compared to experiments. Furthermore, for the turbulent energy dissipation a constant value was chosen instead of returning the values from the applied k - ϵ model.

This work

Since the coupling of CFD and PBM advanced very well in the last years, as shown in the above selected examples, the predictability of a combined CFD-PBM tool for the layout of industrial columns can be further investigated. Therefore, in the present work, a combination of computational fluid dynamics (CFD) and droplet populations balance modeling (DPBM) is applied to simulate the drop size distributions and flow fields in a segment of a liquid-liquid RDC extractor. The simulations are carried out in the commercial CFD code Fluent. The liquid-liquid flow is modeled using a

Reynolds averaged turbulence model in conjunction with the Eulerian two-fluid equations. As a first approach, in previous work the simulated flow fields for an iso-optical test system were validated by particle image velocimetry (PIV) measurements taken on a pilot scale column and a suitable turbulence model, namely the realizable k - ϵ model was chosen for the simulation of the two-phase flow and the coupling of CFD and DPBM (Drumm & Bart 2006). Two theoretical models for coalescence and breakup, the models of Luo & Svendsen (1996) and Coulaloglou & Tavlarides (1977) are implemented in the CFD code as user defined functions (UDF). Finally, simulated droplet distributions for the system toluene-water are compared to experimental measurements by Simon (2004).

Geometry and operating conditions

The basis of the investigations are the experiments conducted by Simon in a 5 RDC compartments section of a column with 150 mm diameter. For the systems water-toluene and water-butylacetate the in- and outlet droplet size distributions of the rising droplets were measured for different stirrer revolutions. The RDC column was operated at different throughputs for the aqueous (50-100 l/h) and the organic phase (50-100 l/h). The stirrer revolution was varied between 150 and 250 rpm.

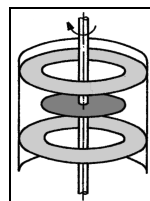


Figure 1: Sketch of a Rotating Disc Contactor compartment

Numerical Scheme

A 2D axis symmetric grid of the column was modeled in Gambit. Because of the rotational symmetry of a Rotating Disc Contactor (Fig.1) the 2D grid can be adopted without losing information. Previous work showed that a 2D grid delivers reliable results regarding the hydrodynamics of a RDC (Drumm & Bart 2006). For the boundary conditions the common approach with one pressure outlet condition at the top and one velocity-inlet at the bottom was applied, but assumptions for the volume fraction of the dispersed phase at the in- and outlets had to be made. The surfaces of the rotating disc and the column wall were defined with no-slip wall boundary conditions. All flow conditions, as well the droplet distribution at the inlet, were the same as in the experiments (Simon, 2004). Quadrilateral elements with a grid space of 1mm were adopted to map the flow domain. The computational grid is depicted in Fig. 2. Standard wall functions modeled the near wall region. The simulations were carried out unsteadily reducing the time step from 0.1 to 0.001 s. The simulations were first carried out using the first order implicit solver. After convergence was reached it

was switched to the second order implicit solver to gain the final solution. For the discretisation in space first order upwind schemes and the QUICK scheme were used except for the pressure terms where the body force weighted scheme was used. The simple algorithm was used for the pressure-velocity coupling. For the under-relaxation factors standard values were used without modification. For the description of the population balances 15 classes are used. The governing equations of the flow and the population balances as well as the implementation of the investigated coalescence and breakup kernels are described in detail in the following chapters.

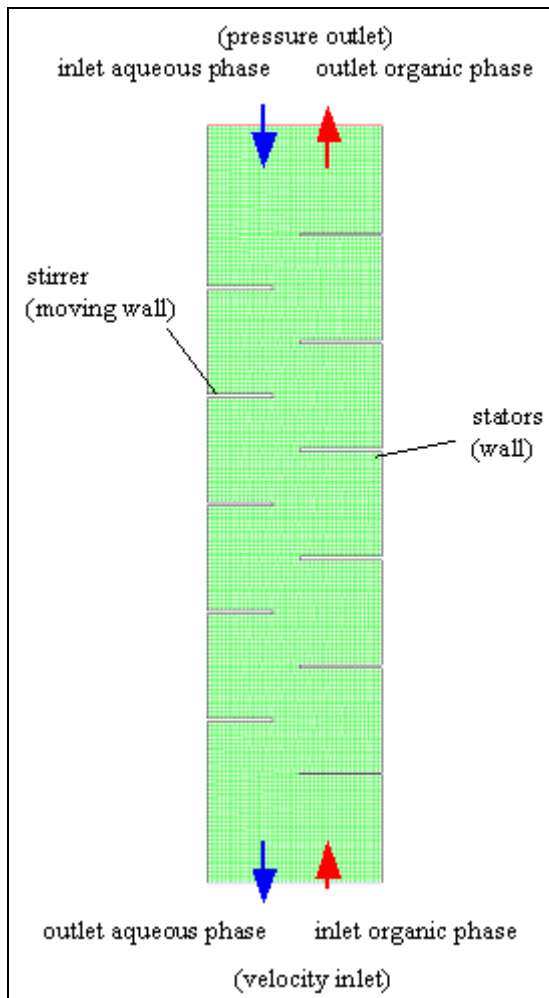


Figure 2: Computational grid, boundary conditions are given in brackets

Flow equations

An Euler-Euler model where both phases are treated mathematically as interpenetrating continua was applied for the two-phase simulations of the extraction column. The conservation equations are solved for each phase. The continuity equations for the liquid phase 1 is

$$\frac{\partial(\alpha_i \rho_i)}{\partial t} + \nabla \cdot (\alpha_i \rho_i \bar{u}_i) = 0 \quad (1)$$

where α is the volume fraction, which represents the space occupied by each phase, ρ is the phase density, u is the phase velocity. The conservation of momentum for phase 1 is

$$\frac{\partial(\alpha_i \rho_i \bar{u}_i)}{\partial t} + \nabla \cdot (\alpha_i \rho_i \bar{u}_i \bar{u}_i) - \nabla \cdot \tau_i = -\alpha_i \nabla p + \alpha_i \rho_i g + F_k \quad (2)$$

where τ is the stress-strain tensor, p is the pressure shared by all phases, g is the gravitational acceleration and F represents the interfacial forces.

In addition to (1) and (2) the summation equation for the volume fractions must be satisfied:

$$\alpha_1 + \alpha_2 = 1 \quad (3)$$

The inter-phase interaction term consists of different momentum exchange mechanisms. Only the drag force was taken into account, while the virtual mass force and the lift force can be neglected for a liquid-liquid interaction as shown by Wang and Mao (2005) in a stirred tank. The drag force is calculated in Fluent as

$$F_{c,d} = K_{c,d} (\bar{u}_d - \bar{u}_c) \quad (4)$$

where the subscripts c and d stand for the two liquid phases, while K represents the interphase momentum exchange coefficient. The exchange coefficient for a liquid-liquid mixture can be written in the following general form:

$$K_{c,d} = \frac{\rho_d \alpha_c \alpha_d f}{\tau_d} \quad (5)$$

where f is the drag coefficient and τ the particulate relaxation time.

$$\tau_d = \frac{\rho_d d_d^2}{18 \mu_c} \quad (6)$$

In the above equation d_d is the Sauter mean diameter of the droplets of the dispersed liquid phase and μ is the dynamic viscosity. For the description of the drag coefficient the model of Schiller & Naumann (1935) is applied

$$f = \frac{C_D \text{Re}}{24} \quad (7)$$

$$C_D = \begin{cases} 24(1 + 0.15 \text{Re}^{0.687}) / \text{Re} & \text{Re} \leq 1000 \\ 0.44 & \text{Re} > 1000 \end{cases} \quad (8)$$

With the relative Reynolds number Re defined as

$$\text{Re} = \frac{\rho_c |\bar{u}_d - \bar{u}_c| d_d}{\mu_c} \quad (9)$$

The drag force results finally in

$$F_{c,d} = \frac{3\rho_c \alpha_c \alpha_d C_D |\bar{u}_d - \bar{u}_c| \left(|\bar{u}_d - \bar{u}_c| \right)}{4d_d} \quad (10)$$

For the consideration of the multiphase turbulence the Fluent mixture turbulence model was used, which is an extension of the single-phase model, together with the realizable k- ε model. The k and ε equations for the realizable k- ε model are

$$\frac{\partial}{\partial t} (\rho_m k) + \nabla \cdot (\rho_m \bar{u}_m k) = \nabla \cdot \left(\frac{\mu_{t,m}}{\sigma_k} \nabla k \right) + G_{k,m} - \rho_m \varepsilon \quad (11)$$

$$\frac{\partial}{\partial t} (\rho_m \varepsilon) + \nabla \cdot (\rho_m \bar{u}_m \varepsilon) = \nabla \cdot \left(\frac{\mu_{t,m}}{\sigma_k} \nabla \varepsilon \right) + \rho_m C_1 S \varepsilon \quad (12)$$

$$-\rho_m C_2 \frac{\varepsilon^2}{k + \sqrt{\mu \varepsilon}}$$

$$C_1 = \max \left(0.43, \frac{\eta}{\eta + 5} \right) \quad (13)$$

$$\eta = S \frac{k}{\varepsilon} \quad (14)$$

where S is the strain rate tensor. G_k in eq. 11 represents the generation of turbulence kinetic energy due to the mean velocity gradients. The density, velocity and turbulent viscosity of the mixture are:

$$\rho_m = \alpha_c \rho_c + \alpha_d \rho_d \quad (15)$$

$$\bar{u}_m = \frac{\alpha_c \rho_c \bar{u}_c + \alpha_d \rho_d \bar{u}_d}{\alpha_c \rho_c + \alpha_d \rho_d} \quad (16)$$

$$\mu_{t,m} = \rho_m C_\mu \frac{k^2}{\varepsilon} \quad (17)$$

C_1 , C_2 and C_μ in eq. 12 and eq. 17 are model constants, whereas default values were used. One of the noteworthy features is that the production term in the ε equation does not involve the production of k as the other k- ε models. It is believed that the present form represents the spectral energy transfer better. This model has been extensively validated for a wide range of flows, including rotating homogeneous shear flows, free flows including jets and mixing layers, channel and boundary layer flows, and separated flows. For all these cases, the performance of the model has been found to be substantially better than that of the standard k- ε model

(Fluent user's guide 2005). Own investigations gave the same insight (Drumm & Bart 2006).

Population Balance Model

For the description of the PBM a number density function $n(\bar{x}, \phi, t)$ can be postulated, which denote the spatial position \bar{x} of a droplet as an external coordinate and the droplet volume ϕ as an internal coordinate. The total number of droplets in the entire system is then

$$\int_{\Omega_\phi} \int_{\Omega_x} n dV_x dV_\phi \quad (18)$$

The local average number density in physical space (per unit volume) is given by

$$N(\bar{x}, t) = \int_{\Omega_\phi} n dV_\phi \quad (19)$$

and the total volume fraction of all particles is given by

$$\alpha(\bar{x}, t) = \int_{\Omega_\phi} n V(\phi) dV_\phi \quad (20)$$

The transport equation for the number density function is finally given as

$$\frac{\partial}{\partial t} [n(V, t)] + \nabla \cdot [un(V, t)] = S(V, t) \quad (21)$$

where $S(V, t)$ are the source terms for coalescence and breakup of the droplets and can be further written as

$$S(V, t) = B^C(V, t) - D^C(V, t) + B^B(V, t) - D^B(V, t) \quad (22)$$

B^C and D^C are the birth and death rates of droplets of volume V due to coalescence. The birth and death rates are given by

$$B^C(V, t) = \frac{1}{2} \int_0^V a(V - V', V') n(V - V', t) n(V', t) dV' \quad (23)$$

$$D^C(V, t) = \int_0^\infty a(V, V') n(V, t) n(V', t) dV' \quad (24)$$

The birth and death rates B^B and D^B of particles of volume V due to breakage are given by

$$B^B(V, t) = \int_{\Omega_V} \nu g(V') \beta(V | V') n(V', t) dV' \quad (25)$$

$$D^B(V, t) = g(V) n(V, t) \quad (26)$$

Breakage and Coalescence Kernels

Two theoretical models for coalescence and breakup, the models of Luo & Svendsen (1996) and Coualaloglou & Tavlarides (1977) are written as C functions, compiled and implemented in Fluent as user defined functions. The breakage rate expression in eq. 25 is expressed as

$$g(V')\beta(V|V') \quad (27)$$

where $g(V')$ is the breakage frequency, i.e. the fraction of particles of volume V' breaking per unit time and $\beta(V|V')$ is the probability density function (PDF), which describes the distribution of the daughter droplets.

The coalescence kernel in eq. 23 and eq. 24 is defined as the product of two quantities, the collision frequency h and the coalescence efficiency λ .

$$a(V, V') = h(V, V') \cdot \lambda(V, V') \quad (28)$$

Model of Coualaloglou & Tavlarides (1977)

The well known model of Coualaloglou & Tavlarides considers drop deformation and breakup under the influence of local pressure fluctuations in a locally isotropic flow field. The coalescence term uses the frequently applied structure of the product of drop-drop collision frequency and coalescence efficiency. The following expressions of the model of Coualaloglou & Tavlarides were written as user defined functions:

$$g(d) = C_1 \cdot \frac{\varepsilon^{1/3}}{d^{2/3}(1+\alpha)} \exp\left(-\frac{C_2\sigma(1+\alpha)^2}{\rho_d \varepsilon^{2/3} d^{5/3}}\right) \quad (29)$$

where d is the diameter of the breaking droplet, α the volume fraction of the dispersed phase, ρ_d the density of the dispersed phase and σ the interfacial tension.

$$h(d_1, d_2) = C_3 \frac{\varepsilon^{1/3}}{1+\alpha} (d_1 + d_2)^2 (d_1^{2/3} + d_2^{2/3})^{1/2} \quad (30)$$

$$\lambda(d_1, d_2) = \exp\left(-C_4 \frac{\mu_c \rho_c \varepsilon}{\sigma^2} \left(\frac{d_1 d_2}{d_1 + d_2}\right)^4\right) \quad (31)$$

The originally used normal density function as by Valentas et al. (1966), which assumes binary breakage, was also adopted here.

$$\beta(d_1^3 | d_2^3) = \frac{2.4}{d_2^3} \exp\left(-\frac{4.5(2d_1^3 - d_2^3)^2}{d_2^6}\right) \quad (32)$$

It is obvious that the most important value, describing both coalescence and breakup, is the turbulent energy dissipation. The used values for the turbulent energy dissipation ε and the volume fraction α are returned for each cell from the Fluent solver.

Model of Luo & Svendsen (1996)

The second investigated model is the one by Luo & Svendsen (1996). The model is also based on the theories of isotropic turbulence and probability and contains no unknown or adjustable parameter. The break-up frequency is based on the arrival of turbulent eddies to the surface of the droplets. The global frequency of particles of size d is calculated as

$$g(d) = 0.923 \cdot (1+\alpha) \left(\frac{\varepsilon}{d^2}\right)^{1/3} \int_0^{0.5} \int_{\xi_{\min}}^1 \frac{(1+\xi)^2}{\xi^{11/3}} \exp\left(-\frac{12c_f\sigma}{\beta\rho_c\varepsilon^{2/3}d^{5/3}\xi^{11/3}}\right) d\xi df_v \quad (33)$$

where ξ is the ratio between the diameter of the turbulent eddy and the breaking droplet. β is a numerical constant equal 2.41. Luo determined the constant to be 2.0. C_f is the coefficient of surface area, which includes the ratio between the volume of one of the daughter droplets and the mother droplet.

$$c_f = f_v^{2/3} + (1 - f_v)^{2/3} - 1 \quad (34)$$

$$f_v = \frac{d_2^3}{d_1^3} \quad (35)$$

The first part of the double integral in eq. 33 can be solved when using the incomplete gamma function, while the second integral has to be solved numerically. For the second integral 10 equidistant points from 0 to 0.5 for the discretisation of f_v were used. The daughter PDF is obtained out of the integral when the partial breakage rate for a constant f_v is divided by the overall breakage rate.

$$\beta(f_v, v) = \frac{2 \int_{\xi_{\min}}^1 \frac{(1+\xi)^2}{\xi^{11/3}} \exp\left(-\frac{12c_f\sigma}{\beta\rho_c\varepsilon^{2/3}d^{5/3}\xi^{11/3}}\right) d\xi}{v \int_0^1 \int_{\xi_{\min}}^1 \frac{(1+\xi)^2}{\xi^{11/3}} \exp\left(-\frac{12c_f\sigma}{\beta\rho_c\varepsilon^{2/3}d^{5/3}\xi^{11/3}}\right) d\xi df_v} \quad (36)$$

The collision frequency and probability in the Luo & Svendsen model result from the kinetic gas theory and are

$$h(d_1, d_2) = \frac{\pi}{4} (d_1 + d_2)^2 \beta^{0.5} \varepsilon^{1/3} (d_1^{2/3} + d_2^{2/3})^{1/2} \quad (37)$$

$$\lambda(d_1, d_2) = \exp \left(-C_1 \frac{[0.75(1 + \xi^2)(1 + \xi^3)]^{1/2}}{\left(\frac{\rho_d}{\rho_c} + \gamma\right)^{1/2} (1 + \xi)^3} We^{1/2} \right) \quad (38)$$

C_1 is a unknown constant of order unity, γ is the virtual mass coefficient and ξ is the droplet size ratio d_1/d_2 . Both relations can be easily implemented in the user defined function.

Solution of population balance equations

The population balance equations are solved by the discrete method (CM) (Hounslow et al. 1988, Litster et al. 1995). The volume coordinate was discretised using a geometric factor as $V_{i+1}/V_i = 2^q$ (Litster et al. 1995), where q was chosen to be 0.5. In Fluent the PBE is written in terms of volume fraction of droplet size i for the CM

$$\frac{\partial}{\partial t} [\rho_d \alpha_i] + \nabla \cdot [\rho_d u_d \alpha_i] = \rho_d V_i S \quad (39)$$

where α_i is the volume fraction of droplet size i and is defined as

$$\alpha_i = N_i V_i = V_i \int_{V_i}^{V_{i+1}} n(V, t) dV \quad (40)$$

A fraction of α , called f_i , is introduced as a solution variable. This fraction is defined as

$$f_i = \frac{\alpha_i}{\alpha} \quad (41)$$

where α is the total volume fraction of the dispersed phase. The particle birth and death rates are then defined as follows

$$B^C_i = \sum_{K=1}^N \sum_{j=1}^N a_{kj} N_k N_j x_{kj} \xi_{kj}, \quad (42)$$

$$D^C_i = \sum_{j=1}^N a_{ij} N_i N_j, \quad (43)$$

$$B^B_i = \sum_{j=i+1}^N g_j N_j \beta(V_i | V_j), \quad (44)$$

$$D^B_i = g_i N_i. \quad (45)$$

The values ξ and x preserve the reassignment to the classes if the resulting aggregated droplet lies between the classes.

$$\xi_{kj} = \begin{cases} 1 & \text{for } V_i < V_{ag} < V_{i+1}, \text{ where } i \leq N-1 \\ 0 & \text{otherwise} \end{cases} \quad (46)$$

$$V_{ag} = [x_{kj} V_i + (1 + x_{kj}) V_{i+1}] \quad (47)$$

where

$$x_{kj} = \frac{V_{ag} - V_{i+1}}{V_i - V_{i+1}} \quad (48)$$

Finally, for the coupling with the fluid dynamics the Sauter mean diameter of the droplets is calculated in every time step and returned to the drag force (eq. 10).

$$d_{32} = \frac{\sum N_i d_i^3}{\sum N_i d_i^2} \quad (49)$$

Results and Discussion

In the following section the results of the simulations for the system toluene-water and the operating conditions conducted by Simon (2004) are shown. Both flow fields for the phases, as well as droplet distributions and a comparison with experiments, is presented. First, flow fields for the stirrer revolutions 150 and 300 rpm are presented for the model of Coualaloglou & Tavlarides. Fig.3 shows the simulated 2D velocity vectors and 2D velocity magnitude in the aqueous phase without considering the dominating swirl velocity, since the developed two-phase flow field is better visible then. Although the aqueous phase flows from top to bottom the vortices reverse at the positions between the stators and are directed to the top because the throughput of the ascending droplets is high enough to modify the flow pattern (Drumm & Bart, 2006). The same trend is obvious in Fig. 4 for 300 rpm. The higher stirrer revolution makes for a higher acceleration outwards, towards the column wall. For the sake of completeness in Fig.5 the contours of the velocity magnitude for a stirrer revolution of 150 rpm also considers the swirl velocity to make the dominance of the swirl velocity visible.

In Fig. 6 one can see the path of the dispersed phase, with an average volume fraction of 6%, through the compartment. The droplets do not penetrate the outer regions of the compartment and accumulate under stirrer and walls. Same observations were also made in experiments (Drumm & Bart, 2006). In Fig. 7 the volume fraction of the dispersed phase is depicted for a stirrer revolution of 300 rpm. The droplets penetrate the region between the stators much more, while the holdup in one extraction compartment increases to 9 %. This agrees well with measurements by Modes (1999), where the holdup in a RDC with the same operating conditions and the same geometry was measured around 10%.

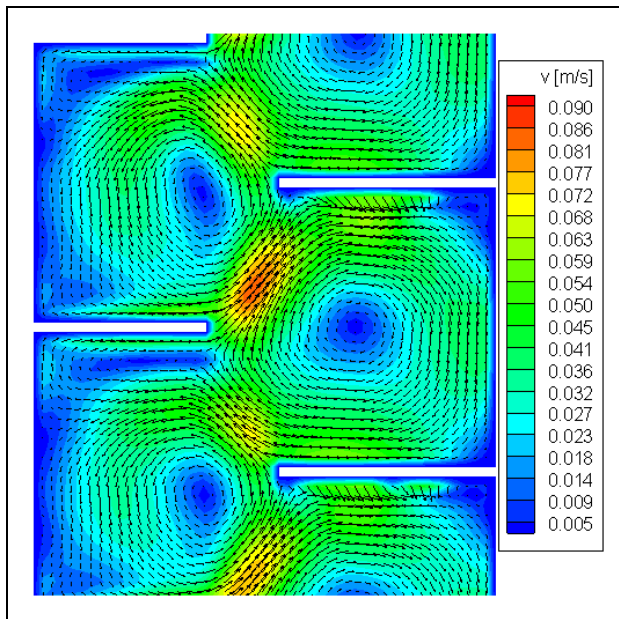


Figure 3: Simulated two-phase flow field for the system toluene-water, predicted velocity vectors (2D-plane) and velocity magnitude (2D) in the aqueous phase, $V_{aq}=100$ l/h, $V_{org}=100$ l/h, $n=150$ min⁻¹

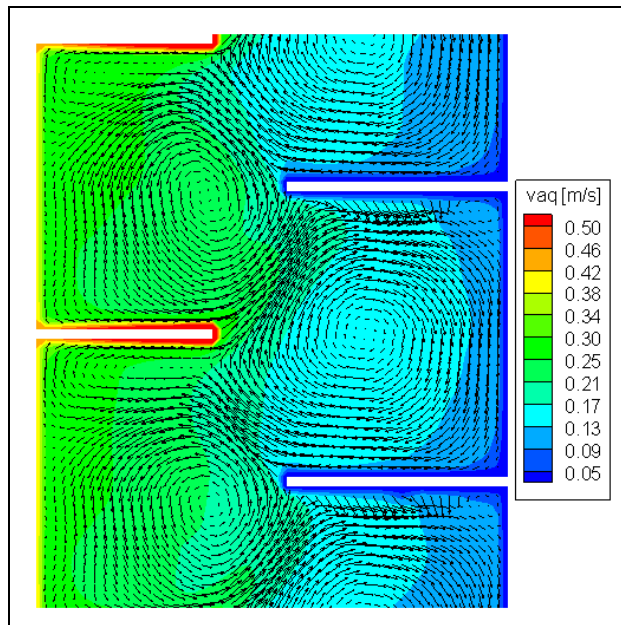


Figure 5: Simulated two-phase flow field for the system toluene-water, predicted velocity vectors (2D-plane) and velocity magnitude (3D) in the aqueous phase, $V_{aq}=100$ l/h, $V_{org}=100$ l/h, $n=150$ min⁻¹

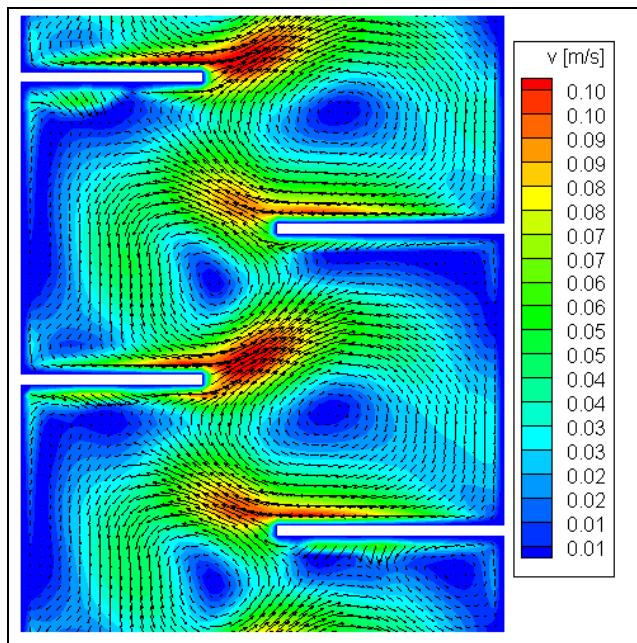


Figure 4: Simulated two-phase flow field for the system toluene-water, predicted velocity vectors (2D-plane) and velocity magnitude (2D) in the aqueous phase, $V_{aq}=100$ l/h, $V_{org}=100$ l/h, $n=300$ min⁻¹

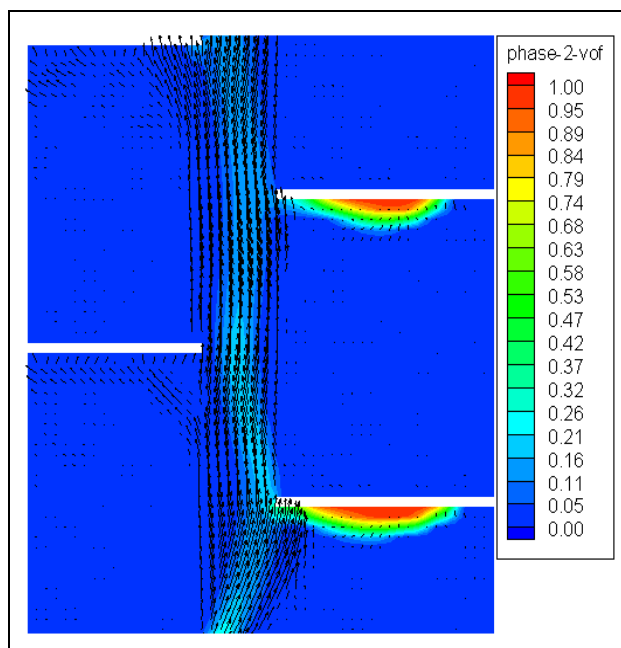


Figure 6: Simulated two-phase flow field for the system toluene-water, predicted velocity vectors (2D-plane) and volume fraction of the organic phase, $V_{aq}=100$ l/h, $V_{org}=100$ l/h, $n=150$ min⁻¹

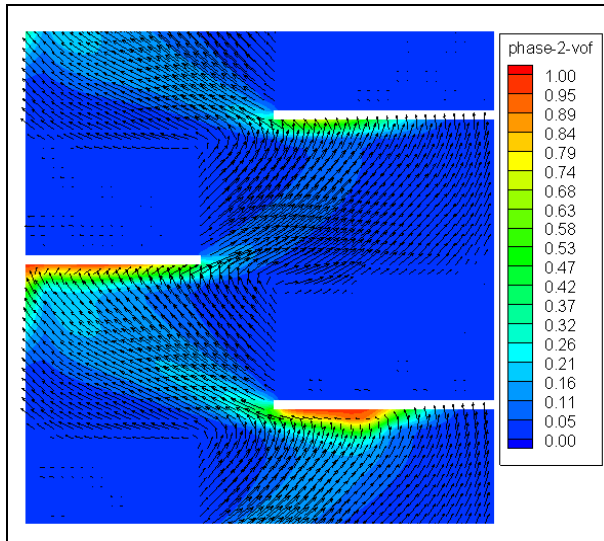


Figure 7: Simulated two-phase flow field for the system toluene-water, predicted velocity vectors (2D-plane) and volume fraction of the organic phase, $V_{aq}=100$ l/h, $V_{org}=100$ l/h, $n=300$ min⁻¹

Besides the flow fields and the volume fractions of the phases main interest is in the prediction of the droplet size distribution and the Sauter mean diameter, since the ratio of volume fraction and droplet diameter defines the liquid-liquid interfacial area available for mass transfer. Therefore, in Fig. 8 and Fig. 9 volume cumulative drop size distributions are depicted for the breakup and coalescence models of Coualoglou & Tavlarides (Fig. 8) and Luo & Svendsen (Fig. 9) for the system toluene-water. The volume fraction and the energy dissipation are from CFD simulations and the calculated Sauter mean diameter influences the drag force calculation. The model of Coualoglou & Tavlarides is able to predict the drop size distribution very accurately because of the adjustment of the parameters $C_3=0.005$ and $C_4=1.0E11$ in the coalescence terms. For the adjustable parameters in the breakup terms, constant values $C_1=0.005$ and $C_2=0.1$ were taken. For the model of Luo & Svendsen, the coalescence efficiency returns too high values when the parameter c_1 in eq. 38 is of order unity. Therefore the parameter c_1 was set to 7.0 for the simulation. The model of Luo & Svendsen still predicts a too wide distribution. However, the model of Luo & Svendsen allows for a major predictability, since no other parameters were adjusted. In consideration of this fact the model gave good results. Also, there are some possibilities to improve the model of Luo & Svendsen. For instance, only binary breakup is assumed in the model, which is suitable for gas bubbles but not for droplets, where more than two daughter droplets are formed. The Luo & Svendsen daughter droplet size distribution cannot match the physical situation, is very simple when examined separately and overestimates unequal breakage (Lasheras et al. 2002). This contradicts experimental investigations by Andersson & Andersson (2006), where equal sized breakup was the most probable outcome for drop breakup. In further simulations the simple PDF could be replaced by experimental correlated PDF (Modes 1999). Another key factor in the

description of the breakage rate is the double integral in eq. 33 where it is assumed that only a turbulent eddy, which is smaller than the droplet, cause breakage. New investigations by Andersson & Andersson (2006) or Eastwood et al. (2003) also showed that eddies bigger than the size of the fluid particle can cause breakup. Future work could take these facts into consideration for a further improvement of the prediction of the droplet size distribution. Also the coalescence kernel could be further improved or replaced by a more suitable coalescence model.

Finally, in Fig. 10 the predicted and measured Sauter mean diameter is compared. As for the cumulative drop size distribution the model of Coualoglou & Tavlarides predicts the Sauter mean diameter with a relative deviation of less than 5 %, while the model of Luo & Svendsen is almost 25 % deviant for a stirrer revolution of 150 rpm.

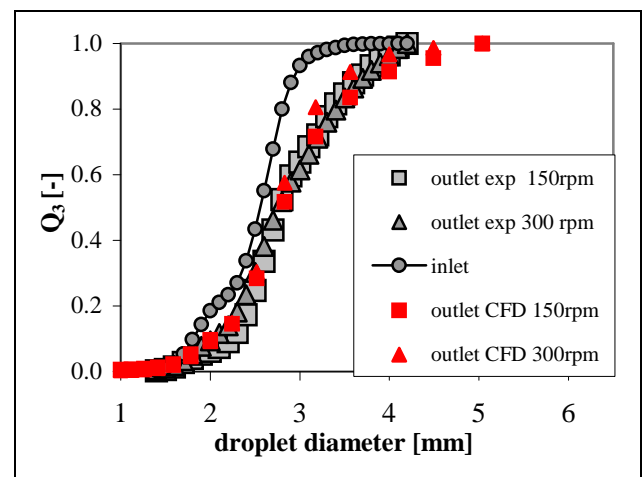


Figure 8: Measured and simulated volume cumulative drop size distribution Q_3 for the system toluene-water, $V_{aq}=100$ l/h, $V_{org}=100$ l/h, $n=150$ min⁻¹, 300 min⁻¹, Coualoglou & Tavlarides

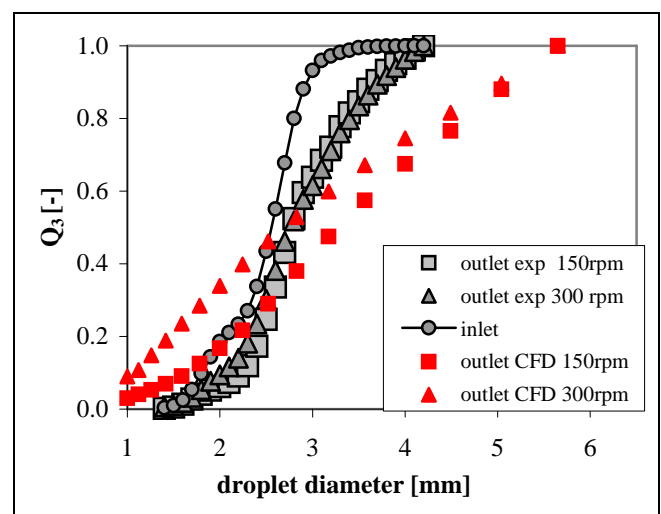


Figure 9: Measured and simulated volume cumulative drop size distribution Q_3 for the system toluene-water, $V_{aq}=100$ l/h, $V_{org}=100$ l/h, $n=150$ min⁻¹, 300 min⁻¹, Luo & Svendsen

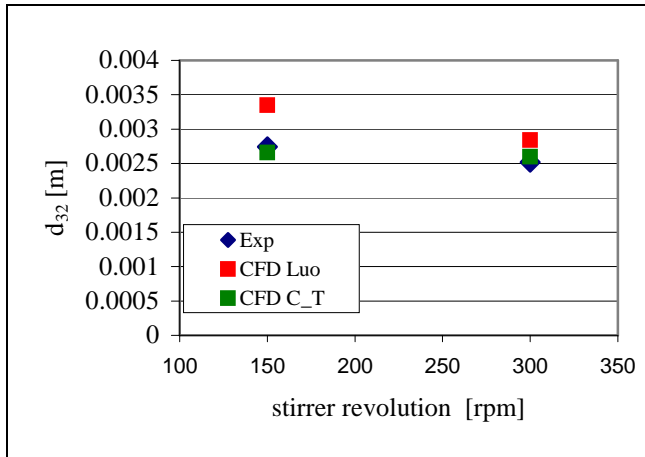


Figure 10: measured and simulated Sauter mean diameter of the droplets at the outlet of the RDC segment for the system toluene-water

Conclusions

In this work, a combination of CFD and DPBM in the framework of Fluent was applied to simulate the drop size distributions and flow fields in a 5 compartment section of a liquid-liquid RDC extractor. The liquid-liquid flow was modeled using the realizable $k-\epsilon$ turbulence model in conjunction with the Eulerian two-fluid equations. Two theoretical models for coalescence and breakup, the models of Luo & Svendsen (1996) and Coualoglou & Tavlarides (1977) were implemented in the CFD code as user defined functions. A complete coupling was applied, where the volume fraction and the energy dissipation in the source terms of the PBM were taken from CFD simulations and the calculated Sauter mean diameter influenced the drag force term for the flow field.

Simulated droplet distributions for the system toluene-water were compared to literature data by Simon (2004). Recapitulating, the Euler-Euler approach is able to describe the flow conditions as well as the holdup in a liquid-liquid extraction column, when a suitable turbulence model is chosen. For the model of Coualoglou & Tavlarides, the first results for the system toluene-water showed that the combined CFD-DPBM approach is able to predict the droplet size distribution in a RDC extractor very accurately, when the parameters in the model are adjusted. On the other hand, the model of Luo & Svendsen allowed for a major predictability, since only one parameter was changed and also gave acceptable results in terms of the droplet size distribution and the Sauter mean diameter. Possible improvements in the model of Luo & Svendsen were figured out and will be addressed in future work.

The first results of the linked CFD-PBM model show that the CFD-PBM tool is able to predict flow fields, holdup, both droplet distributions and Sauter mean diameter in a liquid-liquid extraction column. In comparison to the currently used DPBM codes in the introduction, the link of

CFD and PBM provides a prediction, where no experiments are needed, and in terms of the Luo & Svendsen model at most one parameter has to be adjusted.

Future Work

The following aspects will be considered in future work:

a) Breakup dominated test system

Since the system toluene-water is coalescence dominated, in the next step another test system like butylacetate-water should be investigated in terms of the application of the different coalescence and breakup kernels.

b) Coalescence and breakup models

The mentioned drawbacks of the model of Luo & Svendsen will be further investigated for another improvement of the prediction. More up to date models, e.g. the model of Andersson & Andersson (2006), should be implemented to gain a better basis for comparison and understanding, of what a complete model should contain.

c) CFD considerations -

near wall treatment and multiphase turbulence model

Own single-phase simulations have shown that the near wall treatment (e.g. wall functions, two layer model) has a big impact on the predicted turbulent energy dissipation, while the influence on the velocities of the flow field can be neglected. In a next step different near wall treatments and their influence on the predicted droplet size distribution should be investigated and compared. Instead of the Fluent mixture multiphase turbulence model other multiphase turbulent models could be considered (Sato 1981).

d) Column simulation

In the present work, a RDC segment with 5 compartments was simulated and compared to experimental results. In one of the next steps, when suitable coalescence and breakup closures are found it should be taken in consideration to simulate a whole column. By the means of the 2D grid of the RDC column this should be enabled with justifiable numerical effort.

Acknowledgements

This work was financially supported by the Deutsche Forschungsgemeinschaft (DFG).

Nomenclature

a	coalescence rate (s^{-1})
c_f	coefficient of surface area
C_D	drag coefficient
d	droplet diameter (m)

f	drag coefficient
f	solution variable
f_v	breakup fraction
F	interaction force (N)
g	acceleration (ms^{-2})
g	breakage frequency (s^{-1})
G	turbulence production term ($m^{-3}s^{-1}$)
h	collision frequency (s^{-1})
k	turbulent kinetic energy (m^2s^{-2})
K	exchange coefficient ($kg s^{-1}m^{-3}$)
n	number density function (m^{-6})
N	local average number density (m^{-3})
p	pressure (Nm^{-2})
Re	Reynolds number
S	strain rate (1/s)
u	velocity (ms^{-1})
t	time (s)
V	volume (m^3)
We	Weber number
x	coordinate (m)

Greek letters

α	volume fraction
β	probability density function
β	numerical constant
δ	Kronecker delta
ε	energy dissipation (m^2/s^3)
ϕ	droplet volume (m^3)
γ	virtual mass coefficient
λ	coalescence efficiency
ν	kinematic viscosity (m^2s^{-1})
ν	number of daughter droplets
μ	viscosity ($kgm^{-1}s^{-1}$)
ρ	density (kgm^{-3})
σ	interfacial tension (Nm^{-1})
τ	shear stress (Nm^{-2})
τ	particulate relaxation time (s)
ξ	size ratio between eddy and droplet
ξ	size ratio droplets
ξ	pivot rearrangement variable

Subscripts

1,2	coalesced droplet 1 and 2
ag	aggregation
c,d	continuous and dispersed phase
l	phase l
k	phase k
m	mixture

Abbreviations

CFD	computational fluid dynamics
CM	classes method
DPBM	droplet population balance model
PBM	population balance model
MUSIG	Multiple-Size-Group

QUICK	Quadratic Upwind Interpolation for Convective Kinematics
PIV	Particle Image Velocimetry
rpm	revolutions per minute

References

- Alopaeus, V., Koskinen, J. & Keskinen, K. I. Simulation of the population balances for liquid-liquid systems in a nonideal stirred tank. Part 1 description and qualitative validation of the model. Chem. Eng. Sci., Vol.54, 5887-5899 (1999)
- Andersson, R., Andersson, B. Modeling the breakup of fluid particles in turbulent flows. AIChE J, Vol. 52, 6, 2031-2038, (2006)
- Andersson, R., Andersson, B. On the breakup of fluid particles in turbulent flows. AIChE J., Vol. 52, 6, 2020-2030, (2006)
- Attarakih, M., Bart, H.-J., Lagar, L. & Faqir, N. LLECMOD: A Windows-based program for hydrodynamics simulation of liquid-liquid extraction columns. Chem. Engng. Proc., Vol. 45, 113-123 (2006)
- Coulaloglou, C. A. & Tavlarides, L. L. Description of interaction processes in agitated liquid-liquid dispersions. Chem. Eng. Sci., Vol. 32, 1289-1297 (1977)
- Drumm, C. & Bart, H.-J. Hydrodynamics in a RDC extractor: single and two-Phase PIV measurements and CFD simulations. Chem. Eng. Technol., Vol. 29; No. 11, 1297-1302 (2006)
- Eastwood, C. D., Armi, L. & Lasheras, J. C. The breakup of immiscible fluids in turbulent flows. J. of Fl. Mech., Vol. 502, 309-333 (2004)
- Fluent Inc. Fluent 6.2 user's guide (2005)
- Gourdon, C., Casamatta, G. A. & Muratet, G. Population balance based modelling. in Liquid – Liquid Extraction Equipment. Ed.: J.C. Godfrey and M.J. Slater, John Wiley & Sons, West Sussex, 141-226 (1994)
- Hounslow, M. J., Ryall, R. L. & Marshall, V. R. A discretized population balance for nucleation, growth and aggregation. AIChE J., Vol. 34, 11, 1821-1832 (1988)
- Hulburt, H. M. & Katz, S. Some problems in particle technology. Chem. Eng. Sci., Vol. 19, 555-574 (1964).
- Kronberger, T., A. Ortner, A., Zulehner, W. & Bart, H.-J. Numerical simulation of extraction columns using a drop population model. Comp. Chem. Eng., Vol. 19, 639-644 (1995)

Litster, J. D., Smit, D. J., Hounslow, M. J. Adjustable discretization population balance for growth and aggregation. *AICHE Journal*, Vol. 41, 3, 591-603 (1995)

Lo, S. Application of population balance to CFD modelling of gas-liquid reactors. Proc. "Trends in numerical and physical modelling for industrial multiphase flows", Corse (2000)

Luo, H. & Svendsen, H. F. Theoretical model for drop and bubble breakup in turbulent dispersions. *AICHE J.*, Vol. 42, 5, 1225-1233 (1996)

Modes, G. Grundlegende Studie zur Populationsdynamik einer Extraktionskolonne auf Basis von Einzeltropfenuntersuchungen, Ph.D. thesis, University Kaiserslautern, Germany (1999)

Sanyal, J., Marchisio, D. L., Fox, R. O., Dhanasekharan, K. On the comparison between population balance models for CFD simulation of bubble columns. *Ind. Eng. Chem. Res.*, Vol. 44, 5063-5072 (2005)

Schiller, L. & Naumann, Z. Über die grundlegenden Berechnungen bei der Schwerkraftaufbereitung. *Ver. Dtsch. Ing.*, Vol. 77, 143 (1935)

Schmidt, S.A., Simon, M., Attarakih, M., Lagar, L. G. & Bart, H.-J. Droplet population balance modelling - hydrodynamics and mass transfer. *Chem. Eng. Sci.*, Vol. 61, 246-256 (2006)

Simon, M. Koaleszenz von Tropfen und Tropfenschwärmen. Ph.D. Thesis, University Kaiserslautern, Germany (2004)

Steinmetz, T., Schmidt, S., Attarakih & M., Bart, H.-J. Droplet population balancing for column simulation, Proc. of the International Solvent Extraction Conference (ISEC 2005), Beijing, China, *China Academic Journal (compact disc version) Electronic Publishing House*, 997-1003 (2005)

Valentas, K.J., Bilous, O. & Amundson, N. R. Analysis of breakage in dispersed phase systems. *Ind. Engng. Chem. Fundl.*, Vol. 5, 2, 271-279 (1966)

Vikhansky, A., Kraft, M., Simon, M., Schmidt, S. & Bart, H.-J. Droplets population balance in a Rotating Disc Contactor: an inverse problem approach. *AICHE J.*, Vol. 52, 4, 1441-1450 (2006)

Wang, F. & Mao, Z.-S. Numerical and experimental investigation of liquid-liquid two-phase flow in stirred tanks. *Ind. Eng. Chem. Res.*, Vol. 44, 5776-5787 (2005)

Wulkow, M., Gerstlauer, A. & Nieken, U. Parsival: A tool for the simulation of crystallization processes. *Chem. Tech.*, Vol. 51, 5, 249-252 (1999)

Publication III

Reprinted from Proceedings 6th International Conference on Computational Fluid Dynamics in the Oil & Gas, Metallurgical and Process Industries CFD 2008, Johansen, S.T., Olsen, J.E., Ashrafiyan, A (Eds.), Trondheim, **2008**,

Christian Drumm, Menwer Attarakih, Sudarshan Tiwari, Jörg Kuhnert, Hans-Jörg Bart,
Implementation of the Sectional Quadrature Method of Moments in a CFD code.

Reprinted with permission from SINTEF (The Foundation for Scientific and Industrial Research at The Norwegian University of Science and Technology).

IMPLEMENTATION OF THE SECTIONAL QUADRATURE METHOD OF MOMENTS IN A CFD CODE

Christian DRUMM¹, Menwer ATTARAKIH², Sudarshan TIWARI³, Jörg KUHNERT³ and Hans-Jörg BART^{1*}

¹ Lehrstuhl f. Thermische Verfahrenstechnik, TU Kaiserslautern, POB 3049, 67653 Kaiserslautern, Germany

² Faculty of Eng. Tech., Chem. Eng. Dept., Al-Balqa Applied University, POB 15008, 11134 Amman, Jordan

³ Fraunhofer Institut Techno- und Wirtschaftsmathematik, Fraunhofer-Platz 1, 67663 Kaiserslautern, Germany

* E-mail: bart@mv.uni-kl.de

ABSTRACT

In this work, the Sectional Quadrature Method of Moments (SQMOM) is implemented in the commercial CFD code Fluent for solving the population balance equation in a combined CFD-Population Balance Model (PBM). The SQMOM is introduced via user-defined functions (UDF) and user-defined scalars. The SQMOM offers the possibility to use a multi-fluid model depending on the number of primary particles in the SQMOM. Normally, a two-fluid model is applied in CFD-PBM models. Hereby, all droplets (particles) move in the same velocity field, characterized by the Sauter mean diameter. As a start, an Eulerian three-fluid model is tested whereas two fluids, respectively two primary particles in the SQMOM are defined for the dispersed phase and continuity and momentum equations are solved for each fluid. Aggregation and breakage are considered in the population balance model which is coupled to the fluid dynamics in order to describe droplet behaviour in a stirred liquid-liquid extraction column. Some case studies show the accuracy of the SQMOM-three-fluid model and the possible advantage of this model in comparison to a common two-fluid model. Results of the three-fluid SQMOM simulation are compared to results of a two-fluid simulation using the Quadrature method of moments which was also introduced via UDF.

Keywords: CFD, Population balances, multi-fluid model, Sectional Quadrature Method of Moments

NOMENCLATURE

a coalescence frequency [$1/(m^3s)$]
B birth due to aggregation or breakage
 C_D drag coefficient
D death due to aggregation or breakage
d diameter [m]
f drag coefficient
F interaction force [N]
g gravity [m/s^2]
g breakage frequency [$1/(m^3s)$]
L abscissa [m]
m moment [m^{k-3}]
n number density function [$1/m^6, 1/m^4$]
 N_f number of fluids
 N_{pp} number primary particles (sections)
 N_{sp} number secondary particles (weights/abscissa)
p pressure [Pa]

S source terms [m^{k-3}/s]
t time [s]
u velocity [m/s]
V volume [m^3]
x coordinate [m]
w weights

Greek

α volume fraction [-]
 β probability density function [1/m]
 δ Kronecker delta
 ρ density [kg/m^3]
 τ stress-strain tensor [N/m^2]
 τ particulate relaxation time [s]
 μ dynamic viscosity [kg/ms]

Subscripts / superscripts

32 Sauter mean diameter
C coalescence
B breakage
c continuous phase
d dispersed phases
<i> ith section
i ith dispersed section (phase)
k kth moment
l phase

INTRODUCTION

In recent years, CFD simulations have been used with great success in chemical engineering applications and allowed the prediction of local hydrodynamic details in equipment encountered in many industrial processes. One of the widely used multiphase models for CFD simulations is the Eulerian multiphase model which can describe a dispersed multiphase flow and accounts for interactions between the dispersed phase and the continuous phase. Generally, a two-fluid model is applied successfully for a two-phase problem, whereas the Sauter mean diameter represents the different sizes of the particles in the dispersed phase. (e.g. Drumm & Bart, 2006; Wang & Mao, 2005). If the particle size distribution is very wide or multimodal this approach is more likely to fail. Recent research also investigated

multi-fluid models to consider different sizes of the particles in the dispersed phase to overcome these restrictions (Hosoakwa et al., 2007; Hjertager, 2007). However, particle-particle interactions such as breakage or aggregation were not considered.

In this connection, the population balance modelling (PBM) forms the cornerstone for modelling the complex behaviour of dispersed phase systems (e.g. liquid-liquid, gas-liquid, precipitation) and accounts for the particle interactions such as breakage and aggregation (Ramkrishna, 2000). When the particle size distribution is modelled instead of using averaged particle sizes, dependencies on the particles sizes (e.g. for mass transfer in gas-liquid and liquid-liquid) are considered.

Today, the focus is on combined CFD-PBM models because of the mutual benefits and the strong interdependency between particle interactions and fluid dynamics. Combined CFD-PBM models are widely used nowadays (Sanyal et al., 2005; Drumm et al., 2008; Lo & Rao, 2007; Krepper et al., 2007; Petitti et al., 2007). Currently applied CFD-PBM models are normally based on the two-fluid Multiple Size Group (MUSIG) Model (Lo, 2000), where all particles in the PBM share the same velocity field and only one momentum equation is solved for all particle classes. The particle size distribution is modelled with PBM while only averaged particle sizes as the Sauter mean diameter are coupled to the drag term and used for the influence on the fluid dynamics. A new strategy as in the inhomogeneous MUSIG model tries to divide the dispersed phase into a number of N velocity groups, where each of the velocity groups is characterized by its own velocity field, to get rid of the common simplification (Krepper et al., 2007). As a drawback, this approach is based on the CPU-time consuming classes method (CM).

For the solution of the PBM, CM (Hounslow et al., 1988; Ramkrishna, 2000) and the Quadrature Method of Moments (QMOM) (Marchisio et al., 2003) are normally used in the coupled models. In the CM the particle population is discretized into a finite number of intervals that are used to track the population density directly. The CM is particularly useful when the particle sizes do not vary widely. On the other hand, one limitation of the finite difference schemes is their inability to predict accurately integral quantities (low-order moments as an especial case) associated with populations of sharp shapes (Ramkrishna, 2000; Attarakih, et al., 2006). The QMOM as first introduced by McGraw (1997) is found very efficient from accuracy and computational cost point of view. Unlike the CM, the QMOM has a drawback of destroying the shape of the distribution and the information about the distribution is only stored in its moments. The QMOM was recently analyzed and tested using different case studies concerned with crystallization (Grosch et al., 2007). The authors highlighted the problem of ill-conditioning associated with either the standard or direct QMOM when the number of abscissas increases.

The SQMOM (Attarakih et al., 2008) as an adaptive method combines the advantages of the CM and the QMOM and minimizes their drawbacks. The SQMOM is based on the concept of primary and secondary particles, where the primary particles are responsible for

the distribution reconstruction (classes), while the secondary ones (method of moments) are responsible for breakage and coalescence events and carry detailed information about the distribution. The method can track accurately any set of low-order moments with the ability to reconstruct the shape of the distribution. The SQMOM has three major advantages over the different QMOM analyzed by Grosch et al. (2007): First, the inversion of the moment problem using the product difference algorithm or the direct QMOM is no longer needed since explicit analytical expressions are now derived. Second, the problem of ill-conditioning is reduced due to the limited number of abscissas to two. Third, the convergence of the solution could now be tested by increasing the number of sections, which is not available at all in the standard QMOM (Attarakih et al., 2008). First attempts, using only one primary particle were recently carried out to couple the SQMOM with a CFD code for the simulation of an extraction column (Drumm et al., 2008). In this case, the SQMOM is equivalent to the QMOM.

Coupling of the SQMOM to a CFD code

Summarising, there are different possibilities for combined CFD-PBM models. The PBM itself accounts for the modelling of the size distribution rather than averaged particle sizes. Common CFD-PBM models are still limited to two-fluid models while first attempts of multi-fluid models were already carried out. For the PBM, the SQMOM seems to be a very attractive alternative beside the numerous solution methods. This contribution now focuses on a combined CFD-PBM model, whereas the SQMOM is applied for the solution of the PBM. In comparison to the present models, a more accurate and less CPU-time consuming multi-fluid approach is achieved when the SQMOM is applied. Two primary particles are applied, whereas one momentum equation is solved for each primary particle and two secondary particles ($N_{sp}=2$ corresponding to four moments) are sufficient to account for particle interactions. The SQMOM is incorporated in Fluent by the use of user defined scalars and user-defined functions for the source terms. In principle, the coupled model is applicable in many engineering fields, in the following we focus on a liquid-liquid extraction problem. Therefore, simulations were carried out for a Rotating Disc Contactor extraction column using the system toluene-water. The paper is structured as follows: first, the governing equations of the three-fluid model as well as the PBM, the SQMOM and the coupling between CFD and PBM are introduced. After that, the SQMOM simulation results are shown and compared to results of the QMOM. Finally, a summary and conclusions are given.

CFD-PBM MODEL

Multi-fluid model

A three-fluid model based on the Eulerian approach, where all phases are treated mathematically as interpenetrating continua, was applied for the coupling. Here we consider three phases (fluids), one for the liquid phase and two phases for the dispersed phase

resulting from the use of two primary particles. The conservation equations are solved for each phase. The continuity equation for the phase 1 is:

$$\frac{\partial(\alpha_i \rho_i)}{\partial t} + \nabla \cdot (\alpha_i \rho_i \mathbf{u}_i) = \rho_i S_i. \quad (1)$$

The conservation of momentum for phase 1 is:

$$\frac{\partial(\alpha_i \rho_i \mathbf{u}_i)}{\partial t} + \nabla \cdot (\alpha_i \rho_i \mathbf{u}_i \mathbf{u}_i) - \nabla \cdot \boldsymbol{\tau}_i = -\alpha_i \nabla p + \alpha_i \rho_i \mathbf{g} + \mathbf{F}_i + \rho_i \mathbf{u}_i S_i. \quad (2)$$

The source terms in eqs. 1 and 2 represents the transfer of dispersed phase mass and momentum due to breakage and coalescence processes that causes droplets to move between the sections in the SQMOM. In addition to eqs. 1 and 2 the constraint for the volume fractions must be satisfied:

$$\sum_{i=1}^{N_f} \alpha_i = 1. \quad (3)$$

In this work, only the drag force was taken into account for the inter-phase interaction term, while the virtual mass force and the lift force can be neglected for liquid-liquid interactions. (Drumm & Bart, 2006, Wang & Mao, 2005). The drag force between the continuous and the two dispersed phases is represented by:

$$\mathbf{F}_{c,d} = \frac{3\rho_c \alpha_c \alpha_d C_D |\mathbf{u}_d - \mathbf{u}_c| (\mathbf{u}_d - \mathbf{u}_c)}{4d_{32,d}}. \quad (4)$$

Here, the model of Schiller & Naumann (1935) is applied for the evaluation of C_D . For the calculation of the multiphase turbulence, the Fluent mixture turbulence model can be used, which is an extension of the single-phase model, together with the realizable k- ϵ model (Fluent, 2006). The realizable k- ϵ model delivers reliable results for the investigated extraction column (Drumm & Bart, 2006). However, here we focus on the implementation of the SQMOM and the multi-fluid model and not on the prediction of the hydrodynamics and turbulences. Therefore laminar flow is assumed in the present simulations. More details about the governing equations can be found elsewhere (Drumm & Bart, 2007; Fluent, 2006).

Population Balance Model

Population balance equation and QMOM

The population balance is a continuity statement written in terms of the particle number concentration. The general derivation based on the Reynolds transport theorem is given in Ramkrishna (2000). The transport equation for the number density concentration n can be given as:

$$\frac{\partial}{\partial t} [n(V,t)] + \nabla \cdot [\mathbf{u}n(V,t)] = S(V,t), \quad (5)$$

where $S(V,t)$ is the source term for breakage and coalescence due to birth and death rates (B and D respectively) and can be further expanded as:

$$S(V,t) = B^C(V,t) - D^C(V,t) + B^B(V,t) - D^B(V,t). \quad (6)$$

In the sectional or classes methods CM (e.g. Hounslow et al., 1988; Ramkrishna, 2000) the particle size is discretized into a number of sections, where the population in each section is considered to behave like a single particle. On the other hand, in the methods of moments as the QMOM (McGraw, 1997; Marchisio et al., 2003), the transport equation is written for the moments of the distribution. The k^{th} moment of the distribution is defined as:

$$m_k(x,t) = \int_0^{\infty} n(d,x,t) d^k dd. \quad (7)$$

Accordingly, the transport equation for the moments is:

$$\alpha_d \rho_d \frac{\partial}{\partial t} (m_k) + \alpha_d \rho_d \nabla \cdot (\mathbf{u}_d m_k) = \alpha_d \rho_d S_k. \quad (8)$$

The QMOM is based on the following quadrature approximation of the moments:

$$m_k = \int_0^{\infty} n(d,x,t) d^k dL = \sum_{i=1}^N w_i L_i^k, \quad (9)$$

where the quadrature approximation of order N is defined by its N weights w_i and N abscissas L_i and can be calculated in terms of the first $2N$ moments m_0, \dots, m_{2N-1} using the product-difference (PD) algorithm (Gordon, 1968). A generalization and detailed investigation of the quadrature method of moments have been presented recently by Grosch et al. (2007). The authors highlighted various error sources and investigated also the ill-conditioned map from the moments to the abscissas and weights.

The Sectional Quadrature Method of Moments

In the SQMOM framework of discretization, the single particles from the sections of the CM will be called the primary particles (N_{pp}) and they will be responsible for the reconstruction of the distribution. Unfortunately, a large number of primary particles in the classical sectional methods is required, not only to reconstruct the shape of the distribution, but also to estimate the desired integral quantities associated with the distribution, which are normally predicted with low accuracy. To overcome this fundamental problem of the sectional methods, N_{sp} secondary particles are generated in each section (i) with positions (abscissas: $d_j^{<i>$) and weights ($w_j^{<i>$) where $i=1,2,\dots,N_{pp}$; $j=1,2,\dots,N_{sp}$. The secondary particles are exactly equivalent to the number of quadrature points in the QMOM. The way in which the SQMOM works is started by dividing the particle size into contiguous sections (N_{pp} primary particles). Each section is then seeded by the desired number of secondary particles which carry detailed information

about the distribution. In this framework, the active particle interactions such as breakage and coalescence occur through interactions between the secondary particles. Note that $N_{sp} \times N_{pp}$ particles are contributing in the breakage and coalescence events. Due to the increase of the number of interacting particles, more information is gathered about the distribution itself. The distribution could be reconstructed from the secondary particles by averaging the total weights of the secondary particles with respect to the section width Δd_i and locating them at the mean size of the secondary particles. In pure mathematical sense, the SQMOM is equivalent to applying the QMOM to each section of an arbitrary width: $[d_{i-1/2}, d_{i+1/2}]$, $i=1,2,\dots,N_{pp}$, resulting in a set of sectional moments that could be written as:

$$m_k^{<i>}(x,t) = \int_{d_{i-1/2}}^{d_{i+1/2}} n(d,x,t) d^k dd. \quad (10)$$

Note that four moments are sufficient for each section to carry detailed information about the distribution when the number of secondary particles equals two. Within this context two sets of quadratures are analytically derived avoiding problems associated with the PD-algorithm.

The two equal weights and abscissas can be calculated by the moments m_0 , m_1 and m_3 .

$$L_{1,2} = m_1 \pm \frac{1}{\sqrt{3}} \sqrt{\frac{m_3}{m_1} - m_1^2}, \quad (11)$$

$$w_{1,2} = \frac{1}{2} m_0, \quad (12)$$

where all the sectional moments appearing in eq.11 are normalized with respect to the zero moment. Now, The transport equation (eq.8) is solved for each sectional moment.

$$\alpha_i \rho_d \frac{\partial}{\partial t} (m_k^{<i>}) + \alpha_i \rho_d \nabla \cdot (\mathbf{u}_d m_k^{<i>}) = \alpha_i \rho_d S_k^{<i>}. \quad (13)$$

The source terms normally consist of vector and matrices multiplication to account for the N_{pp} primary and N_{sp} secondary particles. In the present case, we have applied two primary particles ($N_{pp}=2$) and two secondary particles ($N_{sp}=2$). For this simple case, the source terms for death and birth due to coalescence and breakage can be written without matrices as:

$$B_k^{C <i>} = \sum_{k=1}^{i \times N_{sp}} \sum_{j=k}^{i \times N_{sp}} \left(1 - \frac{1}{2} \partial_{k,j} \right) w_j^{<i>} \cdot w_k^{<i>} \cdot \left(L_j^{<i>3} + L_k^{<i>3} \right)^{k/3} \cdot a(L_j^{<i>}, L_k^{<i>}) \quad (14)$$

$$D_k^{C <i>} = \sum_{j=1}^{N_{sp}} w_j^{<i>} \cdot L_j^{<i>k}. \quad (15)$$

$$\sum_{m=1}^{N_{pp}} \left(a(L_j^{<i>}, L_1^{<m>}) \cdot w_1^{<m>} + a(L_j^{<i>}, L_2^{<m>}) \cdot w_2^{<m>} \right) B_k^{B <i>} = \sum_{m=i}^{N_{pp}} \sum_{j=1}^{N_{sp}} \left(\int_{d_{i-1/2}}^{\min(d_{i+1/2}, d_j^{<i>})} L_j^{<m>k} \cdot w_j^{<m>} \cdot g(L_j^{<m>}) \cdot L^k \beta(L | L_j^{<m>}) \partial L \right) \quad (16)$$

$$D_k^{B <i>} = \sum_{j=1}^{N_{pp}} L_j^{<i>k} \cdot w_j^{<i>} \cdot g(L_j^{<i>}). \quad (17)$$

Here, the source terms account for movements between the sections due to the birth and death terms. The generality of the SQMOM was proved by showing that all the related sectional and quadrature methods appearing in the literature for solving the population balance equation are merely special cases. When the number of secondary particles equals one the CM is recovered. On the other hand, when the number of primary particles (sections) equals one, the classical QMOM is recovered. More details about this approach can be found in the original paper of Attarakih et al. (2008).

Coupling CFD and PBM in Fluent

The moments for the primary particles are defined as user-defined scalars in Fluent. Each primary particle receives its own fluid inside the dispersed phase. The weights and abscissas (eq. 11-12) are calculated at the beginning of each time step and stored in user-defined memory. The source terms (eq. 14-17) were written as user-defined functions and added to the transport equation of each sectional moment (eq. 13). Therefore eight user-defined scalars were used, respectively four moments for each section. By means of the equal weights and abscissas it would even be possible to consider only three moments (m_0 , m_1 and m_3), while m_2 is estimated by interpolation between the available moments. In addition, the third moment m_3 could also replace the continuity equation of the dispersed phase resulting in another reduction of computational costs. The source term in eq. 13 represents the local transfer of droplet phases between the sections due to breakage and coalescence of droplets. Therefore, the source terms of the third moments which account for the movement between the sections are coupled to the continuity and momentum equations of the corresponding fluid (eq. 1 & eq. 2). For coupling with the fluid dynamics the Sauter mean diameter of the droplets is calculated in each section at each time step and returned to the drag force of the respective phase in Eq. (4). So each section moves with its own velocity field based on the Sauter mean diameter of this section.

$$d_{32}^{<i>} = \frac{m_3^{<i>}}{m_2^{<i>}}. \quad (18)$$

Concerning the breakage and coalescence frequencies, constant kernels for coalescence and breakage were used at this early stage of numerical experimentation. However, in future, when models for coalescence and breakage are used, governing values e.g. the turbulent energy dissipation ε or the volume fraction α could be returned for each cell from the solver. The velocity of the dispersed phases in eq. 13 is derived from the Navier-Stokes equations, thus a complete two-way coupling between CFD and PBM is assured.

Numerical Schemes & column geometry

The simulations were carried out for a 5-compartment section of a Rotating Disc Contactor extraction column with 150 mm inner diameter (Fig.1). A water-toluene system was considered with toluene as the dispersed phase. The drop size distribution of the toluene droplets was assumed as two monodisperse equal volume fractions with one peak at 2 mm and the other one at 4 mm. In a common multi-fluid model the Sauter mean diameter of the dispersed phase would be 2.7 mm. The RDC column was operated countercurrently at identical throughputs of 100 l/h for the aqueous and the organic phases respectively. The stirrer speed was set to 150 rpm.

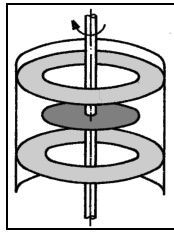


Figure 1: Sketch of a Rotating Disc Contactor compartment.

Three test cases were investigated: one without breakage and coalescence, one assuming pure breakage and the third one is with pure coalescence:

Test case	1	2	3
Aggregation a	0	0	1. E-8
Breakage g	0	0.2	0
Daughter distribution β	uniform		

Table 1: Test cases

A 2D axis symmetric grid of the column was modeled in Gambit. Because of the rotational symmetry of a Rotating Disc Contactor, the 2D grid can be adopted without losing information. Previous work showed that a 2D grid delivers reliable results regarding the hydrodynamics of an RDC (Drumm & Bart, 2006, Drumm & Bart, 2007). For the boundary conditions the common approach with one pressure outlet condition at the top and one velocity-inlet at the bottom was applied. Quadrilateral elements with a grid space of 1 mm were adopted to map the flow domain. The computational grid is depicted in Fig. 2. Standard wall functions were used for modelling the near wall region. For the under-relaxation factors standard values were used without

modification and an under-relaxation factor of 0.5 was applied for the moments.

RESULTS

In the following section the results of the simulations for the system toluene-water are shown. The simulations were carried out for the introduced three-fluid model using the SQMOM with two primary particles and compared to results of a common two-fluid model using the QMOM. For comparison, the equal weights and abscissas are also applied in QMOM instead of using the PD-algorithm. For the SQMOM the global upper (7 mm) and lower boundaries (0.001 mm) of the droplet size were defined at the beginning and the sections were seeded by the secondary particles. Because of the two equal volume monodisperse droplet distributions, the sectional moments at the inlet of the organic phase become:

$$m_0^{<1>} = 1.25E8, m_1^{<1>} = 250000, m_2^{<1>} = 500, m_3^{<1>} = 1$$

$$m_0^{<2>} = 1.56E7, m_1^{<2>} = 62500, m_2^{<2>} = 250, m_3^{<2>} = 1$$

For the two-fluid model only one set of moments is considered as:

$$m_0 = 5.27E7, m_1 = 140625, m_2 = 375, m_3 = 1$$

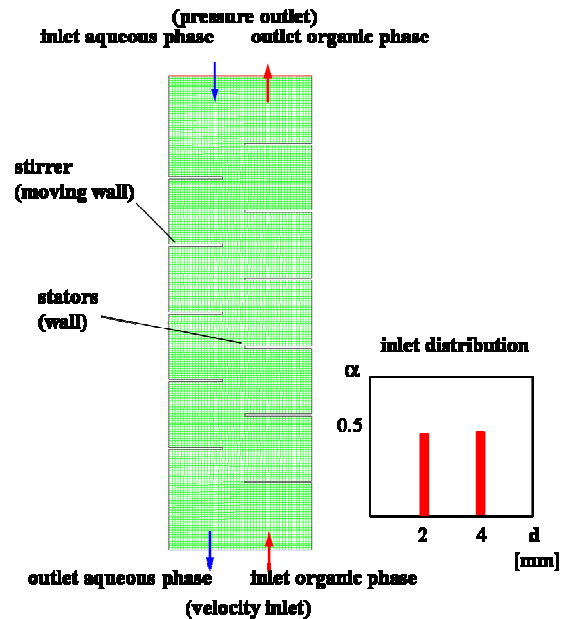


Figure 2: Computational grid and inlet drop size distribution

Test case 1: no source terms

First, the results for test case 1 are shown. The test case without source terms was chosen to test the evolution of the user-defined scalars and to show the major differences between the three-fluid and two-fluid model. In Fig. 3 the Sauter mean diameters of the two sections with SQMOM (eq. 18) are depicted. The sectional d_{32} remain constant through the column when the source terms are set to zero as expected.

In Fig. 4 one can see the volume fractions and the path of the two dispersed phases (fluids) through the compartments. The droplets do not penetrate the outer regions of the compartment and accumulate under the stirrer and the stators. The first primary particle (2 mm, first section) accumulates much more under stirrer and stators in comparison to the second primary particle (4 mm, second section), since bigger droplets have a higher rising velocity and therewith a smaller holdup than small droplets.

The global d_{32} calculated by means of eq. 19 is depicted in Fig. 5. It is calculated by summing up the third and second moments over all sections:

$$d_{32}^{<global>} = \frac{\sum \alpha^{<i>} \cdot m_3^{<i>}}{\sum \alpha^{<i>} \cdot m_2^{<i>}} \quad (19)$$

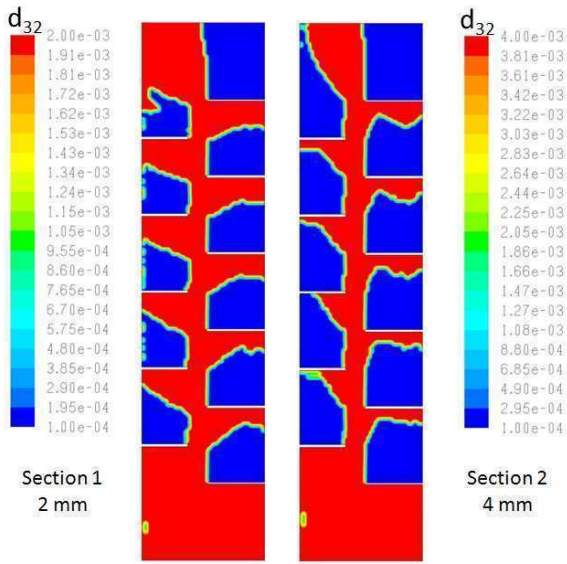


Figure 3: Three-fluid model, sectional d_{32} without source terms

The d_{32} using the QMOM (two-fluid model) as well as the volume fraction are depicted in Fig. 6.

It is obvious from Fig. 5 and Fig. 6 that the two-fluid model cannot account for the differences in the drop size distribution. The influence of the two monodisperse distributions is blurred and neither reflected by the volume fraction or the d_{32} . The two-fluid model presents a trade-off which is suitable for narrow distributions or monomodal distributions but not for the chosen bimodal one. The selected distribution is even a narrow distribution and was chosen as a case study to point out possible benefits of the multi-fluid model. On the other hand, in previous work it could be shown that the two-fluid model is able to predict holdup and path of the dispersed phase for a real extraction column where the droplet size in a monomodal distribution ranged from around 1 to around 5 mm (Drumm & Bart, 2007)

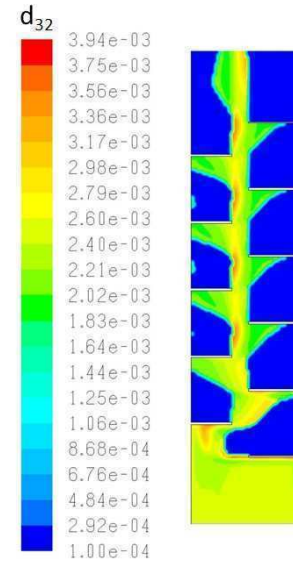


Figure 5: Three-fluid model, global d_{32} without source terms

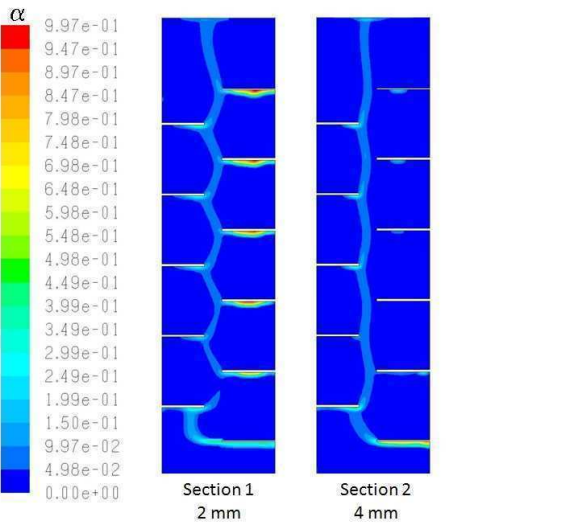


Figure 4: Three-fluid model, sectional volume fraction without source terms

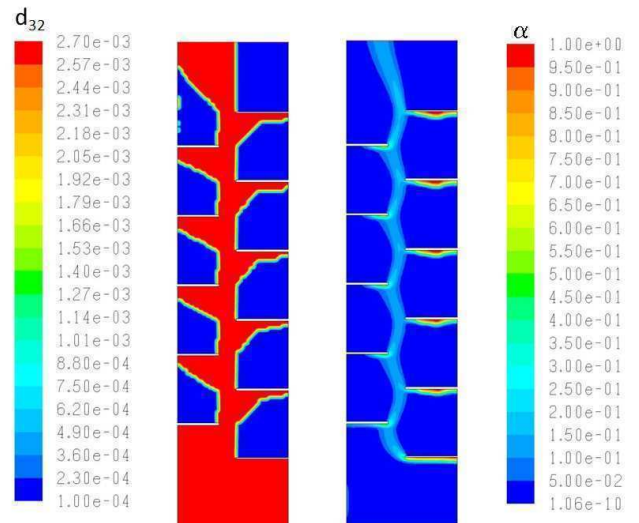


Figure 6: Two-fluid model, d_{32} and volume fraction without source terms

Test case 2: Breakage only

The case of pure breakage was considered to show the movement of the droplets between the two sections in SQMOM.

First, the SQMOM was applied in a two-fluid model to validate the correct implementation of the algorithm in Fluent. This case allows for a comparison, since the global d_{32} resulting from the SQMOM with two primary particles and the QMOM should be almost equal. Attarakih et al. (2008) investigated the influence of the number of primary and secondary particles on the convergence of the first four moments. It is evident that the order of convergence is increased by increasing both the primary and secondary particles due to the increasing accuracy of evaluating the unclosed integrals in the PBE. Nevertheless, the influence is small enough to allow for a qualitative comparison. The main differences are now that the real moments of the distribution are considered in the two sections of SQMOM, while only the global set of moments is considered in QMOM. The global d_{32} using the SQMOM ($N_{pp}=2$) and the QMOM both for a two-fluid model are depicted in Fig. 7. The diameter at the outlet (top) is nearly equal around 1.8 mm for both the SQMOM with two primary particles and the QMOM. In SQMOM, the contribution of total mass in the first section increases to around 85% at the outlet because of the breakage into this section. The result shows the correct implementation of the SQMOM and the correct movement of mass between both sections.

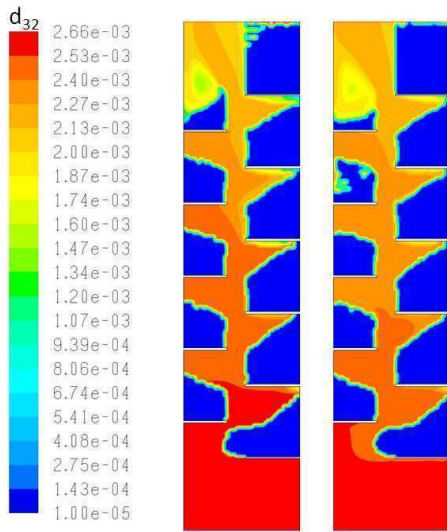


Figure 7: Global d_{32} : SQMOM ($N_{pp}=2$, left) and QMOM (right), two-fluid model

In the next step, the three-fluid model was applied for the SQMOM ($N_{pp}=2$). All source terms were considered in the governing equations. As in the two-fluid case, the second section in SQMOM is almost empty at the outlet since the entire droplet volume in the second section breaks into the first section because of the constant breakage. The volume fraction of both sections considering mass movement between the fluids due to the source terms is depicted in Fig.8. The holdup of the

second section decreases because of the breakup into the first section and results in accumulation of mass in the first section. Now it is clear that almost only the first section contributes to the global d_{32} because of the empty second one (Fig. 8).

The sectional d_{32} are depicted in Fig. 9 and confirm this fact. The d_{32} in the second section reaches the lower boundary instantly and is interpolated to be located between the boundaries while the d_{32} in section 1 decreases to around 1.7 mm and dominated the overall d_{32} .

Finally, the overall d_{32} calculated by means of eq. 19 is depicted in Fig. 10. As in Fig. 7, the diameter at the outlet is 1.8 mm, respectively in the region (1.6 – 2.1) mm due to the volume fraction of both fluids. The same behavior as in Fig. 5 is also observed: the influence of the different sections and drop sizes respectively is accounted for in the three-fluid model.

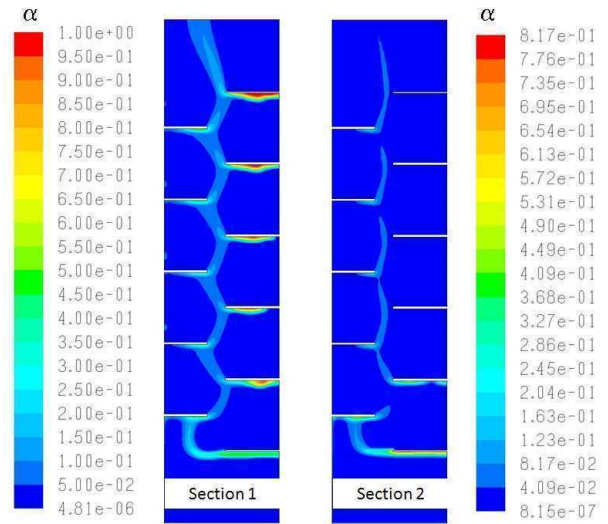


Figure 8: sectional volume fraction: SQMOM (three-fluid model)

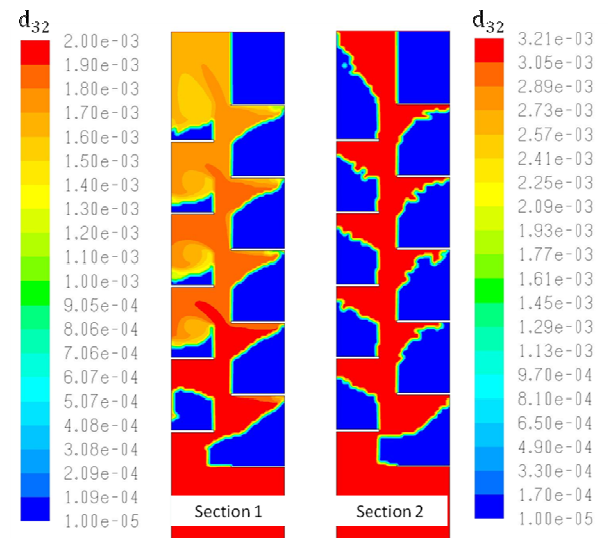


Figure 9: Sectional d_{32} : SQMOM (three-fluid model)

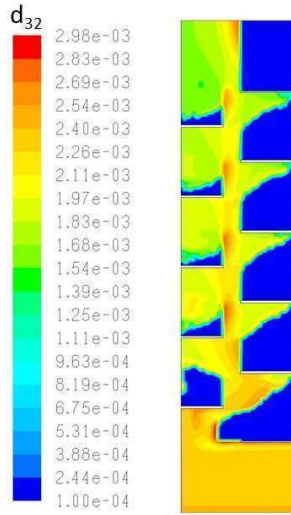


Figure 10: Global d_{32} : SQMOM (three-fluid model)

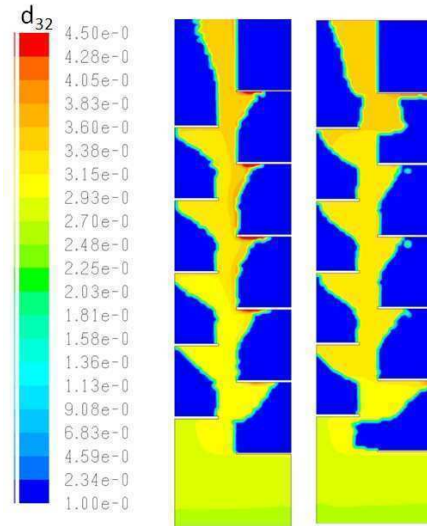


Figure 11: Global d_{32} : SQMOM (left) and QMOM (right), two-fluid model

Test case 3: Coalescence only

A constant aggregation was assumed in the third test case. Again, a two-fluid model was considered first to test the evolution of SQMOM separately. For this case, the second section in SQMOM was empty at the inlet and all sectional moments were set to zero, while the sectional moments of the first section were equal to the moments in the QMOM. Fig. 11 compares the global Sauter mean diameter in the column section as predicted by the SQMOM and QMOM. The Sauter mean diameter at the outlet (top) is nearly equal to 3.5 mm using both methods. In SQMOM, the contribution of total mass in the second section increases to around 30% at the outlet because of the coalescence into this section.

As in the previous case, in the next step the SQMOM was applied in the three-fluid model to show the different behavior. The volume fraction of both sections considering mass movement between the fluids is depicted in Fig.12. The holdup of the first section decreases because of the droplet coalescence into the second section and results in the accumulation of mass in the second section. Finally, Fig. 13 shows the global d_{32} . The d_{32} at the outlet is now in the region 3 – 5.2 mm depending on the volume fraction of the respective phase.

Recapitulatory, the results of the implemented SQMOM are nearly equal to the results of the QMOM for the Sauter mean diameter when the two-fluid model is applied. The comparison for the two-fluid model shows the correct implementation of SQMOM in Fluent. Furthermore, the local transfer of mass between the sections is working accurately. The source terms for the continuity and momentum equations were considered in the three-fluid model. The impact of the droplet breakage and coalescence on the volume fractions due to the movement between the sections is correctly described and makes a great visual impact. It is obvious that multi-fluid models (a three-fluid model here) can account for size-specific volume fractions and velocities and will improve the predictability of coupled CFD-PBM solvers.

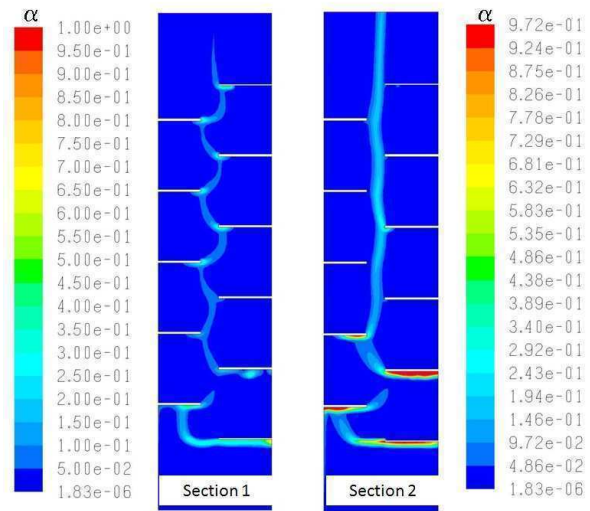


Figure 12: sectional volume fraction: SQMOM (three-fluid model)

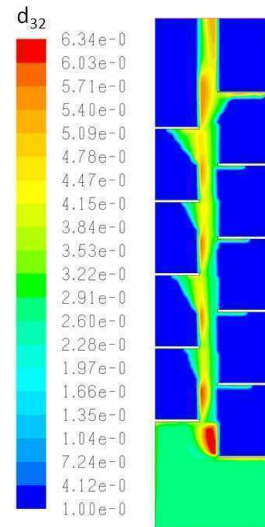


Figure 13: Global d_{32} : SQMOM (three-fluid model)

CONCLUSIONS

The SQMOM was incorporated in the commercial CFD code Fluent via user-defined subroutines. First results of the coupled CFD-PBM algorithm using the SQMOM and a three-fluid model were presented and compared to a two-fluid-QMOM model which was also written as subroutines. A complete two-way coupling is achieved between the fluid dynamics and the PBM. Constant kernels in the model account for breakage and coalescence. Simulation results for three test cases show the accuracy and benefit of the three-fluid model using SQMOM in comparison to the two-fluid model using the QMOM. The local movement of the droplets between the two fluids in the SQMOM is working smoothly while the overall Sauter mean diameter is calculated correctly. In future work, models for breakage and coalescence can be easily integrated and will allow for a prediction of the real drop size distribution in a column. The SQMOM represents a perfect basis to couple CFD and PBM in a multi-fluid model. The multi-fluid model accounts for the proper description of the fluid dynamics while the SQMOM allows for an accurate description of the particle size distribution. An unlimited amount of additional fluids or primary particles could also be easily added, while only the computational power sets the limit. A multi-fluid model can describe size-specific particle behaviour as velocities or hold-up much better and can further improve the predictability of coupled CFD-PBM solvers.

ACKNOWLEDGMENTS

The authors would like to thank the Deutsche Forschungsgemeinschaft (DFG) for the financial support.

REFERENCES

- ATTARAKIH, M. M., BART, H.-J., & FAQIR, N. M. (2006), "Numerical solution of the bivariate population balance equation for the interacting hydrodynamics and mass transfer in liquid-liquid extraction columns", *Chem. Eng. Sci.*, **61**, 113-123.
- ATTARAKIH, M. M., DRUMM, C. & BART, H.-J. (2008), "Solution of the population balance equation using the sectional quadrature method of moments", accepted for publ. in *Chem. Eng. Sci.*
- DRUMM, C. & BART, H.-J., (2006), "Hydrodynamics in a RDC extractor: single and two-Phase PIV measurements and CFD simulations", *Chem. Eng. Techn.*, **29**, 11, 1297-1302.
- DRUMM, C. & BART, H.-J., (2007), "Coupling of CFD with DPBM: Drop size distributions and flow fields in a RDC extractor", *Proc. of the 6th International Conference on Multiphase Flow ICMF-2007*, M. Sommerfeld (Ed.), Leipzig, Germany, July 9-13.
- DRUMM, C., TIWARI, S., ATTARAKIH, M. M., KUHNERT, J. & BART, H.-J., (2008), "CFD-PBM coupled model using the finite point set method and the SQMOM", *Proc. International Solvent Extraction Conference (ISEC 2008)*, Tucson, USA, September 15-19.
- FLUENT, (2006), *Fluent 6.3 User's guide*, Fluent, Inc., Lebanon, USA.
- GORDON, R.G., (1968), "Error bounds in equilibrium statistical mech.", *Journal Mathematical Physics*, **9**, 655-672.
- GROSCHE, R., BRIESEN, H., MARQUARDT, W. & WULKOW, M., (2007), "Generalization and numerical investigation of QMOM", *AIChE Journal*, **53**, 207-224.
- HOUNSLOW, M. J., RYALL, R. L. & MARSHALL, V. R., (1988), "A discretized population balance for nucleation, growth and aggregation", *AIChE Journal*, **34**, 1821-1832.
- KREPPER, E., FRANK, T., LUCAS, D., PRASSER, H.-M. & ZWART, P.J., (2007), "Inhomogeneous MUSIG model – a population balance approach for polydispersed bubbly flows", *Proc. of the 6th International Conference on Multiphase Flow ICMF-2007*, M. Sommerfeld (Ed.), Leipzig, Germany, July 9-13.
- HJERTAGER, B.H., (2007), "Multi-fluid CFD analysis of chemical reactors", In: *Multiphase reacting flows: modelling and simulation*, D.L. Marchisio & R.O. Fox (Eds.), Vol. 492 CISM Series, Springer, Wien, 125-179.
- HOSOAKWA, S., SOU, A. & TOMIYAMA, A., "Multi-fluid simulation of turbulent bubbly pipe flows", *Proc. of the 6th International Conference on Multiphase Flow ICMF-2007*, M. Sommerfeld (Ed.), Leipzig, Germany, July 9-13.
- LO, S., (2000). "Application of population balance to CFD modelling of gas-liquid reactors", *Proc. "Trends in numerical and physical modeling for industrial multiphase flows"*, Corsica, France.
- LO, S. & RAO, P., (2007). "Modeling of droplet breakup and coalescence in an oil-water pipeline", *Proc. of the 6th International Conference on Multiphase Flow ICMF-2007*, M. Sommerfeld (Ed.), Leipzig, Germany, July 9-13.
- MARCHISIO, D.L., PIKTURNA, J.T., FOX, R.O., VIGIL, R.D. & BARRESI, A.A., (2003), Quadrature method of moments for population-balance equations, *AIChE J.*, **49**, 1266-1276.
- MARCHISIO, D.L., VIGIL, R.D. & FOX, R.O., (2003), "Implementation of the Quadrature Method of Moments in CFD-codes for aggregation-breakage problems", *Chem. Eng. Sci.*, **58**, 3337-3351.
- MCGRAW, R., (1997), "Description of aerosol dynamics by the Quadrature Method of Moments", *Aerosol Sci. and Tech.*, **27**, 255-265.
- PETITTI, M., CARAMELLINO, M., MARCHISIO, D.L. & VANNI, M., (2007), "Two-scale simulations of mass transfer in an agitated gas-liquid tank", *Proc. of the 6th International Conference on Multiphase Flow ICMF-2007*, M. Sommerfeld (Ed.), Leipzig, Germany, July 9-13.
- RAMKRISHNA, D., (2000), "Population balances: theory and applications to particulate systems in engineering", Academic Press, San Diego.
- SCHILLER, L., NAUMANN, Z., (1935). „Über die grundlegenden Berechnungen bei der Schwerkraftaufbereitung“. *Zeitschrift des Vereines Deutscher Ingenieure*, **77**, 143.

SANYAL, J., MARCHISIO, D. L., FOX, R. O. & DHANASEKHARAN, K., (2005), "On the comparison between population balance models for CFD simulation of bubble columns", *Ind. & Eng. Chem. Res.*, **44**, 5063-5072.

WANG, F. & MAO, Z.-S., (2005), "Numerical and experimental investigation of liquid-liquid two-phase flow in stirred tanks", *Ind. & Eng. Chem. Res.*, **44**, 5776-5787.

Publication IV

Reprinted from Proceedings 6th International Conference on Computational Fluid Dynamics in the Oil & Gas, Metallurgical and Process Industries CFD 2008, Johansen, S.T., Olsen, J.E., Ashrafiyan, A (Eds.), Trondheim, **2008**,

Menwer Attarakih, Dia Zeidan, Christian Drumm, Sudarshan Tiwari, Hussein Allaboun, Hans-Jörg Bart, Jörg Kuhnert,

Dynamic Modelling of Liquid Extraction Columns using the Direct Primary and Secondary Particle Method (DPSPM).

Reprinted with permission from SINTEF (The Foundation for Scientific and Industrial Research at The Norwegian University of Science and Technology).

DYNAMIC MODELLING OF LIQUID EXTRACTION COLUMNS USING THE DIRECT PRIMARY AND SECONDARY PARTICLE METHOD (DPSPM)

Menwer ATTARAKIH^{1*}, Dia ZEIDAN², Christian DRUMM³, Hussein ALLABOUN⁴, Sudarshan TIWARI⁵, Hans-Jörg BART³, and Jörg KUHNERT⁵

¹ Faculty of Eng. Tech., Chem. Eng. Dept., Al-Balqa Applied University, POB 15008, 11134 Amman, Jordan

² Dept. of Basic Sciences, Al-Balqa Applied University, 119117- AL-Salt, Jordan

³ Lehrstuhl f. Thermische Verfahrenstechnik, TU Kaiserslautern, POB 3049, 67653 Kaiserslautern, Germany

⁴ Jordan University of Science & Tech., Chemical Eng. Dep., P.O. Box: 15008, 22110 Irbid, Jordan

⁵ Fraunhofer Institut Techno- und Wirtschaftsmathematik, Fraunhofer-Platz 1, 67663 Kaiserslautern, Germany

- E-mail: attarakih@yahoo.com

ABSTRACT

Dynamic modelling of liquid extraction columns is not so established as that of distillation columns because of the discrete nature of the dispersed phase. The natural framework for taking this into account is the bivariate population balance equation. However, due to the mathematical complexity of the resulting model it is not feasible to use it for dynamic and online control purposes. To reduce the complexity of these models without losing the dynamic information, the concept of the primary and secondary particle method is utilized to reduce the bivariate population balance model to a self-contained dynamic one. In this model one primary and one secondary particles are only used, which correspond to conserving the total number and volume concentrations. These particle internal properties are tracked directly and coupled through the mean positions of the particle along the size and solute concentration coordinates. The secondary particle could be envisaged as fluid particle carrying information about the distribution as it evolves in space and time. The reduced model is shown to be hyperbolic with nonlinear source terms. Four contact waves are identified with two distinct positive and negative speeds. Accordingly, special discretization technique based on the upwind scheme with Flux Vector Splitting is used. The unsteady state analysis reveals that the dominant time constant is due to the solute concentration in the continuous phase. On the contrary, the response of the dispersed phase mean properties is relatively very fast compared to the solute concentration one.

Keywords: Dynamic Modelling, Population balances, Two liquid phase flow, Primary and Secondary Particle Method.

NOMENCLATURE

A_c	column cross-sectional area [m ²]
c	solute concentration [kg/m ³]
B, D	birth and death source terms [1/m ³ /s]
D_x	axial dispersion coefficients [m ² /s]
d	droplet diameter [m]
d_{vs}	Sauter mean droplet diameter [m]
d_{30}	Mass-number mean droplet diameter [m]
F	Flux vector as given by Eq.(21)

$f_{d,cy} \partial d \partial c_y$	the number of droplets with d and $c_y \in [d, d + \partial d] \times [c_y, c_y + \partial c_y]$ [1/m ³]
H	column height [m]
K_{oy}	overall mass transfer coefficient [m/s]
K_s	slowing factor due to column geometry [-]
m	solute distribution coefficient [-]
m'	modified solute distribution coefficient [-]
N	total number concentration [1/m ³]
N_{pp}, N_{sp}	number of primary and secondary particles respectively [-].
P	vector of physical properties [$\mu \rho \sigma$]
Q	volumetric flow rate [m ³ /s]
t	time [s]
u	velocity [m/s]
U	vector of conservative variables
v	droplet volume [m ³]
v_{in}	feed mean droplet volume [m ³]
X	total solute concentration in x-phase [kg/m ³]
Y	total solute concentration in y-phase [kg/m ³]
z	space coordinate [m]

Greek Symbols

α	total phase holdup [-]
Γ	breakage frequency [1/s]
ϑ	mean number of daughter droplets [-]
λ	eigenvalue [s]
$\mu_r^{<i>}$	r th moment in the i th section
μ	viscosity [Pa.s]
π	droplet interaction source terms as defined by Eq.(13).
ρ	density [kg/m ³]
σ	interfacial tension [N/m]
τ	time constant [s]
Υ	source term that represents the net number of droplet produced by breakage and coalescence [1/s]

ψ	internal and external coordinates vector ($[d, c_y, z, t]$)
ω	coalescence frequency [m^3/s]

Subscripts

x, y	continuous and dispersed phases respectively
s	slip velocity
t	terminal velocity

Superscripts

b	breakage
c	coalescence
*	equilibrium
\square	derivative with respect to time
–	mean value
in	inlet
out	outlet

INTRODUCTION

Liquid-liquid extraction columns are one of the major multiphase contacting equipment that received a wide industrial acceptance in many fields of engineering such as hydrometallurgical, nuclear, petrochemical, pharmaceutical, and food industries (Lo et al., 1983, Bart, 2001). However, the optimal design and control of such equipment has not yet been fulfilled and still dependent on the time consuming and expensive scale up methods based on laboratory scale pilot plants.

The understanding of liquid-liquid extraction columns dynamic behaviour can be notably used in the design of process control strategy or the start-up and shutdown procedures (Hufnagl et al., 1991, Weinstein et al., 1998, Mjalli, 2005, Xiaojin et al., 2005). The attempts to model this dynamic behaviour are founded because of the discrete nature of the dispersed phase. This is due to the complex nature of the macroscopic dispersed phase interactions as well as the microscopic interphase mass transfer occurring in the continuously turbulent flow field. These macroscopic interactions such as droplet breakage and coalescence coupled to the interphase mass transfer result in a distributed population of droplets. This population is distributed not only in the spatial domain of the contacting equipment, but also randomly distributed with respect to the droplet state (properties) such as size, concentration and age. Accordingly, the state of any droplet is represented by a bivariate (joint) density function $f_{d,c_y}(d, c_y; t, z) \partial d \partial c_y$ accounting for the number of droplets having sizes and concentrations in the ranges $[d, d + \partial d] \times [c_y, c_y + \partial c_y]$ per unit volume of the contactor. This allows the discontinuous macroscopic (breakage and coalescence) and the continuous microscopic (interphase mass transfer) events to be coupled in a single spatially distributed population balance equation. Unfortunately, the full dynamic investigation and control of liquid-liquid extraction columns could be problematic; partially due to their multiphase nature, and partially due

to the difficulty of online measurements of important output variables. Due to this, many of the impeded modules in the commercial flowsheeting packages used in process design for liquid extraction columns are still based on the pseudo homogeneous or simplified stagewise population balance models that are not able to capture the essential column dynamics. Actually, the natural modelling approach that reflects the dispersion phase details is by using the bivariate population balance framework (Attarakih et al., 2006, 2008). However, due to the size and mathematical complexity of the resulting model it is not feasible to use it for dynamic and online control purposes or as an impeded module in process design flowsheeting programs, where short computational times are needed. To reduce the complexity of these models without losing the dynamic information, it is obvious that a suitable reduction technique is needed. Accordingly, the concept of the primary and secondary particle method (PSPM) (Attarakih, et al., 2008) is utilized to reduce the bivariate population balance model to a self contained dynamic model with one primary and one secondary particles. The secondary particle could be envisaged as fluid particle carrying information about the whole distribution as it is evolved in space and time. This information reflects the particle - particle interactions (breakage and coalescence) and transport (convection and diffusion). On the other hand, the primary particle carries the mean properties of the population such as total number concentration; mean droplet diameter, dispersed phase holdup and so on. So, the main objective of this work is to develop a reduced mathematical model (from the bivariate population balance equation) capable of describing the dynamic behaviour of liquid-liquid extraction columns that has a distributed physical rather than stagewise nature.

THE MATHEMATICAL MODEL

The Bivariate Population Balance Equation

The general spatially distributed population balance equation (SDPBE) describing the coupled hydrodynamics and mass transfer in liquid extraction columns in a one spatial domain could be written as (Attarakih et al., 2006):

$$\frac{\partial f_{d,c_y}(\psi)}{\partial t} + \frac{\partial [u_y f_{d,c_y}(\psi)]}{\partial z} + \frac{\partial [c_y f_{d,c_y}(\psi)]}{\partial c_y} = \frac{Q_y^{\text{in}}}{A_c} \frac{f_{d,c_y}^{\text{in}}}{v^{\text{in}}}(d, c_y; t) \delta(z - z_y) + \mathcal{Y}\{\psi\} \quad (1)$$

In this equation the components of the vector $\psi = [d, c_y, z, t]$ are those for the droplet internal state (diameter and solute concentration), the external coordinate (column height) (z) and the time (t) where the velocity along the concentration coordinate (c_y) is (\dot{c}_y). The bivariate volume source term ($\mathcal{Y}\{\psi\}$) represents the net number of droplets produced by breakage and coalescence per unit volume and unit time

in the coordinates range $[\zeta, \zeta + \partial\zeta]$ (ζ accounts for droplet size and solute concentration) and is rather complex due to the appearance of many double integrals in the death and birth terms (Attarakih, et al., 2006). The left hand side is the continuity operator in both the external and droplet internal states. The first term on the right hand side is a point source term representing the rate at which the droplets entering the column with volumetric flow rate ($Q_{y,in}$) that is perpendicular to the column cross-sectional area (A_c) at a location (z_y) with an inlet number density (f_{d,c_y}^{in}) satisfying the normalization condition and (v^{in}) is the mean volume of the droplets leaving the distributor (see Fig.(1)). The dispersed phase velocity (u_y) relative to the walls of the column is determined in terms of the relative (slip) velocity with respect to the continuous phase (u_s) and the continuous phase velocity (u_x) with respect to the walls of the column as follows:

$$u_y = u_s - u_x \quad (2)$$

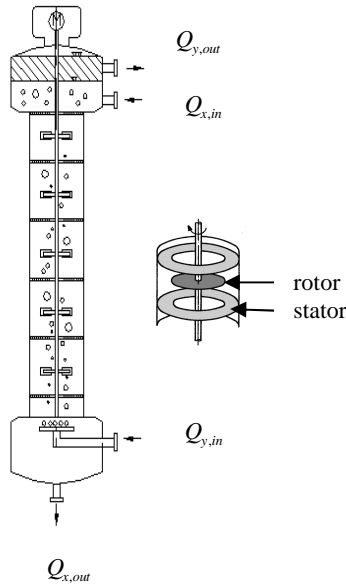


Figure 1: A Rotating Disc Contactor (RDC) and one compartment internal geometry.

The slip velocity (u_s) is given by an algebraic velocity model assuming that the liquid droplets could reach their equilibrium velocity in a short period of time compared to the system relaxation time (Manninen et al., 1996). It could be related to the single droplet terminal velocity, (u_t) to take into account the droplet swarm (the effect of the dispersed phase holdup: α_y) and the flow conditions in a specific equipment:

$$u_s = K_s (1 - \alpha_y) u_t(d, \mathbf{P}) \quad (3)$$

The elements of the vector \mathbf{P} consists of the system physical properties ($[\mu \rho \sigma]$), and K_s is a slowing factor taking into account the effect of the column internal geometry (presence of stators and rotor disks as

shown in Fig.(1)) on the droplet terminal velocity ($0 < K_s \leq 1$) (Modes et al., 1999). A useful guide for selecting the suitable droplet terminal velocity based on the shape of the droplet (rigid, oscillating or circulating), and hence on the system physical properties, could be found in Gourdon et al. (1994).

The solute concentration in the continuous phase (c_x) is predicted using a component solute balance on the continuous phase:

$$\frac{\partial(\alpha_x c_x)}{\partial t} - \frac{\partial}{\partial z} \left(u_x \alpha_x c_x + D_x \frac{\partial(\alpha_x c_x)}{\partial z} \right) = \frac{Q_x^{in} c_x^{in}}{A_c} \delta(z - z_y) - \int_0^\infty \int_0^{c_y, \max} \dot{c}_y v(d) f_{d,c_y}(\psi) \partial d \partial c_y \quad (4)$$

Note that the volume fraction of the continuous phase (α_x) satisfies the physical constraint: $\alpha_x + \alpha_y = 1$. The left hand side of Eq.(4) as well as the first term on the right hand side have the same interpretations as those given in Eq.(1); however, with respect to the continuous phase. The last term appearing in Eq.(4) is the total rate of solute transferred from the continuous to the dispersed phase, where the liquid droplets are treated as moving point sources. The presence of the diffusion flux in the second term of Eq.(4) is to take into account the nonideal behavior of the turbulent continuous flow (Lo et al., 1983).

DROPLET INTERACTION FUNCTIONS

The source term appearing in Eq.(1) could be expanded as:

$$\Upsilon = B^b(d, c_y; t, z) - D^b(d, c_y; t, z) + B^c(d, c_y; t, z) - D^c(d, c_y; t, z) \quad (6)$$

where B^b and B^c are the rate of droplets birth due to droplet breakage and coalescence respectively, and D^b and D^c are the rates of droplet loss (death) due to droplet breakage and coalescence respectively.

Droplet Breakage

For droplet breakage in an RDC column, it is experimentally observed that the droplet breakage is mainly determined by the action of the shearing force resulting from the rotating disk (Cauwenberg et al., 1997; Schmidt et al., 2006). Cauwenberg et al. (1997) suggested a correlation for breakage probability (fraction of mother droplets that are broken up) to a modified Weber number. This takes into account the critical rotor speed below which the shear force is not enough to exceed the droplet surface energy. As reported by Schmidt et al. (2006) it is the interfacial tension rather than the other physical properties (viscosity or density) that play the major role in the droplet breakage. Since the measurement of the non-equilibrium interfacial tension as a function of solute concentration is not yet well established, it is of great importance to include at least the effect of the equilibrium interfacial tension on the droplet breakage. Schmidt et al. (2006) studied the effect of the equilibrium solute concentration (acetone) on the

interfacial tension, and hence the breakage probability in a segment of an RDC column based on the single droplet experiments. They found that the breakage probability increases as the equilibrium interfacial tension decreases for the two studied systems (water-acetone-toluene and water-butyl acetate). Within this context they followed Cauwenberg et al. (1997) and correlated the breakage probability using the two aforementioned chemical systems.

Droplet Coalescence

Generally speaking, droplet coalescence is less understood than droplet breakage since it involves the interaction between two droplets and the intervening liquid film from the continuous phase. The physiochemical properties of this film and the turbulent fluctuations play an important role in droplet coalescence. Coalescence is believed to occur if the contact time between any two randomly coalescing droplets exceeds the time required for the complete intervening film drainage and rupture (Coulaloglou & Tavlarides, 1977). These authors expressed the coalescence frequency as a product of collision rate and coalescence efficiency based on the kinetic theory of gases and the film hydrodynamics with two fitting parameters.

Mass Transfer Coefficients

The dispersed phase individual mass transfer coefficient is found dependent on the behavior of the single droplet in the sense whether it is stagnant, circulating or oscillating (Kumar and Hartland, 1999). In the present work, the simplified model of Handlos and Baron (1957) as well as the correlation of Kumar and Hartland (1999) are used. However, the criterion based on the Reynolds number as suggested by Zhang et al. (1985) may be used as a guide for selecting the proper mass transfer model. The individual mass transfer coefficient for the continuous phase is essentially subjected to the aforementioned classification procedure, where two models are used to predict it. The first simple one is based on the film coefficient equation as recommended by Weinstein et al. (1998) and Wang and Wang (2007), and the second one is based on the correlation of Kumar and Hartland (1999) for RDC liquid-liquid extraction columns.

Now, once the individual mass transfer coefficients are estimated, the rate of change of solute concentration in the liquid droplet (\dot{c}_y) is expressed in terms of the droplet volume average concentration and the overall mass transfer coefficient (K_{oy}):

$$\dot{C}_y = \frac{6K_{oy}}{d} (c_y^*(c_x) - c_y(z, t)) \quad (7)$$

Note that (K_{oy}) may be function of the droplet diameter and time depending on the internal state of the droplet; that is, whether it is circulating or behaving like a rigid sphere. The overall mass transfer coefficient is usually expressed using the two-resistance theory in terms of the individual mass transfer coefficients for the continuous and the dispersed phases (Lo et al., 183) and $c_y^* = mc_x$,

where m is the distribution coefficient. Note that c_y^* is the maximum attainable thermodynamic equilibrium solute concentration.

Boundary Conditions

Concerning the boundary conditions, we adopted those of Wilburn (1964) (See Attarakih et al. (2004) for details). The initial conditions are taken as zero dispersed phase holdup and zero or uniform solute concentration in the continuous phase. The inlet bivariate number density is taken as: $f_{d,c_y}^{in}(d, c_y; t) = f_d^{in}(d; t) \times c_y^{in}$. This means that all the inlet droplets have the same uniform solute concentration.

THE PRIMARY AND SECONDARY PARTICLE CONCEPT

The population balance equation given by Eq. (1) represents an infinite number of integro-partial differential equations due to the continuous variation of the internal droplet states from their minimum to maximum physical limits. So, these variables have to be sampled at finite number of grid points so that the resulting set of equations could be tractable. The classical framework for solving such integral equations is the finite difference schemes in which particle states are discretized into a finite number of sections. The population density in each section is considered to behave like a single particle placed usually at the middle. Unfortunately, these methods are inaccurate for tracking the integral properties associated with the population density function due the inconsistency between those obtained from the continuous and discrete population densities (Ramkrishna, 2000, Attarakih, 2008). To overcome this problem of internal inconsistency, the primary and secondary particle method (PSPM) is developed (Attarakih et al., 2008). In this method, the population density in each section is represented by a single particle that is called primary particle which characterized by its total number concentration and mean size (position). This particle is responsible for the reconstruction of the distribution and is associated with a finite number of secondary particles with their own local number concentrations and sizes. The interaction between these secondary particles in different sections, due to breakage and coalescence events, results in a new particle with no representative size due to the discrete approximation of the distribution. Because the newly-birthed particle could now conserve a finite set of low order moments (actually two per secondary particle), the resulting set of discrete population balance equations are internally consistent with respect to a desired number of low order moments. In pure mathematical sense, the secondary particles are exactly equivalent to the number of quadrature points in Gauss-like quadratures or the Quadrature Method Of Moments (QMOM) (McGraw, 1997).

The first step in the PSPM is to envisage the dispersed phase as contiguous N_{pp} primary particles. Each primary particle is associated with the desired number of secondary particles which carry detailed information

about the distribution. The active particle mechanisms such as breakage and coalescence occur through interactions between these secondary particles. It is obvious now that $N_{sp} \times N_{pp}$ particles are contributing in the breakage and coalescence events. Due to the increase of the number of interacting particles, more information is gathered about the distribution itself. This distribution could be reconstructed from the secondary particles by averaging the total weights of the secondary particles with respect to the smallest domain containing these particles associated with the i th primary particle and locating them at the mean size of the secondary particles. Mathematically, the above presentation is equivalent to applying the QMOM to each size partition of an arbitrary width: $[d_{i-1/2}, d_{i+1/2}]$: $i = 1, 2, \dots, N_{pp}$ resulting in a set of low order moments: $\mu_r^{<i>$: $r = 0, 2, \dots, 2N_{sp} - 1$, in each section. The number concentration and the size of each secondary particle are calculated by the inversion of the sectional moment problems (Attarakih et al., 2008). The PSPM could be viewed as an optimum and general framework that combines the advantages of the finite difference schemes and the QMOM, while minimizes their drawbacks. It has the advantage of being self-contained in terms of distribution reconstruction in contrast to the conventional QMOM. To keep the presentation clear the one-primary and one secondary particle model will be presented in detail in the next section.

THE DIRECT ONE-PRIMARY ONE-SECONDARY PARTICLE MODEL (DOPOSPM)

The direct one-primary and one-secondary particle model is the simplest discrete model that can represent the continuous population balance equation. This representation is of moderate accuracy and reflects all the features contained in the continuous population balance equation. For example, the model conserves both total number and volume (mass) concentrations and is exact when the breakage and coalescence frequencies are constants. This corresponds to following directly (and hence the name Direct) the total number concentration (N), volume fraction (α) and the solute concentration (\bar{c}) by solving their transport equations. To derive these equations, the bivariate density function is considered as a Dirac delta function with weight (N) and locations (\bar{d} and \bar{c}):

$$f_{d,c_y}(d, c_y, t, z) = N(t, z) \delta(d - \bar{d}(t, z)) \delta(c - \bar{c}(t, z)) \quad (8)$$

For $z \in (z_y, z_x)$, where z_y and z_x are the inlets of the dispersed and continuous phases respectively. This is equivalent to replacing the bivariate density function by one-primary and one-secondary particle (in this special case they are identical) with weight (N) and internal states (\bar{d} : mean diameter and \bar{c} : mean solute concentration). The total number, volume and mean solute concentrations are defined by:

$$N = \int_0^\infty \int_0^{c_y^*} f_{d,c_y} \partial d \partial c_y \quad (9)$$

$$\alpha_y = \int_0^\infty \int_0^{c_y^*} v f_{d,c_y} \partial d \partial c_y \quad (10)$$

$$\bar{c}_y = \frac{\int_0^\infty \int_0^{c_y^*} c_y v f_{d,c_y} \partial d \partial c_y}{\int_0^\infty \int_0^{c_y^*} v f_{d,c_y} \partial d \partial c_y} \quad (11)$$

To get the transport equation for the total number concentration (N), Eq.(8) is substituted in Eq.(1) and both sides are integrated with respect to d and c_y from (0 to ∞) and from (0 to c_y^*) respectively. Doing this, the following transport equation is arrived to:

$$\frac{\partial N}{\partial t} + \frac{\partial(u_y N)}{\partial z} = \frac{1}{A_c} \frac{Q_y^{in}}{v_{in}} \delta(z - z_y) + \pi \quad (12)$$

$$\pi = (\vartheta(\bar{d}) - 1) \Gamma(\bar{d}, \bar{c}_y) N - \frac{1}{2} \omega(\bar{d}, \bar{d}, \bar{c}_y) N^2 \quad (13)$$

Note that in the last equation the first term is the rate of formation of particles with breakage frequency (Γ). The mean number of daughter particles is given by (ϑ) that is determined by integrating the daughter droplet distribution function with respect to (d). This distribution is determined using single droplet experiments in small devices (Schmidt et al., 2006). The second term in Eq.(13) is the net rate of droplet death due to coalescence of two droplets of the same mean size and concentration with frequency (ω). It is clear that droplet breakage and coalescence follow first and second order mechanisms based on (N) respectively. The transport equation for (α) and (\bar{c}_y) are derived by multiplying Eq.(1) by $v(d)$ for (α) and $c_y v(d)$ for (\bar{c}_y), substituting Eq.(8) in (1) and integrating from (0 to ∞) and (0 to c_y^*) with respect to d and c_y respectively to get:

$$\frac{\partial \alpha_y}{\partial t} + \frac{\partial(u_y \alpha_y)}{\partial z} = \frac{Q_y^{in}}{A_c} \delta(z - z_y) \quad (14)$$

$$\frac{\partial[Y]}{\partial t} + \frac{\partial(u_y Y)}{\partial z} = \frac{Q_y^{in}}{A_c} c_y^{in} \delta(z - z_y) + \frac{6K_{oy}(\bar{d}, \bar{c}_y)}{\bar{d}} (m' X - Y) \quad (15)$$

The solute balance in the continuous phase is found directly by substituting Eq.(8) in the integral of the right hand side of Eq.(4):

$$\frac{\partial X}{\partial t} + \frac{\partial}{\partial z} \left[-u_x X - D_x \frac{\partial X}{\partial z} \right] = \frac{Q_x^{in}}{A_c} c_x^{in} \delta(z - z_x) - \frac{6K_{oy}(\bar{d})}{\bar{d}} (m'X - Y) \quad (16)$$

Where:

$$X = \alpha_x c_x, \quad Y = \alpha_y c_y, \quad m' = \frac{\alpha_y}{\alpha_x} m$$

The mean particle diameter (\bar{d}) can be found from the mean mass of the secondary particle:

$$\bar{d} = \begin{cases} \sqrt[3]{\frac{6 \alpha_y}{\pi N}}, & N > \sqrt{\varepsilon} \\ d_{vs}, & \text{otherwise} \end{cases} \quad (17)$$

Where (ε) is the machine precision and (d_{vs}) is the Sauter mean diameter estimated from the available correlations in extraction columns. For example, Ladha (1990) correlated the Sauter mean diameter in the RDC column as function of the system physical properties, rotor speed and the effect of mass transfer direction. Note that the value of (d_{vs}) in Eq.(17) is not critical and can be taken for example as the feed mean droplet diameter. This is only required to avoid the division by zero in the regions where there is no particle concentration. Note that the mean droplet diameter given by Eq.(17) is physically the mass-number mean diameter. It is the mean diameter of secondary particle whose mass is given as the ratio between its volume and number concentrations. This diameter is known in the particulate solid literature as d_{30} .

To close the model, an expression for the continuous phase velocity (u_x) is derived by adding the continuity equations for the dispersed and continuous phases assuming that the density of both phases is constant. This assumption is justified when low mass transfer fluxes are encountered and the two liquids are considered to be incompressible. The resulting expression is (Attarakih et al., 2006):

$$u_x = \alpha_y(z, t) u_s(\bar{d}, \bar{c}_y, z) - \alpha_y(H, t) u_s(\bar{d}, \bar{c}_y, H) + \Delta_x(z) \frac{Q_x^{in}}{Ac} + \Delta_y(z) \frac{Q_y^{in}}{Ac} \quad (18)$$

Where:

$$\Delta_x = \begin{cases} 1, & z \leq Z_x \\ 0, & \text{otherwise} \end{cases} \quad \text{and} \quad \Delta_y = \begin{cases} 1, & z < Z_y \\ 0, & \text{otherwise} \end{cases} \quad \text{and}$$

(H) is the height at the exit of the dispersed phase from the top of the column (see Fig.(1)). The discontinuity appearing in the continuous phase velocity (u_x) due to the presence of the two step functions (Δ_x and Δ_y) is physically understood by referring to the column geometry given in Fig.(1). The lower and upper settling zones are designed to separate the heavy and light phases at the bottom and top of the column respectively.

So, the velocity of the continuous phase is zero in the upper settling zone to allow the coalescence of the light phase droplets to disengage from the column.

The mathematical model given by the system of Eqs.(12) to (16) and the associated algebraic closure equations is coupled through the convective and source terms and is dominated by macro and micro convection transport with discontinuous breakage and coalescence events. The time scale of these events is considered too small compared to that of convection and diffusion transport mechanisms. To get more insight into the mathematical characteristics, the hyperbolic nature of the model will be investigated in the next section.

The Hyperbolicity of the DOPOSPM

The system of equations (Eqs.(12) to 16) comprising the DOPOSPM is first written in the following standard conservation form:

$$\partial_t U + \partial_z F(U) = S(U) \quad (19)$$

where U is a four-component column vector containing the conservative variables defined over the domain $z \in (0, H)$ and is given by: $U = (N \quad \alpha_y \quad Y \quad X)^T$. In this vector the first component is the total number concentration, the second one is the total volume concentration and the third and fourth components are the total solute concentrations in the dispersed and continuous phases respectively. The flux vector $F(U)$ is given by: $F(U) = (Nu_y \quad \alpha_y u_y \quad Yu_y \quad -Xu_x)^T$ and the source term vector is given by:

$$S(U) = \begin{pmatrix} (Q_y^{in} / A_c v^{in}) \delta(z - z_y) + \pi \\ (Q_y^{in} / A_c) \delta(z - z_y) \\ (Q_y^{in} c_y^{in} / A_c) \delta(z - z_y) + 6K_{oy} (m'X - Y) / \bar{d} \\ (Q_x^{in} c_x^{in} / A_c) \delta(z - z_x) - 6K_{ox} (m'X - Y) / \bar{d} \end{pmatrix} \quad (20)$$

The hyperbolic nature of the system given by Eq.(19) is identified by finding the eigenvalues of the numerical flux $F(U)$ given above. Now, if $u_1 = N$, $u_2 = \alpha_y$, $u_3 = Y$ and $u_4 = X$, then the numerical flux vector is given by:

$$F(U) = \begin{pmatrix} u_1 u_y(u_1, u_2) \\ u_2 u_y(u_1, u_2) \\ u_3 u_y(u_1, u_2) \\ -u_4 u_x(u_1, u_2) \end{pmatrix} \quad (21)$$

Note that, in writing the above numerical flux the continuous and dispersed phase velocities are assumed to be weak functions of u_3 and u_4 (the solute concentration in both phases) (Gerstlauer, 1999). Moreover, the dispersed phase holdup in industrial

liquid-liquid extraction columns ranges usually from (10 to 15) percent (Schmidt, 2005) and hence the dependency of u_x and u_y on the dispersed phase holdup (u_2) is also weak as appears in Eq.(3). Consequently, the predicted dispersed phase velocity is higher than that with including the term $(1-u_2)$. On the other hand, the dependency of u_t (terminal droplet velocity) on (u_1) is only significant for high rates of breakage or coalescence. In case of dominant droplet breakage u_y is smaller than that in the case of dominant droplet coalescence and is nearly constant for the case of negligible droplet breakage and coalescence. Based on this brief discussion, the dependency of u_t on u_1 is suppressed in the derivation of the Jacobian matrix ($\partial_U F(U)$). Accordingly, the eigenvalues of the Jacobian matrix are given by:

$$\lambda_{1,2,3} = u_y \quad (22)$$

$$\lambda_4 = -u_x \quad (23)$$

These eigenvalues are exact for spray liquid-liquid extraction columns where the droplet swarm effect ($1-\alpha_y$) and breakage and coalescence are negligible (u_y and u_x is independent of u_1). Since all the eigenvalues are real, the system of conservation laws given by Eq.(19) is hyperbolic (Toro, 1999) with two opposite distinct waves propagating along the column. These are namely, the x -phase solute concentration wave (from top to bottom) and the y -phase (from bottom to top) waves (number, volume and solute concentrations respectively) that have identical velocities given by u_y .

To identify the type of these waves, it is sufficient to study all the characteristic fields (λ_j -field, $j=1,2,3,4$) by finding $\nabla \lambda_j(U) \cdot V^{(j)}(U)$, where $V^{(j)}(U)$ are the right eigenvector corresponding to λ_j . Since u_y and u_x are assumed to be constants (as discussed above), then it is clear that:

$$\nabla \lambda_j(U) \cdot V^{(j)}(U) = 0, \quad j=1,2,3,4 \quad (24)$$

So, all the waves propagating along the column height are contact waves characterized by a single jump discontinuity connecting the left (U_L) and right (U_R) states in a linearly degenerate field (Toro, 1999). For example, the number and volume concentration waves enter at the bottom of the column as a discontinuity jump and move toward the top with speed u_y .

The Dominant Time Constant in the DOPOSPM

From dynamic point of view, the time constants (reciprocal of the eigenvalues) prevailing in the system are given by: $\tau_y = H/|u_y|$ and $\tau_x = H/|u_x|$. According

to Eq.(2), $u_y > |u_x|$ in order for the dispersed phase droplets to ascend up the column. Usually, the column should be operated under certain conditions to avoid heavy entrainment of the dispersed phase droplets by satisfying the condition: $u_y > |u_x|$ (Lo et al., 1983).

Based on this industrial fact, the dominant time constant is attributed to the continuous phase and hence is given by: $\tau_x = H/|u_x|$. So, the response of the solute concentration in the continuous phase is expected to have a sluggish response compared to that of the dispersed phase. As a consequence of this, the dispersed phase variables (number and volume concentrations and the mean droplet diameter) are expected to reach equilibrium (steady state) rapidly as noticed by many researches (Al Khani et al., 1989, Hufnagl et al., 1991, Weinstein et al., 1998). The above time constants are functions of rotor speed, column geometry, system physical properties and secondary particle mean diameter and concentration.

NUMERICAL SOLUTION OF THE DOPOSPM

As mentioned above, the DOPOSPM consists of a system of conservation laws that are dominated by convection. For such type of problems there is standard numerical recipes generated over decades of research in the computational fluid dynamics (CFD) (Toro, 1999). The major difficulty lies in the convective terms where special discretization techniques are required when nonsmooth profiles are expected to appear. One of the popular methods of discretization is the finite volume method that makes use of the conservation nature of the partial differential equations, and hence handle discontinuous profiles successfully (although with front smearing). As a first attempt to solve the system given by Eq.(19), the first order upwind scheme with Flux Vector Splitting (FVS) is chosen due to the explicit form of the eigenvalues given by Eqs.(22) and (23). The key feature of this method is that the discretization of the convective flux is performed according to the sign of the wave propagation speed (the eigenvalues). The name upwind comes from the fact that discretization is performed using grid points on the side from which information flows. So, for numerical approximation of the system (19) the column height (specified by the domain: $0 \leq z \leq H$) is discretized into L spatial cells $C_i = [z_{i-1/2}, z_{i+1/2}]$ with $i=1,2,\dots,L$. Now, introducing the sliding cell average for the arbitrary quantity $g(z,t)$:

$$g_i = \frac{1}{\Delta z} \int_{z_{i-1/2}}^{z_{i+1/2}} g(\zeta,t) d\zeta$$
 one can integrate the system (19) over the cell C_i and the time interval: $T_i = [t, t + \Delta t]$ to get:

$$U_i^{n+1} = U_i^n - \lambda_n (F_{i+1/2}^n - F_{i-1/2}^n) + S(U_i^n) \quad (25)$$

where $U_i^n = U_i(z_i, t^n)$ and $F_{i+1/2}^n = F(t^n, z_i + \Delta z/2)$ is called the numerical flux at the right interface of the cell C_i . Since the values of the vector (U) is known only at the discrete grid points ($z_{i-1/2} < z_i \leq z_{i+1/2}$) at the time

level (t^n), the unknown values of the numerical fluxes at the cell interfaces have to be estimated by reconstruction from their known values (U_i^n). Depending on the sign of the Jacobian eigenvalues, the system (25) could be written as:

$$U^{n+1} = U^n - \frac{\Delta t^n}{\Delta z} E^n + \Delta t^n S(U^n) \quad (26)$$

where the matrix E is a tridiagonal matrix whose elements are given by:

$$e_{i,i-1} = \frac{\Delta t^n}{\Delta z} [\lambda_j^+]_{i-1}^n, \quad i = 2, 3, \dots, L \quad (27)$$

$$e_{i,i} = 1 - \frac{\Delta t^n}{\Delta z} [\lambda_j^+ - \lambda_j^-]_i^n, \quad i = 1, 2, \dots, L \quad (28)$$

$$e_{i,i+1} = -\frac{\Delta t^n}{\Delta z} [\lambda_j^-]_{i+1}^n, \quad i = 1, 3, \dots, L-1 \quad (28)$$

$$\Delta t_x^n = C_{cfl} \frac{\Delta z}{\max_i |\lambda_{x,i}^n|} \quad (29)$$

$$\Delta t_y^n = C_{cfl} \frac{\Delta z}{\max_i |\lambda_{y,i}^n|} \quad (30)$$

$$\Delta t^n = \min(\Delta t_x^n, \Delta t_y^n) \quad (31)$$

and C_{cfl} is the Courant number that should lie in the interval (0,1) to force the numerical stability of the scheme (26). The positive and negative eigenvalues are defined as: $\lambda_j^+ = \max(0, \lambda_j)$ and $\lambda_j^- = \min(0, \lambda_j)$ where $j = x$ and y for the continuous and dispersed phase respectively. Note that in deriving the matrix E the numerical flux is assumed to satisfy the homogeneity condition (Toro, 1999):

$$F(U) = A(U)U \quad (32)$$

Since u_y and u_x are assumed to be weak functions of the conservative variables (U). Finally, The elements of the source term ($S(U^n)$) are obtained simply by applying the sliding average (g_i) to Eq.(20). The time step given by Eq.(31) is adaptive and is estimated at each integration step.

NUMERICAL RESULTS AND DISCUSSION

In this work we considered a pilot plant RDC liquid-liquid extraction column having 0.15 m diameter and 2.55 m total height. This column is available in the laboratory of the institute of process engineering at the

University of Kaiserslauter. The technical specifications of this column are given in Table (1).

In all the numerical simulations, the inlet feed distribution is taken as a normal distribution fitted to the experimental data of Schmidt et al. (2006). The minimum and maximum droplet diameters for the inlet feed distribution are $d_{min} = 0.025$ mm and $d_{max} = 8$ mm such that negligible number of droplets exists outside this range. The two chemical systems used are those of the EFCE denoted by system 1 and system 2, where system 1 is water-acetone-toluene and system 2 is water-acetone-n-butyl acetate. The physical properties of these systems are available online (<http://www.dechema.de/Extraktion>). The individual mass transfer coefficients as predicted from the relations reported in Zhang et al. (1985) and Weinstein et al. (1998) are denoted as mass transfer model 1 and those of Kumar and Hartland (1999) are denoted as mass transfer model 2.

Column diameter	0.15	Column height	2.550
Stator diameter	0.105	Dispersed phase inlet	0.250
Rotor diameter	0.090	Continuous phase inlet	2.250
Compartment height	0.030		

Tab. 1: RDC column geometry (all dimensions are in m)

The inlet solute concentrations in the continuous and dispersed phases are taken 100 and 0 kg/m³ respectively and the total flow rate of each phase is taken 2.778×10^{-5} m³/s. The terminal droplet velocity is evaluated from the Vignes (1965) correlation for system 1 and from that of Klee and Treybal (1957) for system 2 based on the procedure described by Gourdon et al. (1994). The slowing factor of Modes (2000) is utilized. Before we start our full numerical simulation of the present model, we want to gain some trust in the performance of the DOPOSPM discrete form (given by the system (26)) by comparing its predictions with some available analytical solutions. For this purpose we derived analytical solutions for two special cases: the first one is dynamic analytical solution for the DOPOSPM in the case of no breakage or coalescence, stagnant continuous phase ($Q_x^{in} = 0$) and in the absence of mass transfer. The second case is a steady state solution in the absence of droplet breakage and coalescence. The details of these solutions will be published separately.

The DOPOSPM Validation

The numerical solution of the DOPSPM is compared to the analytical one by showing the evolution of the dispersed phase holdup along the column height at different times. The number of spatial cells used here is 200 and the C_{cfl} number is taken as 0.95. The chemical components are those of system (1) with toluene being the dispersed phase fed at the bottom of the column at 0.0 m (see Table 1), while the terminal velocity model is that of Vignes (1965) as described above. The mean

droplet size in the feed is taken as 4 mm with standard deviation of 0.5 mm.

Fig.(2) shows the analytical solution for the holdup wave propagating along the column from the bottom . As expected, this is a contact wave (discontinuity jump) traveling with constant speed ($u_y = u_s$) since u_x is zero (stagnant continuous phase). It is evident that the numerical solution approximates very well the analytical one and captures the moving discontinuity along the column.

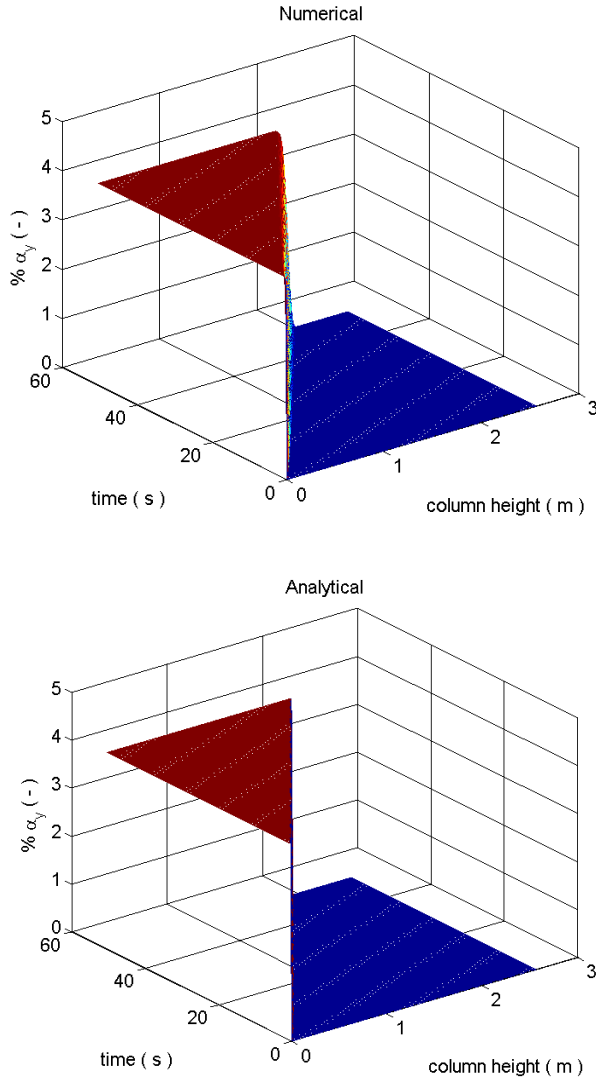


Fig.(2): Comparison between analytical and numerical holdup wave propagation along the column height at different times. The agitator speed is 100 rpm.

The steady state velocity profiles (u_x and u_y) are obtained analytically in the case of no droplet breakage and coalescence or numerically in the presence of these two mechanisms. After that the system of Eqs.(15) and (16) are solved analytically for the steady state X and Y profiles. Since the moving discontinuities disappeared at steady state, all the profiles are smooth along the column and can be solved for with the desired accuracy. To get more insight into the convergence properties of the discrete DOPOSPM, a cross sectional profile at $t = 50$ s is plotted in Fig.(3). Note that the x -axis is zoomed to focus on the moving front. It is clear that as

the number of special cells is increased, the numerical solution converges to the analytical one. Since the spatial discretization scheme is only first order accurate, the convergence is rather slow at the upper part of the front. Note that the holdup profile is constant along the column height since the secondary particle moves with constant mean diameter as defined by Eq.(17). In this case it is equal to that of the inlet feed distribution ($\bar{d}^{in} = 3.6$ mm). The same is valid for the total number concentration wave ($N(t, z)$).

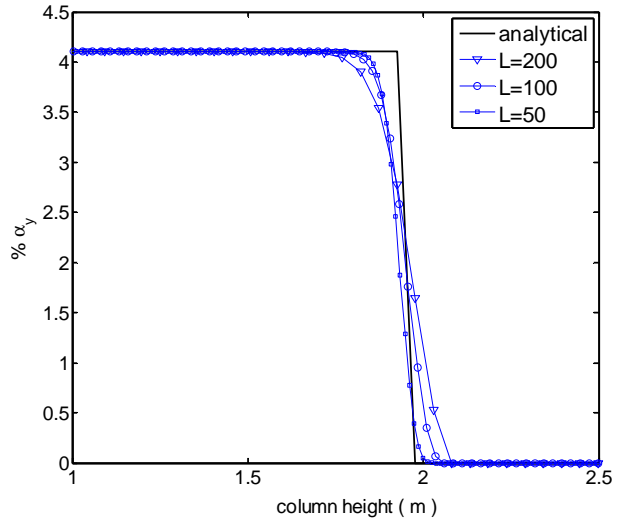


Fig.(3): Convergence of the numerical holdup profiles to the analytical solution by increasing the number of spatial cells for the same case simulated in Fig.(2) at $t = 50$ s. The agitator speed is 100 rpm.

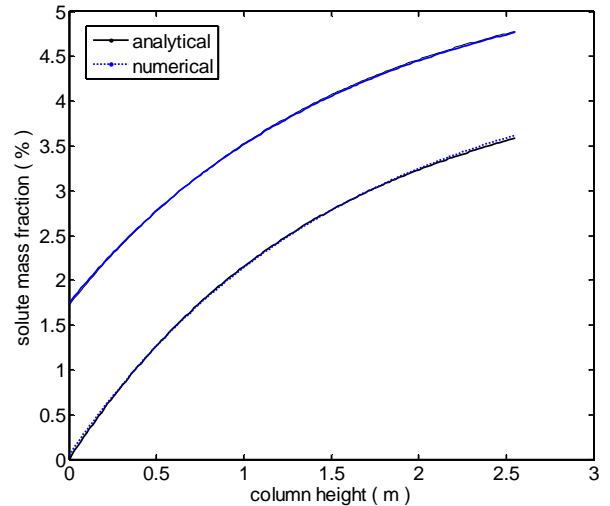


Fig. (4): Comparison between analytical and numerical solutions for the solute mass fractions along the column. Droplet breakage and coalescence are neglected. The number of spatial cells is 150.

Fig.(4) shows the steady state profiles for solute mass fractions (e.g. $x = X / (\alpha_x \rho_x)$ and $y = Y / (\alpha_y \rho_y)$) in both phases along the column height, where droplet breakage and coalescence are neglected. It is clear that the numerical solution converged to the analytical one using only 150 spatial cells. As stated above, the

remarkable accuracy of the first order upwind scheme is due to the disappearance of discontinuities at steady state.

Dynamic Behavior of the RDC Column

To investigate the dynamic behavior of the pilot plant RDC extraction column, several step changes are introduced in the important input variables. The two contact wave due to solute concentration in the continuous phase and the second one due to the solute concentration in the dispersed phase are first studied. This is done by introducing simultaneous step changes in the inlet solute concentration in the continuous dispersed phases respectively. The initial conditions for both variables are taken as zeros (physically, this corresponds to filling the column using pure water from the top and pure toluene from the bottom) and no droplet breakage and coalescence or mass transfer are considered. As shown in Fig.(5), the two concentration waves are moving in opposite directions according to the sign of the eigenvalues given by Eqs.(22 and 23)

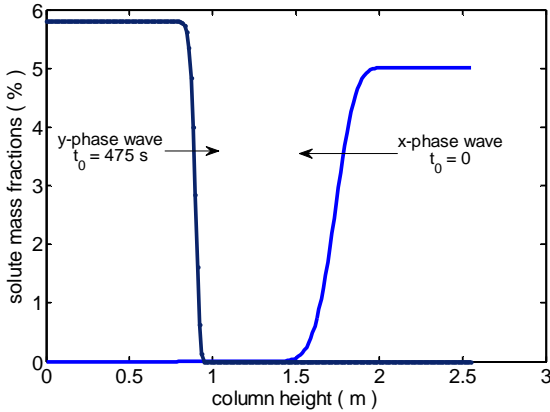


Fig.(5): The propagation of the x and y phases concentration profiles along the column. Droplet breakage, coalescence and mass transfer are neglected. The number of spatial cells is 200 and the final simulation time is 500 s. The time of step change in the y-phase inlet concentration occurred at 475 s.

As expected, the y-phase concentration wave moves faster than the x-phase wave due to the large time constant of the x-phase (This is why the step change in the y-phase concentration is made at 475 s). This behaviour is proved experimentally by Hufnagl et al.(1991). Since no mass transfer is considered in this case, the two waves continue moving until they leave the column without any interaction. Note that the x-phase moving profile is smeared out due to the numerical diffusion inherent to the first order upwind scheme. However, the y-phase profile continues moving with almost sharp front. This is because the time integration step is based on the higher y-phase velocity as selected by Eq.(31). This results in satisfying the C_{cfl} number for the dispersed phase upwind scheme rather than the continuous phase one. As a consequence, the C_{cfl} number for the x-phase is less than that when it flows alone in the column. The natural result of this is the numerical diffusion seen in Fig.(5).

To investigate the effect of the mass transfer on the propagating concentration waves, the mass transfer source term appearing in Eqs.(15) and (16) is included. Since the two phases are initially solute free, each propagating wave interacts with the surrounded fluid due to mass transfer. So, by referring to Fig.(6) the y-phase concentration profile is smeared due to the transfer of the solute to the pure x-phase in the region $z \in [0,1]$. Similarly, the solute in the x-phase is transferred to the pure y-phase in the region $z \in [1.5,2.5]$. In the region $z \in (1,1.5)$ no mass transfer occurs since the two phases are solute free.

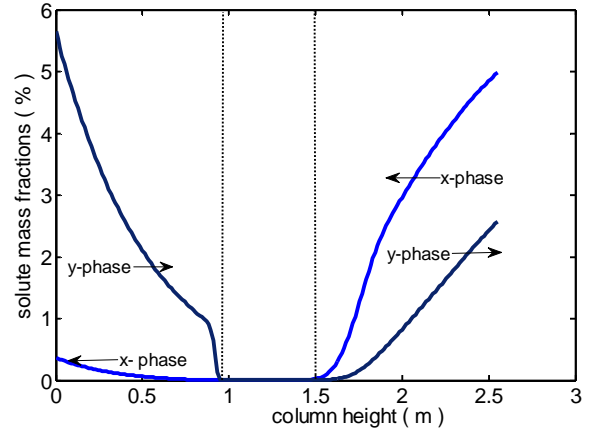


Fig.(6): The propagation of the x and y phases concentration profiles along the column in the presence of mass transfer. Droplet breakage and coalescence are neglected. The number of spatial cells is 200 and the final simulation time is 500 s. The time of step change in the y-phase inlet concentration occurred at 475 s.

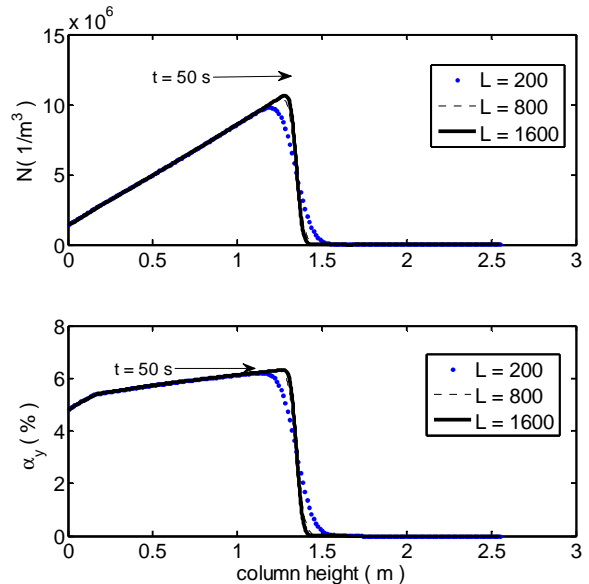


Fig.(7): Propagation of the total number and volume waves in stagnant continuous phase along the column height in the presence of droplet breakage at rotor speed of 200 rpm.

So, the presence of the mass transfer source term smears out the sharp concentration fronts moving along the column. Now, the effect of droplet breakage on the

moving holdup profile will be investigated. Fig.(7) shows the moving total number (N) and volume concentration (α_v) profiles in the presence of droplet breakage at 200 rpm rotor speed in a stagnant continuous phase. The breakage frequency and the daughter droplet distribution are from the work of Schmidt et al. (2006). It is evident that the two profiles are now increasing and smeared due to the decreasing size of the secondary particle along the column height because of droplet breakage. This in reality leads to droplets of different sizes and hence different residence times. So, there exists a residence time distribution that causes the volume fraction and number concentrations to be diffused along the column height. This phenomenon is called the forward mixing of the dispersed phase. To be sure that the front smearing is not because of numerical diffusion, a high number of spatial cells is used (200, 800 and 1600 cells). By referring to Fig.(7) it is clear that the numerical diffusion is minimized and the moving front is correctly captured. Fig.(8) depicts the secondary particle number concentration as function of size and column height. First, the number concentration is increasing along the column height due to droplet breakage. Second, the secondary particle mean diameter (d_{30}) decreases continuously along the column height due to droplet breakage. As mentioned above, this reflects the different droplet size distribution along the column.

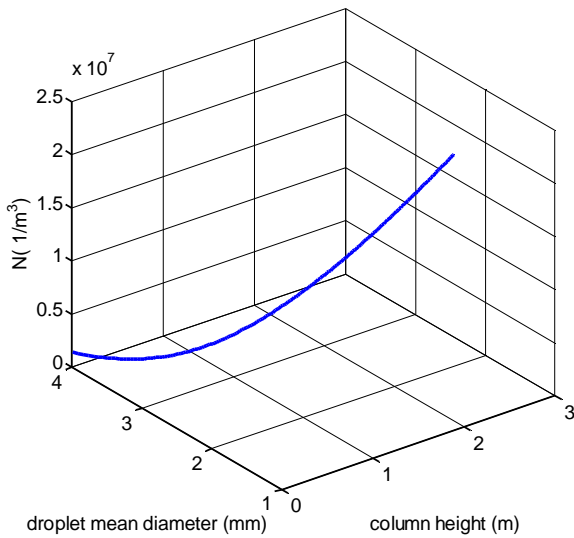


Fig.(8): Secondary particle total number concentration as function of its mean droplet diameter and column height in the presence of droplet breakage and stagnant continuous phase.

In actual extraction columns, both droplet breakage and coalescence do exist. To simulate this, we use the same previous case but now with simultaneous droplet breakage and coalescence. The coalescence frequency is that of Coualoglou and Tavlarides (1977) with parameters taken from Schmidt et al. (2006). Fig.(9) shows the total number and volume concentrations moving along the column height. Comparing this to Fig.(7), it is clear that both concentrations are reduced

due to droplet coalescence according to the second order source term in Eq.(13). Since droplet coalescence is accompanied by the reduction of total number and volume fraction, this results (according to Eq.(17)) in the reduction of the mean droplet diameter.

Again, the convergence of the first order upwind scheme is assured by using large number of spatial cells (400 and 800). Due to the negativity of the coalescence source term (see Eq.(13)), the C_{cfl} number is decreased from 0.95 in the case of droplet breakage to 0.6 to avoid spurious oscillations near the sharp moving fronts. For this case, high resolution schemes with TVD (Total Variation Diminishing) nature are actually needed.

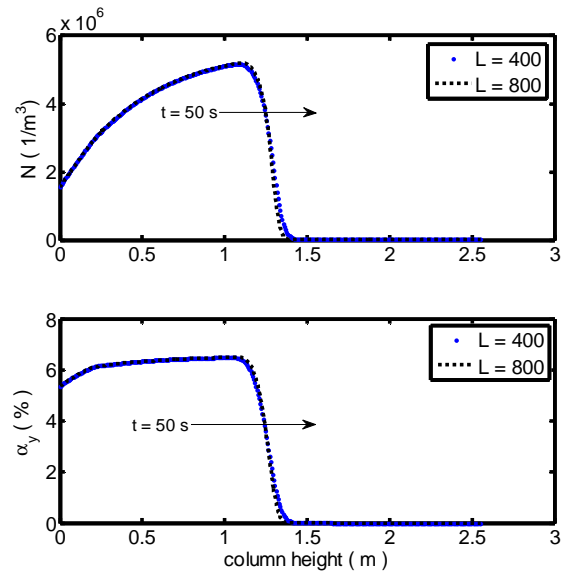


Fig.(9): Propagation of the total number and volume waves along the column height in the presence of droplet breakage and coalescence at rotor speed of 200 rpm.

CONCLUSIONS

A reduced mathematical model is derived based on the concept of the direct primary and secondary particle method. The model is derived from the detailed bivariate population balance equation describing the coupled hydrodynamics and mass transfer in liquid extraction columns. The model is capable of describing droplet breakage and coalescence without any specific assumption about the shape of the distribution. The averaged quantities in the reduced model were: total number, volume and solute concentrations. The model equations are comprised of a set of conservation laws that are highly coupled through the secondary particle mean diameter. Characteristic filed analysis shows that the model is hyperbolic with four contact waves; three of which are moving in the positive z -axis and one in the opposite direction. The first order upwind scheme with Flux Vector Splitting (FVS) is found accurate enough to capture the moving discontinuities at relatively high C_{cfl} number. Due to the negativity of the coalescence source term and the increase of the mean particle size, the moving sharp fronts are smeared by numerical diffusion and hence high resolution schemes are needed in this case. Because of the reduced number of conservation

laws (compared to the full population balance model), the model comes as a compromise between computational cost and numerical accuracy. However, if high accuracy is needed, the model is already extended to multi-primary one secondary particle model. Accordingly, the full dynamic response of the extraction column could be predicted in short computational times. In this regard, the model is suitable for control purposes and for simulation packages using the modular approach. Concerning the column dynamics, the hydrodynamics of the column responds faster than mass transfer.

ACKNOWLEDGMENTS

The authors would like to thank the Deutsche Forschungsgemeinschaft (DFG) for the financial support.

REFERENCES

- ATTARAKIH, M.M., BART, H.-J., STEINMETZ, T., DIETZEN, M. & FAQIR, N. M., (2008), "LLECMOD: A Bivariate Population Balance Simulation Tool for Liquid-Liquid Extraction Columns" *Open Chemical Engineering Journal*, **2**, 10 – 34.
- ATTARAKIH, M. M., DRUMM, C., BART, H.-J. and FAQIR, (2008), "Solution of the population balance equation using the sectional quadrature method of moments", accepted for publ. in *Chem. Eng. Sci.*
- ATTARAKIH, M., H.-J. BART, and N. FAQIR (2006), "Numerical Solution of the Bivariate Population Balance Equation for the Interacting Hydrodynamics and Mass Transfer in Liquid-Liquid Extraction Columns", *Chem. Eng. Sci.*, **61**: p. 113-123.
- AL KHANI, S. D., GOURDON, C., CASAMATTA, G., (1989) "Dynamic and steady-state simulation of hydrodynamics and mass transfer in liquid-liquid extraction column". *Chem. Eng. Sci.*, **44**, 1295-1305.
- BART, H.-J., (2001), "Reactive Extraction", Berlin, Springer.
- CAUWENBERG, V., DEGREVE, J., SLATER, M. J., (1997), "The interaction of solute transfer, Contaminants and drop break-up in rotating disc contactors: Part II. The coupling of mass transfer and breakage process via interfacial tension". *Can. J. Chem. Eng.*, **75**, 1056-1066.
- COULALOGLOU, C. A., TAVLARIDES, L. L., (1977), "Description of interaction processes in agitated liquid-liquid dispersions", *Chem. Eng. Sci.*, **32**, 1289-1297.
- GERSTLAUER, A., (1999), "Herleitung und Reduktion populationsdynamischer Modelle am Beispiel der Flüssig-Flüssig-Extraktion". *Fortschritt-Berichte VDI Reihe*, **3**, 612.
- GOURDON, C., CASAMATTA, G., MURATET, G., (1994), "Population balance based modelling of solvent extraction columns", in: Godfrey, J. C. Slater, M. J. (Eds.), *Liquid-liquid extraction equipment*, John Wiley & Sons, New York, p. 137-226.
- HUFNAGL, H., McIntyre, M., BLASS, E., (1991) "Dynamic behaviour and simulation of a liquid-liquid extraction column". *Chem. Eng. Tech.*, **14**, 301-306.
- KLEE, A. J., and TREYBAL, R. E., (1956), "Rate of rise or fall of liquid drops." *AIChE*, **2**, 444-447.
- KUMAR, A. and HARTLAND, S., (1999), "Correlations for prediction of mass transfer coefficients in single drop systems and liquid-liquid extraction columns". *Trans. Inst. Chem. Eng.*, **77** (Part A), 372-384.
- LADDHA, G.S. and T.E. DEGALEESAN, (1976), "Transport phenomena in liquid extraction", New Delhi: Tata McGraw-Hill.
- Lo, T.C., M.H.I. Baird, and C. Hanson, *Handbook of solvent extraction*. 1983, New York: John Wiley and Sons.
- MANNINEN, M., TAIVASSALO, V., KALLIO, S., (1996), "On the mixture model for multiphase flow", *Technical Research Center of Finland*, VTT Publications, ESPOO, report No. 288.
- MCGRAW, R., (1997), "Description of aerosol dynamics by the Quadrature Method of Moments", *Aerosol Sci. and Tech.*, **27**, 255-265.
- MJALLI, F.S., (2005), "Neural network model-based predictive control of liquid-liquid extraction contactors". *Chem. Eng. Sci.*, **60**, 239-253.
- MODES, G., BART, H.-J., RODRIGUES-PERANCHO, D., BRÖDER, D., (1999), "Simulation of the fluid dynamics of solvent extraction columns from single droplet parameters". *Chem. Eng. Tech.*, **22**, 231-236.
- RAMKRISHNA, D., (2000), "Population balances: theory and applications to particulate systems in engineering", Academic Press, San Diego.
- SCHMIDT, S. A., SIMON, M., ATTARAKIH, M. M., LAGAR, L., BART, H.-J., (2006), "Droplet population balance modelling - hydrodynamics and mass transfer", *Chem. Eng. Sci.*, **61**, 246-256.
- TORO, E. F., (1999), "Riemann solvers and numerical methods for fluid dynamics". 2nd ed. Berlin: Springer.
- VIGNES, A., (1965), "Hydrodynamique des dispersions." *Genie Chimique*, **93**, 129-142.
- WEINSTEIN, O., SEMIAT, R., LEWIN, D. R., (1998), "Modeling, simulation and control of liquid-liquid extraction columns", *Chem. Eng. Sci.*, **53**, 325-339.
- WANG, T. and WANG, J., (2007), " Numerical simulation of gas-liquid mass transfer in bubble columns with a CFD-PBM coupled model", *Chem. Eng. Sci.*, **62**, 7107-7118.
- WILBURN, N. P., (1964), "Mathematical determination of concentration profiles in two-phase continuous countercurrent extractors", *Ind. Eng. Chem. Fund.*, **3**, 189-195.
- XIAOJIN, T., L. GUANGSHENG, and W. JIADING (2005), "An improved dynamic combined model for evaluating the mass transfer performances in extraction columns.", *Chem. Eng. Sci.*, **60**, 4409-4421.
- ZHANG, S. H., Yu, S. C., ZHOU, Y. C., SU, Y. F., (1985), "A model for liquid-liquid extraction column performance- the influence of drop size distribution on extraction efficiency", *Can. J. Chem. Eng.*, **63**, 212-226.

Publication V

Reprinted from Proceedings 6th International Conference on Computational Fluid Dynamics in the Oil & Gas, Metallurgical and Process Industries CFD 2008, Johansen, S.T., Olsen, J.E., Ashrafian, A (Eds.), Trondheim, **2008**,

Sudarshan Tiwari, Christian Drumm, Vikash Sharma, Jörg Kuhnert, Menwer Attarakih, Axel Klar, Hans-Jörg Bart,

A Mesh-Free CFD-Population Balance Equation Coupled Model

Reprinted with permission from SINTEF (The Foundation for Scientific and Industrial Research at The Norwegian University of Science and Technology).

A MESHFREE CFD-POPULATION BALANCE EQUATION COUPLED MODEL

Sudarshan TIWARI^{1,*}, Christian DRUMM³, Vikash K. SHARMA², Joerg KUHNERT¹, Menwer ATTARAKIH⁴, Axel KLAR²
and Hans-Joerg BART³

¹ Fraunhofer Institute for Industrial Mathematics, Fraunhofer-Platz 1, 67663 Kaiserslautern, Germany

² Fachbereich Mathematik, TU Kaiserslautern, POB 3049, 67653 Kaiserslautern, Germany

³ Lehrstuhl f. Thermische Verfahrenstechnik, TU Kaiserslautern, POB 3049, 67653 Kaiserslautern, Germany

⁴ Al-Balqa Applied University, Faculty of Eng. Tech., Chemical Eng. Department, 11134 Amman, Jordan

*E-mail: tiwari@itwm.fhg.de

ABSTRACT

In this contribution we focus on the meshfree method for coupling fluid dynamic equations and the droplet population balance equation. As a meshfree method we consider our own developed method, called the Finite Pointset Method, which is a mesh-free, Lagrangian, particle method. We have considered the liquid-liquid two-phase flow which consists of an aqueous continuous and an organic dispersed phase. A two-fluid model is considered. In the momentum equations of both phases a drag force, as a function of the Sauter mean diameter, is added. The Sauter mean diameter is obtained from solving the population balance equation, which is solved numerically by the Sectional Quadrature Method of Moments with upto 5 primary particles.

Keywords: CFD, Meshfree particle method, Population balance equation, Multiphase flow

INTRODUCTION

In this paper we use a meshfree Lagrangian method, called the Finite Pointset method (FPM). We first start filling the fluid domain by finite number of points (or clouds or particles), which are the numerical grids. These points move with fluid velocities and together with them carry all fluid quantities, like velocities, pressures, etc., which are necessary to solve fluid dynamic equations. One of the most important process of this method is the maintenance of the good quality of particle distribution. After a movement of particles, they may scatter from each other and create holes in the computational domain and the method becomes unstable. Therefore, one has to add new particles if there exists holes. Moreover, particles may come very close to each other, in this case one can keep one particle and remove other closer ones, see Drumm et al. (2008b) for details.

In most of the multiphase flows the secondary phase consists normally of moving bubbles, particles and droplets. Since the FPM is a fully Lagrangian method, it is a natural choice for the dispersed phase. Moreover, FPM is also an appropriate numerical method for simulations of, for examples, free surface flows as well as flows with complicated and rapidly changing geometry since the classical methods like finite difference, finite element, finite volume methods are quite complicated and time consuming due to the reconstruction of mesh in each time step. A first approach for Lagrangian meshfree method for solving fluid dynamic equations is the method of Smoothed Particle Hydrodynamics (SPH). SPH was originally invented to solve problems in astrophysics without geometry (Lucy (1977), Gingold and Monaghan (1977)). This method has been further extended to solve varieties of problems like compressible flows, incompressible flows, multiphase flows and others, see papers by Monaghan (1992) and Morris (2000) and references therein. The main difficulty of SPH is the incorporation of boundary conditions and higher order spatial derivatives.

Another widely used approach for solving fluid dynamics equations in a meshfree framework is the moving least squares (MLS) or weighted least squares method (Belytschko et al. (1996), Dilt (1996), Kuhnert (1999), Tiwari and Manservisi (2002)). With this approach boundary conditions can be implemented in a natural way just by placing particles on boundaries and prescribing boundary conditions on them (Kuhnert (1999)).

We extended the least squares method to the Chorin's projection method for the Navier-Stokes equations (Tiwari and Kuhnert (2002), Tiwari and Kuhnert (2007)). The Poisson solver has been adopted in the least squares approximation procedure with the constraint that this equation and the corresponding boundary condition must

be satisfied on each particle.

Recently, we have applied FPM in the two-fluid model in a liquid-liquid extraction column (Drumm et al. (2008b)). Furthermore, we have incorporated the population balance equation (PBE) in the two-fluid model (Tiwari et al. (2008)), where the PBE is solved by the sectional quadrature method of moments (SQMOM) (Attarakih et al. (2007)). A brief overview of SQMOM is presented in Drumm et al. (2008a), in this proceedings.

In our earlier work (Tiwari et al. (2008)), we have used only one primary particle, which is equivalent to classical quadrature method of moments (QMOM) (Marchisio et al. (2003)). In this paper, we have used upto 5 primary particles. We have considered three cases: only breakage, only aggregation and breakage and aggregation both with constant kernels. The main purpose of this paper is to incorporate the SQMOM with more than one primary particle in our FPM code. Therefore, the simulations are performed in a two-dimensional geometry for primary particles equal to 1, 2 and 5.

The paper is organized as follows. First, we present the governing equations and numerical schemes. Then, we introduce a meshfree method, the FPM, for solving numerical schemes and the coupling strategy of the two-fluid model. Finally, we present some numerical results.

Governing equations and numerical scheme

Two-fluid model

We consider the two-fluid model for multiphase flows, where both phases are liquids. We call them as primary phase (aqueous continuous phase) and secondary phase (organic dispersed phase). All the quantities with the index c denotes the continuous phase and the index d denotes the dispersed phase. In this paper we consider all equations in the Lagrangian form. The continuity equations for the continuous and dispersed phases are

$$\frac{d\alpha_c}{dt} = -\alpha_c(\nabla \cdot \mathbf{v}_c) \quad (1)$$

$$\frac{d\alpha_d}{dt} = -\alpha_d(\nabla \cdot \mathbf{v}_d), \quad (2)$$

where α_c and α_d are the volume fractions, \mathbf{v}_c and \mathbf{v}_d are the velocity vectors and $\frac{d}{dt}$ is the material derivative.

In addition to (1) and (2) the volume fractions must satisfy the following constraint

$$\alpha_c + \alpha_d = 1. \quad (3)$$

The conservation of momentum for the continuous phase is given by

$$\frac{d\mathbf{v}_c}{dt} = -\frac{\nabla p}{\rho_c} + \frac{1}{\alpha_c \rho_c} \nabla \cdot \boldsymbol{\tau}_c + \mathbf{g} + \frac{1}{\alpha_c \rho_c} \mathbf{F}_{drag} \quad (4)$$

and the secondary phase is given by

$$\frac{d\mathbf{v}_d}{dt} = -\frac{\nabla p}{\rho_d} + \frac{1}{\alpha_d \rho_d} \nabla \cdot \boldsymbol{\tau}_d + \left(1 - \frac{\rho_c}{\rho_d}\right) \mathbf{g} - \frac{1}{\alpha_d \rho_d} \mathbf{F}_{drag}, \quad (5)$$

where ρ_c and ρ_d are the densities, p is the pressure shared by both phases, \mathbf{g} is the gravitational force and \mathbf{F}_{drag} represents the interfacial forces and $\boldsymbol{\tau}$ is the stress tensor, for example, for the continuous phase it is given by

$$\boldsymbol{\tau}_c = \alpha_c \mu_c [\nabla \mathbf{v}_c + (\nabla \mathbf{v}_c)^T - \frac{1}{3} (\nabla \cdot \mathbf{v}_c) \mathbf{I}], \quad (6)$$

where μ_c is the dynamic viscosity of the continuous phase. The inter-phase interaction term consists of different momentum exchange mechanisms. Only the drag force was taken into account, while the virtual mass force and the lift force can be neglected for a liquid-liquid interaction as shown by Wang and Mao (2005) in a stirred tank. The interfacial momentum transfer (drag force) between two phases is given by

$$\mathbf{F}_{drag} = \frac{3}{4} \alpha_d \rho_c \frac{C_D}{d_{32}} |\mathbf{v}_d - \mathbf{v}_c| (\mathbf{v}_d - \mathbf{v}_c), \quad (7)$$

where d_{32} is the diameter of the droplets of the dispersed liquid phase and the drag force coefficient C_D is given by (Schiller and Naumann (1935))

$$C_D = \begin{cases} \frac{24}{Re} (1 + 0.15 Re^{0.687}) & \text{if } Re \leq 1000 \\ 0.44 & \text{if } Re > 1000 \end{cases}$$

and Re is the relative Reynolds number defined as

$$Re = \frac{\rho_c |\mathbf{v}_d - \mathbf{v}_c| d_{32}}{\mu_c}. \quad (8)$$

If the breakage and aggregation between droplets are not taking place, like in the mono-dispersed phase, the diameter of the droplet d_{32} is considered to be constant. In general, this is not constant and droplets are assumed to have a spectrum of sizes. This spectrum can be computed with the help of the PBE.

Population balance equation

The superstructure of the PBE and the general derivation based on the Reynolds transport theorem is given in Ramkrishna (2000). In the present case this equation can be written as

$$\frac{\partial f(V, \mathbf{x}, t)}{\partial t} + \nabla \cdot (\mathbf{v}_d f(V, \mathbf{x}, t)) = S(f(V, \mathbf{x}, t), V, \mathbf{x}, t), \quad (9)$$

where

$$\begin{aligned} S = & -\Gamma(V) f(V, \mathbf{x}, t) + \\ & \int_V^{V_{max}} \Gamma(V', \mathbf{x}, t) \beta(V|V') f(V', \mathbf{x}, t) dV' \\ & - f(V, \mathbf{x}, t) \int_{V_{min}}^{V_{max}} \omega(V, V') f(V', \mathbf{x}, t) dV' \\ & + \frac{1}{2} \int_{V_{min}}^V \omega(V - V', V') f(V - V', \mathbf{x}, t) f(V', \mathbf{x}, t) dV' \end{aligned}$$

and $f(V, \mathbf{x}, t)$ is the number density function with particle size V as an independent variable. The vector \mathbf{v}_d is the same particle velocity introduced in previous subsection. The source term S in (9) consists of loss term (preceded by minus sign) and gain term (preceded by plus sign) due to breakage and aggregation collisions of droplets. The breakage and aggregation of droplets are governed by breakage and aggregation frequencies, respectively. The breakage frequency $\Gamma(V)$ represents the fraction of droplets breaking per unit time, while the aggregation frequency $\omega(V, V')$ accounts for the probability of successful collisions between a pair of droplets. The splitting of mother droplet of size V' to daughter droplets having a spectrum of sizes is given by the daughter particle distribution $\beta(V|V')$.

The above equation (9) is an integro-partial differential equation and has no general solution. Hence, one has to solve the equation by numerical techniques. Several numerical schemes have been reported and many of them are problem specific, see Attarakih et al. (2006) for the review of the numerical schemes. We are looking for the one which is feasible to couple with the flow solver. The Quadrature Method of Moments (QMOM) is one of the suitable methods to incorporate easily into flow solvers, however, it may suffer from the ill-conditioned eigenvalue problem in the product-difference algorithm, which is pointed out by Attarakih et al. (2007). They have shown that Sectional QMOM (SQMOM) is more stable and compared the numerical solutions with the available analytical solutions of the PBE. In this paper we incorporate the SQMOM for the PBE into the FPM code. A brief description of SQMOM is presented in the same proceedings, see Drumm et al. (2008a). For more details of SQMOM, we refer to Attarakih et al. (2007).

For the coupling of momentum equations with the PPE one can construct the wide range of classes of droplets based on their sizes, however, the considerations of individual classes may not be feasible in the computer simulations since momentum equations have to be solved for each class. Currently, the applied CFD-PBE models are based on the two-fluid Multiple Size Group (MUSIG) Model (Lo (2002)), where all droplets in the PBE share the same velocity field and only one momentum equation is solved for all droplet classes based on the area averaged droplet size, also called as Sauter mean diameter denoted by d_{32} . A new strategy, the inhomogeneous MUSIG model tries to divide the dispersed phase into a number N so-called velocity groups, where each of the velocity groups is characterized by its own velocity field, to get rid of the common simplifications (Krepper et al. (2007)). As a drawback, this multi-fluid approach is based on the CPU-time consuming classes methods. So, the SQMOM seems to be another interesting alternative, since each primary particle could move with its own velocity group and hence having its own momentum equation resulting also

in a multi-fluid model depending on the number of primary particles. Unlike, the classes methods the accuracy of resolving the population balance source term using the SQMOM is insensitive to the number of primary particles. This in turn gives more flexibility in specifying the number of primary particles, where more particles could be added to reconstruct the shape of the distribution with almost the same accuracy. As a benefit, in comparison to the inhomogeneous MUSIG model, SQMOM is less CPU-time consuming, since it is based on the computational less expensive quadrature method of moments.

Numerical scheme for primary liquid phase

We solve the primary liquid phase with the FPM in combination with Chorin's pressure projection method (Chorin (1968)). In this work we decompose the pressure into hydrodynamic and dynamic pressures, i.e. $p = p_{hyd} + p_{dyn}$. The scheme consists of two fractional steps and is of first order accuracy in time. In the first step we compute the intermediate velocities \mathbf{v}^* and in the second step we correct the velocity with the constraint that velocity fulfills the continuity equation. In our numerical scheme, we substitute the value of $\nabla \cdot \mathbf{v}_c$ which appeared in the stress strain tensor τ_c from the equation (1). Moreover, after some manipulations, we obtain

$$\nabla \cdot \tau_c = \nabla \cdot (\alpha_c \mu_c \nabla) \mathbf{v}_c + \Theta(\mathbf{v}_c, \alpha_c \mu_c, \nabla) = \nabla \cdot (\kappa \nabla \mathbf{v}_c) + \Theta(\mathbf{v}_c, \kappa, \nabla), \quad (10)$$

where Θ is some straight forward, but lengthy term and $\kappa = \alpha_c \mu_c$. Moreover, the operator $\nabla \cdot (\kappa \nabla \mathbf{v}_c)$ can be re-expressed by

$$\nabla \cdot (\kappa \nabla \mathbf{v}_c) = \frac{1}{2} [\Delta(\kappa \mathbf{v}_c) + \kappa \Delta \mathbf{v}_c - \mathbf{v}_c \Delta \kappa]. \quad (11)$$

This means, once we construct the shape functions for the Laplace operator Δ , then the differential operator $\nabla \cdot (\kappa \nabla \mathbf{v}_c)$ can be approximated by combination of Δ applied to different functions. Hence the momentum equation (4) can be re-expressed in the simple form

$$\begin{aligned} \frac{d\mathbf{v}_c}{dt} &= -\frac{\nabla p}{\rho_c} + \frac{1}{\alpha_c \rho_c} [\nabla \cdot (\kappa \Delta) \mathbf{v}_c + \Theta(\mathbf{v}_c, \kappa, \nabla)] \\ &\quad + \frac{3}{4} \frac{\alpha_d}{\alpha_c} \frac{C_D}{d_{32}} |\mathbf{v}_d - \mathbf{v}_c| (\mathbf{v}_d - \mathbf{v}_c) + \mathbf{g} \\ &= -\frac{\nabla p}{\rho_c} + \frac{1}{\alpha_c \rho_c} \nabla \cdot (\kappa \Delta) \mathbf{v}_c - G_c \mathbf{v}_c + \mathbf{H}, \end{aligned} \quad (12)$$

where $G_c = \frac{C_D}{d_{32}} |\mathbf{v}_d - \mathbf{v}_c|$ and the vector \mathbf{H} consists of all the forces as source terms.

In the following we describe the projection scheme for continuous liquid flow in the FPM framework.

(i) Initialize :

$$p_{dyn}^{n+1} := p_{dyn}^n \quad (13)$$

(ii) Compute α_c^{n+1} implicitly by

$$\alpha_c^{n+1} = \frac{\alpha_c^n}{1 + \Delta t (\nabla \cdot \mathbf{v}_c^n)} \quad (14)$$

(iii) Compute the actual hydrostatic pressure p_{hyd}^{n+1} from

$$\nabla \cdot \left(\frac{1}{\rho_c} \nabla p_{hyd}^{n+1} \right) = \nabla \cdot \mathbf{g} \quad (15)$$

with boundary conditions

$$\frac{\partial p_{hyd}^{n+1}}{\partial \mathbf{n}} = \mathbf{g} \cdot \mathbf{n} \text{ on } \Gamma_{wall} \text{ and } \Gamma_{inflow}, \quad (16)$$

$$p_{hyd}^{n+1} = p_{hyd}^0 \text{ on } \Gamma_{outflow} \quad (17)$$

(iv) Establish preliminary pressure

$$\tilde{p} = p_{hyd}^{n+1} + p_{dyn}^n \quad (18)$$

(v) Compute implicitly the intermediate velocity \mathbf{v}_c^* from

$$\left[(1 + \Delta t G_c) I - \frac{\Delta t}{\alpha_c^{n+1} \rho_c} \nabla \cdot (\kappa \nabla) \right] \mathbf{v}_c^* = \mathbf{v}_c^n - \frac{\Delta t}{\rho_c} \nabla \tilde{p} + \Delta t \mathbf{H}^n \quad (19)$$

(vi) Correct the velocity

$$\mathbf{v}_c^{n+1} = \mathbf{v}_c^* - \frac{\Delta t}{\rho_c} \nabla \epsilon^{n+1} \quad (20)$$

with the constraint (continuity equation)

$$\nabla \cdot \mathbf{v}_c^{n+1} = -\frac{1}{\alpha_c^n} \frac{d\alpha_c}{dt} = -\frac{1}{\alpha_c^n} \frac{\alpha_c^{n+1} - \alpha_c^n}{\Delta t} \quad (21)$$

(vii) Updating the dynamic pressure

$$p_{dyn}^{n+1} = p_{dyn}^n + \epsilon^{n+1}, \quad (22)$$

where ϵ^{n+1} is obtained from (this is obtained taking divergence on (20))

$$\nabla \cdot \left(\frac{1}{\rho_c} \nabla \epsilon^{n+1} \right) = \frac{1}{\Delta t} \left[\frac{1}{\alpha_c^n} \frac{\alpha_c^{n+1} - \alpha_c^n}{\Delta t} + \nabla \cdot \mathbf{v}_c^* \right] \quad (23)$$

with boundary conditions similar to p_{hyd} given in (16).

(viii) Move the particles

$$\mathbf{x}_c^{n+1} = \mathbf{x}_c^n + \Delta t \mathbf{v}_c^{n+1}. \quad (24)$$

We note that in the left hand side of equation (19) the operator $(1 + \Delta t G_c) I - \frac{\Delta t}{\alpha_c \rho_c} \nabla \cdot (\kappa \nabla)$ and the left hand side of equation (23) give rise to the construction of a large sparse matrices, each line of which containing the local, discrete approximation of the operators. The right hand sides appear as a load vector. Hence equations (15), (19) and (23) represent large sparse linear systems, which we solve in the meshfree framework with the help of the FPM. In addition to that we approximate the gradient vectors with the help of the FPM. In the next chapter, we demonstrate how to approximate the Laplace operator by the Finite Pointset Method.

Numerical scheme for secondary phase

Once the velocity, pressure and volume fraction of the continuous phase is known, we interpolate them into the dispersed phase particles from the surrounding clouds of continuous phase particles from the least squares approximation. Then, the following steps are followed to compute the quantities on the secondary phase.

(i) Compute α_d^{n+1} implicitly by

$$\alpha_d^{n+1} = \frac{\alpha_d^n}{1 + \Delta t (\nabla \cdot \mathbf{v}_d^n)} \quad (25)$$

and normalize the volume fractions in order to fulfill the consistency condition (3) as follows

$$\alpha_d^{n+1} = \frac{\alpha_d^{n+1}}{\alpha_d^{n+1} + \alpha_c^{n+1}} \text{ and } \alpha_c^{n+1} = \frac{\alpha_c^{n+1}}{\alpha_d^{n+1} + \alpha_c^{n+1}} \quad (26)$$

(ii) compute the velocity \mathbf{v}_d^{n+1} implicitly as

$$\left[(1 + \Delta t G_d) I - \frac{\Delta t}{\alpha_d^{n+1} \rho_d} \nabla \cdot (\kappa \nabla) \right] \mathbf{v}_d^{n+1} = \mathbf{v}_d^n - \Delta t \left[\frac{\nabla p^{n+1}}{\rho_d} + \left(1 - \frac{\rho_c}{\rho_d} \right) \mathbf{g} + G_d \mathbf{v}_c^{n+1} \right], \quad (27)$$

where $G_d = \frac{3}{4} \frac{\rho_c}{\rho_d} \frac{C_D}{d_{32}} \|\mathbf{v}_c^n - \mathbf{v}_d^n\|$ and $\kappa = \alpha_d^{n+1} \mu_d$.

(iii) Move particles

$$\mathbf{x}_d^{n+1} = \mathbf{x}_d^n + \Delta t \mathbf{v}_d^{n+1}. \quad (28)$$

FPM for the coupled equations

The basis of the computations in FPM is a point cloud, which represents the flow field. The points of the cloud are referred to as particles or numerical grids. They are carriers of all relevant physical information. The particles have to completely cover the whole flow domain, i.e. the point cloud has to fulfill certain quality criteria (particles are not allowed to form "holes" which means particles have to find sufficiently many neighbors; also, particles are not allowed to cluster; etc.). The point cloud is a geometrical basis, which allows for a numerical formulation making FPM a general finite difference idea applied to continuum mechanics. That especially means, if the point cloud would reduce to a regular cubic point grid, then FPM would reduce to a classical finite difference method. The idea of general finite differences also means that FPM is not based on a weak formulation like Galerkin's approach. Rather, FPM is a strong formulation which models differential equations by direct approximation of the occurring differential operators. The method used is a moving least squares idea which was especially developed for FPM.

Coupling Strategy

To simulate the above presented equations for two-phase flows we establish the separate cluster of points for each phase. Each of these separate cluster of points will act as a numerical grid to approximate the governing differential equations for each phase. These point clouds are decoupled from each other, however they are able to exchange any kind of information among the clusters. In this situation we have to interpolate the quantities at an arbitrary particle in one phase from the surrounding cluster of particles from other phase. The interpolation is obtained with the help of the least squares approximation (Dilt (1996), Kuhnert (1999)).

Meshfree discretization for the Laplace operator

The discretization is a generalized finite difference method. The first idea on the generalized finite difference method is presented in (Liszka and Orkisz (1980)), where the sparse linear system is directly derived from the Taylor series expansion. The constraint least squares method is presented by Tiwari and Kuhnert (2002), where the Poisson equation and the boundary conditions are added in the Taylor series expansion as constraints. The comparison of both methods are presented in (Illiev and Tiwari (2002)). It is found that the method presented by Tiwari and Kuhnert is more stable. We still encounter some instability problem during the simulation, where the distribution of neighbor particles are so bad that the iterative method of the sparse linear system do not converge. Therefore, we need to add extra strong condition such that the iterative method converges. As we have seen in the numerical schemes, we need to construct the Laplace operator for the velocities and the pressure equations. Therefore, we consider here the numerical scheme for the Poisson equation and the solutions of the velocity as well as pressure equations can be obtained in the similar fashion.

Consider the computational domain $\Omega \subset R^v, v = 1, 2, 3$. Consider a set of clouds, grids or particles $P(\mathbf{x}, h) = \{\mathbf{x}_i : \mathbf{x}_i \in \Omega, i = 1, \dots, N\}$. The distribution of particles is not necessarily to be uniform and can be quite arbitrary. Typical distribution of particles, for examples in 2D, looks like in Fig. 1.

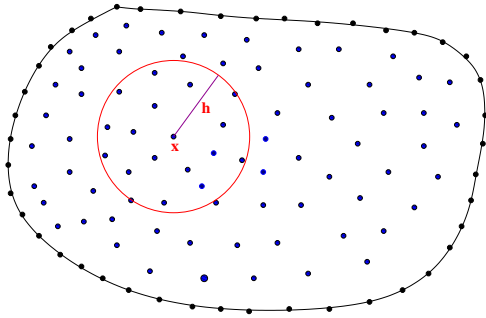


Figure 1: Fluid domain with particles

Let $f(\mathbf{x})$ be a scalar function and f_i its values at \mathbf{x}_i for $i = 1, 2, \dots, N$. In order to limit the number of points we associate a weight function $w = w(\mathbf{x}_i - \mathbf{x}; h)$ with small compact support, where h determines the size of the support, as shown in Fig. 1. In SPH, h is known as smoothing length. The smoothing length defines a set of neighboring particles around \mathbf{x} . The weight function can be quite arbitrary but in our computations, we consider a Gaussian weight function. Let $N(\mathbf{x}, h) = \{\mathbf{x}_i : i = 1, 2, \dots, m\}$ be the set of m neighboring points of \mathbf{x} . For consistency reasons some obvious restrictions are required, namely for example, in 2D, if we want the second order approximation there should be at least 6 neighbor particles including this central particle and they should neither be on the same line nor on the same circle. Hence we define the size of h such that the minimum number of neighbors is guaranteed for the approximation of derivatives. Hence, new particles will have to be brought into simulations as the particle distribution becomes too sparse or, logically, particles will have to be removed from the computation as they become too dense (Drumm et al. (2008b)).

Consider the Poisson equation

$$\Delta f = \psi \text{ in } \Omega \in R^3 \quad (29)$$

with the boundary conditions

$$f = g_1 \text{ on } \Gamma_D \quad \text{and} \quad \frac{\partial f}{\partial \mathbf{n}} = g_2 \text{ on } \Gamma_N, \quad (30)$$

where Γ_D and Γ_N denote the Dirichlet and Neumann boundaries, respectively.

As in the classical discretization method, we construct the shape functions $\phi_i, i = 1, \dots, m$ such that

$$\Delta f \approx \sum_{i=1}^m \phi_i f_i. \quad (31)$$

To construct ϕ_i we consider m Taylor series expansions of $f(\mathbf{x}_i)$ about \mathbf{x}

$$\begin{aligned} f(\mathbf{x}_i) = & f(\mathbf{x}) + dx_i f_x + dy_i f_y + dz_i f_z + \frac{1}{2} dx_i^2 f_{xx} + \\ & dx_i dy_i f_{xy} + dx_i dz_i f_{xz} + \frac{1}{2} dy_i^2 f_{yy} + \\ & dy_i dz_i f_{yz} + \frac{1}{2} dz_i^2 f_{zz} + O(\|\mathbf{dx}_i\|^3), \end{aligned} \quad (32)$$

for $i = 1, \dots, m$, where $dx_i = x_i - x$, $dy_i = y_i - y$, $dz_i = z_i - z$ and f_x is the partial derivative of f with respect to x , f_{xx} is the second order partial derivative with respect to x and so on.

Now we multiply (32) by ϕ_i and sum over 1 to m

$$\begin{aligned} \sum_{i=1}^m \phi_i f_i = & \left(\sum_{i=1}^m \phi_i \right) f + \left(\sum_{i=1}^m \phi_i dx_i \right) f_x + \left(\sum_{i=1}^m \phi_i dy_i \right) f_y + \\ & \left(\sum_{i=1}^m \phi_i dz_i \right) f_z + \left(\frac{1}{2} \sum_{i=1}^m \phi_i dx_i^2 \right) f_{xx} + \left(\sum_{i=1}^m \phi_i dx_i dy_i \right) f_{xy} + \end{aligned}$$

$$\begin{aligned} & \left(\sum_{i=1}^m \phi_i dx_i dz_i \right) f_{xz} + \left(\frac{1}{2} \sum_{i=1}^m \phi_i dy_i^2 \right) f_{yy} + \\ & \left(\sum_{i=1}^m \phi_i dy_i dz_i \right) f_{yz} + \left(\frac{1}{2} \sum_{i=1}^m \phi_i dz_i^2 \right) f_{zz} + O(\|d\mathbf{x}_i\|^3). \end{aligned} \quad (33)$$

From the expression (33) we obtain the approximation of the Laplace operator

$$\Delta f \approx \sum_{i=1}^m \phi_i f_i + O(\|d\mathbf{x}_i\|^3). \quad (34)$$

if the following conditions satisfy

$$\begin{aligned} \sum_{i=1}^m \phi_i &= 0, \quad \sum_{i=1}^m \phi_i dx_i = 0, \quad \sum_{i=1}^m \phi_i dy_i = 0, \quad \sum_{i=1}^m \phi_i dz_i = 0, \\ \sum_{i=1}^m \phi_i dx_i^2 &= 2, \quad \sum_{i=1}^m \phi_i dx_i dy_i = 0, \quad \sum_{i=1}^m \phi_i dx_i dz_i = 0, \\ \sum_{i=1}^m \phi_i dy_i^2 &= 2, \quad \sum_{i=1}^m \phi_i dy_i dz_i = 0, \quad \sum_{i=1}^m \phi_i dz_i^2 = 2. \end{aligned} \quad (35)$$

It consists of 10 constraints (35) and we denote them by G_1, \dots, G_{10} . We observe in the classical finite difference approximation that the sum of all coefficients equals to zero, where the first condition in (35) also fulfills the same condition. Moreover, in order to obtain a stable linear system, we add one more condition that the coefficient on the central particle must be negative, similar to the classical finite difference discretization. Therefore, we consider the additional condition

$$\phi(x_i = x) = -\frac{\beta}{h^2}, \quad (36)$$

where β is a non-negative small number and h is the smoothing length. Hence, we have 11 constraints (35 - 36) for the approximation of the Laplace operator.

Now, we minimize the functional

$$J = \sum_{i=1}^m \frac{\phi_i^2}{w_i} \quad (37)$$

with respect to constraints G_1, \dots, G_{11} . From the Euler-Lagrange theorem, this constrained minimization is equivalent to

$$\frac{\partial J}{\partial \phi_i} + \sum_{j=1}^{11} \lambda_j \frac{\partial G_j}{\partial \phi_i} = 0, \quad i = 1, \dots, m, \quad (38)$$

where $\lambda_1, \dots, \lambda_{11}$ are the Lagrange multipliers. More explicitly we express

$$\begin{aligned} 2\phi_i/w_i + \lambda_1 + dx_i \lambda_2 + dy_i \lambda_3 + dz_i \lambda_4 + dx_i^2 \lambda_5 + \\ dx_i dy_i \lambda_6 + dx_i dz_i \lambda_7 + dy_i^2 \lambda_8 + \\ dy_i dz_i \lambda_9 + dz_i^2 \lambda_{10} + \lambda_{11} \delta_{ix} = 0, \end{aligned} \quad (39)$$

for $i = 1, \dots, m$, where

$$\delta_{ix} = \begin{cases} 1, & \text{if } x_i = x \\ 0, & \text{else.} \end{cases}$$

The above system of equations can be written in the matrix form

$$M\mathbf{a} = \mathbf{b}, \quad (40)$$

where M is a geometrical matrix and $\mathbf{a} = [\lambda_1, \dots, \lambda_{11}]^T$, $\mathbf{b} = -2[\phi_1/w_1, \dots, \phi_m/w_m]^T$. In general we have $m > 11$, therefore the linear system (40) is overdetermined and we obtain the solution from the weighted least squares method and the solution is explicitly given by

$$\mathbf{a} = (M^T W M)^{-1} (M^T W) \mathbf{b}. \quad (41)$$

The vector $(M^T W)\mathbf{b}$ can be written explicitly with the help of conditions (35)

$$\begin{aligned} (M^T W)\mathbf{b} = \\ (-2) \left(\begin{array}{cccccccccc} 0 & 0 & 0 & 0 & 2 & 0 & 0 & 2 & 0 & 2 & -\frac{\beta}{h^2} \end{array} \right)^T. \end{aligned}$$

Hence, we can compute the Lagrange multipliers $\lambda_i, i = 1, \dots, 11$ from (41) and substituting them in (39), the shape functions $\phi_i, i = 1, \dots, m$ can be expressed by

$$\begin{aligned} \phi_i = -\frac{w_i}{2} (\lambda_1 + dx_i \lambda_2 + dy_i \lambda_3 + dz_i \lambda_4 + dx_i^2 \lambda_5 + \\ dx_i dy_i \lambda_6 + dx_i dz_i \lambda_7 + dy_i^2 \lambda_8 + \\ dy_i dz_i \lambda_9 + dz_i^2 \lambda_{10} + \delta_{ix} \lambda_{11}). \end{aligned} \quad (42)$$

If the particle \mathbf{x} belongs to the Neumann boundary, then the constraints are given by

$$\sum_{i=1}^m \phi_i = 0, \quad \sum_{i=1}^m \phi_i d\mathbf{x}_i = \mathbf{n} \quad (43)$$

and the matrix M and the vector $(M^T W)\mathbf{b}$ can be computed accordingly.

Once we compute the Lagrange multipliers as above, we then obtain the approximation (31) for the particle \mathbf{x} . Hence, if we consider \mathbf{x}_j an arbitrary particle and \mathbf{x}_{j_i} its neighbors of number $m(j)$, then we have the following sparse linear system of equations for the unknowns $f_j, j = 1, \dots, N$

$$\sum_{i=1}^{m(j)} \phi_{j_i} f_{j_i} = \psi_j. \quad (44)$$

In this sparse linear system the neighbor particle index gives the entry of the matrix components. This linear system can be solved by any iterative solvers. In this paper, we have solved this by the stabilized biconjugate gradient (BiCgStab) method. The above scheme for the Poisson equation gives the second order convergence, see (Illiev and Tiwari (2002)).

NUMERICAL TESTS

Our main goal is to incorporate the SQMOM in the FPM code to simulate a 3D stirred extraction column and observe the effect of increment of the primary particles. The detailed studies in 3D geometry is time consuming, therefore, in this paper, we have considered a two-dimensional domain with 5 compartments as sketched in Fig. 2, which is the slice of 3D extraction column, where the rotors are fixed. The extension of the code to three dimensional stirred extraction column is straight forward.

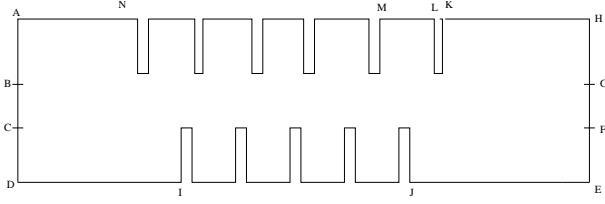


Figure 2: 2D computational domain

The size of the domain is $310\text{ mm} \times 48\text{ mm}$. On the left boundary $BC = 4\text{ mm}$ is the inflow boundary for primary phase and the rest is no-slip boundary for the primary phase and outflow boundary for the secondary phase. On the right wall $FG = 4\text{ mm}$ is inflow boundary for the droplet and the rest EF and GH are the no-slip boundary for the secondary phase and outflow boundary for the primary phase. Rest of the walls are considered as no-slip boundary for both phases. The size of compartments is $ML = 29\text{ mm}$ and they are separated by $LK = 1\text{ mm}$. The length of other walls like $AN = KH = 80\text{ mm}$ and $DI = JE = 94\text{ mm}$. The dimensions are the same in the 3D domain. The volume flow of the aqueous (water) and organic (butyl-acetate) phases are 100 l/h which corresponds to the inflow velocities equal to 0.0342 m/s . The densities of the aqueous and organic phases are 1000 kg/m^3 and 880 kg/m^3 , respectively. The viscosities for the aqueous and organic phases are 0.001 kg/(ms) and 0.0007 kg/(ms) . Moreover, the gravitational force acts in the positive x -direction. The moments in the inlet boundary of the dispersed phase are $m_0 = 6.4e7$, $m_1 = 160000$, $m_2 = 400$, $m_3 = 1$ such that the Sauter mean diameter is 2.5 mm . If we use more primary particles, then we generate the moments in the section, where this Sauter diameter falls in and in the rest of the section we set sectional moments equal to zero. For all three cases the simulations have been run upto 5.1 secs , where a quasi-steady state is reached. The smoothing length $h = 0.0035\text{ mm}$ such that the total number of particles for both phases is around 15000 initially. The total number of particles varies around this initial number during the simulations. The user CPU time in the dual Intel Xeon 5148LV (2.33 GHz.) is 331 minutes.

Case 1: Breakage only

In our first test case, we have considered only the breakage with constant kernel equal to 1. A parabolic distribution with constant $C = 1$ is taken into account, see Marchisio et al. (2003) for models of parabolic distribution. In Figs. 3, 4 and 5 we have plotted the Sauter mean diameter for primary particles equal to 1, 2 and 5, respectively. The size of d_{32} is decreasing from 2.5 mm to below 1.8 mm in the outlet. For primary particle equal to 1 it is around 1.3 mm , which may be underpredicted.

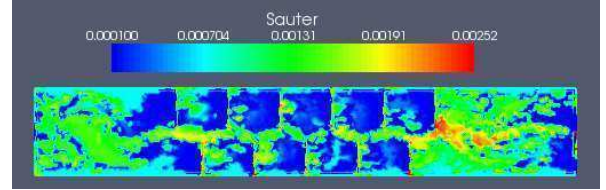


Figure 3: d_{32} for breakage only with 1 primary particle

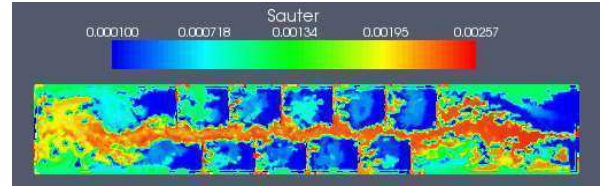


Figure 4: d_{32} for breakage only with 2 primary particles

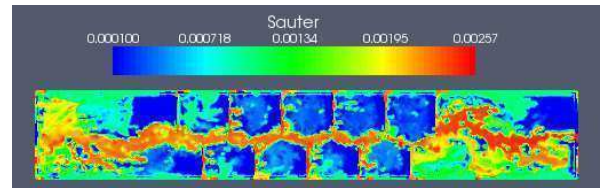


Figure 5: d_{32} for breakage only with 5 primary particles

Case 2: Aggregation only

As a second test case, we have considered only the aggregation with constant kernel equal to $1E - 7$. As in the case 1, Figs. 6, 7 and 8 exhibit d_{32} for primary particles equal to 1, 2 and 5, respectively. For the primary particles equal to 2 and 5 d_{32} in the outlet is around 4.8 mm . As in the case 1 d_{32} is again underpredicted for the primary particle equal to 1. These results have to be verified with help of experiments.

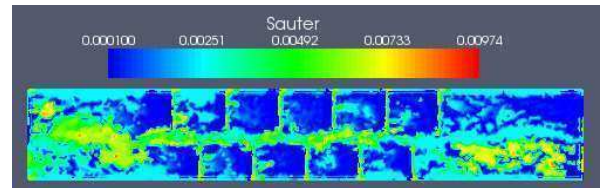


Figure 6: d_{32} for aggregation only with 1 primary particle

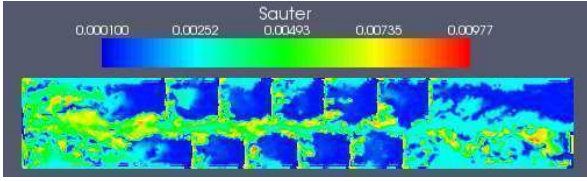


Figure 7: d_{32} for aggregation only 2 primary particles

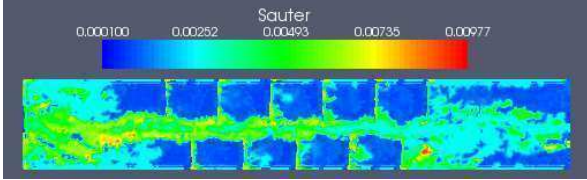


Figure 8: d_{32} for aggregation only with 5 primary particles

Case 3: Breakage and aggregation

In our final test case, we have considered both breakage and aggregation with constant kernels equal to cases 1 and 2. In Figs. 9, 10 and 11 we have plotted the Sauter mean diameters for primary particles 1, 2 and 5, respectively.

We note that we have used 2 secondary particles for each sections. The primary particle equal to 1 is equivalent to the classical QMOM (Marchisio et al. (2003)). Attarakih et al. (2007) have compared the moments obtained from the SQMOM simulations with the exact ones for primary particles 2 and higher, they have shown that increasing the number of primary particle from 2 to 4 gives the moments quite closer to the exact ones. In Figs. 10 and 11, we see qualitatively the Sauter mean diameters is quite better than the ones in Fig. 9.

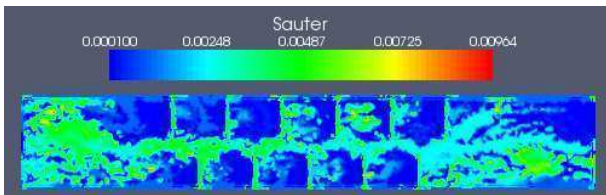


Figure 9: d_{32} for breakage and aggregation with 1 primary particle

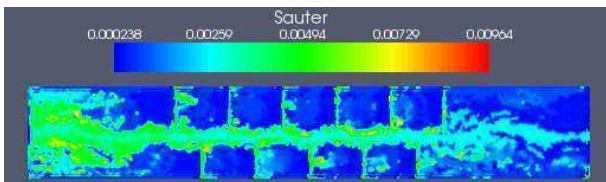


Figure 10: d_{32} for breakage and aggregation with 2 primary particles

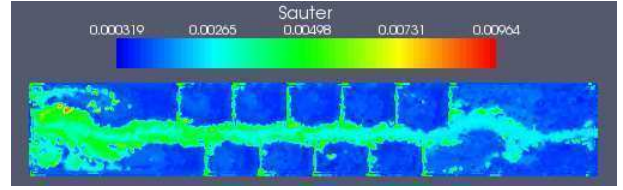


Figure 11: d_{32} for breakage and aggregation with 5 primary particles

Similar observations can be obtained also in the volume fractions for the dispersed phase, which are plotted in Figs. 12-14.

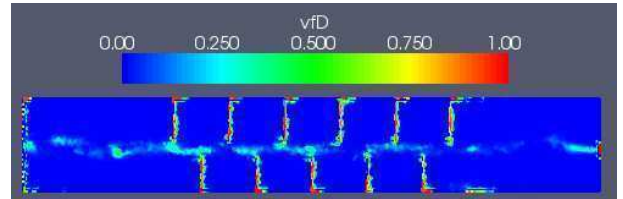


Figure 12: Volume fraction for dispersed phase for 1 primary particle

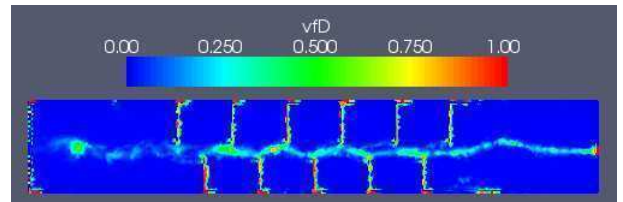


Figure 13: Volume fraction for dispersed phase for 2 primary particles

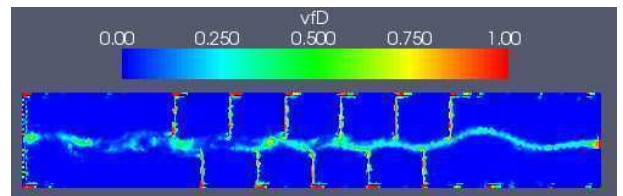


Figure 14: Volume fraction for dispersed phase for 5 primary particles

Finally, we have plotted the velocity contour for the primary particles 1, 2 and 5 in Figs. 15, 16 and 17, respectively.

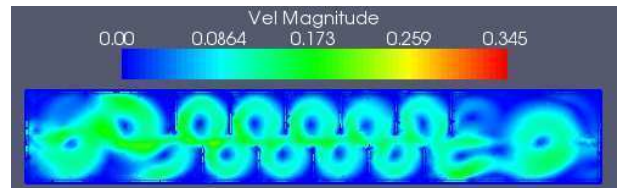


Figure 15: Velocity contour for continuous phase for 1 primary particle

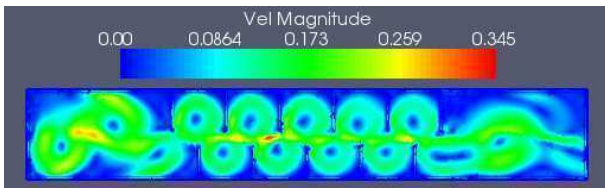


Figure 16: Velocity contour for continuous phase for 2 primary particle

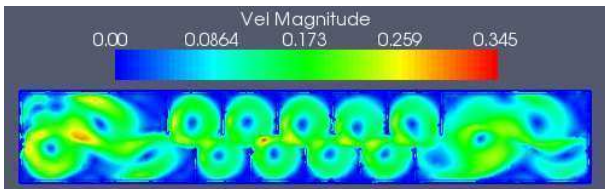


Figure 17: Velocity contour for continuous phase for 5 primary particles

All the plots of the Sauter mean diameters, volume fractions and velocity counters show that the simulation results for primary particles 2 and 5 are close each other and have some discrepancies with the simulation results of 1 primary particle. Nevertheless, the results show that even a small number of primary particles deliver reliable results making the SQMOM very attractive from computational point of view. Furthermore, the number of primary particles could be fitted to the particular needs of problems, while the number of secondary particles in each section is equal to 2.

CONCLUSION

A meshfree Lagrangian particle method, called Finite Pointset Method (FPM) is presented for the coupled model of CFD and population balance equation. A two-fluid model is considered. Two separate decoupled clusters of particles are established for the continuous and dispersed phases. Each phase is computed in their respective clusters of point and the information between phases have been exchanged through the least squares method from one cluster of points to another and vice versa. The Sauter mean diameter is computed from the solution of population balance equation, which is solved by the sectional QMOM. The SQMOM was successfully implemented in FPM. Constant aggregation and breakage kernels have been used. Two dimensional geometry is considered to see the effect of the more primary particles. In future, three dimensional stirred extraction column will be considered with real models for aggregation and breakage and the simulated results will be compared with the experimental one. Moreover, a turbulence model will be included to model the real aggregation and breakage kernels.

ACKNOWLEDGMENT

The authors would like to thank the Deutsche Forschungsgemeinschaft DFG for the financial support.

REFERENCES

- M.M. Attarakih, H.-J. Bart, and N.M. Faqir. Numerical solution of the bivariate population balance equation for the interacting hydrodynamics and mass transfer in liquid-liquid extraction column. *Chem. Eng. Sci.*, 61(1):113, 2006.
- M.M. Attarakih, C. Drumm, and H.-J. Bart. Solution of the population balance equation using the sectional quadrature method of moments. In *3rd International Conference on Population Balance Modelling*. Quebec, Canada, 2007.
- T. Belytschko, Y. Krongauz, D. Organ, M. Flemming, and P. Krysl. Meshless methods: An overview and recent developments. *Comput. Methods Appl. Mech. Eng.*, 139:3, 1996.
- A. Chorin. Numerical solution of the Navier-Stokes equations. *J. Math. Comput.*, 22:745, 1968.
- G.A. Dilt. Moving least squares particle hydrodynamics I, consistency and stability. Technical Report Hydrodynamics methods group, Los Alamos National Laboratory, 1996.
- C. Drumm, M. M. Attarakih, S. Tiwari, J. Kuhnert, and H.-J. Bart. Implementation of the sectional quadrature method of moments in a CFD code. In *6th Int. Conf. on CFD in Oil & Gas*. Norway, 2008a.
- C. Drumm, S. Tiwari, J. Kuhnert, and H.-J. Bart. Finite pointset method for simulation of the liquid-liquid flow field in an extractor. *Comp. Chem. Eng.*, in Press, 2008b.
- R.A. Gingold and J.J. Monaghan. Smoothed particle hydrodynamics: theory and application to non-spherical stars. *Mon. Not. Roy. Astron. Soc.*, 181:375, 1977.
- O. Illiev and S. Tiwari. A generalized (meshfree) finite difference discretization for elliptic interface problems. Numerical Methods and Applications, Lecture Notes in Computer Sciences (I. Dimov, I. Lirkov, S. Margenov and Z. Zlatev, eds.), springer, page 443, 2002.
- E. Krepper, T. Frank, D. Lucas, H.-M. Prasser, and P.J. Zwart. Inhomogeneous MUSIG model - a population balance approach for polydispersed bubbly flows. In *6th International Conference on Multiphase Flow*. Leipzig, Germany, 2007.
- J. Kuhnert. *General smoothed particle hydrodynamics*. PhD Thesis, University of Kaiserslautern, Germany, Shaker Verlag, 1999.
- T. Liszka and J. Orkisz. The finite difference method on arbitrary irregular grid and its application in applied mechanics. *Computers & Structures*, 11:83, 1980.
- S. Lo. Application of population balance to CFD modelling of gas-liquid reactors. In *Trends in Numerical and Physical Modelling for Industrial Multiphase Flows*. Corsica, France, 2002.
- L.B. Lucy. A numerical approach to the testing of the fission hypothesis. *Astron. J.*, 82:1013, 1977.

D.L. Marchisio, J.T. Piktorna, R. O. Fox, R.D. Vigil, and A.A. Barresi. Quadrature method of moments for population balance equation. *AIChE J.*, 49:1266, 2003.

J.J. Monaghan. Smoothed particle hydrodynamics. *Annu. Rev. Astron. Astrop.*, 30:543, 1992.

J.P. Morris. Simulating surface tension with smoothed particle hydrodynamics. *J. Comput. Appl. Meth.*, 155(2):263, 2000.

D. Ramkrishna. *Population Balances*. Academic Press, San Diego, 2000.

L. Schiller and Z. Naumann. A drag coefficient correlation. *Z.Ver.Deutsch.Ing.*, 77:318, 1935.

S. Tiwari and J. Kuhnert. A meshfree method for incompressible fluid flows with incorporated surface tension. *revue aurope'enne des elements finis*, 11:965, 2002.

S. Tiwari and J. Kuhnert. Modeling of two-phase flows with surface tension by Finite Pointset Method (FPM). *J. Comp. Appl. Math.*, 203:376, 2007.

S. Tiwari and S. Manservisi. Modeling incompressible Navier-Stokes flows by LSQ-SPH. *The Nepali Math. Sci. report*, 20, 2002.

S. Tiwari, C. Drumm, M.M. Attarakih, J. Kuhnert, and H.-J. Bart. Coupling of the CFD and the Droplet Population Balance Equation with the Finite Pointset Method. To appear in *Lecture Notes in Comput. Sci. Eng.*, Springer, 2008.

F. Wang and Z.-S. Mao. Numerical and experimental investigation of liquid-liquid two phase flow in stirred tanks. *Ind. & Eng. Res.*, 44:5776, 2005.

Publication VI

Reprinted from Proceedings International Solvent Extraction Conference ISEC 2008, Moyer, B. (Ed.), Vol.2, 1177, published by Canadian Institute of Mining, Metallurgy and Petroleum, Montreal, **2008**.

Christian Drumm, Sudarshan Tiwari, Menwer Attarakih, Jörg Kuhnert, Hans-Jörg Bart,
CFD-PBM coupled model using the Finite Pointset Method and the SQMOM.

Reprinted with permission from Canadian Institute of Mining, Metallurgy and Petroleum (CIM).

ISBN: 1-894475-80-1 (Volume I)

ISBN: 1-894475-81-X (Volume II)

CFD-PBM COUPLED MODEL USING THE FINITE POINTSET METHOD AND THE SQMOM

C. Drumm,¹ S. Tiwari,² M. M. Attarakih,³ J. Kuhnert,² and H.-J. Bart^{1*}

¹*Lehrstuhl f. Thermische Verfahrenstechnik, TU Kaiserslautern, Postfach 3049, 67653 Kaiserslautern, Germany.* ²*Fraunhofer Institut Techno- und Wirtschaftsmathematik, Fraunhofer-Platz 1, 67663 Kaiserslautern, Germany.* ³*Faculty of Engineering Tech., Chem. Eng. Dept, Al-Balqa Applied University, PO. Box 15008, 11134 Amman, Jordan.*
**Corresponding author email address: bart@mv.uni-kl.de*

ABSTRACT

This contribution focuses on a combined Computational Fluid Dynamics (CFD) and Droplet Population Balance Model (DPBM), where the DPBM is solved as part of the CFD code. The coupling is done with the help of the Finite Pointset Method (FPM), which is a meshfree, Lagrangian, particle method. The droplet population balance equations are solved by the Sectional Quadrature Method of Moments (SQMOM). First simulations of the coupled algorithms are presented for an RDC extractor in which droplet coalescence and breakage (with constant kernels) are used.

INTRODUCTION

In the simulation and layout of liquid-liquid extraction columns the dispersed phase is classically assumed as a pseudo homogeneous phase. The state of the art for the design of extraction columns is to use the dispersion or back mixing model, where one parameter accounts for all deviations from the ideal plug flow behaviour. Recent research focussed on the droplet population balance models DPBM that take into account droplet transport (rise and backmixing) and interaction (breakage and coalescence) [1, 2]. In typical DPBM codes, the dispersion model is still used for the description of the hydrodynamics and results from small scale devices (single droplet experiments) are needed to predict Sauter mean diameters and hold-up profiles [1, 2]. The coupling of Computational Fluid Dynamics (CFD) with DPBM allows for a further improvement, since now the turbulent flow in an extraction column is fully resolved and described by CFD with much less simplifications. Neither pilot plant experiments nor parameters are needed, since all required parameters in the DPBM equations (e.g. the turbulent energy dissipation, velocities of the droplets) come from CFD, provided that the CFD predictions are accurate. Recent investigations show that CFD can predict the two-phase counter-current flow field in a Rotating Disc Contactor (RDC) [3, 4].

Only a few researchers investigated combined CFD-DPBM models in the field of liquid-liquid extraction so far but achieved encouraging results for the combined models [5, 6].

Hence, this contribution focuses on a combined Computational Fluid Dynamics (CFD) and Droplet Population Balance Model (DPBM) to eliminate the classical simplifying assumptions imposed on this promising field of research. The coupling is done with the help of the Finite Pointset Method (FPM), which is a meshfree, Lagrangian, particle method. FPM is an in-house development of the Fraunhofer Institute. In comparison to a commercial code the source code is fully modifiable, which eases the implementation of the DPBM. As a further benefit, the DPBM equations are solved by the Sectional Quadrature Method of Moments [7]. This method is found to track accurately any set of low-order moments with the ability to reconstruct the shape of the distribution. In this way, it combines the advantages of the classes methods (CM) [8] and the Quadrature Method of Moments (QMOM) [9], and at the same time it minimizes their drawbacks. For the validation of the coupled algorithm, a five compartment section of a Rotating Disc Contactor (RDC) was modelled in three dimensions. As a starting step, constant breakage and coalescence kernels were assumed and simulations using the system butylacetate-water were carried out for the same operating conditions as in experiments of Simon [10].

THE POPULATION BALANCE EQUATION

The superstructure of the population balance equation and the general derivation based on the Reynold transport theorem is given in Ramkrishna [11]. The spatially distributed population balance equation could be written as:

$$\frac{\partial f(v, \xi, t)}{\partial t} + \nabla \cdot (uf(v, \xi, t)) = \rho\{f(v, \xi, t), v, \xi, t\}. \quad (1)$$

Since the particles are assumed to have in general a spectrum of sizes, this spectrum could be represented by a number density function with particle size as an independent variable. So, let $f(v, \xi, t)\partial v$ be the average number of particles per unit volume of a fixed subspace at time t , then the above number continuity equation is formally interpreted as: The first term on the left hand side denotes the accumulated particles of size v , the second term is the convection of the particles along the physical space ξ while, the source term on the right hand side represents the net number of particles produced due to breakage and coalescence per unit time and volume of physical space.

THE FINITE POINTSET METHOD

The FPM is a numerical method for solving fluid dynamic equations. This is a meshfree, Lagrangian method. The basis of the computations is a point cloud which is referred to as particles or numerical grid points. Particles move with the fluid velocity and they carry all relevant physical information. The point cloud represents the flow field, where they have to cover completely the whole flow domain, i.e. the point cloud should fulfill

certain adaptivity criteria (particles are not allowed to form "holes" which means particles have to find sufficiently many neighbors; also, particles are not allowed to cluster; etc.). The point cloud is a geometrical basis, which allows for a numerical formulation, making FPM a general finite difference idea applied to continuum mechanics. FPM is a strong formulation technique which models differential equations by direct approximation of the occurring differential operators. The method uses a moving least squares idea which was especially developed for FPM. The primary (continuous) phase is modeled by the Navier-Stokes equations. The motion of the secondary (dispersed) phase is calculated by solving the equation of motion in which the inertia, drag and buoyancy forces are taken into account. The coupling strategy within FPM framework is as follows: the separate point clouds are established for each phase. Primary and secondary phase equations are solved in their respective point clouds. These point clouds are decoupled from each other; however the necessary information like velocities, volume fractions, etc. will be exchanged between these clouds. A complete two-way coupling is achieved in which the Sauter mean diameter of the droplets is calculated in every time step and substituted in the drag force, while the velocity of the droplets in the convective term of the DPBM is derived from the Navier-Stokes equations. This method is found to be appropriate for multiphase problems, e.g. a two-phase immiscible flow and details about the numerical approach can be found elsewhere [4, 12].

THE SECTIONAL QUADRATURE METHOD OF MOMENTS

In the finite difference or sectional methods (e.g. [8]) the particle size is discretized into a finite number of sections, whereas the population in each section is considered to behave like a single particle. In the SQMOM framework of discretization, this single particle will be called the primary particle and it will be responsible for the reconstruction of the distribution. Unfortunately, large number of primary particles in the classical sectional methods is required, not only to reconstruct the shape of the distribution, but also to estimate the desired integral quantities associated with the distribution. The interaction between primary particles in different sections, due to breakage and coalescence events, results in a new primary particle with no representative size due to the discrete approximation of the distribution. Because the newly-birthed particle could not conserve any of its low order moments but one, the rest of the low-order moments are predicted with low accuracy and hence the associated integral quantities. To overcome this fundamental problem of the sectional methods, N_{sp} secondary particles in the SQMOM are generated in each section (i) with positions (abscissas: $d_j^{<i>}$) and weights ($w_j^{<i>}$) where $i = 1, 2, \dots, N_{pp}$, $j = 1, 2, \dots, N_{sp}$). The secondary particles are exactly equivalent to the number of quadrature points in Gauss-like quadratures or the QMOM [9]. Accordingly, each secondary particle could conserve or reproduce two low-order moments and in general $2N_{sp}$ moments in each section. The way in which the SQMOM works is started by dividing the particle size into contiguous sections (N_{pp} primary particles). Each section is then seeded by the desired number of secondary particles which carry detailed information about the distribution. In this framework, the

active particle mechanisms such as splitting and coalescence occur through interactions between the secondary particles. It is obvious now that $N_{sp} \times N_{pp}$ particles are contributing in the splitting and aggregation events. Due to the increase of the number of interacting particles, more information is gathered about the distribution itself. This distribution could be reconstructed from the secondary particles by averaging the total weights of the secondary particles with respect to the section width (Δd_i) and locating them at the mean size of the secondary particles. In pure mathematical sense, the above presentation is equivalent to applying the QMOM to each section of an arbitrary width: $[d_{i-1/2}, d_{i+1/2}]$: $i = 1, 2, \dots, N_{pp}$ resulting in a set of sectional moments that could be written as:

$$\mu_r^{<i>}(\xi, t) = \int_{d_{i-1/2}}^{d_{i+1/2}} d^r f(d, \xi, t) \partial d, \quad r = 0, 2, \dots, 2N_{sp} - 1 \quad (2)$$

More details about this approach can be found in the original paper of Attarakih et al.[7].

RESULTS

In this section results of the simulations using the system butyl acetate-water are shown. Volume flow rates in the simulations are 100 L/h for both the aqueous and organic phases, while the stirrer speed is 150 rpm. As a starting point, constant kernels for breakage (1.0) and coalescence (1.0E-10), which were fitted to experimental data, are considered in the DPBM and only one primary particle is chosen in the SQMOM. In this case the SQMOM corresponds exactly to the QMOM; however, with efficient numerical implementation. In Fig. 1 the simulated Sauter mean diameters ($d_{32} = \mu_3/\mu_2$) in the five compartment section are shown. The Sauter mean diameter is increasing from a value of 2.2 mm to around 2.7 mm and matches the experimental value of the Sauter mean diameter (around 2.6 mm [9]). In future simulations, real breakage and coalescence models will be considered to allow for a prediction of the drop size distribution. Furthermore, more than one primary particles will be applied, whereas, each class will move with their own mean diameter by solving separate Navier-Stokes equations. A comparison of the SQMOM with analytical solutions showed that it is extremely accurate when an appropriate number of primary or secondary particles are used [7]. The results of the volume fraction in Fig. 2 show that the droplets accumulate under stirrers and stators and rise mainly through the middle of the compartment without penetrating the outer regions. The same observations were also made in experiments [3]. Fig.3 shows the simulated 2D velocity vectors and 2D velocity magnitude in a xz -plane in the aqueous phase without considering the dominating swirl velocity in y -direction, since the developed two-phase flow field is better visible then. Although the aqueous phase flows from top to bottom the vortices reverse at the positions between the stators and are directed to the top because the throughput of the ascending droplets is high enough to modify the flow pattern. In Fig.4 the contours of the velocity

magnitude also consider the swirl velocity. The velocities near the stirrer correspond to the tip velocity ($v_{tip}=0.7$ m/s) and decreases through the compartment to zero at the column wall. A detailed comparison of simulated and measured flow fields and velocities in single- and two-phase flows using a constant diameter for the droplets in the same geometry showed that FPM is able to predict the flow fields and velocities [4].

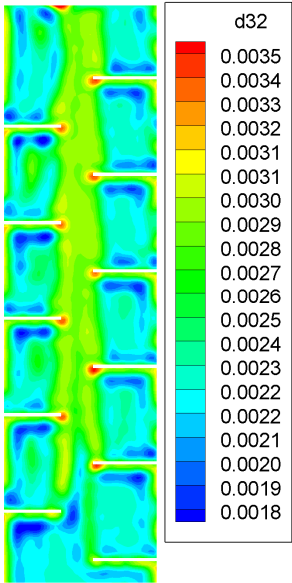


Figure 1. The simulated Sauter mean diameter (left)

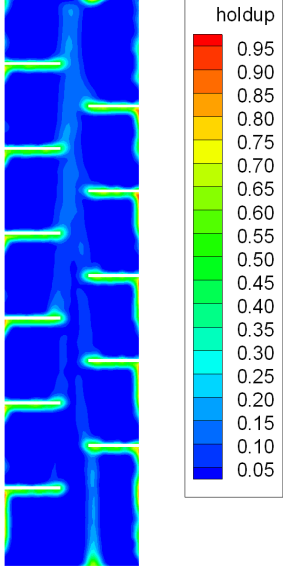


Figure 2. The simulated volume fraction of the dispersed phase (right)

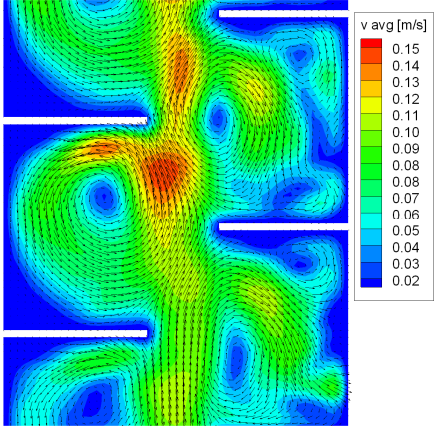


Figure 3. The simulated velocity vectors and magnitude (axial and radial velocity) in one compartment

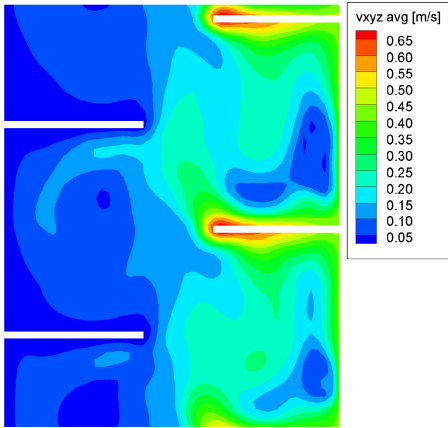


Figure 4. The simulated velocity magnitude (axial, radial and swirl velocity) in one compartment

CONCLUSIONS

First results of the coupled CFD-PBM algorithm using the FPM and the SQMOM were presented. A complete two-way coupling is achieved and the coupled model accounts for breakage and coalescence. FPM is able to predict the flow fields and velocities in an RDC extractor. The SQMOM is found extremely accurate and the flexibility of the method through its reduction to the standard QMOM when the number of primary particles equals one makes it very attractive from computational point of view. The constant kernels were fitted to experimental data and predict suitable results. Models for breakage and coalescence can be easily integrated and will allow for a prediction of the drop size distribution.

ACKNOWLEDGMENTS

This work was financially supported by the Deutsche Forschungsgemeinschaft (DFG).

REFERENCES

1. M. M Attarakih, H.-J. Bart and N. M. Faqir, "Numerical solution of the bivariate population balance equation for the interacting hydrodynamics and mass transfer in liquid-liquid extraction columns", *Chem. Eng. Sci.*, **61**(1), 113-123 (2006).
2. S. A. Schmidt, M. Simon, M.M. Attarakih, L. Lagar, H.-J. Bart, "Droplet population balance modelling - hydrodynamics and mass transfer", *Chem. Eng. Sci.*, **61**(1), 246-256, (2006).
3. C. Drumm and H.-J. Bart, "Hydrodynamics in a RDC extractor: single and two-phase PIV measurements and CFD simulations", *Chem. Eng. Techn.*, **29**(11), 1-8 (2006).
4. C. Drumm, S. Tiwari, J. Kuhnert and H.-J. Bart, "Finite Pointset Method for Simulation of the Liquid-Liquid Flow Field in an Extractor", submitted *Comp. Chem. Eng.*, (2007).
5. C. Drumm, M. M Attarakih and H.-J. Bart, "Coupling of CFD with DPBM for a RDC extractor", submitted for publication in *Chem. Eng. Sci.*, special issue 3rd International Conference on Population Balance Modelling, Quebec, Canada, 19-21 Sep. 2007.
6. A. Vikhansky, M. Kraft, M. Simon, S. Schmidt and H. J. Bart, "Droplets population balance in a rotating disc contactor: an inverse problem approach", *AIChE Journal*, **52**(4), 1441-1450 (2006).
7. M. M Attarakih, C. Drumm, H.-J. Bart, "Solution of the Population Balance equation using the Sectional Quadrature Method of Moments", submitted for publication in *Chem. Eng. Sci.*, special issue 3rd International Conference on Population Balance Modelling, Quebec, Canada, 19-21 Sep. 2007.
8. M. J. Hounslow, R. L. Ryall and V. R. Marshall, "A discretized population balance for nucleation, growth and aggregation", *AIChE Journal*, **34**(11), 1821-1832 (1988).
9. R. McGraw, "Description of aerosol dynamics by the quadrature method of moments", *Aerosol Sci. & Tech.*, **27**(2), 255-265 (1997).
10. M. Simon, "Koaleszenz von Tropfen und Tropfenschwärmen", Dr.-Ing. Thesis, TU Kaiserslautern, Kaiserslautern, Germany, 2002.
11. Ramkrishna, D. , *Population Balances*, Academic Press, San Diego, 2000.
12. S. Tiwari and J. Kuhnert, "Modeling of two-phase flows with surface tension by Finite Pointset Method (FPM)", *J. Comp. Appl. Math.*, **203**(2), 376-386 (2007).

Publication VII

Reprinted from Computers & Chemical Engineering, 32, 2946-2957, **2008**,

Christian Drumm, Sudarshan Tiwari, Jörg Kuhnert, Hans-Jörg Bart,

Finite Pointset Method for Simulation of the Liquid-Liquid Flow Field in an Extractor.

Reprinted with permission from Elsevier.

<http://dx.doi.org/10.1016/j.compchemeng.2008.03.009>



Finite pointset method for simulation of the liquid–liquid flow field in an extractor

Christian Drumm^a, Sudarshan Tiwari^b, Jörg Kuhnert^b, Hans-Jörg Bart^{a,*}

^a Lehrstuhl f. Thermische Verfahrenstechnik, TU Kaiserslautern, Gottlieb-Daimler-Strasse, 67663 Kaiserslautern, Germany

^b Fraunhofer Institut Techno- und Wirtschaftsmathematik, Fraunhofer-Platz 1, 67663 Kaiserslautern, Germany

ARTICLE INFO

Article history:

Received 22 October 2007

Received in revised form 20 March 2008

Accepted 20 March 2008

Available online 8 April 2008

Keywords:

CFD

FPM

Meshfree method

Extraction column

Liquid–liquid flow

PIV

ABSTRACT

Finite pointset method (FPM) is applied for the simulation of the single- and two-phase flow field in a rotating disc contactor (RDC) type extraction column. FPM is a numerical method to solve fluid dynamic equations. This is a Lagrangian and meshfree particle method, where the particles move with fluid velocity and carry all information necessary for solving fluid dynamic quantities. The simulations are validated by single- and two-phase 2D particle image velocimetry (PIV) measurements. In addition, the results are compared to simulations of the commercial CFD code Fluent. The results show that FPM can predict the one- and two-phase flow field in the RDC, whereas the predicted velocities are in good agreement with the experimental ones. FPM also bears comparison with the results of the commercial CFD code Fluent.

© 2008 Elsevier Ltd. All rights reserved.

1. Introduction

Liquid–liquid extraction is a separation process, which is based on the different distribution of the components to be separated between two liquid phases. Liquid–liquid extraction processes are widely applied in chemical and biochemical industries. Classical extraction equipments are mixer-settler cascades and different types of counter-current extraction columns like the RDC type, which is analyzed here. The simulation of these counter-current liquid–liquid extraction columns still requires improvement. Today, the layout of an extractor is mainly based on manufacturer's knowledge and simplified models, e.g. the HTU-NTU concept methods, where 1D flow models, such as the back flow or dispersion model, are used to account for the non-idealities of the flow. In most cases these models are too simple to describe the real hydrodynamic behavior. That is why the design of extraction columns often requires pilot plant experiments and is time and money consum-

ing. On the other hand, there is an ongoing claim by the industry for more straightforward, faster and money saving simulation methods.

Computational fluid dynamics (CFD) are one possibility in this direction, since CFD can predict the 3D flow field in an extraction column and also account for the non-idealities. In addition to the flow field, CFD simulations can deliver single design parameters as the residence time of the droplets (Modes & Bart, 2001). Current research in the last years also focused on the link of CFD and the population balance models (PBM) (Vikhansky & Kraft, 2004). PBM can specify droplet movement, coalescence and breakage of the dispersed phase and consider the particulate behavior of the droplets in an extraction column. For a successful combination of CFD and PBM and a general application of CFD in the field of liquid–liquid extraction columns, the performance of CFD simulations for extraction columns should be tested. In recent years, only a few working groups focused on the simulation of the hydrodynamics in counter-current stirred liquid–liquid extraction columns. The authors often helped themselves by only considering the single-phase flow in the column (Fei, Wang, & Wan, 2000; Modes & Bart, 2001). Two-phase flow fields were simulated and investigated only by Rieger, Weiss, Weigley, Bart, and Marr (1996), You and Xiao (2005), Vikhansky & Kraft (2004) and Drumm and Bart (2006). Only the latter showed a complete comparison of the simulated flow field with experiments.

In this paper we present the simulations of liquid–liquid two-phase flows in an extraction column. The primary (continuous)

Abbreviations: BiCgStab, stabilized biconjugate gradient; CFD, computational fluid dynamics; FPM, finite pointset method; ILA, intelligent laser application; LDA, laser doppler anemometry; PBM, population balance model; PIV, particle image velocimetry; RANS, Reynolds averaged Navier–Stokes; RDC, rotating disc contactor; SPH, smoothed particle hydrodynamics.

* Corresponding author.

E-mail addresses: cdrumm@mv.uni-kl.de (C. Drumm), tiwari@itwm.fhg.de (S. Tiwari), kuhnert@itwm.fhg.de (J. Kuhnert), bart@mv.uni-kl.de (H.-J. Bart).

Nomenclature

\vec{a}	vector
\vec{b}	vector
B	Ball of radius h with center \vec{x}
C_D	drag coefficient
d_d	droplet diameter
dx	difference of x -coordinate of i th particle to central particle
f	scalar
\vec{F}	interfacial force
\vec{g}	gravity force
h	radius of interaction of neighboring particle
\vec{H}	force
I	identity matrix
J	quadratic functional
m	number of neighbor particle
M	geometrical matrix
N	total number of particle
$O(N)$	capital order of N
p	pressure
p_{dyn}	dynamic pressure
p_{hyd}	hydrostatic pressure
P	set of neighbor particles
R^v	v -dimensional Euclidean space
Re	relative Reynolds number
S	stress tensor
t	time
\vec{v}	velocity vector
w	weight function
W	diagonal matrix
\vec{x}	position vector

Greek letters

α	volume fraction
β	constant
Γ	boundary
δ	Dirac delta function
η	constant factor for the Gaussian weight function
λ	Lagrange multiplier
μ	dynamic viscosity
ν	dimension in Euclidean space
ρ	density
ϕ	shape function for spatial derivative approximation
ψ	a scalar function
Ω	computational domain

Subscript

32	Sauter mean diameter
l	primary phase
d	dispersed phase
N	Neumann boundary
D	Dirichlet boundary
i	particle index
in	inflow
out	outflow
w	wall

phase is modeled by the Navier–Stokes equations. The motion of the secondary (disperse) phase is calculated by solving the equation of motion in which the inertia, drag and buoyancy forces are taken into account.

We solve both types of equations by the finite pointset method (FPM). FPM is a Lagrangian and meshfree method for solving fluid dynamic equations. Meshfree methods are originally developed to simulate fluid dynamics problems. Smoothed particle hydrodynamics (SPH) is referred to as the first meshfree method (Lucy, 1977; Monaghan, 1992). Since then it has been extended to simulate the compressible Euler equations in fluid dynamics and was applied to a wide range of problems (see Hu & Adams, 2006; Liu & Liu, 2003; Monaghan, 1994; Morris, 2000). The implementation of the boundary conditions is the main problem of the SPH method. Our approach differs from the method of SPH in approximations of derivatives and the treatment of boundary conditions. In its original formulation, SPH is easy for implementation, but it provides poor accuracy/convergence (Duarte & Oden, 1996; Griebel & Schweitzer, 2000). Further, variety of meshfree methods were proposed in the last decade for solving fluid dynamics and solid mechanics problems. Detailed discussion on the development of meshfree methods and on their application, can be found, e.g., in Belytschko, Krongauz, Organ, Flemming, and Krysl (1996), Griebel and Schweitzer (2002, 2005, 2006), Liu, Liu, and Lam (2003) and other references there.

FPM is suitable to handle, for examples, flow problems with complicated and rapidly changing geometry (Kuhnert, Tramecon, & Ullrich, 2000), free surface flows (Tiwari & Kuhnert, 2002) and multiphase flows (Tiwari & Kuhnert, 2007). In our previous works we have presented the simulations of two-phase immiscible flows using FPM (Tiwari & Kuhnert, 2007), where we have considered a class of points, where the phases are distinguished by the color for each fluid particle and advect the color function which results in tracking the interface accurately. The normal and the curvature of the interface can be computed from the color function. In this paper, we do not use the color function, instead we establish the separate cluster of points for each phase. Each of these separate cluster of points will act as a numerical grid to approximate the governing differential equations for each phase. These point clouds are decoupled from each other, however they are able to communicate any kind of information among the clusters. A detailed description of FPM is presented in Section 3.

For the validation of the simulations particle image velocimetry measurements are conducted. The PIV technique allows the recording of a complete flow velocity field in a plane of the flow within a few microseconds (Kompenhans, Raffel, & Willert, 1998). Most publications of PIV velocity measurements concern measurements in single-phase flows. While literature concerning velocity measurements in gas–liquid flow is also available, literature concerning liquid–liquid problems is seldom. For example, Bujalski, Yang, Nikolov, Solnordal, and Schwarz (2006) conducted single-phase water CFD simulations and PIV measurements in a pulsed extraction column, which is normally operated in a two-phase mode. In a common dense liquid–liquid system PIV measurements are not possible because of the different refractive index of the phases. Laser Doppler anemometry (LDA) velocity measurements are still possible but do not allow a comparison of the whole velocity profile (Rieger et al., 1996). The problem can be overcome when apply a refractive index matching technique (Budwig, 1994). In the present work, the refractive index matching technique as used by Augier, Masbernat, and Guiraud (2003) is adopted. The technique makes the measurement of the flow field in the aqueous phase possible and also allows for a phase discrimination. In addition the simulations are also compared to simulations of the commercial CFD code Fluent. The approach of the Fluent simulations was already described elsewhere (Drumm & Bart, 2006), therefore, it is not described in detail in this paper. We have used the same geometry for Fluent and FPM simulations.

In Section 2, we present the mathematical model. In Section 3 we present the basic idea of FPM and FPM schemes for two-phase flows.

In Section 4, the essential PIV setup is summarized shortly, while Section 5 contains results and comparisons of the single-phase as well as two-phase flows and some summary and conclusions are presented in Section 6.

2. Governing equations and numerical scheme

2.1. Governing equations

The governing equations for the continuous liquid phase of multiphase flows can be derived from the Navier–Stokes equations for single-phase flow. In this paper we consider all equations in the Lagrangian form. The continuity equation for the primary liquid phase is

$$\frac{d\alpha_l}{dt} = -\alpha_l(\nabla \cdot \vec{v}_l), \quad (1)$$

where the index l stands for the liquid phase, α_l the volume fraction, \vec{v}_l the velocity vector for the liquid phase and d/dt is the material derivative. Similarly, the continuity equation for the secondary phase is given by

$$\frac{d\alpha_d}{dt} = -\alpha_d(\nabla \cdot \vec{v}_d), \quad (2)$$

where the index d denotes the quantities for the secondary (dispersed) phase. In addition to (1) and (2) the volume fractions must satisfy the following constraints

$$\alpha_l + \alpha_d = 1. \quad (3)$$

The conservation of momentum for the liquid phase is given by

$$\frac{d\vec{v}_l}{dt} = -\frac{\nabla p}{\rho_l} + \frac{1}{\alpha_l \rho_l} \nabla \cdot S_l + \vec{g} + \frac{1}{\alpha_l \rho_l} \vec{F}_l \quad (4)$$

where ρ_l is the liquid density, p the pressure, which is same for both phases, \vec{g} the gravitational force, \vec{F}_l the interfacial forces and S_l is the stress tensor.

$$S_l = \alpha_l \mu_l [\nabla \vec{v}_l + (\nabla \vec{v}_l)^T - \frac{1}{3}(\nabla \cdot \vec{v}_l)I], \quad (5)$$

where μ_l is the dynamic viscosity of the liquid. The inter-phase interaction term consists of different momentum exchange mechanisms. Only the drag force was taken into account, while the virtual mass force and the lift force can be neglected for a liquid–liquid interaction as shown by Wang and Mao (2005) in a stirred tank. The interfacial momentum transfer (drag force) between two phases is given by

$$\vec{F}_l = \frac{3}{4} \alpha_d \rho_l \frac{C_D}{d_d} |\vec{v}_d - \vec{v}_l| (\vec{v}_d - \vec{v}_l), \quad (6)$$

where d_d is the diameter of the droplets of the dispersed liquid phase and C_D is given by Schiller and Naumann (1935)

$$C_D = \begin{cases} \frac{24}{Re} (1 + 0.15 Re^{0.687}) & \text{if } Re \leq 1000 \\ 0.44 & \text{if } Re > 1000 \end{cases}$$

and Re is the relative Reynolds number defined as

$$Re = \frac{\rho_l |\vec{v}_d - \vec{v}_l| d_d}{\mu_l}. \quad (7)$$

Similarly, the momentum balance equation for the dispersed phase is given by

$$\frac{d\vec{v}_d}{dt} = -\frac{\nabla p}{\rho_d} + \left(1 - \frac{\rho_l}{\rho_d}\right) \vec{g} + \frac{1}{\alpha_d \rho_d} \vec{F}_d, \quad (8)$$

where $\vec{F}_d = -\vec{F}_l$. In both phases the particle positions are given by

$$\frac{d\vec{x}_l}{dt} = \vec{v}_l \quad (9)$$

$$\frac{d\vec{x}_d}{dt} = \vec{v}_d. \quad (10)$$

In order to fulfill the volume fractions constraint we renormalize α_l and α_d after computing from Eqs. (1) and (2) in every time step as

$$\alpha_l = \frac{\alpha_l}{\alpha_l + \alpha_d} \quad \text{and} \quad \alpha_d = \frac{\alpha_d}{\alpha_l + \alpha_d}. \quad (11)$$

2.2. Numerical scheme for primary liquid phase

We solve the primary liquid phase with the FPM in combination with Chorin's pressure projection method (Chorin, 1968). In this work we decompose the pressure into hydrodynamic and dynamic pressures, i.e. $p = p_{\text{hyd}} + p_{\text{dyn}}$. The scheme consists of two fractional steps and is of first order accuracy in time. In the first step we compute the intermediate velocities \vec{v}^* and in the second step we correct the velocity with the constraint that velocity fulfills the continuity equation. In our numerical scheme, we substitute the value of $\nabla \cdot \vec{v}_l$ which appeared in the stress strain tensor S_l Eq. (5). Moreover, after some calculations, we obtain

$$\nabla \cdot S_l = \nabla \cdot (\alpha_l \mu_l \nabla \vec{v}_l) + \Theta(\vec{v}_l, \alpha_l \mu_l, \nabla) = \nabla \cdot (\kappa \nabla \vec{v}_l) + \Theta(\vec{v}_l, \kappa, \nabla) \quad (12)$$

where Θ is some straight forward, but lengthy term and $\kappa = \alpha_l \mu_l$. Moreover, the operator $\nabla \cdot (\kappa \nabla \vec{v}_l)$ can be re-expressed by

$$\nabla \cdot (\kappa \nabla \vec{v}_l) = \frac{1}{2} [\Delta(\kappa \vec{v}_l) + \kappa \Delta \vec{v}_l - \vec{v}_l \Delta \kappa]. \quad (13)$$

This means, once we construct the shape functions for the Laplace operator Δ , then the differential operator $\nabla \cdot (\kappa \nabla \vec{v}_l)$ can be approximated by combination of Δ applied to different functions. Hence the momentum Eq. (4) can be re-expressed in the simple form

$$\begin{aligned} \frac{d\vec{v}_l}{dt} &= -\frac{\nabla p}{\rho_l} + \frac{1}{\alpha_l \rho_l} [\nabla \cdot (\kappa \nabla \vec{v}_l) + \Theta(\vec{v}_l, \kappa, \nabla)] \\ &\quad + \frac{3}{4} \frac{\alpha_d}{\alpha_l} \frac{C_D}{d_d} |\vec{v}_d - \vec{v}_l| (\vec{v}_d - \vec{v}_l) + \vec{g} \\ &= -\frac{\nabla p}{\rho_l} + \frac{1}{\alpha_l \rho_l} \nabla \cdot (\kappa \nabla \vec{v}_l) - G_1 \vec{v}_l + \vec{H}, \end{aligned} \quad (14)$$

where $G_1 = (3/4)(\alpha_d/\alpha_l)(C_D/d_d)|\vec{v}_d - \vec{v}_l|$ and the vector \vec{H} consists of all the forces as source term.

In the following we describe the projection scheme for continuous liquid flow in the FPM framework.

(i) Initialize:

$$p_{\text{dyn}}^{n+1} := p_{\text{dyn}}^n \quad (15)$$

(ii) Move the particles

$$\vec{x}_l^{n+1} := \vec{x}_l^n + \Delta t \vec{v}_l^n \quad (16)$$

(iii) Compute α_l^{n+1} implicitly by

$$\alpha_l^{n+1} = \frac{\alpha_l^n}{1 + \Delta t (\nabla \cdot \vec{v}_l^n)} \quad (17)$$

(iv) Compute the actual hydrostatic pressure p_{hyd}^{n+1} from

$$\nabla \cdot \left(\frac{1}{\rho_l} \nabla p_{\text{hyd}}^{n+1} \right) = \nabla \cdot \vec{g} \quad (18)$$

with boundary condition

$$\frac{\partial p_{\text{hyd}}^{n+1}}{\partial \vec{n}} = \vec{g} \cdot \vec{n} \text{ on } \Gamma_w \text{ and } \Gamma_{\text{in}}, \quad p_{\text{hyd}}^{n+1} = p_{\text{hyd}}^0 \text{ on } \Gamma_{\text{out}} \quad (19)$$

(v) Establish preliminary pressure

$$\tilde{p} = p_{\text{hyd}}^{n+1} + p_{\text{dyn}}^n \quad (20)$$

(vi) Compute implicitly the intermediate velocity \tilde{v}_1^* from

$$\left[(1 + \Delta t G_1) I - \frac{\Delta t}{\alpha_1 \rho_1} \nabla \cdot (\kappa \nabla) \right] \tilde{v}_1^* = \tilde{v}_1^n - \frac{\Delta t}{\rho_1} \nabla \tilde{p} + \Delta t \tilde{H}^n \quad (21)$$

(vii) Correct the velocity

$$\tilde{v}_1^{n+1} = \tilde{v}_1^* - \frac{\Delta t}{\rho_1} \nabla \epsilon^{n+1} \quad (22)$$

with the constraint (continuity equation)

$$\nabla \cdot \tilde{v}_1^{n+1} = -\frac{1}{\alpha_1^n} \frac{d\alpha_1}{dt} = -\frac{1}{\alpha_1^n} \frac{\alpha_1^{n+1} - \alpha_1^n}{\Delta t} \quad (23)$$

(viii) Updating the dynamic pressure

$$p_{\text{dyn}}^{n+1} = p_{\text{dyn}}^n + \epsilon^{n+1} \quad (24)$$

where ϵ^{n+1} is obtained from (which we obtain taking divergence on (22))

$$\nabla \cdot \left(\frac{1}{\rho_1} \nabla \epsilon^{n+1} \right) = \frac{1}{\Delta t} \left[\frac{1}{\alpha_1^n} \frac{\alpha_1^{n+1} - \alpha_1^n}{\Delta t} + \nabla \cdot \tilde{v}_1^* \right] \quad (25)$$

with boundary conditions similar to p_{hyd} given in (19).

We note that in the left-hand side of Eq. (21) the operator $(1 + \Delta t G_1) I - (\Delta t / \alpha_1 \rho_1) \nabla \cdot (\kappa \nabla)$ and the left-hand side of Eq. (25) give rise to the construction of a big sparse matrices, each line of which containing the local, discrete approximation of the operators. On the right-hand sides appear a load vector. Hence Eqs. (18), (21) and (25) represent big sparse linear systems. In summary, in each time step, we construct the approximation of Laplace operator, and with the help of this operator we solve the equations for all three velocity components and the pressure Poisson equations. In addition to that, we need to approximate the gradient vectors. In the next section, we demonstrate how to approximate gradient and the Laplace operators by the finite pointset method.

2.3. Numerical scheme for secondary phase

In order to solve the differential equations for each phase separately, we need to exchange the flow quantities from one phase to another and vice versa. After solving the equations on the primary phase particles, we interpolate the pressure, volume fraction and velocity on each particle in the secondary phase from the cluster of the primary phase. Since we have established the cluster of points for each phase separately, we have to interpolate the quantities at an arbitrary particle in one phase from the surrounding cluster of particles from the other phase. This can be easily achieved with the help of least squares method, described in the next section.

The following steps are followed to compute the quantities on secondary phase.

(i) Move particles

$$\tilde{x}_d^{n+1} := \tilde{x}_d^n + \Delta t \tilde{v}_d^n \quad (26)$$

(ii) Compute α_d^{n+1} implicitly by

$$\alpha_d^{n+1} = \frac{\alpha_d^n}{1 + \Delta t (\nabla \cdot \tilde{v}_d^n)} \quad (27)$$

and normalize the volume fractions in order to fulfill the consistency condition (3) as follows

$$\alpha_d^{n+1} = \frac{\alpha_d^{n+1}}{\alpha_d^{n+1} + \alpha_1^{n+1}} \quad \text{and} \quad \alpha_1^{n+1} = \frac{\alpha_1^{n+1}}{\alpha_d^{n+1} + \alpha_1^{n+1}} \quad (28)$$

(iii) compute the velocity \tilde{v}_d^{n+1} implicitly by

$$\tilde{v}_d^{n+1} = \frac{\tilde{v}_d^n + \Delta t [-(\nabla p^{n+1} / \rho_d) + (1 - (\rho_1 / \rho_d)) \vec{g} + G_d \tilde{v}_1^{n+1}]}{1 + \Delta t G_d}, \quad (29)$$

where $G_d = (3/4)(\rho_1 / \rho_d)(C_D / d_d) \|\tilde{v}_1^n - \tilde{v}_d^n\|$.

3. Finite pointset method

The basis of the computations in FPM is a point cloud, which represents the flow field. The points of the cloud are referred to as particles or numerical grids. They are carriers of all relevant physical information. The particles have to completely cover the whole flow domain, i.e. the point cloud has to fulfill certain quality criteria (particles are not allowed to form “holes” which means particles have to find sufficiently many neighbors; also, particles are not allowed to cluster; etc.). The point cloud is a geometrical basis, which allows for a numerical formulation making FPM a general finite difference idea applied to continuum mechanics. That especially means, if the point cloud would reduce to a regular cubic point grid, then FPM would reduce to a classical finite difference method. The idea of general finite differences also means that FPM is not based on a weak formulation like Galerkin’s approach. Rather, FPM is a strong formulation which models differential equations by direct approximation of the occurring differential operators. The method used is a moving least squares idea which was especially developed for FPM.

3.1. Initialization of point cloud

The most important parameter in the FPM is the average distance between the particles h . We allow this parameter as a user defined smoothed function in space $h(\vec{x})$ and it has a variation less than 1.

In general, our computational domain has a boundary with piecewise linear shell functions. For example, line segments in 2D and triangles or quadrilaterals in 3D. In the first step, we establish one particle in the center of each shell element. Then, these particles are the sources for other new particles and we establish new particles which have minimum distance $ah(\vec{x})$ and maximum distance $h(\vec{x})$, where a is a positive constant, for examples, $a = 0.2$. Then we use these established particles as the source of new particles as long as the boundary is filled and the minimum and maximum distance satisfied.

To initialize the interior particles we start the boundary particles as the source. We first construct one layer inside the domain. The available particles are the sources for other new interior particles and then we successively insert particles till the center is reached and above minimum and maximum distance conditions are satisfied. After completion of initialization, we apply once more hole filling and removing closed algorithm, which are described in the following sections.

It is not necessary that our initial particle distribution has to be placed in regular lattice. Since the particles move with fluid velocity, the regularity will be destroyed within few time iterations. Then they may cluster or scatter. Therefore, we need to monitor in every two to three time steps to maintain the good quality of particle distribution with the help of adding and removing mechanism.

3.2. Neighbor searching

Searching neighbors of particles is the most important and time consuming part of the meshfree method. After the initialization, particles are numbered from 1 to N and for each index one has direct access to the position \bar{x}_i . The fundamental operation to be done on the point cloud is to find neighbors for a point inside a ball with given radius h . In our simulation we have assumed constant h all over the domain Ω .

We construct a voxel data structure which contains the computational domain. The voxels form a regular grid of squares respectively cubes in 2D and 3D with side length h . For each voxel, the indices of points are contained in it. Moreover, for each point it is known, in which voxel it is contained and which are the points inside the radius h .

We establish three types of lists. The first list requires to loop over all points and computing its voxel. This is of complexity $O(N)$. The second list can be obtained from the first list by sorting with respect to the voxel indices. This is of complexity $O(N \log N)$. Of course, in time dependent problems, one generates the lists just once from scratch, and then in the following update from the previous time step.

Hence, for a point \bar{x}_i , all points inside the ball $B(\bar{x}_i, h)$ need to be found. The second list gives direct access to the voxel, where this point is contained in. Now all points in the voxel and its 8 (in 2D) and 26 (in 3D) neighboring voxels are tested for being inside the ball. The indices of the points in these voxels are given by the first list. Since each voxel contains $O(1)$ points, this operation is of constant effort. Hence the total complexity of a neighborhood search for every point is $O(N)$. Finally, the neighborhood information is saved in the third list.

3.3. Filling hole

Finding a hole in the point cloud is a more tricky task, since provided is only information where points are and not where there are none. An important fact is that the center of a void circle of maximal radius must be a Voronoi point. The Voronoi cell (Voronoi, 1907) of point \bar{x}_i is the set of all points closer to \bar{x}_i than to any other point. If the points are in general position, $\nu + 1$ Voronoi cells meet in one point, called the Voronoi point.

Finding all Voronoi points in 2D can be done in $O(N \log N)$ time, e.g. by Fortune's planesweep algorithm (Fortune, 1987). In 3D, the Voronoi points can be found in $O(N^2)$ time by converting the problem to finding a 4D convex hull. As for hole filling the Voronoi points are only to be detected locally, subdivision algorithms can reduce the effort to $O(N \log N)$ (Shewchuk, 1999).

Obviously in 3D, but also in 2D, constructing the full Voronoi diagram can be too expensive for a large number of points. This is in some sense satisfying, since the complexity of meshing a point cloud in 3D is one major motivation for putting our focus on meshless methods. If the Voronoi diagram was easy to compute, so would be the Delaunay triangulation. For the task of identifying holes, the existing voxel (or octree) structure can be used to construct local, partially overlapping, Voronoi diagrams. If the point cloud is not too deformed, this approach successfully identifies the largest holes in $O(N)$ time, since the number of points considered locally is of order $O(1)$. Once the too largest holes are identified, new points are inserted, which is for each new point of complexity $O(1)$. After the insertion of new particles we use the moving least squares interpolation for approximation of fluid dynamic quantities.

3.4. Removing points

Particles which are too clustered are thinned by merging pairs of close by points into a single one. By an iterative application, also large clusters can be thinned out. The two closest points can be found in $O(N)$ time by looping over all points and for each point finding its closest neighbor by checking all points in its circular neighborhood. With the same procedure, one can find the k shortest distances, as well as all points closer than a given distance d_{\min} . Removing a point is negligible effort. Introducing a new point is of complexity $O(1)$, since it is one interpolation problem using all neighboring points.

One prescribes a minimum distance between two points. Assume two points closer than this distance are detected. Then both are removed and replaced by a new point, i.e. the two particles are merged into a new single one. Let the two particles have the positions \bar{x}_k and \bar{x}_l , and let the data \bar{u}_k and \bar{u}_l be associated data vectors. The new particle is inserted in the center of mass of the two particles, and the data is linearly interpolated.

$$\bar{x} = (\bar{x}_k + \bar{x}_l)/2 \quad \bar{u} = (\bar{u}_k + \bar{u}_l)/2. \quad (30)$$

Note that the position of the new particle is actually not too important, since the two particles are close by anyhow (i.e. one could place the new particle at a position of one of the two removed ones). The data, however, must be interpolated equally. An alternative to the mean value of the data vector, one can use the higher order moving least squares approximations.

3.5. Approximation of model equations by FPM

As we have already mentioned in the previous section we need to interpolate flow quantities from one cluster point to the other one in order to perform two-way coupling. In addition to that we have to approximate the spatial derivatives in each phase and solve the Poisson equation for the primary phase. In this section, we describe the numerical scheme for solving the Poisson equation by FPM. For the details of FPM and its applications, we refer one of our previous paper (Tiwari & Kuhnert, 2007) and references there in.

Consider the Poisson equation

$$\nabla \psi = f \quad \text{in } \Omega \in \mathbb{R}^3 \quad (31)$$

with the boundary conditions

$$\psi = g \quad \text{on } \Gamma_D \quad \text{and} \quad \frac{\partial \psi}{\partial \bar{n}} = h \quad \text{on } \Gamma_N, \quad (32)$$

where Γ_D and Γ_N denote the Dirichlet and Neumann boundaries, respectively. The numerical discretization is a generalized finite difference method. The first idea on the generalized finite difference method is presented in Liszka and Orkisz (1980), where the sparse linear system is directly derived from the Taylor's series expansion. The constrained least squares method is presented in Tiwari and Kuhnert (2002), where the Poisson equation and the boundary condition are added in the Taylor series expansion as constraint. The comparison of both methods is presented in Iliev and Tiwari (2002). It is found that the method presented by Tiwari and Kuhnert is more stable. We still encounter some instability problem during the simulation, where the distribution of neighbor particles are so bad that the iterative method of the sparse linear system does not converge. Therefore, we need to add extra strong conditions such that the iterative method converges.

Consider the finite set of points \bar{x}_i for $i = 1, 2, \dots, N$ in $\Omega \cup \Gamma$. We want to construct the differential operators at every particle position from its neighboring cloud of points. Let \bar{x} be an arbitrary particle position. We introduce a weight function such that

the particles sitting closer to \bar{x} has higher influence than those sitting far from it. Moreover, in order to restrict the number of points we consider a weight function $w = w(\bar{x}_i - \bar{x}; h)$ with small compact support, where h determines the size of the support. The weight function can be quite arbitrary, however it makes sense to choose a Gaussian weight function of the form

$$w_i = w(\bar{x}_i - \bar{x}; h) = \begin{cases} \exp(-\eta \frac{\|\bar{x}_i - \bar{x}\|^2}{h^2}), & \text{if } \frac{\|\bar{x}_i - \bar{x}\|}{h} \leq 1 \\ 0, & \text{else,} \end{cases} \quad (33)$$

where η is a positive constant and is considered to be in the range of 2–6, depends upon users. Let $P(\bar{x}, h) = \{\bar{x}_i : i = 1, 2, \dots, m\}$ be the set of m neighbor points of $\bar{x} = (x, y, z)$ in a ball of radius h . We note that the central particle \bar{x} is one element of the neighbor set $P(\bar{x}, h)$. For consistency reasons, some obvious restrictions are required, for example, in 2D if we want the second order approximation of derivatives at a arbitrary particle, there should be at least six particles including this central particle and they should neither be on the same line nor on the same circle. Hence we define the size of h such that the minimum number of neighbors is guaranteed for the approximation of derivatives. Hence, new particles will have to be brought into play as the particle distribution becomes too sparse or, logically, particles will have to be removed from the computation as they become too dense.

As in the classical discretization method, we construct the shape functions $\phi_i, i = 1, \dots, m$ such that

$$\Delta \psi \approx \sum_{i=1}^m \phi_i \psi_i. \quad (34)$$

In order to construct ϕ_i we consider m Taylor series expansions of $\psi(\bar{x}_i)$ about \bar{x}

$$\begin{aligned} \psi(\bar{x}_i) = & \psi(\bar{x}) + dx_i \psi_x + dy_i \psi_y + dz_i \psi_z + \frac{1}{2} dx_i^2 \psi_{xx} + dx_i dy_i \psi_{xy} \\ & + dx_i dz_i \psi_{xz} + \frac{1}{2} dy_i^2 \psi_{yy} + dy_i dz_i \psi_{yz} \\ & + \frac{1}{2} dz_i^2 \psi_{zz} + O(\|d\bar{x}_i\|^3), \end{aligned} \quad (35)$$

for $i = 1, \dots, m$, where $dx_i = x_i - x, dy_i = y_i - y, dz_i = z_i - z$.

Now we multiply (35) by ϕ_i and sum over 1 to m

$$\begin{aligned} \sum_{i=1}^m \phi_i \psi_i = & \left(\sum_{i=1}^m \phi_i \right) \psi + \left(\sum_{i=1}^m \phi_i dx_i \right) \psi_x + \left(\sum_{i=1}^m \phi_i dy_i \right) \psi_y \\ & + \left(\sum_{i=1}^m \phi_i dz_i \right) \psi_z + \left(\frac{1}{2} \sum_{i=1}^m \phi_i dx_i^2 \right) \psi_{xx} \\ & + \left(\sum_{i=1}^m \phi_i dx_i dy_i \right) \psi_{xy} + \left(\sum_{i=1}^m \phi_i dx_i dz_i \right) \psi_{xz} \\ & + \left(\frac{1}{2} \sum_{i=1}^m \phi_i dy_i^2 \right) \psi_{yy} + \left(\sum_{i=1}^m \phi_i dy_i dz_i \right) \psi_{yz} \\ & + \left(\frac{1}{2} \sum_{i=1}^m \phi_i dz_i^2 \right) \psi_{zz} + O(\|d\bar{x}_i\|^3). \end{aligned} \quad (36)$$

From the expression (36) we obtain the approximation of the Laplace operator

$$\Delta \psi \approx \sum_{i=1}^m \phi_i \psi_i + O(\|d\bar{x}_i\|^3) \quad (37)$$

if the following conditions satisfy

$$\begin{aligned} \sum_{i=1}^m \phi_i = 0, \quad \sum_{i=1}^m \phi_i dx_i = 0, \quad \sum_{i=1}^m \phi_i dy_i = 0, \\ \sum_{i=1}^m \phi_i dz_i = 0, \quad \sum_{i=1}^m \phi_i dx_i^2 = 2, \quad \sum_{i=1}^m \phi_i dx_i dy_i = 0, \\ \sum_{i=1}^m \phi_i dx_i dz_i = 0, \quad \sum_{i=1}^m \phi_i dy_i^2 = 2, \\ \sum_{i=1}^m \phi_i dy_i dz_i = 0, \quad \sum_{i=1}^m \phi_i dz_i^2 = 2 \end{aligned} \quad (38)$$

It consists of 10 constraints (38) and we denote them by G_1, \dots, G_{10} . We observe in the classical finite difference approximation that the sum of all coefficients equals to zero, where the first condition in (38) also fulfills the same condition. Moreover, in order to obtain a stable linear system, we add one more condition that the coefficient on the central particle must be negative, similar to the classical finite difference discretization. Therefore, we consider the additional condition

$$\phi(x_i = x) = -\frac{\beta}{h^2}, \quad (39)$$

where β is a non-negative small number and the constant h is the size of compact support. Hence, we have 11 constraints (38 – 39) for the approximation of the Laplace operator.

Now, we minimize the functional

$$J = \sum_{i=1}^m \frac{\phi_i^2}{w_i} \quad (40)$$

with respect to constraints G_1, \dots, G_{11} . From the Euler–Lagrange theorem, this constrained minimization is equivalent to

$$\frac{\partial J}{\partial \phi_i} + \sum_{j=1}^{11} \lambda_j \frac{\partial G_j}{\partial \phi_i} = 0, \quad i = 1, \dots, m, \quad (41)$$

where $\lambda_1, \dots, \lambda_{11}$ are the Lagrange multipliers. More explicitly we express

$$\begin{aligned} 2\phi_i/w_i + \lambda_1 + dx_i \lambda_2 + dy_i \lambda_3 + dz_i \lambda_4 + dx_i^2 \lambda_5 + dx_i dy_i \lambda_6 \\ + dx_i dz_i \lambda_7 + dy_i^2 \lambda_8 + dy_i dz_i \lambda_9 + dz_i^2 \lambda_{10} + \lambda_{11} \delta_{ix} = 0, \end{aligned} \quad (42)$$

for $i = 1, \dots, m$, where

$$\delta_{ix} = \begin{cases} 1 & \text{if } x_i = x \\ 0 & \text{else} \end{cases}$$

The above system of equations can be written in the matrix form

$$M\bar{a} = \bar{b}, \quad (43)$$

where

$$M = \begin{pmatrix} 1 & dx_1 & dy_1 & dz_1 & dx_1^2 & dx_1 dy_1 & dx_1 dz_1 & dy_1^2 & dy_1 dz_1 & dz_1^2 & \delta_{1x} \\ \vdots & \vdots \\ 1 & dx_m & dy_m & dz_m & dx_m^2 & dx_m dy_m & dx_m dz_m & dy_m^2 & dy_m dz_m & dz_m^2 & \delta_{mx} \end{pmatrix},$$

$\bar{a} = [\lambda_1, \dots, \lambda_{11}]^T, \bar{b} = -2[\phi_1/w_1, \dots, \phi_m/w_m]^T$. In general we have $m > 11$, therefore the linear system (43) is overdetermined and we obtain the solution from the weighted least squares method and the solution is explicitly given by

$$\bar{a} = (M^T W M)^{-1} (M^T W \bar{b}), \quad (44)$$

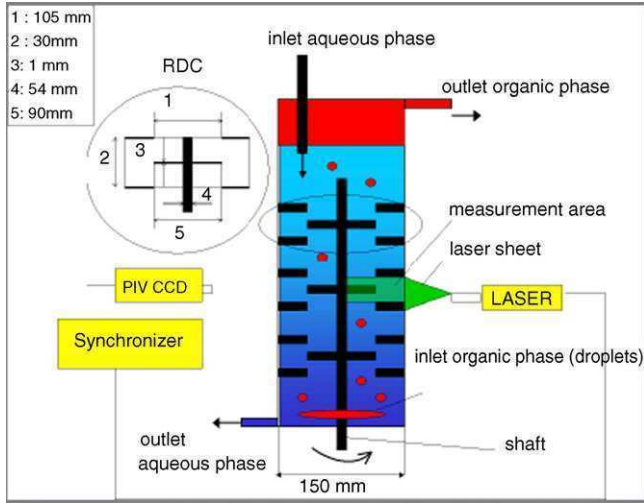


Fig. 1. Experimental setup.

if $M^T W M$ is nonsingular, where $W = \text{diag}[w_1, \dots, w_m]$. The vector $(M^T W) \bar{b}$ can be written explicitly with the help of conditions (38)

$$(M^T W) \bar{b} = (-2) \begin{pmatrix} 0 & 0 & 0 & 0 & 2 & 0 & 0 & 2 & 0 & 2 & -\frac{\beta}{h^2} \end{pmatrix}^T.$$

Hence, we can compute the Lagrange multipliers $\lambda_i, i = 1, \dots, 11$ from (44) and substituting them in (42), the shape functions $\phi_i, i = 1, \dots, m$ can be expressed by

$$\phi_i = -\frac{w_i}{2} (\lambda_1 + dx_i \lambda_2 + dy_i \lambda_3 + dz_i \lambda_4 + dx_i^2 \lambda_5 + dx_i dy_i \lambda_6 + dx_i dz_i \lambda_7 + dy_i^2 \lambda_8 + dy_i dz_i \lambda_9 + dz_i^2 \lambda_{10} + \delta_{ix} \lambda_{11}) \quad (45)$$

If the particle \bar{x} belongs to the Neumann boundary, then the constraints are given by

$$\sum_{i=1}^m \phi_i = 0 \quad (46)$$

$$\sum_{i=1}^m \phi_i d\bar{x}_i = \bar{n} \quad (47)$$

and the matrix M and the vector $(M^T W) \bar{b}$ can be computed accordingly.

Similarly, we can compute other derivatives, where the matrix M remains the same, only the constraints will be different which result different vectors $(M^T W) \bar{b}$. For examples, to compute ψ_x we have

$$(M^T W) \bar{b} = (-2) \begin{pmatrix} 0 & 1 & 0 & 0 & 0 & 0 & 0 & 0 & 0 & 0 & -\frac{\beta}{h^2} \end{pmatrix}^T$$

and to compute ψ_{xx} we have

$$(M^T W) \bar{b} = (-2) \begin{pmatrix} 0 & 0 & 0 & 0 & 2 & 0 & 0 & 0 & 0 & 0 & -\frac{\beta}{h^2} \end{pmatrix}^T$$

and so on.

Once we compute the Lagrange multipliers as above, we then obtain the approximation (34) for the particle \bar{x} . Hence, if we consider \bar{x}_j an arbitrary particle and \bar{x}_{j_i} its neighbors of number $m(j)$, then we have the following sparse linear system of equations for

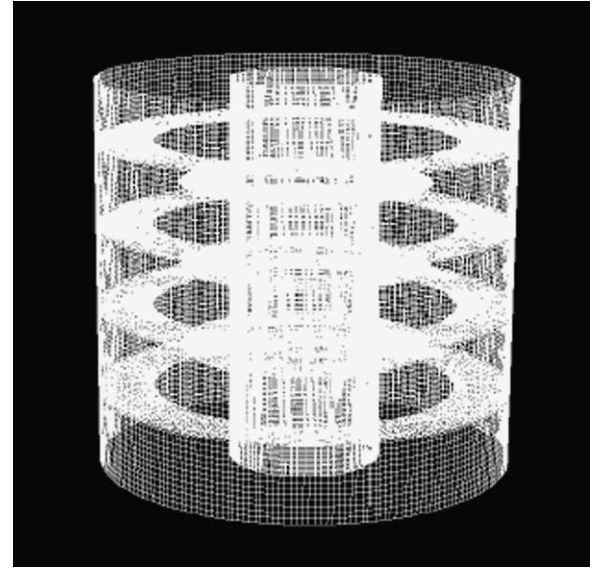
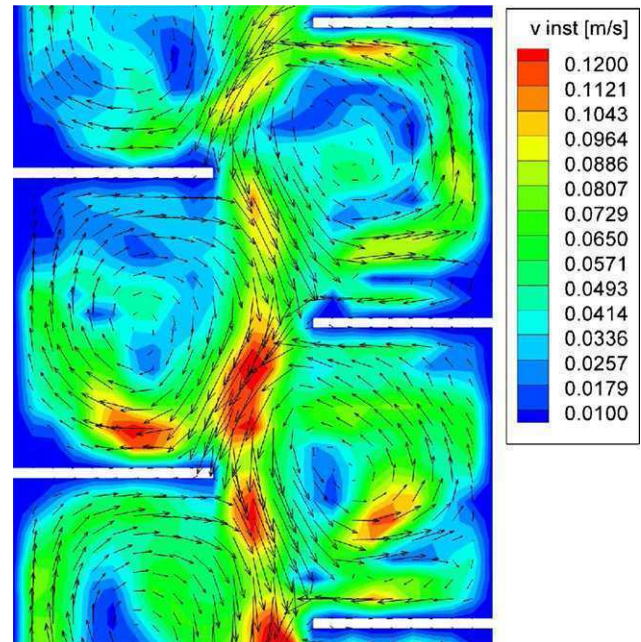


Fig. 2. Numerical grid.

the unknowns $\psi_j, j = 1, \dots, N$

$$\sum_{i=1}^{m(j)} \phi_{j_i} \psi_{j_i} = f_j. \quad (48)$$

In this sparse linear system the neighbor particle index gives the entry of the matrix components. This linear system can be solved by any iterative solvers. In this paper, we have solved this by the stabilized biconjugate gradient (BiCGStab) method. The above scheme for the Poisson equation gives the second order convergence (see Iliev & Tiwari, 2002).

Fig. 3. FPM, simulated instantaneous velocity magnitude and vectors in 2D xz -plane, single-phase flow.

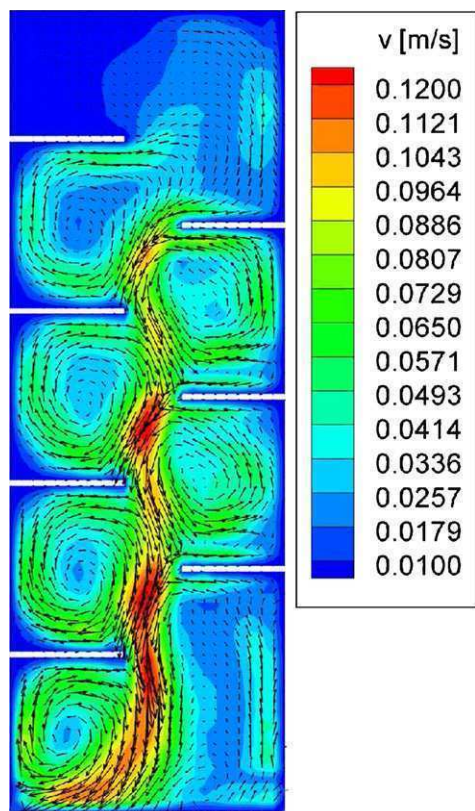


Fig. 4. FPM, average velocity magnitude and vectors in 2D xz -plane, single-phase flow.

4. Experimental PIV setup

A 1 m section of a 150 mm diameter column with 5 RDC compartments as internals was used as the experimental basis. The experimental setup together with the dimensions of the RDC compartments is depicted in Fig. 1. The column can be operated in one and two-phase conditions, the aqueous phase entering at the top and leaving at the bottom, while the second phase is fed into the column through a distributor at the bottom. The distributor generates

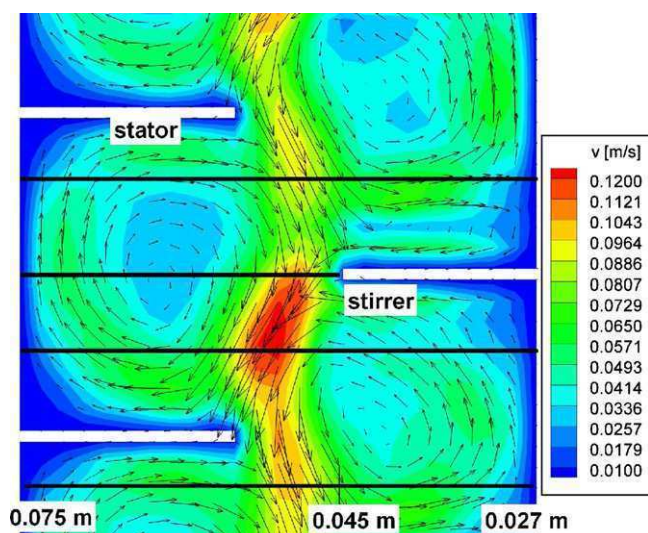


Fig. 5. FPM, averaged velocity magnitude and vectors in 2D xz -plane in one compartment and planes for comparison, single-phase flow.

droplets in the millimeter range ($d_{23} = 2.5$ mm). Variable rotation of the disc stirrers was warranted by an agitator. The optical measurement area (48 mm \times 30 mm) in one extraction compartment is the height of one compartment and the symmetry region from the shaft to the wall of the column. The RDC column was operated at throughputs of 200 l/h for the single-phase flow and 100 l/h for the aqueous phase and organic phase in the two-phase flow. The stirrer revolution was varied between 150 and 300 rpm.

An ILA (Intelligent Laser Applications GmbH) PIV system was used. The laser sheet is generated by two 25 mJ double pulsed Nd:Yag lasers (Minilite Continuum) operated at a frequency between 1 and 4 Hz. The laser sheet was expanded by a cylindrical lens to a thickness of around 2 mm, while the height of the laser sheet in the column was around 0.1 m. The wavelength of the lasers is 532 nm. Each laser pulse is composed of two flashes separated by a delay between 0.5 and 1 ms. A 12-bit digital CCD camera (PCO Sensicam) records pictures with a resolution of 1280×1024 pixels, whereas the measurement area used 970×600 pixels of the CCD array, thus one pixel is 0.05 mm in real length scale. A square perspex box filled with water was placed outside the cylindrical glass column to minimize the effect of optical distortion. The ILA synchronizer synchronized the laser and the cameras.

In the single-phase scenario water was used. In a common dense liquid–liquid system PIV measurements are not possible because of the different refractive index of the phases, where the dispersed second phase masks the measurement area. Therefore, an iso-optical system introduced by Augier et al. (2003) was applied for the two-phase measurements. The iso-optical liquid–liquid system is composed of n-heptane as the dispersed phase and a water–glycerine mixture (44 wt% water), which have the same refractive index at a temperature of 25 °C. The heptane droplets do

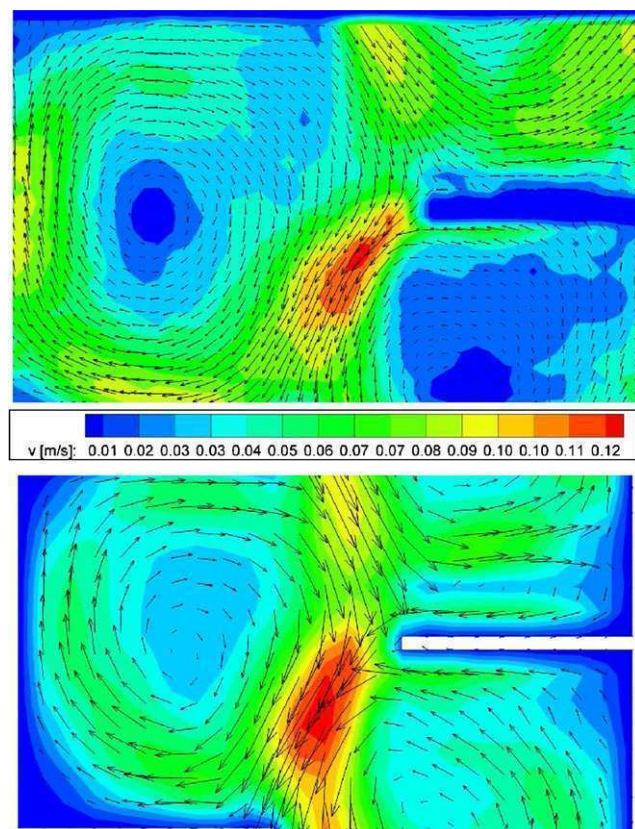


Fig. 6. Comparison PIV–FPM, measured (top) and simulated (bottom) average velocity magnitude and vectors in 2D xz -plane in one compartment, single-phase flow.

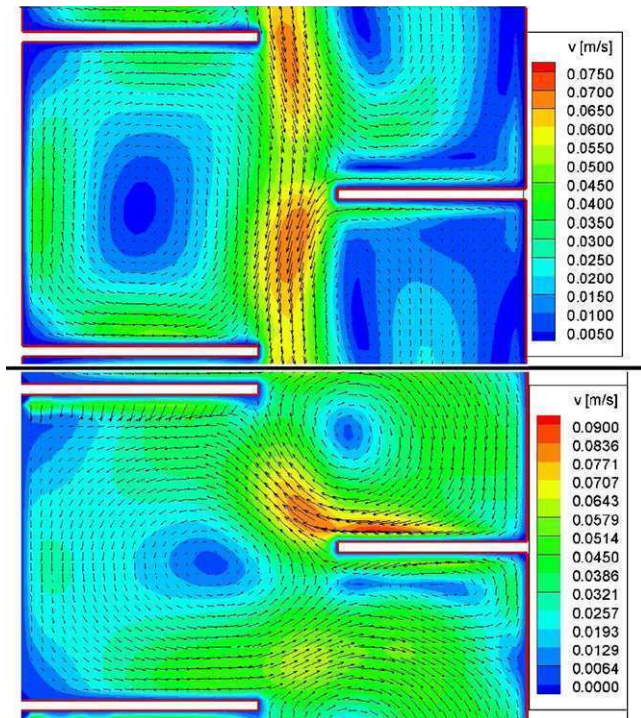


Fig. 7. Fluent single-phase (top) and two-phase (bottom) flow simulations.

not mask the measurement area and allow a clear view. Furthermore, a small quantity of the fluorescent dye Rhodamine 6G only soluble in the aqueous phase is dissolved to enhance the phase discrimination. The dye emits a 560 nm wavelength orange light in the continuous phase. Hollow spherical glass particles with a diameter of 10 μm and a density of 1100 kg/m^3 seeded the flow. Therewith almost neutral buoyancy is assured for both the single ($= 1000 \text{ kg}/\text{m}^3$ for water) and two-phase scenario ($= 1180 \text{ kg}/\text{m}^3$ for glycerine–water mixture). The interrogation areas for the cross correlation were 64×64 pixel with a 50% overlapping, followed by an 32×32 pixel adaptive cross correlation. Local median filters were used to eliminate outliers, which were interpolated. One hundred pairs of pictures were taken to filter the effects of turbulence for the determination of ensemble-averaged velocity fields.

5. Numerical results

Simulations were carried out on the geometry depicted in Fig. 2. As a matter of course the grid was removed for the FPM simulations to release the vantages of a meshfree method. The volume flows, systems and stirrer revolutions in the single- and two-phase

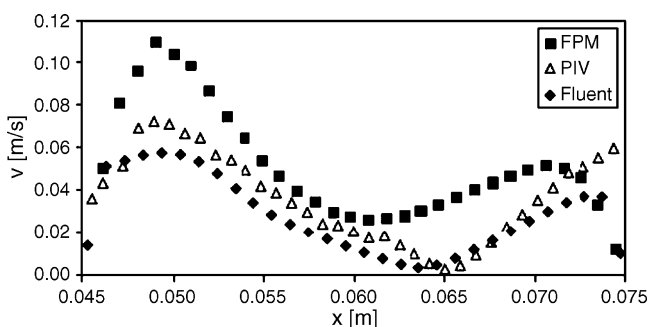


Fig. 8. Comparison PIV–FPM–Fluent, measured and simulated average velocity magnitude in 2D xz -plane at stirrer level, single-phase flow.

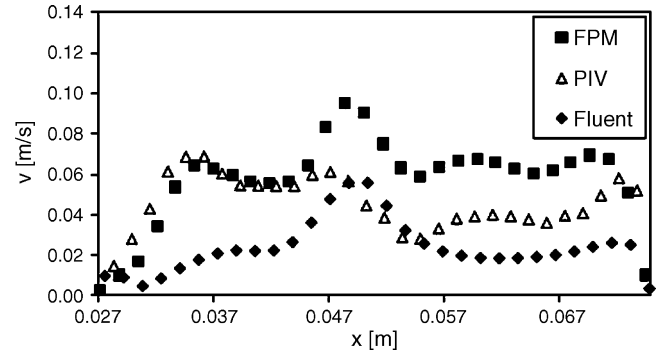


Fig. 9. Comparison PIV–FPM–Fluent, measured and simulated average velocity magnitude in 2D xz -plane at upper half compartment height, single-phase flow.

simulations are the same as in the pilot plant column described in Section 4. In this paper we focus on FPM and want to compare FPM to PIV experiments and standard CFD approaches. Therefore, in the Fluent simulations just the standard $k-\epsilon$ model was used for the closure of turbulence without considering more suitable turbulence models. A comparison of different closures for turbulence in the framework of Fluent was done already elsewhere (Drumm & Bart, 2006). Since only 2D PIV measurements were possible in the extractor, the velocities are compared in the PIV measurement plane (xz -plane). The instantaneous velocities resulting from FPM simulations are shown in Fig. 3. To compare these results with the average velocities of PIV and Fluent (RANS $k-\epsilon$ model) time-averaged velocities were computed using 50 instantaneous velocity profiles after steady state was reached. Around 10–20 s were simulated in order to reach this steady state, whereas the time step in FPM simulations was around $1.5\text{E}-3$ and around 230,000 particles have been used for each phase.

5.1. Single-phase simulation results

In the shown results of the single-phase scenario, the volume flow of the aqueous phase is 200 l/h and the stirrer revolution is 150 rpm. Contours of average velocity magnitude and vectors from the FPM simulations for the whole geometry are shown in Fig. 4. The velocities from FPM, PIV and Fluent are compared along three different lines inside the compartment. The position of these lines, which are at the stirrer level (0.045–0.075 m) and halfway between the stirrer and the upper and lower stators of one extraction compartment (0.027–0.075 m), are shown in Fig. 5. A qualitative comparison between the PIV measurements and the FPM simulations is visible in Fig. 6. It can be seen that the FPM simulations are in good agreement with the experiments. As expected, the highest

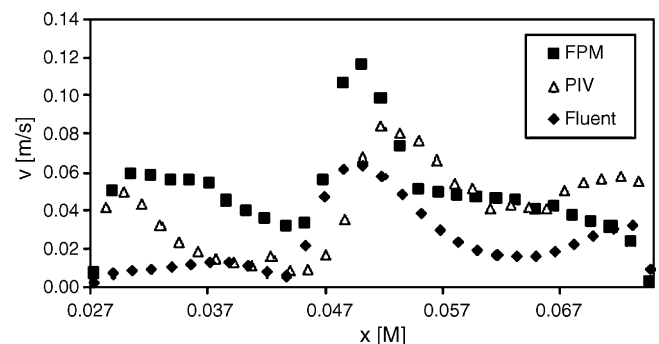


Fig. 10. Comparison PIV–FPM–Fluent, measured and simulated average velocity magnitude in 2D xz -plane at lower half compartment height, single-phase flow.

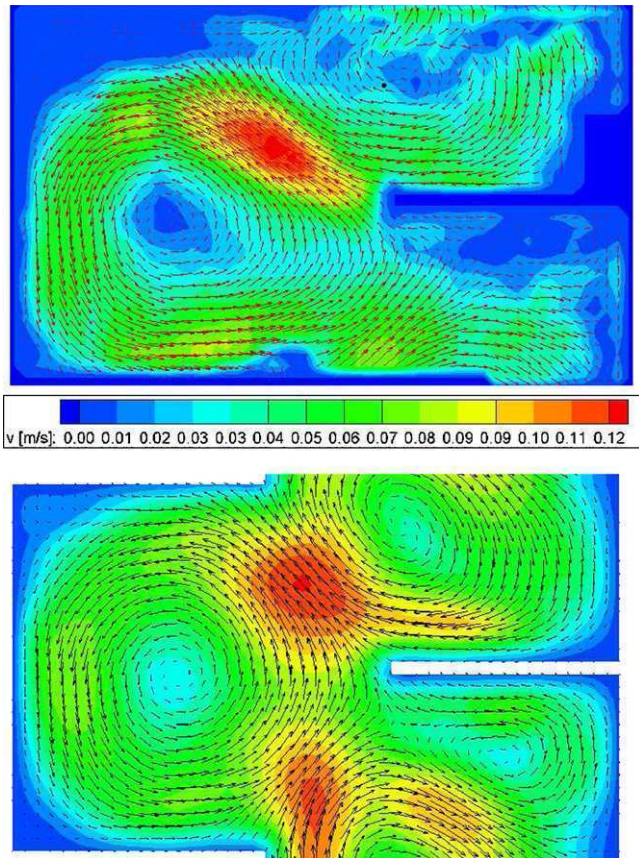


Fig. 11. Comparison PIV–FPM, measured (top) and simulated (bottom) average velocity magnitude and vectors in 2D xz -plane in one compartment, two-phase flow.

velocities are near the stirrer tip. From the velocity vectors and the contours, two big vortices can be estimated in the compartment; one between the stators and the other between the stirrer. A small third vortex is visible above the stirrer because the flow field turns around at this position towards the stirrer tip. All these phenomena are obvious in both the FPM simulations and experiments in Fig. 6. Results of the Fluent simulations are shown in the upper part of Fig. 7. In contrast to FPM, the big vortex between the stirrers is not well developed in Fluent using the standard $k-\epsilon$ model. The maximum velocity at the stirrer tip is also better predicted by FPM (Fig. 6), while Fluent under-predicts this value (Fig. 7). On the other hand, FPM tends to over-predict the velocities in the dead zones in the middle of each big vortex. The comparisons for the velocities

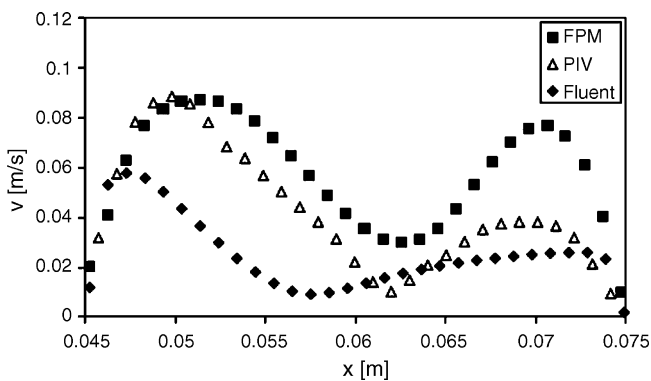


Fig. 12. Comparison PIV–FPM–Fluent, measured and simulated average velocity magnitude in 2D xz -plane at stirrer level, two-phase flow.

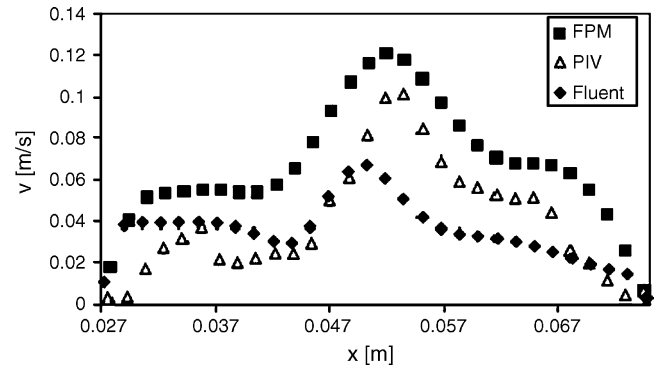


Fig. 13. Comparison PIV–FPM–Fluent, measured and simulated average velocity magnitude in 2D xz -plane at upper half compartment height, two-phase flow.

along the different lines are shown in Figs. 8–10. For the velocities at the stirrer level it is obvious that FPM over-predicts the velocities at the stirrer level, while Fluent under-predicts these velocities. An explanation for the deviation near the stirrer could be the fact that the field of maximum velocities near the stirrer tip is more broad in FPM. For the comparisons at the upper and lower half compartment height, FPM can predict the velocity profile better than Fluent, also because the vortices are better developed, again comprising a slight over-prediction for FPM and an under-prediction for Fluent. Recapitulatory, one can say that FPM matches the overall experimental data and can describe all flow phenomena such as vortices, whereas at some points FPM tends to over-predict the velocities.

5.2. Two-phase simulation results

In the shown results of the two-phase scenario, the volume flow of the aqueous phase is 100 l/h, the volume flow of the organic phase is 100 l/h and the stirrer revolution is 150 rpm. The Sauter mean diameter of the droplet distribution ($d_{32} = 0.0025$ m) was used in the drag term in Eq. (6) for both the FPM and Fluent simulations. The Fluent results, applying the standard $k-\epsilon$ model together with the Euler–Euler multiphase model, are depicted in Fig. 7 (lower part). Contours of average velocity magnitude and vectors from the FPM simulations and the PIV measurements are shown in Fig. 11. As in the single-phase scenario, the FPM simulations are in good agreement with the experiments (Fig. 11). Still, two big vortices can be estimated in the compartment; one between the stators and the other between the stirrer. Because of the rising droplets the vortices shift or turn around and are directed to the top of the column, so that the vortex between the stirrer moves to the position above the stirrer and vice versa. The small third vortex is now visible under the stirrer because of the opposite rotating direction.

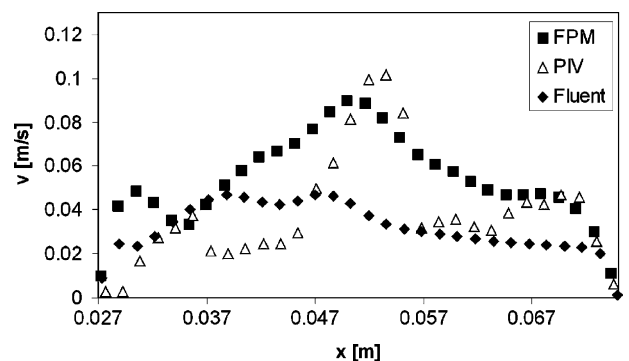


Fig. 14. Comparison PIV–FPM–Fluent, measured and simulated average velocity magnitude in 2D xz -plane at lower half compartment height, two-phase flow.

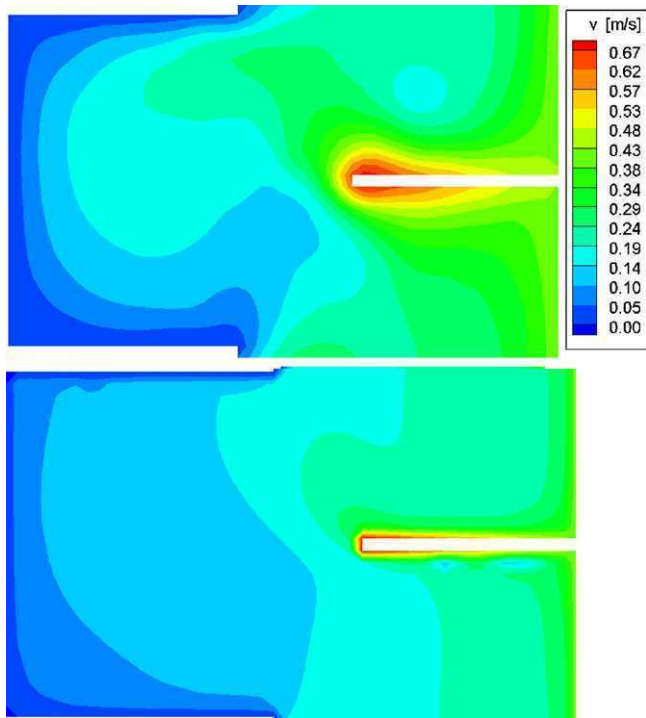


Fig. 15. Comparison FPM–Fluent, simulated velocity magnitude including swirl velocity, two-phase flow.

Again FPM can predict all these flow phenomena. The velocities from FPM, PIV and Fluent are again compared along the three different lines Figs. 11–14. FPM correctly predicts the shape of the velocity profile along the lines through the compartment. However, the same trends as in the single-phase case can be recognized; FPM slightly tends to overestimate the velocities while the velocities are undervalued in the Fluent simulation. The overall prediction is reasonable. It has to be pointed out that especially the velocities in the 2D PIV measurement area are hard to predict since they are only results of the shear stresses while the main velocity is normal to the xz -plane. Although no experimental measurements in this direction are possible, in Fig. 15, the simulated overall velocity including the velocity vertical to the 2D xz -plane is depicted. The maximum velocity near the stirrer is the track speed of the stirrer tip ($v = 0.7$ m/s). From the stirrer to the wall the velocity is decreasing to zero. While the velocities at the boundaries are predicted correctly and are the same in both FPM and Fluent, it is again obvious that FPM predicts a higher velocity in the y -direction between the stirrers and from the stirrer to the wall.

6. Summary and conclusions

Single- and two-phase simulations of a RDC extractor were carried out in the framework of the meshfree code FPM and compared to 2D PIV measurements. In addition to that the results were also compared to Fluent simulations where the standard $k-\epsilon$ model was applied. The results show that FPM can predict the one- and two-phase flow field in the RDC, whereas all flow phenomena such as vortices can be described. FPM matches the overall experimental data and the predicted velocities are in good agreement with the experimental ones. Both methods predict reliable flow fields whereas FPM do not pale in comparison to the commercial CFD code. At some points FPM tends to overestimate the velocities while the velocities are undervalued in the Fluent simulation. Recapitulatory, one can say that FPM was successfully applied to model the

flow fields in a stirred extraction column. In future, meshfree methods like the FPM have to be considered as an attractive alternative to classical mesh based methods like finite difference, finite element methods in the field of chemical engineering. Since FPM is a fully Lagrangian method, it is more suitable for the simulation of the secondary phase in chemical engineering problems: here the secondary phase consists normally of moving bubbles, particles and droplets.

Acknowledgement

We would like to thank the Deutsche Forschungsgemeinschaft (DFG) for the financial support of our research.

References

- Augier, F., Masbernat, O., & Guiraud, P. (2003). Slip velocity and drag law in a liquid–liquid homogeneous dispersed flow. *AIChE Journal*, 49(9), 230.
- Belytschko, T., Krongauz, Y., Organ, D., Flemming, M., & Krysl, P. (1996). Meshless methods: An overview and recent developments. *Computer Methods in Applied Mechanics and Engineering*, 139, 3.
- Budwig, R. (1994). Refractive index matching methods for liquid flow investigations. *Experiments in Fluids*, 17, 350.
- Bujalski, J. M., Yang, W., Nikolov, J., Solnordal, C. B., & Schwarz, M. P. (2006). Measurement and CFD simulation of single-phase flow in solvent extraction pulsed column. *Chemical Engineering Science*, 61(9), 2930.
- Chorin, A. J. (1968). Numerical solution of the Navier–Stokes equations. *Mathematics of Computation*, 22, 745.
- Drumm, C., & Bart, H.-J. (2006). Hydrodynamics in a RDC extractor: Single- and two-phase PIV measurements and CFD simulations. *Chemical Engineering and Technology*, 29(11), 1.
- Duarte, C. A., & Oden, J. T. (1996). H-p clouds and h-p meshless methods. *Numerical Methods for Partial Differential Equations*, 1.
- Fei, W., Wang, Y., & Wan, Y. (2000). Physical modeling and numerical simulation of velocity fields in rotating disc contactor via CFD simulation and LD measurement. *Chemical Engineering Journal*, 78, 131.
- Fortune, S. J. (1987). A sweepline algorithm for Voronoi diagrams. *Algorithmica*, 2, 153.
- Griebel, M., & Schweitzer, A. (2000). A particle-partition of unity method for the solution of elliptic, parabolic, and hyperbolic PDEs. *SIAM Journal of Scientific Computing*, 22, 853.
- Griebel, M., & Schweitzer, A. (2002). *Lecture notes in computational science and engineering*, Vol. 26: Meshfree methods for partial differential equations I. Springer.
- Griebel, M., & Schweitzer, A. (2005). *Lecture notes in computational science and engineering*, Vol. 43: Meshfree methods for partial differential equations II. Springer.
- Griebel, M., & Schweitzer, A. (2006). *Lecture notes in computational science and engineering*, Vol. 57: Meshfree methods for partial differential equations III. Springer.
- Hu, X. Y., & Adams, N. A. (2006). A multi-phase sph method for macroscopic and mesoscopic flows. *Journal of Computational Physics*, 213(2), 844.
- Iliev, O., & Tiwari, S. (2002). A generalized (meshfree) finite difference discretization for elliptic interface problems. In I. Dimov, I. Lirkov, S. Margenov, & Z. Zlatev (Eds.), *Numerical Methods and Applications, Lecture Notes in Computer Sciences* (p. 480). Springer.
- Kompenhans, J., Raffel, M., & Willert, C. E. (1998). *Particle image velocimetry—A practical guide*. Berlin: Springer.
- Kuhnert, J., Tramecon, A., & Ullrich, P. (2000). Advanced air bag fluid structure coupled simulations applied to out-of position cases. In *EUROPAM conference proceedings*.
- Liszka, T., & Orkisz, J. (1980). The finite difference method on arbitrary irregular grid and its application in applied mechanics. *Computers & Structures*, 11, 83.
- Liu, G. R., & Liu, M. B. (2003). *Smoothed particle hydrodynamics: A meshfree particle method*. Singapore: World Scientific.
- Liu, M. B., Liu, G. R., & Lam, K. Y. (2003). Modeling incompressible flows using a finite particle method. *Applied Mathematical Modelling*, 29(12), 1252.
- Lucy, L. B. (1977). A numerical approach to the testing of the fission hypothesis. *Astronomical Journal*, 82, 1013.
- Monaghan, J. J. (1992). Smooth particle hydrodynamics. *Annual Review of Astronomy and Astrophysics*, 30, 543.
- Monaghan, J. J. (1994). Simulating free surface flows with SPH. *Journal of Computational Physics*, 110, 399.
- Modes, G., & Bart, H.-J. (2001). CFD simulation of nonideal dispersed phase flow in stirred extraction column. *Chemical Engineering and Technology*, 24(12), 1242.
- Morris, J. P. (2000). Simulating surface tension with smoothed particle hydrodynamics. *International Journal for Numerical Methods in Fluids*, 33(3), 333.
- Rieger, R., Weiss, C., Weigley, G., Bart, H.-J., & Marr, R. (1996). Investigation the process of liquid–liquid extraction by means of computational fluid dynamics. *Computers and Chemical Engineering*, 20(12), 1467.
- Schiller, L., & Naumann, Z. (1935). A drag coefficient correlation. *Zeitschrift Verein deutscher Ingenieure*, 77, 318.

- Shewchuk, J. R. (1999). *Lecture notes on Delaunay mesh generation*. Lecture notes. University of California at Berkeley.
- Tiwari, S., & Kuhnert, J. (2002). A meshfree method for incompressible fluid flows with incorporated surface tension, revue europe'enne des elements finis. *Journal of Computational Applied Mathematics*, 11, 965.
- Tiwari, S., & Kuhnert, J. (2007). Modeling of two-phase flows with surface tension by finite pointset method (FPM). *Journal of Computational Applied Mathematics*, 203, 376.
- Vikhansky, A., & Kraft, M. (2004). Modeling of a RDC using a combined CFD-population balance approach. *Chemical Engineering Science*, 59, 2597.
- Voronoi, G. (1907). Nouvelles applications des parameters continus la theorie des formes quadratiques. *Journal fur Die Reine Angewandte Mathematik*, 133, 161.
- Wang, F., & Mao, Z.-S. (2005). Numerical and experimental investigation of liquid–liquid two-phase flow in stirred tanks. *Industrial and Engineering Chemical Research*, 44, 5776.
- You, X., & Xiao, X. (2005). Simulation of the three-dimensional two-phase flow in stirred extraction columns by Lagrangian–Eulerian method. *Chemical and Biochemical Engineering Quarterly*, 19(1), 1.

Publication VIII

Reprinted from Book Meshfree Methods for Partial Differential Equations IV, Series: Lecture Notes in Computational Science and Engineering , Vol. 65, Griebel, Michael; Schweitzer, Marc Alexander (Eds.), **2008**,

Sudarshan Tiwari, Christian Drumm, Menwer Attarakih, Jörg Kuhnert, Hans-Jörg Bart
Coupling of the CFD and the Droplet Population Balance Equation with the Finite Pointset Method.

Reprinted with permission from Springer.

Coupling of the CFD and the Droplet Population Balance Equation with the Finite Pointset Method

Sudarshan Tiwari¹, Christian Drumm², Menwer Attarakih³, Jörg Kuhnert¹, and Hans-Jörg Bart²

¹ Fraunhofer-Institut für Techno- und Wirtschaftsmathematik (ITWM)
Fraunhofer-Platz 1, D-67663 Kaiserslautern, Germany
tiwari@itwm.fraunhofer.de, kuhnert@itwm.fhg.de

² Lehrstuhl f. Thermische Verfahrenstechnik, TU Kaiserslautern,
Gottlieb-Daimler-Strasse, 67663 Kaiserslautern, Germany
cdrumm@mv.uni-kl.de, bart@mv.uni-kl.de

³ Al-Balqa Applied University, Faculty of Eng. Tech., Chemical Eng. Department,
11134 Amman, Jordan
attarakih@yahoo.com

Summary. In this paper we present the liquid-liquid two-phase flow simulations of a stirred extraction column with the help of our own developed meshfree method called the Finite Pointset Method (FPM). The primary (continuous) phase is modeled by the incompressible Navier-Stokes equations. The motion of the secondary (dispersed) phase is simulated by solving the equation of motion in which inertia, drag and buoyancy forces are taken into account. The size of the droplets is obtained by solving the droplet population balance equation (DPBE). The DPBE is solved by the Sectional Quadrature Method of Moments (SQMOM). The coupling between both phases is performed by considering the momentum transfer from each phase. In this work, some simulations in two and three dimensional cases with constant breakage and aggregation kernels are presented.

Key words: Multiphase Flows, Droplet Population Balance Equations, Mesh-free Method, FPM, Liquid-Liquid Extraction, Sectional Quadrature Method of Moments

1 Introduction

Liquid-liquid extraction is a separation process, which is based on the difference of the distribution of the components to be separated between two liquid phases. Liquid-liquid processes are widely applied in chemical and biochemical industries. In the simulation and design of liquid-liquid extraction

columns the dispersed phase is classically assumed as a pseudo homogeneous phase, where one parameter accounts for all deviations from the ideal plug flow behavior. Nowadays, the population balance equation (PBE) forms the cornerstone for modeling polydispersed (discrete) systems arising in many engineering applications such as liquid-liquid extraction. To account for this polydispersed nature, the dispersed phase is represented in terms of a density function. In contrast to the classical approach, the evolution of this density function is dictated by different active mechanisms such as breakage and coalescence. Furthermore, the accurate prediction of the dispersed phase evolution depends strongly on the proper modeling of the continuous flow fields and hydrodynamics in which the droplets are dispersed. Up to now the design of an extraction columns without experimental pilot plant experiments has not been feasible. In current droplet population balance model (DPBM) codes [1], the dispersion model is still used for the description of the hydrodynamics and results from small scale devices (single droplet experiments) are needed to predict Sauter mean diameters and hold-up profiles [2, 18]. On the other hand, Computational Fluid Dynamics (CFD), based on a mono-disperse assumption, can predict the flow fields and hydrodynamics in a stirred RDC extraction column and deliver all necessary information for the DPBM [7, 8]. Finally, in order to properly model drop size distributions and flow fields in an extraction column without the need for pilot plant or small scale device experiments, the population balance must be coupled with turbulent CFD modeling. Only a few researchers investigated combined CFD-DPBM models in the field of liquid-liquid extraction so far but achieved encouraging results for the combined models [6, 23]. Hence, this contribution focuses on a combined CFD and DPBM to advance in this promising field of research. The coupling is done with the help of the Finite Pointset Method (FPM), which is a meshfree, Lagrangian, particle method. FPM is an in-house development of the Fraunhofer Institute. Our main goal is to incorporate the DPBM into the FPM code. In comparison to a commercial code the FPM source code is fully modifiable, which eases the implementation of the DPBM. The DPBM equations are solved by the Sectional Quadrature Method of Moments (SQMOM)[3]. This method is found to track accurately any set of low-order moments with the ability to reconstruct the shape of the distribution, so it unites the advantages of the classes method (CM)[10] and the Quadrature Method of Moments (QMOM) [15], while it minimizes the drawbacks. The SQMOM is based on the concept of primary and secondary particles, where the primary particles are responsible for the distribution reconstruction (CM), while the secondary ones are responsible for breakage and coalescence events and carry information about the distribution (QMOM). As a first attempt in the coupling procedure, the normal limitation that only one set of Navier-Stokes equations is solved for all droplets [13] have been retained. Accordingly, only one primary particle is used in the SQMOM which is equal the QMOM using 4 moments for this special case, however with efficient numerical implementation. For validation of the coupled algorithm, a five compartment section of a Rotating Disc Con-

tactor (RDC) was modeled in 2D and 3D. The simple 2D model of the column was used to estimate the parameters for breakage and coalescence, which is not feasible in a complex and CPU-time consuming 3D model. In this paper constant breakage and aggregation kernels are assumed and simulations for the system butylacetate-water were carried out for the same operating conditions as in experiments of Simon [19].

The paper is organized as follows: in section 2, the governing equations are presented, while in section 3, the strategy to incorporate the DPBM in FPM code and numerical schemes for these equations. Section 4 contains results and comparisons of the two phase flows and some conclusions are presented in section 5.

2 Governing equations

2.1 Multiphase flows

We consider the two-fluid model for multiphase flows, where both phases are liquids. We call them as primary phase (aqueous continuous phase) and secondary phase (organic dispersed phase). All the quantities with the index c denotes the continuous phase and the index d denotes the dispersed phase. In this paper we consider all equations in the Lagrangian form. The continuity equations for the continuous and dispersed phases are

$$\frac{d\alpha_c}{dt} = -\alpha_c(\nabla \cdot \mathbf{v}_c) \quad (1)$$

$$\frac{d\alpha_d}{dt} = -\alpha_d(\nabla \cdot \mathbf{v}_d), \quad (2)$$

where α_c and α_d are the volume fractions, \mathbf{v}_c and \mathbf{v}_d are the velocity vectors and $\frac{d}{dt}$ is the material derivative.

In addition to (1) and (2) the volume fractions must satisfy the following constraint

$$\alpha_c + \alpha_d = 1. \quad (3)$$

The conservation of momentum for the continuous phase is given by

$$\frac{d\mathbf{v}_c}{dt} = -\frac{\nabla p}{\rho_c} + \frac{1}{\alpha_c \rho_c} \nabla \cdot S_c + \mathbf{g} + \frac{1}{\alpha_c \rho_c} \mathbf{F}_{drag} \quad (4)$$

and the secondary phase is given by

$$\frac{d\mathbf{v}_d}{dt} = -\frac{\nabla p}{\rho_d} + \frac{1}{\alpha_d \rho_d} \nabla \cdot S_d + \left(1 - \frac{\rho_c}{\rho_d}\right) \mathbf{g} - \frac{1}{\alpha_d \rho_d} \mathbf{F}_{drag}, \quad (5)$$

where ρ_c and ρ_d are the densities, p is the pressure shared by both phases, \mathbf{g} is the gravitational force and \mathbf{F}_{drag} represents the interfacial forces and S is the stress tensor, for example, for the continuous phase it is given by

$$S_c = \alpha_c \mu_c [\nabla \mathbf{v}_c + (\nabla \mathbf{v}_c)^T - \frac{1}{3}(\nabla \cdot \mathbf{v}_c)I], \quad (6)$$

where μ_c is the dynamic viscosity of the continuous phase. The inter-phase interaction term consists of different momentum exchange mechanisms. Only the drag force was taken into account, while the virtual mass force and the lift force can be neglected for a liquid-liquid interaction as shown by Wang and Mao [24] in a stirred tank. The interfacial momentum transfer (drag force) between two phases is given by

$$\mathbf{F}_{drag} = \frac{3}{4} \alpha_d \rho_c \frac{C_D}{d_{32}} |\mathbf{v}_d - \mathbf{v}_c| (\mathbf{v}_d - \mathbf{v}_c), \quad (7)$$

where d_{32} is the diameter of the droplets of the dispersed liquid phase and the drag force coefficient C_D is given by Schiller and Naumann [17]

$$C_D = \begin{cases} \frac{24}{Re}(1 + 0.15Re^{0.687}) & \text{if } Re \leq 1000 \\ 0.44 & \text{if } Re > 1000 \end{cases}$$

and Re is the relative Reynolds number defined as

$$Re = \frac{\rho_c |\mathbf{v}_d - \mathbf{v}_c| d_{32}}{\mu_c}. \quad (8)$$

If the breakage and aggregation between droplets are not taking place, like in the mono-dispersed phase, the diameter of the droplet d_{32} is considered to be constant. In general, this is not constant and droplets are assumed to have a spectrum of sizes. This spectrum can be computed with the help of the population balance equation. One can construct the wide range of classes of droplets based on their sizes, however, the considerations of individual classes may not be feasible in the computer simulations since momentum equations have to be solved for each class. Currently, the applied CFD-PBM models are based on the two-fluid Multiple Size Group (MUSIG) Model [13], where all droplets in the PBM share the same velocity field and only one momentum equation is solved for all droplet classes based on the area averaged droplet size, also called as Sauter mean diameter denoted by d_{32} . This quantity can be computed with the help of the solution of the population balance equation, described in the following subsection. A new strategy, the inhomogeneous MUSIG model tries to divide the dispersed phase into a number N so-called velocity groups, where each of the velocity groups is characterized by its own velocity field, to get rid of the common simplifications. Typically 2-3 velocity groups may be sufficient to capture the fluid dynamics.

The population balance is solved as M subdivisions (classes) of each velocity group, resulting in a multi-fluid approach in which $N \times M$ population balance equations are solve [11]. As a drawback, this multi-fluid approach is based on the CPU-time consuming classes method, where 20-30 or even more classes (scalars) are required to capture the shape of the distribution. In this connection, the SQMOM seems to be another interesting alternative,

since each primary particle could move with its own velocity group and hence having its own momentum equation resulting also in a multi-fluid model depending on the number of primary particles. As a benefit, in comparison to the inhomogeneous MUSIG model, SQMOM is less CPU-time consuming, since it is based on the computationally less expensive quadrature method of moments. For example, 6 additional scalars for the moments are required when two velocity groups are applied (3 for each primary particle, the 3rd moment can replace the continuity equation) compared to 20-30 or even more additional scalars in the classes method. The SQMOM and the concept of primary and secondary particles are described in section 3.4.

2.2 Droplet population balance equation (DPBE)

The superstructure of the DPBE and the general derivation based on the Reynolds transport theorem is given in [16]. In the present case this equation can be written as

$$\frac{\partial f(V, \mathbf{x}, t)}{\partial t} + \nabla \cdot (\mathbf{v}_d f(V, \mathbf{x}, t)) = S(f(V, \mathbf{x}, t), V, \mathbf{x}, t), \quad (9)$$

where

$$\begin{aligned} S = & -\Gamma(V)f(V, \mathbf{x}, t) + \int_V^{V_{max}} \Gamma(V', \mathbf{x}, t) \beta(V|V') f(V', \mathbf{x}, t) dV' \\ & - f(V, \mathbf{x}, t) \int_{V_{min}}^{V_{max}} \omega(V, V') f(V', \mathbf{x}, t) dV' \\ & + \frac{1}{2} \int_{V_{min}}^V \omega(V - V', V') f(V - V', \mathbf{x}, t) f(V', \mathbf{x}, t) dV' \end{aligned}$$

and $f(V, \mathbf{x}, t)$ is the number density function with particle size V as an independent variable. The vector \mathbf{v}_d is the same particle velocity introduced in previous subsection. The source term S in (9) consists of loss term (preceded by minus sign) and gain term (preceded by plus sign) due to breakage and aggregation collisions of droplets. The breakage and aggregation of droplets are governed by breakage and aggregation frequencies, respectively. The breakage frequency $\Gamma(V)$ represents the fraction of droplets breaking per unit time, while the aggregation frequency $\omega(V, V')$ accounts for the probability of successful collisions between a pair of droplets. The splitting of mother droplet of size V' to daughter droplets having a spectrum of sizes is given by the daughter particle distribution $\beta(V|V')$.

The above equation (9) is an integro-partial differential equation and has no general solution. Hence, one has to solve the equation by numerical techniques. Several numerical schemes have been reported and many of them are problem specific (see Attarakih et al [2]) for the review of the numerical schemes. We are looking for the one which is feasible to couple with the flow

solver. The Quadrature Method of Moments (QMOM) is one of the suitable methods to incorporate easily into flow solvers, however, it may suffer from the ill-conditioned eigenvalue problem in the product-difference algorithm, which is pointed out by Attarakih et al [3]. We present some simulations in two and three dimensional case with constant breakage and aggregation kernels. They have shown that Sectional QMOM (SQMOM) is more stable and compared the numerical solutions with the available analytical solutions of the DPBE. In this paper we incorporate the SQMOM for the DPBE into the FPM code. In the next section we give brief description of the SQMOM, see [3] for details.

3 Numerical methods

3.1 FPM for solving coupled equations

The basis of the computations in FPM is a point cloud, which represents the flow field. The points of the cloud are referred to as particles or numerical grids. They are carriers of all relevant physical informations. The particles have to cover completely the whole flow domain, i.e. the point cloud has to fulfill certain quality criteria (particles are not allowed to form "holes" which means particles have to find sufficiently many neighbors; also, particles are not allowed to cluster; etc.). The point cloud is a geometrical basis, which allows for a numerical formulation making FPM a general finite difference idea applied to continuum mechanics. As a special case, if the point cloud is reduced to a regular cubic point grid, then the FPM would reduce to a classical finite difference method. The idea of general finite differences also means that FPM is not based on a weak formulation like Galerkin's approach. Rather, FPM is a strong formulation which models differential equations by direct approximation of the occurring differential operators. The method used is a moving least squares idea which was especially developed for FPM. In the earlier publications we have reported about the FPM in details, see [12, 20, 21, 22]. Due to the restriction of the space, we do not repeat the same details in this paper.

To simulate the above presented equations for two-phase flows we establish the separate cluster of points for each phase. Each of these separate cluster of points will act as a numerical grid to approximate the governing differential equations for each phase. These point clouds are decoupled from each other, however they are able to exchange any kind of information among the clusters. In this situation we have to interpolate the quantities at an arbitrary particle in one phase from the surrounding cluster of particles from other phase. This can be easily achieved with the help of least squares method, described in [12, 20, 21, 22].

3.2 Numerical Scheme for primary liquid phase

The primary liquid phase is solved using the FPM in combination of Chorin's pressure projection method [4]. In this work we decompose the pressure into hydrodynamic and dynamic pressures, i. e. $p = p_{hyd} + p_{dyn}$. The scheme consists of two fractional steps and is of first order accuracy in time. In the first step we compute the intermediate velocities \mathbf{v}^* and in the second step we correct the velocity with the constraint that velocity fulfills the continuity equation. In our numerical scheme, we substitute the value of $\nabla \cdot \mathbf{v}_c$ which appeared in the stress strain tensor S_c from the equation (1). Moreover, after some manipulations, we obtain

$$\nabla \cdot S_c = \nabla \cdot (\alpha_c \mu_c \nabla) \mathbf{v}_c + \Theta(\mathbf{v}_c, \alpha_c \mu_c, \nabla) = \nabla \cdot (\kappa \Delta) \mathbf{v}_c + \Theta(\mathbf{v}_c, \kappa, \nabla) \quad (10)$$

where Θ is some straight forward, but lengthy term and $\kappa = \alpha_c \mu_c$. Moreover, the operator $\nabla \cdot (\kappa \nabla \psi)$ can be re-expressed by

$$\nabla \cdot (\kappa \nabla \mathbf{v}_c) = \frac{1}{2} [\Delta(\kappa \mathbf{v}_c) + \kappa \Delta \mathbf{v}_c - \mathbf{v}_c \Delta \kappa]. \quad (11)$$

This means, once we construct the shape functions for the Laplace operator Δ , then the differential operator $\nabla \cdot (\kappa \nabla \mathbf{v}_c)$ can be approximated by combination of Δ applied to different functions. Hence the momentum equation (4) can be re-expressed in the simple form

$$\begin{aligned} \frac{d\mathbf{v}_c}{dt} &= -\frac{\nabla p}{\rho_c} + \frac{1}{\alpha_c \rho_c} [\nabla \cdot (\kappa \Delta) \mathbf{v}_c + \Theta(\mathbf{v}_c, \kappa, \nabla)] \\ &\quad + \frac{3}{4} \frac{\alpha_d}{\alpha_c} \frac{C_D}{d_{32}} |\mathbf{v}_d - \mathbf{v}_c| (\mathbf{v}_d - \mathbf{v}_c) + \mathbf{g} \\ &= -\frac{\nabla p}{\rho_c} + \frac{1}{\alpha_c \rho_c} \nabla \cdot (\kappa \Delta) \mathbf{v}_c - G_c \mathbf{v}_c + \mathbf{H}, \end{aligned} \quad (12)$$

where $G_c = \frac{C_D}{d_{32}} |\mathbf{v}_d - \mathbf{v}_c|$ and the vector \mathbf{H} consists of all the forces as source term.

In the following we describe the projection scheme for continuous liquid flow in the FPM framework.

(i) Initialize :

$$p_{dyn}^{n+1} := p_{dyn}^n \quad (13)$$

(ii) Compute α_c^{n+1} implicitly by

$$\alpha_c^{n+1} = \frac{\alpha_c^n}{1 + \Delta t (\nabla \cdot \mathbf{v}_c^n)} \quad (14)$$

(iii) Compute the actual hydrostatic pressure p_{hyd}^{n+1} from

$$\nabla \cdot \left(\frac{1}{\rho_c} \nabla p_{hyd}^{n+1} \right) = \nabla \cdot \mathbf{g} \quad (15)$$

with boundary condition

$$\frac{\partial p_{hyd}^{n+1}}{\partial \mathbf{n}} = \mathbf{g} \cdot \mathbf{n} \text{ on } \Gamma_{wall} \text{ and } \Gamma_{inflow}, \quad p_{hyd}^{n+1} = p_{hyd}^0 \text{ on } \Gamma_{outflow} \quad (16)$$

(iv) Establish preliminary pressure

$$\tilde{p} = p_{hyd}^{n+1} + p_{dyn}^{n+1} \quad (17)$$

(v) Compute implicitly the intermediate velocity \mathbf{v}_c^* from

$$\left[(1 + \Delta t G_c) I - \frac{\Delta t}{\alpha_c^{n+1} \rho_c} \nabla \cdot (\kappa \nabla) \right] \mathbf{v}_c^* = \mathbf{v}_c^n - \frac{\Delta t}{\rho_c} \nabla \tilde{p} + \Delta t \mathbf{H}^n \quad (18)$$

(vi) Correct the velocity

$$\mathbf{v}_c^{n+1} = \mathbf{v}_c^* - \frac{\Delta t}{\rho_c} \nabla \epsilon^{n+1} \quad (19)$$

with the constraint (continuity equation)

$$\nabla \cdot \mathbf{v}_c^{n+1} = -\frac{1}{\alpha_c^n} \frac{d\alpha_c}{dt} = -\frac{1}{\alpha_c^n} \frac{\alpha_c^{n+1} - \alpha_c^n}{\Delta t} \quad (20)$$

(vii) Updating the dynamic pressure

$$p_{dyn}^{n+1} = p_{dyn}^n + \epsilon^{n+1} \quad (21)$$

where ϵ^{n+1} is obtained from (this is obtained taking divergence on (19))

$$\nabla \cdot \left(\frac{1}{\rho_c} \nabla \epsilon^{n+1} \right) = \frac{1}{\Delta t} \left[\frac{1}{\alpha_c^n} \frac{\alpha_c^{n+1} - \alpha_c^n}{\Delta t} + \nabla \cdot \mathbf{v}_c^* \right] \quad (22)$$

with boundary conditions similar to p_{hyd} given in (16).

(viii) Move the particles

$$\mathbf{x}_c^{n+1} = \mathbf{x}_c^n + \Delta t \mathbf{v}_c^{n+1} \quad (23)$$

We note that in the left hand side of equation (18) the operator $(1 + \Delta t G_c) I - \frac{\Delta t}{\alpha_c \rho_c} \nabla \cdot (\kappa \nabla)$ and the left hand side of equation (22) give rise to the construction of a large sparse matrices, each line of which containing the local, discrete approximation of the operators. The right hand sides appear as a load vector. Hence equations (15), (18) and (22) represent large sparse linear systems, which we solve in the meshfree framework with the help of the FPM. In addition to that we approximate the gradient vectors with the help of the FPM.

3.3 Numerical Scheme for secondary phase

Once the velocity, pressure and volume fraction of the continuous phase is known, we interpolate them into the dispersed phase particles. Then, the following steps are followed to compute the quantities on secondary phase.

(i) Compute α_d^{n+1} implicitly by

$$\alpha_d^{n+1} = \frac{\alpha_d^n}{1 + \Delta t (\nabla \cdot \mathbf{v}_d^n)} \quad (24)$$

and normalize the volume fractions in order to fulfill the consistency condition (3) as follows

$$\alpha_d^{n+1} = \frac{\alpha_d^{n+1}}{\alpha_d^{n+1} + \alpha_c^{n+1}} \quad \text{and} \quad \alpha_c^{n+1} = \frac{\alpha_c^{n+1}}{\alpha_d^{n+1} + \alpha_c^{n+1}} \quad (25)$$

(ii) compute the velocity \mathbf{v}_d^{n+1} implicitly as

$$\left[(1 + \Delta t G_d) I - \frac{\Delta t}{\alpha_d^{n+1} \rho_d} \nabla \cdot (\kappa \nabla) \right] \mathbf{v}_d^{n+1} = \mathbf{v}_d^n - \Delta t \left[\frac{\nabla p^{n+1}}{\rho_d} + \left(1 - \frac{\rho_c}{\rho_d}\right) \mathbf{g} + G_d \mathbf{v}_c^{n+1} \right] \quad (26)$$

where $G_d = \frac{3}{4} \frac{\rho_c}{\rho_d} \frac{C_D}{d_{32}} \|\mathbf{v}_c^n - \mathbf{v}_d^n\|$, $\kappa = \alpha_d^{n+1} \mu_d$.

(iii) Move particles

$$\mathbf{x}_d^{n+1} = \mathbf{x}_d^n + \Delta t \mathbf{v}_d^{n+1} \quad (27)$$

3.4 SQMOM for the DPBE

There exist many numerical methods in the literature as attempts to solve certain type of the PBEs. In the sectional methods (e.g. [10]) the particle size (here it is denoted by the particle diameter D) is discretized into finite number of sections. One limitation of the finite difference schemes is their inability to predict accurately integral quantities (low-order moments as a especial case) associated with populations of sharp shapes [16, 2]. A Large number of primary particles in the classical sectional methods is required, not only to reconstruct the shape of the distribution, but also to estimate the desired integral quantities associated with the distribution. The quadrature method of moments (QMOM) as first introduced by McGraw [15] is found very efficient from accuracy and computational cost point of view. Unlike the sectional methods, the QMOM has a drawback of destroying the shape of the distribution and the information about the distribution is only stored in its moments. On the other hand, the QMOM tracks the population moments and hence it conserves the integral quantities.

The idea behind the SQMOM is to divide the population density function into sections followed by the application of the QMOM to each section. In the SQMOM framework of discretization, the single particle from the sectional methods will be called the primary particle N_{pp} and it will be responsible for the reconstruction of the distribution. To overcome the fundamental problem of the sectional methods, N_{sp} secondary particles are generated in each section with positions (abscissas) and weights that are given by: $D_j^{<i>}, w_j^{<i>}; j = 1, \dots, N_{sp}, i = 1, N_{pp}$, respectively. Note that, the secondary particles are exactly equivalent to the number of quadrature points in Gauss-like quadrature or the QMOM [15, 14, 9]. Accordingly, each secondary particle could conserve or reproduce two low-order moments and in general moments in each section; and hence the method is given the name Sectional QMOM (SQMOM). The way in which the SQMOM works is started by dividing the particle size into (N_{pp} primary particles) contiguous sections. Each section is then seeded by the desired number of secondary particles which carry detailed information about the distribution. In this framework, the active particle mechanisms such as splitting and aggregation occur through interactions between the secondary particles. Therefore, $N_{sp} \times N_{pp}$ particles are contributing in the splitting and aggregation events. The distribution could be reconstructed from the secondary particles by averaging the total weights of the secondary particles with respect to the section width (ΔD_i). These operations of averaging are carried out for all primary particles as follows:

$$\bar{w}_i(\mathbf{x}, t) = \frac{1}{\Delta D_i} \sum_{j=1}^{N_{sp}} w_j^{<i>}, \bar{D}_i(\mathbf{x}, t) = \frac{\sum_{j=1}^{N_{sp}} w_j^{<i>} D_j^{<i>}}{\sum_{j=1}^{N_{sp}} w_j^{<i>}}, i = 1, \dots, N_{pp} \quad (28)$$

In pure mathematical sense, the above presentation is equivalent to applying the QMOM to each section of an arbitrary width $[D_{i-1/2}, D_{i+1/2}]$, $i = 1, \dots, N_{pp}$ resulting in a set of sectional moments that could be written as

$$m_r^{<i>}(\mathbf{x}, t) = \int_{D_{i-1/2}}^{D_{i+1/2}} D^r f(D, \mathbf{x}, t) dD, \quad r = 0, 1, \dots, 2N_{sp} - 1. \quad (29)$$

To this end it remains how to relate the positions and weights (appearing in (28) of the secondary particles in the i th section to the sectional moments of the unknown function $f(D, \mathbf{x}, t)$ given by (29). The sectional moments $m_r^{<i>}$ can be approximated by the weights and abscissas of the secondary particles

$$m_r^{<i>}(\mathbf{x}, t) = \sum_{j=1}^{N_{sp}} w_j^{<i>} (D_j^{<i>})^r, \quad r = 0, 1, \dots, 2N_{sp} - 1. \quad (30)$$

Now, the problem of sectional moments could be stated as: Given a set of sectional moments $m_r^{<i>}$ for $r = 0, 1, \dots, 2N_{sp} - 1$ and $i = 1, 2, \dots, N_{pp}$, find a set of weights $w_j^{<i>}$ and abscissas $D_j^{<i>}$ of the secondary particles for

$j = 1, 2, \dots, N_{sp}$ and $i = 1, 2, \dots, N_{pp}$. Although, the set of weights and positions of the secondary particles is unique for a specified number of sectional moments, there are several ways for finding them. The product-difference algorithm of Gordon and the direct tracking of the weights and positions are examples of these methods [9, 14]. It is worthwhile to mention here that these methods were only applied to population densities with a whole section ranging from zero to infinity. These methods suffer from ill-conditioning if the number of secondary particles is large (usually if greater than four) [2]. This increase in the number of secondary particles in a one-population section could only increase the accuracy of the integration quadrature at the expense of solving a large eigenvalue problem. To overcome this difficulty, the number of secondary particles is fixed to one or two in each section in the SQMOM and the accuracy of the integration quadrature is achieved by controlling the width of each section (like adaptive integration). In this way, analytical solutions are derived for the weights and positions of secondary particles using equal-weight quadratures. In order to obtain the abscissas and weights of the secondary particles analytically three low order moments are considered [6]. To conserve the total droplet number, length and mass in each section, $m_r^{<i>}, r = 0, 1, 3, i = 1, 2, \dots, N_{pp}$ are chosen, where Eq.(30) is reduced to three nonlinear algebraic equations which are analytically solved for the secondary particle weights and abscissas

$$w_{1,2}^{<i>}(\mathbf{x}, t) = \frac{1}{2}\hat{m}_0^{<i>}, \quad D_{1,2}^{<i>}(\mathbf{x}, t) = \hat{m}_1^{<i>} \mp \frac{1}{3}\sqrt{\frac{\hat{m}_3^{<i>}}{\hat{m}_1^{<i>}} - (\hat{m}_1^{<i>})^2}, \quad (31)$$

where $\hat{m}_r = m_r/m_0$.

Finally, the continuity equation for the r th sectional moment could be written in Lagrangian form as

$$\begin{aligned} \frac{dm_r^{<i>}(\mathbf{x}, t)}{dt} + (\nabla \cdot \mathbf{v}_d)m_r^{<i>}(\mathbf{x}, t) = \\ -D_r^{<i>}[\Gamma^{<i>} \bullet w^{<i>}]^T + \sum_{m=1}^{N_{pp}} C_r^{<i,m>}[\Gamma^{<i>} \bullet w^{<i>}]^T + \\ \sum_{k=1}^{i \times N_{sp}} \left[\sum_{j=k}^{i \times N_{sp}} \Psi_{k,j,r}^{<i>} \omega_{j,k} w'_j w'_k - \eta_k \sum_{n=1}^{N_{pp} \times N_{sp}} (d'_k)^r \omega_{k,n} w'_k w'_n \right], \quad (32) \end{aligned}$$

where $r = 0, 1, \dots, 2N_{sp} - 1, i = 1, 2, \dots, N_{pp}$ and the symbols T and \bullet are used for matrix transpose and element by element multiplication, respectively. The matrices $D^{<i>}$ and $w^{<i>}$ contain the secondary abscissas and weights in the i th section. The matrix $\Gamma^{<i>}$ contains the breakage frequencies and $C^{<i,m>}$ consists of integrals that preserve the low-order moments of the newly birthed particles in the i th section due to splitting of a mother particle of size $d_j^{<m>}$. The function η_k is used to select the secondary particles disappearing due to aggregation in the i th section, while $\Psi_{r,k,j}^{<i>}$ is an aggregation

matrix whose nonzero elements represent the successful aggregation events between any pair of secondary particle with abscissas and weights that are given by the augmented vectors: D' and w' , respectively. This matrix preserves exactly the first $2N_{sp}$ low-order moments of the newly birthed particles by aggregation. The velocity of the dispersed phase \mathbf{v}_d is calculated in the momentum equation of the dispersed phase. Once the moments are computed as above, the important parameters like Sauter mean diameter is defined as the ratio between the third and second moments

$$d_{32}^{<i>}(\mathbf{x}, t) = m_3^{<i>} / m_2^{<i>} \quad (33)$$

and the volume fraction can be computed from the third moment

$$\alpha_d^{<i>}(\mathbf{x}, t) = S_V m_3^{<i>}(\mathbf{x}, t), \quad (34)$$

where S_V is a shape factor, for example, if the droplets are spherical, $S_V = \pi/6$. Note that, in the case of two fluid model, where one considers only one primary particle, $d_{32}^{<i>} = d_{32}$ and $\alpha_d^{<i>} = \alpha_d$. If one considers the primary particle more than one, we obtain the multi-fluid model, where one has to establish the same number of primary particle of droplets and the volume fraction is equal to the sum of all volume fractions of primary particle. In this paper, we have considered only one class of primary particles. Hence, together with the continuity and momentum equations for the two-phase flows equations, we have to solve for each primary particle the additional $2N_{sp}$ transport equations for the moments (32).

4 Numerical examples

Our main goal is to incorporate the SQMOM in the FPM to simulate the 3d extraction column as shown in Fig.1, which consist of rotors and stators. The rotor rotates with 150 *rpm*. The volume flow of the aqueous (water) and organic (butyl-acetate) phases are 100 *l/h* which corresponds to the inflow velocities equal to 0.0342 *m/s*. On the top plane the small central ring is the inflow boundary for the aqueous phase and the rest is the outflow boundary for organic phase. Similarly, on the bottom the small central ring is the inflow boundary for the organic phase and the rest is the outflow boundary for the aqueous phase. The rest of the boundaries are the no-slip boundaries for both phases. The densities of the aqueous and organic phases are 1000 *kg/m³* and 880 *kg/m³*, respectively. The viscosities for the aqueous and organic phases are 0.001 *kg/(ms)* and 0.0007 *kg/(ms)*. Moreover, the gravitational force acts in the negative *z*-direction. The moments in the inlet boundary of the dispersed phase are $m_0 = 1145352.0$, $m_1 = 2863.3805$, $m_2 = 7.15845$, $m_4 = 0.01789$ such that the abscissas are: 1.63 *mm* and 2.58 *mm* and both weights equal to 39699.25. These moments are used for the experiments by Simon [19]. The droplets Sauter mean diameter in the experiments of Simon was $d_{32} =$

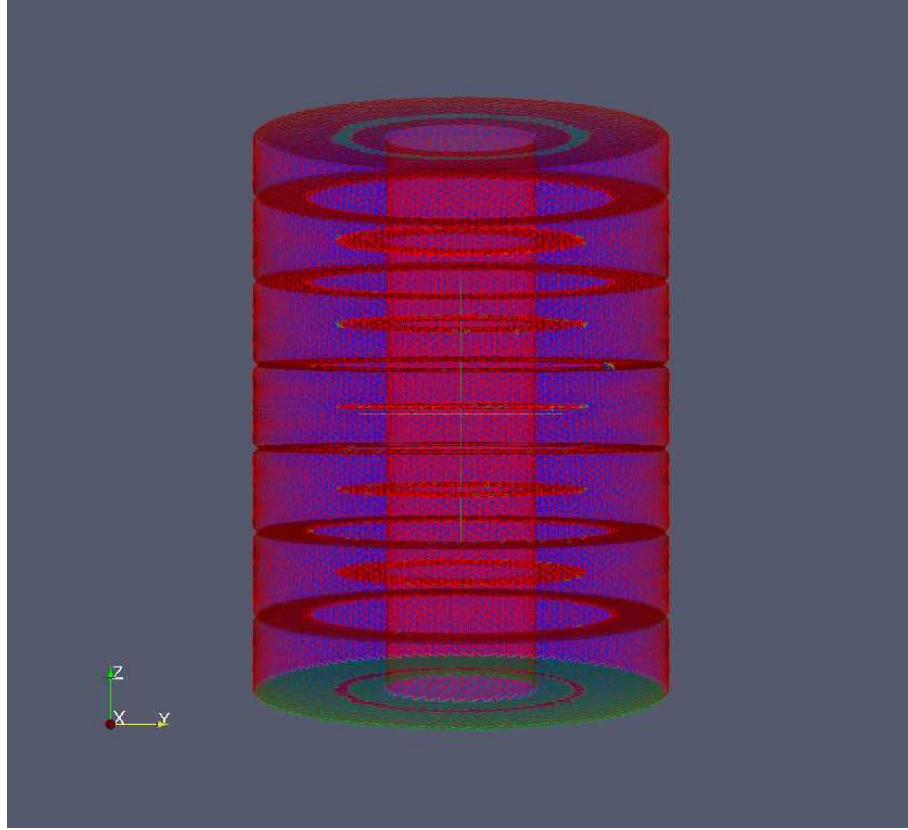


Figure 1. 3D extraction column

2.6 mm at the outlet. In this paper we have considered constant breakage and aggregation kernels. The computations are continued until the flow reached quasi-steady state. In order to find some estimation on the aggregation and breakage kernel, we performed some parameter study in $2D$ geometry where the rotor is fixed. The 2D computational domain is depicted in Fig. 2, where 5 compartments (as in the 3D domain) are considered. The size of the domain is $310\text{ mm} \times 48\text{ mm}$. On the left boundary $BC = 4\text{ mm}$ is the inflow boundary for primary phase and the rest is no-slip boundary for the primary phase and outflow boundary for the secondary phase. On the right wall $FG = 4\text{ mm}$ is inflow boundary for the droplet and the rest EF and GH are the no-slip boundary for the secondary phase and outflow boundary for the primary phase. Rest of the walls are considered as no-slip boundary for both phases. The size of compartments is $ML = 29\text{ mm}$ and they are separated by $LK = 1\text{ mm}$. The length of other walls like $AN = KH = 80\text{ mm}$ and $DI = JE = 94\text{ mm}$. The dimensions are the same in the 3D domain. The approach of the

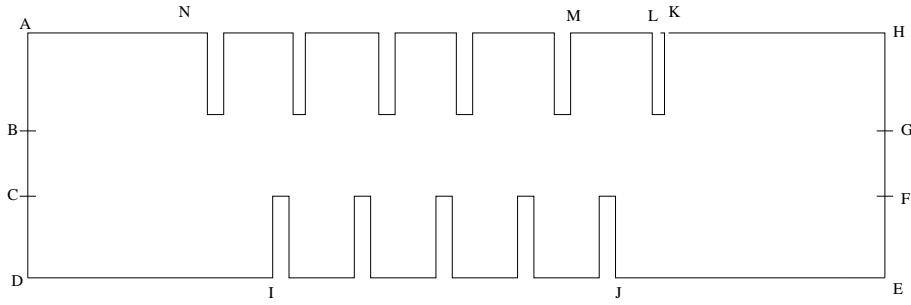


Figure 2. 2d computational domain

2D domain for parameter studies was chosen because parameter studies are not feasible (large CPU time) in a complex 3D domain.

The following approach is followed: we have considered three cases: only breakage, only aggregation and breakage and aggregation both. In Fig.3 we have plotted the Sauter mean diameter for all three cases. Best results were achieved for the constant breakage kernel of magnitude equals 1.0 and a constant aggregation kernel of magnitude equals $1e - 10$. On the top the results are only with the breakage. Here we see the breakage take place mainly in the middle of the domain. The Sauter mean diameter is decreasing from 2.5 mm to below 2 mm at the outlet. In the middle we have plotted the Sauter diameter for aggregation only. The diameter is increasing to around 4.5 mm. In the bottom, we see the Sauter diameter for both breakage and aggregation. As in the experiment, we have obtained the Sauter diameter approximately equal to 2.6 mm. In the next step, the same breakage and coalescence kernels were applied in the 3D domain. The results are depicted in Figs. 4 and 5. As in the 2D domain, the Sauter diameter is equal to 2.6 mm and can match the experiments. Now it is obvious that the same parameters, which were achieved in the CPU-time saving 2D domain, are also suitable for the simulation of the real column. This is possible, since only constant kernels were applied. Real models for coalescence and breakage (e.g. [5]) are strong functions of the energy input (turbulent energy dissipation). Since the main purpose of this work is to couple the FPM and the SQMOM (CFD-PBM) this simplification seems to be a good starting point to focus on the basic principles without considering complex models. The current approach allows for a good description of the real column behavior but it is not adequate for a prediction of the Sauter mean diameter. That's why real models should and will be applied in future work.

The results of the velocity magnitudes and vectors are shown in Fig. 5. Two large vortices can be estimated in the compartment; one between the stirrers and the other between the stirrer. Because of the rising droplets the vortices shift or turn around and are directed to the top of the column, so that the vortex between the stirrer moves to the position above the stirrer and vice

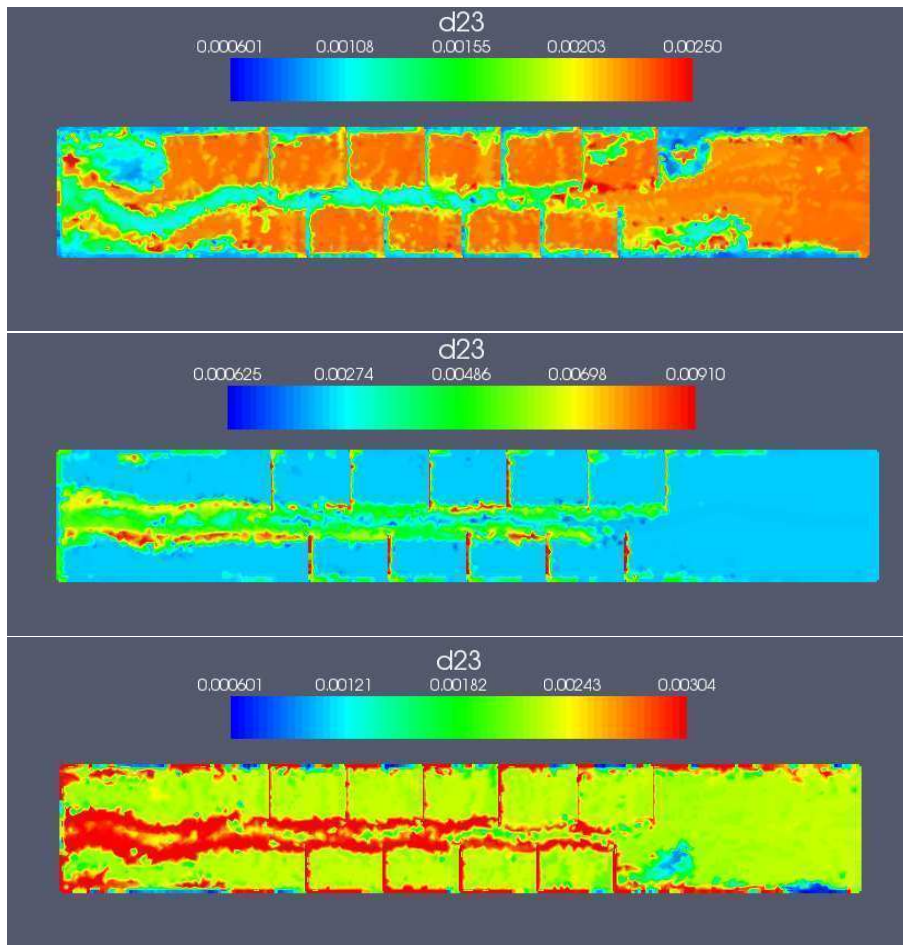


Figure 3. Sauter mean diameter with breakage only (top), aggregation only (middle) and breakage and aggregation (bottom)

versa. As expected, the highest velocities are near the stirrer decreasing to zero near the wall. It could already be shown that FPM can predict flow fields and velocities in the stirred extraction column, whereas all flow phenomena such as vortices can be described. In addition, the FPM results match the overall experimental data and the predicted velocities are in good agreement with the experimental ones [8]. The results of the holdup of the dispersed phase are shown in the right hand side of Fig. 4. It can be seen that the organic droplets accumulate under stirrer and stators and move mainly through the middle of the column without penetrating the outer regions of the column. This agree well with the real column behavior, since the same observations were also seen in experiments [7].

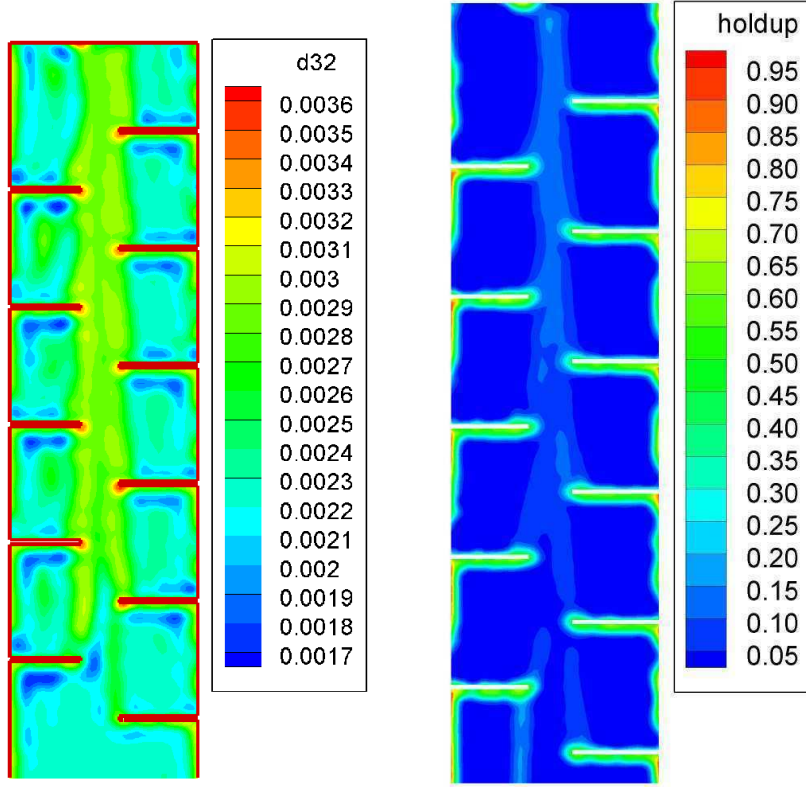


Figure 4. Sauter diameter in m (left) and Holdup of dispersed phase(right)

Convergence study

For the purpose of convergence study, we have considered a simple 2D rectangular geometry of size $[1, 1.5] m \times [0, 1.5] m$. For the liquid phase it is considered as a closed tank without in- and outflow boundaries. The gravity acts in the negative y -direction. For the droplet, we considered the top boundary as the outflow and the interval $[1.145, 1.16] m$ on the bottom as the inflow boundary with the velocity $v = (0, 0.01) m/s$. Both effects of aggregation and breakage have been considered with constant kernels. The rest of the parameters are same as in the above mentioned numerical examples. We have simulated upto 10 seconds. In this time state Table1 shows the size of h as well as the corresponding total number of particles in both phases and maximum velocities of both phases. Here, we see that the scheme converges, but not with the expected order. In Fig. 6, we have plotted the velocity field for the continuous phase with $h = 0.02 m$ at the time $t = 8.86 s$.

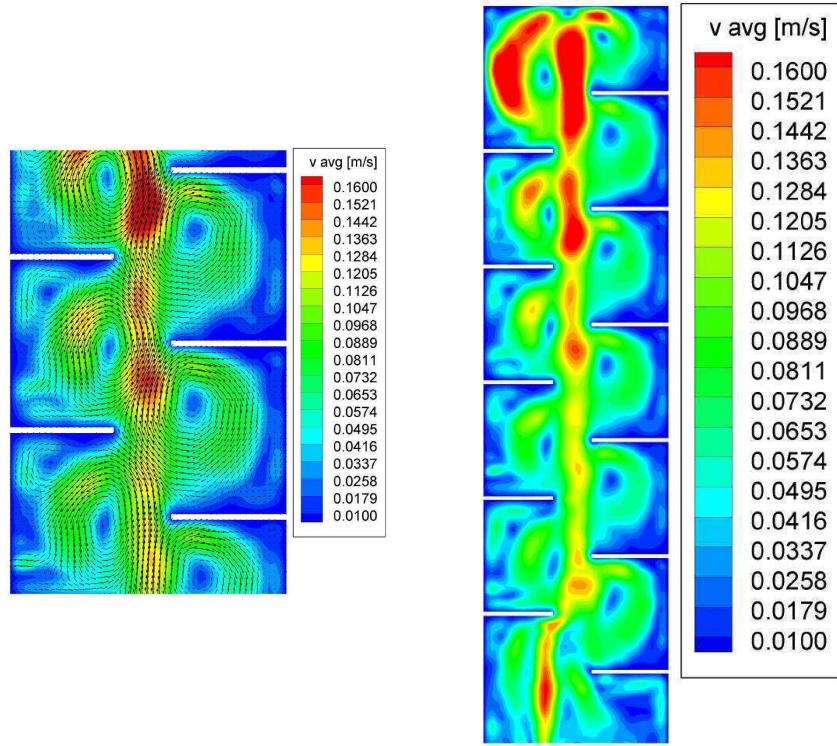


Figure 5. velocity contour of continuous phase

Table 1.

h	N	$\ \mathbf{v}_c\ _{max}$	$\ \mathbf{v}_d\ _{max}$
0.08	1548	0.8031	1.0148
0.04	5628	0.6220	0.8058
0.02	21451	0.5512	0.7538
0.01	83133	0.5333	0.7216
0.0075	145840	0.5304	0.7022

5 Conclusion

In this paper we have considered the coupling of CFD with DPBM. The PBE is solved using the SQMOM with one primary particle. We have considered constant breakage and aggregation kernels and they have been fitted to experimental data in a 2D domain in which the numerical results are close to experimental ones. The same parameters were applied in the 3D domain and produce suitable results for the Sauter mean diameter, holdup and aqueous

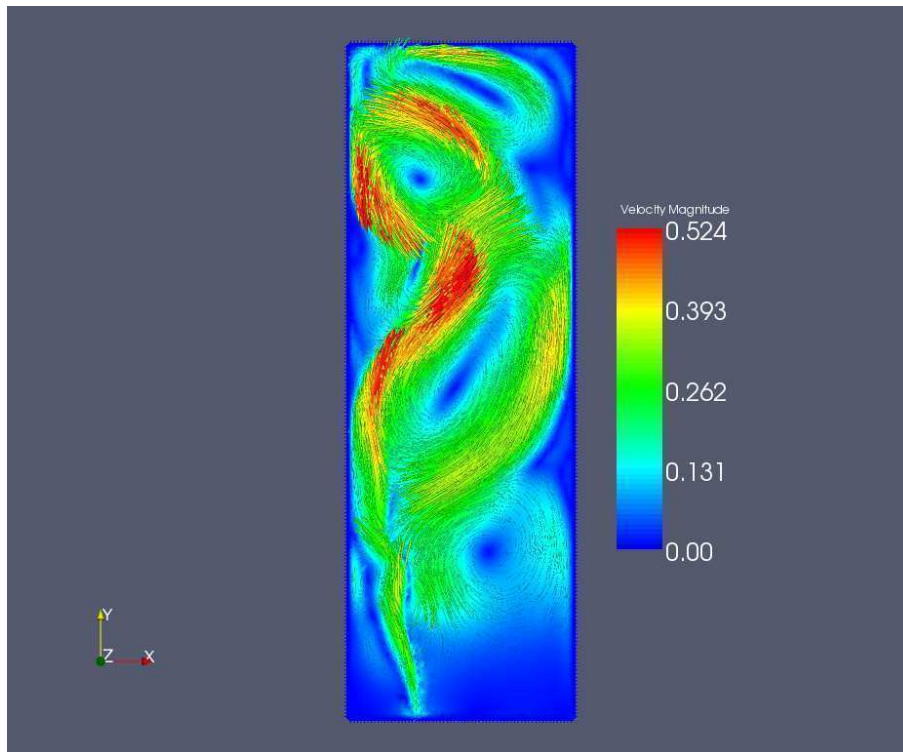


Figure 6. Velocity contour for continuous phase

phase velocities. In summary, the coupling of FPM and SQMOM is accomplished using one primary particle resulting in a two-fluid model and constant kernels for breakage and coalescence. In future work, more primary particles will be considered to achieve a multi-fluid CFD-DPBM model. Furthermore, instead of the constant breakage and aggregation kernels real coalescence and breakage models will be used in the DPBE to permit a prediction of the column behavior. Such kernels in general depend on the turbulent energy, therefore, the turbulence model will be included in the FPM code.

Acknowledgment: We would like to thank the “Deutsche Forschungsgemeinschaft (DFG)” for the financial support of our research.

References

1. M. M. Attarakih, H.-J. Bart, L.G. Lagar and N.M. Faqir, *LLECMOD: A Windows-based program for hydrodynamics simulation of liquid-liquid extraction columns*, Chem. Eng. Proc., **45**(2), (2006), 113–123.

2. M. M. Attarakih, H.-J. Bart and N.M Faqir, *Numerical solution of the bivariate population balance equation for the interacting hydrodynamics and mass transfer in liquid-liquid extraction column*, Chem. Eng. Sci., **61**(1), (2006), 113–123.
3. M. M. Attarakih, C. Drumm and H.-J. Bart, *Solution of the population balance equation using the sectional quadrature method of moments*, submitted in Chem. Eng. Sci., special issue 3rd international conference on population balance modelling, Quebec, Canada, 19–21 Sept. 2007.
4. A. Chorin, *Numerical solution of the Navier-Stokes equations*, J. Math. Comput., **22** (1968), 745–762.
5. C. A. Coualoglou and L. L. Tavlarides, *Description of interaction processes in agitated liquid-liquid dispersions*, Chem. Eng. Sci., **32**, (1977), 1289-1297.
6. C. Drumm, M. M. Attarakih and H.-J. Bart, *Coupling of CFD with DPBM for a RDC extractor*, submitted in Chem. Eng. Sci., special issue 3rd international conference on population balance modelling, Quebec, Canada, 19–21 Sept. 2007.
7. C. Drumm and H.-J. Bart, *Hydrodynamics in a RDC extractor: single and two-phase PIV measurements and CFD simulations*, Chem. Eng. Techn., **29**(11), (2006), 1–8.
8. C. Drumm, S. Tiwari, J. Kuhnert and H.-J. Bart, *Finite pointset method for simulation of the liquid-liquid flow field in an extractor*, (2007), submitted Comp. Chem. Eng..
9. R. G. Gordon, *Error bounds in equilibrium statistical mechanics*, J. Math. Phys. **9**, (1968), 655–663.
10. M.J. Hounslow, R.L. Ryall and V.R. Marshall, *A discretized population balance for nucleation, growth and aggregation*, AIChE Journal, **34**(11), (1988), 1821–1832.
11. E. Krepper, T. Frank, D. Lucas, H.-M. Prasser and P.J. Zwart, *Inhomogeneous MUSIG model - a population balance approach for polydispersed bubbly flows*, Proceedings of the ICMF-2007, M. Sommerfeld (Ed.), 6th International Conference on Multiphase Flow, Leipzig, (2007).
12. J. Kuhnert, *An upwind finite pointset method (FPM) for compressible Euler and Navier-Stokes equations*, (M. Griebel and M. A. Schweitzer, eds.), Lecture Notes in Computational Science and Engineering, vol. 26, Springer, 2002, pp. 239–249.
13. S. Lo, *Application of population balance to CFD modelling of gas-liquid reactors*, Proc. "Trends in numerical and physical modelling for industrial multiphase flows", Corsica, France, 2002.
14. L.D. Marchisio and R.O. Fox, *Solution of the population balance equations using the direct quadrature method of moments*, J. Aerosol Sci. **36**, (2005), 43–73.
15. R. McGraw, *Description of aerosol dynamics by the quadrature method of moments*, Aerosol Sci. & Tech., **27**(2), (1997), 255–265.
16. D. Ramkrishna, *Population Balances*, Academic Press, San Diego, 2000.
17. L. Schiller and Z. Naumann, *A drag coefficient correlation*, Z. Ver. Deutsch. Ing., **77**, (1935), 318.
18. S. A. Schmidt, M. Simon, M. M. Attarakih, L. Lager and H.-J. Bart, *Droplet population balance modelling - hydrodynamics and mass transfer*, Chem. Eng. Sci., **61**(1), (2006), 246–256.
19. M. Simon, *Koaleszenz von Tropfen und Tropfenschwärmen*, Dr. Ing. Thesis, TU Kaiserslautern, Germany, 2002.
20. S. Tiwari and J. Kuhnert, *Finite pointset method based on the projection method for simulations of the incompressible Navier-Stokes equations*, (M. Griebel and

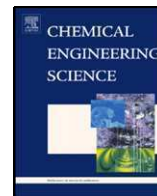
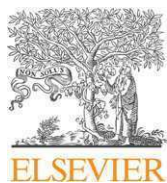
- M. A. Schweitzer, eds.), Lecture Notes in Computational Science and Engineering, vol. 26, Springer, 2002, pp. 373–387.
21. S. Tiwari and J. Kuhnert, *A numerical scheme for solving incompressible and low Mach number flows by Finite Pointset Method*, (M. Griebel and M. A. Schweitzer, eds.), Lecture Notes in Computational Science and Engineering, vol. 43, Springer, 2005, pp. 191–206.
 22. S. Tiwari, S. Antonov, D. Hietel, J. Kuhnert and R. Wegener, *A Meshfree Method for Simulations of Interactions between Fluids and Flexible Structures*, (M. Griebel and M. A. Schweitzer, eds.), Lecture Notes in Computational Science and Engineering, vol. 57, Springer, 2006, pp. 249–264.
 23. A. Vikhansky, M. Kraft, M. Simon, S. Schmidt and H.-J. Bart, *Droplets Population balance in a rotating disc contactor: an inverse problem approach*, *AIChE Journal*, **52**(4), (2006), 1441–1450.
 24. F. Wang and Z.-S. Mao, *Numerical and experimental investigation of liquid-liquid two-phase flow in stirred tanks* *Ind. Eng.Chem. Res.*, **44**, (2005), 5776.

Publication IX

Reprinted from Chemical Engineering Science, 64, 721-732, **2009**,
Christian Drumm, Menwer M. Attarakih, Hans-Jörg Bart,
Coupling of CFD with DPBM for an RDC extractor.

Reprinted with permission from Elsevier.

<http://dx.doi.org/10.1016/j.ces.2008.05.041>



Coupling of CFD with DPBM for an RDC extractor

Christian Drumm^a, Menwer M. Attarakih^b, Hans-Jörg Bart^{a,*}

^aLehrstuhl für Thermische Verfahrenstechnik, TU Kaiserslautern, P.O. Box 3049, 67653 Kaiserslautern, Germany

^bFaculty of Engineering Technology, Chemical Engineering Department, Al-Balqa Applied University, P.O. Box 15008, 11134-Amman, Jordan

ARTICLE INFO

Article history:

Received 14 November 2007

Received in revised form 4 April 2008

Accepted 22 May 2008

Available online 1 June 2008

Keywords:

Computational fluid dynamics

Population balance

Extraction

Multiphase flow

Coalescence

Breakup

ABSTRACT

For the design of counter-current liquid–liquid extraction columns, there is a strong industrial demand for more straightforward, faster and money-saving simulation methods. One possibility in this direction that has a great potential is the coupling of computational fluid dynamics (CFD) with population balance models (PBM). Therefore, a combination of CFD and droplet population balance modelling (DPBM) is applied to simulate the drop size distributions and flow fields in a liquid–liquid RDC extractor. The simulations are carried out in the commercial CFD code Fluent. The liquid–liquid flow is modelled using a Reynolds averaged turbulence model in conjunction with the Eulerian two-fluid equations. Models for coalescence and breakup, from Luo and Svendsen [1996. Theoretical model for drop and bubble breakup in turbulent dispersions. *A.I.Ch.E. Journal* 42, 1225–1233] Coualoglou and Tavlarides [1977. Description of interaction processes in agitated liquid–liquid dispersions. *Chemical Engineering Science* 32, 1289–1297] and a mixed model [Martínez-Bazán, C., Montañés, J.L., Lasheras, J.C., 1999. On the breakup of an air bubble injected into a fully developed turbulent flow. Part 1. Breakup frequency. *Journal of Fluid Mechanics* 401, 157–182; Prince, M.J., Blanch, H.W., 1990. Bubble coalescence and break-up in air-sparged bubble columns. *A.I.Ch.E. Journal* 36, 1485–1499] are implemented in the CFD code as user defined functions. For the solution of the PBM a classes method (CM) [Kumar, S., Ramkrishna, D., 1996. On the solution of population balance equations by discretization—I. A fixed pivot technique. *Chemical Engineering Science* 51, 1311–1332] and the quadrature method of moments (QMOM) [Marchisio, D.L., Pikturna, J.T., Fox, R.O., Vigil, R.D., Barresi, A.A., 2003a. Quadrature method of moments for population-balance equations. *A.I.Ch.E. Journal* 49, 1266–1276] are used. Simulated droplet distributions for the systems toluene–water and butyl acetate–water are compared to experimental measurements. The model of Luo and Svendsen was modified to predict the droplet size distribution. The mixed model allows the prediction of the Sauter mean diameter without any adjustable parameter. Pros and cons of the combined model as well as future needs and trends such as multi-fluid CFD–PBM models are discussed. The results show that the link of PBM and CFD is a suitable design tool which can significantly improve the layout of industrial columns.

© 2008 Elsevier Ltd. All rights reserved.

1. Introduction

Liquid–liquid extraction is a separation process, which is based on the different distribution of the components to be separated between two liquid phases. Liquid–liquid extraction processes are widely applied in chemical and biochemical industries. Classical extraction equipments used are mixer–settler cascades and different types of counter-current extraction columns like the rotating disc contactor (RDC) type, which is investigated here. The simulation of these counter-current liquid–liquid extraction columns still demands improvement. The state of the art for the design of extraction

columns is to use the HTU–NTU or height equivalent to a theoretical plate (HETP) concept together with the dispersion or back-mixing model to account for the nonidealities of the flow (Thornton, 1992). Only one parameter accounts for all deviations from the ideal plug flow in these models and they are too simple to describe the real hydrodynamic behaviour (Bart and Stevens, 2004). The assumptions also overlook the droplets interactions and hence their effects on the coupled hydrodynamics and mass transfer. Consequently, the design of extraction columns often requires pilot plant experiments that are time and money consuming. On the other hand there is an ongoing claim by the industry for more straightforward, faster and money-saving simulation methods. Simulation methods that show these abilities are droplet population balance modeling (DPBM) and computational fluid dynamics (CFD).

* Corresponding author. Tel.: +49 631 2052414.
E-mail address: bart@mv.uni-kl.de (H.-J. Bart).

In recent years, CFD simulations have been used with great success in chemical engineering applications and allowed the prediction of local hydrodynamic details in equipment encountered in many industrial processes. One of the widely used multiphase models for CFD simulations is the Eulerian multiphase model which can describe a dispersed multiphase flow and accounts for interactions between the dispersed phase and the continuous phase. However, only a few working groups focused on the CFD simulations of the hydrodynamics in counter-current stirred liquid–liquid extraction columns. The majority of these groups considered only single-phase flow in the column (Modes and Bart, 2001; Fei et al., 2000). Two-phase flow fields were simulated and investigated by Rieger et al. (1996), You and Xiao (2005), Vikhansky and Kraft (2004) and Drumm and Bart (2006). Only the latter showed a complete comparison of the simulated flow field to experiments. Generally, a two-fluid model is applied successfully for a two-phase problem, whereas a constant Sauter mean diameter represents the different sizes of the particles in the dispersed phase. (e.g. Drumm and Bart, 2006; Wang and Mao, 2005). If the particle size distribution is very wide or multimodal this approach is more likely to fail. Recent research also investigated multi-fluid models to consider different sizes of the particles in the dispersed phase to overcome these restrictions (Tomiya and Shimada, 2001; Hosokawa et al., 2007).

DPBM, with its origin in crystallization (Hulburt and Katz, 1964), can specify droplet movement, coalescence and breakage of the dispersed phase and consider the particulate behaviour in an extraction column (Gourdon et al., 1994). Current DPBM codes by Attarakih et al. (2006) or Kronberger et al. (1995) also use simplified models, e.g. the dispersion model for the hydrodynamics. The codes are based on average compartment conditions (pseudo-homogeneous) and contain only one external coordinate. It could be shown by Steinmetz et al. (2005) and Schmidt et al. (2006) that the population balance modelling (PBM) based on these codes (Attarakih et al., 2006) is able to predict the holdup profile and the Sauter mean diameter of the droplets in a liquid–liquid extraction column. Although this approach has a huge advantage over the currently used design methods, there are still experiments in small lab-scale devices necessary. These are needed to establish correlations for the droplet rising velocities, the dispersion coefficient in the dispersion model and to fit adjustable parameters in the coalescence and breakage kernels.

The coupling of CFD and DPBM can eliminate these simplifications and shortcomings of stand-alone DPBM codes. Drop size distributions strongly influence mass transfer and hydrodynamics in an extraction column. As to this, the turbulent flow in a stirred column is significantly involved in the breakage and coalescence of the droplets. Therefore, due to the strong interdependency between droplet interactions and fluid dynamics, a combination of CFD and DPBM is recommended, where both methods can benefit from each other. CFD can predict the hydrodynamics and turbulence and give a fully resolved local resolution of the two phase flow in all three external coordinates, while the PBM can account for the droplet coalescence and breakup and predict the size distribution of the dispersed phase.

First publications adopted this approach using the simplification of a one-way coupling. This means that only the result of the flow simulation is used for the calculation of the drop size distributions, while the influence of the drops on the flow field is neglected. A multi-block approach, where the investigated geometry is subdivided into sub-regions, is another alternative in that respect. Alopaeus et al. (1999) divided the investigated stirred tank into 11 sub-regions, while the turbulent energy dissipation entering the population balances came from CFD simulations by integrating over the volumes of the sub-regions. They stated that by assuming a stirred extraction column to be homogeneous, a serious error might be

introduced, since turbulent energy dissipation is several orders of magnitude greater near the impeller than far from it. Schlauch (2006) simulated a liquid–liquid stirred tank by means of the CFD code Feat-flow and the commercial PBM code Parsival (Wulkow et al., 1999) using also a one-way coupling. The tank is subdivided into four regions, and only the velocity fields of the CFD simulations enter the PBM code.

These simplifications in the coupling procedure can be reduced by implementing the population balance equations in a CFD code. Lo (2000) implemented the population balance equations in the commercial CFD code CFX via the multiple-size-group (MUSIG) model of Lo. Herewith a complete coupling is achieved by dividing the bubble size distribution into a number M of discrete size classes. The basic assumption in this coupling is that bubbles of all sizes share a common velocity field through coupling the Sauter mean diameter to the drag term. Sanyal et al. (2005) implemented a classes-method (CM) and a method of moments (MOM) in the CFD code Fluent in conjunction with the Eulerian multiphase model. Since the main focus of the work was the investigation of alternative approaches for solving the population balance equations and not the detailed modelling of the hydrodynamics in a column, the results were not compared to experiments. Furthermore, for the turbulent energy dissipation a constant value was chosen instead of returning the values from the applied $k-\epsilon$ model. Nowadays, combined CFD–PBM models are widely investigated in the gas–liquid and liquid–liquid fields (e.g. Andersson et al., 2004; Chen et al., 2005; Jakobsen et al., 2005; Lehr et al., 2002; Moilanen et al., 2007; Olmos et al., 2001; Vikhansky and Kraft, 2004; Wang et al., 2006). All the references are based on the assumption that the particle size distribution is modelled with PBM while only averaged particle sizes as the Sauter mean diameter are coupled to the fluid dynamics. Current research tries to eliminate the drawback of the present models and focuses on an inhomogeneous MUSIG model where the dispersed phase is divided into a number of different velocity groups or classes, where each of the classes is characterized by its own velocity field. The PBM is then applied to the sub-size groups, which are within each of the velocity groups (Krepper et al., 2007). According to the authors, 2–3 velocity groups should be sufficient. Bhole et al. (2008) even realized size-specific bubble velocities by solving momentum equations for each bubble class, where the number of velocity groups is equal the number of classes in the CM. As a drawback, these two approaches are based on the CPU time consuming CM and additional equations for the conservation of momentum have to be solved for each velocity group. In this connection, another interesting alternative seems to be the Sectional Quadrature Method of Moments (SQMOM) (Attarakih et al., 2008), which combines the approaches of the CM and the QMOM, whereas a small number of classes (e.g. 1, 2 or 3) can be used as moving classes or velocity groups as suggested by Krepper et al. (2007), while only 3–4 moments could be solved inside each class to reproduce the moments and to account for breakage and coalescence. A lot of computational effort could be saved in comparison to the inhomogeneous MUSIG model when only two or three velocity groups are applied. For this reason the SQMOM is recently coupled with the finite pointset method, a meshfree CFD code (Drumm et al., 2008a) and also incorporated in Fluent in the framework of a three-fluid model (Drumm et al., 2008b).

Since the coupling of CFD and PBM advanced very well in the last years, as shown in the above selected examples, the predictability of a combined CFD–PBM tool for the layout of stirred extraction columns can be further investigated. Coupled CFD–PBM simulations for a stirred extractor are almost nonexistent and can only be found in Vikhansky and Kraft (2004). Therefore, in the present work, a combination of CFD and DPBM is applied to simulate the drop size distributions and flow fields in a five-compartment segment of a liquid–liquid RDC extractor. The simulations are carried out in the

commercial CFD code Fluent 6.3. The liquid–liquid flow is modeled using a Reynolds averaged turbulence model in conjunction with the Eulerian two-fluid equations. In previous work, the simulated flow fields of the two-fluid model with constant d_{32} were compared to particle image velocimetry (PIV) measurements, taken on the same pilot scale column, and agreed well with each other (Drumm and Bart, 2006). The turbulence has been modelled by the realizable $k-\epsilon$ model, which delivers the best results for the present two-phase flow (Drumm and Bart, 2006). Two theoretical models for coalescence and breakup, the models of Luo and Svendsen (1996) and Coualoglou and Tavlarides (1977), as well as a mixed model, where the breakup kernel comes from Martínez-Bazán et al. (1999) and the coalescence kernel from Prince and Blanch (1990) are implemented in the CFD code as user defined functions (UDF). For the solution of the PBM a CM (Kumar and Ramkrishna, 1996) and the QMOM (Marchisio et al., 2003a) are used.

Here we retain the assumption of the two-fluid model, which was successfully applied for wide gas–liquid distributions ranging from around <1 to >20 mm (e.g. Sanyal et al., 2005; Chen et al., 2005). Therefore, it should also be sufficient for the description of the monomodal narrower drop size distribution (1–5 mm) in the present liquid–liquid problem. We focus on the prediction of the drop size distribution, varying QMOM, CM and closures for coalescence and breakage, in a proved, tested and cost-efficient framework, namely the two-fluid model. On the other hand, combined CFD–PBM multi-fluid models are still under development and highly CPU-time consuming.

Finally, simulation results of the aqueous and dispersed phase fluid dynamics are given and simulated drop size distributions for the system toluene–water and butyl acetate–water are compared to the experimental measurements of Simon (2004). The paper is organized as follows: governing equations as well as the coalescence and breakage models are introduced in Section 2. In Section 3, the results of the simulations are presented and compared to the experimental data with respect to the solution methods of the PBM (CM and QMOM) and the applied breakage and coalescence models. Pros and cons of the combined model as well as future needs and trends such as multi-fluid CFD–PBM models are also discussed. A summary and conclusions are given in Section 4.

2. Numerical approach

2.1. Numerical scheme

The simulations are carried out in the commercial CFD code Fluent 6.3. The basis of the investigations are experiments conducted by Simon (2004) in a five-compartment section of an RDC column with 150 mm diameter. Therefore, a 2D axis-symmetric grid of the column was modelled in Gambit. Because of the rotational symmetry of an RDC (Fig. 1) the 2D grid can be adopted without losing information. Previous work showed that a 2D grid delivers reliable results regarding the hydrodynamics of an RDC (Drumm and Bart, 2006). Concerning the boundary conditions the common approach with one pressure outlet condition at the top and one velocity-inlet at the bottom was applied. However, assumptions for the volume fraction of the dispersed phase at the in- and outlets had to be made. The surfaces of the rotating disc and the column wall were defined with no-slip wall boundary conditions. All flow conditions, as well as the droplet distribution in the CM and QMOM at the inlet, were the same as in the experiments. Quadrilateral elements with a grid space of 1 mm were adopted to map the flow domain (10000 cells). The computational grid is depicted in Fig. 2. Standard wall functions modelled the near wall region. The simulations were carried out unsteadily reducing the time step from 0.1 to 0.001 s, using the first order implicit solver. For the discretisation in space first order

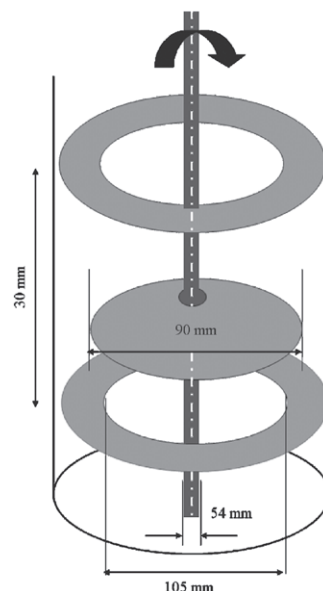


Fig. 1. Rotating disc contactor (outer diameter 150 mm).

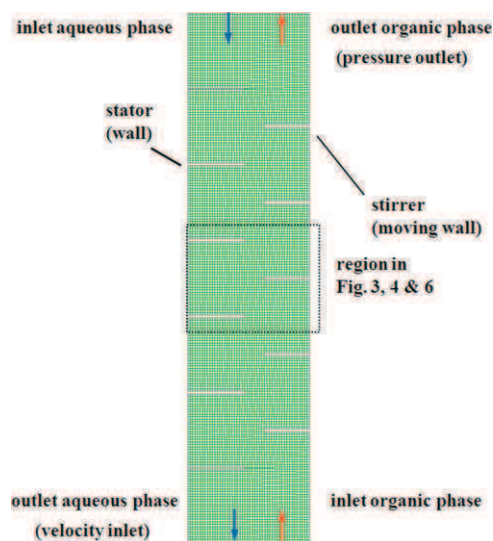


Fig. 2. Computational grid for a five-compartment RDC column (the boundary conditions are given in brackets).

upwind schemes were used for the population balance equations and the first order upwind and the QUICK scheme were used for the flow equations. The SIMPLE algorithm was used for the pressure–velocity coupling. Concerning the under-relaxation factors, standard values were used without modification. The governing equations of the flow and the population balances as well as the implementation of the investigated coalescence and breakup kernels are described in detail in the following sections.

2.2. Two-fluid model

An Euler–Euler model where both phases are treated mathematically as interpenetrating continua was applied for the two-phase simulations of the extraction column. The conservation equations are

solved for each phase. The continuity equation for the liquid phase l is

$$\frac{\partial(\alpha_l \rho_l)}{\partial t} + \nabla \cdot (\alpha_l \rho_l \vec{u}_l) = 0, \quad (1)$$

where α is the volume fraction, which represents the space occupied by each phase, ρ is the phase density and u is the phase velocity. The conservation of momentum for phase l is

$$\frac{\partial(\alpha_l \rho_l \vec{u}_l)}{\partial t} + \nabla \cdot (\alpha_l \rho_l \vec{u}_l \vec{u}_l) - \nabla \cdot \tau_l = -\alpha_l \nabla p + \alpha_l \rho_l \vec{g} + F_k, \quad (2)$$

where τ is the stress–strain tensor, p is the pressure shared by all phases, g is the gravitational acceleration and F represents the interfacial forces. In addition to Eqs. (1) and (2) the constraint for the volume fractions must be satisfied:

$$\alpha_1 + \alpha_2 = 1. \quad (3)$$

The interphase interaction term F_k consists of different momentum exchange mechanisms. Only the drag force was taken into account, while the virtual mass force and the lift force can be neglected for liquid–liquid interactions as shown by Wang and Mao (2005) in a stirred tank. The drag force is calculated as

$$F_{c,d} = \frac{\rho_d \alpha_c \alpha_d f}{\tau_d} (\vec{u}_d - \vec{u}_c), \quad (4)$$

where the subscripts c and d stand for the two liquid phases, while f is the drag coefficient and τ_d the particulate relaxation time:

$$\tau_d = \frac{\rho_d d_d^2}{18 \mu_c}. \quad (5)$$

In the above equation d_d is the Sauter mean diameter of the droplets of the dispersed liquid phase and μ is the dynamic viscosity. For the evaluation of the drag coefficient, the model of Schiller and Naumann (1935) is applied:

$$f = \frac{C_D Re}{24}, \quad (6)$$

$$C_D = \begin{cases} 24(1 + 0.15 Re^{0.687})/Re, & Re \leq 1000, \\ 0.44, & Re > 1000. \end{cases} \quad (7)$$

With the relative Reynolds number Re defined as

$$Re = \frac{\rho_c |\vec{u}_d - \vec{u}_c| d_d}{\mu_c}. \quad (8)$$

The drag force results finally in

$$F_{c,d} = \frac{3 \rho_c \alpha_c \alpha_d C_D |\vec{u}_d - \vec{u}_c| (\vec{u}_d - \vec{u}_c)}{4 d_d}. \quad (9)$$

For the calculation of the multiphase turbulence, the Fluent mixture turbulence model was used, which is an extension of the single-phase model, together with the realizable $k-\varepsilon$ model (Fluent, 2005). Our own previous investigations lead to the conclusion that the current model is the most suitable available multiphase-model in Fluent for the description of the liquid–liquid flow (Drumm and Bart, 2006).

2.3. Population balance model

For the description of the PBM a number density function $n(x, V, t)$ can be postulated, which denotes the spatial position x of a droplet as an external coordinate and the droplet volume V as an internal

coordinate. The transport equation for the number density function n is given by

$$\frac{\partial}{\partial t} [n(V, t)] + \nabla \cdot [\vec{u} n(V, t)] = S(V, t), \quad (10)$$

where $S(V, t)$ are the source terms for coalescence and breakup of the droplets and can be further written as

$$S(V, t) = B^C(V, t) - D^C(V, t) + B^B(V, t) - D^B(V, t). \quad (11)$$

B^B , D^B , B^C and D^C are the birth and death rates of droplets of volume V due to coalescence and breakup. The birth and death rates are given by

$$B^C(V, t) = \frac{1}{2} \int_0^V a(V - V', V') n(V - V', t) n(V', t) dV', \quad (12)$$

$$D^C(V, t) = \int_0^\infty a(V, V') n(V, t) n(V', t) dV', \quad (13)$$

$$B^B(V, t) = \int_V^\infty g(V') \beta(V|V') n(V', t) dV', \quad (14)$$

$$D^B(V, t) = g(V) n(V, t). \quad (15)$$

The aggregation kernel a in the coalescence equations accounts for the probability of successful collisions between pairs of droplets. It is defined as the product of two quantities, the collision frequency h and the coalescence efficiency λ :

$$a(V, V') = h(V, V') \cdot \lambda(V, V'). \quad (16)$$

The breakage rate expression includes the breakage frequency g , which represents the fraction of droplets splitting per unit time and the probability density function (PDF) β , which describes the distribution of the daughter droplets from the splitting mother particle V' :

$$g(V') \beta(V|V'). \quad (17)$$

For the solution of the population balance equation the CM and the QMOM (McGraw, 1997; Marchisio et al., 2003a) are used. Widely applied schemes for the method of classes are by Hounslow et al. (1988) and Kumar and Ramkrishna (1996). A review of various methods is given in Ramkrishna (2000). The governing equations for both solution methods are summarized in the following sections.

2.3.1. Classes method

In Fluent the PBM is written in terms of the volume fraction of droplet size i for the CM:

$$\frac{\partial}{\partial t} [\rho_d \alpha_i] + \nabla \cdot [\rho_d u_d \alpha_i] = \rho_d V_i S_i, \quad (18)$$

where α_i is the volume fraction of droplet size i and is defined as

$$\alpha_i = N_i V_i = V_i \int_{V_i}^{V_{i+1}} n(V, t) dV. \quad (19)$$

All droplet volume fractions sum to the total volume fraction of the dispersed phase:

$$\sum_{i=1}^M \alpha_i = \alpha_d. \quad (20)$$

In writing the source terms of Eq. (18) the fixed pivot technique of Kumar and Ramkrishna (1996) has been used. The droplet birth

and death rates conserving both numbers and mass are defined as follows:

$$B_i^C = \sum_{\substack{j \geq k \\ V_{i-1} \leq (V_j + V_k) \leq V_{i+1}}} \left(1 - \frac{1}{2} \delta_{j,k}\right) a_{kj} \eta N_k N_j, \quad (21)$$

$$D_i^C = N_i \sum_{j=1}^M a_{ij} N_j, \quad (22)$$

$$B_i^B = \sum_{j=1}^M g_j N_j B_{ij}, \quad (23)$$

$$D_i^B = g_i N_i. \quad (24)$$

The value η preserves the reassignment to the classes if the resulting coalesced droplet V lies between the classes:

$$\eta = \begin{cases} \frac{V - V_{i-1}}{V_i - V_{i-1}} & \text{if } V_{i-1} < V < V_i, \\ \frac{V_{i+1} - V}{V_{i+1} - V_i} & \text{if } V_i < V < V_{i+1}. \end{cases} \quad (25)$$

The value B_{ij} is the contribution to group i due to breakage of a droplet of size V_j :

$$B_{ij} = \int_{V_i}^{V_{i+1}} \frac{V_{i+1} - V}{V_{i+1} - V_i} \cdot \beta(V, V_j) dV + \int_{V_{i-1}}^{V_i} \frac{V - V_{i-1}}{V_i - V_{i-1}} \cdot \beta(V, V_j) dV. \quad (26)$$

More details about this approach could be found elsewhere (Kumar and Ramkrishna, 1996; Ramkrishna, 2000).

2.3.2. Quadrature method of moments

By using the QMOM the transport equation is solved for the k th moment that is defined as

$$m_k(x, t) = \int_0^\infty n(L, x, t) L^k dL, \quad (27)$$

where L is the droplet size. By applying the last equation to the population balance equation (10), the transport equation can be written as

$$\frac{\partial}{\partial t} (\rho_d m_k) + \nabla \cdot (\rho_d u_d m_k) = \rho_d S_k. \quad (28)$$

Note that the QMOM is based on the following quadrature approximation:

$$m_k = \int_0^\infty n(L, x, t) L^k dL = \sum_{i=1}^N w_i L_i^k, \quad (29)$$

whereas the quadrature approximation of order N is defined by its N weights w_i and N abscissas L_i and can be calculated in terms of the first $2N$ moments m_0, \dots, m_{2N-1} through the product–difference algorithm. A detailed explanation can be found in Marchisio et al. (2003a, b). The source term S_k for death and birth due to coalescence and breakage can be written as

$$B_k^C = \frac{1}{2} \sum_{i=1}^N w_i \sum_{j=1}^N w_j \cdot (L_i^3 + L_j^3)^{k/3} \cdot a(L_i, L_j), \quad (30)$$

$$D_k^C = \sum_{i=1}^N L_i^k \cdot w_i \sum_{j=1}^N w_j \cdot a(L_i, L_j), \quad (31)$$

$$B_k^B = \sum_{i=1}^N w_i \int_0^\infty L^k \cdot g(L_i) \cdot \beta(L, L_i) dL, \quad (32)$$

$$D_k^B = \sum_{i=1}^N w_i \cdot L_i^k \cdot g(L_i). \quad (33)$$

Given a set of moments the most likely particle size distribution can be reconstructed based on the statistically most probable distribution for turbulent flames (Pope, 1979), which was adapted for crystallization problems by Baldyga and Orciuch (2001):

$$n(L) = B_0 \exp\left(\sum_{i=0}^{2N-1} A_i L^i\right). \quad (34)$$

The equation for the k th moment is now written as

$$m_k = \int_0^\infty L^k B_0 \exp\left(\sum_{i=0}^{2N-1} A_i L^i\right) dL, \quad (35)$$

$$k = 0, 1, \dots, 2N - 1.$$

Given $2N$ moments, the coefficients B_0 and A_i can be found by a globally convergent Newton–Raphson method to reconstruct the particle size distribution. The method was also applied for reconstruction in the work of Sanyal et al. (2005). Other reconstruction techniques could be found in the work of John et al. (2007).

2.4. Coupling CFD and PBM

Finally, for the coupling with the fluid dynamics the Sauter mean diameter of the droplets is calculated in every time step and returned to the drag force in Eq. (4). This is also the main drawback of the model, since only one set of Navier–Stokes equations is solved for all droplet classes and all classes have the same velocity evaluated at the Sauter mean diameter:

$$d_{32} = \frac{\sum N_i d_i^3}{\sum N_i d_i^2} \quad \text{or} \quad d_{32} = \frac{m_3}{m_2}. \quad (36)$$

Nevertheless, as stated in the introduction it is the cost-efficient standard approach in the coupling of CFD and PBM so far. The governing values in the source terms for coalescence and breakage, e.g. the turbulent energy dissipation ε or the volume fraction α are returned for each cell from the Fluent solver. The velocity u_d in Eqs. (18) and (28) is derived from the Navier–Stokes equations, thus a complete two-way coupling between CFD and PBM is assured. Using this approach, all information come from the simulation and the need for experimental data and geometrically dependent correlations is eliminated.

2.5. Breakup and coalescence closures

Two theoretical models for coalescence and breakup, the models of Luo and Svendsen (1996) and Coulaloglou and Tavlariades (1977) are coded in C programming language, compiled and implemented in Fluent as UDF. In addition, a mixed model was chosen, where the breakage kernel was adopted from Martínez-Bazán et al. (1999) and the coalescence kernel comes from Prince and Blanch (1990). The different breakup and coalescence models were varied in the simulations using both the CM and QMOM.

2.5.1. Model of Coulaloglou and Tavlariades (1977)

The well-known model of Coulaloglou and Tavlariades considers drop deformation and breakup under the influence of local pressure fluctuations in a locally isotropic flow field. The coalescence term uses the frequently applied structure of the product of drop–drop collision frequency and coalescence efficiency. The model is given by the following set of equations:

$$g(d) = C_1 \cdot \frac{\varepsilon^{1/3}}{d^{2/3}(1 + \alpha)} \exp\left(-\frac{C_2 \sigma(1 + \alpha)^2}{\rho_d \varepsilon^{2/3} d^{5/3}}\right), \quad (37)$$

$$h(d_1, d_2) = C_3 \frac{\varepsilon^{1/3}}{1 + \alpha} (d_1 + d_2)^2 (d_1^{2/3} + d_2^{2/3})^{1/2}, \quad (38)$$

$$\lambda(d_1, d_2) = \exp \left(-C_4 \frac{\mu_c \rho_c \varepsilon}{\sigma^2 (1 + \alpha)^3} \left(\frac{d_1 d_2}{d_1 + d_2} \right)^4 \right), \quad (39)$$

where σ is the interfacial tension and ε the turbulent energy dissipation. C_1 – C_4 are adjustable parameters. The originally used normal density function for the daughter droplet distribution of Valentas et al. (1966), which assumes binary breakage, is also adopted here

$$\beta(d_1^3 | d_2^3) = \frac{2.4}{d_2^3} \exp \left(-\frac{4.5(2d_1^3 - d_2^3)^2}{d_2^6} \right). \quad (40)$$

2.5.2. Model of Luo and Svendsen (1996)

The second investigated model is the one by Luo and Svendsen. The model is also based on the theories of isotropic turbulence and probability and contains no unknown or adjustable parameter. The breakup frequency is based on the arrival of turbulent eddies to the surface of the droplets. The global frequency of particles of size d is given by

$$g(d) = \frac{1}{2} \cdot 0.923 \cdot (1 - \alpha) \left(\frac{\varepsilon}{d^2} \right)^{1/3} \int_0^1 \int_{\xi_{\min}}^1 \frac{(1 + \xi)^2}{\xi^{11/3}} \times \exp \left(-\frac{12c_f \sigma}{\beta_0 \rho_c \varepsilon^{2/3} d^{5/3} \xi^{11/3}} \right) d\xi dfv, \quad (41)$$

where ξ is the ratio between the diameter of the turbulent eddy and the breaking droplet. Note that β_0 is a numerical constant equal to 2 derived from the kinetic gas theory. C_f ($C_f = f_v^{2/3} + (1 - f_v)^{2/3} - 1$) is the coefficient of surface area, which includes the ratio f_v between the volume of one of the daughter droplets and the mother droplet. The first part of the double integral in Eq. (41) can be solved by using the incomplete gamma function, while the second integral has to be solved numerically. For the second integral 10 equidistant points from 0 to 0.5 for the discretisation of f_v were used. The daughter PDF is obtained from the integral when the partial breakage rate for a constant f_v is divided by the overall breakage rate:

$$\beta(f_v, v, v) = \frac{2 \int_{\xi_{\min}}^1 ((1 + \xi)^2 / \xi^{11/3}) \exp(-12c_f \sigma / (\beta_0 \rho_c \varepsilon^{2/3} d^{5/3} \xi^{11/3})) d\xi}{v \int_0^1 \int_{\xi_{\min}}^1 ((1 + \xi)^2 / \xi^{11/3}) \exp(-12c_f \sigma / (\beta_0 \rho_c \varepsilon^{2/3} d^{5/3} \xi^{11/3})) d\xi dfv}. \quad (42)$$

The collision frequency and efficiency in the model result from the kinetic gas theory and are given by

$$h(d_1, d_2) = \frac{\pi}{4} (d_1 + d_2)^2 \beta_0^{0.5} \varepsilon^{1/3} (d_1^{2/3} + d_2^{2/3})^{1/2}, \quad (43)$$

$$\lambda(d_1, d_2) = \exp \left(-C_1 \frac{[0.75(1 + \xi^2)(1 + \xi^3)]^{1/2}}{((\rho_d / \rho_c) + \gamma)^{1/2} (1 + \xi)^3} We^{1/2} \right). \quad (44)$$

C_1 is an unknown constant of order unity, γ is the virtual mass coefficient and ξ is the droplet size ratio d_1/d_2 .

2.5.3. Mixed model

Finally, the third investigated model is a mixed one, where the kernels are adopted from Martínez-Bazán et al. (1999) (breakup) and Prince and Blanch (1990) (coalescence). Martínez-Bazán et al. proposed a model based on purely kinematic ideas. For a particle to break, its surface has to be deformed by the turbulent stresses. Similar approaches for the breakup description were chosen by Schmidt et al. (2006):

$$g(d) = \frac{K \sqrt{\beta_0 (\varepsilon d)^{2/3} - 12(\sigma / (\rho d))}}{d}. \quad (45)$$

Hereby, K is an adjustable parameter ($K=0.25$) in the original model, which was set to $K=1$. Note that β_0 is now equal to 8.2 in the

model of Martínez-Bazán. The aggregation term in the model of Prince and Blanch is similar to the model of Luo and Svendsen. Here only the turbulent collision rate of the model was considered, while the buoyancy drive and laminar shear collision rates were neglected. The collision rate of droplets and the likelihood of collisions resulting in coalescence are

$$h(d_1, d_2) = 0.089\pi (d_1 + d_2)^2 \varepsilon^{1/3} (d_1^{2/3} + d_2^{2/3})^{1/2}, \quad (46)$$

$$\lambda(d_1, d_2) = \exp \left(-\frac{(d_1 d_2 / (4(d_1 + d_2)))^{5/6} \rho_c^{1/2} \varepsilon^{1/3}}{4\sigma^{1/2}} \ln \left(\frac{h_0}{h_c} \right) \right). \quad (47)$$

Here h_0 is the initial film thickness while h_c is the critical film thickness where rupture occurs, whereas a value of 10^4 was assumed for the ratio. For the breakup kernel in the model of Prince and Blanch, the predicted breakage frequency is a few orders of magnitude higher and cannot give reliable results without a strong adjustment. Instead of the binary breakup assumptions in the other models, a beta distribution (Bahmanyar and Slater, 1991), which can describe more than two daughter droplets was chosen. First simulations were carried out by assuming binary breakup ($x_m = 2$)

$$\beta(d_1, d_2) = 3 \cdot x_m (x_m - 1) \left(1 - \left(\frac{d_1}{d_2} \right)^3 \right)^{(x_m - 2)} \frac{d_2^5}{d_1^6}. \quad (48)$$

3. Results and discussion

In the following section the results of the simulations for the systems toluene–water and butyl acetate–water for the operating conditions conducted by Simon (2004) are shown and compared to the experimental results. Volume flow rates in all simulations are 100 l/h aqueous phase and 100 l/h organic phase, while the stirrer revolution was varied between 150 and 300 rpm.

3.1. Hydrodynamics

First of all, results of the fluid dynamics in the aqueous and dispersed phase are shown. Flow fields for the stirrer rotational speeds 150 and 300 rpm are presented for the model of Coualoglou and Tavlarides using the system toluene–water. Fig. 3 shows the simulated 2D velocity vectors (xy -components) and velocity magnitude in the aqueous phase without considering the dominating swirl velocity (z -component), since the developed two-phase flow field is better visible then. Although the aqueous phase flows from top to bottom, the vortices reverse at the positions between the stators and are directed to the top because the throughput of the ascending droplets is high enough to modify the flow pattern. The same trend is obvious for 300 rpm. The higher stirrer rotational speed causes a higher acceleration outwards and towards the column wall. In Fig. 4 the contours of the velocity magnitude also consider the swirl velocity to make the dominance of the swirl velocity visible. The velocities near the stirrer correspond to the tip velocities (0.7 and 0.14 m/s) and decreases through the compartment to 0 at the column wall. A detailed comparison of simulated and measured flow fields and velocities in single- and two-phase flows using a constant diameter for the droplets in the same geometry showed that the CFD model is able to predict the flow fields and velocities (Drumm and Bart, 2006). Flow fields are only shown for the model of Coualoglou and Tavlarides, since they are only dependent on the results of the Sauter mean diameter. Since the aim of this study is to predict the drop size distribution or Sauter mean diameter, flow fields look alike for the different models, when the predicted Sauter mean diameter matches the experimental one. In the present study, the drop size distribution does not vary so much to have an influence on the aqueous

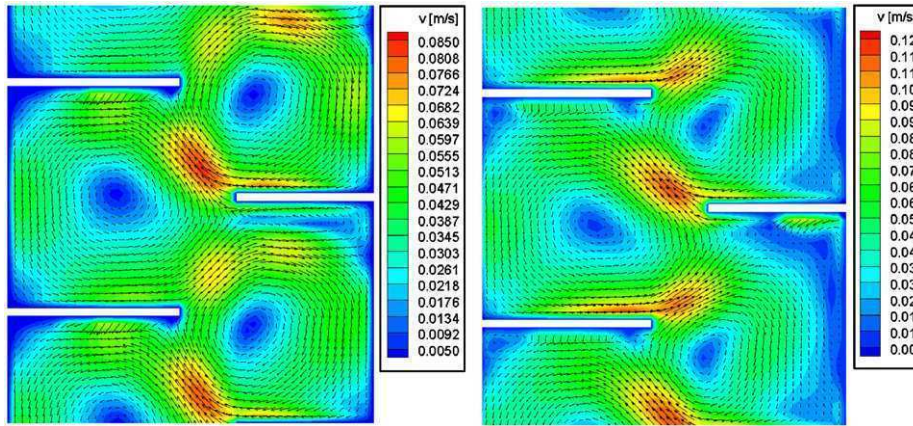


Fig. 3. Predicted velocity vectors and velocity magnitude (axial and radial velocities) in the aqueous phase, 150 rpm (left), 300 rpm (right).

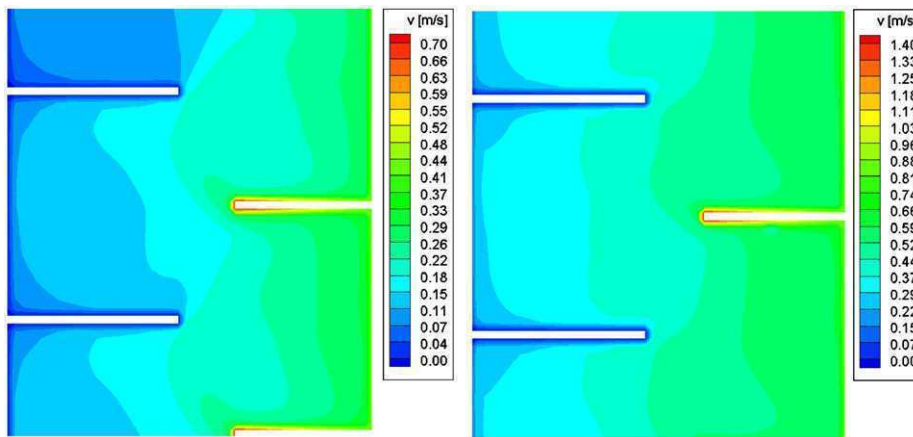


Fig. 4. Predicted overall velocity magnitude (axial, radial and swirl velocities) in the aqueous phase, 150 rpm (left), 300 rpm (right).

flow fields, when the coupled CFD–PBM model without a constant diameter is used.

However, the influence of the different drop sizes is blurred in the present model because it is assumed that all droplets with different sizes move in the same velocity based on the Sauter mean diameter as in the MUSIG model by Lo (2000). This assumption is examined further by showing velocities of the dispersed phase. Rise velocities of toluene drops in stagnant water are depicted in Fig. 5 for different drop diameters. Experimental data of Modes (2000), Wegener et al. (2007) and Gourdon et al. (1994) are plotted together with the predicted velocities from the applied drag law of Schiller and Naumann (1935). Note that Wegener et al. (2007) measured transient rise velocities, while the other authors measured stationary velocities. The former authors observed first a pseudo-terminal (dashed line) velocity followed by a deformation of the drops and an oscillation of the drop velocity (dotted line). It can be seen (Fig. 5) that the drag law can describe the rise velocities as a function of the drop size diameters with small deviation. On the other hand, it is obvious that the assumption of the two-fluid model results in large errors for droplets at the left-most around 1.5 mm and right-most position (4.5 mm) of the distribution. The size-specific rise velocities point at the main drawback of the two-fluid model and confirms the future need for investigations in multi-fluid frameworks, which already started (Bhole et al., 2008; Krepper et al., 2007; Drumm et al., 2008b). In this connection it is worthwhile to mention that the benefit of the two-fluid model is the moderate computational effort which is anyway very high in coupled CFD–PBM models. The same accounts for the QMOM,

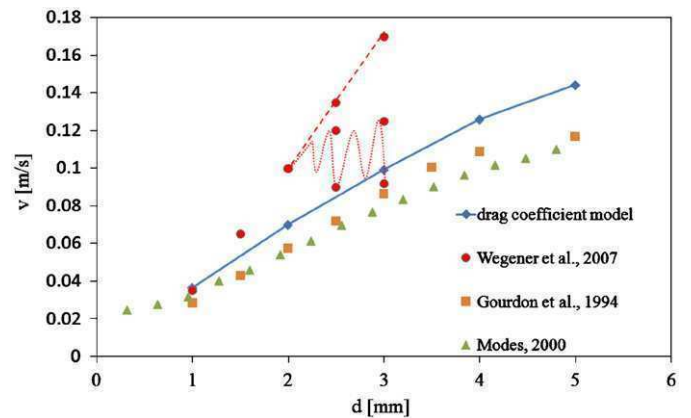


Fig. 5. Rise velocity of toluene drops for different drop diameters, comparison of experimental literature data and the prediction from the drag law (Eq. (7)).

where the number of scalars is extremely low, which is of primary importance for CFD application (Marchisio et al., 2003a). A multi-fluid CFD–PBM will further increase the computational effort. The so far investigated multi-fluid models applied only 2D grids in the simulations. It is questionable if 3D simulations using the very accurate multi-fluid model based on the CM as in Bhole et al. (2008) is actually possible on currently available personal computers. One has to

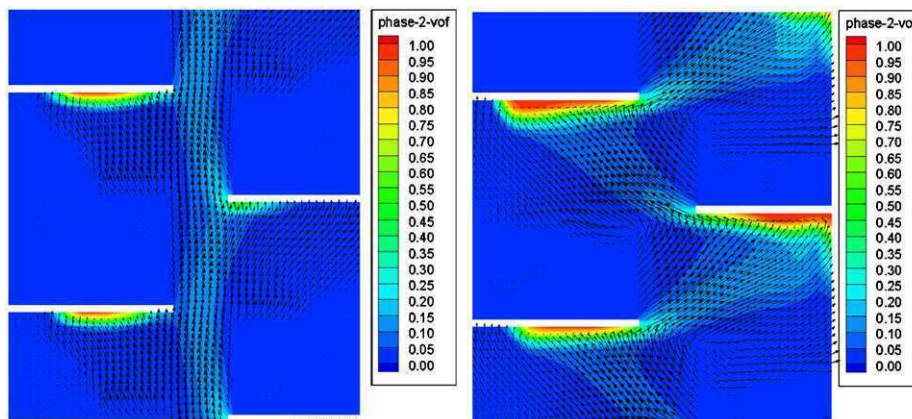


Fig. 6. Predicted velocity vectors (axial and radial velocities) and volume fraction of the dispersed phase, 150 rpm (left), 300 rpm (right).

make a compromise between limited computing power and accuracy, whereas the two-fluid model and the QMOM seem reasonable and worthwhile assumptions in the past and present, while multi-fluid models (both CM and especially MOM) present the future with increasing computing power.

Simulation results for the holdup of the organic phase are depicted in Fig. 6. One can see the path of the dispersed phase for a stirrer revolution of 150 and 300 rpm through the compartment. The droplets do not penetrate the outer regions of the compartment and accumulate under stirrer and walls. Same observations were also made in experiments (Drumm and Bart, 2006). The average volume fraction in one compartment for 150 rpm is around 6%. For 300 rpm the droplets penetrate the region between the stators much more, while the holdup in one extraction compartment increases by 9%. This agrees well with measurements by Modes (2000), where the holdup in an RDC with the same operating conditions and the same geometry was measured around 10% for 300 rpm. While the two-fluid model cannot describe size-specific drop velocities, the results for the holdup are reasonable. For the present liquid–liquid problem the two-fluid model seems less problematic as for common gas–liquid problems, where the bubble size distribution is wider and the absolute bubble velocities and the size-specific influence on the velocities are higher (see e.g. Sanyal et al., 2005; Bhole et al., 2008).

3.2. Drop size distributions

Regarding the drop size distributions, first of all, the discussion should focus on the two solution methods (CM and QMOM) and the influence of the number of classes and moments, respectively. For the model of Coualoglou and Tavlarides (using one set of parameters), different scenarios were carried out for the CM and the QMOM varying the number of classes ($N_c = 8, 15$ and 29) and the number of moments ($N_m = 4, 6$ and 8). The volume coordinate in the CM was discretised using a geometric factor as $V_{i+1}/V_i = 2^{1/q}$ (Litster et al., 1995), where q was chosen to be 2. Fig. 7 shows the volume cumulative drop size distributions dependent on the applied number of classes for the system toluene–water. It can be seen that the drop size distributions for 8 classes is slightly deviant from 15 and 29 classes, while the refinement from 15 to 29 classes produces almost the same distribution. For the QMOM, the moments were computed from the experimental drop size distribution at the inlet. The drop size distribution is reconstructed from the moments as described in Eq. (42). Fig. 8 shows the reconstructed drop size distribution for the different number of tracked moments. The reconstructed distributions are almost identical using 4, 6 and 8 moments at the inlet and outlet of the section. The outlet reconstruction, using 8 moments,

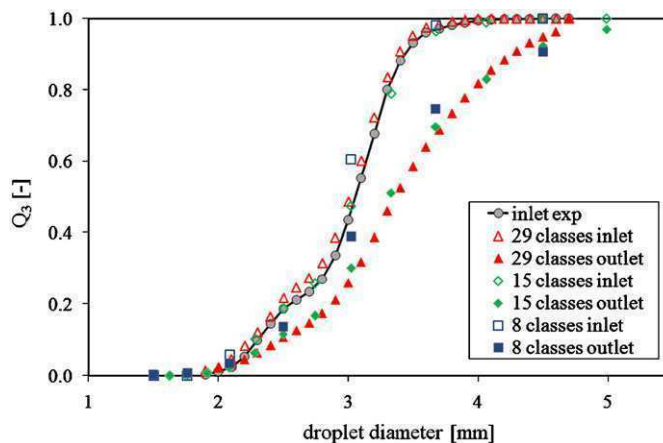


Fig. 7. Influence of the number of classes on the predicted drop size distribution, cumulative volume drop size distribution Q_3 for the system toluene–water (model of Coualoglou and Tavlarides).

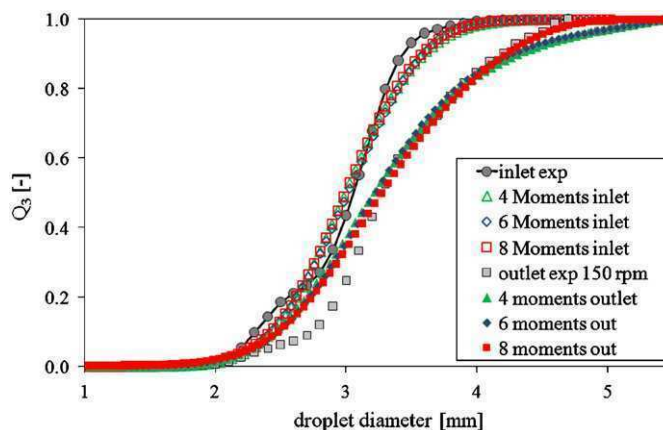


Fig. 8. Influence of the moments (4, 6 and 8 moments) on the reconstruction, cumulative volume drop size distribution Q_3 for the system toluene–water (model of Coualoglou and Tavlarides).

deviates slightly but insignificantly at the head of the distribution (around 4.5 mm). For all three cases the d_{32} is 2.83 mm with a maximum deviation around 0.01% between 4 and 8 moments. The following conclusions can be drawn: 15 classes in the CM are sufficient for

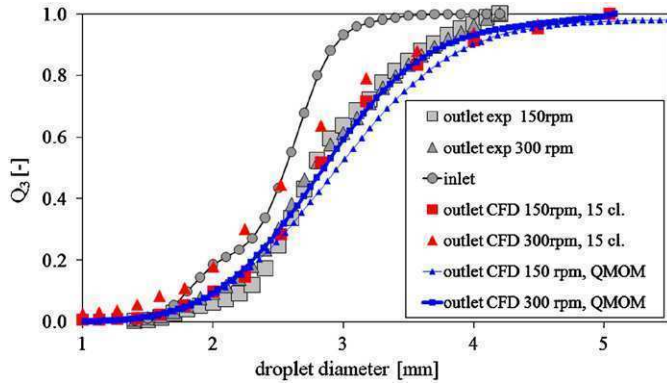


Fig. 9. Cumulative volume drop size distribution Q_3 for the system toluene-water as predicted using the CM and QMOM (model of Coualoglou and Tavlarides).

the description of the problem and seem to be a good trade-off, the number of tracked moments (4, 6 or 8) does not significantly influence the reconstruction of the distributions for the present problem. Sanyal et al. (2005) made the same observations and stated that at least 12–18 classes in the CM are required and 6 moments in the QMOM are sufficient to accurately describe the evolution of the bubble diameters (1–20 mm) in a bubble column. Krepper et al. (2007) specified 20 classes for a bubble size distribution ranging from 1 to almost 30 mm. Marchisio et al. (2003a) stated that the order of magnitude of the errors was very similar in the QMOM when the number of nodes was increased, with three nodes (6 moments) offering the best trade-off between number of scalars and accuracy. In the following simulations, the QMOM was used with 6 moments also as a trade-off, although 4 moments would probably be sufficient, especially since we only focus on the correct prediction of the Sauter mean diameter and not on the perfect reconstruction of the distribution. Reconstructed distributions are only shown for a better comparison of both methods in terms of the drop size distribution. For the system toluene–water 15 (Coualoglou and Tavlarides) and 16 classes (Luo and Svendsen, mixed model) were applied below, while 16 up to 25 classes were applied for the system butyl acetate–water because of the wider distribution.

Regarding the different breakage and coalescence closures, first, the model of Coualoglou and Tavlarides was applied and the parameters in the model were adjusted to match the experimental data. The parameter fitting is not feasible with CFD due to high computational burden (Moilanen et al., 2007). Therefore, the used parameters in the present study cannot be regarded as universally applicable parameters and are only one possible parameter set in the present case. In Fig. 9, measured and simulated volume cumulative drop size distributions at the in- and outlets of the column section are depicted for the system toluene–water. Because of the four adjustable parameters the model of Coualoglou and Tavlarides described the droplet size distribution accurately. Both CM (15 classes) and QMOM (6 moments) using the same parameter set give reliable results. In terms of the QMOM the number of scalars to be tracked is reduced from 15 to 6. This comes together with a lower CPU time and no lower and upper limit on the classes (Marchisio et al., 2003a). The QMOM does not only track the moments with high accuracy but also allows for a reconstruction of the distribution. The results show that a description of experimental data is easily achieved when adjustable parameters are used.

For the model of Luo and Svendsen, the simulation results are shown in Figs. 10 and 11. It can be seen in Fig. 10 that the original model overestimates the coalescence. Therefore, the only parameter in the model c_1 in the coalescence efficiency (Eq. (44)), which is normally of order unity, was adjusted. Good predictions were achieved

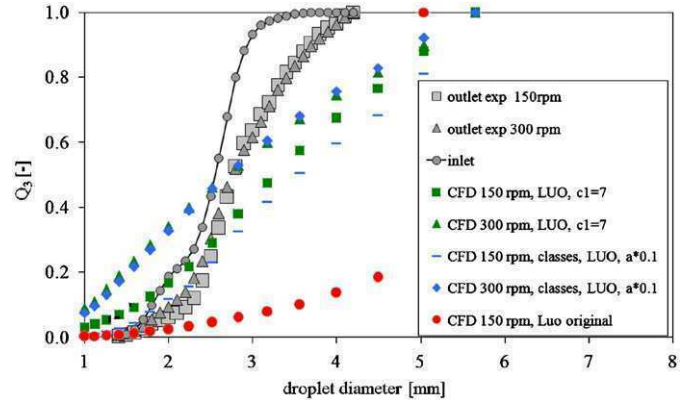


Fig. 10. Cumulative volume drop size distribution Q_3 for the system toluene–water as predicted using the CM (model of Luo and Svendsen).

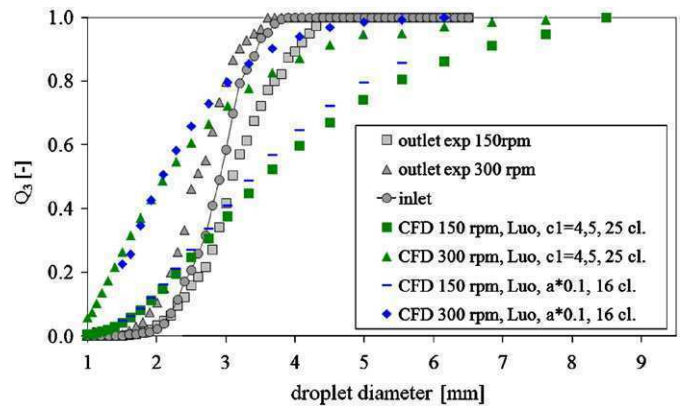


Fig. 11. Cumulative volume drop size distribution Q_3 for the system butyl acetate–water as predicted using the CM (model of Luo and Svendsen).

when the parameter c_1 was set to 7.0 for toluene–water. Chen et al. (2005) tested the model of Luo and Svendsen in a CFD–PBM model for a bubble column and made similar observations that the model predicted coalescence rates are about a factor of 10 higher than the predicted breakup rate. They proposed a constant decrease in the coalescence kernel by a factor 10 (increase breakage 10-fold, respectively). Lo (2000) and Olmos et al. (2001) also multiplied the coalescence rate by a constant less than 1. When the whole coalescence kernel is reduced by a factor of 10 almost the same results were achieved (see Fig. 10). For the system butyl acetate–water the parameter c_1 in the model of Luo and Svendsen had to be set to 4.5 because of the different system properties in comparison to the system toluene–water. On the other hand, this factor is again equal to a constant reduction of factor 10 (see Fig. 11). So the constant factor for the whole coalescence kernel is still valid and seems to be independent from the applied system. The model of Luo and Svendsen allows for a major predictability, since the constant factor 0.1 is more an engineering estimate than an adjustment. One could obtain “better” comparison against experimental data by tweaking this factor but would lose the predictive nature of CFD (Chen et al., 2005).

Recapitulating, the model of Luo and Svendsen overestimates the collision frequency (underestimates breakup). Chen et al. (2005) justified this because of the wrong prediction of the turbulent energy dissipation in the simulation. It has to be pointed out that the investigated models are strong functions of the turbulent energy dissipation. Own investigations, comparing simulations to PIV measurements in single-phase flows, which will be addressed in a

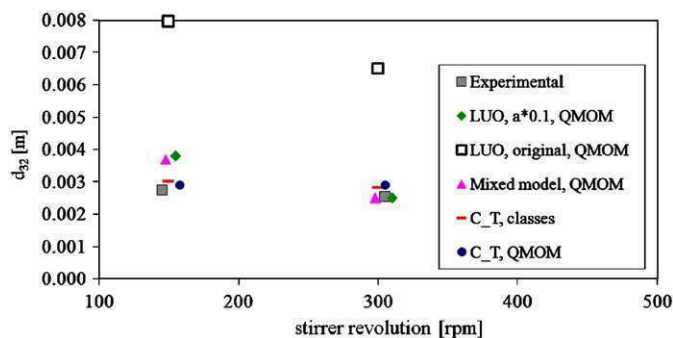


Fig. 12. Sauter mean diameters d_{32} for the system toluene–water using different breakup and coalescence closures.

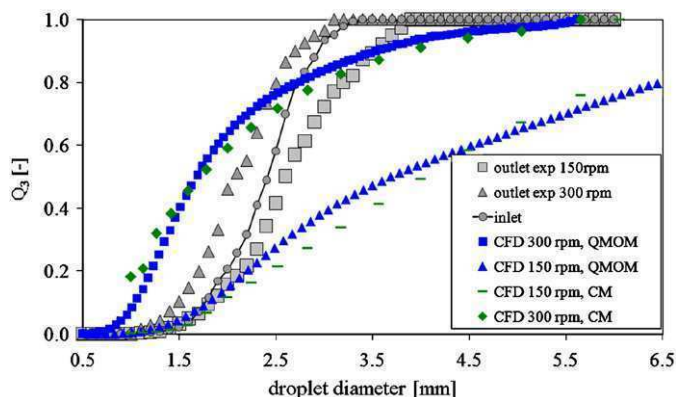


Fig. 13. Cumulative volume drop size distribution Q_3 for the system butyl acetate–water as predicted using the CM and QMOM (mixed model).

forthcoming publication, show that the $k-\varepsilon$ models can predict the volume averaged turbulent energy dissipation with a small error. Unfortunately, the PIV measurements were not possible for the two-phase case, but it is well known that multiphase turbulence still demands improvement (Andersson et al., 2004). If another turbulence model is applied, the present results will probably change. Also the near wall treatment (e.g. wall functions and two layer model) has a big impact on the predicted turbulent energy dissipation. The currently applied turbulence model was chosen because it could predict flow fields phenomena in the RDC extractor, but there is no assurance that it is equally suitable for the prediction of the turbulent energy dissipation in the liquid–liquid flow. In general, experimental investigations or direct measurements of the dissipation rate for two-phase flows were not found in the literature.

There are some possibilities to improve the model of Luo and Svendsen which was developed to model bubble behaviour. For instance, only binary breakup is assumed in the model, which is suitable for bubbles but normally not for droplets, where more than two daughter droplets are formed (Schmidt, 2006). Modes (2000) measured the number of daughter droplets around 2.2 for the present RDC extractor. Therefore, the binary breakage assumption is not far from reality in the present case, but could deviate for other column types (e.g. Kühni column up to 12 daughter droplets, Schmidt, 2006). The Luo and Svendsen daughter droplet size distribution cannot match the physical situation, is very simple when examined separately and overestimates unequal breakage (Lasheras et al., 2002). This contradicts experimental investigations by Andersson and Andersson (2006), where equal sized breakup was the most probable outcome for drop breakup. In further simulations the simple PDF could be replaced by experimentally correlated PDF (Modes, 2000). Another key factor in the description of the breakage rate is the double integral in Eq. (41) where it is assumed that only a turbulent eddy, which is smaller than the droplet, causes breakage. New investigations by Andersson and Andersson (2006) or Eastwood et al. (2004) also showed that eddies bigger than the size of the fluid particle can cause breakup. Future work could take these facts into consideration for a further improvement of the prediction of the droplet size distribution. Also the dominating coalescence kernel could be further improved or replaced by a more suitable coalescence model.

Because of the inconsistencies in the model of Luo and Svendsen the mixed model was chosen. The breakup kernel of Martínez-Bazán is very simple and gives results in the same order of magnitude as the model of Luo and Svendsen, while the CPU time is much lower. On the other hand, because of slightly different assumptions the collision frequency in the model of Prince and Blanch is four times less than in the model of Luo and Svendsen. For the system toluene–water the predicted Sauter mean diameters using the QMOM are visible in Fig. 12. The results for the system butyl acetate–water are visible in Fig. 13. Again the CM and the QMOM was carried out and as before

the drop size distribution can be reconstructed from the moments and approximates the results of the CM. The results for 150 rpm are slightly deviant, while the prediction for the higher stirrer speed (300 rpm) is very good. The mixed model gives results with a deviation less than 30% for the Sauter mean diameters independent of the system, whereas no parameters had to be adjusted. The results show that a prediction of the droplet size distribution is possible, even when no adjustable parameters are used.

As a concluding overview, the Sauter mean diameters for different simulation cases using the system toluene–water are depicted in Fig. 12. The predicted Sauter mean diameters for the model of Coualaloglou and Tavlarides reflect the experimental data accurately because of the adjustable parameters. The original model of Luo and Svendsen calculates a Sauter mean diameter, which is more than 100%, oversized. When the parameter c_1 is adjusted or the whole aggregation kernel is tweaked by a factor 0.1 the deviation is less than 30% for both systems in respect to the experiments. For the mixed model the deviation for the Sauter mean diameter is less than 30% for both systems without using any adjustable parameters.

4. Summary and conclusions

In this work, a combination of CFD and DPBM in the framework of Fluent was applied to simulate the drop size distributions in a five-compartment section of a liquid–liquid RDC extractor. The liquid–liquid flow was modeled using the realizable $k-\varepsilon$ turbulence model in conjunction with the Eulerian two-fluid equations. For the solution of the PBM the CM (Kumar and Ramkrishna, 1996) and the QMOM (McGraw, 1997; Marchisio et al., 2003a, b) were used. Theoretical models for coalescence and breakup, the models of Luo and Svendsen (1996), Coualaloglou and Tavlarides (1977) and a mixed model (Martínez-Bazán et al., 1999; Prince and Blanch, 1990) were implemented in the CFD code as UDFs. A complete coupling was applied, where the velocity of the dispersed phase in the convective term of the PBM and the volume fraction and energy dissipation in the source terms of the PBM were taken from CFD simulations. On the other hand the calculated Sauter mean diameter influenced the drag force term of the flow field.

Good agreement was obtained compared to the experimental drop holdup, path of the droplets and velocity fields, showing that the coupled model can predict the hydrodynamics in a stirred extraction column. Terminal velocities were presented, which can be predicted from the applied drag law. Although the two-fluid model cannot describe size-specific velocities it presents a reasonable and worthwhile assumption for coupled CFD–PBM simulations, where a lot of additional scalars have to be solved and the computing power

is the limiting factor. Nevertheless, multi-fluid models will further improve the coupled simulations with increasing computing power in the future. Especially the method of moments (as the SQMOM) appears to be the correct choice in this connection to counter-balance the necessary additional computing power for the additional momentum equations and to account for a high accuracy.

Regarding the drop size distribution, the QMOM using 6 moments, gives accurate results together with a much lower CPU time and no limits on the classes. In the CM, 16 classes (toluene–water), respectively 25 classes (butyl acetate–water) are sufficient. For the model of Coulaloglou and Tavlarides, the results for the system toluene–water showed that the combined CFD–DPBM approach is able to describe the droplet size distribution in an RDC extractor very accurately, when the parameters in the model are adjusted. The model of Luo and Svendsen allows for a straightforward predictability, since only one parameter was changed and gave also acceptable results in terms of the droplet size distribution and the Sauter mean diameter. In this connection, it is noteworthy that the constant scaling factor of 0.1 for the whole coalescence kernel could be successfully applied for both systems. For the mixed model, reliable results were obtained for both systems, without any adjustable parameter.

The results show that a prediction of the droplet size distribution is possible, even when no adjustable parameters are used. However, a lot of future work is needed to allow for a prediction of the drop size distribution in extractions columns without any adjustable parameters. Mainly, there seems to be a need for more investigations on multiphase turbulence models and experimental work. Some general possible model improvements for the model of Luo and Svendsen were mentioned. The performance for an entire extraction column, different test systems and stirrer geometries should also be further investigated in this connection. In summary, the present coupled CFD–PBM model removed some prior assumptions and simplifications and could be further improved in future work when more than one velocity groups are applied in the framework of a multi-fluid model for the dispersed phase.

Notation

a	coalescence kernel
A_i	reconstruction coefficient
B_0	reconstruction coefficient
B	birth rates
$B_{i,j}$	contribution due to breakage
c_f	coefficient of surface area
C	adjustable parameters
C_D	drag coefficient
d	droplet diameter
d_{32}	Sauter mean diameter
D	death rates
f	drag coefficient
f_v	breakup fraction
F	interaction force
g	gravity
g	breakage frequency
h	collision frequency
h_0	initial film thickness
h_c	critical film thickness
K	adjustable parameter
L	droplet size
L	abscissa
m_k	kth moment
M	total number of classes
N_i	local average number density

n	number density function
p	pressure
Re	Reynolds number
S	source term
S_k	moment source term
t	time
u	velocity
V	volume
w	weight
We	Weber number
x	coordinate
x_m	number daughter droplets

Greek letters

α	volume fraction
β_0	numerical constant
β	probability density function
γ	virtual mass coefficient
δ	Kronecker delta
ε	turbulent energy dissipation
η	reassignment variable
λ	coalescence efficiency
μ	viscosity
μ_t	turbulent viscosity
ξ	size ratio eddy/droplet droplet/droplet
ρ	density
σ	interfacial tension
τ	relaxation time

Subscripts

c, d	continuous and dispersed phase
l	liquid phase l
m	mixture

Abbreviations

CFD	computational fluid dynamics
CM	classes method
DPBM	droplet population balance model
MOM	method of moments
MUSIG	multiple-size-group
PBM	population balance model
PDF	probability density function
PIV	particle image velocimetry
QMOM	quadrature method of moments
SQMOM	sectional quadrature method of moments
rpm	revolutions per minute

Acknowledgement

This work was financially supported by the Deutsche Forschungsgemeinschaft (DFG).

References

- Alopaevs, V., Koskinen, J., Keskinen, K.I., 1999. Simulation of the population balances for liquid–liquid systems in a nonideal stirred tank. Part 1 description and qualitative validation of the model. *Chemical Engineering Science* 54, 5887–5899.
- Andersson, R., Andersson, B., 2006. On the breakup of fluid particles in turbulent flows. *A.I.Ch.E. Journal* 52 (6), 2020–2030.
- Andersson, R., Andersson, B., Chopard, F., Noren, T., 2004. Development of a multi-scale simulation method for design of novel multiphase reactors. *Chemical Engineering Science* 59, 4911–4917.
- Attarakih, M.M., Bart, H.-J., Lagar, L.G., Faqir, N.M., 2006. LLECMOD: a Windows-based program for hydrodynamics simulation of liquid–liquid extraction columns. *Chemical Engineering Processing* 45, 113–123.
- Attarakih, M.M., Drumm, C., Bart, H.-J., 2008. Solution of the population balance equation using the sectional quadrature method of moments. In: *Chemical Engineering Science*, this issue, doi:10.1016/j.ces.2008.05.006.

- Bahmanyar, H., Slater, M.J., 1991. Studies of drop-break-up in liquid–liquid systems in a rotating disc contactor part I: conditions of no mass transfer. *Chemical Engineering Technology* 14, 79–89.
- Baldyga, J., Orciuch, W., 2001. Barium Sulphate precipitation in a pipe—an experimental study and CFD modelling. *Chemical Engineering Science* 56, 2435–2444.
- Bart, H.-J., Stevens, G., 2004. Reactive solvent extraction. In: Kertes, M., Sengupta, A.K. (Eds.), *Ion Exchange and Solvent Extraction*, vol. 17. Marcel Dekker, New York, pp. 37–82.
- Bhole, M.R., Joshi, J.B., Ramkrishna, D., 2008. CFD simulation of bubble columns incorporating population balance modeling. *Chemical Engineering Science* 63, 2267–2282.
- Chen, P., Sanyal, J., Dudukovic, M.P., 2005. Numerical simulation of bubble column flows: effect of different breakup and coalescence closures. *Chemical Engineering Science* 60, 1085–1101.
- Coulaloglou, C.A., Tavlirides, L.L., 1977. Description of interaction processes in agitated liquid–liquid dispersions. *Chemical Engineering Science* 32, 1289–1297.
- Drumm, C., Bart, H.-J., 2006. Hydrodynamics in a RDC extractor: single and two-phase PIV measurements and CFD simulations. *Chemical Engineering Technology* 29, 1297–1302.
- Drumm, C., Tiwari, S., Attarakih, M.M., Kuhnert, J., Bart, H.-J., 2008a. CFD–PBM coupled model using the finite point set method and the SQMOM. In: *Proceedings of the International Solvent Extraction Conference 2008 (ISEC)*, Tucson, USA.
- Drumm, C., Attarakih, M.M., Tiwari, S., Kuhnert, J., Bart, H.-J., 2008b. Implementation of the Sectional Quadrature Method of Moments in a CFD code. In: *Proceedings of the 6th International Conference on CFD in the Process Industries CFD 2008*, Trondheim, Norway.
- Eastwood, C.D., Armi, L., Lasheras, J.C., 2004. The breakup of immiscible fluids in turbulent flows. *Journal of Fluid Mechanics* 502, 309–333.
- Fei, W.Y., Wang, Y.D., Wan, Y.K., 2000. Physical modeling and numerical simulation of velocity fields in rotating disc contactor via CFD simulation and LDV measurements. *Chemical Engineering Journal* 78, 131–139.
- Fluent 6.2 user's guide, 2005. Fluent, Inc., Lebanon.
- Gourdon, C., Casamatta, G.A., Muratet, G., 1994. Population balance based modelling. In: Godfrey, J.C., Slater, M.J. (Eds.), *Liquid–Liquid Extraction Equipment*. Wiley, West Sussex, pp. 141–226.
- Hosokawa, S., Sou, A., Tomiyama, A., 2007. Multi-fluid simulation of turbulent bubbly pipe flows. In: Sommerfeld, M. (Ed.), *Proceedings of the 6th International Conference on Multiphase Flow, ICMF-2007*, Leipzig.
- Hounslow, M.J., Ryall, R.L., Marshall, V.R., 1988. A discretized population balance for nucleation, growth and aggregation. *A.I.Ch.E. Journal* 34, 1821–1832.
- Hulburt, H.M., Katz, S., 1964. Some problems in particle technology. *Chemical Engineering Science* 19, 555–574.
- Jakobsen, H.A., Lindborg, H., Dorao, C.A., 2005. Modeling of bubble column reactors: progress and limitations. *Industrial & Engineering Chemistry Research* 44, 5107–5151.
- John, V., Angelov, I., Öncül, A.A., Thévenin, D., 2007. Techniques for the reconstruction of a distribution from a finite number of its moments. *Chemical Engineering Science* 62, 2890–2904.
- Krepper, E., Frank, T., Lucas, D., Prasser, H.-M., Zwart, P.J., 2007. Inhomogeneous MUSIG model—a population balance approach for polydispersed bubbly flows. In: Sommerfeld, M. (Ed.), *Proceedings of the 6th International Conference on Multiphase Flow, ICMF-2007*, Leipzig.
- Kronberger, T., Ortner, A., Zulehner, W., Bart, H.-J., 1995. Numerical simulation of extraction columns using a drop population model. *Computers and Chemical Engineering* 19, 639–644.
- Kumar, S., Ramkrishna, D., 1996. On the solution of population balance equations by discretization—I. A fixed pivot technique. *Chemical Engineering Science* 51, 1311–1332.
- Lasheras, J.C., Eastwood, C., Martínez-Bazán, C., Montañés, J.L., 2002. A review of statistical models for the break-up of an immiscible fluid immersed into a fully developed turbulent flow. *International Journal of Multiphase Flow* 28, 247–278.
- Lehr, F., Millies, M., Mewes, D., 2002. Bubble-size distributions and flow fields in bubble columns. *A.I.Ch.E. Journal* 48, 2426–2442.
- Litster, J.D., Smit, D.J., Hounslow, M.J., 1995. Adjustable discretization population balance for growth and aggregation. *A.I.Ch.E. Journal* 41, 591–603.
- Lo, S., 2000. Application of population balance to CFD modelling of gas–liquid reactors. In: *Proceedings of the Trends in Numerical and Physical Modeling for Industrial Multiphase Flows*, Corsica, France.
- Luo, H., Svendsen, H.F., 1996. Theoretical model for drop and bubble breakup in turbulent dispersions. *A.I.Ch.E. Journal* 42, 1225–1233.
- Marchisio, D.L., Pikturna, J.T., Fox, R.O., Vigil, R.D., Barresi, A.A., 2003a. Quadrature method of moments for population-balance equations. *A.I.Ch.E. Journal* 49, 1266–1276.
- Marchisio, D.L., Vigil, R.D., Fox, R.O., 2003b. Implementation of the quadrature method of moments in CFD codes for aggregation-breakage problems. *Chemical Engineering Science* 58, 3337–3351.
- Martínez-Bazán, C., Montañés, J.L., Lasheras, J.C., 1999. On the breakup of an air bubble injected into a fully developed turbulent flow. Part 1. Breakup frequency. *Journal of Fluid Mechanics* 401, 157–182.
- McGraw, R., 1997. Description of aerosol dynamics by the quadrature method of moments. *Aerosol Science and Technology* 27, 255–265.
- Modes, G., 2000. Grundlegende Studie zur Populationsdynamik einer Extraktionskolonne auf Basis von Einzeltropfenuntersuchungen, Dr.-Ing. Thesis TU Kaiserslautern. Shaker Verlag, Aachen.
- Modes, G., Bart, H.-J., 2001. CFD simulation of nonideal dispersed phase flow in stirred extraction columns. *Chemical Engineering Technology* 24, 1242–1245.
- Moilanen, P., Laakonen, M., Visuri, O., Aittamaa, J., 2007. Modeling local gas–liquid mass transfer in agitated viscous shear-thinning dispersions with CFD. *Industrial & Engineering Chemistry Research* 46, 7289–7299.
- Olmos, E., Gentric, C., Vial, C., Wild, G., Midoux, N., 2001. Numerical simulation of multiphase flow in bubble column reactors. Influence of bubble coalescence and break-up. *Chemical Engineering Science* 56, 6359–6365.
- Pope, S.B., 1979. Probability distributions of scalars in turbulent shear flow. In: *Turbulent Shear Flows 2: Selected Papers from the Second International Symposium on Turbulent Shear Flows*. Springer, Berlin, pp. 7–16.
- Prince, M.J., Blanch, H.W., 1990. Bubble coalescence and break-up in air-sparged bubble columns. *A.I.Ch.E. Journal* 36, 1485–1499.
- Ramkrishna, D., 2000. *Population Balances: Theory and Applications to Particulate Systems in Engineering*. Academic Press, San Diego.
- Rieger, R., Weiss, C., Wigley, G., Bart, H.-J., Marr, R., 1996. Investigating the process of liquid–liquid extraction by means of computational fluid dynamics. *Computers and Chemical Engineering* 20, 1467–1475.
- Sanyal, J., Marchisio, D.L., Fox, R.O., Dhanasekharan, K., 2005. On the comparison between population balance models for CFD simulation of bubble columns. *Industrial & Engineering Chemistry Research* 44, 5063–5072.
- Schlauch, S., 2006. Numerical simulation of stirred liquid–liquid systems. *Proc. Appl. Math. Mech.* 6, 541–542.
- Schiller, L., Naumann, Z., 1935. Über die grundlegenden Berechnungen bei der Schwerkraftaufbereitung. *Zeitschrift des Vereines Deutscher Ingenieure* 77, 143.
- Schmidt, S.A., 2006. Populationsdynamische Simulation gerührter Extraktionskolonnen auf der Basis von Einzeltropfen- und Tropfenschwarmuntersuchungen. Dr.-Ing. Thesis TU Kaiserslautern. Shaker Verlag, Aachen.
- Schmidt, S.A., Simon, M., Attarakih, M., Lagar, L.G., Bart, H.-J., 2006. Droplet population balance modelling—hydrodynamics and mass transfer. *Chemical Engineering Science* 61, 246–256.
- Simon, M., 2004. Koaleszenz von Tropfen und Tropfenschwärmen. Dr.-Ing. Thesis TU Kaiserslautern, Kaiserslautern.
- Steinmetz T, Schmidt S, Attarakih M, Bart, H.-J., 2005. Droplet population balancing for column simulation. In: *Proceedings of the International Solvent Extraction Conference (ISEC 2005)*. China Academic Journal (compact disc version) Electronic Publishing House, Beijing, pp. 997–1003.
- Thornton, J.D., 1992. *Science and Practice of Liquid–Liquid Extraction*. Oxford University Press, Oxford.
- Tomiyama, A., Shimada, N., 2001. A numerical method for bubbly flow simulation based on a multi-fluid model. *Journal of Pressure Vessel Technology* 123, 510–516.
- Valentas, K.J., Bilous, O., Amundson, N.R., 1966. Analysis of breakage in dispersed phase systems. *Industrial & Engineering Chemistry Fundamental* 5, 271–279.
- Vikhansky, A., Kraft, 2004. Modelling of a RDC using a combined CFD-population balance approach. *Chemical Engineering Science* 59, 2597–2606.
- Wang, F., Mao, Z.-S., 2005. Numerical and experimental investigation of liquid–liquid two-phase flow in stirred tanks. *Industrial & Engineering Chemistry Research* 44, 5776–5787.
- Wang, T., Wang, J., Jin, Y., 2006. A CFD–PBM coupled model for gas–liquid flows. *A.I.Ch.E. Journal* 52, 125–140.
- Wegener, M., Grünig, J., Stüber, J., Paschedag, A.R., Kraume, M., 2007. Transient rise velocity and mass transfer of a single drop with interfacial instabilities—experimental investigations. *Chemical Engineering Science* 62, 2967–2978.
- Wulkow, M., Gerstlauer, A., Niekem, U., 1999. Parsival: a tool for the simulation of crystallization processes. *Chemische Technik* 51, 249–252.
- You, X., Xiao, X., 2005. Simulation of the three-dimensional two-phase flow in stirred extraction columns by Lagrangian–Eulerian method. *Chemical and Biochemical Engineering Quarterly* 19, 1–11.

Publication X

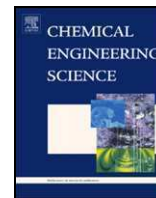
Reprinted from Chemical Engineering Science, 64, 742-752, **2009**,

Menwer Attarakih, Christian Drumm, Hans-Jörg Bart,

Solution of the population balance equation using the sectional quadrature method of moments (SQMOM).

Reprinted with permission from Elsevier.

<http://dx.doi.org/10.1016/j.ces.2008.05.006>



Solution of the population balance equation using the sectional quadrature method of moments (SQMOM)

Menwer M. Attarakih^{a,*}, Christian Drumm^b, Hans-Jörg Bart^b

^aAl-Balqa Applied University, Faculty of Engineering Technology, Chemical Engineering Department, PO. Box 15008, Marka 11134, Amman, Jordan

^bTU Kaiserslautern, Lehrstuhl für Thermische Verfahrenstechnik, POB 3049, 67653 Kaiserslautern, Germany

ARTICLE INFO

Article history:

Received 12 November 2007

Received in revised form 11 March 2008

Accepted 5 May 2008

Available online 16 May 2008

Keywords:

Population balance

Agglomeration

Model reduction

Simulation

Quadrature methods

Sectional methods

ABSTRACT

A discrete framework is introduced for simulating the particulate physical systems governed by population balance equations (PBE) with particle splitting (breakage) and aggregation based on accurately conserving (from theoretical point of view) an unlimited number of moments associated with the particle size distribution. The basic idea is based on the concept of primary and secondary particles, where the former is responsible for distribution reconstruction while the latter is responsible for different particle interactions such as splitting and aggregation. The method is found to track accurately any set of low-order moments with the ability to reconstruct the shape of the distribution. The method is given the name: the sectional quadrature method of moments (SQMOM) and has the advantage of being not tied to the inversion of large sized moment problems as required by the classical quadrature method of moments (QMOM). These methods become ill conditioned when a large number of moments are needed to increase their accuracy. On the contrary, the accuracy of the SQMOM increases by increasing the number of primary particles while using fixed number of secondary particles. Since the positions and local distributions for two secondary particles are found to have an analytical solution, no large moment inversion problems are anymore encountered. The generality of the SQMOM is proved by showing that all the related sectional and quadrature methods appearing in the literature for solving the PBE are merely special cases. The method has already been extended to bivariate PBEs.

© 2008 Elsevier Ltd. All rights reserved.

1. Introduction

The population balance equation (PBE) forms nowadays the cornerstone for modeling polydispersed (discrete) systems arising in many engineering applications such as aerosols dynamics, nanoparticle generation, crystallization, precipitation (protein precipitation), mining (granulation), liquid–liquid (liquid–liquid extraction (physical and reactive), emulsion polymerization, activated sludge flocculation), gas–liquid (bubble column reactors, bioreactors, nucleate boiling, evaporation, condensation), gas–solid (fluidized bed reactors), combustion processes (turbulent flame reactors) and microbial systems (multivariable cell population) (Randolph and Larson, 1988; Ramkrishna, 2000; Rosner et al, 2003; Cameron et al., 2005; Dhanasekharan et al., 2005). The population balance modeling lays down a modern approach for modeling the complex behavior of such systems. This complex behavior is in part a consequence of the multiscale processes that take place. For example the particle forces are

strongly dependent on the shape and size of the particles, which can affect the terminal velocity (Sha et al., 2006). For this reason, the modeling of the particle size distribution can bring new possibilities for getting more accurate prediction of polydispersed systems behavior. In this way, the PBE can be used to improve the modeling of two-phase flow problems. To account for this polydispersed nature, the dispersed phase is represented in terms of a density function. The evolution of this density function is dictated by the different active mechanisms involved such as splitting (breakage), aggregation (coalescence), growth, and so on. The accurate prediction of the dispersed phase evolution depends strongly on the proper modeling of the different processes including the continuous flow field in which the particles are dispersed (Rosner et al, 2003; Sha et al., 2006).

The challenges in modeling these processes are due to the discrete nature of particles whose states are not only affected by the particle–particle interactions, but also due to interaction of these particles with their continuous environment. The results of these interactions lead to different active mechanisms such as particle splitting, attrition, aggregation, growth and nucleation. The resulting model equations of these mechanisms range from integro-differential to integro-partial differential equations with no general

* Corresponding author. Tel.: +962 6 5158587; fax: +962 6 4894294.

E-mail address: attarakih@yahoo.com (M.M. Attarakih).

analytical solutions. As a result of this, the numerical solution of these types of problems has been an active area of research for the last three decades. However, most numerical methods have focused on the specifics of the problem of interest. Accordingly, there exist many numerical methods in the literature as attempts to solve certain type of PBEs. These methods range from simple finite difference schemes (FDS) or sectional methods using linear grids (in terms of particle diameters) to Galerkin and orthogonal collocations methods on finite elements. An exhaustive review of the available numerical methods is presented by Attarakih et al. (2004a, 2006) and Cameron et al. (2005). In the FDS the particle population is discretized into a finite number of intervals that are used to track the population density directly. The FDS are particularly useful when the particle sizes do not vary widely. On the other hand, one limitation of the FDS is their inability to predict accurately integral quantities (low-order moments as a special case) associated with populations of sharp shapes (Ramkrishna, 2000; Attarakih et al., 2006). The quadrature method of moments (QMOM) as first introduced by McGraw (1997) to solve the PBE with pure growth is found very efficient from accuracy and computational cost point of view. Unlike the FDS (sectional) methods, the QMOM has a drawback of destroying the shape of the distribution and the information about the distribution is only stored in its moments. The r th moment is defined by integrating the population number density function with respect to certain population property (e.g. particle sizes) weighted with this property raised to its r th power. When r equals zero the zero moment represents the total number of particles per unit volume; on the other hand, when r equals three the third moment represents the volume fraction (volume concentration) of the particles. The QMOM tracks the population moments (e.g. the zero and third moments) rather than its size and hence it does not depend on the minimum and maximum particle sizes. A closure problem arises since the integral terms appearing in the PBE could not be written generally in terms of the moments only. This closure is due to the specific forms of the breakage and aggregation frequencies which depend in turn on the type of the physical application of the PBE. The QMOM is used here in order to close approximately these integrals by using a Gauss-like quadrature (numerical integration). The solution for the abscissas (nodes) and weights used in this quadrature requires the solution of an eigenvalue problem in terms of the population low-order moments. These eigenvalues are roots of a polynomial equation resulting from the approximation of the number density function (integrand) by a polynomial of a specified degree that equals the desired number of low-order moments (Piskunov and Golubev, 2002). Unfortunately, as the number of the low-order moments increases, the solution of the associated eigenvalue problem becomes difficult due to ill conditioning (increasing of round off errors). Or equivalently, if the weights and abscissas are tracked directly (Marchisio and Fox, 2005) the solution of the resulting linear system becomes ill conditioned and hence difficult to solve with sufficient accuracy. A recent comparison between the QMOM and the FDS could be found in Attarakih et al. (2006).

So, the objective of this work is to answer the question: Is it possible to have a numerical scheme that retains the advantages of the QMOM without destroying the shape of the distribution? The answer to this question seems to be yes. It is found that all the attempts made previously to increase the accuracy of the FDS such as the fixed and moving pivot techniques (Ramkrishna, 2000) or the conservative discretization approach (CDA) of the present authors (Attarakih et al., 2004b) are all merely limited answers to the above question. Here, a unified and general numerical approach for a wide class of population balance problems is introduced, which will serve as a valuable computational interface for revealing important similarities in the dynamical behavior of particulate and dispersed phase systems. The idea is based on dividing the particle state (for example, the particle

size) into arbitrary contiguous partitions. In each partition, the population density function is represented by primary particles carrying sufficient information about the shape of the original distribution. The population in a given partition is allowed to interact with that in the others through what is called the secondary particles. These particles carry enough information about the local variations of the population density function through their local low-order moments. Since the evolution of the population density function in time and space is governed by the number of primary and secondary particles in each section, and hence their sectional moments, the method is given the name: The Sectional Quadrature Method Of Moments (SQ-MOM). In this way, the SQMOM combines the idea of self-distribution reconstruction (since it resembles the FDS) and the QMOM. However, the difficulty encountered in solving the ill-conditioned eigenvalue problem associated with the QMOM is avoided here by considering small number of secondary particles (small size eigenvalue problem) at the expense of increasing the number of primary particles (increasing the number of sections).

In the following sections, the method is introduced and thoroughly tested using the available analytical solutions when it is possible. It is found that the SQMOM is very accurate in solving the PBEs, furnish a Gauss-like quadrature to evaluate any integral quantities associated with the population density and converges very fast as the number of primary and secondary particles is increased. The extension of the method to a bivariate case is also introduced as a bivariate SQMOM (BVSQMOM).

2. The PBE

The superstructure of the PBE and the general derivation based on the Reynold transport theorem is given in Ramkrishna (2000). However, a special case of this equation required to introduce the SQMOM is stated in Eqs. (1) and (2) below. This does not mean that the SQMOM is limited to this special case, but the additional features of the detailed PBE are easily added if they are required. The PBE describing particle splitting, aggregation, entering and leaving a fixed homogeneous subspace could be stated as

$$\tau \frac{\partial f(v, t)}{\partial t} = f^{\text{in}}(v, t) - f(v, t) + \tau \rho \{f(v, t), v, t\} \quad (1)$$

$$\begin{aligned} \rho = & -\Gamma(v)f(v, t) + \int_v^{v_{\text{max}}} \Gamma(v', t)\beta(v|v')f(v', t)\delta v' \\ & - f(v, t) \int_{v_{\text{min}}}^{v_{\text{max}}} \omega(v, v')f(v', t)\delta v' \\ & + \frac{1}{2} \int_{v_{\text{min}}}^v \omega(v - v', v')f(v - v', t)f(v', t)\delta v' \end{aligned} \quad (2)$$

Since the particles are assumed to have in general a spectrum of sizes, this spectrum could be represented by a number density function with particle size as an independent variable. So, let $f(v, t)\delta v$ be the average number of particles per unit volume of a fixed subspace at time t ; then the above number continuity equation is formally interpreted as: The first term on the left-hand side denotes the accumulated particles of size v during a space time of magnitude τ . The first two terms on the right-hand side is the net number of particles entering and leaving a given homogeneous subspace during a space time τ . The source term (due to splitting and aggregation as given by Eq. (2)) is rather complex and consists of two parts: The formation terms (preceded by plus signs) and loss terms (preceded by minus signs). The splitting and aggregation of particles are governed by splitting and aggregation frequencies, respectively. The splitting frequency ($\Gamma(v)$) represents the fraction of particles splitting per unit time, while the aggregation frequency ($\omega(v, v')$) accounts for the probability of successful collisions between a pair of particles. The splitting of a mother particle of size v' to daughter particles

having a spectrum of sizes is given by the daughter particle distribution $\beta(v|v')$. For the case of binary breakage the integral of this daughter particle distribution should be equal to two and the distribution itself vanishes for $v \geq v'$. The functional forms of these frequencies are problem dependent and dictate the particular cases of the PBEs (Ramkrishna, 2000).

3. Splitting frequency

To complete the description of particle splitting, models for splitting frequency as well as the daughter particle distribution should be completely defined. Unfortunately, these models are problem dependent and hence could not be generally defined without resource to the equipment geometry. As an example, for droplet splitting in liquid–liquid dispersions, it is experimentally observed that the droplet splitting is mainly determined by the action of the shearing force resulting from the rotating discs as well as turbulent energy dissipation of the continuous phase (Cauwenberg et al., 1997). On the other hand, particle splitting during granulation is governed by the high shear forces during collision of particles with each other and the wall or impeller (Cameron et al., 2005). Nevertheless, the splitting frequency is usually proportional to the particle size and is a function of the continuous environment physical properties (mainly the surface tension), particle residence time, and the energy input. The daughter particle distribution is usually correlated using a certain type of the β -distribution (Schmidt et al., 2006).

4. Aggregation frequency

Aggregation (coalescence) results from the successful collision between at least two particles to produce a new composite particle. In general, the particle aggregation is more complex than the particle splitting since it involves the interaction between two particles and the intervening film from the continuous environment in case of liquid and gas bubbles. For solid particles, the success of collisions could be a function of binder and powder physical properties, particle size and operational factors such as powder velocity and bed height (Cameron et al., 2005). The aggregation frequency is usually correlated as a product of collision rate and coalescence efficiency based on the kinetic theory of gases (Coulaloglou and Tavlarides, 1977; Schmidt et al., 2006).

5. The primary and secondary particles concept

In the finite difference or sectional methods the particle size (here it is denoted by the particle diameter: d) is discretized into finite number of sections: N_{pp} . The population in each section is considered to behave like a single particle, and hence it is concentrated at a representative size usually at the middle of the section. In the present framework of discretization, this single particle will be called the primary particle and it will be responsible for the reconstruction of the distribution. In this way, the greater the number of primary particles (N_{pp}), the more accurate is the reconstruction of the distribution. Unfortunately, large number of primary particles in the classical sectional methods is required, not only to reconstruct the shape of the distribution, but also to estimate the desired integral quantities associated with the distribution (such as the total number of particles and the mean particle size). This in turn increases the computational loads extensively when the PBE is coupled, for example, with CFD packages (Marchisio and Fox, 2005).

The interaction between primary particles in different sections, due to breakage or/and coalescence events for example, results in a new primary particle with no representative size due to the discrete approximation of the distribution. Because the newly birthed particle could not conserve any of its low-order moments but

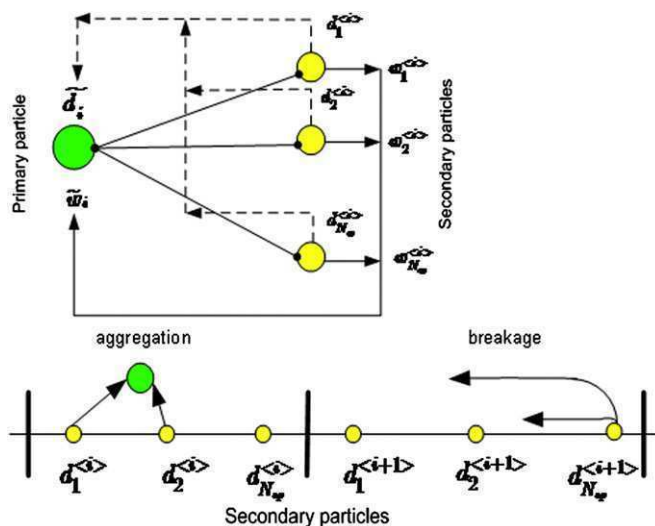


Fig. 1. The concept of primary and secondary particles. The upper panel is the secondary particle interactions leading either to splitting or aggregation, while the lower panel shows how the primary particles are reconstructed from the secondary ones.

one (if it is located at the middle of the section), the rest of the low-order moments are predicted with low accuracy and hence the associated integral quantities. To overcome this fundamental problem of the sectional methods, N_{sp} secondary particles are generated in each section with positions (abscissas) that are given by: $d_j^{(i)}$: $j = 1, 2, \dots, N_{sp}, i = 1, 2, \dots, N_{pp}$ (see Fig. 1 upper panel). Note that the number of the secondary particles that dictates the desired number of low-order moments to be conserved. It is clear from this presentation that each primary particle has its own secondary particles identified by their positions (sizes) and total number concentration associated with them (weights: $w_j^{(i)}$: $j = 1, 2, \dots, N_{sp}, i = 1, 2, \dots, N_{pp}$) as it is shown in Fig. 1). This results from partitioning the population density in each section between these particles, according to the variation of the population density in this section, by assigning weights ($w_j^{(i)}$: $j = 1, 2, \dots, N_{sp}, i = 1, 2, \dots, N_{pp}$) to each particle. It is found that the value of the weights and the location of the particles depend on the shape of the number density function, where the positions of the secondary particles reflect the shape of this function in the i th section. The secondary particles are exactly equivalent to the number of quadrature points in Gauss-like quadratures or the QMOM. Accordingly, each secondary particle could conserve or reproduce two low-order moments and in general $2N_{sp}$ moments in each section; and hence the method is given the name sectional QMOM (SQMOM). The way in which the SQMOM works are started by dividing the particle size into N_{pp} contiguous sections. Each section is then seeded by the desired number of secondary particles which carry detailed information about the distribution. In this framework, the active particle mechanisms such as splitting and aggregation occur through interactions between the secondary particles because at this stage the primary particles are not yet formed. It is obvious from Fig. 1 (the upper panel) that $N_{sp} \times N_{pp}$ particles are contributing in the splitting and aggregation events. Due to the increase of the number of interacting particles, more information is gathered about the distribution itself. This distribution could be reconstructed from the secondary particles by averaging the total weights of the secondary particles with respect to the section width (Δd_i) and locating it at the mean size of the secondary particles as shown in Fig. 1 (the lower panel).

These operations of averaging are carried out for all primary particles as follows:

$$\tilde{w}_i(t) = \frac{1}{\Delta d_i} \sum_{j=1}^{N_{sp}} w_j^{(i)}, \quad i = 1, 2, \dots, N_{pp} \quad (3)$$

$$\tilde{d}_i(t) = \frac{\sum_{j=1}^{N_{sp}} w_j^{(i)} d_j^{(i)}}{\sum_{j=1}^{N_{sp}} w_j^{(i)}}, \quad i = 1, 2, \dots, N_{pp} \quad (4)$$

In a purely mathematical sense, the above presentation is equivalent to applying the QMOM to each section of an arbitrary width: $[d_{i-1/2}, d_{i+1/2}] : i = 1, 2, \dots, N_{pp}$ resulting in a set of sectional moments that could be written as

$$\mu_r^{(i)}(t) = \int_{d_{i-1/2}}^{d_{i+1/2}} d^r f(d, t) \delta d, \quad r = 0, 2, \dots, 2N_{sp} - 1 \quad (5)$$

6. The sectional moment problem

Note that the classical QMOM as introduced by McGraw (1997) treats the population as a whole quantity without paying attention to any local variation of the density function between the limits of integration $((0, \infty))$. This is because the first use of the QMOM by Gordon (1968) who was interested only in integrating functions over the domain: $(0, \infty)$. The only restriction that Gordon placed on the distribution function is that $F(d, t)$ (the cumulative distribution of $f(d, t)$) is a nondecreasing function and the values of its first $2N_{sp}$ moments exist.

The idea behind the SQMOM is to divide the population density function into sections (sub-regions) followed by the application of the QMOM to each section. It is clear to this point that any section of $F(d, t)$ ($d \in [d_{i-1/2}, d_{i+1/2}]$) will remain nondecreasing even when $f(d, t)$ vanishes in certain sections. In the especial case where $f(d, t) = 0$ (especially at the two ends of the distribution due to regulatory conditions, Motz et al., 2002), the population density function is uniformly distributed and hence the positions of the secondary particles could be set arbitrarily. So, there is no need for the QMOM in this especial case. It is obvious that by applying the QMOM to certain sections of the population, the rules of Gordon (1968) were not violated. This in fact allows the application of the classical QMOM to any arbitrary section of the population resulting in a set of local particle positions (abscissas) and weights. To this end, it remains how to relate the positions and weights of the secondary particles in the i th section (appearing in Eqs. (3) and (4)) to the sectional moments of the unknown function $f(d, t)$ given by Eq. (5).

Now, let the population density in the i th section $[d_{i-1/2}, d_{i+1/2}] : i = 1, 2, \dots, N_{pp}$ be represented in terms of local secondary particles weights and positions in the following form:

$$f^{(i)}(d, t) = \sum_{j=1}^{N_{sp}} w_j^{(i)}(t) \delta(d - d_j^{(i)}(t)) \quad (6)$$

where $\delta(d - d_j^{(i)})$ is the Dirac delta function placed at the secondary particle position: $d_j^{(i)}$ with strength $w_j^{(i)}$. Note that the positions and weights of the secondary particles are functions of time to follow the temporal evolution of the population density function. Similarly, the whole population density could now be reconstructed using the same form of Eq. (6), but now making use of the mean weights and positions assigned to the primary particles given by Eqs. (3) and (4):

$$f(d, t) = \sum_{i=1}^{N_{pp}} \tilde{w}_i(t) \delta(d - \tilde{d}_i(t)) \quad (7)$$

To relate the sectional moments $(\mu_r^{(i)})$ to the positions and weights of the secondary particles, Eq. (6) is substituted formally into Eq. (5) to get

$$\mu_r^{(i)}(t) = \sum_{j=1}^{N_{sp}} w_j^{(i)}(d_j^{(i)})^r, \quad r = 0, 2, \dots, 2N_{sp} - 1 \quad (8)$$

Note that with Eqs. (5) and (8) at hand, Eqs. (3) and (4) could be rigorously derived by taking the zero and first sectional moments $(\mu_0^{(i)}, \mu_0^{(i)})$ and by applying the mean value theorem of integrals to Eq. (5).

Now, the problem of sectional moments could be stated as: Given a set of sectional moments $(\mu_r^{(i)} : r=0, 1, \dots, 2N_{sp}-1, i=1, 2, \dots, N_{pp})$, find a set of weights and positions of the secondary particles $(d_j^{(i)}, w_j^{(i)} : j = 1, 2, \dots, N_{sp}, i = 1, 2, \dots, N_{pp})$. Although, the set of weights and positions of the secondary particles is unique for a specified number of sectional moments, there are several ways for finding them. The product-difference algorithm of Gordon (1968) and the direct tracking of the weights and positions (Piskunov and Golubev, 2002; Marchisio and Fox, 2005) are examples of these methods. It is worthwhile to mention here that these methods were only applied to population densities with a whole section ranging from zero to infinity. As stated in Section 1, these methods suffer from ill conditioning if the number of secondary particles is large (usually if greater than four) (Attarakih et al., 2006). This increase in the number of secondary particles in a one-population section could only increase the accuracy of the integration quadrature at the expense of solving a large eigenvalue problem. To overcome this difficulty, the number of secondary particles is fixed to one or two in each section and the accuracy of the integration quadrature is achieved by controlling the width of each section (like adaptive integration, Gerald and Wheatly, 1994). In this way, analytical solutions are derived for the weights and positions of secondary particles using two types of quadratures: the unequal and equal-weight quadratures as they will be described in the following sections.

6.1. The two-unequal-weight quadrature

In this type of quadrature the first four low-order sectional moments are used to find two secondary particle positions and weights. The product-difference algorithm of Gordon (1968) as described by McGraw (1997) is simplified analytically resulting in the following set of algebraic equations:

$$d_{1,2}^{(i)}(t) = -\frac{1}{2}\psi \mp \frac{1}{2}\sqrt{\psi^2 - 4\chi} \quad (9)$$

$$w_{1,2}^{(i)}(t) = \left(\frac{\sigma}{\tilde{d} - d_{1,2}} \right)_{(i)}^2 \frac{\mu_0^{(i)}}{1 + [\sigma/(\tilde{d} - d_{1,2})]_{(i)}^2} \quad (10)$$

where

$$\psi = \left(\frac{\hat{\mu}_1 \hat{\mu}_2 - \hat{\mu}_3}{\sigma^2} \right)_{(i)}, \quad \chi = \left(\frac{\hat{\mu}_1 \hat{\mu}_3 - \hat{\mu}_2^2}{\sigma^2} \right)_{(i)},$$

$$\sigma^2 = (\hat{\mu}_2 - \hat{\mu}_1^2)_{(i)}, \quad \hat{\mu}_r = \frac{\mu_r}{\mu_0}, \quad \tilde{d} = \hat{\mu}_1$$

6.2. The two-equal-weight quadrature

Here the inequality constraint of the two weights is relaxed resulting in two secondary particles of equal weights. This corresponds to assuming uniform population density in any given section and since there is only three unknowns $(d_1^{(i)}, d_2^{(i)}, w_1^{(i)} = w_2^{(i)})$, only three low-order moments are needed. Choosing the first three low-order moments $(\mu_r^{(i)} : r=0, 1, 2, i=1, 2, \dots, N_{pp})$ results in a quadrature

the same as that proposed by Yoon and McGraw (2004). Unfortunately, if the diameter is chosen as the particle size, the total particle mass is not conserved which is essential in any numerical solution of the PBE (Ramkrishna, 2000; Marchisio and Fox, 2005). To overcome this problem, $\mu_r^{(i)} : r = 0, 1, 3, i = 1, 2, \dots, N_{pp}$ are chosen by excluding $\mu_2^{(i)}$ which will be accurately estimated using Eq. (8). Doing this, Eq. (8) is reduced to three nonlinear algebraic equations which are analytically solved for the secondary particle positions and weights:

$$d_{1,2}^{(i)}(t) = \hat{\mu}_1^{(i)} \mp \frac{1}{\sqrt{3}} \sqrt{\frac{\hat{\mu}_3^{(i)}}{\hat{\mu}_1^{(i)}} - (\hat{\mu}_1^{(i)})^2} \quad (11)$$

$$w_{1,2}^{(i)}(t) = \frac{1}{2} \mu_0^{(i)} \quad (12)$$

these equations are found to produce results that are comparable in accuracy to that produced by the set of Eqs. (9) and (10), however, with reduced computational cost (solving $3N_{pp}$ ordinary differential equations instead of $4N_{pp}$). Moreover, the two-unequal-weight quadrature breaks down when the population approaches a monodispersed density (placed at d_0) with moments: $\mu_r^{(i)} = d_0^r : r = 0, 1, 3, i = 1, 2, \dots, N_{pp}$. On the other hand, the two-equal-weight quadrature predicts correctly the positions of the two secondary particles that are placed at $d_0(d_{1,2}^{(i)}(t) = \hat{\mu}_1^{(i)} = d_0)$.

7. Discretization of the PBE using the SQMOM

The discretization of the general PBE is performed by partitioning the particle size (diameter) into contiguous sections of an arbitrary width: $[d_{i-1/2}, d_{i+1/2}] : i = 1, 2, \dots, N_{pp}$. Each section is then seeded by a fixed and equal number of secondary particles, where their positions and weights are found by applying Eqs. (9) and (10) or (11) and (12) to the sectional moments of the initial condition: $f(d, 0) = f_0(d)$. Once these positions and weights are available, one primary particle is constructed per section using Eqs. (3) and (4). These primary particles reflect the shape of the original initial distribution. Now, with these secondary particles at hand, the splitting and aggregation events can take place using the specified frequency functions: $\Gamma(d), \omega(d, d')$. For a given section ($i : 1, 2, \dots, N_{pp}$) and at a given instant of time one mother particle is picked for splitting and two secondary particles for aggregation. This should account for preserving the sectional moments of the birthed and lost particles by either splitting or aggregation. The sectional moments (written in terms of the positions and weights of the secondary particles (Eqs. (9) and (10))) are then advanced in time according to the general PBE given by Eqs. (1) and (2). Mathematically, this is equivalent to applying the sectional moment transformation given by Eq. (5) to the PBE described by Eqs. (1) and (2). This starts by multiplying both sides of Eqs. (1) and (2) by d^r and integrating with respect to d over the section width: $[d_{i-1/2}, d_{i+1/2}] : i = 1, 2, \dots, N_{pp}$. Note that the unclosed integrals (could not be written in terms of $\mu_r^{(i)}$ due to the specific forms of the splitting and aggregation frequencies) are closed by the help of Eq. (6). The transformed equations could be written as

$$\tau \frac{\partial \mu_r^{(i)}(t)}{\partial t} = (\mu_r^{(i)}(t))_{in} - \mu_r^{(i)}(t) + \tau \rho(d'(t), w'(t)) \quad (13)$$

$$\begin{aligned} \rho = & -D_r^{(i)} [\Gamma^{(i)} \bullet w^{(i)}]^T + \sum_{m=i}^{N_{pp}} C_r^{(i,m)} [\Gamma^{(i)} \bullet w^{(i)}]^T \\ & \times \sum_{k=1}^{i \times N_{sp}} \left\{ \sum_{j=k}^{i \times N_{sp}} \Psi_{k,j,r}^{(i)} \omega_{j,k} w'_j w'_k - \eta_k \right. \\ & \left. \times \sum_{n=1}^{N_{sp} \times N_{pp}} (d'_k)^r \omega_{k,n} w'_k w'_n \right\} \quad (14) \end{aligned}$$

$$\pi_{r,j}^{(i,m)} = \int_{d_{i-1/2}}^{\min(d_{i+1/2}, d_j^{(m)})} d^r \beta(d|d_j^{(m)}) \hat{c} d \quad (15)$$

$$\eta_k = \begin{cases} 1 & \text{if } (i-1)N_{sp} + 1 \leq k \leq iN_{sp} \\ 0 & \text{otherwise} \end{cases} \quad (16)$$

$$\Psi_{k,j,r}^{(i)} = \begin{cases} (1 - \frac{1}{2} \delta_{kj}) & \text{if } (d_{i-1/2})^3 \leq [(d'_k)^3 + (d'_j)^3]^{r/3} < (d_{i+1/2})^3 \\ 0 & \text{otherwise} \end{cases} \quad (17)$$

where

$$D_r^{(i)} = [(d_1^{(i)})^r \quad (d_2^{(i)})^r \quad \dots \quad (d_{N_{sp}}^{(i)})^r]$$

$$\Gamma^{(i)} = [\Gamma(d_1^{(i)}) \quad \Gamma(d_2^{(i)}) \quad \dots \quad \Gamma(d_{N_{sp}}^{(i)})]$$

$$w^{(i)} = [w_1^{(i)} \quad w_2^{(i)} \quad \dots \quad w_{N_{sp}}^{(i)}]$$

$$C^{(i,m)} = \begin{bmatrix} \pi_{0,1}^{(i,m)} & \dots & \pi_{0,N_{sp}}^{(i,m)} \\ \vdots & \dots & \vdots \\ \pi_{2N_{sp}-1,1}^{(i,m)} & \dots & \pi_{2N_{sp}-1,N_{sp}}^{(i,m)} \end{bmatrix}$$

$$d' = [d_1^{(1)} \quad \dots \quad d_{N_{sp}}^{(1)} \quad \dots \quad d_1^{(N_{pp})} \quad \dots \quad d_{N_{sp}}^{(N_{pp})}]$$

$$w' = [w_1^{(1)} \quad \dots \quad w_{N_{sp}}^{(1)} \quad \dots \quad w_1^{(N_{pp})} \quad \dots \quad w_{N_{sp}}^{(N_{pp})}]$$

$$r = 0, 1, \dots, 2N_{sp} - 1, i = 1, 2, \dots, N_{pp}, \quad \text{and} \\ \delta_{kj} \text{ is the Kronecker delta.}$$

and the symbols: T and \bullet are used for matrix transpose and element by element multiplication, respectively.

Note that the integral appearing in Eq. (15) preserves the low-order moments of the newly birthed particles in the i th section due to splitting of a mother particle of size $d_j^{(m)}$. This integral could be easily evaluated if the form of the daughter particle distribution ($\beta(d|d_j^{(m)})$) is known. The function (η_k) is used to select the secondary particles disappearing due to aggregation in the i th section, while $\Psi_{r,k,j}^{(i)}$ is a sparse aggregation matrix whose nonzero elements represent the successful aggregation events between any pairs of secondary particles with locations and weights that are given by the augmented vectors: d' and w' . This matrix (Eq. (17)) preserves exactly the first $2N_{sp}$ low-order moments of the newly birthed particles by aggregation. Since the number of secondary particles is arbitrary, the discretized PBE preserves in theory an infinite number of low-order moments as its continuous counterpart. However, from a practical point of view only a finite number of low-order moments are required to generate an accurate integration quadrature over a number of sections having a specified width. In this way, by limiting the number of secondary particles to one or two and unlike the classical QMOM, there is one extra degree of freedom to control the accuracy of the integration quadrature; that is, the section width.

The system given by Eqs. (9) and (10) or (11) and (12) along with Eqs. (13)–(17) is a differential algebraic equation (DAE) system that could be reduced to only a differential one by substituting Eqs. (9) and (10) or (11) and (12) into Eqs. (13)–(17). Note that it is clear by this combination that the solution of the discretized PBE guarantees the exact preservation (reproduction) of $2N_{sp}$ first low-order moments ($\mu_r : r = 0, 1, \dots, 2N_{sp} - 1$). This makes the present framework of discretization generally consistent and accurate for solving general PBEs without placing any assumption on the shape and type of the distribution or splitting and aggregation functions. Moreover, the accuracy of evaluating integral quantities over the unknown density function $f(d, t)$ is not closely tied to the number of primary particles (sections) as in the case of classical sectional methods. Actually, it is found that when the number of secondary particles is greater than or equal to two, the accuracy of predicted low-order moments

Table 1
The SQMOM and the other sectional methods

Sectional method	No. of primary particles	No. of secondary particles
Classical sectional methods Ramkrishna (2000)	N_{pp}	1 Carries some information about w but none about d
Fixed-pivot technique Ramkrishna (2000)	N_{pp}	1 Carries some information about w and but none about d
Moving pivot technique Ramkrishna (2000)	N_{pp}	1 Carries some information about w and d
Conservative discretization Attarakih et al. (2004b)	N_{pp}	Carries some information about w but none about d
QMOM (McGraw, 1997) and DQMOM (Marchisio and Fox, 2005)	1	N_{sp} Carries detailed information about w and d
SQMOM Present work	N_{pp}	N_{sp} Carries detailed information about w and d

Table 2
Summary of the functions used in the PBE to validate the SQMOM

Case	Inlet feed	β	Γ and ω
1	$f^{\text{in}} = 3 \frac{d^2}{d_0^3} e^{-(d/d_0)^3}$	$\beta = 3\vartheta \frac{d^2}{d^3}, \quad \vartheta = 2$	$\Gamma = d^6, \quad \omega = 0$
2	Lognormal with: Mean = 0.4 mm STD = 0.3 mm	$\beta(d d') = \frac{90\vartheta d^2}{d'^3} \left(\frac{d}{d'}\right)^2 \left(1 - \left[\frac{d}{d'}\right]^3\right)^2$ $\vartheta = 2$	$\Gamma = C_1 \varepsilon^{1/3} \text{erf} \left(\sqrt{C_2 \frac{\varepsilon'}{\rho_c \varepsilon^{2/3} d^{5/3}} + \frac{H_d}{d^{4/3} \varepsilon^{1/3} \sqrt{\rho_c \mu_d}} } \right)$ $\varepsilon = \phi \frac{N_{pp} d_0^3 N^3}{V}$ $C_1 = 0.986 \text{ m}^{-2/3}, C_2 = 0.892 \times 10^{-3}, C_3 = 0.2$ Alopaeus et al. (2002), $\omega = 0$
3	Zero	N.A.	$\Gamma = 0, \quad \omega = d^3 + d'^3$
4	Zero	$\beta = 3\vartheta \frac{d^2}{d^3}, \quad \vartheta = 2$	$\Gamma = K_b d^3, \quad \omega = K_c$
5	Zero	N.A.	$\Gamma = 0, \quad \omega = d^3 + d'^3$ First-order removal constant: $\theta = 0.5$

is sufficient for engineering applications even when the number of primary particles equals one. This fact decouples the evaluation of the integral quantities from the reconstruction of the distribution itself. Accordingly, an accurate shape of the distribution is usually not required and hence a few number of primary particles is sufficient to get an approximate shape of the distribution. Since the section width is arbitrary, d_{\min} and d_{\max} could be chosen to minimize the finite domain error (error induced by not extending the integration limits to zero and infinity in the first and last sections, respectively).

8. The SQMOM and the other sectional methods

The generality of the SQMOM is proved by showing that all the related sectional and quadrature methods appearing in the literature for solving the PBE are merely special cases. This fact is revealed by referring to Table 1 below, where the moving pivot technique, for example, is recovered by using only one secondary particle ($N_{sp} = 1$) and N_{pp} primary particles. The weights and positions of the secondary particle in each section are solved for directly using one-point quadrature to conserve the first (total number of particles) and third (total mass) moments when the internal state of the particle is represented by its diameter. In their original work, Kumar and Ramkrishna (1996) tracked the weights and the positions of the secondary particles directly by solving two system of ODEs comprising the homogeneous PBE by aggregation.

On the other hand, when the number of primary particles (sections) equals one, the classical QMOM is recovered. This means that the super structure of the present discretized PBE could be used to optimize the numerical solution according to the user needs. The user can start constructing the minimum information needed for simulating problems requiring the solution of the PBE with a minimum effort by setting the number of primary particles equal to one. Once the solution has converged an extra information is extracted by increasing the number of primary particles starting from the previous step. This process simulation conceptualizes a hierarchy in the numerical solution of process problems associated with PBEs.

9. Numerical results and discussion

The discretized PBE using the SQMOM described above is applied to the following cases where analytical solution is available for cases 1, 3, 4 and 5:

- Case 1: Splitting in a continuous stirred vessel with simplified splitting functions.
- Case 2: Splitting in a continuous stirred vessel with realized splitting functions.
- Case 3: Aggregation in a batch vessel with sum aggregation frequency.
- Case 4: Simultaneous splitting and aggregation in a batch vessel with constant splitting and aggregation frequencies.
- Case 5: Aggregation in a batch vessel with sum aggregation frequency and first-order removal.

The specific functional forms of the initial condition, inlet feed distribution, daughter particle distribution, splitting and aggregation frequencies are summarized in Table 2.

For the purpose of numerical validation, four cases are presented here for the case of particle splitting and aggregation in a well-mixed vessel where the analytical solution for the PBE is available. For the case of particle splitting (Case 1) in a continuous stirred vessel the analytical solution is given by Attarakih et al. (2004a). For cases 3 and 5 the analytical solution is taken from Gelbard and Seinfeld (1978) and from McCoy and Madras (2003) for case 4. For case 2 a fine grid solution ($N_{pp} = 200$) is used as the reference one using a discretization approach that conserves only the first and third moments of the distribution. The low-order sectional moments are evolved in time using the trapezoidal rule with fixed time step equal to 0.1 s. In all the numerical case studies the particle diameter is partitioned using a linear space: $d : \{d_{1/2} = d_{\min}, d_1, \dots, d_{N_{pp}/2+1} = d_{\max}\}$ and all the average number concentrations are reconstructed using Eqs. (3), (4) and (7) at any given time. The type of quadrature used is the two-equal-weight quadrature unless it is explicitly mentioned.

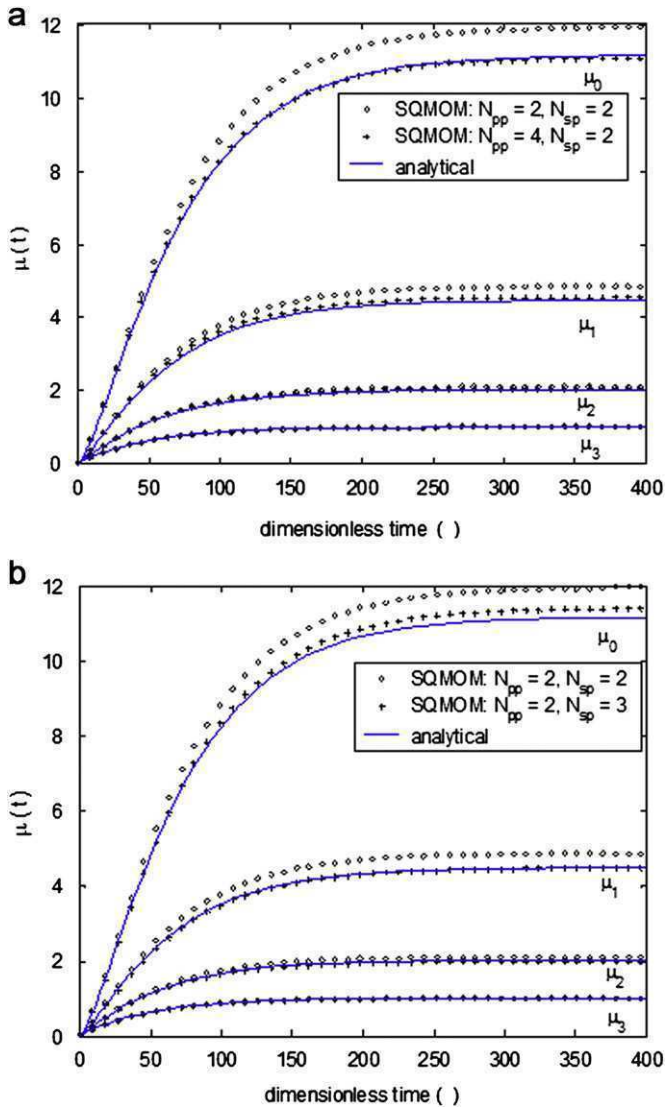


Fig. 2. Case 1: Convergence of the first four moments using the SQMOM for particle breakage in continuous stirred vessel: (a) By varying the number of primary particles (N_{pp}) and (b) by varying the number of secondary particles (N_{sp}). The feed distribution is exponential with respect to the particle volume ($f^{in} = 3d^2e^{-d^3}$), the splitting frequency is proportional to the square of the particle volume ($T = d^6$), the daughter particle distribution is uniform with respect to the mother particle volume ($\beta = 6d^2/d^3$), the initial condition is zero ($f(d,0) = 0$), the minimum and maximum particle sizes are 0.001 and 2, respectively, and the vessel residence time is $\tau = 100$ s.

First, Fig. 2a compares the convergence of the SQMOM at fixed number of secondary particles by varying the number of primary particles from 2 to 4. It is clear that the first two moments (μ_0 and μ_1) are over predicted using only two primary and secondary particles. The inaccuracy is attributed to the sharpness of the distribution as it is evolved in time (see Fig. 3a). By doubling the number of primary particles or equivalently the number of partitions, the width of each partition is decreased resulting in an accurate integration over the sharp distribution as expected. Actually, this fact is true for all Gauss-like quadrature methods. On the other hand, by increasing the number of secondary particles from 2 to 3 as seen in Fig. 2b, the same result is almost obtained, which is expected since the accuracy of the quadrature methods is increased by increasing the number of the quadrature points (secondary particles).

In Fig. 3a, the average number concentration as predicted using the SQMOM is compared with the analytical solution at different pe-

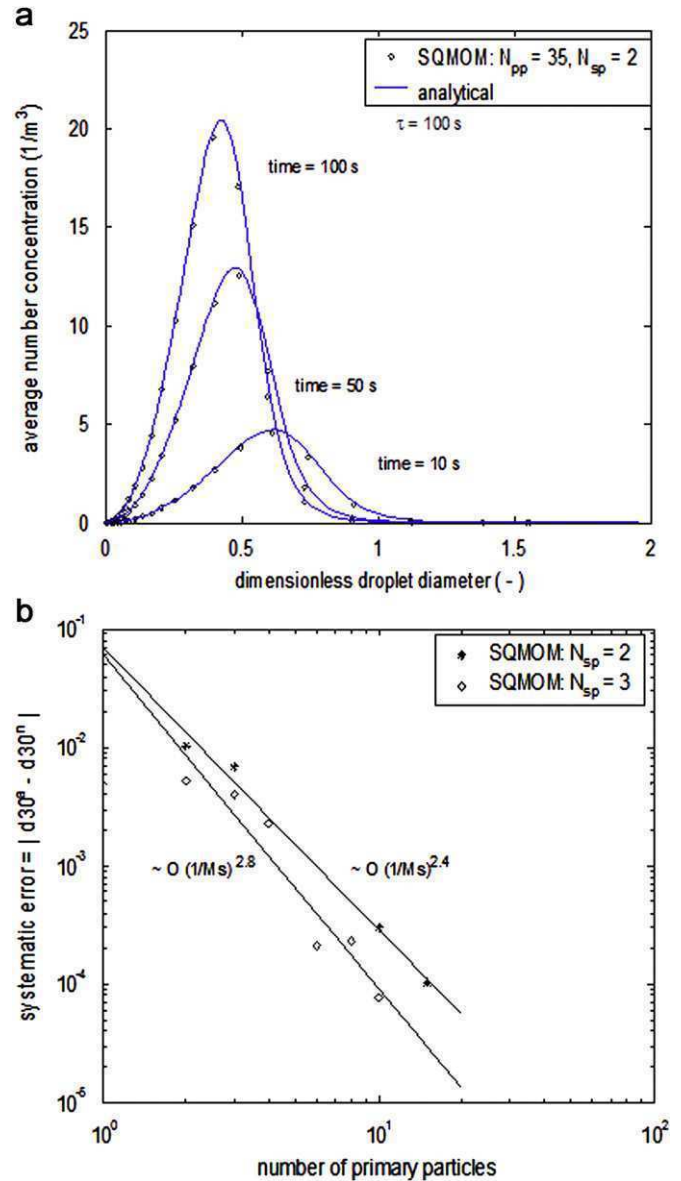


Fig. 3. Case 1: (a) Comparison between the analytical solution and that predicted by the SQMOM for particle splitting in continuous stirred vessel. (b) Convergence of the SQMOM in terms of the systematic error in $d_{30} = \mu_3/\mu_0$. The feed distribution is exponential with respect to the particle volume ($f^{in} = 3d^2e^{-d^3}$), the splitting frequency is proportional to the square of the particle volume ($T = d^6$), the daughter particle distribution is uniform with respect to the mother particle volume ($\beta = 6d^2/d^3$), the initial condition is zero ($f(d,0) = 0$), the minimum and maximum particle sizes are 0.001 and 2, respectively, and the vessel residence time is $\tau = 100$ s.

riods of time. It is clear that using 35 primary particles is enough to follow the shape of the number density function very accurately. However, since the predicted shape of the distribution is not used in the prediction of any integral property, small number of primary particles is found enough to get an idea about the shape of the distribution. Consequently, the location and weights of the secondary particles are used to evaluate any integral over the unknown distribution with the desired accuracy. To get more insight into the convergence properties of the SQMOM, the systematic error (the absolute difference between the analytical and numerical values) based on the mean particle diameter (d_{30}) is studied as function of the number of primary and secondary particles.

It is evident from Fig. 3b that the speed of convergence is increased by increasing the number of both primary and secondary particles due to the increasing accuracy of evaluating the unclosed integrals in the PBE. The increasing accuracy by increasing the number of secondary particles is reported by many researchers (McGraw, 1997; Marchisio and Fox, 2005). Note that the dispersion of the errors in Fig. 3b might be attributed to the numerical errors resulting from the fixed-time step trapezoidal rule.

It is noticed that the resulting set of particle weights and positions are highly nonlinear functions of the low-order moments and numerical integration errors with respect to time could be reduced using higher-order methods such as the fourth-order Runge Kutta method. The numerical accuracy (in the predicted low-order moments and the unclosed integrals) is found to increase by increasing the number of primary particles (sections), while keeping $N_{sp}=2$. This is because, as in any Gauss-like quadrature, the accuracy of the integration increases by decreasing the width of the interval over which the integral is evaluated. If only a rough idea is required about the shape of the distribution, only a few number of primary particles could be used, while keeping the evaluation of the low-order moments and any unclosed integral as accurate as required.

Fig. 4 shows a comparison between the classical CDA of the present author (Attarakih et al., 2004b) and the SQMOM using realized splitting functions (splitting frequency and daughter particle distribution) taken from the work of Alopaeus et al. (2002). These functions describe droplet breakage in a turbulent liquid–liquid dispersion taking into account the effect of the dispersion physical

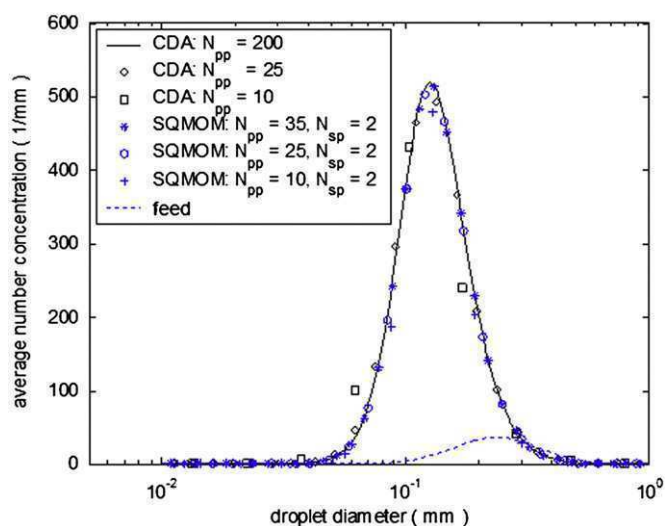


Fig. 4. Case 2: Convergence of the steady state average number density using the SQMOM as compared to the conservation discretization approach (CDA) (Attarakih et al., 2004b) by varying the number of primary particles (N_{pp}) for droplet breakage in continuous stirred vessel with breakage frequency and daughter droplet distribution as given by Alopaeus et al. (2002). The feed is lognormal with mean droplet diameter equals 0.4 mm and standard deviation of 0.3. The initial condition is zero, the rotational speed = 0.35 s^{-1} , the power number = 5 and $\tau = 100 \text{ s}$.

properties and the energy dissipation. Actually, this approach as shown in Attarakih et al. (2004b) is the same the fixed-pivot technique of Kumar and Ramkrishna (1996). It is obvious that 35 primary particles are enough to predict accurately the shape of the distribution as compared with the CDA. Moreover, the prediction of shape of the distribution using the SQMOM is much better (close to the fine grid solution) than that predicted by the CDA using only 10 primary particles. On contrary to the sectional methods, since the large increase in the number of primary particles has negligible effect on the prediction of integral quantities, using small number of primary particles to infer about the shape of the distribution is usually sufficient. To look closely on the computational demand and accuracy of the SQMOM as compared to the classical discretization approach, the four low-order moments as predicted by both methods are compared in Table 3. It is obvious that the SQMOM is superior to the CDA even using small number of primary particles. All the four moments converges very quickly using the SQMOM. If the same accuracy is needed, large number of primary particles is required and hence the computational cost will increase rapidly.

The third example is for particle aggregation in batch stirred vessel where the analytical solution is reported by Gelbard and Seinfeld (1978) for sum aggregation frequency ($\omega = d^3 + d'^3$) and the exponential (with respect to particle volume) initial condition.

Fig. 5a shows the predicted average number density using 25 primary particles and two secondary particles. It is clear how accurately the SQMOM predicts the aggregation events even in the sharp parts of the solution. Also, the first four low-order moments are accurately predicted with the third moment showing an exact mass conservation. It should be emphasized again that the rapid increase in the number of primary particles is not a condition implied by the SQMOM if only integral properties of the distribution are desired which is the usual case. A few number of primary particles (depending on the sharpness of the distribution) are usually enough to get an idea about the shape of the distribution, while maintaining high accuracy in terms of the integral quantities.

So, the computational load of the SQMOM is dependent on the accuracy and details needed by the user. Since it reduces directly to the standard QMOM by setting the number of primary particles equal to one, the computational load is expected to be minimum, however, at the expense of destroying the shape of the distribution.

It is clear that the CPU time grows in quadratic form as a function of primary particles as shown in Fig. 5b. This quadratic form seems to persist even if the number of secondary particles is increased to 3, which is not a requirement of the SQMOM. It is obvious that the numerical cost depends on the number of primary and secondary particles and is proportional to the number of primary particles at a fixed number of secondary particles.

Fig. 6 compares the analytical solution (McCoy and Madras, 2003) with that predicted using the SQMOM using two secondary particles ($N_{sp} = 2$) and different number of primary particles ($N_{pp} = 2, 4, 6, 8, 10$ and 12). It is clear that the primary particles follow accurately the shape of the distribution as their number is increased. For the case of one primary particle the standard QMOM is recovered; however, with analytical solution for the positions (abscissas)

Table 3

Convergence of the first four moments by increasing the number of primary particles using the SQMOM ($N_{sp} = 2$) and the CDA (Attarakih et al., 2004b) for case 3

N_{pp}	SQMOM				N_{pp}	CDA			
	μ_0	μ_1	μ_2	μ_3		μ_0	μ_1	μ_2	μ_3
2	56.932	9.322	1.761	0.395	2	3.104	1.567	0.791	0.399
4	58.424	9.427	1.771	0.399	4	28.706	3.856	0.942	0.399
10	58.799	9.442	1.772	0.399	10	53.215	8.272	1.601	0.399
25	58.803	9.441	1.772	0.399	25	58.529	9.295	1.751	0.399
35	58.803	9.441	1.772	0.399	200	58.785	9.438	1.772	0.399

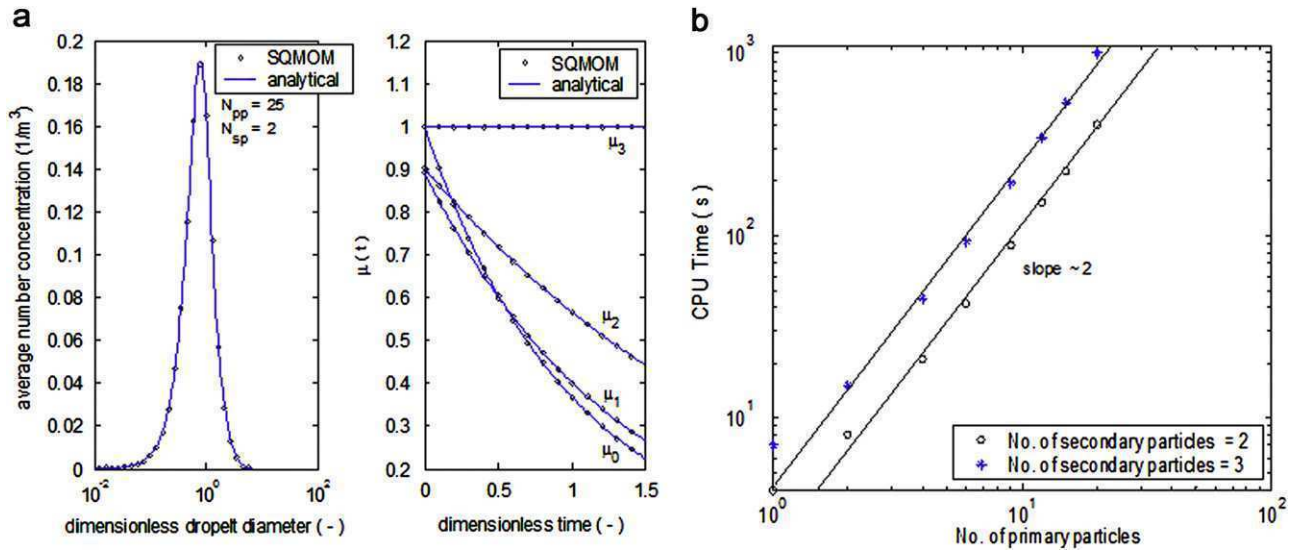


Fig. 5. Case 3: (a) Comparison between the analytical (Gelbard and Seinfeld, 1978) and predicted solutions using the SQMOM for particle aggregation in batch stirred vessel ($d_0 = 1, N_0 = 1$). (b) The effect of primary and secondary particles on the CPU requirements (Pentium PC 1.4 MHz processor and MATLAB 6.5). The aggregation frequency is proportional to the volume of the two aggregating particles ($\omega = d^3 + d^3$) and the initial condition is exponentially distributed with respect to particle volume ($f^m = 3d^2/d_0^3 e^{-d/d_0}$).

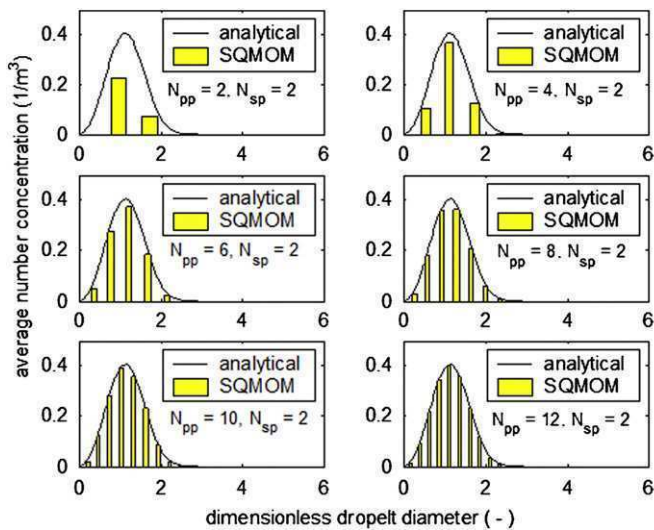


Fig. 6. Case 4: Average number concentration using different primary particles as predicted by the SQMOM with $N_{sp} = 2$ for simultaneous aggregation and splitting in batch stirred tank with dimensionless time $\tau = 10$, constant aggregation frequency = 1, constant splitting frequency = 0.1, $d_{min} = 0.001$ and $d_{max} = 3$. The analytical solution is given by McCoy and Madras (2003).

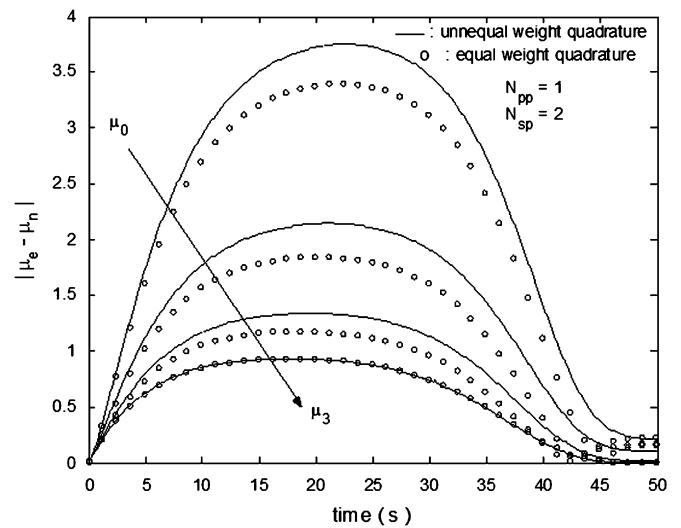


Fig. 7. Case 1: Comparison between the absolute error in the first four moments using the SQMOM with two-unequal- and equal-weight quadratures for the case of particle splitting in a continuous stirred vessel with $\Gamma = d^6$, $\beta = 6d^2/d^3$, $f^m = 3d^2 e^{-d^3}$ and $\tau = 5$ s.

and weights (assumed equal) of the secondary particles that depends only on three low-order moments (μ_0, μ_1 and μ_3).

Fig. 7 compares the two-point quadratures developed in this work (Eqs. (9) and (10) and (11) and (12)) as applied to particle splitting in continuous stirred vessel (case 1). For the sake of fair comparison the differential equation solver: ode45 of MATLAB 6.5 (with SolverRelTol = 1e-3, SolverAbsTol = 1e-6) is used in the cases of two-equal- and unequal-weight quadratures by keeping $\tau = 5$ s and $N_{pp} = 1$.

It is clear that over the whole simulation period the two-equal-weight quadrature is more accurate than the unequal-weight one. This might be attributed to the highly nonlinear form of the unequal-weight quadrature (compare Eqs. (9) and (10) and (11) and (12)). The behavior of the error could be attributed to the moments vari-

ation as a function of time (Fig. 2a); being free of error initially and approaching constant values at steady state. A more complex case study is used to further investigate the accuracy of the two-equal-weight quadrature by considering particle aggregation plus first-order removal.

It is again clear from Fig. 8 that both the two-point quadratures have almost the same accuracy. This might be due to the nonsharp variation of the moments as function of time. The same behavior is observed for the case of particle aggregation in a batch stirred vessel with constant aggregation frequency. It is important to notice that even though the second moment is not involved when the two-equal-weight quadrature is used, it is predicted accurately as shown in Figs. 2a,b, 5a and 8.

10. Extension of the SQMOM to bivariate PBE

The extension of the SQMOM to the bivariate case (BVSQMOM) is carried out in a straightforward manner by using two secondary particles for each internal coordinate. Using the concept of primary particles, each primary particle now is associated with two secondary particles. The location of this bivariate primary particle is found by averaging the positions and weights of its associated secondary particles. A set of algebraic equations are already derived for both coordinates to predict the positions of the secondary particles using a selected number of mixed sectional moments (for example, $\mu_{00}^{(ij)}, \mu_{10}^{(ij)}, \mu_{30}^{(ij)}, \mu_{11}^{(ij)}$ and $\mu_{33}^{(ij)}$: $i = 1, 2, \dots, N_{pp1}, j = 1, 2, \dots, N_{pp2}$). The positions of these secondary particles as predicted by this set of algebraic equations are plotted for the bivariate normal distribution as shown in Fig. 9. On the same figure, the position of the secondary particles using the BVQMOM with principal component analysis (PCA)

(Yoon and McGraw, 2004) are also shown. First, it is clear how the positions of the secondary particles follow the shape of the bivariate distribution when the variance is changed. Second, the BVSQMOM and BVSQMOM-PCA predict almost the same particle positions, although the selected moments for both methods are different. The details of the BVSQMOM will appear in a separate publication with its potential to use effectively direct weight and position tracking: direct SQMOM (DSQMOM).

11. Conclusions

The present framework for solving the PBE based on the concept of the primary and secondary particles is found general where all the previous attempts in literature to overcome the integral problems associated with the unknown number density function are merely special cases of the present framework. In this way, the primary particles are responsible for the distribution reconstruction, while the secondary ones are responsible for splitting, aggregation, etc. events and carry a lot of information about the distribution.

The use of the primary particles circumvent the problem of ill-conditioned eigenvalue problem (for large number of secondary particles) associated with the product-difference algorithm (McGraw, 1997). Within this context two sets of quadratures are analytically derived where the case studies show that the two-equal-weight quadrature is superior to the unequal weight one. The SQMOM is found extremely accurate and converges very fast by increasing either the number of primary or secondary particles, however, at the expense of the computational load. The flexibility of the method through its reduction to the standard QMOM when the number of primary particles equals one makes it very attractive from computational point of view and provides a hierarchy for optimized numerical solutions. The computational load and the degree of details required about the distribution are dependent in a quadratic form on the number of primary particles. An extremely interesting application of the SQMOM is by coupling the PBE to CFD codes. The normal limitation of the existing ways of coupling is the simplification that all characteristic particles (having different sizes) move with the same velocity field based on the Sauter mean diameter (MUSIG model by Lo, 2000). In this connection, the SQMOM seems to be another interesting alternative, since each primary particle will move with its own velocity group and hence having its own momentum equation. For this reason, first attempts were recently carried out to couple the

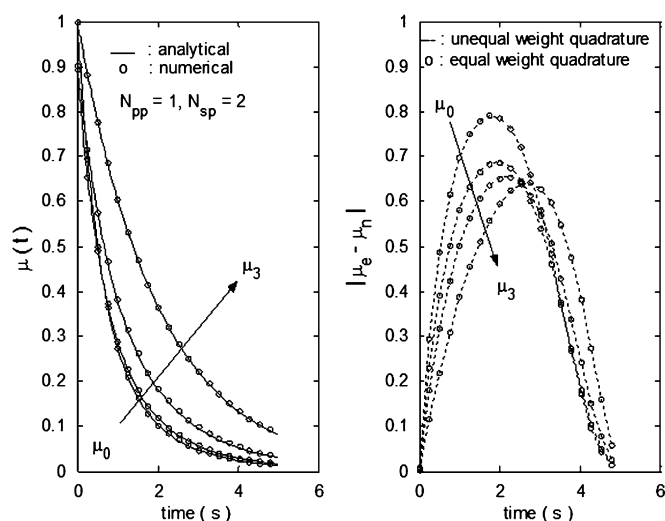


Fig. 8. Comparison between the two-equal- and unequal-weight quadratures for the case of sum aggregation frequency ($\omega = d^3 + d^3$) in batch vessel with first-order removal constant of 0.5 and exponentially distributed initial condition with respect to particle volume ($f^m = (3d^2/d_0^3)e^{-d/d_0}$). (a) Analytical and numerical moments. (b) Absolute error in the numerical moments.

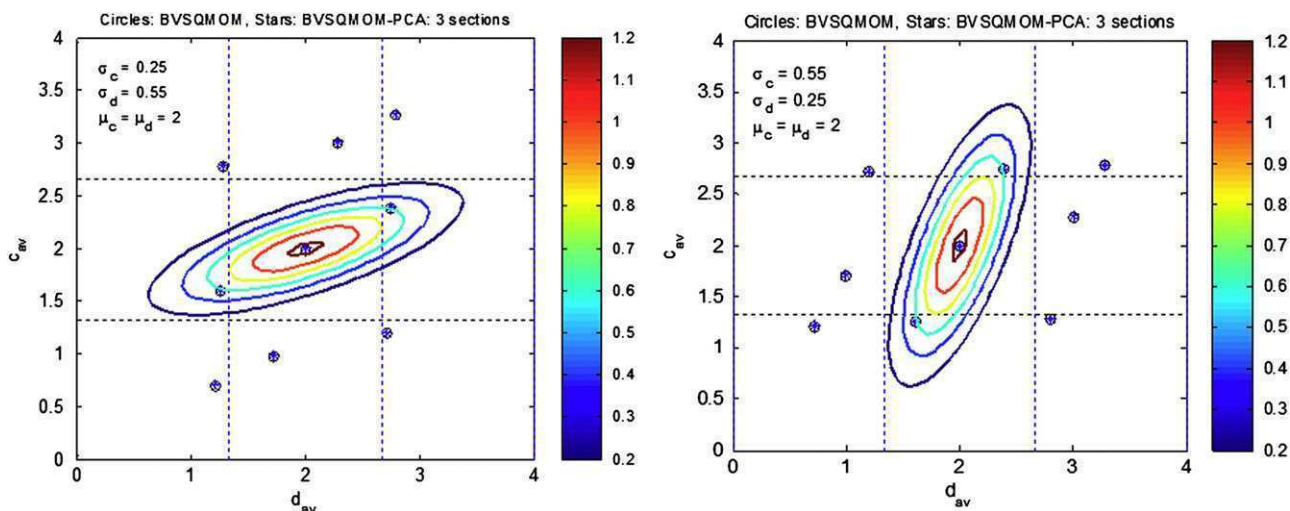


Fig. 9. Average positions (abscissas: c_{av} and d_{av}) of secondary particles as predicted using the BVSQMOM and the BVSQMOM-PCA (Yoon and McGraw, 2004). The contour lines represent a bivariate normal distribution with $\mu_c = \mu_d = 2$ and correlation coefficient = 0.35.

SQMOM with a CFD code for the simulation of a five-compartment RDC extraction column (Drumm et al., 2007). The extension of the SQMOM to a bivariate PBE has been already done based on the primary particle concept with direct tracking of secondary particle weights and positions.

Notation

c_{av}	mean secondary particle size for the bivariate normal distribution, mm
$C^{(i,m)}$	as defined by Eq. (14)
d	particle diameter, mm
d_{av}	mean secondary particle size for the bivariate normal distribution, mm
d_0	mean particle diameter, mm
d_{30}	mean particle diameter ($d_{30} = \mu_3/\mu_0$), mm
d_i	mean i th secondary particle diameter $\in [d_{i-1/2}, d_{i+1/2})$, mm
d'	augmented vector of secondary particle diameters, mm
$d_j^{(i)}$	j th secondary particle diameter $\in [d_{i-1/2}, d_{i+1/2})$, mm
d_{min} and d_{max}	minimum and maximum particle diameter, mm
D_R	rotor diameter, m
$f(v, t)\delta v$	average number of particles per unit volume of a fixed subspace at time t , m^{-3}
$f^{in}(v, t)\delta v$	average number of particles per unit volume entering a fixed subspace at time t , m^{-3}
K_b and K_c	particle splitting and aggregation constants, s^{-1}
N	rotational speed, s^{-1}
N_{pp} and N_{sp}	number of primary and secondary particles, respectively
N_{pp1} and N_{pp2}	number of primary particles in the first and second internal coordinates, respectively
N_0	total number of particles
t	time, s
v	particle volume, mm^3
V	vessel volume, m^3
w'	augmented vector of secondary particle weights, m^{-3}
$w_j^{(i)}$	j th secondary particle weight, m^{-3}
\tilde{w}_i	mean i th secondary particle weight, $mm^{-1} m^{-3}$
Greek letters	
$\beta(d d')\delta d$	number of particles produced when a mother particle of size d' is broken
$\Gamma(v)$	particle splitting frequency, s^{-1}
δ_{kj}	Kronecker delta
ε	average turbulent energy dissipated in the continuous phase, $m^2 s^{-3}$
η	as defined by Eq. (16)
μ_d	dispersed phase viscosity, Pa s
μ_e and μ_n	exact and numerical moments, respectively
$\mu_r^{(i)}$	r th sectional moment $\in [d_{i-1/2}, d_{i+1/2})$, m^{-3}
μ_r	r th total moment $\in (0, \infty)$, m^{-3}
π	as defined by Eq. (15)
ρ_c and ρ_d	continuous and dispersed phase densities, respectively, $kg m^{-3}$
σ	as defined by Eq. (10)

σ'	interfacial tension, $N m^{-1}$
σ_c and σ_d	standard deviation of the bivariate normal density in d and c directions, respectively
τ	stirred vessel time constant, s
ϑ	number of particles produced upon splitting as defined by Eq. (17)
Ψ	
$\omega(v, v')$	particle aggregation frequency, $m^3 s^{-1}$

References

- Alopaeus, V., Koskinen, J., Keskinen, K.I., Majander, J., 2002. Simulation of the population balances for liquid–liquid systems in a nonideal stirred tank: Part 2—parameter fitting and the use of multiblock model for dense dispersions. *Chemical Engineering Science* 57, 1815–1825.
- Attarakih, M.M., Bart, H.-J., Faqir, N.M., 2004a. Numerical solution of the spatially distributed population balance equation describing the hydrodynamics of interacting liquid–liquid dispersions. *Chemical Engineering Science* 59, 2567–2592.
- Attarakih, M.M., Bart, H.-J., Faqir, N.M., 2004b. Solution of the droplet breakage equation for interacting liquid–liquid dispersions: a conservative discretization approach. *Chemical Engineering Science* 59, 2547–2565.
- Attarakih, M.M., Bart, H.-J., Faqir, N.M., 2006. Numerical solution of the bivariate population balance equation for the interacting hydrodynamics and mass transfer in liquid–liquid extraction columns. *Chemical Engineering Science* 61, 113–123.
- Cameron, I.T., Wang, F.Y., Immanuel, C.D., Stepanek, F., 2005. Process systems modelling and applications in granulation: A review. *Chem. Eng. Sci.* 60, 3723–3750.
- Cauwenberg, V., Degreve, J., Slater, M.J., 1997. The interaction of solute transfer, Contaminants and drop break-up in rotating disc contactors: part II. The coupling of mass transfer and breakage process via interfacial tension. *Canadian Journal of Chemical Engineering* 75, 1056–1066.
- Coulaloglou, C.A., Tavlarides, L.L., 1977. Description of interaction processes in agitated liquid–liquid dispersions. *Chemical Engineering Science* 32, 1289–1297.
- Dhanasekharan, K.M., Sanyal, J., Jain, A., Haidari, A., 2005. A generalized approach to model oxygen transfer in bioreactors using population balances and computational fluid dynamics. *Chemical Engineering Science* 60, 213–218.
- Drumm, C., Tiwari, S., Attarakih, M.M., Kuhnert, J., Bart, H.-J., 2007. CFD-PBM coupled model using the finite point set method and the SQMOM, International Solvent Extraction Conference (ISEC), submitted for publication.
- Gelbard, F., Seinfeld, J.H., 1978. Numerical solution of the dynamic equation for particulate systems. *Journal of Computational Physics* 28, 357–375.
- Gerald, C.F., Wheatly, P.O., 1994. *Applied Numerical Analysis*. Addison-Wesley Publishing Company, New York.
- Gordon, R.G., 1968. Error bounds in equilibrium statistical mechanics. *Journal of Mathematical Physics* 9, 655–663.
- Kumar, S., Ramkrishna, D., 1996. On the solution of population balance equations by discretization—II. A moving pivot technique. *Chemical Engineering Science* 51 (8), 1333–1342.
- Lo, S., 2000. Application of population balance to CFD modelling of gas–liquid reactors. In: *Proceedings of Trends in Numerical and Physical Modelling for Industrial Multiphase Flows*, Corsica, France.
- Marchisio, L.D., Fox, R.O., 2005. Solution of the population balance equations using the direct quadrature method of moments. *Journal of Aerosol Science* 36, 43–73.
- McCoy, B.J., Madras, G., 2003. Analytical solution for a population balance equation with aggregation and fragmentation. *Chem. Eng. Sci.* 58, 3049–3051.
- McGraw, R., 1997. Description of aerosol dynamics by the quadrature method of moments. *Aerosol Science and Technology* 27, 255–265.
- Motz, S., Mitrovic, A., Gilles, E.-D., 2002. Comparison of numerical methods for the simulation of dispersed phase systems. *Chemical Engineering Science* 57, 4329–4344.
- Piskunov, V.N., Golubev, A.I., 2002. The generalized approximation method for modeling coagulation kinetics—part 1: justification and implementation of method. *Journal of Aerosol Science* 33, 51–63.
- Randolph, A.D., Larson, M.A., 1988. *Theory of Particulate Processes*. Academic Press, Inc., San Diego.
- Ramkrishna, D., 2000. *Population Balances*. Academic Press, San Diego.
- Rosner, D.E., McGraw, R., Tandon, P., 2003. Multivariate population balances via moment and Monte Carlo simulation methods: an important sol reaction engineering bivariate example and mixed moments for the estimation of deposition, scavenging, and optical properties for populations of nonspherical suspended particles. *Industrial & Engineering Chemistry Research* 42, 2699–2711.
- Schmidt, S.A., Martin, S., Attarakih, M.M., Lagar, L., Bart, H.-J., 2006. Droplet population balance modeling—hydrodynamics and mass transfer. *Chemical Engineering Science* 61, 246–256.
- Sha, Z., Laari, A., Turunen, I., 2006. Multi-phase-multi-size-group model for the inclusion of population balances into the CFD simulation of gas–liquid bubbly flows. *Chemical Engineering & Technology* 29, 550–559.
- Yoon, C., McGraw, R., 2004. Representation of generally mixed multivariate aerosols by the quadrature method of moments: I. Statistical foundation. *Journal of Aerosol Science* 35 (5), 561–576.

Publication XI

Accepted for publication, AIChE Journal

Christian Drumm, Mark W. Hlawitschka, Hans-Jörg Bart

**CFD Simulations and Particle Image Velocimetry Measurements in an Industrial Scale
Rotating Disc Contactor.**

Reprinted with permission from Wiley

<http://dx.doi.org/10.1002/aic.12249>

CFD Simulations and Particle Image Velocimetry Measurements in an Industrial Scale Rotating Disc Contactor

Christian Drumm, Mark W. Hlawitschka, Hans-Jörg Bart

Lehrstuhl für Thermische Verfahrenstechnik, TU Kaiserslautern,

Center of Mathematical and Computational Modeling, TU Kaiserslautern,

P.O. Box 3049, 67653 Kaiserslautern, Germany

Abstract

Fluid dynamics of the single- and two-phase flow in a segment of a Rotating Disc Contactor (RDC) liquid-liquid extraction column with 450 mm inner diameter were studied by performing Computational Fluid Dynamics (CFD) simulations and Particle Image Velocimetry (PIV) measurements. The fluid dynamics were investigated to test the predictivity of CFD at industrial scale. Different turbulence models in conjunction with the Eulerian approach were applied in the single- and two-phase simulations. The turbulent flow characteristics were analysed by Particle Image Velocimetry measurements to validate the CFD simulations. An iso-optical system composed of CaCl_2 /water-butylacetate allows for the two-phase PIV measurements. Local turbulent energy dissipation was derived from velocity gradients in PIV data. In this connection, the influence of the PIV spatial resolution on the measured energy dissipation was also analyzed and different fit functions were tested to scale the measured energy dissipation. Simulated velocity fields as well as the energy dissipation were compared to the experimental PIV data. The results from the simulations and experiments are in good agreement. The work shows, that CFD can predict hydrodynamic characteristics even at bigger scales, but is still subject to some minor restrictions.

Topical Heading

Fluid Mechanics and Transport Phenomena

Keywords

Particle Image Velocimetry, liquid-liquid extraction, CFD, energy dissipation, Rotating Disc Contactor

Introduction

Liquid-Liquid extraction is a separation process, which is based on the different distribution of the separable components between two liquid phases. The process is used primarily when distillation is impractical or too costly to use [1,2]. This unit operation is widely applicable in chemical, biochemical industries, pharmacy and hydrometallurgy. In most modern extraction processes, mechanically agitated columns as pulsed or stirred columns are applied. Stirred extraction columns can range from simple RDC to complicated stirrer geometry as in Kühni columns.

The use of CFD software in many materials processing industries has grown tremendously in recent years. Computational fluid dynamics has been widely utilized for conducting virtual experiments, prototype testing, and parametric studies. Analysis using CFD complements and reduces physical testing, and it can result in a significant time and cost saving. [3].

In the field of liquid-liquid extraction, CFD can predict fluid dynamics and turbulence and gives a fully resolved local resolution of the two-phase flow in an apparatus. It can be used as an aid to scale-up processes from lab or pilot scale to full production. In practice, the layout of extractors is mainly based on experience and empirical or semi-empirical models.

In literature, some good progress has been made in determining stirred column design parameters using CFD simulations both in single-phase [4-8] and two-phase mode [9-13]. Recent work has also dealt with liquid-liquid problems in pulsed extraction columns [14, 15]. Main focus in these references is on the investigation of single- and two-phase velocity fields and flow patterns and residence time distribution studies for the evaluation of the axial dispersion. Comparisons to experimental PIV [12], LDV [4] and LDA [5, 10] data could show that CFD is a suitable design tool for the prediction of the hydrodynamic phenomena such as flow patterns, velocities and backmixing. Only PIV allows the comparison of the whole velocity field, while only discrete points can be compared to LDA and LDV measurements. Over the last years, the Euler-Euler approach emerged as the standard approach to model multiphase problems at higher hold-up and was successfully applied to model stirred RDC extractors of various geometries [5, 10, 11, 12]. The Euler-Lagrange approach, also known as the discrete phase model, is best used for flow regimes where the difference between the volume fractions of the two phases is large. Therefore, the Euler-Lagrange approach was mainly applied to determine dispersion coefficients from a small amount of droplets, but fails to predict column behavior at higher hold-up (above 10%) [5, 7]. Nevertheless, the model was applied by other authors to simulate stirred extraction columns at this lower hold-up [16, 17]. Generally, it is sufficient to apply a two-fluid model in CFD for the description of the dispersed liquid-liquid problem [12, 18]. Drop size distributions in liquid-liquid extractors are usually monomodal and narrow and drop sizes range from around 1 to 5 mm. In this connection, the Sauter mean diameter represents the different sizes of the particles in the dispersed phase, while the influence of the size-specific terminal velocity resulting from the drop size distribution, could be neglected. Multi-fluid models are highly CPU-time consuming and only necessary for wide or multi modal distributions. The coupling of CFD and Population Balance Modelling (PBM) is another promising alternative for an advanced modeling of dispersed multiphase systems [19]. CFD can predict the hydrodynamics and turbulence and give a fully developed local resolution of the two-phase flow in all three external coordinates, while the PBM can account for the droplet coalescence and breakup and analyse the size distribution of the dispersed phase. Nevertheless, these coupled solvers stand and fall with the correct prediction of the fluid dynamics.

In previous work, the single and two-phase flow field of a RDC pilot plant column (150 mm inner diameter) was simulated by means of CFD [12, 19, 20]. The single- and two-phase simulations were validated by PIV measurements. These were the first works which could validate the whole flow field in single- and two-phase operational mode instead of comparing only discrete points as with LDA measurements. In all given citations, CFD was applied for the simulation of pilot scale or lab-scale columns. On the other hand, industrial scale CFD simulations are hardly found because of the high computational load.

Therefore, in the present work, the applicability of CFD is tested for an industrial scale RDC extraction column. An industrial scale 450 mm inner diameter test rig with 3 extraction compartments is investigated. The predictivity of CFD simulations for the bigger scale can be estimated. PIV measurements are conducted in single- and two-phase mode for validation and are compared to the CFD simulations. The aim of this study is to predict the velocity fields in the aqueous phase for the different scales in single- and two-phase (countercurrent) flow and to investigate the distribution of energy dissipation in the extraction compartment, which is one of the most important parameters in liquid-liquid extraction modeling. Stagnant or dead zones of the flow field are also observed in CFD and PIV and compared to each other. Main focus is on the correct prediction of the fluid dynamics and turbulence also to guarantee a successful future coupling with PBM. In PBM the breakage and coalescence kernels are usually strong functions of the energy dissipation. Especially breakage is mainly occurring in the stirrer outflow. That's why for the local energy dissipation the main focus is on this region. In future, with increasing computational power full-scale CFD simulations could be possible without scale-up steps.

The paper is structured as follows: first, the experimental setup and the computational model are described briefly. The results of the CFD simulations and the comparison to the experimental data are presented in the main part of the paper. Single-phase flow results and the analysis of the energy dissipation are followed by the two-phase results. At the end of the paper, a summary and conclusions are given.

Experimental setup

Rotating Disc Contactor

The RDC is the most commonly used extractor for aromatics extraction in the petrochemical industry. The previously investigated pilot plant column with an inner diameter of 150 mm is often applied for scale-up purposes [12]. The layout rule by Kusters [21] was applied for the scale up of the RDC geometry of a DN450 column. Diameter of the shaft was held constant to avoid a 160 mm shaft. The resulting measurement area in the 450 mm test rig is around 10 times larger as in the 150 mm column. The dimensions are compared in Table 1. A sketch of the RDC geometry is given in Fig. (1). Three RDC compartments were installed in the test rig with an overall height of around 1m. The column can be operated at one and two-phase conditions, the aqueous phase entering at the top and leaving at the bottom. A perforated pipe at the bottom of the column served as the dispersed phase distributor, which generates droplets in the mm range. Variable rotation of the disc stirrers is warranted by an agitator. Different rotational speeds (50, 100, 150 200, 300 rpm) were investigated in the test rig. The volume flow of the phases was 1000 l/h in single-phase operating mode and 500 l/h per phase in two-phase mode. The drop sizes in the column were determined from digital photos. The drop size was determined as the Sauter mean diameter ($d_{32} = \sum n_i d_i^3 / \sum n_i d_i^2$) where n_i is the number of identified droplets. The d_{32} was estimated around 2 mm (300 rpm) and 3 mm (100 rpm).

PIV technique

Velocity measurements and the estimation of the turbulent energy dissipation are needed for a comparison with the CFD simulations. PIV measurements are conducted for the validation of the simulations. The PIV technique allows the recording of a complete flow velocity field in a plane of the flow within a few microseconds [22]. Some key data of the PIV setup are given in this chapter. A detailed description of the PIV setup was also given in previous work [12, 20]

An ILA (Intelligent Laser Applications GmbH) 2D PIV system was used. It includes a pair of Nd:YAG Lasers, the CCD camera (PCO SensiCam, 1280x1024 px²) and the ILA synchronizer. The flow is seeded with small tracer particles that follow the flow. A cross section of the flow is illuminated with the use of a laser light sheet. The CCD camera is used to record images of the particles in the illuminated plane. Two subsequent images of the flow, separated by a short time delay, Δt , are divided into small interrogation areas. In the time interval between light pulses, the particles move a short distance. Their displacements are then calculated and can be converted into a velocity vector field by cross correlation when knowing the pulse separation and the image scale. ILA's VidPIV software version 4.6XP was applied for the data analysis. A linear mapping was used to assign the pixels of a picture to physical units. The pulse distance was varied between 250 and 1500 μ s. The interrogation areas for the cross correlation were 64 x 64 pixel with a 50% overlapping, followed by an 32 x 32 pixel adaptive cross correlation. The erroneous vectors were removed and replaced by a global velocity filter and local 3x3 median filters. The outliers were finally interpolated to fill

the holes in the vector field. Images were captured at a rate of 4Hz for 50s. 200 pairs of pictures were taken for the determination of ensemble-averaged velocity fields.

For the single-phase water experiments polyamide tracer particles with a diameter of 50 μm and a density of 1060 kg/m^3 were applied. The density difference between the particles and the water phase and the resulting errors can be neglected. In a two-phase liquid-liquid flow, the presence of the dispersed phase introduces problems to the PIV method, which are not present in single-phase flows. The dispersed phase masks the measurement plane and a clear view on the illuminated plane is not possible. For the two-phase PIV a refractive index matching technique is the method of choice [12]. The measurement of the aqueous phase velocities is possible by the use of an iso-optical system, where the refractive index of both liquid phases is identical. In this work, a system with matching refractive indices was applied which allows the discrimination of the phases and makes an estimation of the phase fractions possible. The system is composed of butylacetate as the dispersed phase and a calcium chloride/water mixture (30/70 wt%) as the continuous aqueous phase. The density of the continuous and the dispersed phases were 1300 and 880 kg/m^3 , respectively. The viscosity of both phases is 0.02 and 0.00074 kg/ms . The fluorescent dye Rhodamine 6G only soluble in the aqueous phase allows the discrimination of the phases. Hollow glass spheres with a diameter of 10 μm and a density of 1100 kg/m^3 only soluble in the aqueous phase seeded the two-phase flow.

The RDC compartment was divided into different zones to increase the resolution of the PIV measurements. The measurement areas are shown in Fig. (2). Zone 1 ranges from the stirrer to the wall and a second zone around the stirrer was chosen for the estimation of the turbulent energy dissipation. The dimensions of zone 1 are obvious from Table 1 and Fig. (1). The dimensions of zone 2 are given in mm in Fig. (2). It was also attempted to measure the area between the shaft and the stirrer tip (left side of the compartment in Fig. (2)). Unfortunately, the illumination of the tracer particles and the overall picture quality in the dense system were not good enough to guarantee reliable measurements. A photograph of the PIV setup is shown in Fig. (3).

Turbulent energy dissipation

PIV offers the possibility to estimate turbulent kinetic energy k and its dissipation rate ε . The approach is shortly described here. The determination of dissipation rate through direct PIV measurement of fluctuating velocity gradients is widely investigated and further information could be found in relevant literature [23-27].

The turbulent kinetic energy and its dissipation rate are derived from the fluctuating velocities and their spatial derivatives. First, the ensemble-averaged velocity field \bar{u} is subtracted from the instantaneous velocity fields u to obtain the local fluctuating velocity fields u' in VidPIV.

$$u' = u - \bar{u} \quad (1)$$

The local energy dissipation ε can be written as:

$$\varepsilon = \nu \left[2 \left(\overline{\left(\frac{\partial u'_i}{\partial x_i} \right)^2} + \overline{\left(\frac{\partial u'_j}{\partial x_j} \right)^2} + \overline{\left(\frac{\partial u'_k}{\partial x_k} \right)^2} \right) + \overline{\left(\frac{\partial u'_i}{\partial x_j} \right)^2} + \overline{\left(\frac{\partial u'_j}{\partial x_i} \right)^2} + \overline{\left(\frac{\partial u'_i}{\partial x_k} \right)^2} + \overline{\left(\frac{\partial u'_k}{\partial x_i} \right)^2} + \overline{\left(\frac{\partial u'_j}{\partial x_k} \right)^2} + \overline{\left(\frac{\partial u'_k}{\partial x_j} \right)^2} + 2 \left(\overline{\left(\frac{\partial u'_i}{\partial x_j} \frac{\partial u'_j}{\partial x_i} \right)} + \overline{\left(\frac{\partial u'_i}{\partial x_k} \frac{\partial u'_k}{\partial x_i} \right)} + \overline{\left(\frac{\partial u'_j}{\partial x_k} \frac{\partial u'_k}{\partial x_j} \right)} \right) \right] \quad (2)$$

where ν is the kinematic viscosity.

Only 5 of the 12 terms can be determined from 2D PIV measurements. The remaining seven terms can be obtained by employing the local isotropy hypothesis [25]. Therefore the equation for ε becomes, in cylindrical coordinates:

$$\varepsilon = \nu \left[2 \overline{\left(\frac{\partial u'_r}{\partial r} \right)^2} + 2 \overline{\left(\frac{\partial u'_z}{\partial z} \right)^2} + 3 \overline{\left(\frac{\partial u'_r}{\partial z} \right)^2} + 3 \overline{\left(\frac{\partial u'_z}{\partial r} \right)^2} + 2 \overline{\frac{\partial u'_r}{\partial z} \frac{\partial u'_z}{\partial r}} \right] \quad (3)$$

The fluctuating velocity fields were exported to Tecplot. Tecplot is a visualization tool, which can analyze complex data. It also serves as a CFD postprocessing software. In Tecplot, the velocity gradients were derived and the energy dissipation was determined.

The turbulent kinetic energy k can also be estimated by a 2D approximation under isotropic flow conditions:

$$k = \frac{1}{2} (\tilde{u}_i^2 + \tilde{u}_j^2 + \tilde{u}_z^2) = \frac{3}{4} (\tilde{u}_i^2 + \tilde{u}_j^2), \quad (4)$$

where \tilde{u}_i are the root-mean-square (rms) values of the instantaneous fluctuating velocity components u'_i .

To fully resolve the spatial behavior of the turbulence quantities of a turbulent three-dimensional flow field, it is necessary to measure down to the Kolmogorov length scale [26]:

$$\eta = \left(\frac{\nu^3}{\varepsilon} \right)^{1/4}. \quad (5)$$

Therefore, for the determination of the turbulent energy dissipation, an additional adaptive cross correlation with a 16 x 16 pixels interrogation area was carried out in VidPIV to improve the spatial resolution. The resulting vector field has a resolution of 8 x 8 pixels because of the 50% overlap.

Computational Model

The simulations were carried out in the CFD code Fluent 6.3. The fluid dynamics of the single-phase water phase was computed by solving the Reynolds averaged Navier-Stokes equations. For modeling the two-phase system, an Eulerian-Eulerian two-fluid approach is used. The conservation equations of continuity and momentum are solved for each phase. The continuity equation for the liquid phase I is:

$$\frac{\partial(\alpha_l \rho_l)}{\partial t} + \nabla \cdot (\alpha_l \rho_l u_l) = 0, \quad (6)$$

where α is the volume fraction, \square which represents the space occupied by each phase, ρ is the phase density, u is the phase velocity. The conservation of momentum for phase I is:

$$\frac{\partial(\alpha_l \rho_l u_l)}{\partial t} + \nabla \cdot (\alpha_l \rho_l u_l u_l) - \nabla \cdot \tau_l = -\alpha_l \nabla p + \alpha_l \rho_l g + F_k, \quad (7)$$

where τ is the stress-strain tensor, p is the pressure shared by all phases, g is the gravitational acceleration and F represents the interfacial forces.

In addition the constraint for the volume fractions must also be satisfied in the two-phase simulations:

$$\alpha_1 + \alpha_2 = 1. \quad (8)$$

For the two-phase flow, the inter-phase interaction term F_k consists of different momentum exchange mechanisms. Only the drag force was taken into account, while the virtual mass force and the lift force were neglected. For the evaluation of the drag coefficient, the model of Schiller & Naumann was applied [28]. In this connection, constant Sauter mean diameters were applied in the simulation, which were estimated by evaluating digital PIV photos from the experiments.

The computational model was a 2D axis-symmetric geometry consisted of 20000 quadrilateral cells with 3 mm grid spacing (see Fig. (4)). For turbulence modeling, the standard k- ϵ , realizable k- ϵ turbulence models and the Reynolds Stress model were applied together with standard wall functions. Details of the different turbulence models can be found in literature [28]. For the calculation of the multiphase turbulence, the Fluent mixture turbulence model was used, which is an extension of the single-phase model [28]. Velocity-inlet and pressure-outlet boundary conditions were applied at the top and bottom of the computational grid. The boundary condition for the single water phase is $v=0.00175$ m/s resulting in 1000 l/h. For the two-phase flow the boundary conditions are $v_{aq}=0.000985$ m/s and $v_{org}=0.0089$ m/s (10% volume fraction at the inlet. Values close to zero were given for the turbulent kinetic energy and the energy dissipation. QUICK differencing schemes were used to discretise the convection terms while PRESTO was used as the discretisation method for pressure. The first order implicit scheme was used for time advancing and the pressure-velocity coupling was done using the PISO algorithm in single-phase and the SIMPLE algorithm in two-phase flow. A time step size between 0.001 and 0.01s was chosen and more than 20s were simulated (100s in two-phase mode). Residuals below 10^{-5} were chosen as convergence criteria (10^{-4} for the two-phase flow). For the two-phase flow, the total volume of the dispersed phase was monitored till it become constant. The computational time for one time step is around 90s using a single 3GHz CPU and two-phase flow. The overall computing time for 10000 time steps at a time step size of 0.01 s (100s real time) is therefore 250h.

Results & Discussion

Single-phase flow

CFD simulations have been performed with three turbulence models, namely the standard k- ϵ , realizable k- ϵ and the RSM. PIV measurements have been conducted for the two different measurement areas shown in Fig. (2). Different stirrer revolutions were investigated at a single-phase water flow rate of 1000 l/h. Since only 2D PIV measurements were possible in the extractor, the velocities are compared in the PIV measurement plane. The velocity magnitude in the PIV measurement plane is calculated from the axial (x-coordinate) and radial velocities (z coordinate). The swirl velocity (y-coordinate) is not compared.

$$u = \sqrt{u_x^2 + u_z^2} \quad (9)$$

Zone 1, from the stirrer to the column wall is the most interesting part of the compartment since it is the mixing zone of the compartment with the highest energy dissipation. PIV contours of average velocity magnitude and velocity vectors of zone 1 at 50rpm are depicted in Fig. (5). A qualitative comparison between the PIV measurements and the CFD simulations is visible in Fig. (6). It can be seen that the CFD simulations are in good agreement with the simulations. As expected, the highest velocities are near the stirrer tip. From the velocity vectors and the contours, one big vortex can be estimated in the compartment between the

stators. The PIV and CFD velocities are compared along a line at the stirrer level from the stirrer to the column wall. The velocities along this line are shown in Fig. (7). The CFD predicted maximum velocity and the velocities at the stirrer level are predicted well by all turbulence models. Only minor discrepancies are visible for the shape of the vortex and the dead zone. The same graphs are shown for 150 rpm (Fig. (8), Fig. (9), Fig. (10)) and 300 rpm (Fig. (11), Fig. (12), Fig. (13)). For the higher stirrer speeds, the shape of the vortices and dead zone are almost identical but at a higher velocity magnitude. Again, all turbulence models can predict the fluid dynamics and the shape of the vortex at 150 rpm (Fig. (9), Fig. (10)). At 300 rpm the standard k-ε fails to predict the shape of the vortex and the maximum velocities (Fig. (12), Fig. (13)). These results can confirm previous work, where the realizable k-ε model and the RSM were best for single-phase flow in a RDC 150 mm pilot plant column [12], while the standard k-ε model could also not meet this accuracy [12,20]. CFD can predict the one-phase flow field in the industrial scale RDC extractor exactly, whereas all flow phenomena such as vortices and dead zones can be described. Grid independency was assured by applying a 1mm grid, which gave the same results at much higher computational load.

Local Turbulent energy dissipation

The turbulent energy dissipation was calculated within the framework of PIV analysis from Eq.(3). Different stirrer speeds, 100, 200 and 300 rpm for a water flow rate of 1000 l/h were investigated. The stirrer Reynolds number range is between 75000 and 4×10^5 . It depends on the rotation per second N , the stirrer diameter D_r , the density ρ_c and the dynamic viscosity η_c [29].

$$\text{Re} = \frac{D_r^2 N \rho_c}{\eta_c} \quad (10)$$

The transition from laminar to turbulent flow in the compartment is expected for a Reynolds number $\text{Re} > 6 \times 10^4$ [29].

The spatial resolution of the PIV measurements affects the magnitude of the measured dissipation rate. To fully resolve the spatial behaviour of the turbulence quantities of a turbulent flow field, it is necessary to measure down to the Kolmogorov length scale. Saarenrinne et al. [27] have shown the turbulent kinetic energy and the dissipation rate spectrums from Helland's theoretical spectrum. From these spectrums it can be seen that to reach 90% of the dissipation rate the spatial resolution Δ should be around 2η , and to reach 65% 9η . On the other hand, to reach 65% of the turbulent kinetic energy the spatial resolution should be only around 90η , and to reach 65% around 20η [27]. Because of the huge compartment area in the industrial scale RDC, ($\text{area}_{\text{compartment}} = 35640 \text{ mm}^2$) a small measurement zone (see Fig. (2), zone 2) at the stirrer was chosen, to increase the spatial resolution. This zone is also of main interest, since the main energy input is at the stirrer and the stirrer tip. In practice, the droplets break in this region at the stirrer wall or in the stirrer outflow. A correct prediction of the turbulent energy dissipation in CFD is crucial for a correct modeling of the breakage and coalescence phenomena and a coupling with Population Balance Models [19]. That's why the measured PIV energy dissipation was compared to the CFD predictions to investigate the predictivity of CFD for the turbulence characteristics. A calculation of the energy dissipation for the whole compartment from the single-phase velocity measurements (see above) did not deliver reliable results because of the lower resolution and the resulting high uncertainties.

The PIV spatial resolution for the different interrogation areas ($64 \times 64 \text{ px}^2$, $32 \times 32 \text{ px}^2$, $16 \times 16 \text{ px}^2$) and the measurement zone is shown in Table 2. The maximum measured energy dissipation for 100 rpm as a function of these spatial resolutions is depicted in Fig. (14). From this figure, it becomes clear, that the smaller measurement zone 2 around the stirrer was necessary to reach a lower spatial resolution together with 16×16 pixels interrogation areas.

In Table 3. the maximum and average values for the energy dissipation and the corresponding Kolmogorov length scales (Eq. (5)) at 100 rpm for PIV and CFD are presented. The average values were calculated by means of an area integral over the whole zone. From this table it can be seen that the spatial resolution is around 5 times the Kolmogorov length scale η for the average energy dissipation. For the maximum value of the energy dissipation only 10η are reached. Therefore, it was assumed that only around 65% of the energy dissipation was measured and the values were scaled in Tecplot by a factor 1.55. The scaled values are also shown in Table 3. and agree well with the average values predicted by CFD. The different turbulence models predict almost identical results for the energy dissipation (see Table 3 & Fig. (15)).

The contours of the energy dissipation in PIV, unscaled (top) and scaled (bottom) are depicted in Fig. (16) and compared to CFD results. It is visible that the scaled energy dissipation in the stirrer outflow agrees well with the CFD results. The maximum values in CFD are higher than the maximum PIV values. The same is also visible in Fig. (17) and Fig. (18), where the scaled energy dissipation is compared along the stirrer level from the stirrer to the column wall. Fig. (17) compares the values close to the stirrer wall, where the PIV measurements were carried out and high values for the energy dissipation are visible. Because of non-idealities and small oscillations of the stirrer in the experiments, it is not possible to measure exactly close to the stirrer wall. This explains the lower measured values close to the stirrer. The higher values in CFD close to the wall can therefore neither be negated nor confirmed from the measurement. At least, the CFD predicted energy dissipation near the stirrer is in the same order of magnitude and seems reasonable based on the slope. In literature, CFD is known to underpredict the dissipation (e.g. [14]), which is not the case here. Note that the small investigated zone is in the near wall regions, which is influenced by the wall effect and the applied wall function.

The CFD predicted energy dissipation near the stirrer is dependent on the grid near the wall and the wall functions. In this work, the standard wall functions were applied without giving closer attention to this aspect, since it is also not possible to compare the near wall values to experimental PIV data. The y^+ values are around 30 and near the optimum [28]. A finer grid (e.g. 1mm) would not be suitable for the near wall regions using the standard wall functions since the wall unit would be far below 30. Some test simulations were also carried out with an enhanced wall treatment applying a fine near wall grid. For the RDC extractor, the grid becomes very fine near the stirrer wall to reach y^+ values around 1. There is a dramatic increase in computational time and no improvement for the velocities. On the other hand, at the vertex of the stirrer even higher values for the energy dissipation were predicted.

In Fig. (18) the energy dissipation is compared in the core flow afar from the wall (see x coordinate). Only a few PIV measurements are available leftmost for this region. In this region, the energy dissipation is one to a few orders of magnitude smaller than near the stirrer. The different turbulent models predict similar results for this region around the dead zone.

The situation of the energy dissipation is worse for 200 and 300rpm. The measured energy dissipation (zone 2) at 200rpm and 300rpm and the corresponding Kolmogorov length scales are given in Table 4. The spatial resolution is now only around 10η for the area average value and around 20η for the maximum values. A scaling based on the rules of thumb of Saarenrinne et al. [26] is now hardly possible. Alekseenko et al. [26] proposed an underestimation coefficient f_ε based on Pao's spectrum:

$$f_\varepsilon = 1 - \exp\left(-\frac{3}{2}\alpha\left(\frac{\pi\eta}{\Delta}\right)^{4/3}\right) \quad (11)$$

where the parameter $\alpha=1.6$. The same authors also developed a fit function to scale the measured values. The fit function reported by Alekseenko et al. [26] is:

$$f_\varepsilon = 1 - \exp\left(-\alpha\left(\frac{3}{2}\left(\frac{\pi\eta}{\Delta}\right)^{4/3} + \left(\frac{\pi\eta}{\Delta - 5.87\eta}\right)^{3.15}\right)\right) \quad (12)$$

where $\Delta > 5.87\eta$. The underestimation coefficients of the turbulent energy dissipation based on Pao's spectrum and the fit function by Alekseenko et al. [26] are shown in Fig. (20). Both correlations were applied to scale the measured values of the energy dissipation. For the fit function, the value of the true energy dissipation was found in the following iterative way. At the first stage f_ε was taken to be equal to unity and approximate value of η was found from $\eta = (\nu^3 f_\varepsilon / \varepsilon_{\text{meas}})^{1/4}$. At the next step f_ε was estimated from Eq.(11) and then η was recalculated. About five iterations are enough for a good convergence [26]. The scaled values for the energy dissipation are also shown in Table 4. Alekseenko et al. have taken the maximum value of ε in the measurement zone as a constant $\varepsilon_{\text{meas}}$. These values are named "PIV scaled max" in Table 4 and the average value for ε is too high, since the values of f_ε are too small in the outer regions. In the next case, the local values of ε were taken as $\varepsilon_{\text{meas}}$ to have an individual scaling parameter ("PIV scaled local" in Table 4). Here the resulting average value becomes smaller than the average in CFD (Table 4). Note that the fit function does not scale values where $\Delta < 5.87\eta$. By applying the fit function, there is no scaling in the outer regions with a satisfying spatial resolution ($\Delta < 5.87\eta$). Finally, f_ε was taken directly from Pao's spectrum in Fig. (19) for the local values of ε as $\varepsilon_{\text{meas}}$ ("PIV scaled Pao" in Table 4). The average value for ε is now higher than the scaled one with the fit function but still lower than the average value in CFD. The maximum value in CFD is always higher than in PIV as discussed above. The good news is that the average value in CFD lies between both underestimation coefficients methods and is in the same order of magnitude. For a bigger measurement area the deviations would be much less since the Kolmogorov length scale is fully resolved in the outer regions of the compartment.

The scaled turbulent energy dissipation with the fit function is compared to the CFD results in Fig. (20) (200 rpm) and Fig. (21) (300rpm). Both methods give the same qualitative and quantitative distribution in the stirrer outflow. The results show that a scaling is possible at higher stirrer speeds but remains difficult especially when the Kolmogorov length scale is only partially resolved ($\Delta > 10\eta$). In Fig. (22) and Fig. (23) the scaled PIV values are plotted at the stirrer level and compared to the CFD results. There is a good agreement for the distance $0.002 < x < 0.014$ m to the stirrer. The RSM delivers the best results especially at 300 rpm. As discussed before, the values close to the stirrer tip (2mm) cannot be compared. All things considered, the CFD results are in good agreement to the scaled PIV measurements although both suffer from uncertainties at the industrial scale and the high energy input.

The huge compartment area in the RDC450 does not allow the estimation of the turbulent energy dissipation or dissipation integral for the whole compartment. For the sake of completeness, the dissipation integrals from CFD are compared to a correlation for the power input in an RDC compartment proposed by Kusters[21]:

$$P = N_p \rho_c N^3 D_r^5 \quad (13)$$

For a comparison with CFD, the mean dissipation can be easily calculated as follows:

$$\bar{\varepsilon} = \frac{P}{\rho_c V_{\text{comp}}} \quad (14)$$

The average energy dissipation by Eq. (14) ranges from 0.01 m²/s³ (100 rpm) to 0.32 m²/s³ at 300 rpm with an impeller power number of 0.3 for the RDC. The predicted mean energy dissipation values from CFD are shown in Table 5 and compared to the results of Eq. (14). The CFD predicted values are now lower. Now for the whole compartment, the effects of the

wall functions are small in comparison to the core flow. It is known that the k- ϵ models underpredict the turbulent properties in stirred tanks or columns [14]. On the other hand, it is questionable if the correlation Eq. (13) can exactly describe the energy input of the RDC at this huge diameter. A stirrer diameter of 0.25 m instead of the present 0.27 m would result in $0.24 \text{ m}^2/\text{s}^3$ mean dissipation value and therefore in some uncertainties in the correlation (Table 5).

Turbulent kinetic energy

Results for the turbulent kinetic energy k in the two PIV measurement zones are depicted in the upper part of Fig. (24) and compared to the CFD results (bottom Fig. (24)). As expected, the turbulent kinetic energy can be easily resolved and does not need high resolutions as for the calculation of the dissipation. In contrast to the energy dissipation, results for the turbulent kinetic energy k seems to be independent of the spatial resolution and contours for both zones (left: zone1, right: zone2) are almost identical and also agree well with the CFD results. For the maximum values of the kinetic energy around 20η are reached for zone 1 and around 10η are reached for the smaller zone 2. The negligible influence of the resolution in this region (resolution below 20η) can confirm the work of Saarenrinne et al. [26].

Recapiulatory, the turbulent kinetic energy is 100% resolved for the RDC 450, while the turbulent energy dissipation can easily be scaled at 100rpm. A scaling for the energy dissipation at higher stirrer speed is also possible.

Two-phase flow

The two-phase flow was investigated at 100 and 300 rpm at volume flow rates of 500 l/h per phase.

The iso-optical system allows the measurement of the velocities in the aqueous phase. Besides the PIV measurements, again all turbulence models were varied in CFD. The velocity fields of the continuous water phase both for CFD simulation and PIV measurements are depicted in Fig. (25) (100 rpm) and Fig. (27) (300 rpm). As in the single-phase flow, one big vortex can be estimated in the compartment between the stators. The vortex shift or turn around now because of the rising droplets. The same behavior was already observed in the pilot plant column [12]. All turbulence models can predict the vortex and the dead zones. However, the vortex in PIV is smaller and compressed and therewith the dead zone is also shifted. The velocities at 100 rpm and 300 rpm are compared along a line at the stirrer level from the stirrer to the column wall in Fig. (26) and Fig. (28). In contrast to the single-phase flow, the deviations are now higher because of the different location of the dead zones and the different shape of the vortices. All turbulence models predict almost identical results at 100 rpm and 300 rpm. Nevertheless, the maximum velocities and the qualitative velocity distribution in the compartment are predicted well. It has to be pointed out that especially the velocities in the 2D PIV measurement area are hard to predict since they are only results of the shear stresses while the main velocity is the swirl velocity normal to the xz -plane.

In Fig. (25) and Fig. (27) the volume fraction in CFD under the stators is smaller than in PIV, which becomes obvious from the velocity vectors in the aqueous phase. It was also noticed that a swirl of dispersed phase developed at 300 rpm at the shaft during the PIV measurements. This phenomenon is depicted in Fig. (29) and compared to the volume fraction in of the dispersed phase in CFD. The same swirl of dispersed phase is predicted in CFD and it is also visible that the droplets do not accumulate under the stators and are dispersed in the compartment. However, a more profound investigation for the volume fraction was not possible in PIV. Finally, the average velocity magnitude and vectors of the whole compartment from CFD are depicted in Fig. (30). It is visible that the velocities at the left side

of the compartment, near to the shaft are very small. This can also explain the accumulation of the dispersed phase near the shaft. The layout rule of Kusters [21] for the shaft would result in a bigger diameter and would probably avoid this effect. As described before, the diameter of the shaft was held constant for the scale-up to avoid a 160 mm shaft.

The differences between PIV and CFD could be explained by the smaller volume fraction under the stators in CFD. Since the droplet diameters were only estimated from the digital photos in the laser measurements and are hard to identify, bigger and smaller diameters in the range 0.5 to 4 mm were also tested in the CFD simulations but did not result in an improvement. The present two-phase model uses a constant Sauter mean diameter and cannot account for coalescence and an accumulation of the droplets under the stators. A coupled CFD-PBM model which can describe the breakage near the stirrer and the coalescence under the stators can describe the local drop size in one compartment and could probably predict better results for the shape of the vortex. In addition, it is well-known that the multiphase models still demand improvement. As expected, the overall prediction of the velocity fields in the RDC450 is reasonable but worse than in the smaller RDC150 pilot plant column in previous work [12].

Conclusions

Single- and two-phase simulations of a RDC extractor at industrial scale were carried out and compared to 2D PIV measurements. Different turbulence models were applied in the CFD simulations. The results show that CFD can predict the one-phase flow field in the industrial scale RDC extractor exactly, while all flow phenomena such as vortices and dead zones can be described. The turbulent energy dissipation was estimated from single-phase PIV measurements and compared to the results of the CFD simulations. The influence of the spatial resolution in PIV on the measured energy dissipation was analysed. Different methods based on a Kolmogorov length scale analysis were applied to scale the local measured energy dissipation. The scaled energy dissipation derived from PIV measurements agree quite well with the CFD results but remains challenging at higher stirrer speeds. CFD can predict the energy dissipation in the stirrer outflow, while no comparison was available directly at the stirrer. A good agreement is reached for the average value, when the energy dissipation is scaled based on Kolmogorov length scale analysis.

For the two-phase flow, CFD fails to correctly predict the shape of the vortices and location of the dead zones, which are both shifted in CFD. Nevertheless, the predicted velocities and the qualitative velocity distribution in CFD are in good agreement with the experimental ones. The work shows, that CFD can predict hydrodynamic characteristics in an industrial scale RDC, but is still subject to improvements.

Notation

D_r	disc diameter, m
F	interaction force, N
f_ε	underestimation coefficient, -
g	gravity constant, m s^{-2}
k	turbulent kinetic energy, $\text{m}^2 \text{s}^{-2}$
n	stirrer revolutions, rpm
N	stirrer revolution, 1/s
N_p	impeller power number, -
P	power input, $\text{kg m}^2 \text{s}^{-3}$
t	time, s
u	instantaneous velocity, m s^{-1}

u'	local fluctuating velocity, m s^{-1}
\tilde{u}	root mean square velocity, m s^{-1}
\bar{u}	mean velocities, m s^{-1}
V_{comp}	volume of an extraction compartment, m^3
x	coordinate, m
y^+	dimensionless wall distance, -

Greek

α	volume fraction, -
Δ	spatial resolution, m
ε	energy dissipation, $\text{m}^2 \text{s}^{-3}$
η	Kolmogorov length scale, m
η_c	dynamic viscosity continuous phase, $\text{kg s}^{-1} \text{m}^{-1}$
ν	kinematic viscosity, $\text{m}^2 \text{s}^{-1}$
ρ	density, kg m^{-3}
ρ_c	density continuous phase, kg m^{-3}
τ	stress-strain tensor, N m^{-2}

Abbreviations

CFD	Computational Fluid Dynamics
LDA	Laser Doppler Anemometry
LDV	Laser Doppler Velocimetry
PIV	Particle Image Velocimetry
RDC	Rotating Disc Contactor
rpm	revolutions per minute
RSM	Reynolds Stress Mod

Acknowledgements

The authors acknowledge the financial support from the Deutsche Forschungsgemeinschaft (DFG).

References

- 1 Erwin, DL. *Liquid-Liquid Extraction. Industrial Chemical Process Design*. New York: McGraw-Hill; 2004.
- 2 Robbins LA, Cusack RW. Liquid-Liquid Extraction Operations & Equipment. In: Perry RH, Green DW, Maloney JO, eds. *Perry's Chemical Engineers' Handbook* (7th Edition). New York: McGraw-Hill; 1997.
- 3 Mukhopadhyay A, Devulapalli B, Dutta A, Grald EW. Computational Fluid Dynamics: A virtual prototyping tool for materials engineering. *JOM*. 2004;56:44-48.
- 4 Fei WY, Wang YD, Wan YK. Physical modeling and numerical simulation of velocity fields in rotating disc contactor via CFD simulation and LDV measurements. *Chem Eng J*. 2000;78:131-139.
- 5 Haderer T, Marr R, Martens S, Siebenhofer M. Bestimmung auslegungsrelevanter hydrodynamischer Kenngrößen einer RDC-Extraktionskolonne mit CFD. *Chem Ing Tech*. 2005;77:1055.
- 6 Modes G, Bart H-J. CFD simulation of nonideal dispersed phase flow in stirred extraction columns. *Chem Eng Technol*. 2001;24:1242-1245.

- 7 Kolb, P, Bart H-J, Fischer L. Entwicklung einer Miniplant-Extraktionskolonne. *Chem Ing Tech.* 2002;74:243-247.
- 8 You X, Bart H-J. Comparison of the Reynolds-averaged Turbulence Models on Single Phase Flow Simulation in Agitated Extraction Columns. *Chin J Chem Eng.* 2003;11:362-366.
- 9 Gurker T, Haderer T, Marr R. CFD supported design in liquid-liquid extraction. In: Moyer BM, ed. Proc. International Solvent Extraction Conference ISEC 2008. 2008;403-408.
- 10 Rieger R, Weiss C, Wigley G, Bart H-J, Marr R, Investigating the process of liquid-liquid extraction by means of computational fluid dynamics. *Comp Chem Eng.* 1996;20:1467-1475.
- 11 Ghaniyari-Benis S, Hedayat N, Ziyari A, Kazemzadeh M, Shafiee M. Three-Dimensional Simulation of Hydrodynamics in a Rotating Disc Contactor using Computational Fluid Dynamics. *Chem Eng Technol.* 2009;32:93-102.
- 12 Drumm C, Bart H-J. Hydrodynamics in a RDC Extractor: Single and Two-Phase PIV Measurements and CFD Simulations. *Chem Eng Technol.* 2006;29:1297-1302.
- 13 Weiss C, Bart H-J. Calculation of Flow Patterns in an RDC based on Computational Fluid-Dynamic Methods. In: Logsdail DH, Slater MJ, eds. *Solvent Extraction in the Process Industry.* London: Elsevier Applied Science. 2003;2:1191-1197.
- 14 Bujalski JM, Yang W, Nikolov J, Solnordal CB, Schwarz MP. Measurement and CFD simulation of single-phase flow in solvent extraction pulsed column. *Chem Eng Sci.* 2006;61:2930-2938.
- 15 Retieb S, Guiraud P, Angelov G, Gourdon C. Hold-up within two-phase countercurrent pulsed columns via Eulerian simulations. *Chem Eng Sci.* 2006;62:4558-4572.
- 16 You X, Xiao X. Simulation of the three-dimensional two-phase flow in stirred extraction columns by Lagrangian-Eulerian method. *Chem Biochem Eng Q.* 2005;19:1-11.
- 17 Vikhansky A, Kraft M. Modelling of a RDC using a combined CFD-population balance approach. *Chem Eng Sci.* 2004;59:2597-2606.
- 18 Wang F, Mao Z-S. Numerical and experimental investigation of liquid-liquid two-phase flow in stirred tanks. *Ind Eng Chem Res.* 2005;44:5776-5787.
- 19 Drumm C, Attarakih MM, Bart H-J. Coupling of CFD with DPBM for a RDC Extractor. *Chem Eng Sci.* 2009;64:721-732.
- 20 Drumm C, Tiwari S, Kuhnert J, Bart H-J. Finite Pointset Method for Simulation of the Liquid-Liquid Flow Field in an Extractor. *Comp Chem Eng.* 2008;32:2946-2957.
- 21 Kosters WCG. Rotating Disc Contactor. In: Lo TC, Baird MHI, Hanson C, eds. *Handbook of Solvent Extraction.* NewYork: John Wiley & Sons; 1983.
- 22 Kompenhans J, Raffel M, Willert CE. *Particle Image Velocimetry - A practical guide.* Berlin:Springer; 1998.
- 23 Saarenrinne P, Piirto M. Turbulent kinetic energy dissipation rate estimation from PIV velocity vector fields. *Exp Fluids.* 2000;29:300-307.
- 24 Baldi S, Ducci A, Yianneskis M. Determination of Dissipation Rate in Stirred Vessels through Direct Measurement of Fluctuating Velocity Gradients. *Chem Eng Tech.* 2004;27:275-281.
- 25 Baldi S, Yianneskis M. On the quantification of energy dissipation in the impeller stream of a stirred vessel from fluctuating velocity gradient measurements. *Chem Eng Sci.* 2004;59:2659-2671.
- 26 Alekseenko SV, Bilsky AV, Dulin VM, Markovich DM. Experimental study of an impinging jet with different swirl rates. *Int J Heat Fluid Flow.* 2007;28:1340-1359.
- 27 Saarenrinne P, Piirto M, Eloranta H. Experiences of turbulence measurement with PIV. *Meas Sci Technol.* 2001;12:1904-1910.
- 28 Fluent Inc. *Fluent 6.3 user's guide.* Lebanon:USA; 2005.
- 29 Bahmanyar H, Slater MJ. Studies of Drop Break-up in Liquid-Liquid Systems in a Rotating Disc Contactor Part I: Condition of no mass transfer. *Chem Eng Technol.* 1991;14:79-89

FIGURES & TABLES

Table 1. Dimensions of the RDC geometry

		RDC DN150	RDC DN450
1 Column diameter [mm]	D_K	150	450
2 Diameter shaft [mm]	D_{shaft}	54	54
3 Compartment height [mm]	H_C	30	90
4 Height stirrer/stator [mm]	H_R	1	3
5 Diameter stirrer [mm]	D_R	90	270
6 Stator inner diameter [mm]	D_s	105	315

Table 2. PIV measurements spatial resolutions

measurement area	PIV resolution (px ²)	spatial resolution (mm)
1 8100 mm ²	32	3.39
	16	1.69
	8	0.85
3 1500 mm ²	32	1.60
	16	0.80
	8	0.40

Table 3. CFD & PIV maximum and average values for ϵ and the corresponding Kolmogorov length scales, 100 rpm

100 rpm	Turbulent energy dissipation ϵ (m ² /s ³)		Kolmogorov length scale η (mm)	
	Maximum value	Average value	minimum	average
PIV	0.19	0.0214	0.0425	0.083
standard k-epsilon	0.64	0.0351	0.0347	0.073
realizable k-epsilon	0.63	0.0342	0.0356	0.074
RSM	0.69	0.0390	0.0353	0.071
<i>PIV scaled</i>	0.38	0.0328	0.0433	0.074

Table 4. CFD & PIV maximum and average values for ϵ at 200 rpm & 300 rpm, PIV measurements scaled with fit functions Fig. (20).

200 rpm	Turbulent energy dissipation ϵ (m ² /s ³)		Kolmogorov length scale η (mm)	
	Maximum value	Average value	minimum	average
PIV measured	0.66	0.075	0.0351	0.0604
PIV scaled max	2.2	0.251	0.0260	0.0447
PIV scaled local	2.2	0.091	0.0260	0.0576
PIV scaled Pao	2.07	0.135	0.0273	0.0522
standard k-epsilon	3.4	0.18	0.0233	0.0485
realizable k-epsilon	3.65	0.199	0.0229	0.0473
RSM	3.7	0.202	0.0228	0.0472
300 rpm	Turbulent energy dissipation ϵ (m ² /s ³)		Kolmogorov length scale η (mm)	
	Maximum value	Average value	minimum	average
PIV measured	1.2	0.276	0.0302	0.0436

PIV scaled max	6.01	1.379	0.0202	0.0292
PIV scaled local	6.01	0.512	0.0202	0.0374
PIV scaled Pao	6.1	0.588	0.0226	0.0361
standard k-epsilon	9.2	0.526	0.0182	0.0371
realizable k-epsilon	10.5	0.623	0.0176	0.0356
RSM	11.5	0.608	0.0172	0.0358

Table 5. CFD mean turbulent energy dissipation for the whole compartment, comparison to correlation by Kusters (Eq. 14)

	Volume-average energy dissipation	
	100 rpm	300 rpm
Standard k-epsilon	0.00813 (0.00842)	0.1306
Realizable k-epsilon	0.0087	0.133
RSM	0.014	0.210
Correlation Eq. 14, ($d_r=0.27$ m)	0.0145	0.32
Correlation Eq. 14, ($d_r=0.25$ m)	0.0088	0.24

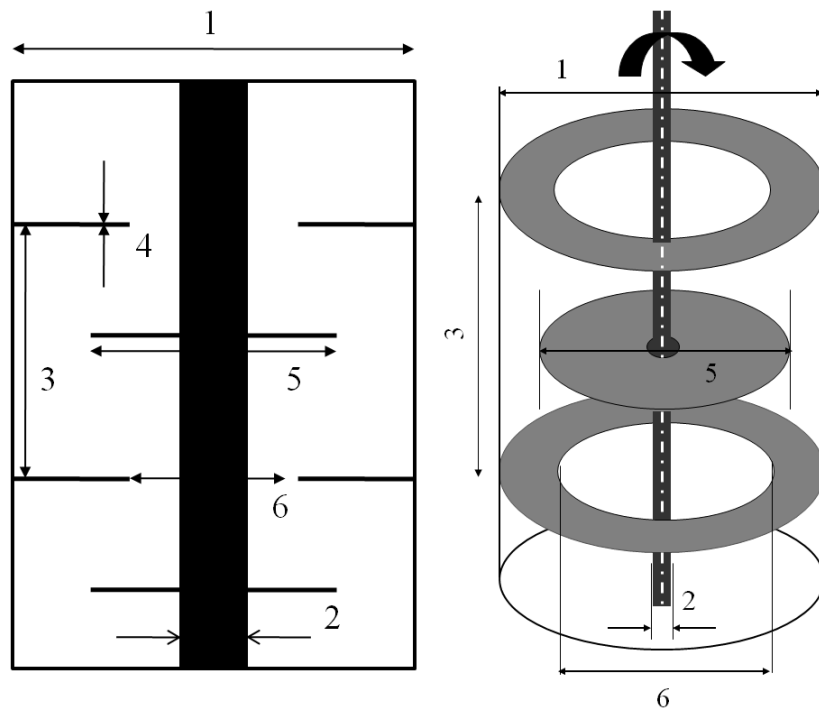


Fig. (1). RDC geometry.

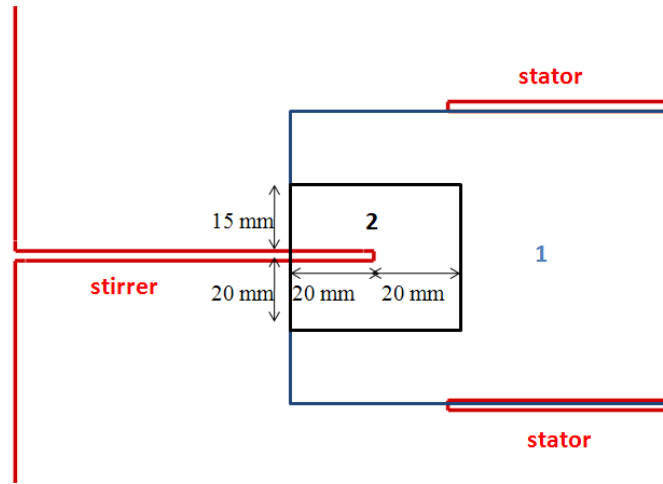


Fig. (2). PIV measurement areas.

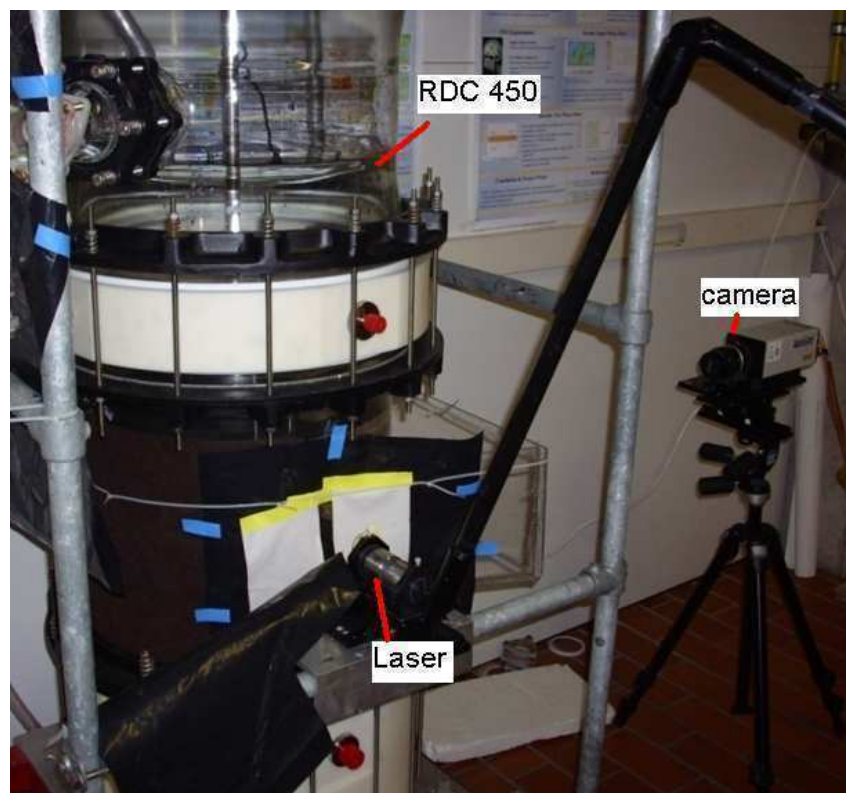


Fig. (3). PIV setup.

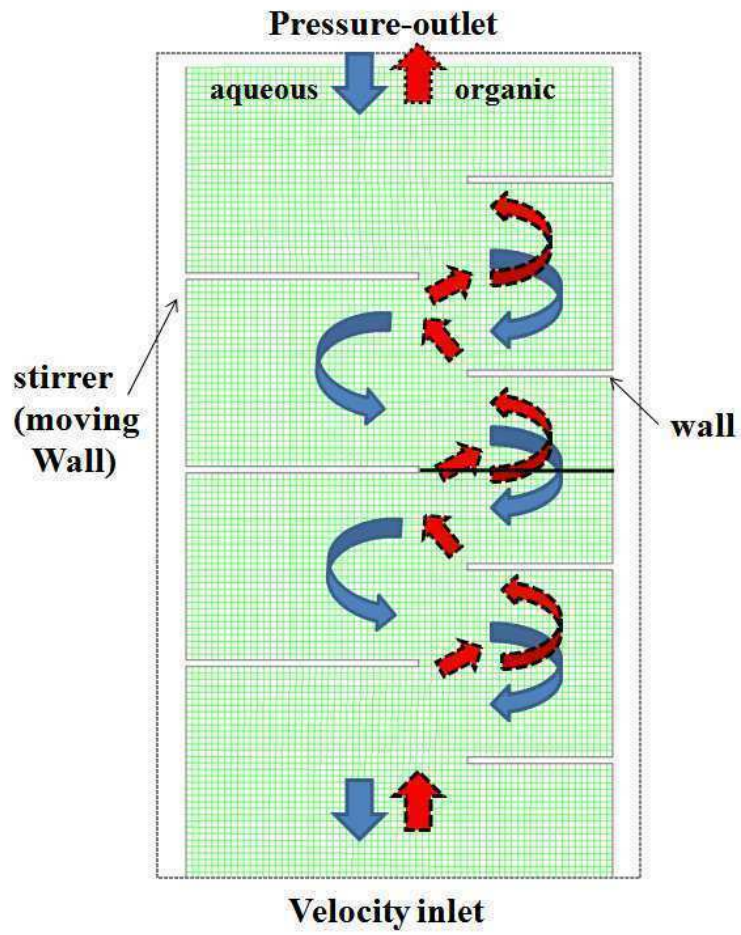


Fig. (4). Computational grid.

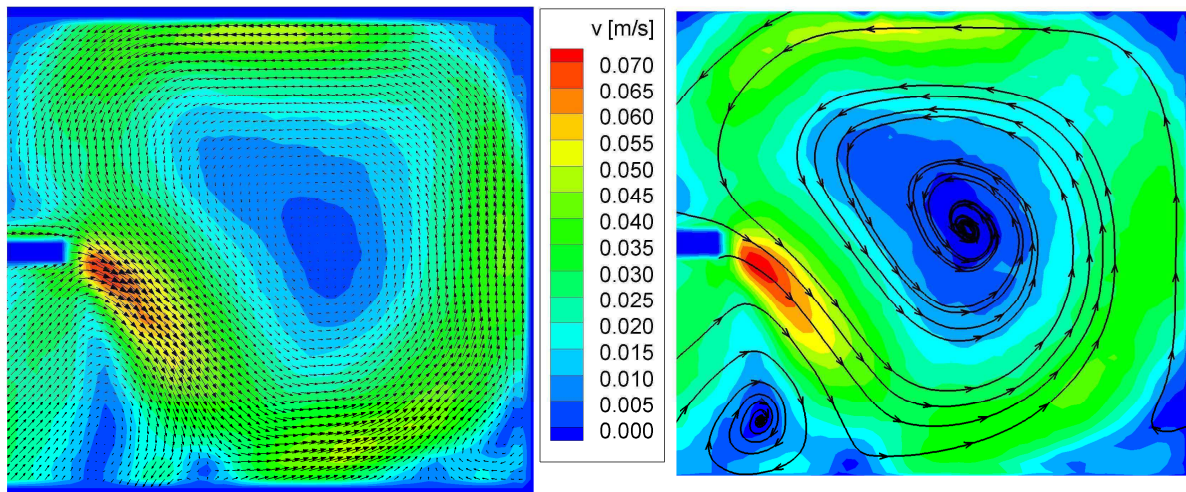


Fig. (5). Single-phase PIV measurements, average velocity magnitude and vectors (left), streamtraces plot (right) zone 1, $n_{\text{stirrer}} = 50$ rpm.

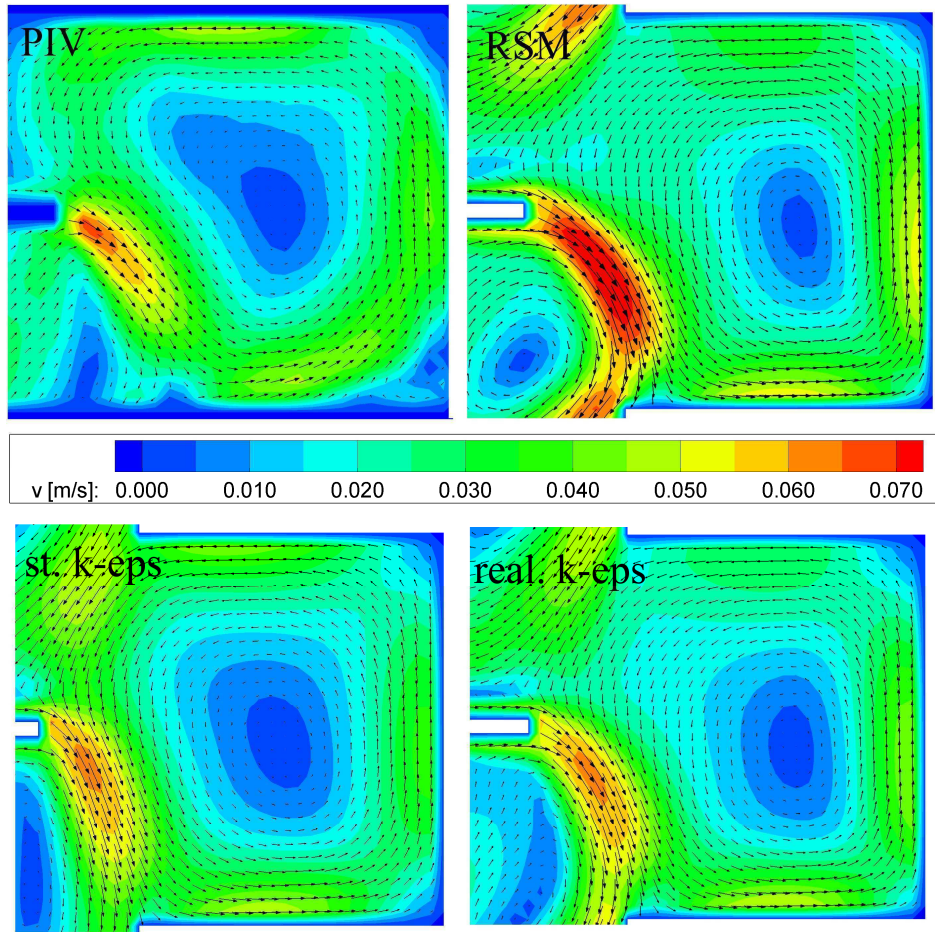


Fig. (6). Comparison PIV-CFD, average velocity magnitude and vectors, zone 1, $n_{\text{stirrer}} = 50$ rpm.

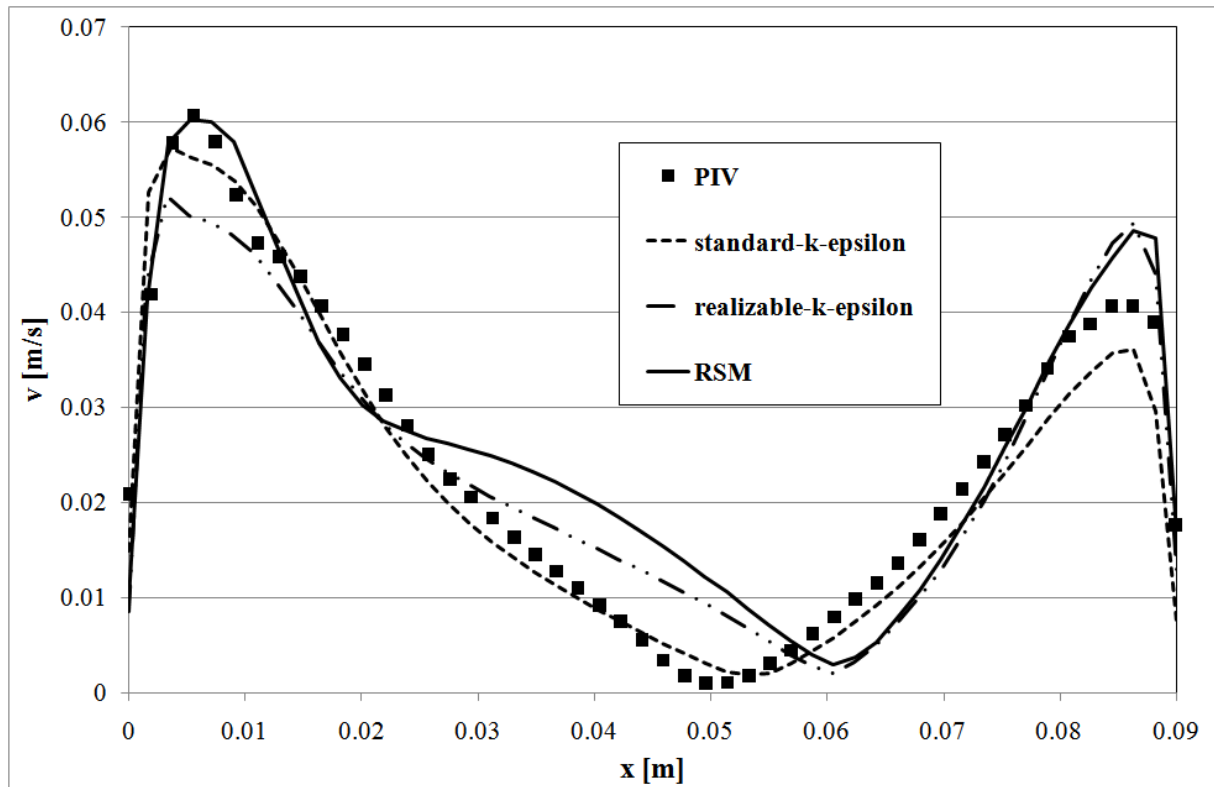


Fig. (7). Comparison PIV-CFD, single-phase measured and calculated average velocity magnitude at stirrer level, zone 1, $n_{\text{stirrer}} = 50$ rpm.

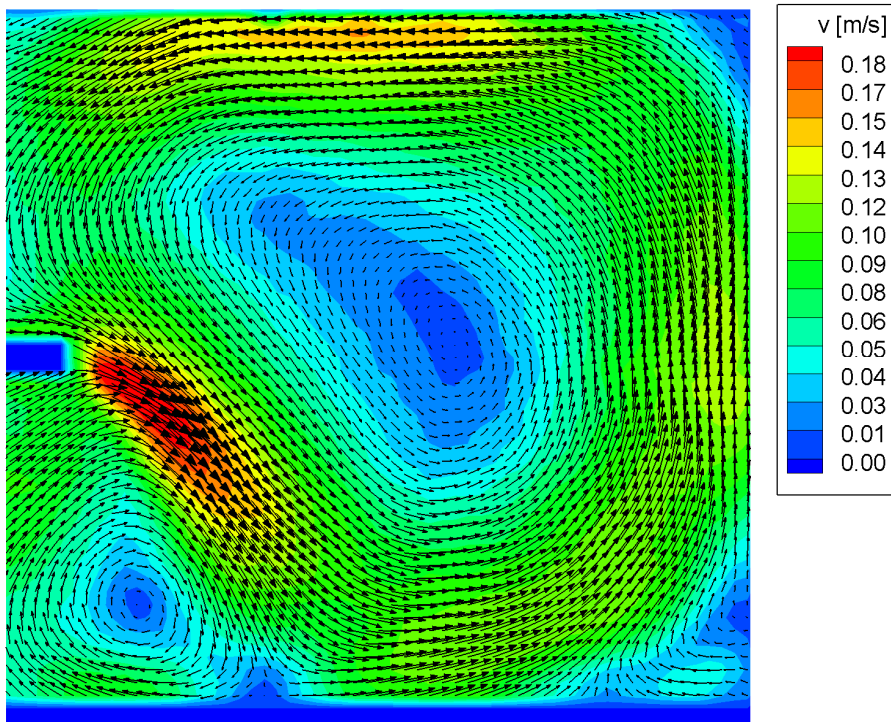


Fig. (8). Single-phase PIV measurements, average velocity magnitude and vectors, zone 1, $n_{\text{stirrer}} = 150$ rpm.

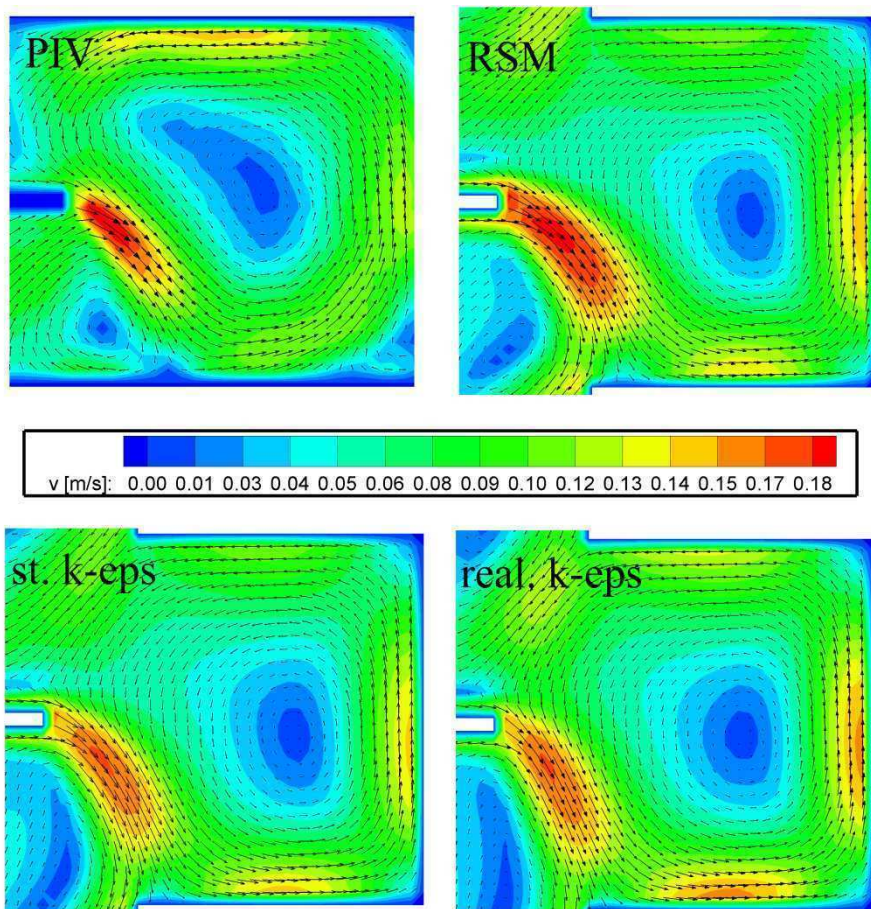


Fig. (9). Comparison PIV-CFD, average velocity magnitude and vectors, zone 1, $n_{\text{stirrer}} = 150$ rpm.

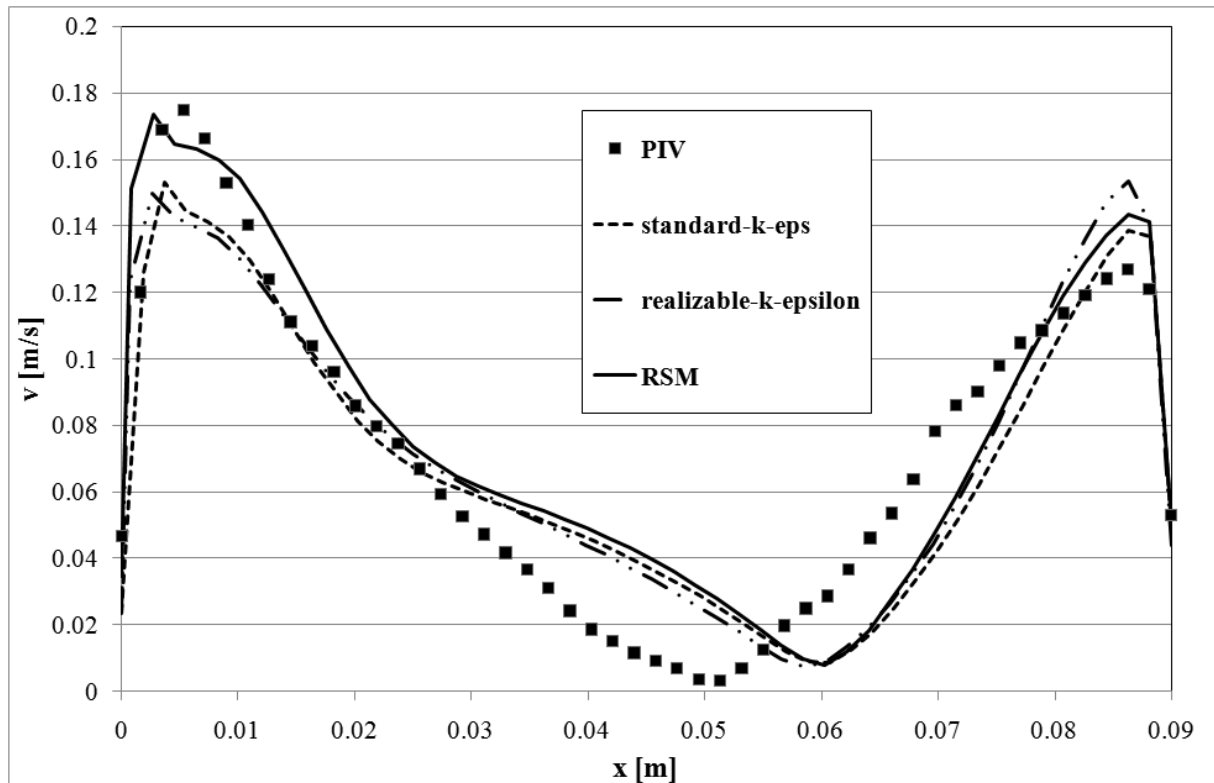


Fig. (10). Comparison PIV-CFD, single-phase measured and calculated average velocity magnitude at stirrer level, zone 1, $n_{\text{stirrer}} = 150$ rpm.

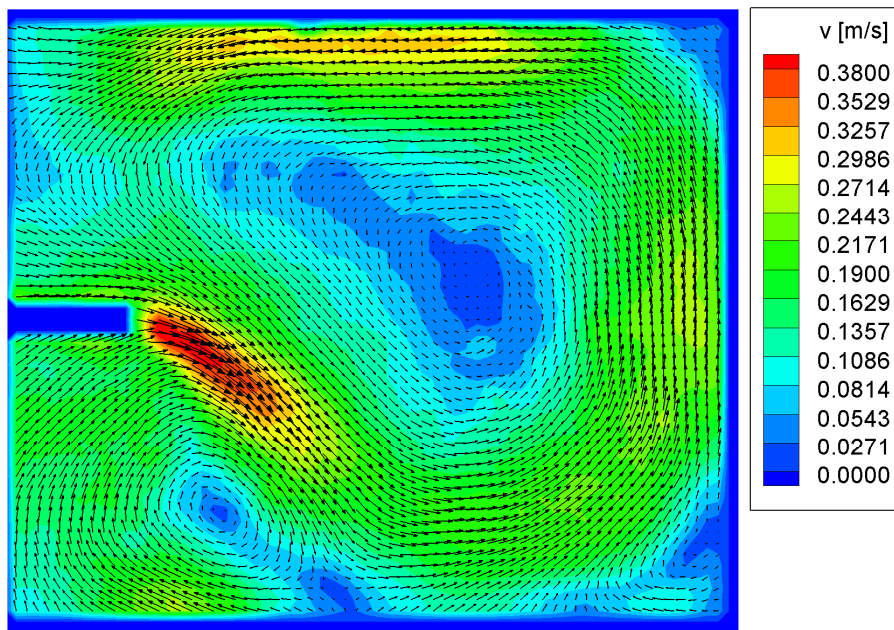


Fig. (11). Comparison PIV-CFD, average velocity magnitude and vectors, zone 1, $n_{\text{stirrer}} = 300$ rpm.

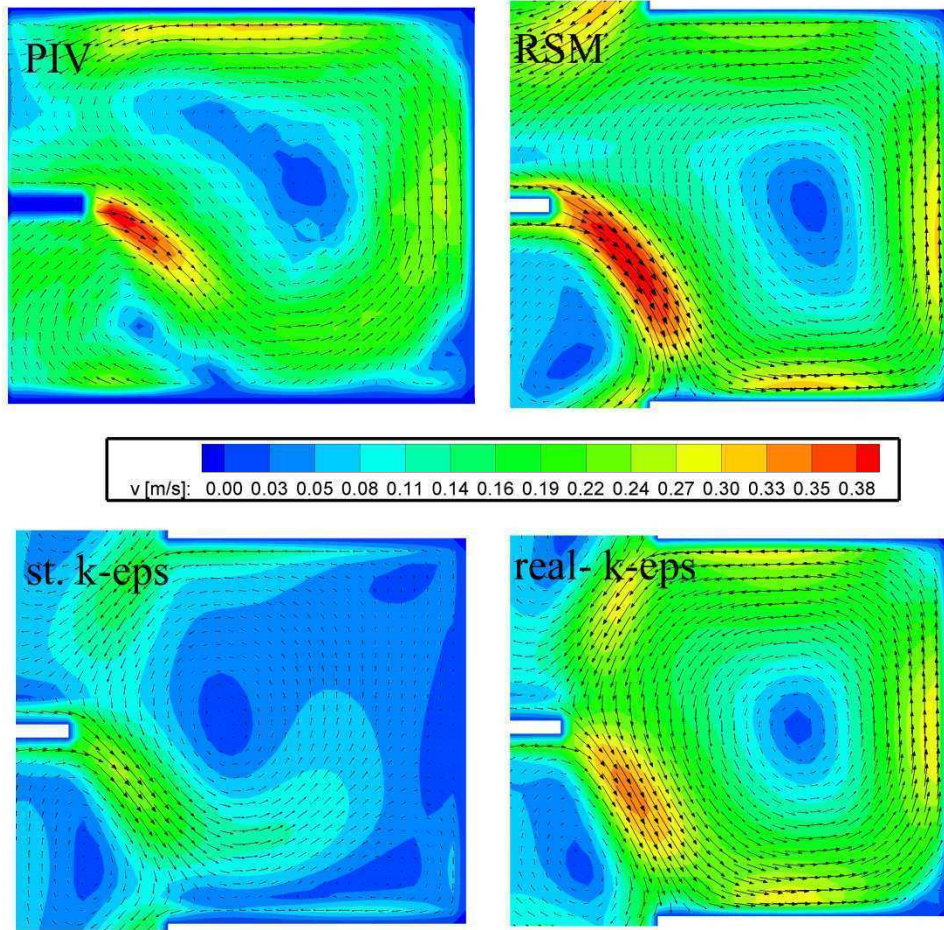


Fig. (12). Comparison PIV-CFD, average velocity magnitude and vectors, zone 1, $n_{\text{stirrer}} = 300$ rpm.

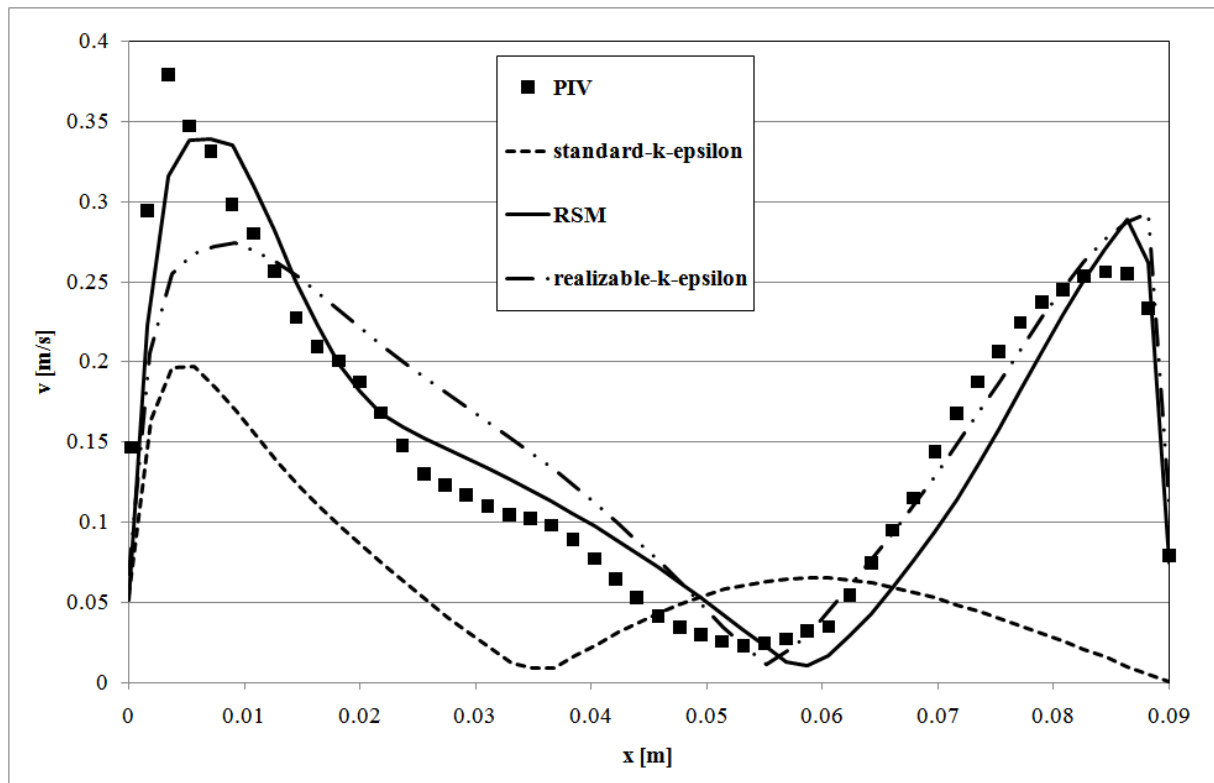


Fig. (13). Comparison PIV-CFD, single-phase measured and calculated average velocity magnitude at stirrer level, zone 1, $n_{\text{stirrer}} = 300$ rpm.

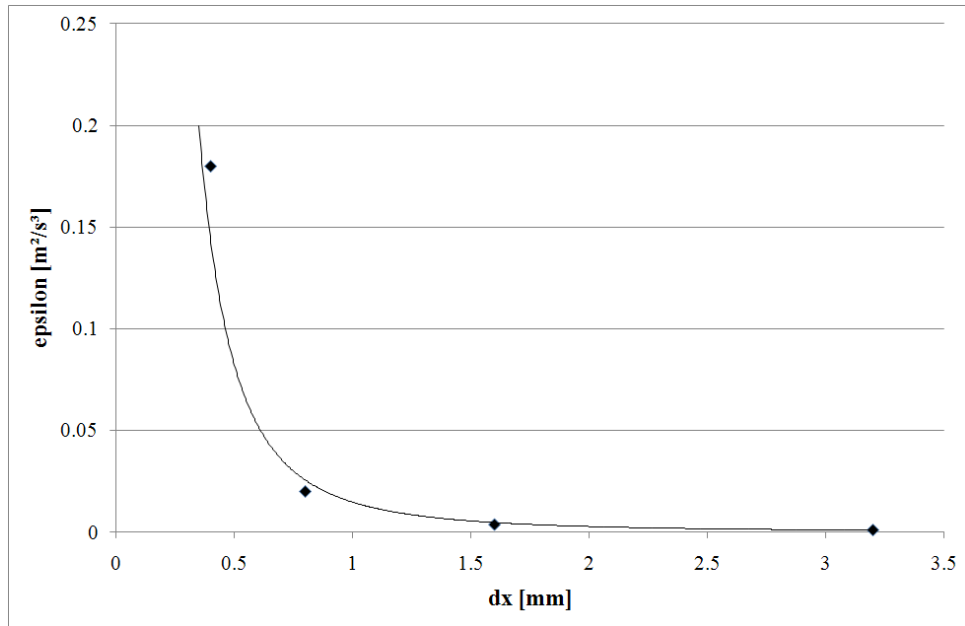


Fig. (14). Influence of the spatial resolution on the measured maximum turbulent energy dissipation in PIV.

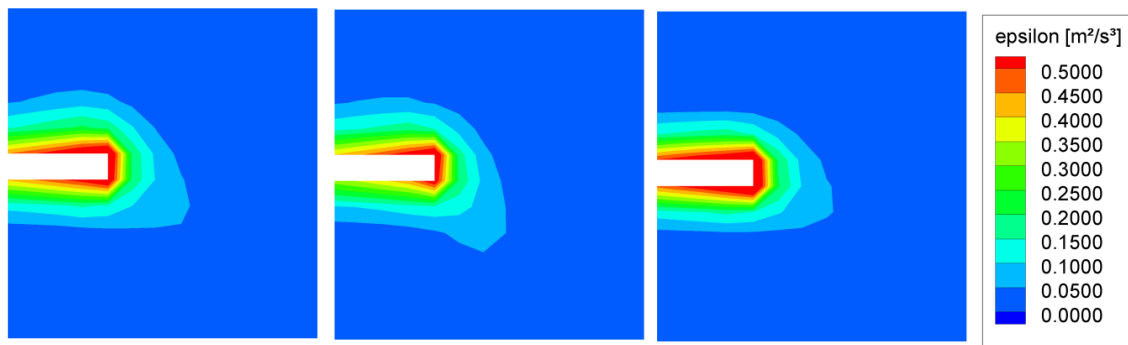


Fig. (15). CFD, turbulent energy dissipation at 100 rpm, standard k-ε, realizable k-ε, RSM (left to right).

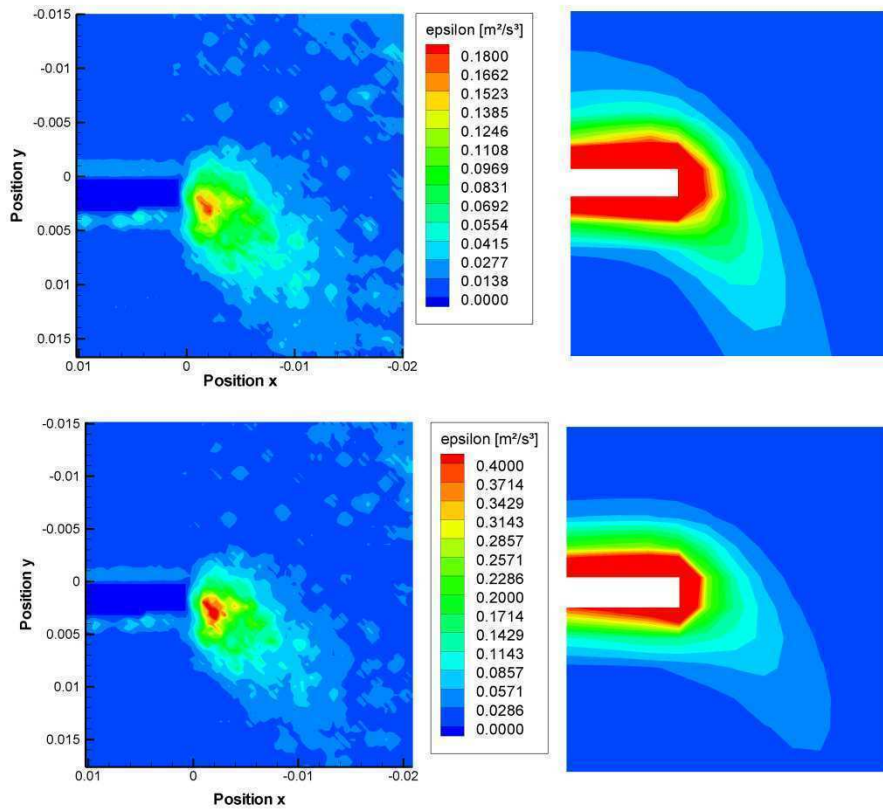


Fig. (16). Turbulent energy dissipation at 100 rpm, Top: PIV 8x8 px² (left), Fluent (right) Bottom: Scaled energy dissipation in PIV based on Kolmogorov length scale analysis 8x8 px² (left), Fluent realizable k-epsilon (right).

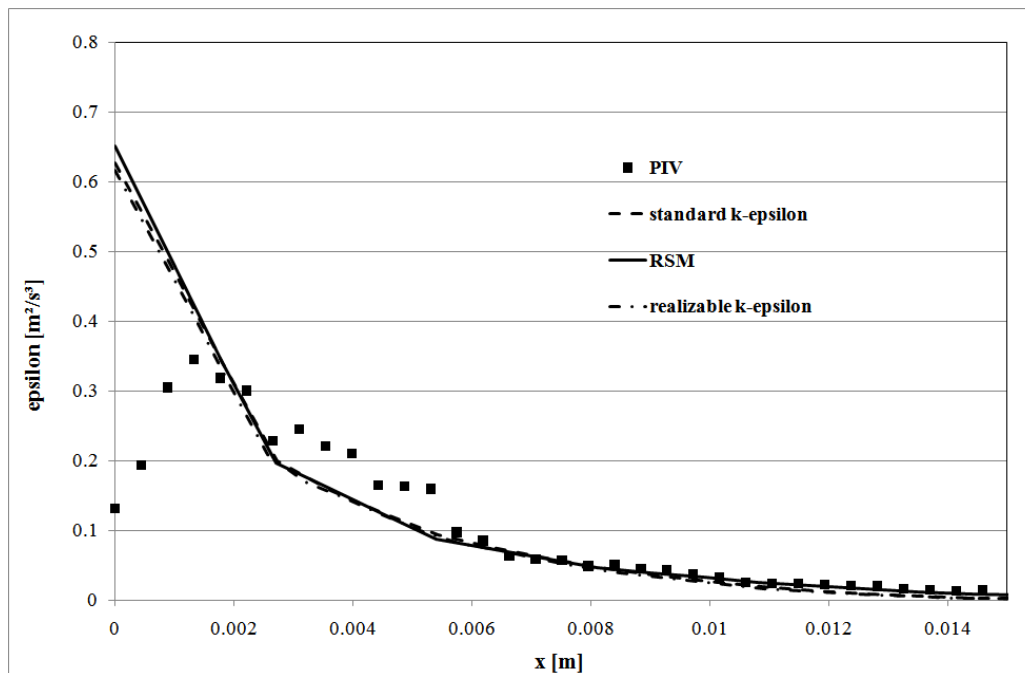


Fig. (17). Comparison turbulent energy dissipation at 100 rpm at the stirrer level, PIV 8x8 px² (scaled), x coordinate distance from the stirrer to the wall.

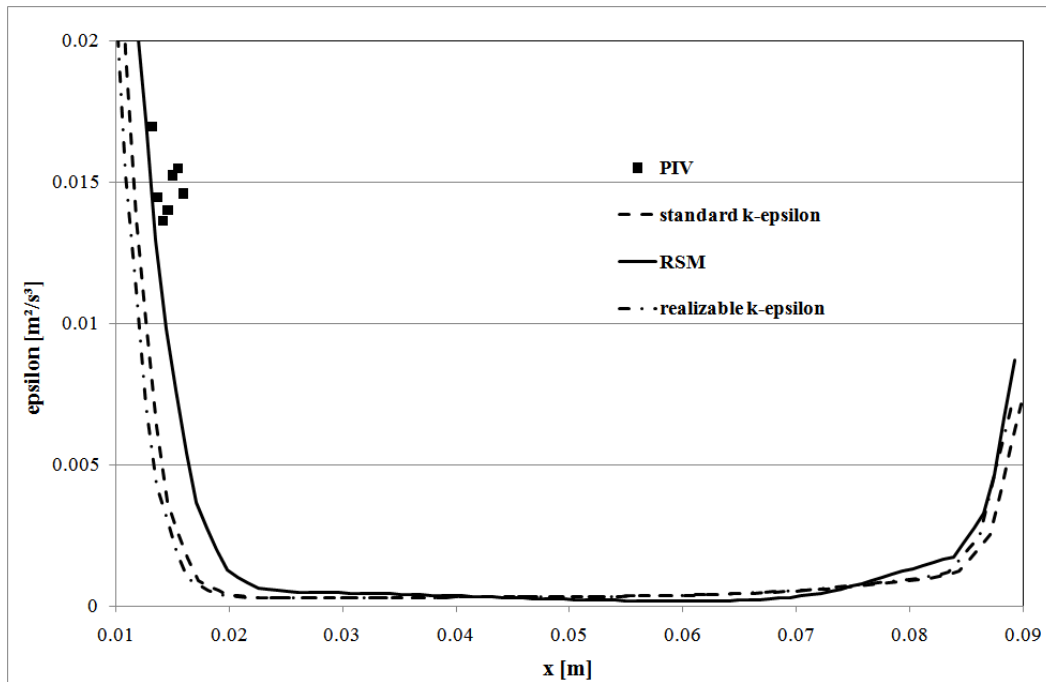


Fig. (18). Comparison turbulent energy dissipation at 100 rpm at the stirrer level (core flow), PIV 8x8 px² (scaled), x coordinate distance from the stirrer to the wall.

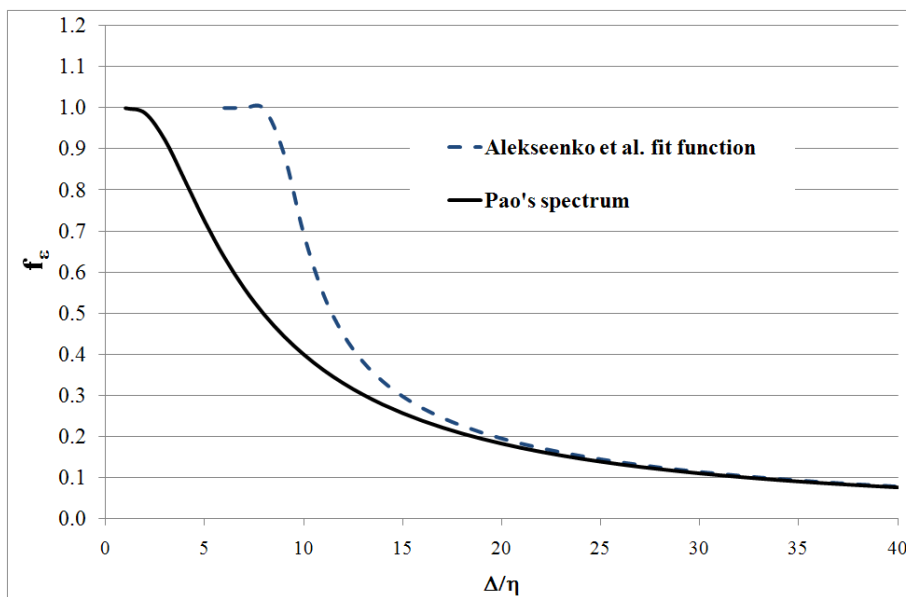


Fig. (19). Influence of the spatial resolution in PIV on the underestimation coefficient of the turbulent energy dissipation, Pao's spectrum & fit function by Alekssenko et al.

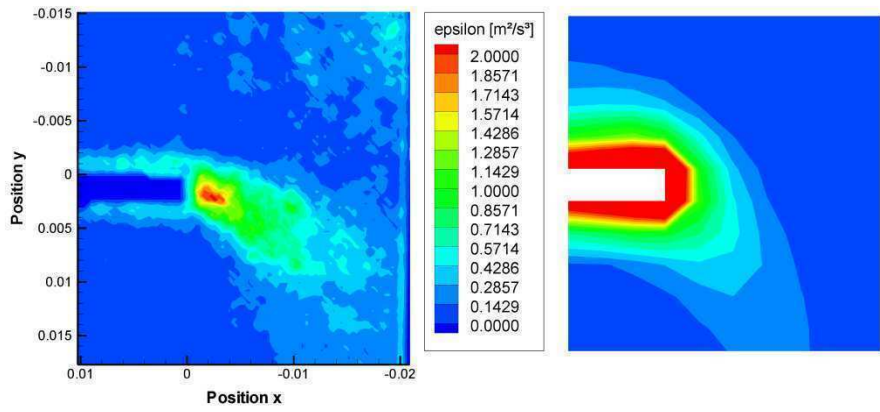


Fig. (20). Turbulent energy dissipation at 200 rpm, scaled energy dissipation in PIV (fit function), PIV 8x8 px² (left), Fluent (realizable k-epsilon) (right).

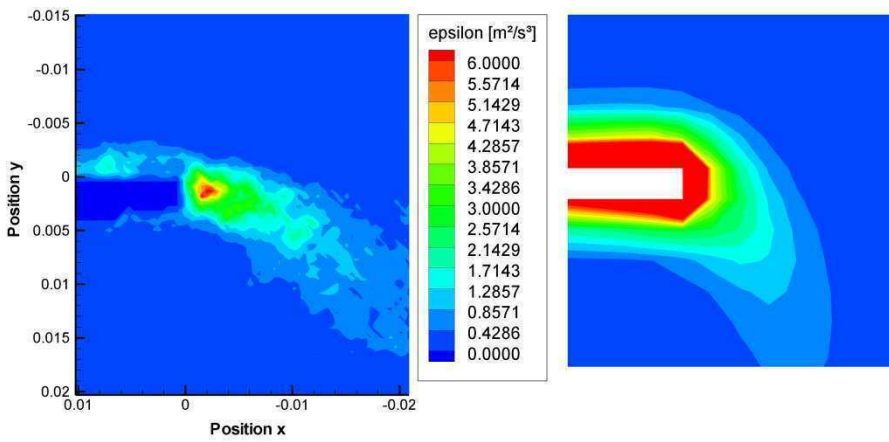


Fig. (21). Turbulent energy dissipation at 300 rpm, scaled energy dissipation in PIV (fit function), PIV 8x8 px² (left), Fluent (realizable k-epsilon) (right).

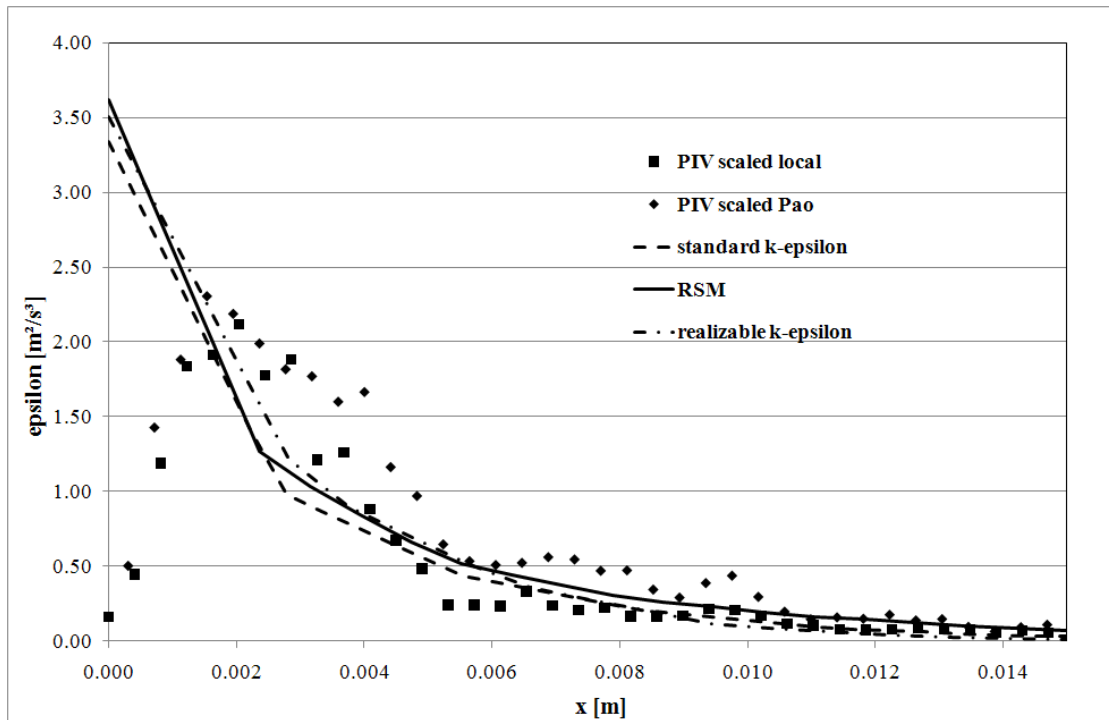


Fig. (22). Comparison turbulent energy dissipation at 200 rpm at the stirrer level, PIV 8x8 px² (scaled) and CFD, x coordinate distance from the stirrer to the wall.

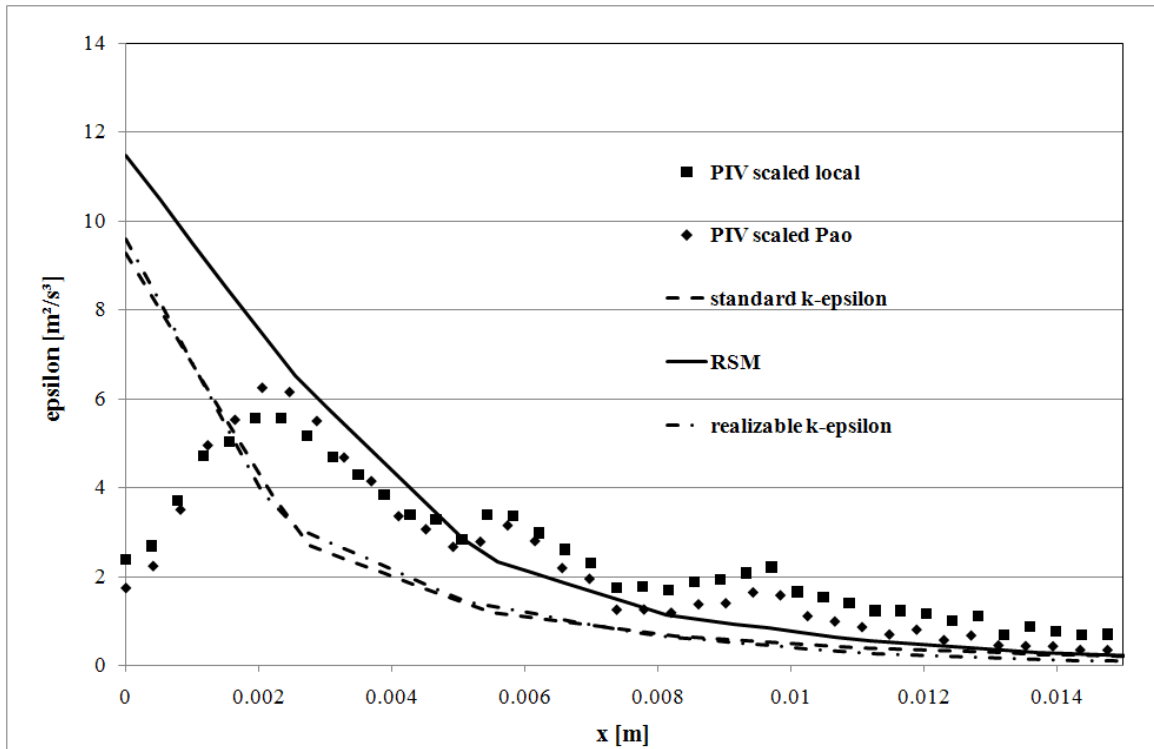


Fig. (23). Comparison turbulent energy dissipation at 300 rpm at the stirrer level, PIV 8x8 px² (scaled) and CFD, x coordinate distance from the stirrer to the wall.

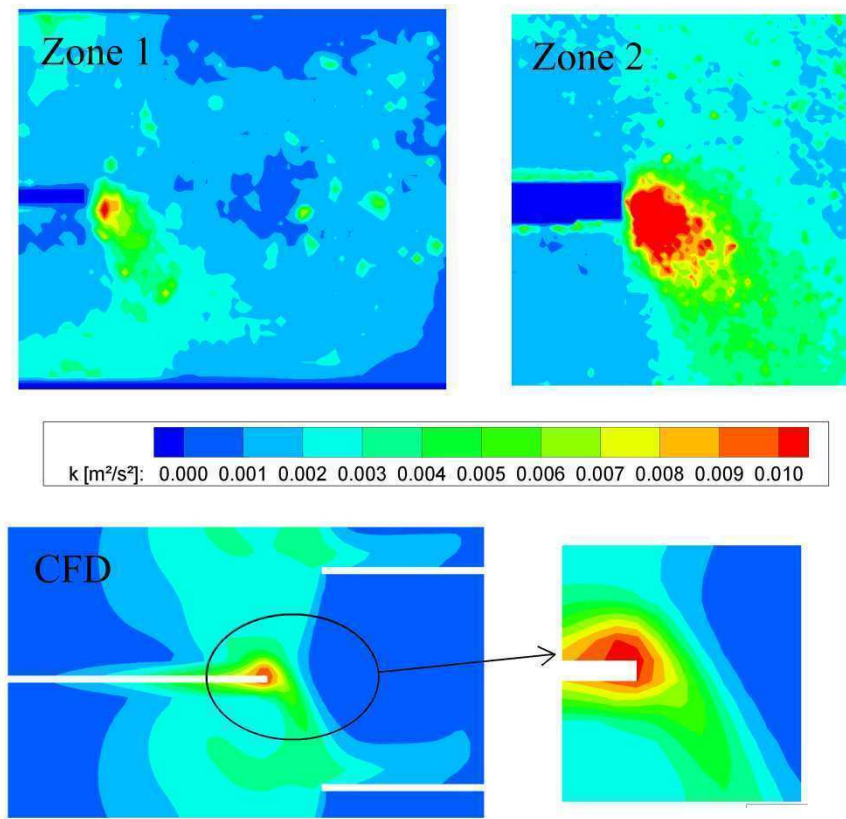


Fig. (24). Turbulent energy k at 100 rpm
 Top: PIV, 16x16 px² (left), 8x8 px² (right), Bottom: Fluent turbulent energy k, standard k-epsilon model.

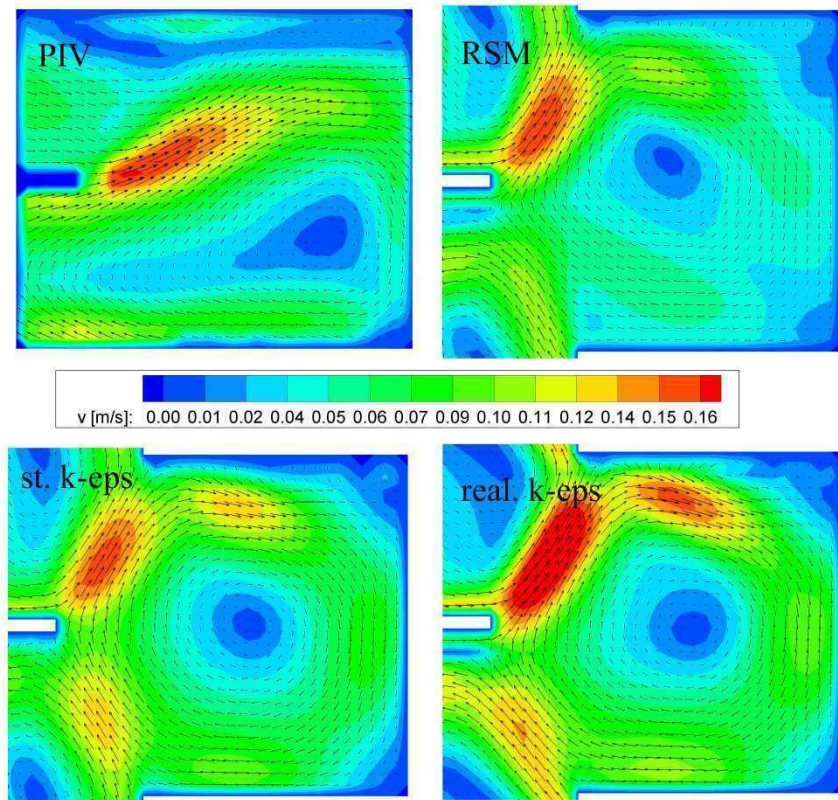


Fig. (25). Comparison PIV-CFD, two-phase average velocity magnitude and vectors in aqueous phase, zone 1, $n_{\text{stirrer}} = 100$ rpm.

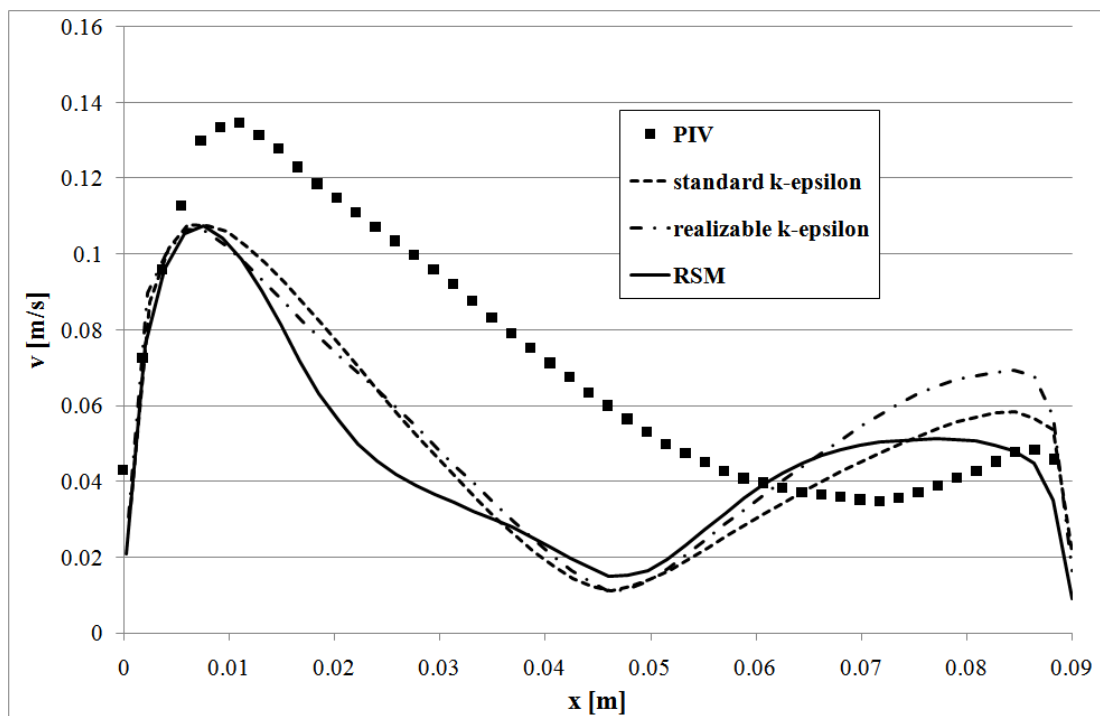


Fig. (26). Comparison PIV-CFD, two-phase measured and calculated average velocity magnitude in aqueous phase at stirrer level, zone 1, $n_{\text{stirrer}} = 100$ rpm.

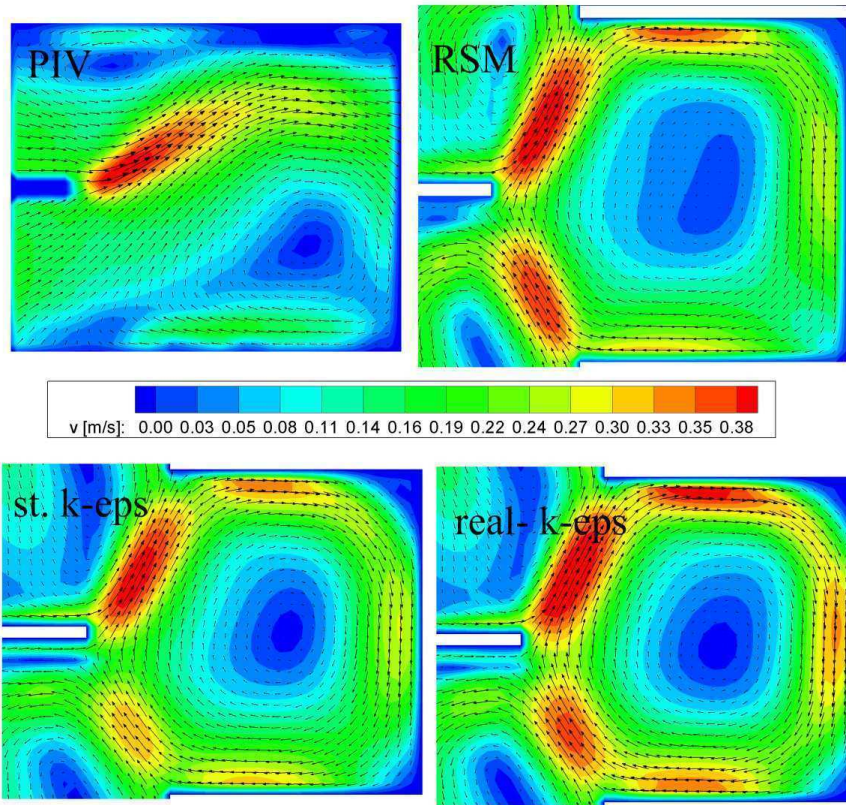


Fig. (27). Comparison PIV-CFD, two-phase average velocity magnitude and vectors in aqueous phase, zone 1, $n_{\text{stirrer}} = 300$ rpm.

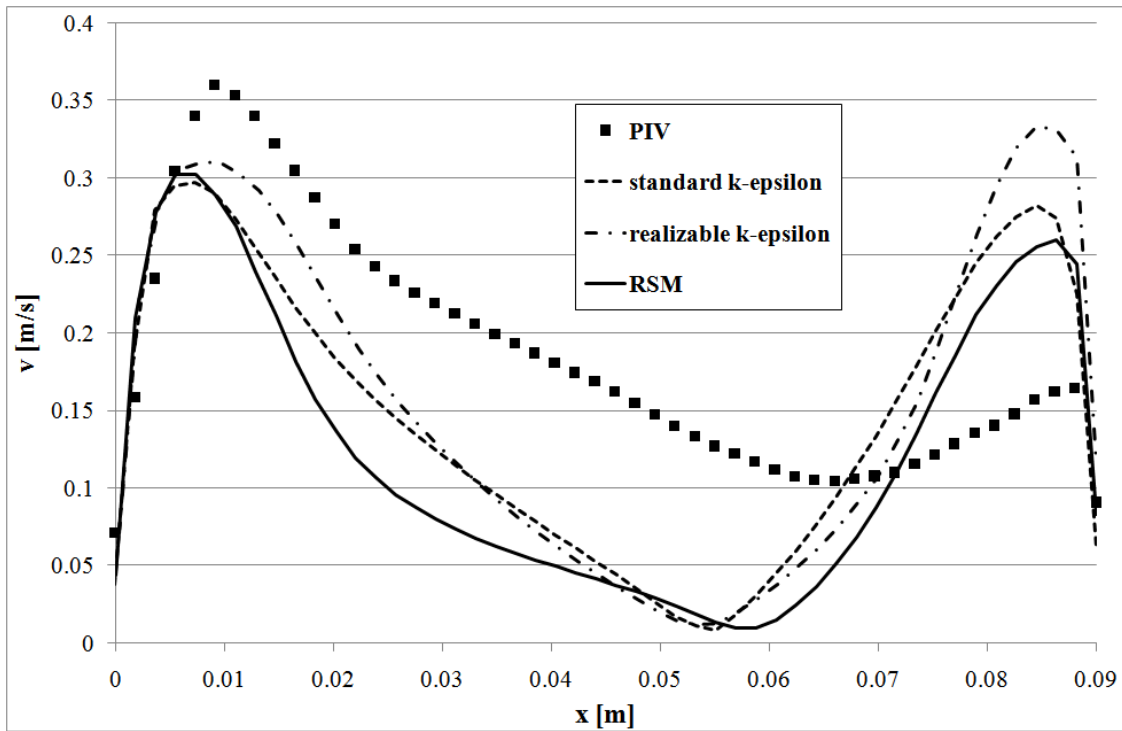


Fig. (28). Comparison PIV-CFD, two-phase measured and calculated average velocity magnitude in aqueous phase at stirrer level, zone 1, $n_{\text{stirrer}} = 300$ rpm.

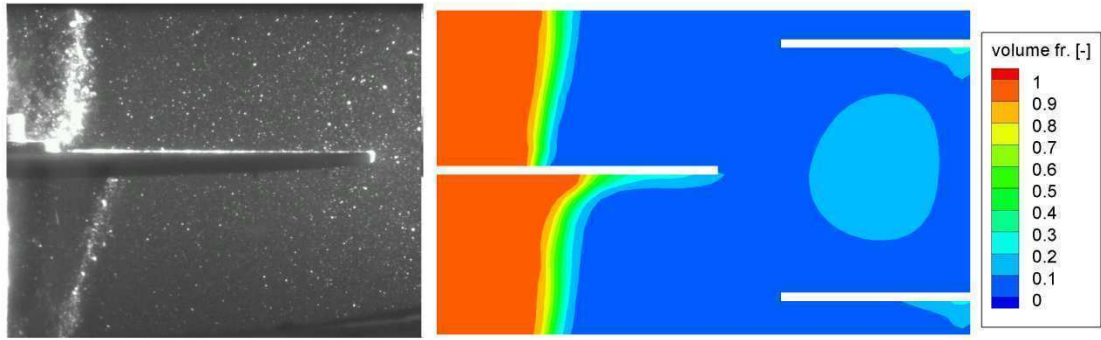


Fig. (29). Swirl near shaft at 300 rpm, PIV picture (left), CFD volume fraction dispersed phase (realizable k-epsilon) (right).

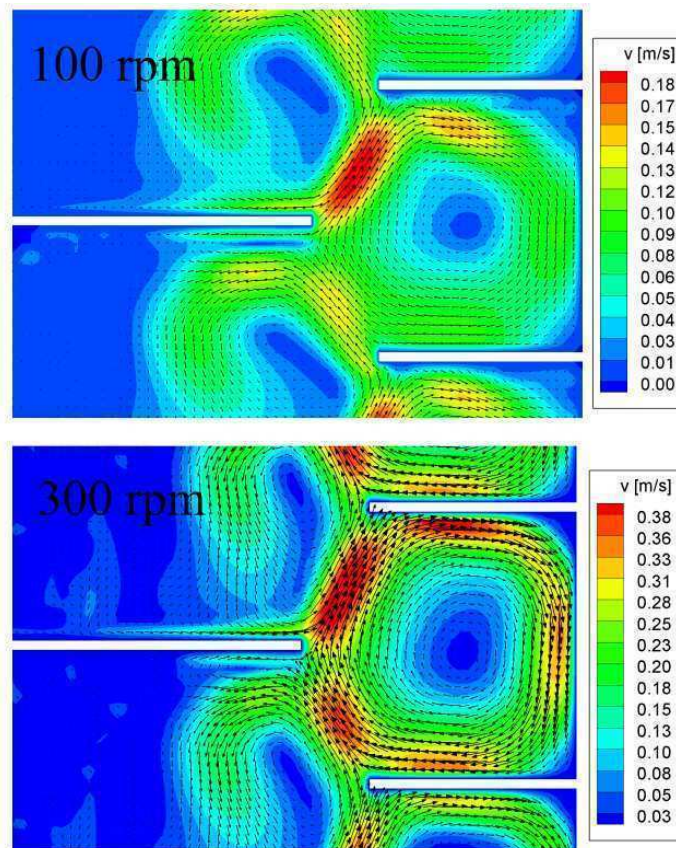


Fig. (30). Two-phase CFD simulation, average velocity magnitude and vectors in aqueous phase in compartment at 100 rpm and 300 rpm, realizable k-epsilon.

Publication XII

Reproduced in parts with permission from Industrial Engineering Chemistry Research , 49 (7), 3442-3451, **2010**. Copyright 2010 American Chemical Society

Christian Drumm, Menwer Attarakih, Mark W. Hlawitschka, Hans-Jörg Bart

One-Group Reduced Population Balance Model for CFD Simulation of a Pilot-Plant Extraction Column.

<http://dx.doi.org/10.1021/ie901411e>

A One-Group Reduced Population Balance Model for CFD Simulation of a pilot-plant extraction column

Christian Drumm^a, Menwer Attarakih^{a,b}, Mark W. Hlawitschka^a, Hans-Jörg Bart^a

^a *Lehrstuhl für Thermische Verfahrenstechnik, TU Kaiserslautern,
Center of Mathematical and Computational Modeling, TU Kaiserslautern,
P.O. Box 3049, 67653 Kaiserslautern, Germany*

^b *Al-Balqa Applied University, Faculty of Eng. Tech., Chem. Eng. Dept., P.O. Box: 15008,
11134-Amman, Jordan*

**Corresponding author: H.-J. Bart, +496312052414, bart@mv.uni-kl.de*

Abstract

In this work, a one-group reduced population balance model based on the One Primary and One Secondary Particle Method (OPOSPM) developed recently by Attarakih et al. [Attarakih, M.M.; Jaradat, M.; Drumm, C.; Bart, H.-J.; Tiwari, S.; Sharma, V.K.; Kuhnert, J.; Klar, A. Solution of the Population Balance Equation using the One Primary and One Secondary Particle Method (OPOSPM). In *Proc. ESCAPE 19*, Cracow, Poland, June 14-17, 2009; Jezowski J., Thullie, J., Eds.; 2009.] is implemented in the commercial Computational Fluid Dynamics (CFD) package FLUENT 6.3 for solving the population balance equation in a combined CFD-Population Balance Model (PBM). The one-group reduced population balance conserves the total number (N) and volume (α) concentrations of the population by solving directly two transport equations for N and α and provides a one-quadrature point for closing the unclosed integrals in the population balance equation. Unlike the published two-equation models, the present method offers accuracy improvement and internal consistency (with respect to the continuous population balance equation) by increasing the number of primary particles (sections). The one-group reduced population balance gives the possibility of a one equation model for the solution of the PBM in CFD based on the mathematically consistent d_{30} instead of the classical d_{32} mean droplet diameter. Droplet breakage and coalescence are considered in the PBM which is coupled to the fluid dynamics in order to describe real droplet behavior in a stirred liquid-liquid extraction column. As a case study, a full pilot plant extraction column of a Rotating Disc Contactor (RDC) type consisting of 50 compartments was simulated with the new model. The predicted results for the mean droplet diameter and the dispersed phase volume fraction (hold up) agree well with literature data. The results show that the new CFD-PBM model is very efficient from computational point of view (two times less than the QMOM and five times less than the method of classes). This is because the one-group reduced population balance requires the solution of only one equation (the total number concentration) when coupled to the CFD solver. It is therefore suitable for fast and efficient simulations of small scale devices and even large scale industrial processes.

Table 1. Dimensions of the RDC extraction column

1 : Column diameter [mm]	D_K	150
2 : Shaft Diameter [mm]	D_{shaft}	54
3 : Compartment height [mm]	H_C	30
4 : Height stirrer/stator [mm]	H_R	1
5 : Diameter stirrer [mm]	D_R	90
6 : Stator inner diameter [mm]	D_s	105

Table 2. Experimental and predicted mean droplet diameters at the top and bottom of the RDC column.

Stirrer speed [rpm]	250	300
$d_{30, \text{in}}$ [mm]	4.28	4.11
$d_{30, \text{out, exp}}$ [mm]	2.95	2.32
$d_{30, \text{out, sim}}$ [mm]	3.03	2.70
Holdup exp [%]	8	10.7
Holdup sim. [%]	7.4	8.6

Table 3. Comparison between the QMOM, CM and the present model (one-group reduced population balance model based on the OPOSPM) in terms of computational time.

Computational time	6 moments QMOM	30 classes CM	OPOSPM	without PBM
1 time step 25 iterations	64 s	160 s	34 s	32 s
4000 time steps at time step size 0.05 s	71 h	178 h	38 h	36 h

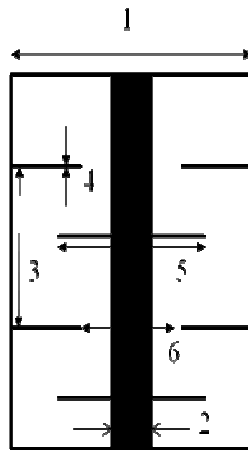


Figure 1. Sketch of a Rotating Disc Contactor compartment.

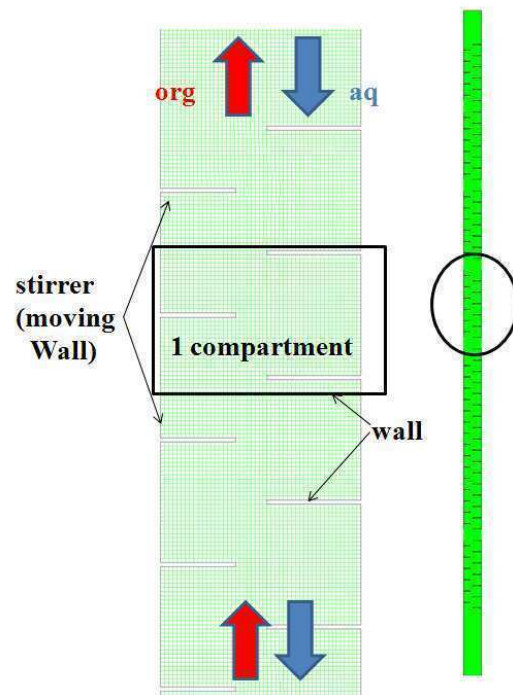


Figure 2. Details of the computational grid.

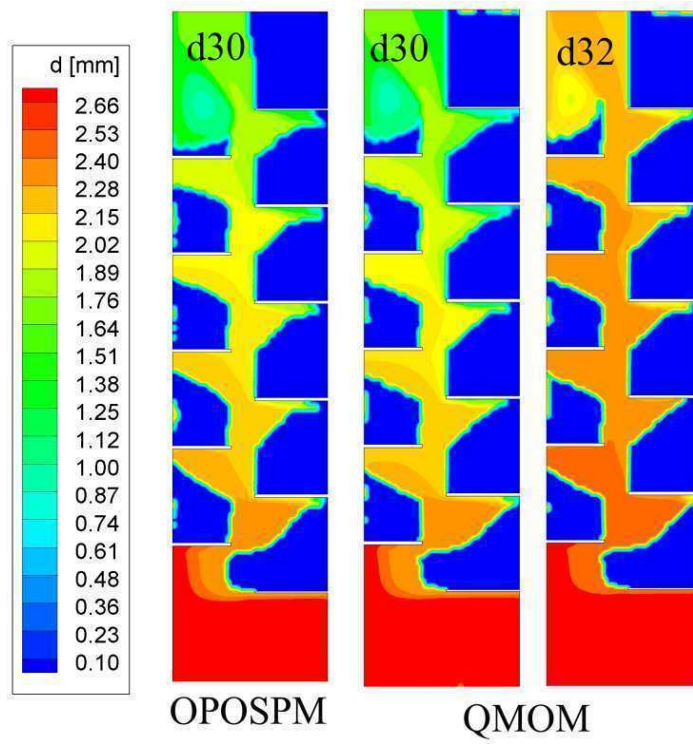


Figure 3. Test case: comparison OPOSPM (d_{30}) and QMOM (d_{30} & d_{32}).

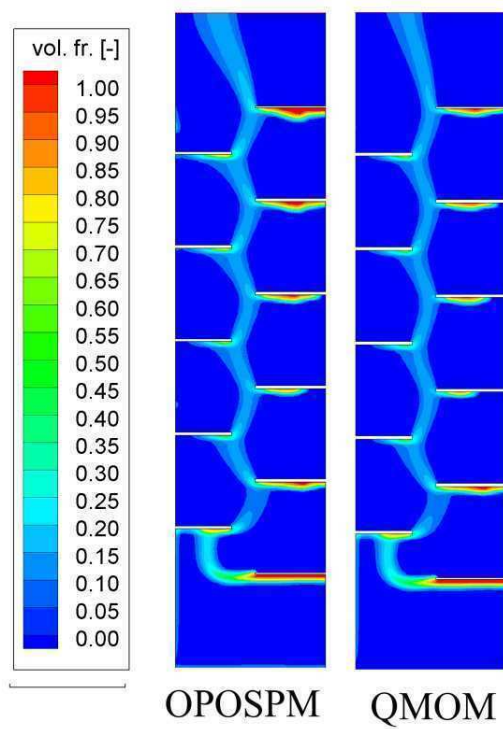


Figure 4. Test case: d_{30} vs d_{32} influences on the fluid dynamics.

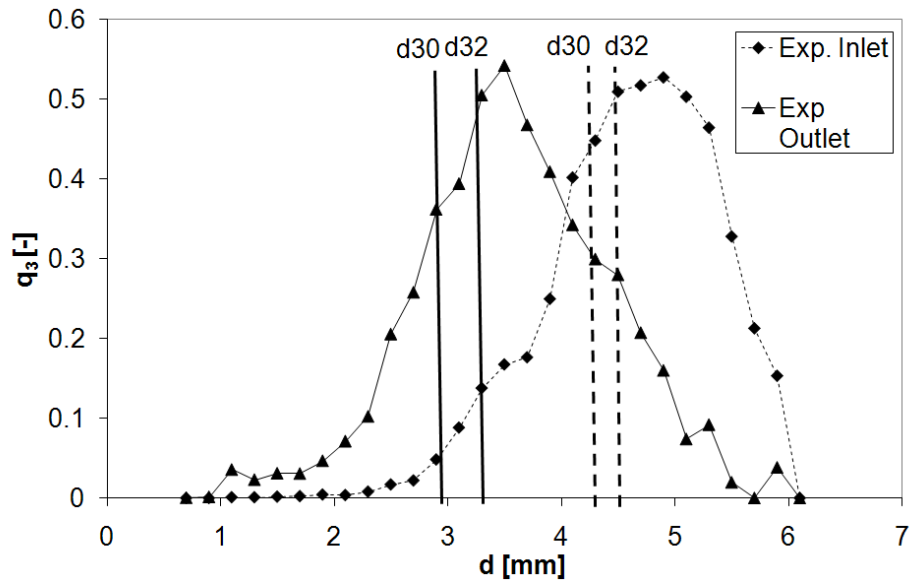


Figure 5. Inlet and Outlet drop size distributions and the calculated mean droplet diameters d_{30} and d_{32} at 250 rpm stirrer speed.

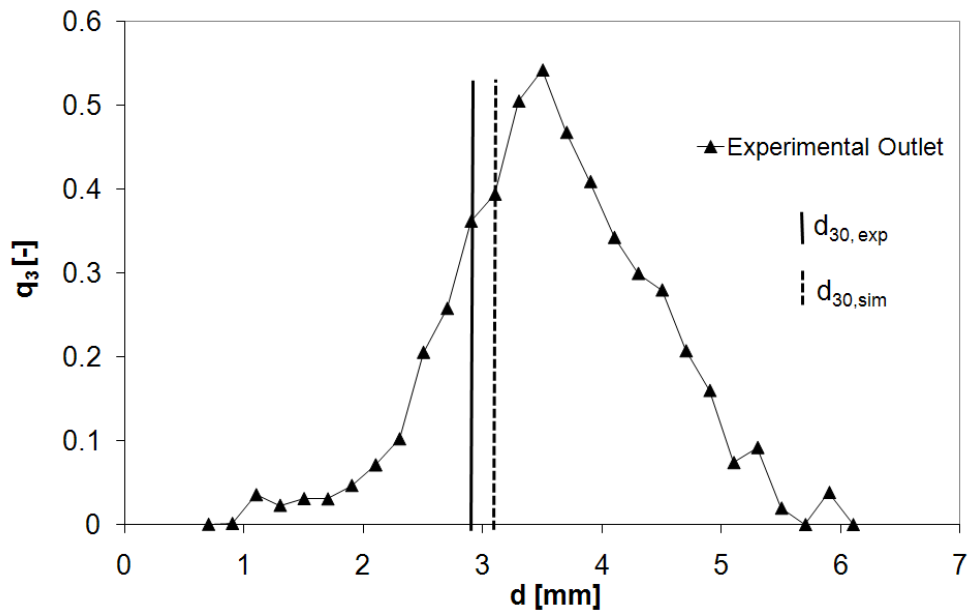


Figure 6. Comparison between predicted and experimental mean mass diameter (d_{30}) at the outlet at 250 rpm stirrer speed.

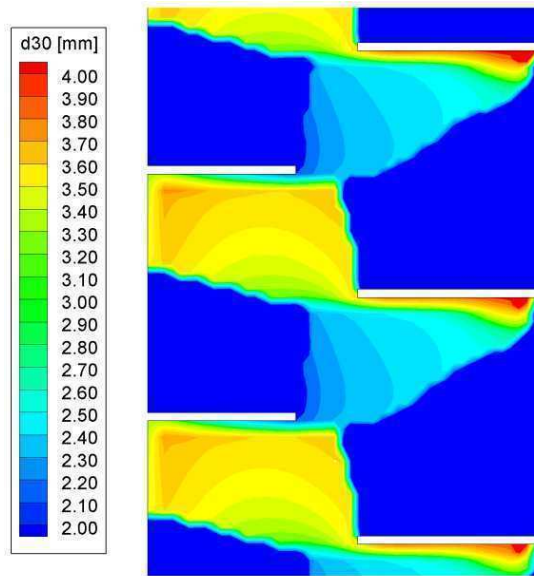


Figure 7. Contours of predicted mean mass droplet diameter d_{30} , inside one compartment at 250 rpm stirrer speed.

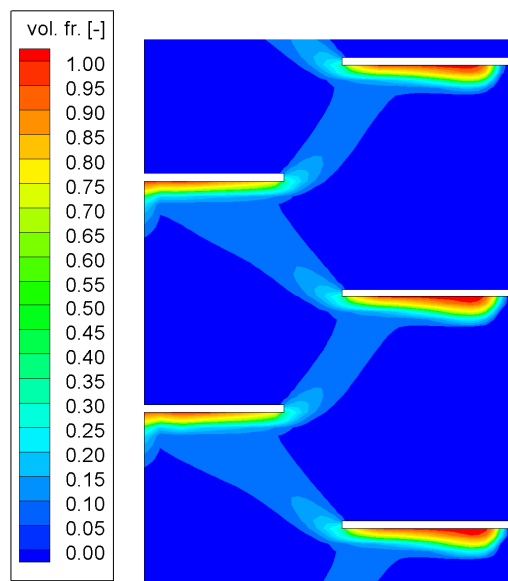


Figure 8. Contours of predicted dispersed phase volume fraction (hold-up) at 250 rpm stirrer speed.

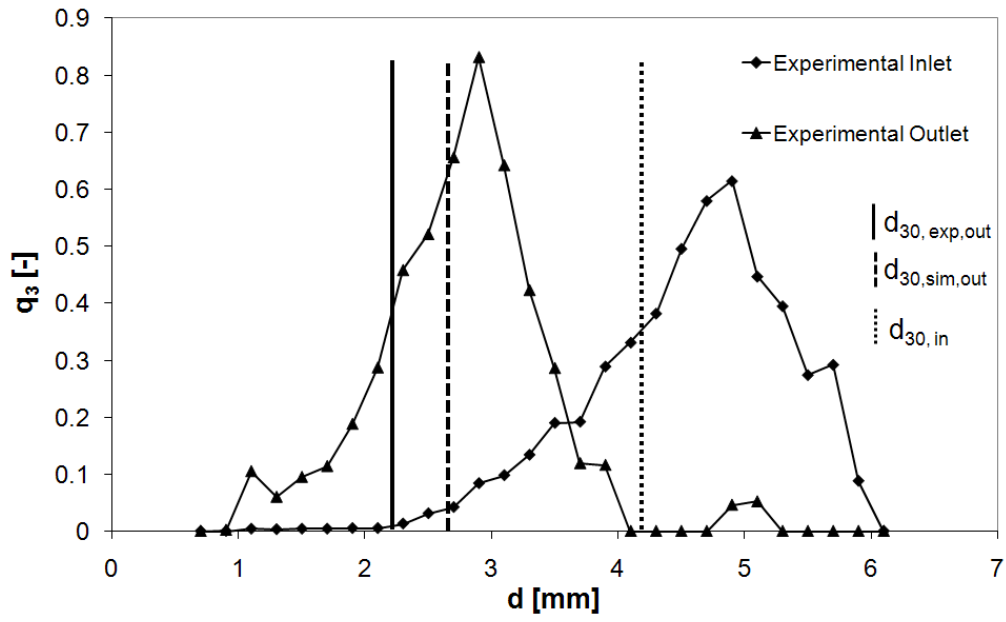


Figure 9. Comparison between predicted and experimental mean mass diameter (d_{30}) at 300 rpm stirrer speed.

Publication XIII

Reprinted from Proc. ESCAPE 19, Jezowski J., Thullie, J. (Eds.), Cracow, Poland, **2009**,
Attarakih, M. M., Jaradat. M., Drumm, C., Bart, H.-J., Tiwari, S., Sharma, V.K., Kuhnert, J.,
Klar, A.

**Solution of the Population Balance Equation using the One Primary and One Secondary
Particle Method (OPOSPM).**

Reprinted with permission from Elsevier.

Solution of the Population Balance Equation using the One Primary and One Secondary Particle Method (OPOSPM)

Menwer Attarakih^{a, b}, Moutasem Jaradat^b, Christian Drumm^b, Hans-Jörg Bart^b,
Sudarshan Tiwari^d, Vikash K. Sharma^c, Jörg Kuhnert^d and Axel Klar^c

^a Faculty of Eng. Tech., Chem. Eng. Dept., Al-Balqa Applied University, POB 15008,
11134 Amman, Jordan

^b Lehrstuhl f. Thermische Verfahrenstechnik, TU Kaiserslautern, POB 3049, 67653
Kaiserslautern, Germany

^c Fachbereich Mathematik, TU Kaiserslautern, POB 3049, 67653 Kaiserslautern,
Germany

^d Fraunhofer Institut Techno- und Wirtschaftsmathematik, Fraunhofer-Platz 1, 67663
Kaiserslautern, Germany

Abstract

A numerical framework is introduced for solving the population balance equation (PBE) based on conserving (selectively) the total number and volume concentrations of the population. The key idea in this work is to represent the distribution by a secondary particle capable of conserving two low-order moments of the distribution. The mean position of the particle is related algebraically to the total volume and number concentrations. In the framework of the SQMOM (Attarakih et al., 2008a) the secondary particle coincides exactly with the primary particle. The resulting discrete model for the PBE consist of two continuity equations for the total number and volume concentrations. These equations are found exact as those derived from the continuous PBE for many popular breakage, aggregation and growth functions. The accuracy of the method could be easily increased by increasing the number of primary particles if needed. The method could be considered as an efficient engineering tool for modeling physical and engineering problems having a discrete and multi-scale nature.

Keywords: population balance, sectional methods, OPOSPM.

1. Introduction

The population balance equation (PBE) proves to be the natural transport equation for modeling many discrete systems such as aerosols dynamics, crystallization, precipitation, liquid-liquid, gas-liquid and combustion processes. The resulting transport equations range from integro-differential to integro-partial differential equations with no general analytical solutions. Accordingly, there exist in the literature many numerical methods as attempts to solve certain type of the PBEs. These methods ranges from simple finite differences (FDS) or sectional methods using linear grids to Galerkin and orthogonal collocations methods on finite elements (Attarakih et al., 2008a). The quadrature method of moments (QMOM) (McGraw, 1997) developed to solve the PBE with pure growth is found very efficient from accuracy and computational cost point of view. Unlike the sectional (FDS) methods, the QMOM has a drawback of destroying the shape of the distribution by retaining information about it only through its moments. On the other hand, one limitation of the finite difference schemes is their inability to

predict accurately integral quantities (low-order moments as a special case) associated with populations of sharp shapes (Ramakrishna, 2000). A recent advance in the numerical methods for solving the PBE is the sectional quadrature method of moments (SQMOM), which combines the advantages of the finite difference schemes and the QMOM (Attarakih et al., 2008a). Despite the accuracy of the SQMOM it still has the disadvantage of direct and simple application to engineering problems where moderate accuracy and fast efficient solutions are needed. So, the objective of this work is to develop a discrete population balance model conserving the most important properties of the discrete system (the total number and volume concentrations) and yet retaining all the features of the PBE. The model should be extendable in such a way that its accuracy is increased as required and at the same time can reconstruct the shape of the distribution. This could be achieved by collapsing the whole population density to a one particle characterized by its mean position (along the particle size space) and its total number and volume concentrations. In terms of the SQMOM, the population is represented by only one primary and one secondary particles and hence the name of the method: the One Primary One Secondary Particle Method (OPOSPM). The method retains the simplicity in structure, ease of explanation and efficient in coding and analyzing multiphase flow problems without losing the essential information offered by the continuous PBE (Attarakih et al., 2008b).

2. The One Primary and One Secondary Particle Method

The spatially distributed population balance equation for a discrete system in which the individual particle property vector $\mathbf{x} = (x_1, x_2, \dots)$ defined in the n -dimensional property space is given by:

$$\frac{\partial f(\mathbf{x}, t)}{\partial t} + \nabla \cdot (\mathbf{u}f) + \nabla \cdot (\dot{\mathbf{x}}f) = S(f, t) \quad (1)$$

In the above equation $f(\mathbf{x}, t)$ is the density of the distribution of particles defined over some range W per unit volume of the physical space R at any given instant of time t ; $\dot{\mathbf{x}}$ is the rate of change of property \mathbf{x} ; \mathbf{u} the particle velocities along the spatial coordinates. The operator on the left hand side of Eq. (1) is a continuity operator and the source term on the right hand side accounts for the instantaneous creation and destruction of particles in this space. The form of this source term depends on the specific processes by which particles appear and disappear from the system (particle breakage, aggregation and growth). Generally S is an integral expression and is given in detail in Ramkrishna (2000). The general solution of Eq.(1) does not exist and hence numerical approximations are resorted to in general. In the finite difference or sectional methods the property of the particle ($x_i = d$) is discretized into finite number of sections, N_{pp} . The population in each section is considered to behave like a single particle, and hence it is concentrated at a representative sizes usually at the middle of each section. In the present framework of discretization, this single particle will be called the primary particle and it will be responsible for the distribution reconstruction. In this way, the greater the number of primary particles, the more accurate is the reconstruction of the distribution. Unfortunately, large number of primary particles is required to estimate accurately the integral quantities of the distribution. This increases extensively the computational loads when the population balance equation is coupled for example to a CFD calculations (Marchisio and Fox, 2005). The interaction between primary particles in different sections, due to breakage event for example, results in a new primary particle with no representative size due to the discrete approximation of the distribution.

Because of the newly-birthed particle could not conserve any of its low order moments but one (if it is located at the middle of the section), the rest of the low-order moments are predicted with low accuracy and hence the associated integral quantities. To overcome this fundamental problem of the sectional methods, secondary particles are generated in each section with positions (abscissas) $d_{30}^{<i>$, $i=1,2,\dots,N_{pp}$ (see Fig.(1)), where the number of these secondary particles dictates the desired number of low-order moments to be conserved. Actually, each secondary particle is capable of conserving only two integral quantities (two low-order moments).

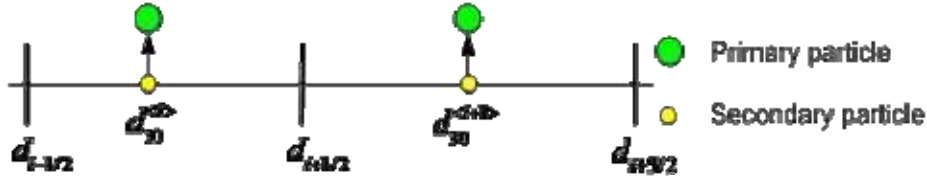


Fig.(1): The concept of primary and secondary particles.

Note that the primary and secondary particles coincide with each other in this case. So, the population density in each section is represented by a single particle whose position (size) is set according to the variation of the population density in this section and is given by:

$$d_{30,i} = \sqrt[3]{\frac{\pi \alpha_i}{6 N_i}} \quad (2)$$

Where N and α are the total number and volume concentrations of the population of real particles (assumed to have spherical shape) in the i th section. By assigning two distinct integral properties (N_i , α_i , $i=1, 2, \dots, N_{pp}$) to each particle, the secondary particles are exactly equivalent to a one-point Gauss-like quadrature according to the QMOM framework (McGraw,1997). Mathematically, this is equivalent to approximating the number density function $f(x_i=d,t)$ in each section by a Dirac delta function having weight N_i and centred at $d_{30,i}$:

$$f^{<i>(d,t) = N_i \delta(d - d_{30,i}) \quad (3)$$

By restricting the number of secondary particles to one, the transport equations for the integral quantities: N and α are obtained from Eq.(1) and (2) by first multiplying Eq.(1) by $(v^m, m=0,1)$ followed by the integration with respect to (d) from zero to infinity to get:

$$\frac{\partial N}{\partial t} + \nabla \cdot (\mathbf{u}N) = (\mathcal{G}(d_{30}) - 1)\Gamma(d_{30})N - \frac{1}{2}\omega(d_{30}, d_{30})N^2 \quad (4)$$

$$\frac{\partial \alpha}{\partial t} + \nabla \cdot (\mathbf{u}\alpha) = G(d_{30})N \quad (5)$$

Where Γ and ω are the breakage and aggregation frequencies respectively, ϑ is the average number of daughter particles produced during breakage and G is the particle velocity (growth rate) along the property coordinate ($x_1=d$) due to mass transfer. The two terms on the right hand side of Eq.(4) represent the net number of particle birth by breakage and loss by aggregation respectively. Note that the above transport equations for number and volume concentrations are coupled through the secondary particle size given by Eq.(2). So, the population balance equation (in one internal property) is now selectively represented by a couple of transport equations conserving both the total number and volume (mass) concentrations of the whole population. Despite the simplicity of these equations, they capture all the relevant features of the continuous population balance equation. The great advantage in this formulation is the disappearance of the convective terms along the particle property coordinates and hence eliminating the difficulties arising from numerical treatment of these terms (Ramkrishna, 2000). Hence, the OPOSPM could be viewed as an efficient tool for handling multiphase flow problems in complex geometries when using detailed CFD modelling and multidimensional PBE. Actually, the only transport equation needed in this coupling is the number continuity given by Eq.(4). This is because Eq.(5) is nothing more than the discrete phase continuity equation which is already built in the commercial CFD software. The OPOSPM is equivalent to taking one secondary and one primary particles using the (SQMOM) (Attarakih, 2008a).

Table 1: Analytical solution of the OPOSPM and the continuous PBE for popular breakage, aggregation frequencies and growth rates.

Case	The OPOSPM	The continuous PBE
Binary breakage in batch vessel: $\Gamma = K_b$	$N = N_0 e^{K_b t}$	$N = N_0 e^{K_b t}$
Binary breakage in batch vessel: $\Gamma = d^3$	$N = N_0 + \alpha_0 t$	$N = N_0 + \alpha_0 t$
Aggregation in batch vessel: $\omega = K_c$	$N = [N_0^{-1} + (0.5 K_c t)]^{-1}$	$N = [N_0^{-1} + (0.5 K_c t)]^{-1}$
Aggregation in batch vessel: $\omega = K_c(d^3 + d^{\beta})$	$N = N_0 e^{-\frac{t}{\tau_c}}, \quad \tau_c = \frac{1}{\alpha_0 K_c}$	$N = N_0 e^{-\frac{t}{\tau_c}}, \quad \tau_c = \frac{1}{\alpha_0 K_c}$
Aggregation in batch vessel: $\omega = K_c(d^3 \times d^{\beta})$	$N = N_0 - 0.5 K_c \alpha_0^2 t$	$N = N_0 - 0.5 K_c \alpha_0^2 t$
Growth in batch vessel: $G = K_g$	$N = \alpha_0 + K_g N_0 t$	$N = \alpha_0 + K_g N_0 t$
Growth in batch vessel: $G = K_g d^3$	$\alpha = \alpha_0 e^{K_g t}$	$\alpha = \alpha_0 e^{K_g t}$
Breakage and aggregation in batch vessel: $\Gamma = K_b$ and $\omega = K_c$	$N = 2(K_b / K_c)N_0 \times [N_0 + 2(K_b / K_c)e^{-K_b t} - N_0 e^{-K_b t}]^{-1}$	

3. Results and Discussion

The simple and compact mathematical form of Eqs.(2), (4) and (5) admits analytical solutions for many popular special cases of the breakage, aggregation and growth rate functions. Here we will restrict our treatment to the spatially homogeneous form of the above equations. Table 1 compares the analytical solution obtained from the OPOSPM (Eqs.(2), (4) and (5)) and that obtained from the continuous population balance equation. First, the analytical solution for the volume concentration (α) is always the same as that obtained from the continuous PBE. Second, the popular constant breakage, aggregation and growth rate functions result in analytical solutions as that obtained from the continuous PBE. Moreover, since the OPOSPM conserves exactly the third moment of the distribution, all the frequency functions for breakage, aggregation and growth rate (with cubic form in d) permit exact analytical solution for the total number concentration. This eases the parameter estimation through the inverse problems and makes the interpretation of the experimental data from the batch or continuous laboratory devices faster when compared to the full numerical solution of the PBE. Despite the low quadrature approximation used in the OPOSPM, it still provides very good approximations of the integral quantities up to the fourth moment of the distribution as shown in Fig.(1). In this figure, the OPOSPM is tested against the known normal distribution. The moments are approximated by: $\mu_r = N \times (d_{30})^r$ and are compared to an adaptive Gaussian quadrature. It is evident that this simple quadrature approximation produced very good results even for the case of fractional moments.

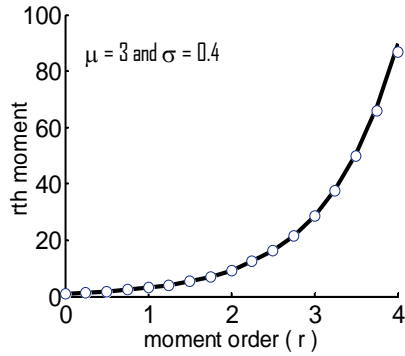


Fig.(1): The r th moment of the normal distribution predicted by the OPOSPM (open circles) and an adaptive Gaussian quadrature (solid line).

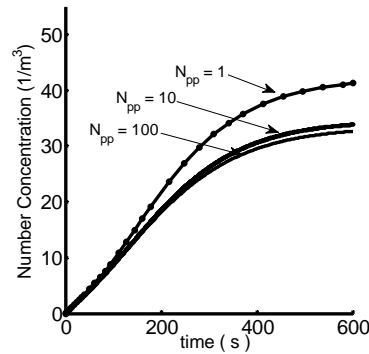


Fig.(2): The effect of increasing the number of primary particles on the total number concentration (N) using practical breakage frequency (Alopaeus et al., 2002) in continuous stirred tank.

Fig.(2) tests the OPOSPM using a rather complex breakage frequency function for liquid-liquid droplets in continuous stirred tank after Alopaeus et al. (2002). For this case the OPOSPM is extended to multi-primary particles in order to check its accuracy. It is clear that the predictions are very good below 200 s and start deviating from the reference solution (100 primary particles) after that. As mentioned above, the OPOSPM provides a compromise between ease of implementation, less computational time and the order of accuracy. Taking into account the error in the correlations for breakage and aggregation frequencies, it is meaningless to have a numerical solution with accuracy

less than that imposed by the physical experimental error. For the same case, Fig.(3) compares the OPOSPM prediction of the mean droplet diameter (d_{30}) to the reference solution. It is clear that the present model predicts well the mean droplet diameter over the whole simulation time. Finally, the extension of the OPOSPM to accommodate more primary particles for the purpose of distribution reconstruction is shown in Fig.(4). The convergence to the analytical solution (solid line) is clear by increasing the number of primary particles (N_{pp}).

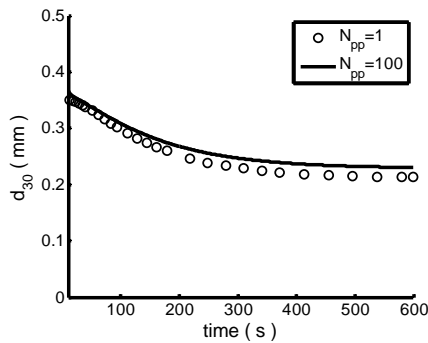


Fig.(3): The effect of increasing the number of primary particles on the droplet mean diameter (d_{30}) using practical breakage frequency (Alopaus et al., 2002) in continuous stirred tank.

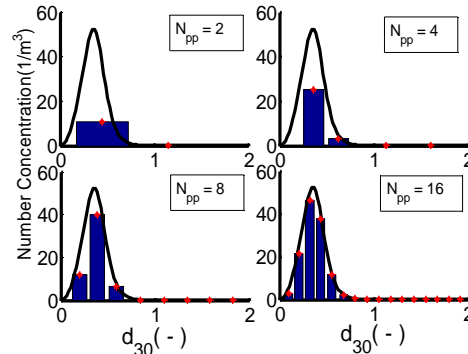


Fig.(4) Reconstruction of the distribution density by increasing the number of primary particles for the case of particle breakage in continuous stirred tank with $\Gamma = d^3$. The solid line is the analytical solution (Attarakih et al., 2004). The final simulation time is 600 units.

4. Conclusions

In this work, an efficient numerical method is derived based on the primary and secondary particle concept for the solution of the PBE. The method consists of two continuity equations for the number and volume concentrations coupled through the particle mean diameter. Despite the low quadrature approximation of the integral properties, the OPOSPM is exact for many popular breakage, aggregation and growth functions. This makes the inverse problems easier and the parameter estimation from the experimental data more robust. The accuracy of the method is easily controlled by increasing the number of primary particles, where a natural distribution reconstruction is then possible. As a final conclusion, the OPOSPM is an efficient and moderately accurate engineering model wherever the PBE is called for as a framework of modeling. In this regard, the method is already applied to the simulation of liquid-liquid extraction columns (Attarakih et al. 2008b).

References

- V. Alopaus, J. Koskinen, K. I. Keskinen, & J. Majander, *Chem. Eng. Sci.*, 57 (2002), 1815.
- M. M. Attarakih, C. Drumm, & H.-J. Bart, *Chem. Eng. Sci.* In press (2008a).
- M. M. Attarakih, M. Jaradat, C. Drumm, H.-J. Bart, S. Tiwari, V. K. Sharma, J. Kuhnert & A. Klar, To appear in ESCAPE19, 14-17-June (2008b), Cracow-Poland.
- M. M. Attarakih, H.-J. Bart, & N. M Faqir, *Chem. Eng. Sci.* 59 (2004), 2547.
- L. D. Marchisio. (2005). *J. Aerosol Sci.*, 36, 43-73.
- R. McGraw, *Aerosol Sci. & Tech.*, 27 (1997), 255.
- D. Ramkrishna. (2000). *Population Balances*, Academic Press, San Diego.

Curriculum Vitae

Diplom-Ingenieur
Christian Drumm



Personal Data

Date/Place of birth: 08/11/1978 in Neunkirchen
Nationality: German
Marital Status: Married, one child

Employment

12/2004 - 10/2009 Scientific Assistant, PhD Student
University Kaiserslautern
Lehrstuhl für Thermische Verfahrenstechnik,
Department of Separation Science and Technology (Prof. H.-J. Bart)

Studies

10/1999 - 11/2004 Process Engineering (Verfahrenstechnik)
University Kaiserslautern
Degree: Diplom, Master of Science.

School education & military service

07/1998 - 04/1999 Basic military service, Panzerartillerielehrbataillon 345, Kusel
07/1989 - 06/1998 Gymnasium Kusel, Degree: Abitur

Languages

German Mother tongue
English Very good in reading, writing and speaking
French Basic knowledges